Molecular emission in regions of star formation

Antoine Gusdorf

École doctorale d'Astronomie et d'Astrophysique d'Île de France

Molecular emission in regions of star formation

THESIS

submitted and publicly defended on November, the 28th, 2008

in fulfilment of the requirements for the

Doctorat de l'Université Paris Sud
Degree of Doctor of Philosophy, Durham University

by

Antoine Gusdorf

Composition du jury

Président :	Laurent Verstraete
Rapporteurs :	Cécilia Ceccarelli Peter Schilke
Examinateurs :	David Flower (co-directeur) Guillaume Pineau des Forêts (co-directeur) Martin Ward

Institut d'Astrophysique Spatiale ;
Centre Universitaire d'Orsay
AND
Atomic and Molecular Physics group ;
Physics Department, Durham University

Mis en page avec la classe thloria.

Remerciements

I sincerely thank David Flower for his patient and quiet supervision of this thesis. I am grateful to have been given the opportunity to learn science and all attached matters over these years. I am particularly glad I could observe his many talents through the years, among which his communication skills, wether written or oral, particularly impressed me. His ability to get to the point, as well as his composed behaviour under any circumstances were a model for me.

I also wish to thank Guillaume Pineau des Forêts, for the dashed intensity of his supervision of this thesis. Over these three years I could greatly benefit from his general vision of the Interstellar Medium processes, which constituted an excellent formation for the early stage researcher that I was. His analysis in his will to share his results with the scientific community were inspirational to me. I will always remember the sheer brilliance of his masters lectures, that contributed to shape my interest in Astrophysics.

I am obviously thankful to both of them to have trained me on the shock code they have been writing, updating, improving and refining for an amount of time that would be indecent to mention here. This process gave me a snapshot of what research should be, endlessly aiming at the most accurate way to understand the physical processes that govern the surrounding world. I also extend my thanks to them for having guided my first steps in the astrophysical world a few years back.

I also wish to thank Sylvie Cabrit, for the generosity of the numerous comments she forwarded me in an unmatched rigorous fashion, everytime I needed. I am aware that the unofficial position she had in this work was not always easy to take, and I am all the more greatful to her for her committment to help me in producing quality science. I am also willing to express my appreciation of her patience to inculcate her rational approach to numerical analysis in me, and to share some of her large observational knowledge with me.

Here is the time and place to also thank Stéphane Olivier, who gave me hope when the sky seemed to be falling over, and whose generous enthousiasm to share his understanding of Physics remains unmatched.

I am very attached to mention the ATMOL group in this thanks section, for having me felt so comfortable in the Durham University environment. Among them, I have a special thought for Steven Wrathmall, who might well be the most welcoming person I have had the chance to meet. His constant attention, assistance, and sympathy undoubtly eased my stay in England. Of particular importance was also Mark Bason, simply for the friendship we had over these three years. The discussions and football skills I shared with those two largely contributed to convert this working time in a nice human experience.

Mirrored thanks in France go to the IAS interstellar medium group, and particularly to those whose thesis accompanied mine through the years. It was always nice to find conversation partners in Mathieu Compiegnes, Nathalie Ysard, Pierre Guillard, Mathieu Vincendon, Manuel Gonzales and Nicolas Flagey. From the teaching point of view, I am very thankful to Laurent Verstraete and Herve Dole to have provided me with the opportunity to share my physical knowledge with the Paris XI University youngsters.

It is with great pleasure that I would like to pay my tribute to Europe, without which the position I had would never have existed. Working in a network environment was definitely

a nice experience. I was specially happy to meet and discuss with Marie Lise Dubernet and Jacques Le Bourlot on a regular basis, thanks to the various summerschools and conferences I was given the opportunity to attend. I was also delighted to share those moments with the colleague I met along the way, Alexandre Faure, Róisín Ní Chuimín, Odysseas Dionatos, Despina Panoglou, Petre Birza and Cristina Apetrei among others.

Of course, I thank my parents for the constant support they expressed through the years, and for the nice way they helped me becoming what I am now. I of course thank my brother and sisters, for the joy of our regular and relaxing encounters in France. I would also like to mention Laurent and Julien, for whom along with my brother, it seemed a matter of principle to celebrate each of my comeback in France with a party.

Last but not least, I am grateful to Marion, for the patience and courage she showed when the sky was not blue, and for the example she set in numerous circumstances.

Table des matières

Table des figures

Abstract

Keywords
magnetohydrodynamics – radiative transfer – shock waves
astrochemistry – atomic processes – molecular processes
stars : formation – circumstellar matter
Infrared : Interstellar medium
ISM : individual objects : L1157 – jets and outflows

Recent observations show that young stars being formed eject matter at several tens of kilometers per second, in the form of jets and outflows that impact the matter whose collapse is at the origin of the formation of the star. The supersonic impact between this jet and the parent interstellar cloud of the star generates a shock front, in the form of a bow-shock, which propagates in the collapsing interstellar gas, and also an inverse shock that propagates along the jet itself. The structure of these shocks depends on their velocity as well as on the physical properties of the gas in which they propagate. Numerical MagnetoHydroDynamical (MHD) simulations of the propagation of such shocks are a way to model the molecular emission arising from these regions, and thus to constrain the physical and chemical properties of the gas in which these molecular lines are emitted. A large grid of shock models is ran, for different values of key parameters such as the shock velocity, the pre-shock density, the magnetic field, ad the shock age. The emission of molecular hydrogen (whose treatment is included inside the shock code) is studied first. Pure rotational and rovibrational excitation diagrams are built for each model, and compared to the available observations of the bipolar outflow L1157. These comparisons confirm the necessity to use non stationary models to be able to interpret the observed column densities of H_2.

The emission of other characteristic molecules in the shocked region is then studied. The radiation transfer is computed thanks to a program based on the LVG (Large Velocity Gradient) approximation. In the case of SiO, comparisons with observed integrated intensities in L1157 are done, independently from the molecular hydrogen results, with a good agreement for stationary shock models and under diverse assumptions regarding the initial repartition of silicon in the dust grains, and oxygen in the gas phase. An attempt to simultaneous fitting of SiO and H_2 observational data is then done, that is their fit by a very same (non stationary) shock model, with encouraging results. To complete this study, CO emission is treated similarly as SiO, and studied over the whole models grid. CO is then added to the list of molecules whose production and emission can be modelled by the same shock model as H_2 and SiO with a satisfying agreement, even if this addition does not yield further constrain on the shock and medium properties.

Résumé

Des observations récentes montrent que les jeunes étoiles en cours de formation éjectent de la matière à des dizaines de kilomètres par seconde, sous la forme de jets et flots impactant le milieu ambiant dont l'effondrement est à l'origine de la formation stellaire. L'impact supersonique entre le jet et le nuage moléculaire parent de l'étoile génère un front de choc sous la forme d'un 'bow-shock' se propageant dans le gaz interstellaire, et qui s'accompagne d'un choc en retour qui se propage le long du jet. La structure de ces chocs dépend de leur vitesse ainsi que des propriétés physiques du gaz dans lequel ils se propagent. Les simulations numériques de type magnétohydrodynamique de propagation de tels chocs permettent de modéliser l'émission moléculaire en provenance de ces régions, et ainsi de contraindre les propriétés du gaz étudié. Une large grille de modèles de chocs est construite, pour différentes plages de valeurs de paramètres caractéristiques parmi lesquels la vitesse de choc, la densité préchoc, le champ magnétique, et l'âge des chocs. L'émission de la molécule de dihydrogène (dont le traitement est inclus dans le code de choc) est d'abord étudiée. Des diagrammes d'excitation (rotationnelle et rovibrationnelle) sont construits pour chaque modèle, et comparés aux observations disponibles pour le flot bipolaire L1157. Ces comparaisons confirment la nécessité d'un recours à des modèles de chocs non stationnaires pour interpréter les densités de colonne observées pour les niveaux de H_2.

L'émission d'autres molécules caractéristiques des régions de choc est ensuite etudiée. Le transfert de rayonnement de ces molécules est simulé à l'aide d'un programme numérique reposant sur l'approximation LVG (Large Velocity Gradient). Dans le cas de la molécule de SiO, des comparaisons avec les intensités integrées observées de la région L1157 sont effectuées indépendamment des résultats relatifs au dihydrogène, avec un bon accord pour des modèles de chocs stationnaires et sous diverses hypothèses de répartition initiale du silicium dans les grains de poussière, et de l'oxygène dans la phase gazeuse. La comparaison simultanée des observations SiO et H_2 est alors réalisée, c'est à dire leur ajustement par un même modèle de choc (non stationnaire), avec des résultats encourageants. Pour compléter cette étude, l'émission de CO est aussi traitée de façon similaire, et étudiée sur les modèles de l'ensemble de la grille. Le monoxyde de carbone est ajouté à la liste des molécules dont la production et l'émission peuvent être modélisées par le même choc que H_2 et SiO avec un accord satisfaisant, même si cet ajout ne génère pas de contrainte supplémentaire par rapport à ces deux molécules.

Modelling molecular outflows

1

Young stars and bipolar outflows

Ce chapitre constitue une introduction générale à la question des flots bipolaires et des jets. Il commence par une présentation sommaire du problème de la formation stellaire ainsi que par une description des premières étapes de la vie d'une étoile, introduction à mes yeux essentielle pour placer cette étude dans le contexte plus global du milieu interstellaire. Puis, les flots bipolaires et les jets, ainsi que leurs interactions avec le milieu environnant sont décrits. Enfin des éléments de modélisation sont fournis dans une dernière partie.

1.1 An introduction to star formation

Stars form from the gravitational collapse of prestellar condensations in molecular clouds, which consist of large, magnetized, and generally gravitationally bound structures, made of gas and dust. In this Section, we study the pre-existing conditions that rule the equilibrium of such structures and the processes that can generate their gravitational collapse, eventually leading to episodes of star formation.

1.1.1 Jeans Criterion

In this Section, we follow Lequeux et al. (2002) to establish the Virial's theorem that translates the equilibrium of self-graviting structures, and to derive the Jean's criterion that indicates whether such a system will collapse or not.

Simplest version of Virial's theorem. Virial's theorem is the fundamental theorem that accounts for the equilibrium of self-graviting structures in the Universe. Let us consider a system of particles whose mass is m_i, whose position is $\mathbf{r}_\mathrm{i}$ relatively to an arbitrary origin, and undergoing a force $\mathbf{F}_\mathrm{i}$. Its momentum of inertia is given by

$$I = \sum_i m_i \mathbf{r}_i^2, \tag{1.1}$$

whose time-derivate writes

$$\frac{d^2 I}{dt^2} = 2\sum_i m_i \mathbf{r}_i \frac{d^2 \mathbf{r}_i}{dt^2} + 2\sum_i m_i \left(\frac{dr_i}{dt}\right)^2, \tag{1.2}$$

leading to

$$\frac{1}{2}\frac{d^2I}{dt^2} = \sum_i m_i \left(\frac{dr_i}{dt}\right)^2 + \sum_i \mathbf{F}_i \cdot \mathbf{r}_i = 2T + \Omega \tag{1.3}$$

In this equation that governs the dynamical evolution of the system :

- T is the kinetic energy of the system, which equals the thermal energy for a system at rest. If the system is not at rest, other terms must be added relative to the macroscopic moves of the gas ;
- Ω is the system's potential energy.

The system's equilibrium condition hence writes : $2T + \Omega = 0$, which is the simple version of Virial's theorem, accounting for the compensation of the gravitational collapse by the particles macroscopic moves.

Jeans mass. For a spherical cloud homogeneously formed of perfect gas, isolated and without macroscopic moves, whose total mass is M :

$$T = T_{\text{thermal}} = \frac{3}{2}\frac{MkT}{\mu m_{\text{H}}}, \tag{1.4}$$

and

$$\Omega = -\frac{3}{5}\frac{GM^2}{R}. \tag{1.5}$$

Using these expressions and developing R in terms of the mass M and density n this form of Virial's theorem leads to an instability criterion, predicting a gravitational collapse for such a system if its mass exceeds a critical mass $M_{\text{crit,th}}$

$$M > M_{\text{crit,th}} = \left(\frac{1}{\mu m_{\text{H}}}\right)^2 \left(\frac{5}{2}\frac{kT}{G}\right)^{3/2} \left(\frac{4}{3}\pi n\right)^{-1/2} \tag{1.6}$$

Jeans length. For modeling purposes, it might be useful to express Jean's criterion in terms of a dispersion relation, as Jeans himself did for an isothermal infinite uniform medium without magnetic field nor macroscopic move, whose density is ρ. Three equations describe this system : the continuity equation, the movement equation, and Poisson equation, given by :

$$\frac{\partial \rho}{\partial t} + \nabla \cdot \rho \mathbf{v} = 0, \tag{1.7}$$

$$\rho\left(\frac{\partial \mathbf{v}}{\partial t} + \mathbf{v} \cdot \nabla \mathbf{v}\right) = -\nabla P - \rho \nabla \Phi, \tag{1.8}$$

$$\nabla^2 \Phi = 4\pi G \rho, \tag{1.9}$$

where Φ is the gravitational potential. The last equation is incorrect for an infinite medium because a uniform density would generate a diverging potential, but does not bear too delicate consequences, as we only consider a perturbation of the system. Using the index '0' for the equilibrium quantities and the index '1' for the perturbative ones, $v = v_1$, $\rho = \rho_0 + \rho_1$, $\Phi = \Phi_0 + \Phi_1$, we can linearize the above equations

$$\frac{\partial v_1}{\partial t} = -\nabla \Phi_1 - \frac{c_S^2}{\rho_0}\nabla \rho_1, \tag{1.10}$$

$$\frac{\partial \rho_1}{\partial t} = -\rho_0 (\nabla \cdot v_1) \tag{1.11}$$

$$\nabla^2 \Phi_1 = 4\pi G \rho_1, \tag{1.12}$$

under the extra assumption that $P/\rho = c_{\rm S}^2 = k_{\rm B} T_k/\mu$ is constant. The combination of these equations then leads to

$$\frac{\partial^2 \rho_1}{\partial t^2} = \rho_0 \nabla^2 \Phi_1 + c_{\rm S}^2 \nabla^2 \rho_1, \tag{1.13}$$

itself leading to the dispersion relation linking the pulsation ω and the wave number $k = 2\pi/\lambda$ for a given perturbation :

$$\omega^2 = k^2 c_{\rm S}^2 - 4\pi G \rho_0. \tag{1.14}$$

The unstable modes for which $\omega^2 < 0$ hence verify :

$$k < k_{\rm J} = \left(\frac{4\pi G \rho_0}{c_S^2} \right)^{1/2} \tag{1.15}$$

Jeans length is $\lambda_{\rm J} = 2\pi/k_{\rm J}$. Jeans mass is the corresponding mass comprised in a cube whose side length is $\lambda_{\rm J}$, and corresponds to the largest mass gravitationally stable in a medium with given density and temperatures. It is also similar to that given by Equation 1.6.

At a given temperature, Jeans mass decreases when the density increases. A collapsing, isothermal gas will then remain unstable as long as it cools sufficiently efficiently to remain isothermal. For a different state equation, $P \propto \rho^\gamma$, we get $M_J \propto \rho^{(3\gamma/2-2)}$. When $\gamma > 4/3$, Jeans mass increases with the density, and the collapsing mass can stabilize.

General expression of Virial's theorem without magnetic field. A more general expression can be obtained from the dynamical equations, here expressed in cartesian coordinates

$$\frac{\partial}{\partial t}(\rho v_j) + \frac{\partial}{\partial x_k} \left(\rho v_j v_k + P \delta_{jk} - \sigma_{jk} + \frac{B^2}{8\pi} \delta_{jk} - \frac{1}{4\pi} B_j B_k \right) = 0 \tag{1.16}$$

or under its vectorial form

$$\rho \frac{D\mathbf{v}}{Dt} = \rho \left(\frac{\partial \mathbf{v}}{\partial t} + \mathbf{v} \cdot \nabla \mathbf{v} \right) = -\nabla P - frac \nabla B^2 8\pi + \frac{1}{4\pi} \mathbf{B} \cdot \nabla \mathbf{B} - \rho \nabla \Phi, \tag{1.17}$$

where $\mathbf{v} = D\mathbf{r}/Dt$, ρ, P, B, and Φ respectively refer to the global velocity, density, pressure, magnetic field, and gravitational potential. $\mathbf{v}$ stands for the macroscopic velocity, the atomic microscopic velocity being accounted for by the pressure P. Multiplying this expression by $\mathbf{r}$ and integrating it over the cloud's volume V, we obtain the successive terms :

- the left hand side term becomes $\int_V \rho \mathbf{r} \cdot \frac{D\mathbf{v}}{Dt} dV = \frac{1}{2} \frac{D^2 I}{Dt^2} - 2T_{\rm macro}$. Indeed $D^2 I/Dt^2 = 2\int_V \rho \mathbf{r} \cdot (D\mathbf{v}/Dt) dV + 2\int_V \rho v^2 dV$, and $T_{\rm macro} = (1/2)\int_V \rho v^2 dV$ is the volumic kinetic energy associated to the macroscopic moves ;

- the thermal pressure term is $-\int_V \mathbf{r}\cdot\nabla P dv = 3\int_V P dV - \int_S P\mathbf{r}\cdot d\mathbf{S} = 3V(\bar{P}-P_{\rm ext})$. $\int_S$ is a surface integral and $\mathbf{S}$ is the vector perpendicular to the cloud's surface. The system is assumed to be in equilibrium with an external pressure P_{ext}, and $\bar{P}$ is the average pressure inside the cloud. In this expression, we used the following equality : $-\int_V \nabla\cdot(\mathbf{r}P)dV + \int_V P\nabla\cdot\mathbf{r}dV = -\int_S P\mathbf{r}\cdot d\mathbf{S} + 3\int_V PdV$, and the fact that $\int_S \mathbf{r}\cdot d\mathbf{S} = 4\pi V$ and $\nabla\cdot\mathbf{r} = 3$;
- similarly, the magnetic pressure gradient is $-(1/8)\int_V \mathbf{r}\cdot\nabla B^2 dV = -(1/8)\int_S B^2\mathbf{r}\cdot d\mathbf{S} + (3/8\pi)\int_V B^2 dV$;
- the magnetic tension term becomes $(1/4\pi)\int_V \mathbf{r}\cdot(\mathbf{B}\cdot\nabla)\mathbf{B}dV = -(1/4\pi)\int_V B^2 dV + (1/4\pi)\int_S(\mathbf{B}\cdot\mathbf{r})\mathbf{B}\cdot d\mathbf{S}$;
- finally $-\int_V \rho\mathbf{r}\cdot\nabla\Phi = \Omega$ is the gravitational potential energy.

The general form for Virial's theorem is then

$$\frac{1}{2}\frac{D^2I}{Dt^2} = 2T_{\rm macro}+\Omega-\int_S(P+P_{\rm mag})\mathbf{r}\cdot d\mathbf{S}+\frac{1}{4\pi}\int_S(\mathbf{B}\cdot\mathbf{r})\mathbf{B}\cdot d\mathbf{S}+3\int_V\left(P+\frac{P_{\rm mag}}{3}\right)dV, \quad (1.18)$$

with $P_{\rm mag} = B^2/8\pi$ and $P = nk_{\rm B}T_{\rm K}$ being the internal thermal pressure. $T_{\rm K}$ is the kinetic temperature.

The equilibrium then writes in the absence of magnetic field :

$$2T_{\rm macro} + \Omega + 3V(\bar{P} - P_{\rm ext}) = 0, \quad (1.19)$$

Virial's equilibrium stability.

1. cloudy sphere without external pressure nor magnetic field.
   In this simple case, the equilibrium writes : $2u + \Omega = 0$, where $u = T_{\rm macro} + (3/2)Mk_{\rm B}\bar{T_{\rm K}}$, where M is the total mass and $T_{\rm K}$ is the kinetic temperature. A radius perturbation of δR induces a variation of $\ddot{I}$:

   $$\frac{1}{2}\delta\ddot{I} = \left(2\frac{\partial u}{\partial R} + \frac{\partial\Omega}{\partial R}\right)\delta R \quad (1.20)$$

   and the stability is assured if $\ddot{I}\dot{I} < 0$, that is if $\ddot{I}\dot{R} < 0$ or $2\partial u/\partial R + \partial\Omega/\partial R < 0$. In a purely thermal system with a polytropic state equation, $u = (3/2)Mk\bar{T_{\rm K}} = 3PV$. The choice of the complementary hypothesis of a polytropic state equation $P \propto \rho^\gamma$, then leads to the influence of γ on the evolution of the system : the stability condition is only verified if $\gamma > 4/3$. In particular :
   - the isothermal virialized systems ($\gamma = 1$) are unstable when isolated and in absence of a magnetic field ;
   - the adiabatic systems ($\gamma = 5/3$) are stable.
2. cloudy isothermal sphere without macroscopic move nor magnetic field.
   In the case of an isothermal sphere without macroscopic moves nor magnetic field the Equation 1.19 becomes (combined with Equations 1.4 and 1.5)

   $$\frac{3}{2}\frac{MkT}{\mu m_{\rm H}} - \frac{3}{5}\frac{GM^2}{R} - 4\pi R^3 P_{\rm ext} = 0 \quad (1.21)$$

In this equation, if (M, T) are given, R depends on $P_{\rm ext}$. Particularly if R is large, internal and external pressure compensate. If $P_{\rm ext}$ increases, the radius decreases, and so does the gravitational term, further reducing the radius : the equilibrium is unstable towards an external pressure increase, possibly leading to the system's collapse.

1.1.2 From a dynamical to a magnetic star formation scenario

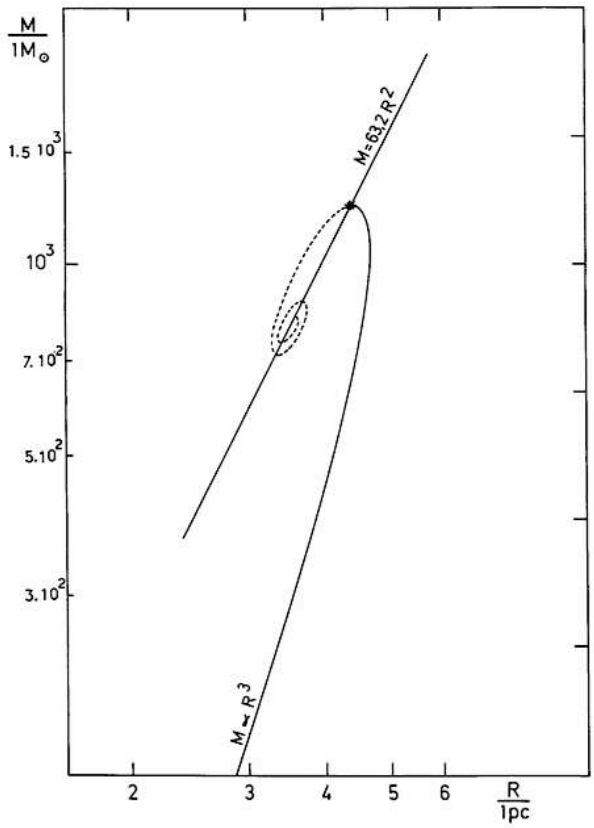

Figure 1.1 – Mass-radius relation for spherical, isothermal, non magnetized clouds in a constant external pressure $P_{\rm ext}/k = 3800$ K cm^{-3}. The critical point ($\star$) corresponds to the highest possible mass, and moves on the straight line of slope 2 with the temperature. It separates the gravitationally stable structures (solid line) from the unstable ones (dashed curve). Taken from Chieze (1987).

The dynamical theory. In this context, the gravitational stability of isothermal spheres with external pressure was the object of focus for the independent works of Bonnor (1956), Ebert (1957), who derived analytical solutions for self-gravitating, ideal gases, and the associated criterion for gravitational collapse. In such conditions of given $(P_{\rm ext}, T)$, Chieze

(1987) obtained a relation linking M and R, shown on Figure 1.1. Correcting the Equation 1.21 in the case of a non homogeneous spherical isothermal sphere in equilibrium, Chieze (1987) also derived the highest possible mass for the Virial's equilibrium

$$\frac{M_{\max}}{1M_{\odot}} = 12.6x_{\star}^{-2}\left(\frac{P_{\rm ext}/k}{3800\,{\rm K\,cm^{-3}}}\right)^{1/2}\left(\frac{R}{1\,pc}\right)^{2}, \qquad (1.22)$$

with $x_{\star} = 0.4466$ for an isothermal sphere, based on observational data for the mass and ardius of clouds and their condensations ($M/M_{\odot} \sim 100(R/1\,{\rm pc})^2$).

In the (M, R) plan, the Figure 1.1 shows the equilibrium state position of an isothermal sphere. The stable equilibrium configuration follows the solid line, whereas the dashed curve corresponds to the unstable ones. The star corresponds to the maximum mass beyond which no equilibrium configuration can be found. For a weaker temperature, with the same external pressure, the critical mass decreases and moves on the indicated straight line.

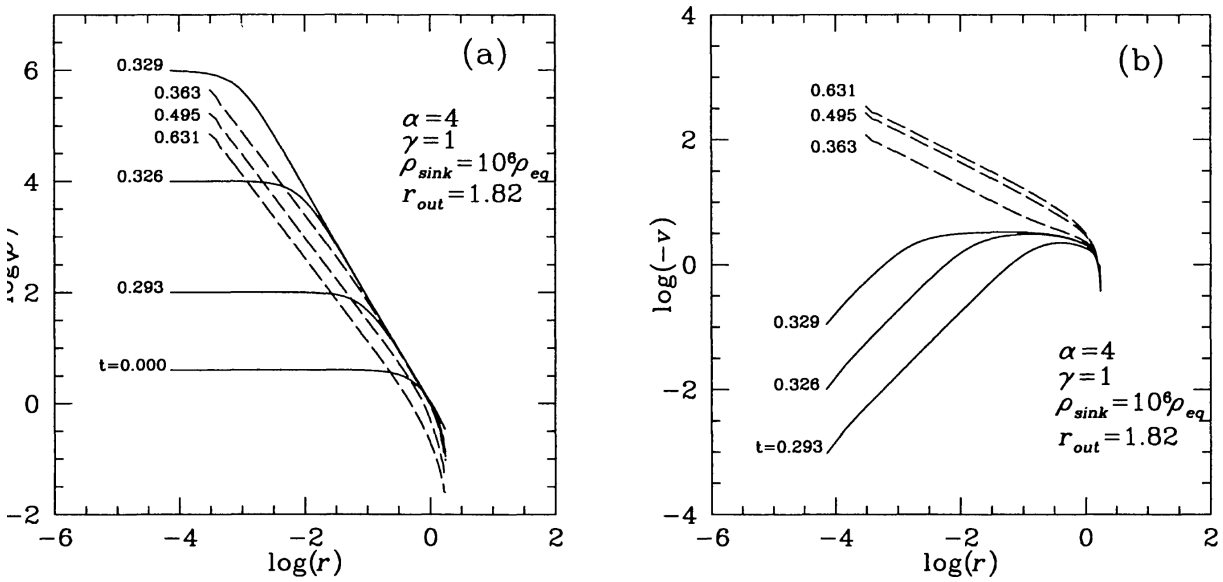

Figure 1.2 – Radial density (left) and infall velocity (right) profiles at various stages of the dynamical collapse. All quantities given in normalized units. The initial configuration is a critical isothermal Bonnor-Ebert sphere with outer radius $r_{\rm out} = 1.82$, four times more massive than allowed by hydrostatic equilibrium. The numbers on the left denote the evolutionary time. When density contrast reaches a value of 10^6, a 'sink' cell is created in the center. The profiles before the formation of the central star are indicated by solid lines, and for later times by dashed lines. Taken from Ogino et al. (1999).

Schmitz (1988), Schmitz (1987) extended these studies to include the effects of rotation in the case of generalized, polytropic equations of state, and recently Lombardi and Bertin (2001) derived the equilibrium condition without imposing any shape or symmetry to the cloud density distribution. Recent computational progresses also allowed for a numerical

hydrodynamical treatment of the gravitational collapse, such as that conducted by Ogino et al. (1999). An example of radial density and infall velocity profile is give on Figure 1.2 for various stages of the isothermal collapse phase. Initially, the gas sphere follows a Bonnor-Ebert critical density profile, but with four times more mass than allowed in an equilibrium state, it is gravitationally unstable and begins to collapse following a free-fall behavior ;

- the density in the outer part decreases, the contraction is retarded from free-fall, building up pressure gradients ;
- the density n the interior grows, and the collapse remains in approximate free-fall, actually speeding up (the free-fall time is given by $t_{\rm ff} = \sqrt(3\pi/32G\bar{\rho})$).

Density changes occur faster and faster on smaller and smaller inner regions, whereas nothing happens in the outer parts. The overall matter distribution is consequently centrally peaked, approaching $\rho \propto r^{-2}$, the density profile of an isothermal sphere. The final central singularity corresponds to the formation of a protostar that grows in mass by accreting the remaining envelope until its exhaustion.

The limits of the dynamical theory. This dynamical theory of gravitational collapse balanced by pressure and microturbulence does not take into account the conservation of angular momentum through the infall nor that of the magnetic field flux. Unfortunately for this theory, measurements of the interstellar magnetic field were made, leading to a typical strength estimate of 3 μG in the diffuse ISM (through Zeeman measurements-Troland and Heiles (1986), pulsar rotation or dispersion measures-Rand and Kulkarni (1989), Rand and Lyne (1994)). Measurements based on synchrotron emission (Davies and Shuter (1963)) or polarization (Chandrasekhar and Fermi (1953)) yielded higher values, but one should keep in mind that these values all depend on the equipartition assumption between magnetic field and other forms of energy (Beck (2001)). In molecular clouds, values ranging from ten to thousands of μG have recently been measured (Crutcher (1999)).

The presence of a magnetic field is of crucial importance for the dynamical theory of star formation. Indeed, under the simple assumption that the magnetic field quickly decreases outside of the cloud, the surface terms vanish in the Equation 1.16, for a considered surface located outside of that of the cloud. For a spherical cloud with a uniform magnetic field, the volume magnetic term becomes $(4\pi R^3/3)(B^2/8\pi)$, so that this equations turns in

$$\frac{3MkT}{\mu m_{\rm H}} - 4\pi R^3 P_{\rm ext} - \frac{1}{R}\left(\frac{3}{5}GM^2 - \frac{1}{3}R^4B^2\right) = 0 \tag{1.23}$$

As long as the ionization is sufficiently high for the field to be frozen to the matter, the flux through the cloud $\phi_{\rm B} = \pi R^2 B$ remains constant, and the opposition to collapse as driven by the magnetic energy remains constant during the collapse. If it cannot prevent this collapse at the beginning, it will not oppose to it as the field is compressed.

Equation 1.23 also shows that for a critical mass $M_{\rm c}$, the magnetic energy equals the gravitational one, with

$$M_{\rm c} = \frac{c_1}{\pi}\left(\frac{5}{9G}\right)^{1/2}\phi_{\rm B} = \frac{c_1^3 5^{3/2}}{48\pi^2}\frac{B^3}{G^{3/2}\rho^2}, \tag{1.24}$$

where c_1 is a corrective factor for the real structure of the cloud. A cloud is dubbed subcritical if magnetostatically stable, and supercritical if not. The very high critical mass yielded by the observed values of the magnetic field impedes the dynamical theory of star formation. Under the assumption that such large and massive structures could be assembled, how could they fragment into objects of stellar masses, when the critical mass remains invariant under spherical gravitational collapse ?

Two other objections contradict the dynamical scenario :

- the excessive rate of star formation it predicts, given that objects should collapse on free-fall timescales, that is orders of magnitude shorter than the ages of typical galaxies ;
- the excessive gap between the angular momentum of the initially idle molecular cloud rotating with the galaxy disk and the small one contained in stars. The dramatic density enhancement associated to the protostar formation should be accompanied by huge angular velocity driving drastically unphysical centrifugal forces. The discovery of bipolar outflows in 1980 unexpectedly and partly solved this paradox, but their existence could not be interpreted without arguments based on the presence of a magnetic field (see the following Sections).

Finally, the turbulence generated in a dynamical scenario does not fit the characteristics of that observed through superthermal linewidths indicating random moves at hypersonic velocities (Mac Low et al. (1998)).

Ambipolar diffusion. To address these problems of magnetic support against fragmentation, local density must be increased without also increasing the magnetic field, thus lowering the magnetic critical mass given by Equation 1.24. This can be done if mass could move across magnetic field lines, which can occur in mostly neutral gas through the process of ion-neutral drift, that is through ambipolar diffusion. We briefly present this effect here following Shu et al. (1987), in the equilibrium, steady-state case (more detailed developments can be found in Kulsrud and Pearce (1969)). This approximation is justified when the ionization is generated by cosmic rays, see for example Lequeux et al. (2002). In this context, the Lorentz force exerted on the charged particles fluid is

$$\frac{\mathbf{j}}{c} \times \mathbf{B} = \frac{1}{4\pi}(\nabla \times \mathbf{B}) \times \mathbf{B}, \tag{1.25}$$

where the current density is given by Ampere's law $\mathbf{j} = (c/4\pi)\nabla \times \mathbf{B}$. This force generates a relative drift between ions and neutrals with an average velocity that can be obtained by balancing it with the drag force (per unit volume), itself driven by the ion-neutral collisions :

$$\mathbf{F}_\mathrm{d} = \rho_\mathrm{i}\rho_\mathrm{n}\gamma(\mathbf{v}_\mathrm{i} - \mathbf{v}_\mathrm{n}), \tag{1.26}$$

where ρ_i, ρ_n, $\mathbf{v}_\mathrm{i}$, $\mathbf{v}_\mathrm{n}$ are the respective density and velocity of ions and neutrals, and γ is a drag coefficient associated to momentum exchange in ion-neutral collisions, with a weak dependence on their nature, and whose magnitude is about 10^{13} cm^{-3} g^{-1} s^{-1}. The drift velocity is consequently

$$\mathbf{v}_\mathrm{d} = \mathbf{v}_\mathrm{i} - \mathbf{v}_\mathrm{n} = \frac{1}{4\pi\gamma\rho_\mathrm{i}\rho_\mathrm{n}}(\nabla \times \mathbf{B}) \times \mathbf{B} \tag{1.27}$$

There is no need to account for the electrons here because their momentum exchange with neutrals is negligible compared to the ion-neutral one. The electrons also follow the ions in there general move, to maintain the charge equilibrium. The ions are coupled to the magnetic field, whose evolution is then given by

$$\frac{\partial \mathbf{B}}{\partial t} + \nabla \times (\mathbf{B} \times \mathbf{v}_\mathrm{i}) = 0, \tag{1.28}$$

whose combination with the previous one results in

$$\frac{\partial \mathbf{B}}{\partial t} + \nabla \times (\mathbf{B} \times \mathbf{v}_\mathrm{n}) = \nabla \times \left\{ \frac{\mathbf{B}}{4\pi\gamma\rho_\mathrm{i}\rho_\mathrm{n}} \times [\mathbf{B} \times (\nabla \times \mathbf{B})] \right\} \tag{1.29}$$

If the right hand side term was nul, corresponding to a high ionization degree, the magnetic field would be coupled to the neutrals move. The right hand side corresponds to the diffusion of the magnetic field in the neutrals fluid. If the magnetic field is uniform in the cloud, the characteristic timescale for ambipolar diffusion is hence given by

$$t_\mathrm{AD} = \frac{R}{v_\mathrm{d}} \simeq \frac{4\pi\alpha\rho_\mathrm{i}\rho_\mathrm{n}R^2}{B^2} \tag{1.30}$$

The first determinations of t_AD in dense molecular clouds through the measurements of the ionization degree yielded values of orders of 10^7 years, that is about 10-20 times longer than the corresponding free-fall time (McKee et al. (1993)). This waiting time for the ambipolar diffusion to occur and the long estimates of molecular clouds lifetimes at that time (30-100 Myr, see Solomon et al. (1987), Blitz and Shu (1980)) triggered the development of the magnetic star formation scenario, preferentially to the simple dynamical collapse.

The magnetic star formation scenario. Shu (1977) thus suggested that the self-similar collapse of initially quasi-static singular isothermal spheres was the most likely description of the star formation process. In his theory, owing to its longer timescale compared to the free-fall one, ambipolar diffusion is supposed to generate the contraction of a quasi-static density structure in an initially magnetically subcritical, isothermal cloud core. During the collapse, the magnetic field is assumed to be no longer important, and it is ignored in the original formulation of the theory. A rarefaction wave propagates outward at the speed of sound, while the cloud material behind it falls freely onto the core , and the matter ahead is at rest. The growth of the central protostar is supposed to end when feedback processes (like bipolar outflows or stellar winds for instance) become important and terminate the infall phase. The density structure predicted by this scenario is essentially indistinguishable from that of the dynamical collapse.

This original model was then extended through numerical analytical investigations, taking into account the effects of rotation, or to finally include those of the magnetic field during the collapse (see Mac Low and Klessen (2004) and references therein).

We expose here some basic elements of Lizano and Shu (1989) , based on the use of Equation 1.23. The collapse is possible if $M > M_\mathrm{c}$ and if the external pressure exceeds a critical value P_m. Fixing the mass M in the equation, its value is obtained by differentiating it with respect to P_ext and R, and writing $dP_\mathrm{ext}/dR = 0$, where R is expressed in function of M and M_c. Two configurations can then be distinguished :

- in the case of sub-critical magnetized clouds, the collapse can occur under the effect of an external pressure increase only if ambipolar diffusion evacuates the magnetic field, which happens in weakly ionized molecular clouds. This configuration is made possible if the mass of the cloud exceeds another critical mass, denoted 'umbral' by the authors. The collapse is slow, hence quasi-static. If the the magnetic pressure largely exceeds the thermal one, Jeans mass is much lower than that of the cloud, and fragmentation into dense cores takes over, possibly leading to low-mass star formation.
- super-critical clouds can globally collapse as a consequence of an external pressure increase (or an internal pressure decrease) : the magnetic field can not prevent the collapse even if its flux is conserved. These clouds can form through the merging of sub-critical ones. In this configuration, the cloud can not remain spherical during its contraction. Generally, there is a regular component of the magnetic field, along which the collapsing material slides and originates the build up of disk-like structure, enhancing the gravitational energy of the cloud, and impeding the effect of the magnetic field. Fragments are formed, of the size of the width of the disk, which themselves can be super-critical and collapse to generate high-mass stars clusters.

Another possibility is the formation of small super-critical cores inside a sub-critical contracting cloud, from small fragments of super-umbral mass. This scenario is better understood than the global super-critical collapse (see Galli and Shu (1993a), Galli and Shu (1993b)), and although its general picture does not sensibly differ from the dynamical scenario, it also predicts the formation of disk-like structures around the protostar, that could correspond to the observed accretion disks.

In spite of the problematic drawbacks of this theory (see next paragraph), the inclusion of strong magnetic fields provided a mechanism to evacuate the angular momentum in collapsing molecular clouds : the occurrence of magnetic braking (Mouschovias and Paleologou (1980)), that could contribute to resolve the angular momentum problem.

Drawbacks of the magnetic scenario. We summarize here the main drawbacks that appear to impede the validity of the magnetic star formation theory. Their emergence was made possible by the progress on both modeling (through the improvements of numerical simulations) and observing (owing to the advent of new observational techniques) fronts. Critical reviews can be found in Whitworth et al. (1996) and Nakano (1998).

1. The singular isothermal spheres hypothesis raises various questions :
   - Although a great number of star formations studied are based on it, the quasi-static, singular, isothermal sphere configuration seems to be the most difficult to realize in nature. Stable equilibrium is only possible if the internal to external density ratio is low, more centrally concentrated cloud only reaching unstable equilibrium states. All paths leading to the establishment of a central singularity are indeed unstable and would collapse before the occurrence of spherical density profile. Moreover, whatever the collapsing scenario, external perturbations tend to break the spherical symmetry and flatten the density profile at small radii ;
   - Star formation from such configurations results in formation of single stars, as the predicted massive disk-like structures resist subfragmentation processes. This

strongly contradicts the much observed nature of binary or higher-order systems (Mathieu et al. (2000), Whitworth et al. (1996)) ;
- High-resolution mapping of the density profiles of prestellar cores reveals flat inner density profiles, thus providing direct evidence against the singular isothermal spheres hypothesis.

2. Many paradoxes also seem to originate in the choice of the ambipolar diffusion as an essential element of the theory :
   - successive numerical studies conducted by Mouschovias and collaborators (see references list in Mac Low and Klessen (2004)) show that the decoupling between matter and magnetic field through ambipolar diffusion occurs over several orders of magnitude in density, showing no clear cut between coupled and de-coupled situation, as the magnetic star formation scenario would require ;
   - recent time-dependent models of chemical evolution and their comparison with observations indicate typical ages of 10^5 years for substructure in molecular clouds, much smaller than the ambipolar diffusion timescale (see van Dishoek et al. (1993), van Dishoeck and Blake (1998), Langer et al. (2000)) ;
   - the standard model assumes that cloud cores in the prestellar phase evolve on ambipolar diffusion timescales, much longer than that of the further accretion phase. This should lead to the observation of a great number of starless cores, whereas the observed fraction of protostellar cores with embedded objects is much larger in practice ;
   - in a scenario where individual cloud core contraction in the prestellar phase is determined by ambipolar diffusion, one would expect age spread in a newly formed group or cluster to considerably exceed the dynamical timescale. On the contrary, numerous observations of clusters show very short age spread, comparable to their dynamical timescale (see for example Hartmann (2001)).
3. A major concern with the dual star formation scenario has also emerged from recent magnetic field measurements in molecular clouds (Crutcher (1999), Bourke et al. (2001)). Although always subject to strong uncertainties, these measurements confirm the results presented in Nakano (1998) : no convincing magnetically subcritical core has ever been observed. Geometrical considerations have been thrown in (Shu et al. (1999)) to weaken this consideration, but they are themselves objected by observations (Ryden (1996), Jones et al. (2001)).
4. Another prediction of the magnetic scenario is the existence of a long lasting quasi-static phase in protostellar evolution while ambipolar diffusion acts, followed by the establishment of the central singularity accompanied by the propagation of a rarefaction wave beyond which the gas remains at rest. Prestellar cores formed this way should show no sign of infall motion, with collapse motions only occurring in the central region. Once again observations show that starless cores exhibit extended infall asymmetries (Lee et al. (2001b)) in contradiction with the inside-out collapse implied by the magnetic theory.
5. Finally the constant accretion rate with time or with respect to the mass of the collapsing fragment predicted by the magnetic theory is also contradicted by observations, that indicate accretion rate decreases with time and increases with the

total mass of the collapsing cloud fragment.

1.1.3 Towards a turbulent star formation theory

All these theoretical and observational shortcomings led various authors to experiment a new scenario, based on the use of the concept of interstellar turbulence, to interpret the star formation process and their observational consequences. Before presenting this new theory, we expose some basic elements on interstellar turbulence.

Evidence for interstellar turbulence. Turbulence can be defined as the gas flow resulting from random motions at many scales. Complete statistical characteristics can be found in Lesieur (1997). Most studies, among which the important contribution from Kolmogorov (1941) were originally orientated towards terrestrial applications, and hence dealing with incompressible turbulence in root-mean-square (rms) subsonic velocities environment at almost constant density. In this configuration, turbulence is initially driven on a large scale L, forming eddies at that scale, that progressively generate smaller eddies, also transferring energy to the smaller scales, all the way down to the dissipation scale $l_{\rm visc}$. At this scale, the energy distribution is determined by viscosity, while that of the top of the cascade (and above), which contains most of the energy, is determined by the driving. Structure functions $S_p(\vec{r}) = \langle\{v(\vec{x}) - v(\vec{x}+\vec{r})\}^p\rangle$ statistically describe the incompressible turbulent flow.

Observationally, the presence of interstellar turbulence was invoked to account for a series of observations related to the velocity dispersion of molecular clouds :

- optical observations of H II regions showed that the extended average of $S_2(\vec{r})$ was correlated with r^β, with β between 0.8 and 1 (Miville-Deschenes et al. (1995)) ;
- millimeter measurements of molecular rotational line widths were large than that predicted by purely thermal considerations ;
- remarkable scaling laws were stressed out between the non thermal part of the internal velocity dispersion and the structures sizes, and between their mass and their size, suggesting a fractal structure for the interstellar medium (see for example Mac Low and Klessen (2004) for a list of publications by Emelgreen and collaborators on the subject). In this case, one must be aware of the fact that the scaling laws point to turbulence, but can not be considered as evidence for it.

To a smaller extent, turbulence in the interstellar also generates scattering, hence influencing the interstellar chemistry (Xie et al. (1995)), and transient (times- and space-wise) strong vorticity gradients regions, hence affecting the gas heating (see Lequeux et al. (2002) for a general overview).

In the interstellar medium, gas flows differ from the idealized description mentioned above :

- it is highly compressible, and supersonic, with Mach numbers ranging from 1 to 50 ;
- the gas is described by a soft equation of state $P \propto \rho^\gamma$, with $0.4 < \gamma < 1.2$, depending on the temperature and density conditions ;
- the driving of turbulence is not uniform and occurs at various scales ;
- the interstellar medium is magnetized, as we have seen in previous Sections.

In addition to this, other processes add to the strong density inhomogeneities , as thermal phase transitions (Wolfire et al. (1995)) or gravitational collapse (Kim and Ostriker (2001)).

Theoretical treatment of interstellar turbulence. The theoretical treatment of interstellar turbulence is a complex subject, owing to the numerous hypothesis mentioned above. MacLow (2002) and Ballesteros-Paredes et al. (2005) provide comprehensive reviews of existing turbulence studies in various configurations, that lie beyond the scope of this introduction. However, we can mention that incompressible turbulence inclusion in the context of star formation results in the substitution of the sound speed in Equation 1.14 by a wavelength-dependent effective sound speed $c^2_{\rm s,eff} = c^2_{\rm s} + 1/3 v^2_{\rm rms}(k)$, where the added term depends on the turbulent power spectrum (Bonazzola et al. (1987)). This way, turbulence may be seen as an additional pressure, and the stability of the system both depends on the total amount of energy and its repartition. In the following, we'll also see that compressional effects can not be left aside when attempting to determine the outcome of star formation. In fact, because Jeans mass dependence on ρ and $c_{\rm s}$ is given by $M_{\rm J} \propto \rho^{-1/2} c^3_{\rm s}$, the above substitution leads to a dependence of the Jeans mass of the form $M_{\rm J} \propto v^3_{\rm rms}$. Compressible turbulence in an isothermal medium causes local density enhancements increasing the density by the square of the Mach number, $\propto v^2_{\rm rms}$, adding a dependence $1/v_{\rm rms}$, leading to $M_{\rm J} \propto v^2_{\rm rms}$ for $v_{\rm rms} \gg c_{\rm s}$, ultimately inhibiting collapse, but leaving room (especially for long driving wavelengths), for local collapse occurrence despite global support.

Origin of interstellar turbulence. The uses of interstellar turbulence to account for observations, or to build an efficient star formation scenario raise the crucial question of its driving mechanisms at different size scales (see the following paragraphs). We briefly present the various possibilities that are currently cited by authors to drive the turbulence, that is its possible energy inputs. This review is taken from the critical enumeration of Mac Low and Klessen (2004), that also includes the input rates estimates of these processes.

1. The shear from galactic rotation could be a source for interstellar turbulence, in a scenario where magnetorotational instabilities allow for it to couple from its large scales to the smaller ones ;
2. Gravitational instabilities could theoretically drive turbulence over two scales :
   - on a local scale, gravitational collapse and consequent motions could be a driving mechanism in molecular clouds. However, because the turbulence decay occurs in less than a free-fall time, it can not delay collapse for longer than a free-fall time ;
   - on a galactic scale, spiral structures can drive turbulence in gas disks, regardless of the presence of spiral arms, although in their absence, numerical works still need improvements in the way they model the stellar component and the treatment of collapse beneath the grid scale ;
3. Protostellar jets and winds are energetic events, but part of their energy is lost through radiative cooling at the wind termination shock, and most of it is deposited into low density gas. In addition to this, it is difficult to imagine how such located

events could generate the increasing power on the largest scale of cloud molecular complexes, as observed ;

4. Massive stars probably dominate the driving in active star-forming galaxies, through various processes :
   - stellar winds are only an efficient source of driving for the more massive (i.e. the most luminous) stars, but they still are important in the first few million years of the lifetime of an OB association ;
   - the ionizing radiation from OB stars can be important very close to young clusters, and it may even terminate the star formation locally. But because almost all of the energy in the ionizing radiation goes towards maintaining the ionization and temperature of the diffuse medium, it does not appear to significantly contribute to the driving of turbulence on a global scale ;
   - the combination of the significant number of their occurrence, their high energy inputs (independent of the star mass) and the associated efficiency of energy transfer towards interstellar gas, supernovae driving appears to be a powerful source of driving, thus providing a large-scale self-regulation mechanism for star formation.

The turbulent paradigm. The first question to address when building a new paradigm of star formation is that of the maintenance of the observed supersonic motions. Indeed, in both magnetized or unmagnetized conditions, supersonic turbulence is shown to decay in less than a free-fall time under molecular clouds conditions (Stone et al. (1998), Mac Low (1999)). In addition to this, contrary to what was primarily thought, recent numerical simulations indicate that magnetohydrodynamical waves do not provide the means to prevent the dissipation of interstellar turbulence. Simultaneously, observational evidence shows that clouds are a few free-fall times old on average, implying there might be continuing energy inputs into the clouds to maintain their turbulence. This continuous energy input could find its origin in the various processes listed above.

We present the most important points for the elaboration of a theory of star formation based on turbulence. These conclusions emerge from recent, three-dimensional, high-resolution numerical simulations of interstellar turbulence (see the list of articles of Klessen and collaborators enumerated in Mac Low and Klessen (2004)), in which a constant kinetic energy input rate is maintained to drive the turbulence, as a consequence of the above first point. The equation of state is isothermal, and to generate turbulent flows, Gaussian velocity fluctuations are introduced. All of these simulations show the importance of density fluctuations generated by highly compressible, self-gravitating turbulence to understanding support against gravity.

1. The turbulence generated by collapse fails to prevent further collapse. Although models of freely collapsing, magnetized gas remain to be done, the study of Balsara et al. (2001) of self-gravitating, decaying, magnetized turbulence indicates that the presence of magnetic field does not extend collapse timescales.
2. While turbulent support against gravitational collapse may act globally, it still allows for local collapse, that occurs when the turbulent velocity field carries enough energy to counterbalance gravitational collapse on global scales. Local collapse in

a globally stable cloud is not predicted by any analytical model. In simulations, though, supersonic flows that generate turbulence support also compress the gas in shocks, locally enhancing its density, and hence reducing its Jeans length. When the supersonic turbulence can support even these density enhancements, and in extreme conditions (a high enough rms velocity, and a small enough driving wavelength), supersonic turbulence can completely prevent collapse.

3. In a context of local collapse, the length scale and strength of energy injection into the system determines the structure of the turbulent flow, and therefore the locations at which stars are most likely formed. The general trends are the following :
   - the larger the scale of driving, the larger shock structures are generated, the more mass is swept up, the more massive are the generated density enhancements (making them more likely to exceed their Jeans mass), the more efficiently the star formation proceeds in these filaments and layers of shocked gas ;
   - the weaker the driving is, the weaker the passing shocks are, the less destructive towards already-formed clumps they will be, thus promoting their further possible collapse.
4. The duality of star formation is also accounted for in the frame of this theory, still according to numerical simulations :
   - large scale driving seems to generate star formation in clusters when the core mass fraction in the cloud is around 20 %, but these clusters are progressively swept up by further shock fronts, leaving room for an isolated way of star formation ;
   - finally freely-decaying turbulence models seem to consistently lead to clustered star formation, whatever the core mass fraction in the cloud.
5. The effects of magnetic fields have also been included in the theory. Indeed, magnetic fields have been suggested to support molecular clouds, thus preventing the collapse of unstable regions, either magnetostatically, or dynamically through MHD waves (Heitsch et al. (2001a), Heitsch et al. (2001b)). In the latter case, the effect of Alfven waves has been investigated, because they are transverse and not subject to damping. The global conclusion is that supersonic turbulence does not cause a magnetostatically supported region to collapse, and that reversely, MHD waves can not prevent collapse in the absence of magnetostatic support (although they can delay it).
6. The timescale predicted by the theory is of a few free-fall times, and is consistent with observations of molecular clouds age and stellar populations. The size scales on which self-similar properties can be observed range from the driving to the dissipation scales. The driving scale is about that of the galactic disk (see the previous paragraph about driving mechanisms), much above the size of the molecular clouds and in agreement with observations, whereas the dissipation length is not well established yet but might be determined by the ambipolar diffusion in typical molecular clouds with very low ionization fractions.
7. The final point of focus of the theory (Mac Low and Klessen (2004)) is the termination means of the star formation processes, that still remain unclear. Feedback from the stars themselves (through ionizing radiation, stellar winds or bipolar outflows) could heat and stir surrounding gas up to prevent further collapse and accretion.

The exhaustion of the reservoir of dense gas, and the action of the same kind of flows that created them are also suggested to interpret the termination of star formation in dense clouds.

Successes of the turbulent paradigm. The theoretical picture described above can successfully be applied to observations of individual star forming regions. We briefly review the agreements induced by the introduction of turbulence in star formation theory.

1. All star formation occur in molecular clouds, and it seems that every giant molecular clouds form stars. The great variety of star forming regions and associated paths of star formation appear to be controlled by the balance between self-gravity and the turbulent velocity field in the interstellar gas. The modes of star formation may not be physically distinct, but the range of qualitatively different behaviors appears over that of possible turbulent flows (see Mac Low and Klessen (2004) for a documented review).
2. The observations of molecular cloud cores, whether they contain a protostellar core or not, can be well compared with gas clumps resulting from numerical models of interstellar cloud turbulence. Again, Mac Low and Klessen (2004) points out the positive agreement in terms of geometry, density profiles, and various additional evidences such as stellar extinction, polarization maps, velocity structure or other statistical measures of structure and dynamics, making these models based on supersonic turbulence the most consistent with observational data.
3. The binary formation offers a serious modeling challenge, as it concerns about 50% of the field star population in the solar neighborhood, and at least the same fraction of pre-main sequence stars. Although it is a natural outcome of the dynamical star formation theory, it has been shown that the growth time of small perturbations in the isothermal phase is small compared to the collapse timescale itself. The formation of multiple stellar systems is hence the result of strong, external perturbations to the collapsing core, or of a subfragmentation that occurs at a later, non-isothermal phase of collapse (after the formation of a protostellar disk). The occurrence of strong external perturbations is natural in turbulent molecular clouds or when stars form in clusters. The quantitative inclusion of magnetic fields, of crucial importance for the development of close binaries through magnetic braking, remains to be done.
4. Stars almost never form in isolation, but instead in groups and clusters. In this context, the turbulence and turbulent fragmentation that prevail in the first place are modified by the inclusion of mutual dynamical interactions that become important because of the number density of protostars and protostellar cores in rich compact clusters. These effects have been studied by a variety of authors and are again listed in Mac Low and Klessen (2004).
5. The observations show that the accretion rate varies strongly over the course of the collapse. While a great number of analytical and numerical studies were aimed at isolated objects, numerical models based on the inclusion of turbulence were designed to investigate the effect of a cluster environment on protostellar mass

accretion rates (see the series of articles by Klessen cited above, Heitsch et al. (2001a) for the most recent ones), in general meeting a satisfying agreement level with the observations.

6. Regarding the question of the distribution of stellar masses at birth, various arguments are currently invoked to account for the shape of the initial mass function. Although none of them seems to be definitive (thus raising the question of the possibility of a deterministic theory for the IMF), the models of self-gravitating, isothermal, supersonic turbulence driven with different wavelengths present the advantage of offering qualitative insight into the processes acting to form the IMF (see Mac Low and Klessen (2004) and references therein for a review of these theories).
7. Beyond the problem of local star formation, Mac Low and Klessen (2004) also discuss the basic development of a unified picture, based on turbulence and cooling, to control the star formation rate and its implications in terms of star formation efficiency. In relation to this, a variety of applications that lie beyond the scope of this introduction are reviewed and approached in the frame of the supersonic turbulence control of star formation, including low surface brightness galaxies, galactic disks, globular clusters, galactic nuclei, primordial dwarfs, and starbust galaxies.

Open questions. In spite of all the observational agreements listed in the previous paragraph, the young theory of star formation based on supersonic turbulence still faces some challenges, that we briefly list here :

- a proper description of the turbulence driven by astrophysical processes remains to be done : on top of the scale, the driving scale still needs clarification in terms of variety and description, whereas at the other end of the cascade, the dissipation length still needs to be found ;
- the determination of the masses of individual stars, which is the result of a complex balance of initial reservoir size, but also accretion and competition or collision with other stars, is yet unclear. The feedback of the newly formed star itself has to be described and included in the models ;
- between the primary galactic value and the stellar one, the proper mechanisms of angular momentum loss or magnetic flux conservation still need to be dealt with, both at stellar scales, where stellar jets are a sign of existing coupling between angular momentum and magnetic flux, and at larger scales, as the observations show substantial lack of flux from the galactic value for example ;
- the hallmark of turbulent support is inefficient, isolated star formation, while efficient, clustered star formation occurs in its absence. In the latter case, it remains unknown how the final properties of the group or clusters depends on the initial turbulence, and how much depends on the properties of gravitationally collapsing gas. The influence of magnetic fields on these properties also remains unclear ;
- the role of turbulence against the competition of gravitational instability in determining the locations and properties of molecular clouds in star-forming galaxies is yet to be determined, as well as the apparent scatter of metallicities in stars of apparently equal ages ;
- the existence of a law linking gas column density to star formation rate also needs

an interpretation in the frame of a turbulent theory ;
- finally, the relative importance of turbulence, rotation, gravitational and thermal instability in the determination of star formation efficiency remain unsolved.

1.1.4 Main stages of early stellar history

Star formation episodes occur in molecular clouds, that can be of two kinds :
- giant molecular clouds such as Orion A tend to produce massive stars ($M \sim 10 - 25 M_\odot$). They are large (several tens of parsecs), massive ($M \sim 10^5 - 10^6 M_\odot$), with an average density of 10^2 cm^{-3}, and a kinetic density of 15-30 K (Blitz (1993), van Dishoek et al. (1993), Williams et al. (2000)) ;
- dark molecular clouds, like ρ Ophiuchi, are smaller (a few parsecs), lighter ($M \sim 10^4 - 10^4 M_\odot$) and colder (10-20 K) structures that only produce low-mass stars (Cernicharo (2001), van Dishoek et al. (1993)).

The formation of low-mass to intermediate-mass star formation (respectively $M \leq 2M_\odot, 2 \leq M \leq 8M_\odot$) can be divided in three stages, described in Andre (2000) :
- the prestellar stage, corresponding to the condensation of a cloud fragment ;
- the protostellar phase, when a star core appears inside the condensation and grows by accreting the surrounding collapsing matter ;
- the pre-main sequency stage, during which the young star contracts quasi-statically.

After that, the hydrogen fusion begins inside the star, which will stay on the main sequency as long as the nuclear reactions compensate the gravitation.

The prestellar phase. The prestellar phase begins with the fragmentation of a molecular cloud in a series of dense and gravitationally bound cores, in which the gravitation is compensated by thermal, magnetic, and turbulent pressure (Mouschovias and Morton (1991), Mouschovias (1991), Vázquez-Semadeni et al. (2000)). These peculiar objects can be seen through molecular tracers of dense gas such as NH_3 (Myers and Benson (1983), Benson and Myers (1989)) and in the dust millimeter and submillimeter continuum (Ward-Thompson et al. (1994), Ward-Thompson et al. (1999)). Their temperature is very low (10-13 K, Myers and Benson (1983), Andre (2000), Andre et al. (2000)), and is the result of the equilibrium between the grain heating by the external interstellar radiation field (Ward-Thompson et al. (2002)), the gas heating by the cosmic rays and the radiative cooling of the grains and gas (through its molecular transitions).

Ambipolar scattering (Shu et al. (1987), Mouschovias and Morton (1991), Mouschovias (1991)), turbulence dissipation (Nakano (1998), Williams et al. (2000)), and/or an external perturbation (Bonnell et al. (1997), Hennebelle and Pérault (2000)) then process these fragments, generating the loss of the magnetic or turbulent support or an external pressure increase. The fragment consequently becomes unstable, and its collapse begins, isothermally (Larson (1969)), or quasistatically (Shu (1977)).

When the central density reaches $n_{H_2} \sim 3 \times 10^{10}$ cm^{-3} (Larson (1969)), the internal region becomes opaque to the dust radiation and the evolution becomes adiabatic. The temperature rises, the collapse slows down. When the density attains 5×10^{12} cm^{-3} (Boss (1995), Bate (1998), Masunaga et al. (1998)), an hydrostatical equilibrium arises in the central region, that leads to the formation of a first protostellar core whose radius is about

$R \sim 5$ UA, and whose mass is $M \sim 0.01 M_\odot$. The collapsing matter increase its density and temperature. When the latter reaches 2000 K, molecular hydrogen dissociation arises, and generates the gravitational collapse of the first core, making room for a second protostellar core of stellar size ($1-3R_\odot$), and ending the prestellar phase (André et al. (2008)). At this stage, the stellar size core is surrounded by a protostellar envelope (possibly gravitationally collapsing).

The protostellar phase. The protostellar phase is the main accreting phase : the surrounding, collapsing matter is accreted by the protostar, whose mass consequently grows. Because the prestellar fragment has a non-zero angular momentum, as a consequence of the conservation of the initial kinetic momentum budget during the collapse (as soon as the surrounding magnetic field stops its braking action, Basu and Mouschovias (1994)), a centrifugal accretion disk forms on the protostar (Terebey et al. (1984), Stahler et al. (1994)). Observations have shown that this accretion phase is associated with powerful matter ejection episodes along the poles, thus evacuating a part of the collapsing envelope's kinetic momentum (Konigl and Pudritz (2000)) : this outflow activity is the central theme of the present study. It leads to the dispersion of the circumstellar material, and consequently to the change in the Spectral Energy Distribution (SED) of the Young Stellar Object (YSO).

Recent progresses in infrared and millimeter observing techniques have allowed for deeper probing of the molecular clouds and for a progressive empirical classification of the YSOs based on the value of their SED in the near- and middle-infrared range. Depending on the value of their infrared spectral index ($\alpha_{\rm IR} = dlog(\lambda F_\lambda)/dlog(\lambda)$), four classes (0, I, II, and III) were first distinguished (see Figure 1.3), of which only the class 0 and I technically belong to the protostellar phase.

Class 0 sources were historically the last ones to be identified, thanks to the progresses of the millimeter radioastronomy. Evidence of star formation activity (through the ejection of a bipolar outflow) was discovered by Andre et al. (1990a), Andre et al. (1990b) around the radiosource VLA 1623, that until then could not be seen in the infrared range, although associated to strong thermal dusty emission at 1.3 mm. This observation led Andre et al. (1993) to define the Class 0 sources as the youngest protostars in the main accretion phase, based on the following observing criteria :

- existence of a stellar core through the detection of a compact source in the centimeter continuum, matter ejection in a bipolar outflow or internal heating source, unlike prestellar condensations ;
- presence of a circumstellar envelope observed through a spatially extended and centrally narrow millimeter continuum, unlike more evolved classes ;
- important fraction ($\gg 0.5\%$) of the bolometric luminosity emitted in the sub-millimeter range, suggesting a greater mass envelope than that of the star, and often corresponding to a cold SED, unlike more evolved stages.

Being still deeply embedded in their envelope, Class 0 sources remain invisible in infrared, and their SED peaks in the sub-millimeter domain. Their maximum age is around 3×10^4 years, although this age could vary with the considered molecular cloud (André et al. (2001)), and hence are of crucial interest to study the initial conditions of the gravitational

collapse.

Class I sources have $\alpha_{\rm IR} > 0$ and SEDs broader than single blackbody functions, resulting from the warm (300-1000 K) dusty emission from the disk or envelope around the hot (3000-5000 K) stellar-like object. They are the youngest objects to be seen in the near infrared at 2 μm, and are typically $1-2\times10^5$ years (Greene et al. (1994), Kenyon and Hartmann (1995)). At this stage, the stellar mass exceeds that of the thinner envelope, and the protostar is surrounded by an accretion disk and associated to a bipolar outflow. A typical example is L1551(see for example Davis et al. (1995)).

The pre-main sequency phase. After the end of the main accretion phase, deuterium burning has begun in the central stellar object (at a temperature of $\sim 10^6$ K), that has almost accreted its final mass. It slides on the birthline (Stahler (1988), Palla and Stahler (2002)), and can be seen in the optical (or infrared if obscured by the molecular cloud) region. During this phase, the star undergoes a quasi-statical contraction over the Kelvin-Helmoltz time ($t_{\rm KH} = GM_\star^2/R_\star L_\star \sim 10^7$ years), much greater than the protostellar one (free-fall time $\sim 10^5$ years). Beyond a temperature of 10^7 K, hydrogen fusion proceeds, and the star reaches the main sequency.

Class II sources are the youngest ones in this phase. They have $-1.5 < \alpha_{\rm IR} < 0$ and SEDs broader than a single temperature blackbody. They are optically visible and show spectra similar to those of cool photospheres. They are surrounded by a (possibly protoplanetar) disk that generates an infrared excess (optically thick) in their SED, and are no longer associated to circumstellar envelopes. They correspond to Classical T Tauri Stars (CTTS), and are 10^6 years old. The youngest ones exhibit faint radio jets and molecular outflows. Recent and careful observations have also revealed the presence of microjets around 30% of the studied T Tauri stars (see the following Section).

Class III sources are more evolved (10^7 years) and are characterized by $\alpha_{\rm IR} < -1.5$. Their SEDs are similar to those of single blackbodies, are visible, and do not show large infrared excess. Their scattered disk is likely to contain planets, and are not surrounded by circumstellar envelopes. No sign of outflow activity can be seen around these objects, also called Weak-line T Tauri Stars (WTTS).

All these characteristics are summarized on Figure 1.3. On this Figure, the bolometric temperature $T_{\rm bol}$ is the temperature of a blackbody having the same mean frequency as the observed SED. This parameter was introduced by Myers and Ladd (1993) and monotonically increases from Class 0 objects to classes I, II, III corresponding to the SED evolution.

1.2 Outflows, Jets and Herbig Haro objects

We here introduce the general phenomenon of bipolar outflows in its broad acceptance. Outflow activity is one of the first manifestations of the formation of a star. Such outflows emerge bipolarly from young stellar objects from Class 0 and Class I, and marginally from Class II stellar objects (see the previous Section), involving similar amounts of energy to

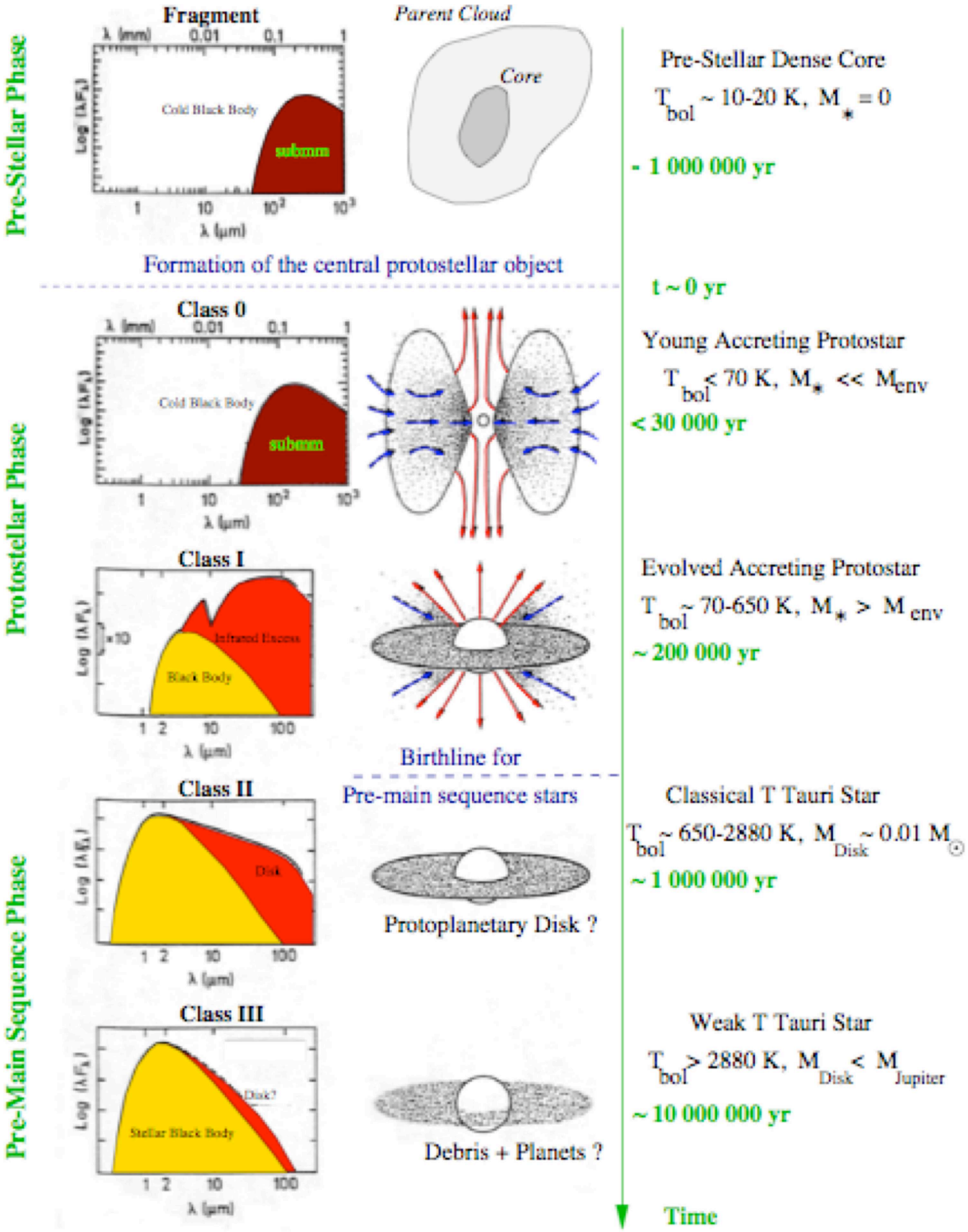

Figure 1.3 – Main stages of low-mass star formation, based on their SED and circumstellar masses. Taken from Andre (2000).

that of the accretion processes, and appear closely linked to them since the earliest stages of the star formation.

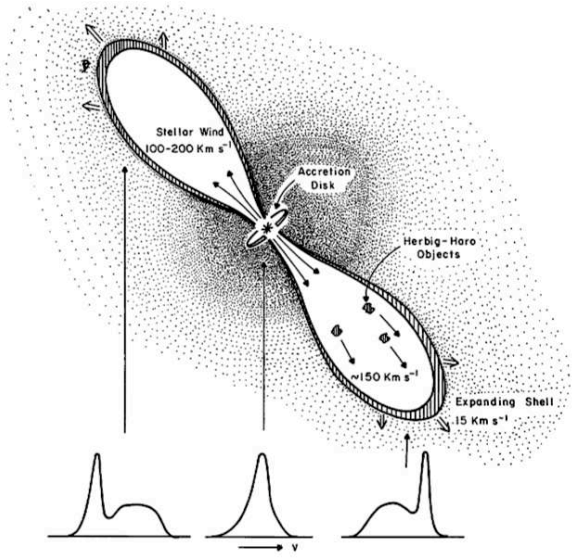

Figure 1.4 – Paradigm proposed by Snell et al. (1980) for the origin of bipolar molecular outflows. Typical CO line profiles from the red and blue CO lobes are sketched at the bottom.

Historically, Herbig (1951) and Haro (1952) were the first ones to identify mass-loss phenomena from young stars through the discovery of small nebulosities with peculiar emission line spectra. The corresponding Herbig-Haro objects were soon linked with stellar winds (Osterbrock (1958)). Schwartz (1975) interpreted them as the result of the interaction between supersonic stellar winds and the surrounding ambient material. Cudworth and Herbig (1979) measured proper motions confirming that the ejection comes from a newly formed star. In 1980, Snell et al. (1980) reported the discovery in CO of a large molecular outflow and suggested a paradigm for the origin of bipolar outflows, in which the outflow traces ambient gas swept-out into a dense, slow bipolar shell by a fast stellar wind collimated by a circumstellar accretion disk (see Figure 1.4). The first rapidly moving, highly collimated jets were then discovered in optical lines (Mundt and Fried (1983)) and in the radio continuum (Bieging et al. (1984)). Almost three decades after, over 600 outflow-related objects have been discovered (http ://casa.colorado.edu/hhcat/), revealing the ubiquity of these energetic episodes. We here describe properties and models that have been compiled through the accumulation of extensive observational data through the years.

1.2.1 Different kinds of outflow activity

It is generally believed that all young stellar objects undergo period of important mass loss, through the emergence of bipolar outflows from a stellar or circumstellar region. A

fast, well collimated stellar wind sweeps up the surrounding ambient molecular gas, leading to the formation of two cavities oriented in opposite directions from the central star. Irregular lobes and incomplete shells form from the displaced molecular gas, generating radiation through ionized, atomic, or molecular gas in various excitation conditions, that can be observed over a wide range of wavelength, from the UV to the radio. Observations consequently reveal a narrow inner beam with knot spacing of 500-1000 AU, traced out to 0.1 pc from the central source, and a series of individual, aligned shocked structures with spacing 0.05–0.2 pc extending up to several pc from the source.

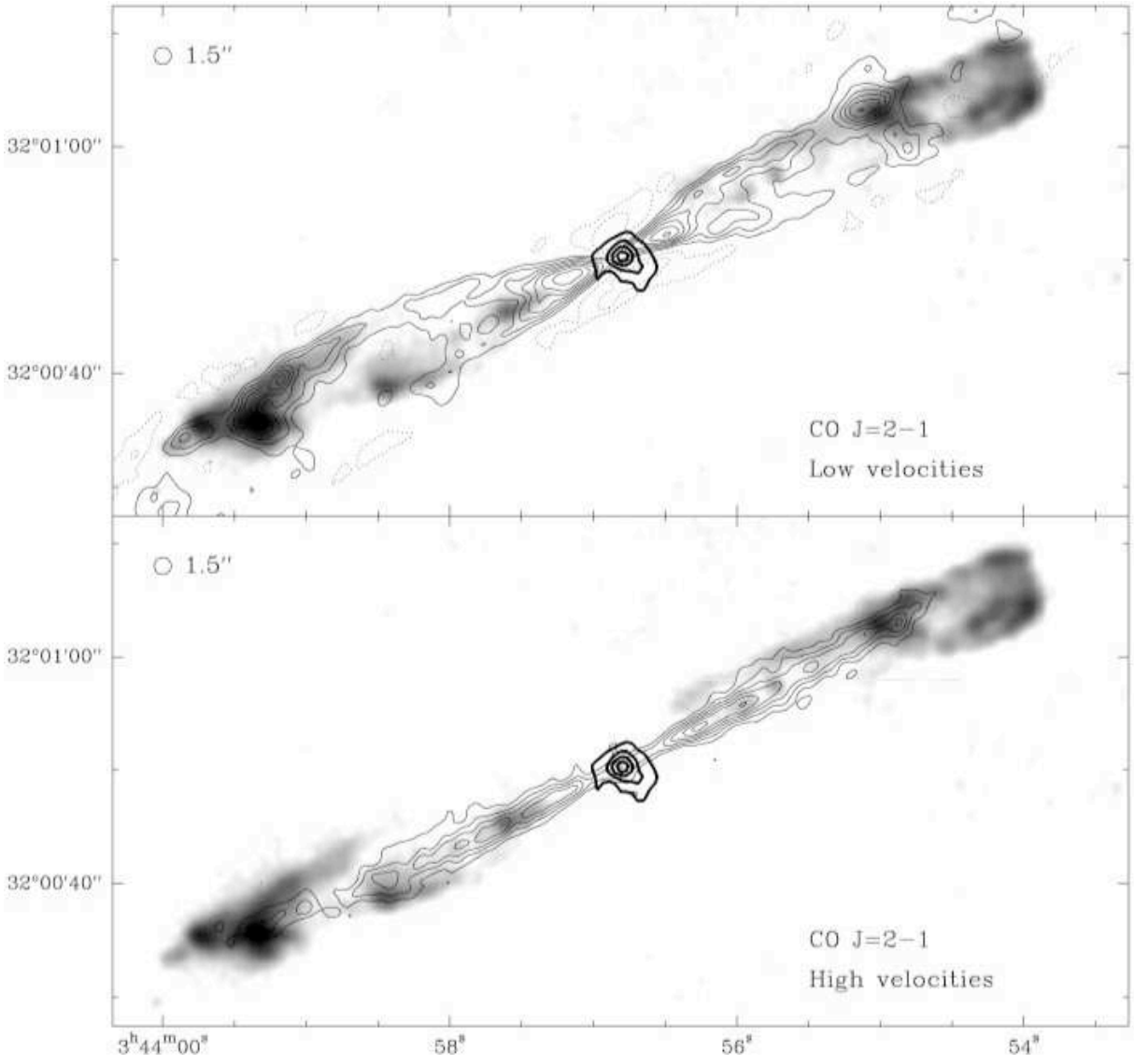

Figure 1.5 – Bipolar molecular outflow (top) and molecular jet (bottom) in the Class 0 source associated with HH211. Taken from Reipurth and Bally (2001), showing grey contours of CO(2 – 1) emission and H_2 at 2.12 μm in shades of grey. The black contour is the continuum emission at 230 GHz.

Molecular components. The molecular component is usually the most massive, because it consists of a large amount of ambient material that has been swept up during the full period of mass-loss. CO emission is associated with the vast majority of observed outflows, whereas the main cooling in these protostellar shocks is due to emission from molecular hydrogen. Water masers are also a typical feature of these environments.

1. Standard CO outflows. High velocities outflows are observed around young stellar objects of very different masses and luminosities. Their collimation and outflowing velocity ranges from 3 to 20 and from 10 to 100 km s^{-1}, with a general trend of higher collimation being associated to higher velocity (Bachiller and Tafalla (1999)). The amount of mass in a given molecular outflow ranges from 10^{-2} (Chernin and Masson (1995)) to 200 $M\odot$ (Russell et al. (1992)). The energy deposited in the CO outflows can reach 10^{47}–10^{48} erg (Garden et al. (1991)). They often exhibit a clumpy or knotty morphology, and principally exist around Class 0 sources, although fainter CO outflows have been observed around Class I and II as well (respectively HH111 and RNO91 for example, in Lee et al. (2000)). Accordingly, measured kinematics timescales range from 10^3 to a few 10^5 years. In class 0 sources, narrow molecular jets extending to 0.05-0.1 pc from the source have been resolved in CO. The typical knot spacing is 1000 AU (Chandler and Richer (2001)). Farther from the central star, 0.1–1 pc along the slow molecular component axis, chains of compact, fast molecular bullets are detected, often associated with rovibrational H_2 emission. These bullets tend to have a regular spacing of typically 0.05–0.2 pc. The best example of a molecular jet (Gueth and Guilloteau (1999)) can be found around the embedded source HH211, that can be seen on Figure 1.5. Two components can be observed :
   - at high velocity, the CO jet traces a highly-collimated linear structure emanated from the protostar, and terminates at the position of a strong H_2 bow-shock. This inner jet is well resolved in its intermediate section when imaged at a resolution of 400 AU, but higher resolution observations reveal a faint, unresolved central beam with a width less than 250 AU (Chandler and Richer (2001)) and broader parts corresponding to small bows. The high velocity component terminates at the position of strong H_2 bow-shocks (see the next paragraph) ;
   - at low velocity, the CO traces a cavity that is located in the wake of these shocks, being observed as extended lobes surrounding the high velocity jet.

   The case of HH211 seems to suggest that the propagation of one or several shocks in a protostellar jet entrain the ambient molecular gas through the large bow-shocks traced by the H_2 line emission and produces the low-velocity molecular outflow with a large opening angle. However, it is not clear yet if the CO molecules belong to the actual protostellar jet and are entrained along the jet in a turbulent cocoon (Raga et al. (1995)), or are formed or excited in shocks propagating down the jet (Raga and Cabrit (1993)).

2. High-excitation H_2 emitting gas. The vibrational transitions of H_2 arise from energy levels > 6000 K above the ground state, and their emission results from collisional excitation in dense regions at temperatures of a few 10^3 K. They are consequently good potential tracers of shocked molecular gas, although the dissociation of molecular hydrogen at high shock speeds can limit their use in extreme conditions. In

spite of the absence of detection around Class II sources, molecular hydrogen is of particular importance in the study of earlier stages of star formation :

- in Class 0 sources, H_2 observations allow for the study of optically invisible outflows (see the following paragraphs), which are still deeply embedded within dense cores. In HH211, as can be seen on Figure 1.5, the molecular hydrogen emission forms long filaments which do not correspond strictly with the axes of the jet. These observations confirm that the H_2 line emission arises in the mixing layer where ambient material is entrained. The observations of bow-shocks stresses the importance of the 'prompt' entrainment at the jet head (Davis and Eisloeffel (1995)) ;
- in Class I sources, shock-excited H_2 emission is usually fainter than in the Class 0 stage, except in several cases, where H_2 bows have been detected well beyond the inner jet beam, with a typical spacing between bows of 0.05–0.2 pc, extending up to a few pc (3.8 pc in the typical case of HH 211) on either side of the central source. Because their dynamical ages (typically several times 10^4 years) reaches the accretion one of their sources, such parsec-scale jets provide fossil records of the evolution of protostars and their activity. A complete review of their properties and utilities is listed by Reipurth and Bally (2001) ;
- in Class II sources, molecular hydrogen emission is not detectable anymore.

3. Water masers. Observations have revealed the presence of water masers within 100 AU of the source in 40 % of the Class 0 objects (Furuya et al. (2001), Chernin (1995)). They only appear in environments where temperatures and densities exceed 200–300 K and 10^8–10^9 cm^{-3} respectively, hence tracing very dense shocks, some with a highly bipolar structure. Some bipolar water masers systems have been mapped, inside a beam diameter of 8-20 AU at a distance of 20-40 AU (see also Claussen et al. (1998), Furuya et al. (1999)). Their multi-epoch observations allow accurate determination of proper motions in the outflowing gas, and hence determination of the flows inclination to the plane of the sky.

Atomic and ionized components. In addition to the molecular emission, optical and centimeter-wavelength jets of ionized material are also observed in episodes of outflow activity. Optical forbidden emission lines indeed provide powerful diagnostics of bipolar activity. Their profiles are blueshifted with respect to the stellar velocity because a thick circumstellar condensation obscures the receding part of the outflow, and they are often double peaked with a high- and a lower-velocity component.

Hα, whose emission is associated to the presence of ionized hydrogen, is a major component in jets and outflows. It is quickly saturated and typical of atomic shock waves 20–150 km s^{-1}, and can thus be used to map the size and shapes of the observed structures. Of a similar use are [SII] emission lines at 67.31 and 67.16 μm, and [NII] emission line at 65.83 μm. Figure 1.6 shows three examples of composite images obtained with the HST from [SII] and Hα components of bright jets from Class I sources.

The [OI] emission line at 63.00 μm (and in to a smaller extent, at 63.63 μm) have also been used because of its brightness in outflow regions. In many objects, it is the

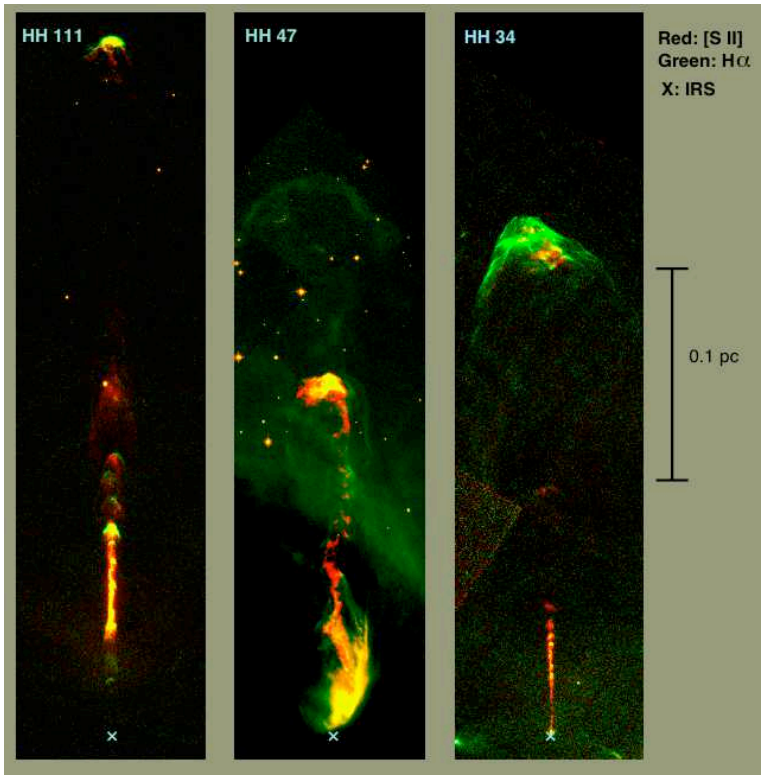

Figure 1.6 – HST images of HH 111, HH 47, and HH 34 on the same linear scale, taken from Reipurth and Bertout (1997).

only emission spatially coincident with the flows, suggesting that their far-IR cooling is strongly dominated by this line (see for example Benedettini et al. (2000)). In addition to these lines, the rich IR emission line spectrum of [FeII] between 1.1 and 2.5 μm offers an excellent opportunity to study the ionized component of the shocked gas in outflows. Four levels are closely spaced, resulting in transitions that are relatively insensitive to the temperature. Because [FeII] emission lines have critical densities much larger than that of [SII], they are a powerful tracer, being less subject to extinction (see for example Giannini et al. (2004) for the example of the use of these lines).

These ionized components do not show the same characteristics at every stage of early star formation :

- in Class 0 sources, no optical jets have yet been detected, either because they are intrinsically faint, or because of the very large $A_v > 1000$ generated by the dust shell that surrounds the central object ;
- in Class I sources, the optical jets become visible in the above lines. The narrow jet beam can be traced out to about 0.1 pc from the central source and contains bright knots with typical spacing of 500–1000 AU, as can be seen on Figure 1.6. This image of three Class I outflows taken with the HST also reveals individual bright and large bow-shaped structures whose apex faces the source, long after the fading of the central jet beam. They are often designated as Herbig-Haro objects, although this category of objects covers a broad range of flows and jets with no real common observational characteristics. Parsec-scale jets, that can be seen in H_2 around various Class I sources, can also have their optical counterpart (HH 111 being an example of these giant flows) ;
- in Class II sources, atomic collimated winds do still appear, but most of the forbidden line flux arises on small scales (less than 100 AU) and can hence be confused with the brighter stellar photosphere. Nevertheless, nearby Class II sources in the Taurus cloud provide useful constraints on jet widths within 800 AU of the star (Woitas et al. (2002), Ray et al. (2007)), showing typical widths of 20-40 AU at a distance of 30-50 AU from the star. Beyond these distances, the jet width grows slowly with the distance, in accordance with the expected 'Mach angle' interpretation value, and matches the larger scale behavior observed for Class I sources at distances greater than 1000 AU. Within this distance, results have been obtained by Hartigan et al. (2004) confirming the value at 50 AU, with a wider opening angle than on larger scales (also see Cabrit (2007) for a review).

Concerning neutral atomic components, Natta et al. (1988) first suggested that a high fraction of neutral matter could be found in the primary winds, and the HI 21-cm line simultaneously began to be detected around a few low-mass YSOs (Lizano et al. (1988), Giovanardi et al. (1992)), through broad wings associated to winds of up to 200 km s^{-1} and mass-loss rates of 10^{-6}–10^{-5} $M_\odot$ yr^{-1}. This detections were not confirmed in important objects such as L1448, possibly impeded by confusion of the background Galactical emission, and mostly because of the poor angular resolution that prevents their precise observations. In addition to this, H I emission modeling in wide-angle winds fails to account for the basic characteristics of the companion CO outflow (Chernin and Masson (1995)).

Radio jets. Radio continuum emission in the centimeter range is also tracing collimated ionized outflows, that is thermal radio jets, which constitute strong evidence for collimated outflows at a small scale (100 AU). Thermal radio continuum emission also emerges at millimeter and shorter wavelengths, tracing heated dust near the object (see the black contours on Figure 1.5). In a few sources, dust emission could also be important at centimeter wavelengths (see for example Chen et al. (1995)). Nevertheless, in most cases, the cm-wavelength emission is interpreted as free-free emission from a thermal jet (Reynolds (1986)). In addition, characteristics of non thermal synchrotron emission have been marginally detected (see for example Curiel et al. (1993)) and included in models (Henriksen et al. (1991)). Anglada (1996) and Rodriguez (1995) provide a detailed review on radio jets around YSOs, whose evolution with the stellar class is the following :

- in Class 0 sources, collimated jets at centimeter wavelengths are resolved within 100 AU of the star. Their transverse width is less than 50 AU on 50 AU scale, consistent with optical sizes (Rodriguez et al. (1995)) ;
- in Class I sources, radio jets are still seen ;
- in Class II sources, radio jets are only seen in the youngest objects of the category. The HL Tau source belongs to the I/II category, and exhibits a jet width that decreases between 50 AU and 10 AU of the source (Eisloffel et al. (2000)).

Microjets. The term 'microjet' refers to high-velocity jets that are seen in optical wavelengths, at such small scales that the lines flux can be confused with the much brighter stellar photosphere. They were only discovered after careful subtraction of the stellar continuum, extending over a few 100 AU in 30% of the T Tauri stars studied (Hirth et al. (1997)). In the other T Tauri stars, microjets are either absent or too cold to emit. Recent sub-arcsecond imaging of these objects shows a jet beam with a knotty morphology (with a typical spacing of 500 AU), and sometimes faint knots out to 0.1 pc (Dougados et al. (2000), Bacciotti et al. (2000)). In many cases, both a low velocity and a high velocity component are detected, with different strengths in various forbidden lines. The latter is spatially more extended, and could result of a jet originating from the star or the very inner part of the accretion disk, whereas the former could come from a slower wind originating from the disk (Kwan and Tademaru (1995)). They might represent the later stages of collimated outflows, without necessarily implying a subsequent later evolution of their central object.

More energetic components. More energetic radiation arise from regions which manifest an outflow activity. UV emission lines and continuum have been detected in a few objects (see Reipurth and Bally (2001) and reference therein). In low-excitation objects, it could emerge from [CIV] and [CIII] lines, whereas fluorescent lines of H_2 are invoked in the case of high-excitation objects. The blue continuum seen in outflows increases in the UV and peaks at 1575 Å, possibly involving atomic or molecular hydrogen.

Many observational problems hamper the detection of UV radiation in outflows, among which the presence of a strong extinction that is not always easy to correct for, or a considerable variability on short timescales. UV lines pose problems anyway : the [CIV] line is observed but never shows shock faster than 100 km s^{-1}, and the [NV] line at

1240 Å should be strong but is never observed.

Further up on the energy scale, parsec-scales that have blown out of their parent cloud could be observable at X-ray wavelengths, through emission produced by fast shocks or absorption lines originating from various ionization states of elements. Bally et al. (2003) report the observations of X-rays in the L1551 region, and investigate their origin and emission mechanisms.

Herbig Haro objects. This term designates the small nebulae with characteristic emission line optical spectra found in star-forming regions, later to be recognized as manifestations of outflow activity from newborn stars. The term has been progressively extended and generalized and can now be associated to all kinds of outflow activity as described above.

1.2.2 Outflows observations and immediate characteristics

Multiplicity. Not all outflows activity consists of bipolar structures. Unipolar CO outflows have been observed (Chernin and Masson (1991), Richer et al. (1992)), and their existence could be explained by swept-up wind models if the protostar is forming on the edge of its parent cloud, or close to an H II region. Quadrupolar outflows driven by the same protostellar condensation have also been observed (see Gueth et al. (2001) for example), and could be resulting of the superposition of two independent outflows, or of single outflows with strong limb-brightening or strong precession of the ejection direction. The first hypothesis raises the question of the causal link between the existence of multiple stellar systems and that of multipolar outflows, without clear answer yet.

Mass-velocity relation. Molecular outflows exhibit a mass-velocity relation with a broken power-law appearance : $M_{\rm CO}(v) \propto v^{\gamma}$, where the slope varies with the flow velocity (from v_{LSR}) in the following way :

- at velocities above this break velocity, the power-law exponent is around -3 to -4, with measurements down to -8, possibly corresponding to a recently accelerated component ;
- at velocities below 6–12 km s^{-1}, the slope varies from -1 to -2.5, perhaps corresponding to a slow, coasting component.

In spite of the possible variation of the break law from 2 to 30 km s^{-1} (see Richer et al. (2000) and references therein), hydrodynamic simulations of jet-driven outflows (see Subsection 1.4.3) predict this slope change that delimits 'prompt' entrainment at the head of the jet, and 'steady-state' entrainment. Richer et al. (2000) also indicates that for low-velocity gas, γ does not depend on the bolometric luminosity over nearly six decades, suggesting a common gas acceleration mechanism. In addition to this, marginal decrease of γ with time for more luminous sources is stressed out, with no such trend in low-luminosity sources.

Proper motions measurements and radial velocities. Proper motions refer to the tangential velocity of the jets or outflows, while radial velocities designate the velocity

along their axes. While the ground-based proper motions studies are limited by poor resolution and are better resolved by HST images (hence providing only bulk motions, and requiring long time between images, introducing the problem of time variability), long-slit spectroscopy is ideally suited to measuring radial velocities, also providing line widths, excitation conditions, and electron densities. The simultaneous determination of both radial and tangential velocity also allows for the derivation of the flow inclination to the plane of the sky, which itself allows for a correction of flow speeds. If the location of the source is known, these measurements can also be used to determine the dynamical age of the flow.

Proper motion and radial velocity measurements show a variety of behaviors :

- in molecular jets a rough linear increase in radial velocity with distance from the source occurs (see next paragraph). Typical proper motions and bulk radial velocities have been measured around 100–200 km s^{-1} with a large spread, and with small associated velocity dispersion. The tangential velocities tend to decline with increasing distance from the flow axes, while the radial ones linearly increase with it, leading to the velocity-distance relation (see next paragraph) ;
- water masers within 100 AU of the source present a much steeper radial gradient in the case of S106 FIR for example (Furuya et al. (1999)), with a line of sight acceleration smaller than expected from this quantity. Proper motions indicate typical velocities of 50km s^{-1} at 25–40 AU from the source ;
- optical jets show broad line profiles in the jet beam, indicating radial velocities of 100–400 km s^{-1} (see for instance Reipurth and Bertout (1997)). A lower velocity component is also detected, though accelerating away from the source. Radial velocities increase with luminosity of the star. Proper motions of 100–500 km s^{-1} can be measured for the knots, again with a very large spread. Low excitation [SII] knots are associated with small-amplitude-velocity jumps (30 km s^{-1}) ;
- Microjets such as DG Tau have also been studied (Hirth et al. (1997), Solf (1997)), in which the maximum [OI] radial velocity and line widths are reached very close to the source. Peak radial velocities of 100–400 km s^{-1} stay constant or decrease with the distance. [NII] emission lines indicate ionization variation with flow speed and distance. Radial velocity asymmetries, and disk winds component can also be detected. Proper motions at 100–200 km s^{-1} are measured for T Tauri jets ;
- large H α-bright or Herbig-Haro bow-shocks tend to be associated with large-radial velocity discontinuities. The measurements of double peaked line profiles consisting of a high-velocity component with a gentle velocity decrease along the flow axis, and a weaker, lower-velocity component with a steep acceleration are well interpreted by models where a fast jet drives a bow-shock with an envelope of entrained ambient material, also accounting for observations of high velocities towards the apex, and decreasing flow speeds towards the wings of the bow-shock. In addition to this, the division of the working surface into a two-shock structure with a bow-shock and a Mach disk (that is, a reverse shock, see Figure 1.12 in Subsection 1.4.3) is confirmed by kinematical arguments based on both radial and tangential velocity measurements.

Velocity-distance relation. Many fairly collimated CO outflows show a linear velocity-distance relation, also called 'Hubble law', where the maximum radial velocity is proportional to the position (Lada and Fich (1996)). To interpret this behavior, the sweeping-up of a dense shell from a power law density distribution by a wide-angle wind (Shu et al. (1991)) or the prompt entrainment of the ambient surrounding gas by a bow-shock at the head of the jet (Downes and Ray (1999), again, see Subsection 1.4.3) have been evoked.

Precession. Many outflows exhibit a more complex shape than the bipolar one. The S-shape symmetry is generally indicative of the precession of the jet axis, as observed in Cep E or L1157(see respectively Eisloffel et al. (1996), Gueth et al. (1998)), although simple bending or misalignment between the structures within the outflow can also be observed (Lee et al. (2000)). In the course of its change of orientation, the jet axis interacts with new material in different portions of the ambient molecular cloud, and can lead to the poor collimation of the outflow (IRAS 20126+4104 Shepherd et al. (2000)), or not (L1157, Gueth et al. (1998)). Precession of the jet axis can occur in Class 0 sources, as L1157, in which two misaligned CO cavities are observed in the blueshifted lobe and can be accurately described by means of a precession model in a narrow cone. In Class I sources, large-scale pronounced changes of orientations have been detected (Reipurth and Bertout (1997)). Such observations are less frequent in Class II sources, although for example Raga et al. (2001) used precessing models to describe the small wiggles in the DG Tau microjet. Orientation changes of the jet axis could be the result of an isotropic accretion from turbulent cloud cores or envelopes, or of the reorientation of the disk associated with the periastron passage of a companion star.

Time variability. Small scale knots or bullets are a common observation in optical jets (HH300, Arce and Goodman (2001)) and microjets, as well as in molecular jets (L1157, Gueth et al. (1998)), with the following properties :

- high-velocity proper motions ;
- very high degree of symmetry ;
- intensity decrease with distance from the source (Raga and Kofman (1992)) ;
- morphology and kinematics of 'mini bow-shocks' in well-resolved knots (Lavalley et al. (1997)) ;
- radial velocity variations and appearance of new knots at the source position over a few years (Solf (1997)), with typical knot spacing of 500-1000 AU.

All these observations strongly support the existence of jet velocity variability in such objects, rather than Kelvin-Helmholtz instability, stationary crossing shocks or traveling jet instabilities. The velocity variability itself seems to originate from intrinsically episodic ejection, or from continuous ejection with frequent ejection bursts, generated by sudden variations in the accretion rate of the forming star.

1.2.3 Outflows estimated properties

Density and excitation conditions. Figure 1.7 shows the most important tracers of outflow activity from young stars. Their excitation generally results from collisions

between outflowing fluid and slower ejecta or ambient gas. Optical and near-IR emission lines require a temperature of at least several thousands degrees to excite, whereas millimeter-wavelength tracers are collisionally excited at temperatures of a few kelvins, at the densities typically fund in molecular clouds or outflow lobes, hence probing the total mass and momentum deposited into outflows over their lifetimes. Particularly the lower rotational states of CO are thermally excited throughout the swept-up gas at the ambient temperature of typical molecular clouds (10 K). [OII] (at 63 μm), and [CII] (at 157 μm) dominate the radiation from warm post-shock gas (50–200 K). Above these temperatures, high-J CO, OH, and rotational, then rovibrational emission lines from H_2 take over. The neutral and singly ionized forbidden optical lines require more powerful outflows, with speeds exceeding 30 km s^{-1}, except in the case of [FeII], that can arise in slower shocks. Higher dissociation states can emit at even greater shock velocities, due to dissociation and consequent ionization, and also to UV shock radiation.

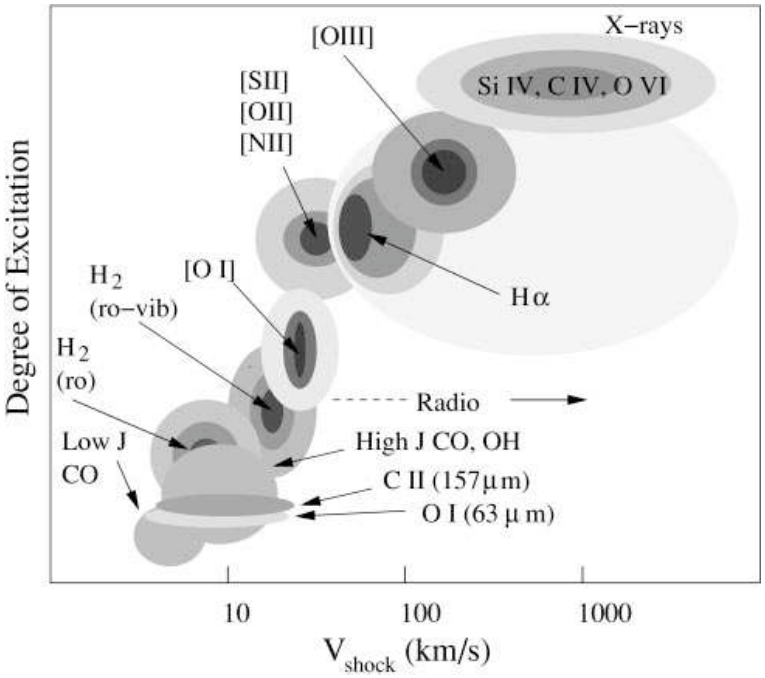

Figure 1.7 – Schematic illustration of the excitation of the most common emission lines associated to stellar outflows in function of the shock velocity. Taken from Reipurth and Bally (2001)

In molecular outflows, CO is very stable, and its line surface brightness is used to determine its column density, which hence allows for the determination of the mass deposited in the outflow. The Large Velocity Gradient is used for transitions with a high critical density (and to resolve the associated non-LTE situations) to constrain the H_2 density, kinetic temperature and species column density along the line of sight. The outer molecular bullets contain gas at a range of temperatures, from 15 to 100 K for the CO component, and for 2000 K for the H_2 one. The density is usually in the 10^4–10^5 cm^{-3}.

In the inner jet beam, the density can reach densities an order of magnitude higher, with temperature conditions of around 100 K.

In HH objects, shock waves at 20–150 km s^{-1} and pre-shock densities of 10–1000 cm^{-3} describe the optical line emission, although some discrepancies remain (Hartigan et al. (2000)). In optical jet beams, forbidden emission line ratios can be used to discriminate among the heating processes that can generate them. Again, shocks with pre-shock densities of 10^2–10^5 cm^{-3} seem to be the dominant line excitation mechanism down to 30 AU of the star. In such objects, the electron density can also be accessed through the use of the [SII] doublet ratio, almost independently from the temperature (Osterbrock (1989)). Different paths can then lead to the estimate of the ionization fraction, and consequently to the density of the considered region (see Cabrit (2000) and references therein). These various paths have been used and compared in the case of DG Tau, allowing to place constraints on shock velocity and magnetic fields for example.

Mass-loss rate estimates from jet observations. Jets and outflows observations also lead to the determination of the mass-loss rate $\dot{M}_j$. The observable mass-loss rate is then either an upper limit (if ambient material is traced by the jet), or a lower limit (if some ejected material does not emit for some reason). Cabrit (2000) provides all necessary details of the various techniques to derive these mass-loss rate values, that we briefly review here.

The first mass-loss rate estimate that can be derived is that of the atomic jet component. Two possible categories of methods can be used :

- the first category is free of extinction corrections, and is based on the dependance of $\dot{M}_j$ on the mean jet density n_j, the mean jet velocity V_j, and its radius r_j (when spatially resolved). Two different assumptions can then be used to derived n_j from the measured density $n_{\rm H}$, itself deduced from the ionization fraction and electronic density for example. In the first one (a), the physical conditions are assumed to be uniform within the observing pixel, and $n_j = n_{\rm H}$. This method is probably an upper limit to the actual value (if the beam is filled with a mixture of high and low density regions). The other estimate (b) assumes that emission comes from a shock wave, in which case $n_j = n_{\rm H} \times \sqrt{C^{-1}}$ is the pre-shock density, and C is the compression factor in the shocked layer where the lines are emitted , estimated from comparisons of observed line ratios with shock models ;
- the second category uses the jet luminosity, is hence subject to uncertainty caused by the extinction correction, but is independent from the jet beam radius determination. Again, two assumptions can be made to derive an estimate of the mass-loss rate. The first one (c) requires that physical conditions are uniform within the observing pixel, and is then based on optically thin forbidden lines luminosity (for example, [OII] at 63 μm, or [SII] at 67.31 μm). The second ones (d) states that the emission traces the cooling of a shock wave, and is based on the [OII] emission line luminosity at 63 μm. It also requires estimates of the shock velocity, number of shocks within the beam, and angle between the shocks and jet flow.

As all these four methods all use the same tracer, Cabrit (2000) compare their results in the case of three bright Class I jets (HH34, HH47, HH111), pointing towards methods (b)

and (c) as the most reliable ones.

The mass flux can also be estimated in molecular components :

- in molecular jets, $\dot{M}_j = MV_\perp/l_\perp$, where M and $l_\perp$ are respectively the jet mass and projected length in the plane of the sky and can be derived from CO maps, and where the projected jet velocity in the plane of the sky $V_\perp$ is assumed to be a characteristic expansion speed ;
- in molecular bullets that are not made of entrained ambient gas (hence tracing jet material), the spacing Δx between bullets can be used to derive the mass-loss parameter. The bullet mass and the projected jet velocity in the plane of the sky $V_\perp$ must also be known in this case.

Eventually, mass flux in the radio jet component can be derived from many parameters such as a supposed uniform ionization fraction, jet opening angle free-free continuum flux, spectral index, jet inclination to the line of sight, and frequency above which emission becomes optically thin. The formula given by Cabrit (2000) also contains the power law variation of the jet width and temperature with distance.

1.2.4 Beyond the scope of this review

high-mass stars outflows. Outflows from more massive, more luminous stars have been the subject of increasing attention recently. Their properties are briefly described in Arce et al. (2007), who also cites Shepherd (2003), Shepherd (2005), and Cesaroni (2005) for more complete reviews. The observations and modeling of such outflows that can consist of CO outflows or H_2 bullets for example, are made difficult by the tendency of massive stars (such as O stars) to form in clusters (which causes the outflows to undergo the collective effects of several driving sources), and also by the fact they reach the main sequence rapidly (hence exposing the outflows to radiation pressure, expanding H II regions, or normal stellar winds). Another selection effect arises from the fact that massive protostars form in massive, high-opacity molecular cloud cores, obscuring the possible outflows. Nevertheless, their study opens up physical regimes that can not be explored in flows from low-mass stars, in terms of associated shock velocities, or temperature for example.

Early-B stars exhibit outflows that can only be highly collimated at the earliest stages, with mass outflow rates from 10^{-5} to a few $\times 10^{-3}$ $M_\odot$ yr^{-1}, momentum rates 10^{-4} to 10^{-2} $M_\odot$ km s^{-1} yr^{-1}, and mechanical luminosity of 10^{-1} to 10^2 $L_\odot$. O stars with bolometric luminosity of more than 10^4 $L_\odot$ generate powerful but generally poorly collimated winds and associated outflows (except in the case of some late O stars), whose momentum rate exceeds 10^{-2} $M_\odot$ km s^{-1} yr^{-1}, more than an order of magnitude higher than that of stellar winds, with a mechanical luminosity $> 10^2$ $L_\odot$. Arce et al. (2007) convincingly argues for a general trend of de-collimation with age for such objects.

Irradiated jets. This term refers to a class of jets from low-mass stars that are embedded within HII regions, and near sources of soft UV radiation. As they are modified by ionization, their physical properties are determined using the methods developed for the analysis of ionized nebulae rather than outflow models. In general, the central star is visible, suffers low extinction, and does not appear to be embedded within opaque cloud

core : the external ionizing UV radiation field has photoablated the surrounding gas, leaving the star and its disk exposed and visible. Reipurth and Bally (2001) compiles the existing observations of these peculiar objects, as well as elements of description of their physics.

The electron density can be easily derived from hydrogen recombination lines or through the use of the red [SII] lines, and can then be combined with velocity field and flow morphology to infer global flow properties. Modeling studies mainly focus on the interpretations of the brightness asymmetry observed in most irradiated jets, possibly depending on that of the protostellar environment or on the rate at which the jet spreads orthogonal to the flow axis. Mass-loss rates and other properties have been estimated for only a few of them (Bally et al. (2000), Bally and Reipurth (2001)).

1.3 Environmental impact on the ambient surrounding gas

1.3.1 Physical impact on the surrounding cloud

Outflows from forming stars inject momentum and energy into the surrounding molecular clouds, at distances ranging from a few AU to a few parsecs. Whereas most studies have concentrated on outflow-core interactions (at typically 0.2 pc from the source), recent progresses in observing techniques now allow for the exploration of smaller (< 0.1 pc) and larger (> 1 pc) scales in nearby star forming regions.

Outflow-envelope interactions. Protostellar winds originate within a few AU from the stars, and they unavoidably interact with the dense circumstellar envelope, whose size is in the range of 10^3–10^4 AU. At this scale, survey studies have been conducted, showing the significant contribution to the observed mass-loss of the surrounding dense gas, as well as the evolution of the corresponding outflow-envelope interaction :

- in Class 0 sources, powerful outflows can modify the distribution and kinematics of gas surrounding a protostar (as around L1157, Beltrán et al. (2004)). Molecular line maps show the circumstellar high-density gas elongations and velocity gradients due to the entrainment of dense envelope gas by the outflow, along the outflow axis ;
- in Class I (L1228, Arce and Sargent (2004)) and Class II (RNO 91, Lee and Ho (2005)), there is an apparent trend of opening angle widening with age. The outflows are eroding the surrounding envelope (by accelerating the ambient gas along their interface with the envelope), and have the potential to further widen the cavities (as the outflow ram pressure is higher than that of the infall).

Even if the pre-protostellar outflow circumstellar matter distribution is less dense along the polar regions, as suggested by different models, (e.g. Hartmann et al. (1996)), the outflow-envelope interactions modify the density distribution and limit the infall region. It has been suggested that the outflow may become wide enough to end the infall process and disperse the associated envelope.

Outflow-core interactions. At the core scale, outflows interactions can generate all sort of disruptive effects, such as :

- shift velocities in the core's medium and high-density gas, in the same sense in position and velocity, as the high-velocity, low density molecular outflow traced by ^{12}CO (see Arce et al. (2007) for a review). Other tracers for low-velocity molecular outflows in dense regions can be used, as ^{13}CO, CS, NH_3, whose shifts are consistent with a momentum-conserving outflow entrainment process. Outflows are also a source of turbulence in the core (e.g. Zhang et al. (2005)) ;
- reshape of the core structure, consequent to sweeping or clearing or to the occurrence of density enhancements along the jet axis (Yu et al. (1999), Tafalla and Myers (1997), Sollins et al. (2004)), favored by its precession (Arce and Goodman (2002a), Arce and Goodman (2002b)). This sweeping up of the gas can ultimately gravitationally unbind it, thus limiting the star formation efficiency (Matzner and McKee (2000)) ;
- core dispersion, that appears to be potentially driven by the outflows in some cases (Fuente et al. (2002), Tafalla and Myers (1997)), although statistical observational dat are still needed to establish such strong conclusions ;
- star formation triggering, when impacting on a pre-existing pre-stellar core along its path (Motoyama and Yoshida (2003)), in only a handful of sources.

Outflow-cloud interactions, far from the source. Giant outflows exist around stars of all masses, as described in Subsection 1.2.1, and can interact at high distances from the source with the parent molecular cloud (Stanke et al. (2000)). Although theoretical and observational work is still needed, a few consequences of these interactions have been studied.

The effects of outflows associated to low-mass stars, able to move 0.1 to 1 solar mass of cloud material are limited to linewidth enhancement of the cloud gas (Arce and Goodman (2001)), and their kinetic energy can marginally reach the gravitational binding of their parent cloud. On the contrary, that of intermediate- and high-mass stars are able to entrain tens to hundreds of solar masses and can potentially generate more damaging events, such as large scale velocity gradients or shells of swept-up gas, and even break the cloud apart (see Arce et al. (2007) and references therein).

Multiple outflow activity, linked with clustered star formation can sweep up gas in significant volumes of the parent cloud into shells (Knee and Sandell (2000)), and be an important source of turbulence inside clouds (Mac Low and Klessen (2004)). Studies have shown that the energy input from outflows can regenerate the observed turbulent motions in molecular clouds on timescales of about 10^6 years (Bally et al. (1996)).

In most extreme cases where the source lies near the edge of a molecular cloud, giant flows can sweep up and expel gas from the parent cloud core and inject it into the surrounding ISM, thus also driving turbulence in the ISM. HH flows can also suffer from deflection from neighbours clouds (as in HH83, Reipurth et al. (1997)) or even neighbours outflows (as in the case of the HH110 flow, Rodríguez et al. (1998)). Flow-cloud collision have been analytically studied by Raga and Canto (1996), and numerically by de Gouveia Dal Pino (1999).

1.3.2 Estimated wind dynamics

The impact from jets and outflows can be quantified in terms of momentum-flux or mechanical luminosity, in the frame of a jet and bow-shock model (see Subsection 1.4.3).

Cold swept-up gas in molecular outflows. The momentum-flux and mechanical luminosity in the flow are defined with respect to low excitation CO lines ($F_{\rm CO} = M_{\rm CO}V_{\rm CO}^2/R_{\rm CO}$ and $L_{\rm CO} = (1/2)M_{\rm CO}V_{\rm CO}^3/R_{\rm CO}$, where M, V, and R are respectively the total flow-mass, velocity, length), and also be related to the wind momentum rate ($F_j = \dot{M}_j V_j$ and $L_j = (1/2)\dot{M}_j V_j^2$) through a simple model of wind/cloud interaction. Detailed discussion of uncertainties sources in the estimate of $F_{\rm CO}$ and $L_{\rm CO}$ are discussed in Cabrit and Bertout (1990), Downes and Ray (1999). In the simplest case of a highly radiative, momentum conserving, planar 'two-shock structure' perpendicular to the jet, $V_{\rm CO}$ is fixed by the equilibrium between shocked ambient gas and shocked jet gas :

$$\rho_a V_{\rm CO}^2 = \rho_j (V_j - V_{\rm CO})^2, \tag{1.31}$$

where ρ_a and ρ_j are the mean ambient and jet density. Multiplying this equation by the shock area A_S, and using $M_{\rm CO} = A_S \rho_a R_{\rm CO}$ leads to the sought relations :

$$F_{\rm CO} = F_j(1 - V_{\rm CO}/V_j)^2 = \eta F_j \tag{1.32}$$
$$L_{\rm CO} = L_j(V_{\rm CO}/V_j)(1 - V_{\rm CO}/V_j)^2 = \epsilon_a L_j \tag{1.33}$$

These formula may require extra numerical factors in η and ϵ_a in more general density distributions or if the wind shock is not radiative.

Ambient shock luminosity. Similarly, the above simple description can be used to calculate the luminosity radiated in the ambient shock (where the flow is accelerated) and in the jet shock (where the jet strikes the flow) :

$$L_{\rm rad}(\text{ambient shock}) = (1/2)\rho_a A_S V_{\rm CO}^3 = L_{\rm CO} = \epsilon_a L_j \tag{1.34}$$
$$L_{\rm rad}(\text{jet shock}) = (1/2)\rho_j A_S (V_j - V_{\rm CO})^3 = L_{\rm CO}(V_j/V_{\rm CO} - 1) = \epsilon_j L_j \tag{1.35}$$

The jet shock is generally expected to be a violently discontinuous, fast and dissociative one, whereas the ambient shock is slower and smoother owing to the magnetic field values reached in dark clouds. $L_{\rm rad}$(ambient shock) can also be directly determined from the measurements of rotational H_2 emission lines.

O I 63 μm luminosity of the wind shock. If the jet shock is indeed dissociative, then the [OI] line at 63 μm is a major coolant for gas below 5000 K, and the method (c) mentioned in Subsection 1.2.3 can be used to estimate $\dot{M}_j$. The largest uncertainty source is the unknown contribution of other regions on the line of sight to the [OI] line at 63 μm (Ceccarelli et al. (1997)).

1.3.3 Shock chemistry

The impact of the outflow on its environment has not only physical consequences. It is also significant in terms of chemistry, as the outflow processes momentarily give rise to processes that are highly unusual in other regions of the interstellar medium.

The peculiar shock chemistry. The propagation of a supersonic protostellar wind through the surrounding ambient medium happens via shock waves. These shock waves compress and heat the gas, and trigger various microscopic processes that do not operate in quiescent environments. Molecular dissociation, endothermic chemical reactions, dust processing (through ice sublimation and grain disruption) result in the existence of a distinct and unusual chemical composition in the close vicinity of YSOs. This transformation through shock chemistry arises quickly, as the timescales involved in the heating and processing of the shocked region are short (a few 10^2 to 10^4 years). Because of the short cooling time (after the passage of the shock), some of these high temperature processes take place only at the earliest stages, and subsequent evolution is dominated by low temperature processes. This evolution, combined with the clearing of the outflow path and the weakening of the main accelerating agent, make these chemical manifestations of the shock interaction vanish as the protostellar object evolves. Chemical anomalies can then be considered as outflow clocks (Bachiller et al. (2001)).

Different kinds of shocks. Different kinds of shocks exist in molecular gas (for more complete explanations, see the Chapter 2) :

- C-shocks occur in magnetized medium, generate continuous changes of the hydrodynamical variables on either side of the shock front, have typical maximum temperatures of 3000 K, and do not generate significant dissociation of molecular hydrogen. The most active molecular chemistry is expected to take place within these shocks, as the temperature jump is high enough to trigger the above processes without disrupting the involved molecules ;
- J-shocks are more violent events, faster, generating higher temperatures, with a discontinuous jump of the hydrodynamical variables on either side of the shock front. Molecules can be significantly dissociated, and only reform over longer timescales.

Both kinds of shocks generate an intensive grain processing that is still the subject of studies (e.g. Flower and Pineau des Forêts (2003), Guillet et al. (2007)), and depletion onto dust grain surfaces in the post-shock region that somehow reduces the abundances of some of the newly formed molecules, but still modifying the chemical composition of both the gas and the solid phases with respect to the pre-shock situation.

Choice of studied outflows. To optimally study the chemistry, the outflow must present some favorable properties in terms of observations :

- the considered outflow region must exhibit little morphological confusion as possible, which favors low-mass Class 0 Sources, on the contrary to high-mass sources that generally exhibit complex structures ;
- the observed outflow must be as clearly delimited as possible from its not-shocked environment, and thus preferably present a high collimation ;

- the orientation in the sky must be favorable to observations, that is a high inclination with respect to the line of sight.

For all these reasons, outflows as L1157 have been extensively studied in various molecular tracers (also see the Chapter 4 for a complete review of existing observations), exhibiting an interesting chemical segregation between molecular broad lines associated with the bow-shock and the narrow profiles from cold quiescent gas observed toward the position of the source.

Molecular enhancements. The consequence of shock chemistry around objects such as L1157 mainly consist of the enhancement of the abundance of many molecules, by factors ranging from a few to a few hundred (e.g CH_3OH, H_2CO, HCO^+, NH_3, HCN, HNC, CN, CS, SO, SO_2). The most extreme case is that of SiO, that is enhanced by a factor 10^6, and is the central subject of this study (see Subsection 5.1.2) for an explanation of these enhancements.

In the cases of CH_3OH and H_2CO for example, the enhancement factor can reach 100 (e.g. Maret et al. (2005)), probably due to their evaporation from grain mantles. Their maximal velocity of their line profiles is usually smaller than that of SiO, maybe because they do not survive at velocities as high as required to form SiO (Garay et al. (2000)) : CH_3OH and H_2CO enhancements with no SiO may be the sign of a weak shock. As these molecules are more volatile than SiO, SiO is expected to re-incorporate the grain mantles earlier, and such an enhancement may simply mark a later stage of the shock evolution. Other promising species that should allow for progresses in the comprehension of shock chemistry are also indicated in Chapter 13.

Other use for molecular tracers. Among these various molecules, there are significant differences in spatial distribution : HCO^+ and CN peak close to the central source, while SO and SO_2 have a maximum in the more distant shocks (OCS presenting the most distant peak), and molecules such as SiO, CS, CH_3OH and H_2CO exhibit an intermediate behavior. Such differences are partly due to excitation conditions, but they are mainly the manifestation of an important gradient in the chemical composition, observed along the outflow, and itself related to the time dependence of shock chemistry.

The chemistry of sulfur is of special interest from that point of view, as it has been designated as a potential chemical clock to date outflows. Many models include H_2S as the main reservoir of S in grain mantles in the pre-shock medium. When the shock passes, H_2S is released into the gas phase, and its abundance decreases after 10^4 years (Charnley (1997)) due to oxidation with O and OH, first producing SO, and then forming SO_2. Models indicate that the SO/H_2S and SO_2/H_2S ratios can be used to obtain the flow age (e.g. Bachiller et al. (2001), Buckle and Fuller (2003)).

Other chemical effects. In addition to these effects, other kinds of shocks associated to jets and outflows can have more drastic effects on the molecular cloud chemistry :

- fast shocks associated with the terminal working surfaces of parsec-scale flows for example, can be highly dissociative. The conditions of the affected region are then reset to its initial chemical state, where large abundances of atomic and ionic species

are present. This 'chemical rejuvenation' can be important in regions like the young cluster NGC1333, where random regions of the molecular cloud are subject to the passage of several outflows, with a time between two successive sweeping by outflow is short compared to the evolutionary timescale of the cloud ;

- molecular abundances in the stationary surrounding gas can also be altered by the radiation field of passing shocks (Viti and Williams (1999)). Low velocity or stationary clumps of several high dipole moment species (such as HCO^+ in HH34, Rudolph and Welch (1992)) thus coincide with the presence of HH objects in the neighborhood. Nevertheless Girart et al. (2005) have found that UV irradiation alone is insufficient to explained the measured enhancements of HCO^+ and that strong heating (as that caused by a shock) is also needed.

Dark sides of chemical studies. One of the major setback with shock chemistry is the extremely poor degree of knowledge that we have. In the case of the sulfur chemistry for example, recent observations seem to indicate that OCS is more abundant than H_2S on ices (van der Tak et al. (2003)), thus questioning the use of the above ratios as chemical clocks in outflows. In addition to this, recent models have raised the question of a more complex sulfur chemistry (Wakelam et al. (2004), Wakelam et al. (2005)) than previously thought.

Examples of our lack of chemical knowledge are frequent. SiO formation is expected to arise thanks to the destruction of the grain cores in shocks, and its manifestation at low velocities is not well understood. Theoretical studies of shock chemistry should involve the effect of UV near the outflow, the chemistry of the atomic component of the jet, the mixing layer chemistry and specific shock-related processes, but such an inclusion can only be at the expense of the CPU time for numerical simulations.

1.3.4 Accretion/ejection correlation in outflows

Interaction of the outflows with their environment at the location of their formation can also be used to constrain models of this formation. One of the means that is frequently used is the accretion/ejection correlation.

Existence of accretion disks. The presence of circumstellar structures of about 10^2 AU and masses in the range of 10^{-3} to 1 $M_\odot$ has been well established due to observations of molecular lines and infrared continua. The properties and frequency rate of these disks have been studied and modeled in different cloud complexes (see for example Mundy et al. (2000), Calvet et al. (2000), Dullemond et al. (2007)). Indeed, disks are necessary to explain various observational facts :

- the asymmetries of the forbidden line profiles observed around YSOs, where the blueshifted profiles are more important than their disk-occulted redshifted counterpart ;
- the spectral energy distributions of the classical TTauri stars, in which IR observations require the typical spectral index of viscous disks ;

- the excess observed in the optical and UV ranges, that is the observed excess continuum to stellar continuum at 5500Å (their ratio is called the 'veiling' of photospheric absorption lines) ;
- the eruptions of FU Ori stars that can be interpreted as consequences of the activity in the accretion disks.

Their properties can be obtained, at the expense of sophisticated models to disentangle the signs of the combined presence of outflow and infall motions in the same regions. Furthermore, with the use of interferometric observations at millimeter wavelength for example, the gas and dust emission from some disks have been observed. In addition to this, increasing observational evidence has been gathered for the existence of a close link between jets and disks surrounding YSOs.

Class I and Class II optical jets In T Tauri stars, a correlation between the [OI] emission line luminosity at 63 μm and the infrared excess luminosity from the disk has been qualitatively reported by various authors (see Cabrit (2000)), suggesting that the ejection processes in Class II sources are powered by disk accretion.

This correlation was later quantified by Hartigan et al. (1995), through the left panel of the Figure 1.8, that plots for the blueshifted part of the jet around T Tauri stars (filled circles) :

- the jet mass-loss rate on the Y-axis, $\dot{M}_j$, calculated via the method (c) mentioned in Subsection 1.2.3, and corrected for interstellar extinction ;
- the accretion rate, $\dot{M}_{\rm acc}$ on the X-axis, based on veiling measurements and other stellar parameters ;

On the same Figure, other points have been added :

- some of the same points, but with a downward correction of a factor 10 for the estimate of $\dot{M}_{\rm acc}$ (open circles, Gullbring et al. (1998)) ;
- three Class I optical jets studied by Hartigan et al. (1994) (stars on the same Figure), with the same estimate of $\dot{M}_j$, and amore appropriate estimate of $\dot{M}_{\rm acc}$ for more embedded objects (see Cabrit (2000)) ;

The Figure provides an order of 0.01 for the $\dot{M}_j/\dot{M}_{\rm acc}$ ratio associated to the sample Hartigan et al. (1995), 0.1 for that of Gullbring et al. (1998), and shows that the jets associated to Class I sources fall on the upper envelope of the correlation found for T Tauri stars jets, showing no significantly different behavior from them.

The right panel of the same Figure plots the wind momentum supply rate $F_j = \dot{M}_j V_j$ (with $V_j = 200$ km s^{-1}) in function of the accretion luminosity ($\dot{L_{\rm acc}} = GM_\star \dot{M}_{\rm acc}/R_\star$ where $M_\star$ and $R_\star$ are the respective stellar mass and radius). For T Tauri stars, the Figure shows that $F_j \simeq$ 10–100 $\dot{L_{\rm acc}}/c$, suggesting that radiation pressure from the accretion shock or disk is insufficient to drive the jets.

Molecular outflows. Molecular outflows also represent a good opportunity to test protostellar ejection mechanisms in relation with accretion processes, in the momentum-conserving limit, that is under the assumption that the wind and molecular flow momenta

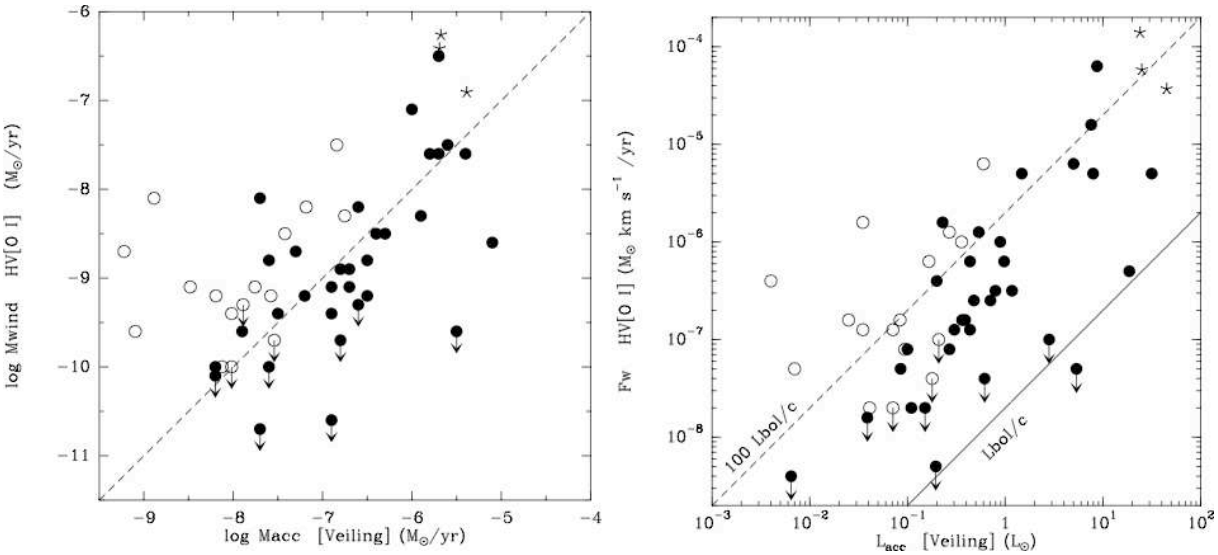

Figure 1.8 – Accretion-ejection correlations in T Tauri stars (see text in Subsection 1.3.4) ; from Cabrit (2000).

are equal, which is justified when the shock cooling times are short compared to flow dynamical timescales (see Dyson (1984)), or when efficient mixing arises at the wind/molecular gas interface (Shu et al. (1991)).

The sample of Richer et al. (2000) shows that the outflows momentum flux and mechanical luminosity ($F_{\rm CO}$ and $L_{\rm CO}$) are correlated with $L_{\rm bol}$ over a range of 5 orders of magnitude. The Figure 1.9 illustrates these existing correlations (left panel : $F_{\rm CO}$ correlation with $L_{\rm bol}$, right panel : $L_{\rm CO}$ correlation with $L_{\rm bol}$) for this sample, mostly containing well defined Class 0 sources. In such young sources, $L_{\rm bol}$ gives a measure of $L_{\rm acc}(\gg L_\star)$. Two lines appear on the left hand side panel of this Figure :

- the solid line shows the maximum momentum flux available in stellar photons in the single-scattering limit (multiple scattering is not likely to occur in the excitation conditions of protostellar winds) ;
- the dashed line shows the typical momentum flux in the ionized component of protostellar winds, inferred from recombination lines or radio continuum data (Panagia (1991)).

Their comparisons with the sample points respectively show that :

- in low-luminosity sources (below $10^4 L_\odot$), $F_{\rm CO} \simeq 100 - 1000 L_{\rm bol}/c$, suggesting that mass-loss is driven by accretion power rather than by radiative pressure ;
- in low-luminosity sources (below $10^4 L_\odot$), $F_{\rm CO} \simeq 10 F_{\rm w,ion}/c$, suggesting that the driving winds must be 90% neutral ;
- in higher luminosity objects, where dust grains provide the main opacity source, the radiation pressure might still have a role.

The right hand side panel of the same Figure shows that $L_{\rm CO}/L_{\rm bol}$ varies from 0.1 (low-luminosity sources) to 0.01(high-luminosity sources). Under the assumption of momentum conservation (also see Subsection 1.3.2), $L_j \gg L_{\rm CO}$: the $L_j/L_{\rm bol}$ ratio is close to

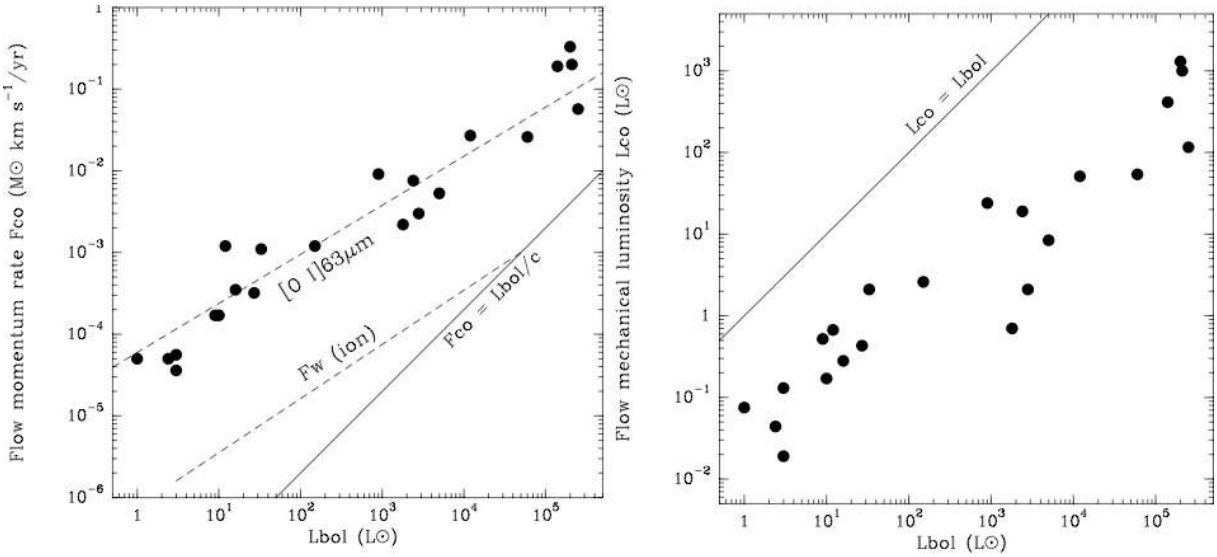

Figure 1.9 – Accretion-ejection correlations in Class 0 molecular outflows (see text in Subsection 1.3.4) ; from Cabrit (2000).

100% (10% for high-mass systems), showing that ejection extracts a large fraction of the accretion power.

Various conclusions can be drawn from there : Cabrit (2000) uses these diagrams to establish that the [OI] emission line intensity at 63 μm is consistent with Class 0 molecular outflows being momentum-driven by radiative, moderate velocity J-type wind-shocks, and discuss their ability to drive the observed molecular outflows. In the other hand, Richer et al. (2000) uses these conclusions to conclude that ejection/accretion ratios derived from this sample is consistent with MHD ejection model for all flow luminosities. In every case, the reader should be kept aware of the strength of the assumption of momentum conservation that was made at the beginning of the study (Richer et al. (2000)).

Accretion/ejection correlations were also investigated in Class I weaker molecular outflows of low-luminosity by Bontemps et al. (1996). Because of their weak CO momentum ($F_{\rm CO} \simeq 100 L_{\rm bol}/c$, see the left panel of Figure 1.10), such objects do not follow an unified behavior with Class 0 sources ($F_{\rm CO} \geq 1000 L_{\rm bol}/c$). In contrast, both Class 0 and Class I are identically correlated to the circumstellar envelope mass $M_{\rm env}$ derived from thermal dust emission ($F_{\rm CO} = 10^{-4} M_{\rm env} \times$ km s^{-1} yr^{-1}, right hand side panel of Figure 1.10).

Since the envelope mass decreases with accretion, this correlation suggests a progressive decay of outflow force over time, perhaps linked to a concurrent decrease in accretion rate over time (Andre (1997)). Again, Cabrit (2000) argues that jets also appears dynamically able to drive molecular outflows in the Class I stage.

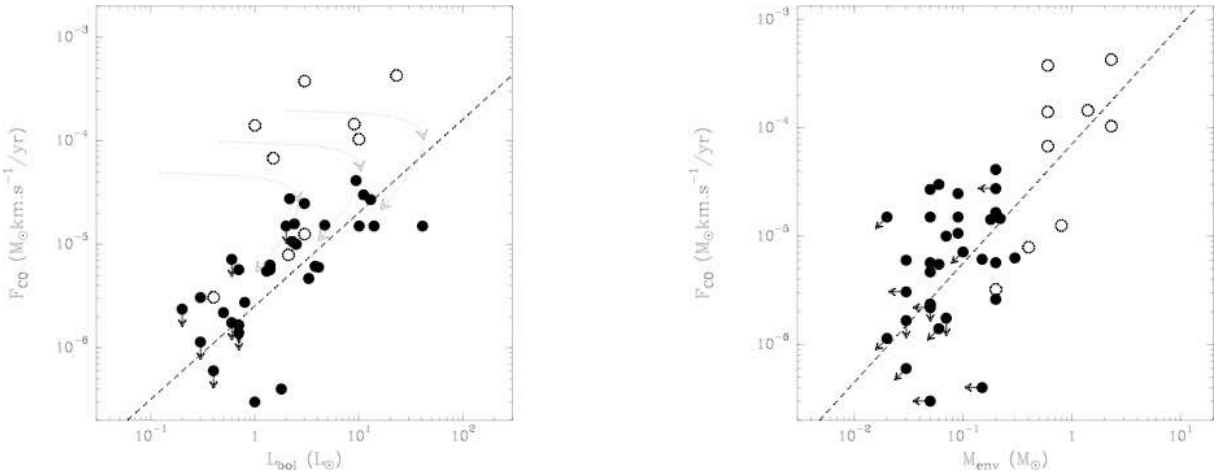

Figure 1.10 – Left panel : correlation of the momentum supply rate in the swept-up molecular flow with the source bolometric luminosity. The dashed line corresponds to $F_{\rm CO} = 100 L_{\rm bol}/c$, open circles to Class 0 sources and filled circles to Class I sources. Dotted curves with arrow show possible time sequences. Right panel : correlation of $F_{\rm CO}$ with the envelope mass. Taken from Bontemps et al. (1996).

1.4 Modelling of outflows

1.4.1 Collimation modelling

In this section, following Cabrit (2007), we present the successive scenarios that were proposed to account for the collimation of outflows, focusing on the most constraining ones, that is the low-luminosity Class II sources.

Collimation by external thermal pressure. The first scenario that was proposed is also the simplest one : the collimation by external pressure. In this model, the initial structure consists of an isotropic wind emitted by a flattened circumstellar structure, and its expansion in the disk plane is limited by an anisotropic thermal pressure gradient that collimates it towards the disk poles. We focus on the most likely steady-state semi-analytical model in the context of high density and moderate speed, in which the wind is highly radiative (Barral and Canto (1981)), although adiabatic models have been considered as well (Konigl (1982)). Three characteristics are used as criterion to study the credibility of such a mechanism to collimate the jet in accordance with observations.

The first one is the waist radius of the cavity created by a wind in these conditions. It is determined by the balance between the wind ram pressure and the thermal one in the disk plane, and therefore depends on the temperature and number density in the disk plane. These parameters are either provided by observations of well-studied disks (see for example Dartois et al. (2003)), or by theoretical calculations in the case of a 'standard' steady viscous accretion disk model in which the viscosity scales as the local disk scale height. Both of these methods provide values that match the observational data of equatorial wind confinement, from which point of view the external thermal pressure

model is hence a satisfying one.

However, to produce a jet, the opening angle of the shocked wind cavity should also be small enough to produce a jet. In a context of thermal pressure confinement, a strong dependence on the ratio of the disk pressure height scale to the waist radius ($\lambda = h/R_0$) of the asymptotic opening angle of the cavity has been demonstrated by Barral and Canto (1981). The opening angle inferred from the typical value of λ for disks around Class II sources suggests an opening angle of 25°, far from the 90° necessary to achieve cylindrical collimation corresponding to a well-focussed jet beam.

In addition to this, the external thermal pressure model predicts the reconfinement of the shocked wind when the disk is immersed in a non-zero pressure medium. In fact, reconfinement could be achieved in principle at a distance where the ambient pressure equals the wind ram pressure. Unfortunately the observations seem to indicate that this reconfinement should arise at less than 50 AU from the star, requiring excessively high ambient densities. Delamarter et al. (2000) have shown these conditions could be found around Class 0/I sources with dense infalling envelopes, but then the previous argument (that is, the excessive opening angle of the shocked wind) contradicts the scenario of external pressure collimation for these objects. For the Class II sources, the combination of the last two ones for Class II sources finally rules out the external pressure as the main agent for jet collimation.

Collimation by external magnetic pressure. Ménard and Duchêne (2004) have exhibited the tendency of jet sources to have their disk axes aligned with the field. It appears consequently relevant to verify if magnetic pressure, instead of thermal one, could significantly contribute to the jet reconfinement, again in the case of a radiative wind shock (see Cabrit (2007) and references therein). Indeed the effect of magnetic tension is this case is to counteract the wind expansion perpendicular to the field lines, leading to an elongated structure along the direction of $\mathbf{B}$.

The approximate, less-constraining relation can be used, similarly as in the case of the thermal pressure to estimate the reconfinement distance, simply balancing the wind ram pressure by the magnetic one. Even in this case, the poloidal component of the magnetic field required to constrain the jet implies that the jet should have trapped a considerable 2–20% of the initial poloidal flux present in the core, which seems to be unlikely because of the concentration of the magnetic field in the star itself, and given its effective diffusion in poorly-ionized, high-density disks. A regeneration of the poloidal flux by a star dynamo effect also seems unlikely on such scales.

Instead of the role of the poloidal flux component, the reconfinement of the jet by a 'turbulent' magnetic pressure has also been invoked, but the magnetic energy density would have to be well above equipartition on large scales, and the processes at stake for the creation and maintaining of such conditions are unclear.

MHD self-collimation. The third collimation process that has been invoked to account for the collimation of jets is the MHD self-collimation. In this case, an MHD wind is launched along a well-organized magnetic field anchored in a rotating object (star, disk, infalling envelope), with a non-zero current flowing across the magnetic surfaces. In this

model, the required poloidal flux is much smaller than in the magnetic collimation process, because the self-collimation is assured by the poloidal component created by the wind itself, and not that of a large scale magnetic field. Although models and comparisons to observations are more difficult in the frame of this scenario (see Cabrit (2007) and references therein), it is currently the most promising one, as it accounts for observed jet widths, collimation scales, and opening angles in Class II sources (see for example Ray et al. (2007)).

high-mass star outflows collimation. For high-mass stars outflows, there is a general trend of decrease of the collimation with age. The young objects are only subject to minimal increased irradiation on the disk and disk-wind by the star, whereas more evolved sources present ultracompact H II regions (and possible powerful water masers). This led authors to propose possible evolutionary sequences, based on the presence of increased radiation from the central star, ionizing the outflow and improving the matter-field coupling (Beuther and Shepherd (2005), Yorke and Sonnhalter (2002), Shepherd (2003)). Increased turbulence in high-mass outflows is also expected to influence their morphology towards decollimation, through the weakening of the conditions for ideal MHD (Fendt and Čemeljić (2002), Pudritz and Banerjee (2005)).

1.4.2 Acceleration modelling

In this section, we again follow the lecture of Cabrit (2007) to expose the various processes proposed to reproduce the observations of acceleration of jets from young stars.

Radiation pressure. The radiative pressure force exerted by photons on the gas at a given distance from a source can easily be expressed as a function of its luminosity and of the photon mean free path in the gas. To drive a wind, this pressure force must overcome the gravity of the central star, a condition for which low-mass (i.e. luminosity) stars fall clearly short. Nevertheless, this condition could be validated for high-mass protostars accreting at very high rates. However, we have seen in Subsection 1.3.4 that radiation pressure fails to account for the high values of flow momentum rate, except perhaps for high-luminosity protostars with high dust opacities. Consequently radiation pressure is ruled out as a general means of driving YSOs jets.

Thermal pressure gradients. Another purely hydrodynamical mechanism, based on thermal pressure gradients, could explain the acceleration of jets from young stars. If the sounds speed at the wind base equals the escape velocity, gas could be accelerated through a sonic point with non-zero velocity.

In this case, the writing of the energy conservation along a streamline yields a minimum initial temperature at the wind base, required to reach a given speed. This temperature is rather high, but have been observed, for example in accretion-related high coronal winds in T Tauri stars (see for instance Dupree et al. (2005)). Unfortunately, the acceleration of the total jet mass-loss rate by this mechanism, given the high coronal temperature that are required, is expected to generate strong X-ray brehmsstrahlung emission, which is not

observed in any case. However, this mechanism could partly participate to the acceleration of jets.

The X-ray emission problem might be overcome in models where the wind is cold at its base, and enthalpy is provided to the flow further up. Unfortunately, given the unavoidable associated losses (such as radiative cooling), the energy required as a specific heat input along the stream line would require a large fraction of the accretion luminosity. As no heating process has been proved that efficiency level, this type of models meets the problem of low efficiency in terms of the driving of stellar winds.

In the case of irradiated jets (see Subsection 1.2.4), the irradiation of the disk surface by strong UV radiation could generate a hot ionized layer in which the sound of speed reaches 10 km s^{-1}. The acceleration of the jet in this situation would not be associated to X-ray emission, making thermal pressure gradients a potential acceleration mechanism, but only for the low-velocity component of the wind, corresponding to a low-mass-loss rate.

Alfven-wave pressure gradients. Alfven waves were suggested by Decampli (1981) as a source of momentum transfer to the flow, under the form of an anisotropic pressure gradient. Such excitation of MHD waves appears possible at the stellar surface or magnetosphere given their deep convective layers and strong magnetic fields, but again the dissipations associated to the propagation of the required coherent Alfven waves (such as acoustic waves) yield excessive necessary value for the wave energy compared to that of the accretion. In addition to this, an efficiency problem would occur, similar as that associated to thermal pressure gradients.

Magneto-centrifugal MHD acceleration. Magneto-centrifugal acceleration presents the nice advantage of being an efficient process. Through this mechanism, a large-scale field exerts a braking torque on a rotating object, transferring momentum towards the outflowing gas, later accelerated by centrifugal and Lorentz forces along the field lines. The rotating object can be the star, disk, or infalling envelope, and the high efficiency of the process is due to that of the conversion from rotation to kinetic energy.

The situation in which the field lines are anchored in the disk imply a high ratio of jet to accretion power, both compatible with the typical observed maximum jet speeds and the current estimates/upper limits on rotation speeds in jets. The jet launching region can either be extended (with an inner edge around five stellar radius), but require a yet to be determined heating source near the disk surface, or consist of a narrow annulus at the inner edge of the disk, in which case higher poloidal speeds and smaller rotation signatures are predicted in the outer regions of the jet.

The field lines can also be anchored in the star, in which case the magneto-centrifugal ejection has been proved to be a natural and fast means to spin down protostars in various situations. However, the correlation with accretion is indirect in this case, and the efficiency of this mechanism depends on the stellar rotation rate. The reconnexion X-wind model of Ferreira et al. (2000), in which the matter is loaded on the field lines not at the stellar surface, but near the corotation point of the disk (where the keplerian rotation velocity equals the stellar rotation one), might overcome these problems. The

episodic mass loading location occurs at the reconnexion point between closed stellar field lines and open disk field. An ejection/accretion correlation is still expected, the mass-loss efficiency may not vary excessively with the stellar rotation, and good agreement with observations of terminal jet speeds, spin down and disk accretion rate evolution is found.

Relaxation of twisted magnetospheric field : magnetic tower. The last ejection mechanism invoked requires particular conditions as the absence of significant disk magnetic field, or the presence of a disk field anti-parallel to the stellar magnetic moment. In such models, closed loops of magnetospheric stellar winds interact with the inner disk, and any small differential twist between them triggers the stretching of magnetic loops , whose complex time-dependent evolution seems to result in outflows. The ejection yielded from such models tend to suffer from a lack of correlation with accretion, and the outflows produced in corresponding numerical simulations show no sufficient collimation (see for example Matt et al. (2002)).

1.4.3 Outflow models review

Our understanding of outflow activity has evolved with the progresses of computational power. Initially analytical, the models used to describe jets and/or outflows are now highly numerical, and include numerous ingredients, such as molecular cooling and chemistry. A detailed review of these models would be out of the scope of this introduction, so we present the basic ideas behind the four classes of existing outflow models, in accordance with Cabrit et al. (1997). Figure 1.11 summarizes the main observable predictions for each of these models class.

Wind-driven shell models. In the wind-driven model, a wide-angle wind blows into the stratified surrounding ambient medium, generating a thin swept-up shell : the outflow shell, hence made of entrained ambient material.

This model was initially developed by Shu et al. (1991), Li and Shu (1996), Matzner and McKee (1999). Recent numerical simulations include that of Delamarter et al. (2000) (spherical wind), Lee et al. (2001a) (atomic axisymmetric wind). The slope of the mass-velocity relation (see Subsection 1.2.2) generally inferred from these models corresponds to the low-velocity component. Wide-angle winds can readily produce outflows with large widths over timescales in agreement with observations, but they fail to generate discrete bow-shock structures in the entrained gas, as seen in many high-resolution CO maps for example, and discrete position-velocity spur structures. The addition of a collimated core with a strong dependence of the velocity field on the angle might be a solution but further work is currently required to validate it.

Gardiner et al. (2003) (MHD collimation effects), and Cunningham et al. (2005) (inclusion of molecular chemistry and cooling, and implementation of an Adaptative Mesh Refinement technique) produced satisfying outflow lobe appearance, but in these cases, no mass-velocity relation nor position-velocity or channel maps were generated, that could be compared to observations.

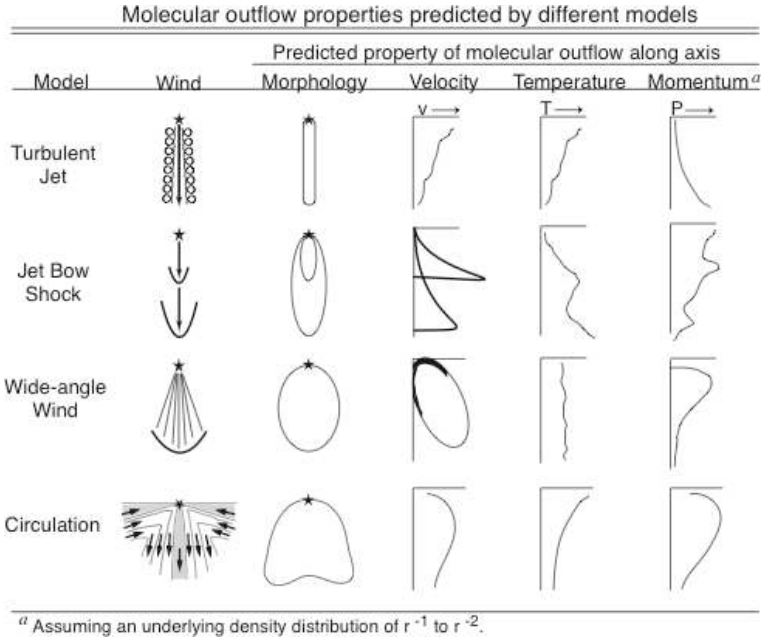

Figure 1.11 – Observable molecular outflows properties predicted by the four classes of models. Taken from Arce et al. (2007).

Turbulent jet models. The jet-driven turbulent model is based on the development of Kelvin Helmholtz instabilities along the jet/environment layer, leading to the formation of a viscous layer in which the ambient gas is entrained in a eventually completely turbulent flow. This model is discussed in Canto and Raga (1991), and Cantó et al. (2003) for example, but only one group has developed numerical simulations that could be compared with observations. Indeed, without including molecular cooling or chemistry, Micono et al. (1998) generated atomic emission predictions, later completed by successful mass-velocity relation predictions Micono et al. (2000). However, these models do currently predict decreasing molecular outflow momentum and velocity with the distance from the source, in contradiction with the observations.

Jet bow-shock models. In the jet-driven bow-shock models, a highly collimated jet of uncertain physical origin propagates into the surrounding ambient medium, producing a thin outflow shell around the jet (see Figure 1.12). The jet-ambient medium impact results in two shocks, a jet shock and a bow-shock, at the head of the jet. Between the shocks, the gas undergoes high pressure conditions and is ejected sideways out of the jet beam, which then interacts with the ambient unperturbed material through a broad bow-shock, producing an outflow cavity surrounding the jet. A variation in the mass-loss rate naturally leads to the production of knotty shocks along the jet axis.

This class of models was first presented by Raga and Cabrit (1993). Recent efforts have been made, that focus on non-magnetic jet bow-shocks models and are stressed out in the brief review of Arce et al. (2007) who cites two groups :

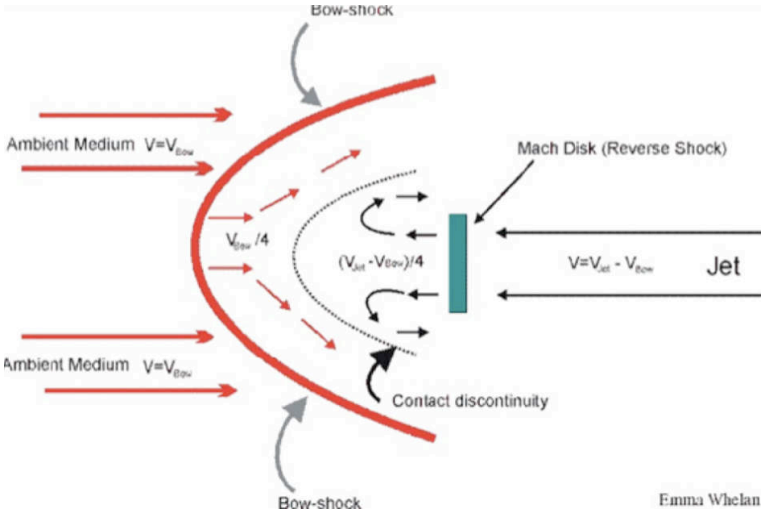

Figure 1.12 – Sketch of the jet bow-shock configuration.

- Downes and Ray (1999), Downes and Cabrit (2003), who simulated low density, axisymmetric, two-dimensional, mainly molecular jets with no chemistry nor cooling below 1000 K, insisting on the resolution of the post-shock region. The initial jet velocities depend on shear and pulsation ;
- Smith and Rosen (2003), Rosen and Smith (2004) investigated fully three-dimensional, mainly molecular flows with cooling and chemistry at all temperatures and an equilibrium assumption for certain reactions, hence under-resolving the post-shock region. The initial jet velocities also vary with shear and pulsation, and also with precession.

The comparative review of the results yielded by these works can be found in Arce et al. (2007), providing different advantages when comparing them to observations owing to their different assumption choices. Nevertheless the degree of satisfaction reached in such comparisons in terms of mass-velocity or position-velocity is rather good. Magnetic fields have also been included in recent simulations (see Arce et al. (2007) and references therein), as well as complex chemistry and instability studies (Lesaffre et al. (2004a), Lesaffre et al. (2004b)).

Generally speaking, this category of models provide outflow widths good agreement with observations of highly collimated outflows, but fail to explain them when the observed outflows are poorly collimated. They also meet difficulties to generate the observed values for outflow momentum. The wandering of the outflow axis, mentioned in Subsection 1.2.2 could mitigate these discrepancies.

Circulation models. In circulation models, the molecular outflows are not made of entrained ambient gas, but of infalling gas, deflected away from the protostar in a central torus of high MHD pressure through a quadrupolar circulation pattern around the protostar, and accelerated above escape speed by local heating. Consequently, most of the infalling circumstellar material is magnetically diverted at large radii into a slow-moving outflow along the polar direction, while infall processes along the equatorial plane. The outflow may still be affected by entrainment from the wind or jet, but only in a limited

extent, to the polar regions. This class of models was suggested by Fiege and Henriksen (1996a), Fiege and Henriksen (1996b), and further numerical simulations brought attraction to these models (Lery et al. (1999), Lery et al. (2002), Lery (2003)), as :

- around low-mass protostars, large outflow-masses can be generated, and satisfactory relation between $F_{\rm CO}$ and $L_{\rm bol}$ can be found in model cases where radiation transport is important. The addition of Poynting flux in the model also allowed for the generation of outflows of sufficient speeds (see for example Combet et al. (2006)) ;
- in outflows from high-mass stars, the observed opening angles and velocity structures can be explained by these models.

Several concerns still remain about the circulation models, namely, the apparent lack of molecular material in the equatorial plane which could feed a circulation flow in objects such as B5 (Velusamy and Langer (1998)), or the direct evidence for fast jets and bow-shock entrainment in some high-mass systems. The existence of unipolar outflows (see Subsection 1.2.2) also contradicts these models, but coud find explanations in other considerations as the formation of the outflow on the edge of a cloud or close to an H II region interface.

Other models. In this paragraph, we can cite the plea of Arce et al. (2007) in favor of combination of jet and wide angle wind models, that would match observations at different wavelengths. Very recently, Machida et al. (2007a), Machida et al. (2007b) managed to account for such a dual outflow to arise, based on the double core collapse occurring at the end of the prestellar phase, as mentioned in Subsection 1.1.4.

Outflows around high-mass protostars. Although most on the simulations work has been focusing on low-mass star outflows. Nevertheless some properties (such as the CO spatial and velocity structure) appear similar over a broad range of luminosities Richer et al. (2000), suggesting common production mechanisms. Recent simulations (disk-outflow connection, Pudritz and Banerjee (2005)) and observations (Beuther et al. (2004)) seem to acknowledge the trend that outflows from high-mass stars could be scaled up versions of that arising around low-mass stars.

1.4.4 Open questions

After this overview of observations and inferred properties of every currently possible manifestations of outflow activity, we briefly review the significant issues that have eluded observational efforts so far.

The nature of the launching and collimating processes remain unclear. The possibility to distinguish one dominant, generic mechanism might be have to be abandoned in favor of a model in which these processes could depend on the stellar evolutionary stage , or on the mass of the forming star. Of particular importance is the role of magnetic fields, whose understanding probably requires more and more observational data. The question of the existence of a big picture over broad ranges of stellar masses and evolutionary ages is still an open one.

The recent progresses in numerical power have allowed for corresponding ones in terms of numerical simulations of all kind. However, the observational distinction between models in which jets are single entities and others where they are integrated with wide-angle winds is not yet entirely clear.

The study of the jet in a multiple stars configuration has to be entirely conducted. The role of the frequently observed companions in the formation and evolution of jets has to be determined. Particularly, the directional stability of jets over long periods of time has to be understood if most sources are binaries.

The connection between the numerous observational manifestations of outflows activity (optical shocks, molecular hydrogen, dust thermal and non thermal emission) has also to be established, preferably in relation within the frame of the rich shock chemistry. This highly peculiar chemistry also needs further understanding : the formation/destruction balance of some species is still unclear. Extensive experimental and theoretical work is still needed on chemical reaction and collision rates, and numerical modelling must include these data as accurately as possible. Progresses must also be achieved in the detection of some high energy signatures, such as X-rays.

From these points of view, the future years look particularly exciting, since it will involve every kind of research area. Observers will be sought thanks to the recent progresses in ground-based detection, but also by the large playing field opened by the arrival of new instruments in the coming years. Modelling teams will have to optimize their use of numerical simulations in accordance with the always improving accuracy and efficiency in terms of calculations power. Chemists (experimentalists and theorists) will also be needed to provide them with always more ingredients to include in the models.

2

Modelling interstellar shocks

Ce chapitre constitue une brève introduction à une simulation des flots bipolaires reposant sur l'utilisation du formalisme des ondes de choc. Ce formalisme est d'abord présenté dans le cadre de la modélisation d'ondes de chocs stationnaires. Les équations sur lesquelles reposent cette modélisation sont ensuite introduites, ainsi que quelques processus microscopiques indispensables. Pour finir, la simulation de chocs non stationnaires à l'aide de chocs stationnaires est expliquée. Le lecteur intéressé pourra trouver une description extensive du code de choc utilisé dans la remarquable présentation de Guillet (2008).

We briefly describe here the ways to model interstellar shocks by means of the shock waves formalism, in two different situations : with or without magnetic field. For an extensive description of the shock code that we used, the interested reader can refer to the remarkable presentation in Guillet (2008).

2.1 Stationary shock models

Whenever a gas is compressed by a 'piston' moving at a speed greater than the sound velocity in the gas, the gas molecules ahead of the compression wave cannot receive a signal that the piston is approaching. The result of this type of motion is that a transition region is set up in the gas across which the properties of the gas change abruptly. In many circumstances this transition region is narrow relative to other dimensions in the gas, and we refer to it as a shock front and treat it as a discontinuity. Across the shock front the density, pressure, velocity, and other parameters of the gas change discretely.

One can define a shock as being the propagation at a supersonic speed of an irreversible, pressure-driven fluid-dynamical disturbance. In fact, even in the case of an adiabatic shock, where the medium does not exchange any heat with the exterior, the gas is heated, and entropy is generated.

Such situations frequently occur in the interstellar medium. Indeed, the temperature is usually low (10 K), and consequently, the sound velocity is low too, about 0.2 km s^{-1}. It is therefore frequent to observe supersonic flows, for example in the expanding ionized regions around hot stars, in the stellar winds of hot stars, in jets associated with star formation, in the explosions of supernovae, or in collision s between interstellar clouds.

2.1.1 Rankine Hugoniot equations

Before presenting the equations that allow us to model the shock, it is useful to recall some thermodynamical relations and definitions. Classically, one denotes by c_p and c_v the specific heats of the gas at constant pressure and volume respectively, with $\gamma = c_\mathrm{p}/c_\mathrm{v}$. In the case of a perfect gas the pressure p, density ρ and temperature T are connected by the equation

$$p = \frac{\rho R T}{m} \tag{2.1}$$

where R is the universal gas constant, and m is the molecular weight in terms of the mass of the hydrogen atom. For adiabatic motion, a fluid element neither gains nor loses heat, and the additional relation holds,

$$p = k\rho^\gamma \tag{2.2}$$

Finally, the entropy of a perfect gas is by definition

$$S = c_\mathrm{v} \log\left(\frac{p}{\rho^\gamma}\right) \tag{2.3}$$

apart from a constant.

We place ourselves then in the reference frame of the shock, and we take the suffixes 1 and 2 to refer to the pre-shock and post-shock region respectively. The conservation laws for mass, momentum, and energy, developed together with the few relations above (see Kendall and C. (1964)), provide the following jump conditions (also called Rankine-Hugoniot equations in a more generic form)

$$\rho_1 v_1 = \rho_2 v_2 \tag{2.4}$$

$$\rho_1 v_1^2 + \rho_1 \frac{kT_1}{\mu} = \rho_2 v_2^2 + \rho_2 \frac{kT_2}{\mu} \tag{2.5}$$

$$\frac{1}{2}\rho_1 v_1^3 + \frac{\rho_1 v_1}{\mu}\left(\frac{5}{2}kT_1 + U_1\right) = \frac{1}{2}\rho_2 v_2^3 + \frac{\rho_2 v_2}{\mu}\left(\frac{5}{2}kT_2 + U_2\right) \tag{2.6}$$

where U is the internal energy of the molecules, v the velocity of the flow in the reference frame of the shock, μ the mean molecular mass, and ρ the mass density. The term $(5/2)kT$ contains the work of the pressure forces and the thermal energy.

Knowing these relations, and considering the relation defining the entropy for a perfect gas (see above Equation 2.3), one can show that the entropy increases during the shock if and only if the pressure in the post-shock region is superior to the one in the pre-shock region. It follows that all shock waves are compression shocks. One can also show, with the help of equation 2.1 that the temperature increases across the shock (all these calculations are provided by Kendall and C. (1964)). Furthermore, if the compression rate is such that $p_2/p_1 \rightarrow \infty$, the density ratio is such that $\rho_2/\rho_1 = (\gamma+1)/(\gamma-1)$. For strong blast waves it sometimes appears that the appropriate value of γ is nearly unity, allowing large density increases.

2.1.2 Single fluid and multi fluids shock models

These two situations, single fluid or multifluid, can be defined with respect with the value of the magnetic field for example, and both correspond to a set of physical conditions that are consequences of this value.

When the magnetic field is weak or non-existent, all components (e.g. atoms, ions, and electrons) may be approximated as having a common flow velocity v. The gas follows the laws of fluid dynamics, and is consequently following matter, momentum and energy conservation laws. The shock corresponds to the supersonic propagation of a pressure variation and is sometimes called 'hydrodynamical'. One can observe J-type shocks ('J' being for Jump), because quantities such as temperature and density undergo a discontinuity (see Figure 2.1). The gas is heated, accelerated and compressed by the shock waves, and then cools down through the emission of its components, atoms or molecules. In the post-shock region, where the gas has enough time to radiate, it cools at constant pressure, which provokes a bigger compression. In sufficiently dense media (molecular clouds, protostellar jets...), one observes mainly the isobaric phase in the J-type shocks. One can also notice that a J-type shock is not a real discontinuity because of the fact that temperature and density change on a spatial scale of about the mean free path. In this situation the medium is called single fluid.

One consequence of the magnetic field, orientated parallel to the shock front, is a partial decoupling of the flows of the different components of the medium through the shock :

- the charged particles gyrate around the magnetic field lines and are consequently coupled to this field ;
- the neutral particles are affected only indirectly by the magnetic field, through collisions with the positive ions (and electrons) ;
- the grains, that are also charged, are coupled to the magnetic field.

The magnitude of the difference between the flow velocities of the charged and the neutral species depends directly on the rate coefficients for the collisional processes between neutral and charged particles. Numerical modelling has shown that the ion-neutral drift velocity can attain a significant fraction of the shock speed, typically several km s^{-1}. The kinetic energy associated with this non thermal motion is sufficiently large to overcome the endothermicities of chemical reactions which would not occur in normal conditions. On the other hand, the conservation of charge implies that ions and electrons move with the same velocity (a relative drift between the two kinds of charge would generate an electric field which would oppose itself to it), but their temperatures are different.

The considered medium is a dense molecular cloud, weakly ionized (and mainly by cosmic ray ionization of molecular hydrogen), with $n_{\mathrm{H}} = n(H) + 2n(H_2) \sim 10^4$ cm^{-3}. In the interstellar medium, the characteristic time of scattering of the magnetic field is generally much longer than to the characteristic time of advection. One can therefore assume that the field is 'frozen' in the ionized fluid. We also assume that this magnetic field is transverse to the flow. In this configuration, Maxwell's equations add up to the fluid dynamics ones, and the shock is deemed 'magnetohydrodynamical' (MHD).

In the charged fluid, compressive, magnetosonic waves can propagate with the velocity :

$$V_{\rm cms} = \sqrt{c^2 + \frac{B^2}{4\pi\rho_{\rm c}}} \simeq \frac{B}{\sqrt{4\pi\rho_{\rm c}}} \tag{2.7}$$

where $\rho_{\rm c}$ is the volume mass of the charged particles, which include ions, electrons, and grains, standing for approximately 1 % of the gas mass. Typically when this velocity exceeds that of the shock, magnetosonic waves propagate faster in the charged fluid than the shock front. Ahead of this shock front, a *magnetic precursor* appears, heating, slowing and compressing the charged fluid of the pre-shock gas before the arrival of the shock front, on spatial scales much larger than the mean free path. This magnetic precursor decouples the neutral and charged fluid, generating ambipolar scattering, that is the friction between the fluids. For a sufficient value of the magnetic field, resulting exchanges of momentum and energy in the precursor are more important, and the neutral fluid itself is likely to be heated, compressed and slowed before the arrival of the shock front.

Because of this slowing down, the neutral fluid also undergoes a velocity jump of a smaller amplitude than in the situation where there is no magnetic field, as one can see on Figure 2.1. Such a shock is called J-shock with magnetic precursor. An order of magnitude of the size of this precursor is provided by the following expression (see for example Draine (1980))

$$L \simeq \frac{8B_0^2}{\mu_0} \frac{\mu_{\rm n} + \mu_{\rm i}}{\rho_{\rm i0}\rho_{\rm n0} < \sigma v >_{\rm in} v_{\rm s}} \tag{2.8}$$

To calculate this characteristic size, one use the conservation of momentum (equation 2.15) in which the two first terms are neglected. Only the elastic ion/neutral collisions are taken into account, and it is assumed that $v_{\rm i} = v_{\rm s}/2$ and $v_{\rm n} = v_{\rm s}$. The complete calculation can be found in Draine (1980).

If the intensity of the magnetic field increases, the size of the precursor increases, and the neutrals (through the ions) are compressed sooner : the discontinuity vanishes, and the shock turns into a C shock (C being for continuous), see Figure 2.1.

The distinction between J shocks and C shocks is relevant with respect to the differences of their characteristics. For example, in a C shock, the maximal temperature (about 500 K at a shock speed of $v_{\rm s} = 10$ km s^{-1}, and a pre-shock density of $n_{\rm H} = 10^4$ cm^{-3}) is much lower that the one that can be reached in a J shock, because the energy is dissipated along a longer distance : ~ 0.1 pc for a C shock, and $\sim 10^4$ pc for a J shock. The critical magnetic field $B_{\rm crit}$ allowing to distinguish J shocks from C shocks can be found analytically only for adiabatic shocks. In practice, the only way to determine $B_{\rm crit}$ is by obtaining numerical solutions for the shock structure for various values of B_0, starting with a small value and increasing B_0 until the J front compression ratio drops to unity.

2.1.3 The shock code inputs

At this point, for clarity reasons, it is useful to precise the choice of some physical and chemical parameters that are of special importance in the shock code that we use, such

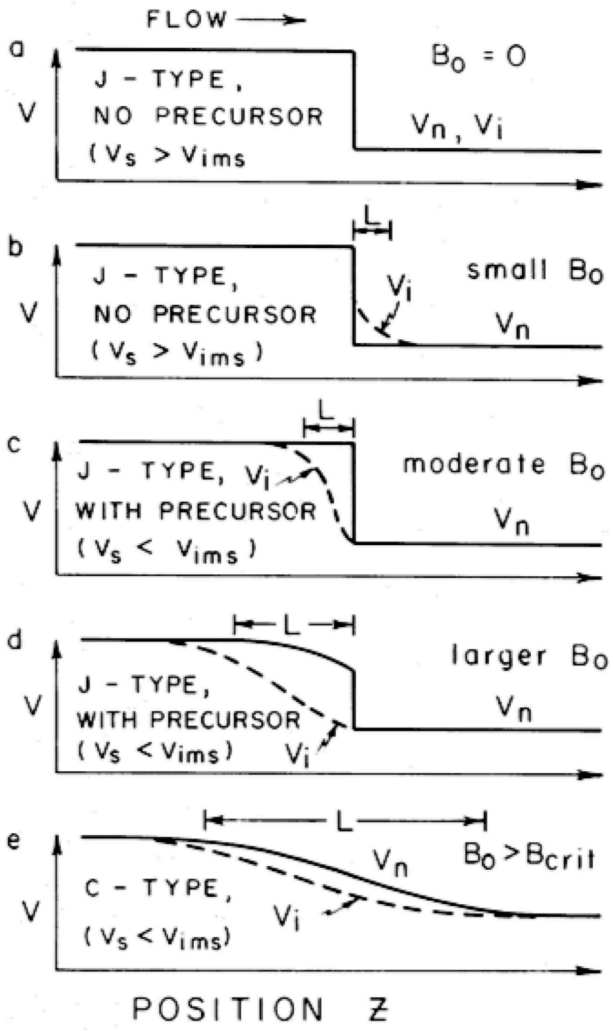

Figure 2.1 – Schematic structure of the velocity of a stationary adiabatic shock wave in poorly ionized medium, as a function of the local magnetic field strength B_0. The velocities are given in the frame where the shock front is idle : v_n is the neutral velocity in the propagation direction of the shock, v_i that of the ions and electrons. The pre-shock medium is on the left hand side of the shock front, the post-shock on its right hand side. L is the shock length, and v_{ims} is the ions magnetosonic speed (the dust grains were ignored in this model).

as the initial condition parameters or such as the variables that are resolved at each point of our models. As we have seen in the previous Subsection, in order to treat stationary C-type shock waves, one must distinguish three fluids when resolving their structure : the charged particles, the neutral particles, and the electrons are hence considered to belong to three different fluids. Consequently, 11 variables related to the physical parameters of these fluids are resolved in the shock code :

- $v_{\rm n}$, $v_{\rm i}$ are the velocities of the neutral and the ionized species ;
- $\rho_{\rm n}$, $\rho_{\rm i}$ are the volume masses of the neutral and the ionized species ;
- $\rho_{\rm neg}$ is the volume mass of the negative ions ;
- $T_{\rm n}$, $T_{\rm i}$, $T_{\rm e}$ are the respective temperatures of the neutral, ionized, and electrons fluid ;
- $n_{\rm n}$, $n_{\rm i}$ are the number densities of the neutral and ionized species ;
- the neutral velocity gradient is the last necessary variable.

To resolve the shock models, initial conditions are required, that are the main specifications related to the kind of shock that is to be modelled :

- the type of shock (C, J, or steady-state to compute the equilibrium state that defines the initial composition of the gas) ;
- the associated number of fluids (1, 2, or 3) ;

Various informations about the initial state of the gas are also required :

- the initial gas temperature ;
- the grains temperatures ;

Of particular importance are the following parameters :

- the shock velocity $v_{\rm s}$;
- the pre-shock density $n_{\rm H}$;
- the magnetic field parameter b.

Regarding the magnetic field, we use the phenomenological law (see Crutcher (1999)) for its intensity

$$B(\mu G) = b\sqrt{n_{\rm H}({\rm cm}^{-3})} \tag{2.9}$$

where b denotes the 'magnetic field parameter', in the pre-shock region.

Output specifications options, numerical parameters (such as the integration time), environment characteristic values (suc as the cosmic ray ionization rate), and some other requirements that will be detailed when convenient in this document, are also present in this file.

2.2 Equations of conservation

As the magnetic field interacts directly only with the charged particles, it is necessary to consider at least a two-fluid model of the shock region. Substantial differences may develop between the flow velocities and kinetic temperatures of the ionized and neutrals fluids.

Whilst the preservation of charge neutrality requires that the flow velocity of the positive ions, v_i, and the electrons, v_e, should be the same, the kinetic temperatures of ions and electrons may differ if Coulomb scattering is insufficiently rapid to maintain a common thermal distribution. Accordingly, we consider a three-fluid model of the medium.

The suffixes n, i, and e will refer to the neutral fluid, the ionized fluid, and the electrons respectively.

Let us denote by z the independent variable, which is the distance from some arbitrary reference point along the positive flow direction. The magnetic induction, which is taken to be perpendicular to the flow, will be denoted by B. We consider a plane-parallel shock in a stationary state, in which the magnetic field is 'frozen' into the ionized gas. All the following equations are given in Flower et al. (1985).

2.2.1 Particle number and density conservation

For the three fluids, conservation of particle number density requires that

$$\frac{d}{dz}\left(\frac{\rho_{\rm n} v_{\rm n}}{\mu_{\rm n}}\right) = \mathcal{N}_{\rm n} \tag{2.10}$$

where $\rho_{\rm n}$ is the mass density of the neutral particle and $\mu_{\rm n}$ the mean molecular weight ; $\mathcal{N}_{\rm n}$ is the number of neutral particles created per unit volume and time.

The corresponding equation for the positive ions is

$$\frac{d}{dz}\left(\frac{\rho_{\rm i} v_{\rm i}}{\mu_i}\right) = \mathcal{N}_{\rm i} \tag{2.11}$$

As we assume charge neutrality, the equation for electrons is identical to 2.11. One can also write the conservation of particle number density for each species

$$\frac{d}{dz}(n_\alpha v_\alpha) = \mathcal{C}_\alpha \tag{2.12}$$

where n_α is the particle number per unit volume, v_α is the velocity of the considered particle, and $\mathcal{N}_\alpha$ is a source term for the species α.

2.2.2 Mass conservation

The equation expressing the conservation of the mass of the neutral particles and of the ionized particles may be written

$$\frac{d}{dz}(\rho_{\rm n} v_{\rm n}) = \mathcal{S}_{\rm n} \quad \text{and} \quad \frac{d}{dz}(\rho_{\rm i} v_{\rm i}) = \mathcal{S}_{\rm i} = -\mathcal{S}_{\rm n} \tag{2.13}$$

considering that neutral mass may be created only through the destruction of ionized mass. $\mathcal{S}_{\rm n}$ is the corresponding source term. The mass of the electrons is negligible.

2.2.3 Momentum conservation

The equation of momentum conservation is, for the neutrals,

$$\frac{d}{dz}\left(\rho_{\rm n} v_{\rm n}^2 + \frac{\rho_{\rm n} k_{\rm B} T_{\rm n}}{\mu_{\rm n}}\right) = \mathcal{A}_{\rm n} \tag{2.14}$$

where T_n is the kinetic temperature of the neutral gas and k_B is Boltzmann's constant ; $\mathcal{A}_\mathrm{n}$ denotes the change in momentum of the neutral fluid per unit volume and time.

In the case of the ion-electron fluid, account must also be taken of the compression of the magnetic field

$$\frac{d}{dz}\left[\rho_\mathrm{i} v_\mathrm{i}^2 + \frac{\rho_\mathrm{i} k(T_\mathrm{i}+T_\mathrm{e})}{\mu_\mathrm{i}} + \frac{B^2}{8\pi}\right] = -\mathcal{A}_\mathrm{n} \tag{2.15}$$

Denoting the unperturbed value of the magnetic induction by B_0, and the shock velocity by v_s, the fact that the field is frozen in the ionized fluid implies that $Bv_\mathrm{i} = B_0 v_\mathrm{s}$, flow velocity being expressed in the frame of reference of the shock. Equation 2.15 then becomes

$$\frac{d}{dz}\left[\rho_\mathrm{i} v_\mathrm{i}^2 + \frac{\rho_\mathrm{i} k(T_\mathrm{i}+T_\mathrm{e})}{\mu_\mathrm{i}} + \frac{B_0^2}{8\pi}\left(\frac{v_\mathrm{s}}{v_\mathrm{i}}\right)^2\right] = -\mathcal{A}_\mathrm{n} \tag{2.16}$$

Once again, the inertia of electrons has been neglected.

2.2.4 Energy conservation

The conservation of energy of the neutral particles may be expressed as

$$\frac{d}{dz}\left[\rho_\mathrm{n} v_\mathrm{n}^3 + \frac{5}{2}\frac{\rho_\mathrm{n} v_\mathrm{n} k T_\mathrm{n}}{\mu_\mathrm{n}} + \frac{\rho_\mathrm{n} v_\mathrm{n} U_\mathrm{n}}{\mu_\mathrm{n}}\right] = \mathcal{B}_\mathrm{n} \tag{2.17}$$

where U_n is the mean internal energy per neutral particle, and $\mathcal{B}_\mathrm{n}$ is the corresponding source term, the change in energy of the neutral fluid per unit volume and time.

For the ion-electron fluid, if we neglect the contribution of the internal energy of the ions, we have

$$\frac{d}{dz}\left[\rho_\mathrm{i} v_\mathrm{i}^3 + \frac{5}{2}\frac{\rho_\mathrm{i} v_\mathrm{i} k(T_\mathrm{i}+T_\mathrm{e})}{\mu_\mathrm{i}} + \frac{B_0^2}{4\pi}\frac{v_\mathrm{s}^2}{v_\mathrm{i}}\right] = \mathcal{B}_\mathrm{i} + \mathcal{B}_\mathrm{e} \tag{2.18}$$

For all these equations of conservation (number, mass, momentum, energy), source terms have to be estimated. These source terms can be the results of different kind of processes arising in the shock context. The most general chemical and physical processes are discussed in Appendix A, and Appendix B deals with the effects of molecular cooling.

2.3 Microscopic processes

2.3.1 The influence of chemistry

Shocks are likely to play an important role in the evolution of the interstellar medium, from a dynamical and chemical point of view. The shock chemistry is indeed very different from the one that one can study in the 'normal' interstellar medium. In fact, whilst they can be neglected in models of the cold, ambient medium, endothermic reactions and those with barriers of up to approximately 1 eV must be considered in shocks. However, there is a compensating reduction in complexity, which is a consequence of the restricted time that an atom or molecule spends within the region of the shock. This time, which is typically

in the range 10^3-10^4 years, is much smaller than the lifetime of a molecular cloud, which may be as long as 10^7 years. It follows that only rapid chemical and physical processes are important within shocks, leading to a simplification of their chemistry.

Through these chemical processes, species are formed or destroyed, ions or neutral added to the corresponding fluids, that then play a role in the thermal balance of the shock, which has an influence on the number of reactions the shock can initiate, and so on. For example, the old question of explaining the amount of CH^+ has perhaps found its solution with the study of interstellar shocks (for further details on this particular aspect, see the Appendix C). Further details about shock chemistry can also be found in Flower (1987), and Pineau des Forets et al. (1997).

The chemical network used in this model takes more than 120 species (see Appendix M) and around 1000 chemical reactions (see Appendix N). The fractional abundances of these species is hence added to the list of unknown variables of the shock code, an their initial value is calculated through the use of a stationary state of the shock code, that simulates the equilibrium state of the considered region. The Figure 2.2 shows the difference of the results obtained with or without taking the chemistry into account.

- in the latter case, the ionization fraction varies only through the differential compression of the ionized and neutral fluids by the shock wave, and has the same value in the pre- and post-shock regions ;
- taking the chemistry into account yields a much lower degree of ionization, leading to weaker ion-neutral coupling, hence broadening the width of the shock wave. Since the energy is dissipated on a larger region as compared to the first case, the maximum temperature is lower (here approximately twice lower).

2.3.2 Grains-neutrals coupling effects

Gas-grains interactions can have important consequences on physical and chemical properties of the shock. In fact, grains can generate formation or removal of molecules of the gas, and their inertia can modify the propagation of the shock, specially in the case of C shocks. Consequently, it is necessary to model the grains behavior with the best accuracy possible.

Interstellar grains population spreads from Polycyclic Aromatic Hydrocarbons (PAH) to much larger particles. Observational constraints on dust in the dense interstellar medium are compatible with models in which spherical and homogeneous grain cores are made of silicate or carbonated material and coated by grain mantles made of various molecular ices. The initial composition of the grains mantles and the elemental depletion into the grains cores is based on observations (see Flower and Pineau des Forêts (2003)). Interstellar grains population spreads from 'Very Small Grains' (VSG), represented by 'Polycyclic Aromatic Hydrocarbons' (PAH), to much larger particles, made of amorphous carbon and silicates. PAH are incorporated with a fractional abundance $n_{PAH}/n_{\rm H} = 10^{-6}$, an upper limit consistent with estimates of the fraction of elemental carbon likely to be present in the form of VSG (Li and Draine (2001), Weingartner and Draine (2001)).

The adopted size distribution for the grains is the one of Mathis et al. (1977), deduced from diffuse interstellar medium observations in the vicinity of the Solar system :

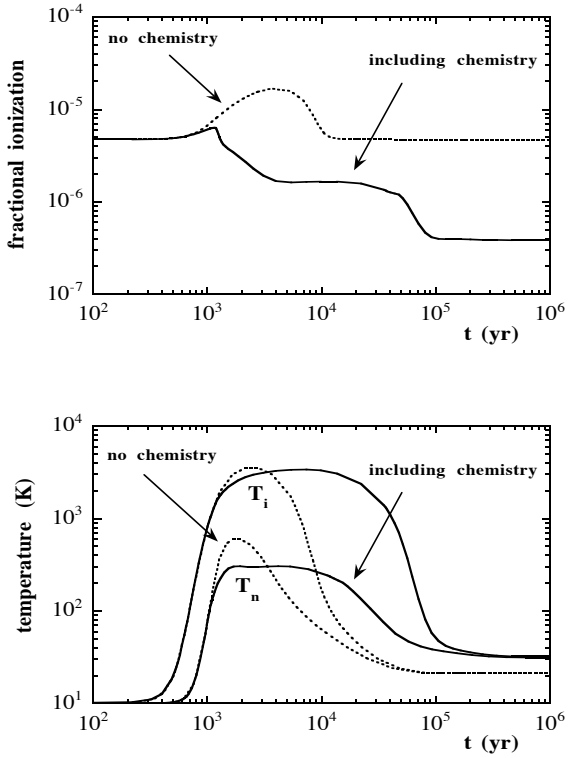

Figure 2.2 – Above : fractional ionization predicted by a model in which $v_{\rm s} = 10$ km s^{-1}, $n_{\rm H} = 10^3$ cm^{-3} and $B_0 = 25\mu$G ; results are compared including and neglecting chemical reactions. Below : Corresponding temperature profiles of the ionized and neutral fluids. Taken from Pineau des Forets et al. (1997).

Tableau 2.1 – Initial repartition of the refractory elements in the gas phase and in the grain mantles and cores (Flower and Pineau des Forêts (2003)). Numbers in parentheses are powers of 10.

element	fractional abundance	gas	mantles	cores
C	3.55(-4)	8.27(-5)	5.53(-5)	2.17(-4)
O	4.42(-4)	1.24(-4)	1.78(-4)	1.40(-4)
Mg	3.70(-5)			3.70(-5)
Si	3.37(-5)			3.37(-5)
Fe	3.23(-5)	1.50(-8)		3.23(-5)

Tableau 2.2 – Initial repartition of chemical species in the grain mantles (Flower and Pineau des Forêts (2003)), relatively to hydrogen (first line), and water ice (second line). Numbers in parentheses are powers of 10.

CO	CO_2	CH_4	NH_3	H_2O
8.3(-6)	1.3(-5)	1.6(-6)	1.6(-5)	1.0(-4)
8.3%	13%	1.6%	16%	100%
CO	CO_2	CH_4	NH_3	H_2O
1.9(-5)	6.2(-6)	7.2(-6)	2.1(-7)	3.7(-6)
19%	6.2%	7.2%	0.21%	3.7%

$dn_g(a)/da \propto a^{-3.5}$, where $dn_g(a)$ is the grain density of grains having a radius between a and a+da. Respective upper and lower limits of the grains radius is assumed to be 0.3 μm and 0.01 μm. With such a distribution, small grains are the most numerous, but large grains provide more contribution to the mass.

The total number density of the grains is also computed

- from the total mass of the refractory grain cores which is 0.78×10^{-2} times that of the gas for the adopted composition of the grain cores ;
- assuming a bulk density of 3 g cm^{-3}.

The thickness of the grains mantles is determined from their molecular composition, assuming a mean number of 5×10^4 molecular binding sites per layer of the mantle and a thickness of 2×10^{-4} μm for each layer, independent of the grains core. This procedure yields an initial mantle thickness of 0.015 μm on the grains cores, whose mean radius is 0.02 μm. However, the sputtering of these grains mantles occurs sufficiently rapidly that the existence of thick ice mantles in the pre-shock gas has little effect on the shock dynamics.

A detailed review of the grains involving processes taken into account, as well as their significant effects on C-shock waves can be found in Flower and Pineau des Forêts (2003). We extract two Tables from this article, 2.1 and 2.2 that respectively provide the initial repartition of refractory elements in the gas phase and dust grains, and the initial

composition of the grain mantles. The refined taking into account of the interactions the grains material is involved in itself gives birth to the necessity of modelling other processes, like erosion, sputtering or fragmentation of the grains (see Guillet et al. (2007) and references therein for a recent analysis).

2.3.3 Dissociation, ionization, and shock structure

An important parameter when one study the emission of molecules in the shock region is the temperature, which influences the abundance as well as the excitation of these molecules. These parameters themselves are then likely to modify the structure of the shock. For example, the dissociation or ionization of an important gas coolant such as H_2 will lead to the slowing of the cooling, that itself can yield the coolant's reformation, having critically modified the structure of the shock in the meantime.

A particular attention must then be brought to a sharp modelling of the ionization and dissociation processes for the most important molecules, but also to an accurate estimate of the ways the cooling occurs during and after the shock wave. One can cite the following processes as ones of importance, all of them being detailed in Le Bourlot et al. (2002) :

- formation, dissociation, and excitation of molecular hydrogen, that will be detailed in Section 3.2 ;
- ionization of H (through collisions with ions or electrons) ;
- cooling via rotational transitions of H_2O, CO, OH, and NH_3 ;
- cooling owing to fine structure transitions of C^+, C, O, and Si^+.

The influence of H_2 is considered in Chapter 3.

2.3.4 Critical velocities

Detailed modelling of such microscopic processes present another major interest for the study of C shocks. Indeed, the heating of the gas provoked by the propagation of the shock can generate the excitation and dissociation of H_2. Since H_2 is the main coolant of the gas in the regions of high temperature, a rapid increase of the kinetic temperature accompanies its dissociation. Owing to the low value of the sound velocity, a sonic point, that is the transformation of the C-type shock into a J-type shock, can then occur. Similarly, ionization of H_2 or H can also limit the maximum shock velocity, v_{crit}, for a C-type shock wave to be able to propagate. Indeed, an increase of the ionization fraction generates a higher coupling between neutral and charged fluids, that yields higher kinetic temperatures, and maybe generate a thermal runaway similar to that observed in J-type shock models. For example, when physico-chemical equations are parallely solved using the conservations equations as described in Section 2.2, for a pre-shock density of 10^4 cm^{-3}, and when the magnetic field parameter $b = 1$, the shock wave remains of C kind below $v_{\rm crit} = 70$ km s^{-1} (see Le Bourlot et al. (2002) for a first review of processes influencing this value).

Charged grains density and consequently gas-grains interactions modelling is also of particular importance regarding the limitation of the speed at which a C shock wave

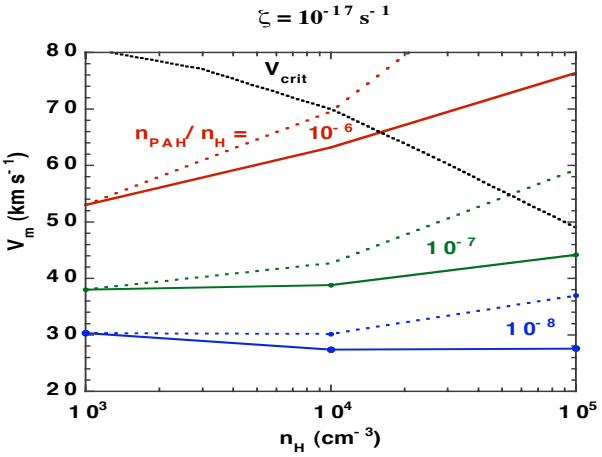

Figure 2.3 – Values of the magnetosonic velocity $v_{\rm m}$, numerically estimated for $10^3 < n_{\rm H} < 10^5$ cm^{-3}, $10^{-8} < n_{\rm PAH}/n_{\rm H} < 10^{-6}$, and $\zeta = 10^{-17}$ s^{-1}. The dash curves show the effects of the correction of collisional decoupling of the charged grains from magnetic field lines. The 'critical' velocity, $v_{\rm crit}$, beyond which the shock turns into a J shock (see Le Bourlot et al. (2002)), is also represented (point curve). Figure taken from Flower and Pineau des Forêts (2003).

can propagate. In fact, a necessary condition for the propagation of a C-type shock wave is that the magnetosonic velocity is greater than the shock velocity. The magnetosonic velocity in the charged fluid is

$$c_{\rm m}^2 = \frac{5k_{\rm B}(T_+ + T_-)}{3(\mu_+ + \mu_-)} + \frac{B^2}{4\pi(\rho_+ + \rho_-)} \tag{2.19}$$

where $T_\pm$ are the temperatures, $\mu_\pm$ are the mean masses and $\rho_\pm$ are the mass densities of the positively and negatively charged fluids; B is the magnetic field strength in the pre-shock gas. The state of charges of grains is computed following Flower and Pineau des Forêts (2003). For instance, an increase of the the fractional abundance of PAH would result in higher values of this speed in the pre-shock gas, thereby enabling C-type shock waves to propagate at higher speeds. An example of the numerical evaluation of the magnetosonic velocity for a given set of parameters is given on Figure 2.3.

2.4 Non stationary shock models

2.4.1 Existence of non stationary shocks

The equations introduced in Section 2.2 incorporate the assumptions that a steady state has been attained ($\partial/\partial t \equiv 0$), and that the flow is one-dimensional along the z-axis. Such an approach presupposes that the time required to attain the steady state is short compared to other time scales characterizing the problem being studied. In particular, this implies that the mechanism driving the shock is maintained for a time which exceeds that required to reach the steady state.

Such assumptions are particularly convenient in the context of interstellar shocks. Indeed, as illustrated in Subsection 2.3.1, chemical abundances can not be left aside and must be integrated to the unknown quantities set, that already comprises the physical parameters of the different fluids. The variables set of the problem is consequently considerably enlarged by such a necessary inclusion, and its size makes it an impossible computational challenge to calculate a time-dependent solution. On the contrary, the resulting steady-state non linear differential equations can be integrated by means of algorithms adapted to 'stiff' problems.

Unfortunately it is very likely that there exist various situations in which the shock propagates but fails to attain a steady state. Chieze et al. (1998) provide an estimate of the characteristic time for recoupling between ions and neutrals, which is also the necessary time to reach a steady state

$$\left[\frac{dv_{\rm n}}{dz}\right]^{-1} \simeq [n_{\rm i} < \sigma v >_{\rm in}]^{-1} \tag{2.20}$$

where $< \sigma v >_{\rm in} \simeq 2 \times 10^{-9}$ cm^{-3} s^{-1} is the rate coefficient for elastic ion-neutral scattering. With the values of $n_{\rm H} = 10^{10}$m^{-3}, $\chi = 10^{-7}$ (degree of ionization), and a shock velocity $v_{\rm s} = 20$ km s^{-1}, one would obtain a time of 3×10^4 years.

From the observational point of view, this value definitely yields the necessity to find a way to model non stationary shock models. Class 0 outflows can be a few thousands of years old ; Gueth et al. (1998) estimated the dynamical age of the blue lobe of L1157 to be between 2000 and 3000 years old, and despite using a method subject to uncertainty, Wakelam et al. (2005) provide the value of 5×10^3 years for the NGC 1333-IRAS 2 flow. Well collimated molecular outflows from massive protostars can also prove to be less than a few times 10^4 years old (Arce et al. (2007)).

In addition to this, previous studies emphasize the necessity of non stationary shock models to account for molecular hydrogen emission observations arising from molecular outflows, in a way that will be detailed in Chapters 3 and 4. One can cite for example Flower et al. (2003), Giannini et al. (2004), Giannini et al. (2006).

2.4.2 Modelling of non stationary shocks

As seen above, the exact solution to this problem would require to solve the set of time-dependent non linear differential equations for the whole set of parameters, including the chemical abundances, given their influence on the shock structure. With over a hundred of chemical species bound by over a thousand of chemical reactions, this solution is simply not conceivable in terms of CPU time.

As a remedy, Chieze et al. (1998) have demonstrated the possibility to approximate non stationary shock waves with a mixture of C-type and J-type shock models, by means of a time stretching/pseudo-viscosity method. Non stationary shock waves have developed a magnetic precursor, but retained a steep J-type discontinuity. In practice, such shock waves are simulated by introducing a discontinuity into the flow at a given value of the fluid flow time, which then becomes a new parameter of the model (see Flower and Pineau des Forêts (1999)). The discontinuity is itself a J-type shock component, that takes over

the C-type shock model. The ionic flow time at which the discontinuity is introduced corresponds to an additional free parameter, that represents the shock age in our study. The termination point of the flow is determined such that the (ion) flow time in the C part of the shock wave, i.e. up to the J-discontinuity, and the flow time behind the discontinuity are equal. We refer to these non stationary models as 'CJ-type', as they possess both C- and J- type characteristics. In terms of input file of the steady shock code, the shock age parameter is the neutral flow time associated to the ionic flow time corresponding to the J-discontinuity inclusion.

We now explain the reason of this choice, following Gusdorf et al. (2008b). In the CJ-type shock models, the termination point of the flow was determined such that the (ion) flow time in the C part of the shock wave, i.e. up to the J-discontinuity, and the flow time behind the discontinuity were equal. In so far as the models are perceived as a set of quasi-time-dependent simulations of the flow, the termination point should correspond to the location of the 'piston' which drives the shock wave.

Let $u_{\rm p}$ be the speed of the piston (which is also the speed of the gas at the surface of the piston) and u_0 be the speed of the gas immediately upstream of the discontinuity, with these speeds being expressed in the shock frame. If $\rho_{\rm p}$ and ρ_0 are the corresponding mass densities, then

$$\rho_{\rm p} u_{\rm p} = \rho_0 u_0 \tag{2.21}$$

from the equation of continuity. Hence

$$u_{\rm p} = \rho_0 u_0 / \rho_{\rm p}. \tag{2.22}$$

The discontinuity advances at u_0 relative to the gas immediately in front of it, and the velocity of the piston, relative to this same gas, is $(u_0 - u_{\rm p})$. Thus, the speed of the discontinuity minus the speed of the piston is $u_{\rm p}$. In other terms, the discontinuity moves away from the piston at speed $u_{\rm p}$. As the discontinuity coincides with the surface of the piston at time $t = 0$, the age of the shock age is

$$t_{\rm s} = \int_0^p [(\rho_{\rm p}/\rho_0)/u_0] dz = [(\rho_{\rm p}/\rho_0)/u_0] \Delta z \tag{2.23}$$

where z is the position coordinate and Δz is the current distance between the discontinuity and the piston ; $t_{\rm s}$ is the time required for the discontinuity to move to its current position from its initial position, at the surface of the piston.

Using $t_{\rm s}$ as defined above to define the shock age has the advantage of removing the ambiguity of the flow times (ion and neutral) : behind the discontinuity, $u_{\rm i} = u_{\rm n}$. Because the flow speed rapidly attains its post-shock value ($= u_{\rm p}$) behind the discontinuity is approximately equal to $t_{\rm s}$. In the time $t_{\rm s}$ required for the discontinuity to separate from the piston and reach its current position, a magnetic precursor develops simultaneously upstream of the discontinuity.

Note, however, that the expression above for $t_{\rm s}$ does not give the shock age exactly, as it assumes that the speed of the discontinuity relative to the piston, $u_{\rm p}$, remains constant, whereas Fig.3d of Lesaffre et al. (2004a) shows that $u_{\rm p}$ decreases steadily as cooling sets in and the size of the velocity jump at the discontinuity decreases, following the growth of the precursor. A more accurate estimate of the age, under the (generally valid) condition

that the width of the region downstream of the J-discontinuity is much smaller than the width of the C part of the shock wave, upstream of the discontinuity (i.e. the 'magnetic precursor'), is the time of flow of the charged fluid through the precursor (Lesaffre et al. (2004b), Eq.(60)). It is this determination of the shock age that has been adopted in the present study.

2.4.3 Shock models

In this subsection, we present general shock profiles for some canonical shock examples. We study various ages of two reference shock models :

- $n_{\rm H} = 10^4$ cm^{-3}, $b = 1$, $v_{\rm s} = 25$ km s^{-1}, ages 175 and 500 years, and the corresponding steady-state, that is the C-type shock with the same input parameters ;
- $n_{\rm H} = 10^4$ cm^{-3}, $b = 1$, $v_{\rm s} = 50$ km s^{-1}, ages 10 and 500 years, and the corresponding steady-state, that is the C-type shock with the same input parameters.

We also present the profiles for corresponding J-type shock waves, computed with $n_{\rm H} = 10^4$ cm^{-3}, $b = 0.1$, and respectively $v_{\rm s} = 25$ and 50 km s^{-1}.

In Figure 2.4, the neutral temperature profile, fluid velocities (charged and neutrals), the compression factor, and the fractional abundance of molecular hydrogen are plotted against the flow time of the charged fluid, $T_{\rm i} = \int (1/v_{\rm i}) dz$, for the models specified above. The C- and CJ-types of shock correspond to different stages of the same shock model. It may be seen that the lower age, of 175 or 10 years respectively is insufficient for a significant magnetic precursor to develop at the corresponding shock speed. Some corresponding relevant quantities are given in Table 2.3.

In all cases, the initial rise in temperature is followed by radiative cooling and compression of the gas as it evolves towards its final, post-shock state. At 25 km s^{-1}, the shock wave is energetic enough to significantly dissociate the ambient molecular hydrogen only in the case of the J-type shock and of the youngest CJ-type one. In fact, in those cases, thanks to the quasi-discontinuous temperature rise, the maximum temperature is attained adiabatically ($\rm T_{max} \simeq 33000$, 32000 K respectively), and consequently much higher than in the C shock model case ($\rm T_{max} \simeq 1800$ K). At intermediate shock age, the J discontinuity starts at a speed slightly smaller than in the youngest case, and the maximum temperature is hence also slightly smaller ($\rm T_{max} \simeq 26000$ K). In the J-type shock wave, the high maximum temperature gives rise to rapid radiative cooling by H_2 and its rovibrational transitions towards approximately 10000 K. This rapid cooling is simultaneous with the drastic dissociation of molecular hydrogen, owing to the temperatures that are reached. The temperature then remains approximately constant in the region where the fractional abundance of molecular hydrogen is low and the cooling of the gas is dominated by atomic oxygen (which is the principal form of the corresponding element) and its fine structure transitions. The corresponding decrease of temperature is accompanied by the re-formation of H_2 (on grains), which then becomes the main coolant again and leads to the post-shock region. Because of the importance of the initial temperature rise, the cooling is very fast. In the CJ-type shocks, a sufficient amount of molecular hydrogen remains in the gas phase to ensure an efficient cooling, before the cut corresponding to

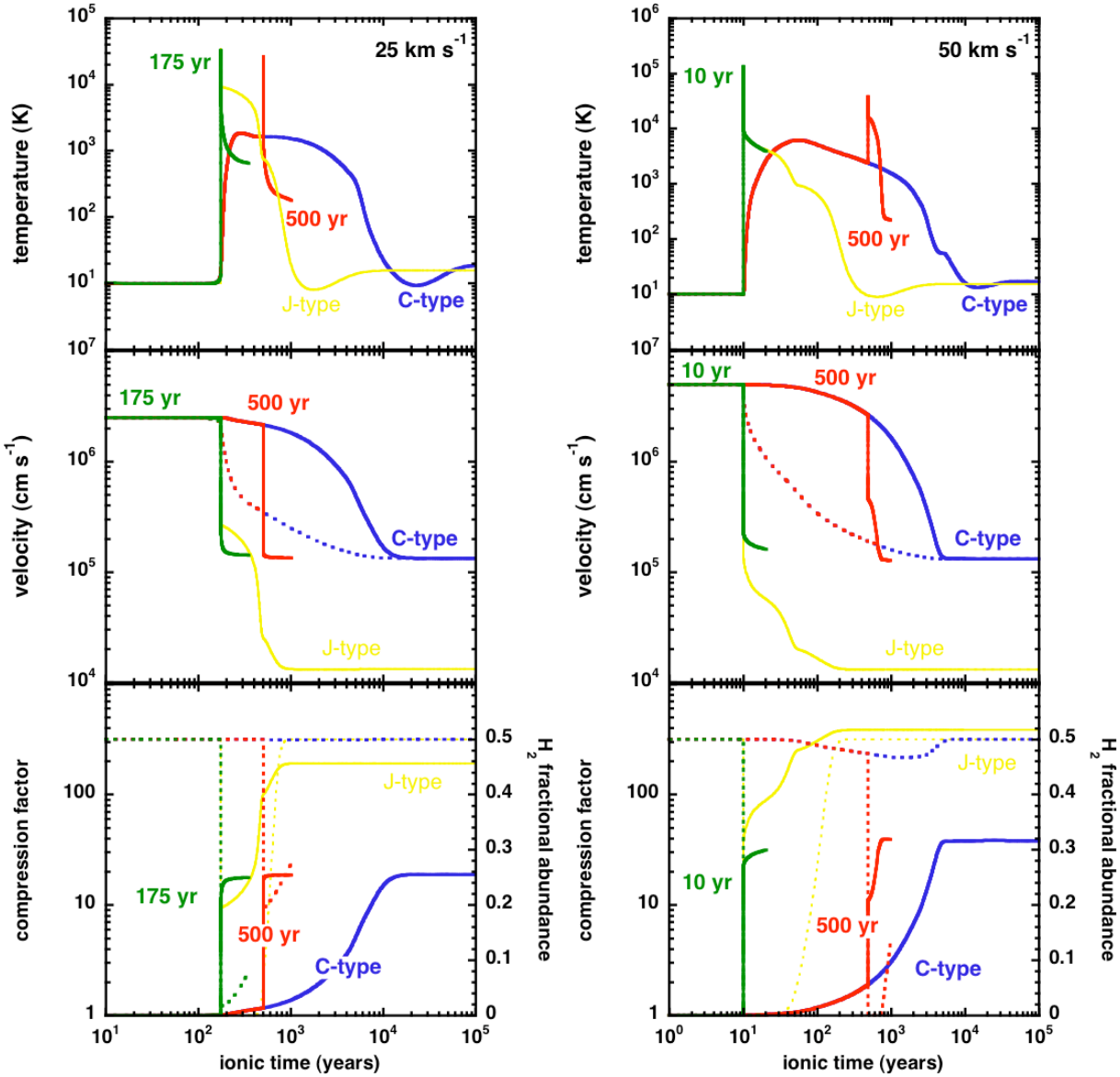

Figure 2.4 – Profiles of C-, CJ-, and J-type shocks specified in Subsection 2.4.3. Left-hand panels : $v_s = 25$ km s^{-1} ; right-hand panels : $v_s = 50$ km s^{-1}. In the middle panels, the full curves correspond to the neutrals and the broken curves to the ions . In the bottom panels, the full curves correspond to the compression factor and the broken curves to the fractional abundance of H_2.

Tableau 2.3 – Characteristic quantities for C-, CJ-, and J-type shocks specified in Subsection 2.4.3 : maximal neutral temperature (T_n max, in kelvin), compression factor (comp, no unit), and minimum molecular hydrogen fractional abundance (H_2 min, no unit).

	25 km s^{-1}				50 km s^{-1}			
	C-type	500 yr	175 yr	J-type	C-type	500 yr	10 yr	J-type
T_n max	1800	26000	32000	33000	6150	38000	130000	130000
comp	18.5	18.5	17.5	190	38	39	31	385
H_2 min	0.5	0.2	0.02	10^{-6}	0.46	10^{-7}	5×10^{-7}	5×10^{-7}

the shock age. In the C shock model, H_2 remains the main coolant through the whole shock : the maximum temperature is not large enough to provoke its dissociation, and only generates a slow radiative cooling, hence a wider shock. The situation is the same at higher velocity, with a much larger dissociation fraction of H_2.

Molecular hydrogen as a diagnosis tool for regions of star formation

3

Molecular hydrogen in regions of star formation

Le dihydrogène est la molécule la plus abondante dans le milieu interstellaire, ainsi que dans les régions de formation stellaire. Sa modélisation dans un code de choc doit donc bénéficier d'une attention particulière. Le chapitre commence donc par une brève description de cette molécule, suivie d'éléments de modélisation qui ont déjà été inclus dans le code de choc dont nous disposons. Les diagrammes d'excitation du dihydrogène et leur utilité dans le cadre de l'étude des flots bipolaires sont ensuite introduits. L'influence des coefficients de taux de collision du dihydrogène par l'atome d'hydrogène sur ces diagrammes d'excitation est enfin discutée.

Molecular hydrogen is the most abundant molecule in the universe, and also in regions of star formation. In addition to this, its molecular characteristics make it of crucial influence in a vast number of physical and chemical processes. For these reasons, H_2 plays a major role in the structure of the shocks waves we consider, and must hence be carefully taken into account in any modeling attempt. This chapter provides the basics on its molecular structure and on its consequent treatment and use. The calculation of its cooling contribution is detailed in Appendix B.

3.1 Molecular hydrogen in molecular outflows

3.1.1 Molecular hydrogen facts

Molecular hydrogen exists in two different forms :

- ortho-H_2 : the two protons of the diatomic molecule have the same direction of spin. The total nuclear spin is I = 1. Only odd values of the rotational quantum number are allowed ;
- para-H_2 : the two protons of the diatomic molecule have opposite directions of spin. The total nuclear spin is I = 0. Only even values of the rotational quantum number are allowed. It is a lower energy state than ortho-H_2.

Transitions between these two forms of H_2 can occur only in reactive reactions, with H atoms or H^+ or H_3^+ ions, for example, which result in a change of the relative orientation

of the individual nuclear proton.

As H_2 is homonuclear, it does not possess a permanent dipole moment : rovibrational transitions within the $X^1\Sigma_g^+$ electronic ground state occur by electronic quadrupole radiation. In addition to this, H_2 has a large rotational constant : 85.25 K. Consequently, its rotational levels are largely spaced : the J = 2 state lies 510 K above J = 0, and J = 3 lies 845 K above J = 1. It follows that the rotational excitation of H_2 becomes important only for temperatures T > 100 K. The $v = 1$ threshold lies approximately 6000 K above the ground state, and consequently rovibrational excitation (such as that at 2.2μm) requires kinetic temperatures T > 1000 K. The full table of H_2 rovibrational levels that were used in the present study is given in Appendix D.

Finally, according to quantum mechanics selection rules, rovibrational transition are possible only when certain conditions between the connected levels rotational quantum numbers are satisfied. Based on these selection rules, notations exist to refer to particular transitions. A typical and useful example when it comes to molecular hydrogen in the interstellar medium is the 1-0 S(1) line at 2.122 μm. The notation stands for the transition : $v' = 1, J' = 3 \longrightarrow v'' = 0, J'' = 1$, based on the expanded notation : O for $J' = J'' - 2$, P for $J' = J'' - 1$ (forbidden), Q for $J' = J''$, R for $J' = J'' + 1$ (forbidden), and S for $J' = J'' + 2$.

3.1.2 Molecular hydrogen in regions of shocks

Generally speaking, molecular hydrogen is of particular importance in the interstellar gas :

- it comprises a significant part of its mass ;
- it helps to define the chemical state of the gas (its ionization state dictates that of the gas, and it is a privileged partner in numerous molecular formation reactions) ;
- it plays a major role in exciting gas coolants (being an abundant molecule, it is an important collision partner for species such as CO, H_2O, SO,...) ;
- it is itself a major coolant of the gas in regions of high temperature.

In regions of shock, the temperatures of thousands of kelvin that are attained (see subsection 2.4.3) are high enough to generate excitation of both rotational and rovibrational transitions, making molecular hydrogen a major coolant for the shocked gas, and a dominant factor to account for the shock structure. Examples of correlation between the shock structure and H_2 fractional abundance can thus be seen on Figure 2.4.

For these reasons, the jet shocked excited regions mainly cool through H_2 quadrupole transitions, and bright rotational and rovibrational lines in that range represent a powerful shock tracer, in the region of the shock where the neutral temperature is comprised around 100-1000 K (Beyond 1000 K, H_2 becomes dissociated, and above 100 K, molecules such as CO, H_2O and OH are the dominant coolers). Due to its very rapid cooling, molecular hydrogen is more suitable to probe shock excitation and gas cooling than CO lines for example, that only provide a time integrated response. Two examples of such a tracing ability are given on Figures 3.1 and 3.2 :

- Figure 3.1 presents two images of the HH211 outflow, already mentioned in Subsection 1.2.1. In this case, the molecular hydrogen 1-0 S(1) line traces the hot gas around 6950 K ;

- Figure 3.2 presents two images of the L1157 outflow. On the left hand side map, the molecular hydrogen 0-0 S(5) line traces the gas at 4590 K.

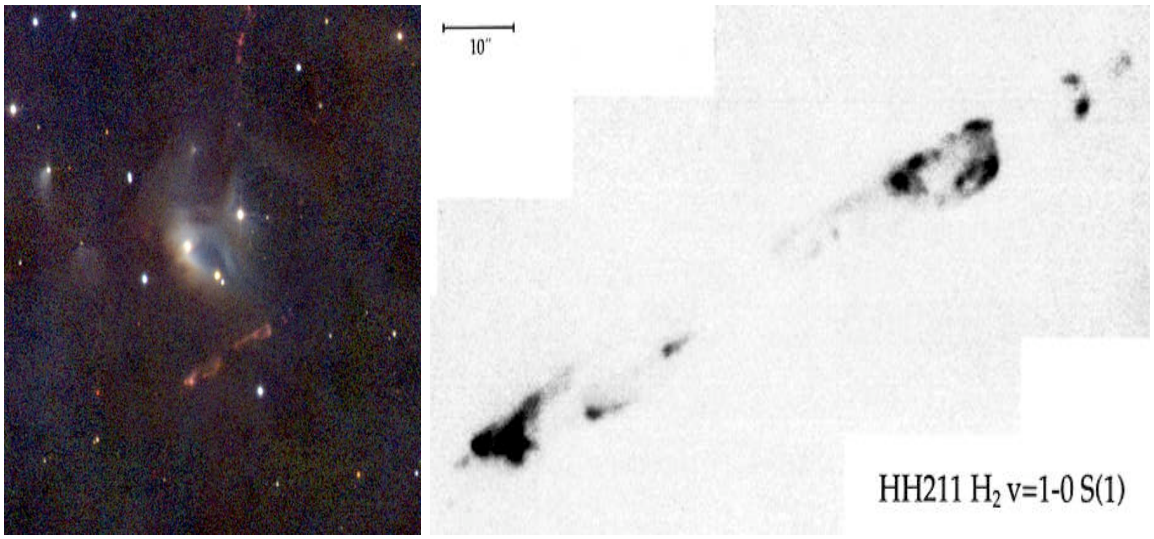

Figure 3.1 – Left : true-colour (J, H, K) near-infrared image of IC348-IR/HH211. Right : high-resolution image of HH211 taken in the H_2 1-0 S(1) line at 1.122 μm. Details on both images are given in McCaughrean et al. (1994).

3.2 The treatment of molecular hydrogen

3.2.1 Taking molecular hydrogen into account

For all the reasons introduced in the previous Subsection, complete numerical simulations of the nonequilibrium gas in shock regions must include a detailed treatment of the physics of H_2. Here we provide some modeling elements that have already been taken into account in the shock code that we use. In this code, H_2 level populations are solved in parallel with the equations of the shock (that is the conservation equations, see Section 2.2), altogether forming a set of N differential equations

$$\frac{dy_i}{dz} = f\left(y_1, ..., y_N, \frac{dy_1}{dz}, ..., \frac{dy_{i-1}}{dz}, z\right) \tag{3.1}$$

where $y_i (i = 1, N)$ are the dependent variables and z, the distance, is the independent variable. Equation 3.1 assumes that a steady state ($\partial y_i/\partial t = 0$) has been attained, but can be used in the fashion described in Section 2.4 to model non stationary shocks. The number of coupled equations, N, is the sum of the number of dynamical variables (10), the number of chemical species (more than 125), and the number of rovibrational levels of H_2 (up to 200).

The fundamental quantity related to molecular hydrogen is the fractional population of the rovibrational (including of course purely rotational) levels. To compute their values

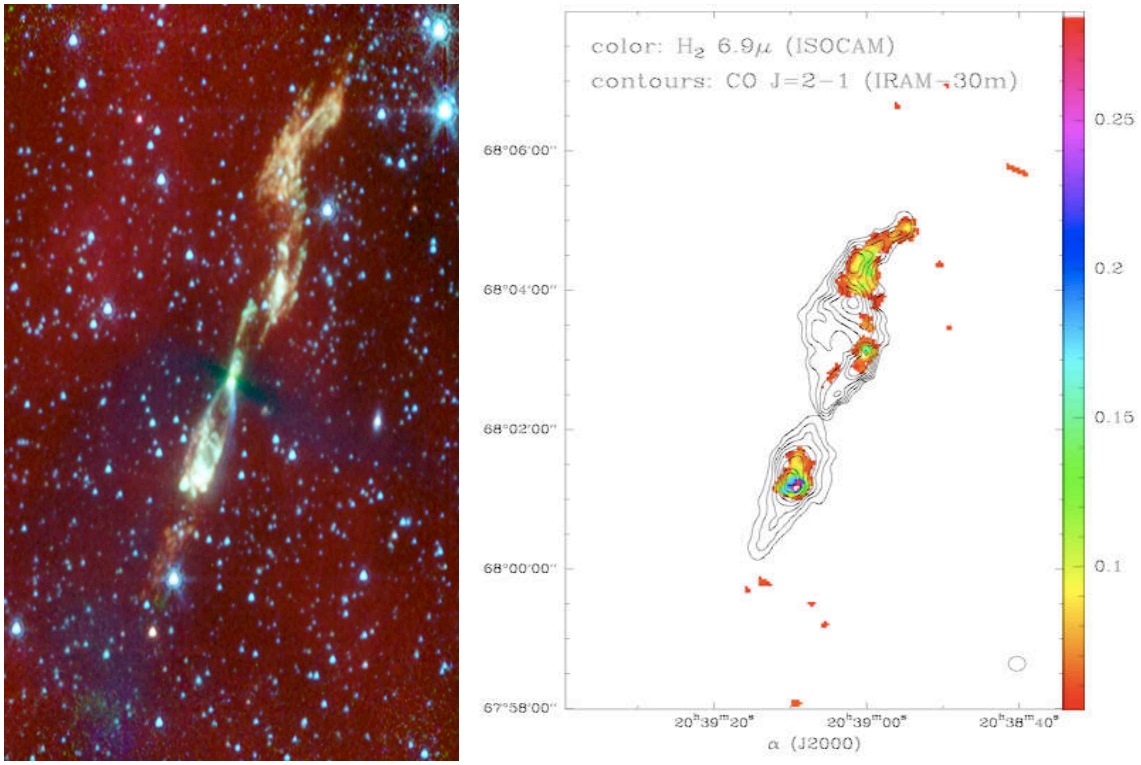

Figure 3.2 – Left : Spitzer telescope image of the L1157 region. Infrared array camera results, in red : 8 μm, green : 4.5 μm, blue : 3.6 μm, Looney et al. (2007). Right : a map of the L1157 outflow (Cabrit et al. (1999)) obtained with ISOCAM in a narrow filter (R $\simeq$ 40), centered on the 0-0 S(5) line at 6.9 μm, and superposed on the CO map of Bachiller and Perez Gutierrez (1997).

at each point of the shock, a great number of processes involving molecular hydrogen must be taken into account, among which :

- ortho to para conversion, through reactive collisions with protons or proton-transferring ions, such as H_3^+, as described in Le Bourlot et al. (1999) and Wilgenbus et al. (2000) ;
- dissociation of H_2 through collisions with H, H_2, He, and electrons, as reviewed by Wilgenbus et al. (2000) and Le Bourlot et al. (2002) ;
- dissociation of H_2 through chemical reactions such as O(H_2,H)OH, or OH(H_2,H)H_2O (see Wilgenbus et al. (2000)) ;
- ionization of H_2 and H through collisions with streaming ions and electrons, with rates detailed in Le Bourlot et al. (2002), and through chemical reactions (see Appendix N for the detail of the chemical reactions network) ;
- population transfer in collisions with H, He, H_2 and grains, using the description of Le Bourlot et al. (2002) ;
- formation of molecular hydrogen on the grains surface ; indeed, H_2 can be dissociated by the shock front, but its re-formation can proceed as soon as the medium has sufficiently cooled down after its passage (see Le Bourlot et al. (2002)).

In the context of interstellar shocks, large velocity gradients exist, and any emitted photon will undergo an important Doppler shifting, and is either absorbed very locally, or escapes the medium (see the Chapter 5 for more complete description of this approximation). In the case of molecular hydrogen, the transition probabilities associated to its rovibrational lines are small, and any emitted photon consequently escapes the medium. The molecular hydrogen emissivity thus simply writes for a given transition $i \rightarrow j$, in K cm^{-3} s^{-1} :

$$\frac{dE_{ij}}{d\omega} = h\nu_{ij} \times A_{ij} \times n_j \tag{3.2}$$

3.2.2 Molecular hydrogen and code inputs

In addition to the shock code inputs already introduced in Subsections 2.1.3 and 2.4.2, a number of parameters relate to the modelling of molecular hydrogen.

Through all this study, the initial H :H_2 abundance ratio is, as every other species fractional abundance, in chemical equilibrium. 150 H_2 levels were included in the computation (up to an energy of 39221 K). The data files associated to collisions between H and H_2 were implemented from Wrathmall et al. (2007).

The shock code also incorporates the possibility for molecular hydrogen to form on grains. In this case, the formation reaction releases an energy of ∼4.5 eV. The lack of knowledge on this formation process leaves the possibility to consider different scenarios (see Flower et al. (2003)) :

- the simplest assumption is that levels are populated in proportion to the statistical (Boltzmann) factor at a temperature of 17249 K, which corresponds to 1/3 of the dissociation of H_2, i.e. in proportion to $g_J \exp(-E_{vJ}/17249)$. The underlying assumption is that 1/3 of the 4.5 eV released by the reaction is under the form of H_2 internal energy ;
- the second assumption consist of a production of vibrationally hot and rotationally cold molecular hydrogen, following the suggestion of Black and van Dishoeck (1987).

To simulate this, the molecular hydrogen is produced in the $J = 0$ and 1 rotational levels of the $v = 6$ manifold (with an ortho :para H_2 ratio equal to 3) ;

- in the third assumption, the molecular hydrogen is produced in the $J = 0$ and 1 rotational levels of the $v = 14$ manifold, at the dissociation limit (with an ortho :para H_2 ratio equal to 3) ;
- we may also assume that levels are populated in proportion to their local fractional number densities.

During this whole study, the first assumption was made. In addition to this, the energy release under the form of kinetic energy, associated to H_2 formation is set to be half of the difference between the dissociation energy of H_2 and its internal energy.

The full list of H_2 rovibrational levels energy that were used can be found in Appendix D.

3.3 Excitation diagrams

As we have seen, H_2 is the main tracer of regions of star formation. In the following subsections we study how to use it to deduce informations on the observed shocks. Though the used quantities-the molecular hydrogen transitions integrated intensities- is a common one, there is a way to dispose of the data that provides a good visualization of the physical conditions of the considered medium : the excitation diagram.

3.3.1 Building of excitation diagrams

Excitation diagrams are just a way to represent the molecular hydrogen spectrum, by plotting the logarithm of the column density of the H_2 rovibrational levels, divided by their statistical weights ($\ln(N_{vJ}/g_J)$, with N_{vJ} in cm^{-2} and g_J), against their excitation energy (E_{vJ}/k_B in K). Such diagrams are very useful to have a first idea of the temperature conditions that exist in the considered regions.

In fact, the measured H_2 line intensities I_{vJ} can be converted into column densities N_{vJ} adopting

$$I_{vJ} = \frac{hc}{4\pi}\sigma A_{vJ} N_{vJ} \tag{3.3}$$

where σ is the wave number, A_{vJ} the transition probability for the rovibrational level v, J, h is Planck's constant, and c is the velocity of light in the vacuum. Column densities can then be compared with those expected from thermal excitation.

The method is the following one. In a thermal distribution, N_{vJ} is proportional to the statistical weight g and the Boltzmann factor $exp(-E_{vJ}/kT_{\rm exc})$. E_{vJ} is the excitation energy of the respective level, g is the product of the nuclear spin statistical weight, which has value of 1 and 3 for even and odd rotational levels J, respectively, and the rotational statistical weight, which is $(2J+1)$. The excitation temperature associated to a transition, T_{exc} is defined by :

$$e^{\frac{h\nu}{kT_{\rm exc}}} = \frac{g_j/n_j}{g_i/n_i} \tag{3.4}$$

where ν is the frequency associated to the $j \rightarrow i$ transition, where n are the level populations associated to the connected levels, and g are their statistical weight. In a situation of local thermal equilibrium, the excitation temperature equals that of the gas. For a uniform excitation temperature, the values $\ln\{N_{vJ}/g\}$ should thus all fall on a straight line plotted versus $E(vJ)$, with a slope proportional to $T_{\rm exc}^{-1}$. One can see that this kind of diagram thus gives a rough estimate of the temperature conditions in the considered region.

From an observational point of view, the advantages of this method are crucial :

- the excitation temperature is a rough estimate of the temperature conditions in the considered region ;
- deviations from LTE can be probed, pointing to excitation conditions of the region ;
- several excitation temperatures can be determined, corresponding to several excitation conditions, and multiple temperature components, reflecting the possible complexity of the shock structure.

From a modelling point of view, the general appearance of the diagram depends not only on the physical parameters of the observed regions, but also to the type of shocks one is trying to identify, allowing for fine constraining assumptions to be made. Flower et al. (2003), Giannini et al. (2004), Giannini et al. (2006) thus provide examples of observed regions for which use was made of such excitation diagrams to describe both the occurrence type of shock and the physical parameters in respectively Cep A West and various Herbig-Haro regions.

3.3.2 Canonical shock examples

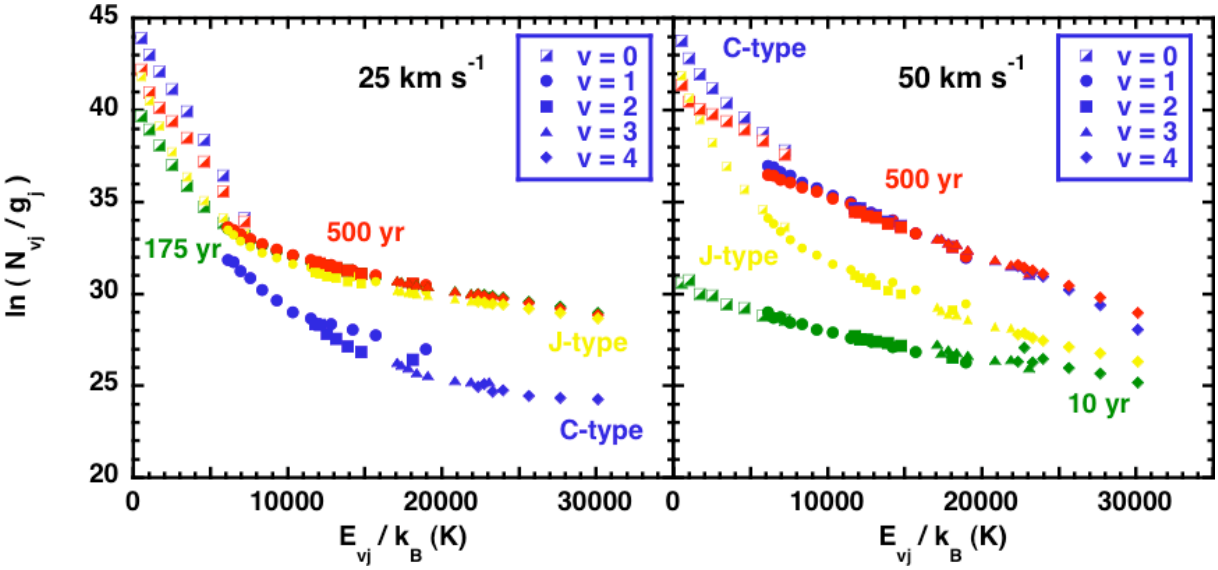

Figure 3.3 – Synthetic H_2 excitation diagrams for the shock models specified in Subsection 2.4.3. Left-hand panel : $v_{\rm s} = 25$ km s^{-1} ; right-hand panel : $v_{\rm s} = 50$ km s^{-1}.

Stationary shock models. As previously stated, through our entire study, the initial ortho-to-para ratio is assumed equal to the statistical equilibrium value of three in our shock models. Indeed, any significant departure from this value would result in a systematic displacement of the ortho with respect to the para levels, and such a behaviour does not appear on the observed excitation diagrams that we use for L1157B1, whether they are purely rotational or rovibrational. For steady C and J shock models, the time over which the integration of H_2 level populations is computed is greater than the necessary time for the post-shock gas to reach thermo-chemical equilibrium, i.e. approximatively 10^5 years. Thus, even if the modeled shock is actually younger, this choice yields no wrong estimate of the excitation, as molecular hydrogen does not emit in the cold post-shock region.

The excitation diagrams obtained for our reference stationary shock models are shown on Figure 3.3, for low (left panel) and high (right panel) shock velocity, for rotational and rovibrational lines. The following trends can be visible :

- at 25 km s^{-1}, the J-type shock is warmer and narrower than the C-type one. Consequently the pure rotational levels ($\lesssim$ 7000 K) are more populated in the C-type shock model, whereas the rovibrational transitions are favored in the J-type shock models ;
- at 50 km s^{-1}, the J-type shock is still warmer and narrower than the C-type one, and the rotational levels are still hence more populated in the C-type shock than in the J-type one. In addition to this, the molecular hydrogen is dissociated in the J-type shock model owing to the very high temperatures generated by the high velocity. As can be seen in Figure 2.4, this dissociation occurs in the warmest part of the shock, which explains the weak values of the rovibrational excitation in this shock.

In both cases, one can note the occurrence of two excitation temperatures in the excitation diagrams, one corresponding to the pure rotational lines, the other, higher than the rotational one, corresponding to the rovibrational transitions.

Non stationary shock models. In cases of non stationary shock models, the molecular hydrogen level populations are computed until the end of the shock, that is the final point that can be seen on the profiles plotted on Figure 2.4. Non stationary shock models present mixed features of C- and J-type shock models, which can also be seen on excitation diagrams :

- in both cases (25 and 50 km s^{-1}), the youngest shock model is both very warm and very rapidly cut, which only generates poor pure rotational emission from molecular hydrogen whose levels are then even less populated than in the case of a J-type shock models ;
- in both cases, the oldest shock models rotational points of the diagram lie between those of the C- and J-type shock models, as expected from a shock model that presents mixed characteristics of C- and J-types ones ;
- at 25 km s^{-1}, the dissociation of H_2 is far less efficient in CJ-type shock models than in J-type shock models, which compensates for the narrow width of these shocks, and accounts for the proximity of CJ- and J-type shock models points on the rovibrational part of the diagram ;

- at 50 km s^{-1}, the dissociation rate of molecular hydrogen in CJ-type shock models is very close to that in the J-type shock model, and the age of the shock, and hence its width, is the key factor to explain the hierarchy in the rovibrational part of the diagram : the youngest shock model is very narrow, and then only generates minor excitation compared to that of the J-type shock model, whereas the oldest one is very broad, almost as the C-type one and consequently generates comparable rovibrational excitation, despite the molecular hydrogen dissociation.

Again, two excitation temperatures seem to emerge from these excitation diagrams, in any case but the particular very young one at 50 km s^{-1}, respectively associated to the pure rotational and rovibrational ones. It is also clear that the comparison of observed and calculated excitation diagrams has the potential not only for type of shock, but also for physical parameters, including the shock age, discrimination.

3.4 H–H_2 collisional rate coefficients

3.4.1 H–H_2 critical densities

As stated in Subsection 3.1.1, H_2 particularly large rotational constant generates important rotational excitation only for T > 100 K, while rovibrational excitation requires T > 1000 K. These temperatures are frequently reached in shocked regions, leading collisions with H to significantly contribute to the rotational excitation of H_2, and possibly to dominate its rovibrational excitation. H is a privileged collision partner when H_2 undergoes dissociation in the shock, that is at high velocity in the case of C-type shock models, or in J-type shock models or non stationary ones. In the shocks that are studied here, the hydrogen atoms resulting from H_2 dissociation do not undergo consequent ionization.

When computing H–H_2 collisional coefficient rates, a special care must consequently be taken both with the representation of the molecule and the choice of the potential energy surface. In the present work, we briefly investigate the differences generated by the choice of a state of the art calculation, described in Wrathmall et al. (2007) or an older set of collisional data, as used in Le Bourlot et al. (1999) or Le Bourlot et al. (2002). The differences between these studies can be summarized as follows :

- in the oldest work, the vibrational motion was treated approximately, by means of a simple harmonic oscillator model, and the potential energy surface that was used was that of Boothroyd et al. (1996) ;
- n the most recent work, the calculations were performed using the most recent H–H_2 potential (Mielke et al. (2002)), and exact numerical representations of the vibrational wavefunctions.

For the purposes of astrophysical applications, the rate coefficients are fitted to the following function of the temperature T

$$log[q(T)] = a + \frac{b}{t} + \frac{c}{t^2} \tag{3.5}$$

where $t = 10^{-3}T + \delta$, and $\delta = 1.0$ to prevent the divergence of the rate coefficient as $t \to 0$, enabling the calculation of both excitation and de-excitation rate coefficients for

Tableau 3.1 – Critical densities (cm^{-3}), n_{crit}, at which the probabilities of collisional and radiative de-excitation are equal, for a selection of transitions of H_2. The collisional partner is H, and the transitions wavelengths are also given, in μm. Numbers in parentheses are powers of 10.

Jup	λ (μm)	file	n_{crit} (100 K)	n_{crit} (500 K)	n_{crit} (1000 K)	n_{crit} (2000 K)
0-0 S(0)	28.2	DRF	1.2(+03)	1.1(+02)	2.2(+01)	4.4(+00)
		SAW	1.1(+03)	7.4(+01)	1.4(+01)	3.3(+00)
0-0 S(1)	17.0	DRF	9.5(+03)	1.0(+03)	2.1(+02)	4.2(+01)
		SAW	4.4(+04)	1.2(+03)	1.6(+02)	3.0(+01)
0-0 S(2)	12.3	DRF	6.1(+04)	7.1(+03)	1.5(+03)	2.9(+02)
		SAW	1.0(+06)	9.4(+03)	8.1(+02)	1.4(+02)
0-0 S(3)	9.66	DRF	8.3(+05)	3.6(+04)	5.1(+03)	8.3(+02)
		SAW	2.0(+06)	2.8(+04)	2.9(+03)	5.1(+02)
0-0 S(4)	8.02	DRF	5.9(+06)	1.7(+05)	1.9(+04)	2.8(+03)
		SAW	3.4(+06)	6.8(+04)	7.9(+03)	1.5(+03)
0-0 S(5)	6.91	DRF	7.9(+06)	3.0(+05)	3.8(+04)	5.6(+03)
		SAW	6.9(+06)	1.6(+05)	1.9(+04)	3.6(+03)
0-0 S(6)	6.11	DRF	1.3(+08)	1.3(+06)	1.0(+05)	1.3(+04)
		SAW	1.5(+07)	3.4(+05)	4.2(+04)	7.6(+03)
0-0 S(7)	5.51	DRF	9.0(+07)	1.7(+06)	1.6(+05)	2.1(+04)
		SAW	3.1(+07)	7.1(+05)	8.5(+04)	1.5(+04)
1-0 S(1)	2.12	DRF	1.9(+11)	5.5(+08)	1.7(+07)	8.4(+05)
		SAW	6.5(+08)	3.5(+06)	2.8(+05)	5.4(+04)
1-0 S(2)	2.03	DRF	1.4(+11)	5.2(+08)	1.8(+07)	9.8(+05)
		SAW	3.2(+08)	2.9(+06)	2.7(+05)	5.1(+04)
2-1 S(1)	2.25	DRF	2.5(+10)	3.9(+08)	2.4(+07)	1.6(+06)
		SAW	1.8(+06)	1.2(+05)	3.8(+04)	2.0(+04)

various temperatures, and also that of the critical density n_{cr}, given by

$$n_{cr} q(j \rightarrow i) = A(j \rightarrow i) \tag{3.6}$$

Indeed even when the dominant excitation mechanism is collisions with H atoms, the populations of the rovibrational levels of H_2 are the results of an equilibrium between radiative and collisional de-excitation. Two limit behaviors can then be distinguished thanks to the critical density :

- if the density is higher than the critical density, collisional de-excitation dominates and the relative level populations tend to a Boltzmann distribution. The values of the collisional rate coefficients are of no other use than the calculation of the critical density ;
- at densities much less than the critical density, collisional excitation is followed by

radiative decay, and so the collisional excitation rates determine the emission line intensities.

However, because of their quadrupolar nature, the spontaneous transition probabilities of H_2 are small, and generate low critical densities in the astrophysical context.

The critical densities with He and H_2 as collision partners for H_2 are given in Appendix E for a selection of transitions of astrophysical interest, showing for example that when H is present, it dominates the vibrational excitation of H_2 over that by H_2 itself. In this Subsection, we focus on the critical densities of H_2 with H, presented in Table 3.1 for Le Bourlot et al. (1999) study (DRF file) and for Wrathmall et al. (2007) ones (SAW file). In this table :

- higher densities appear necessary to thermalize rovibrational as compared with pure rotational transitions ;
- the greater relative importance of H in vibrationally inelastic scattering arises from a comparison of the critical densities with those of the Appendix E ;
- the higher the temperature, the smaller the collision rates, and hence the lower the critical densities ;
- purely rotational transitions critical densities do not differ much at temperatures relevant to the formation of the corresponding emission lines, as the corresponding collisional rate coefficients do not substantially differ between Le Bourlot et al. (1999) and Wrathmall et al. (2007) works ;
- nevertheless rovibrationally inelastic transitions, for which the most recent study yields larger values of the rate coefficients, present accordingly lower associated critical densities.

3.4.2 Application to a C-type shock wave

The rate coefficients for the rovibrational excitation of H_2 by H is expected to play a significant role in C-type shock waves. Indeed the heating generated by a shock wave leads to partial dissociation of H_2, enriching the gas in atomic H. Rotational and rovibrational excitation of H_2 take place, balanced by the spontaneous radiative decay to lower vibrational levels, rather than collisional, with differential behaviors :

- the rotational level populations within a given vibrational state tend to thermalize, even at densities as low as 10^4 cm^{-3}, owing to (vibrationally elastic) collisions between them ;
- the radiative transition probabilities between vibrational manifolds are sufficiently large to prevent thermalization between different vibrational states until higher densities.

Figure 3.4 shows H_2 excitation diagram obtain for a C-type shock with a pre-shock density of $n_{\rm H} = 10^4$ cm^{-3}, a shock velocity $v_{\rm s} = 30$ km s^{-1}, and a magnetic field parameter $b = 1$, with the two different sets of H–H_2 collisional rate coefficients mentioned above. Differences are apparent for $v > 0$, between the results obtained using Wrathmall et al. (2007) rate coefficients and those of Le Bourlot et al. (1999).

In accordance with the critical densities study, for the populations of the $v = 0$ manifold, only the vibrationally elastic (and rotationally inelastic) rate coefficients are important, for which the two sets of data do not show important discrepancies at the tempe-

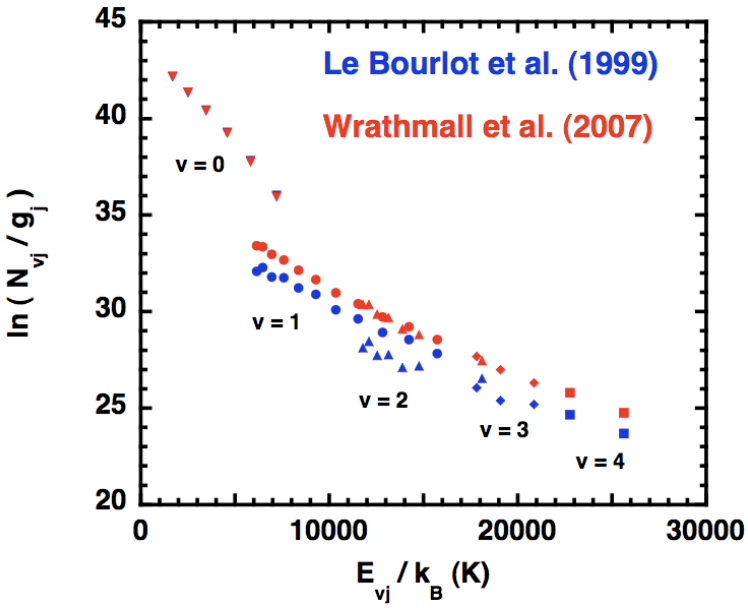

Figure 3.4 – The excitation diagram computed for a C-type shock model (see text Subsection 3.4.2), using the H–H_2 rate coefficients of Le Bourlot et al. (1999) (in blue) and those of Wrathmall et al. (2007) (in red). Results are plotted for rotational levels in vibrational manifolds $0 \leq v \leq 4$. For $v = 0$, the blue and red symbols overlap.

rature at which the corresponding emission lines form. On the contrary, for vibrationally excited levels, the most recent rate coefficients are higher, generating larger populations and column densities.

However the changes are not as important as the actual rate coefficients discrepancies suggest. The heated gas undergoes a compression that leads to an approximate thermalization of the populations of the rotational levels within a rovibrational manifold. Furthermore, to the larger rates of rovibrational excitation corresponds a higher rate of cooling of the gas by H_2. Being a major coolant, the kinetic temperature falls accordingly, exponentially reducing the rates of rovibrational excitation, and then the apparent discrepancies on the excitation diagram of H_2. Such a feedback loop maintains the rate of cooling by H_2 at an approximately constant value.

4

The test case of L1157B1

Dans ce chapitre, le flot L1157 est décrit. Les observations disponibles, ayant contribué à en faire un modèle de 'flot chimiquement actif' sont énumérées, en insistant sur les données existantes en H_2. La suite du chapitre est consacrée à l'ajustement des diagrammes d'excitation observés par les diagrammes modélisés. Les résultats obtenus sur une grille de chocs stationnaires (de types C et J) sont d'abord comparés aux observations. Puis la comparaison avec les chocs non stationnaires est réalisée et accompagnée d'une brève description de la méthodologie utilisée pour réduire l'espace des paramètres libres. La dernière section du chapitre présente les meilleurs résultats obtenus.

4.1 The L1157 outflow

4.1.1 The L1157 region, a chemically active outflow

L1157 is a bipolar outflow driven by a Class 0 protostar (IRAS 20386+6751) of low-luminosity (11 $L_\odot$), located in the constellation Cepheus at a distance of approximately 440 pc. Its high collimation and its high inclination with respect to he line of sight make it favorable to study the effects of the propagation of the outflow in the surrounding medium (see Subsection 1.3.3). L1157 has been studied and observed through the years by means of numerous molecules among which not only the usual known shock tracers (such as SiO, CO for instance) but also a wide range of chemical species (CN, CS, SO, H_2CO ...) that led Bachiller et al. (2001) to deem it as the reference example of a 'chemically active outflow'. This denomination was investigated by Viti et al. (2004), and further justified by the high resolution maps of Benedettini et al. (2007) that stressed out the clumpy structure of the outflow in several molecular lines.

Bachiller et al. (2001), and Beltrán et al. (2004) provide exhaustive reviews of the studies related to L1157. One can additionnally mention the work of Froebrich et al. (2003) that provided FIR maps and photometry of the protostelar object, acquired with the Infrared Space Observatory (ISO) photopolarimeter (PHOT) and Long Wave Spectrometer (LWS). In 2008, Arce et al. (2008) also report the detection of complex organic molecules in the outflow, while its Spitzer IRAC image was released in Looney et al. (2007), revealing a flattened structure around the protostellar source.

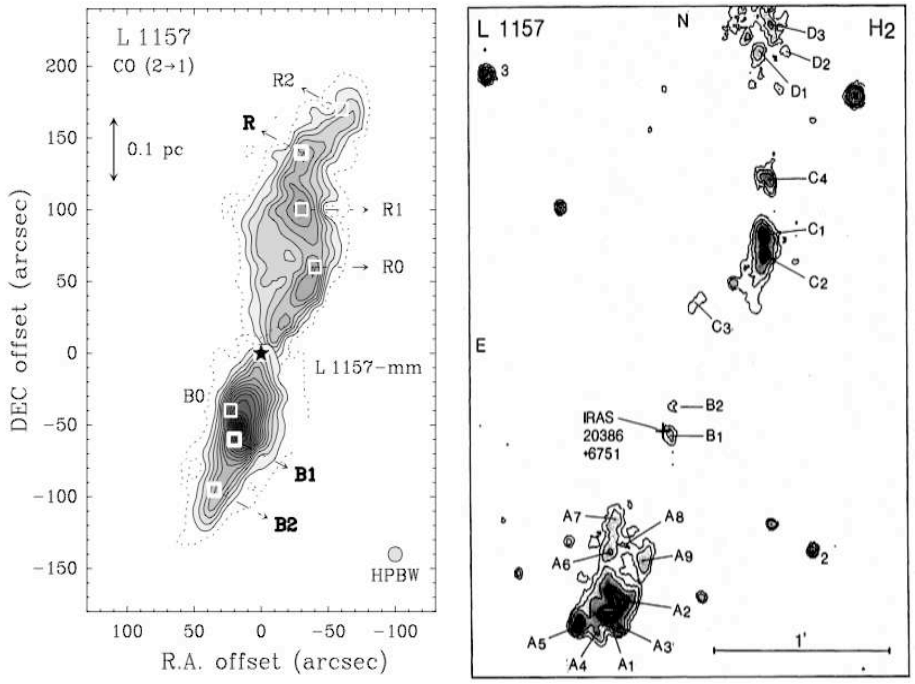

Figure 4.1 – Left : integrated emission of CO (2-1) of the L1157 outflow, taken from Bachiller et al. (2001). Right : H_2 v = 1-0 S(1) + continuum contour/grey scale plot of the L1157 outflow, taken from Davis and Eisloeffel (1995).

Cabrit et al. (1999) compiled observations of the blue lobe of the L1157 outflow in the rotational transitions of molecular hydrogen, and Caratti o Garatti et al. (2006) completed this study by releasing observational data corresponding to a large number of corresponding rovibrational transitions. Nisini et al. (2007) finally reported observations of pure rotational lines of SiO, allowing for us to investigate observations/modelling comparisons thanks to these very efficient shock tracers (Gusdorf et al. (2008a), Gusdorf et al. (2008b) in Appendix O).

Figure 3.2 shows the L1157 molecular outflow as seen by Spitzer, and its H_2 0-0 S(5) map superposed on the CO (2-1) map. Left hand side panel of Figure 4.1 shows the CO (2-1) integrated emission map, with the reference positions in the blue and red lobe (B1, B2, and R0, R1, R, R2 respectively), relating to ISO observations, and which were used for SiO, CO, and rotational H_2 observations in this study. The right hand side figure shows the reference positions associated with rovibrational lines of molecular hydrogan observations.

4.1.2 Molecular hydrogen observations

High energy rotational transitions of CO were conducted by Giannini et al. (2001), and Nisini et al. (2007) provided a complete analysis of SiO excitation in various knots of the blue and red lobes of L1157. Caratti o Garatti et al. (2006) observed a great number of H_2 rovibrational lines mainly in its blue lobe, and Sylvie Cabrit performed corresponding pure rotational lines observations (see Gusdorf et al. (2008b)). Therefore we focus this

Tableau 4.1 – Excitation (rotational and rovibrational) temperatures inferred from observational excitation diagrams for L1157.

$T_{\rm exc}(K)$	without reddening correction	with reddening correction
pix1	1090 ± 110	1080 ± 110
pix2	860 ± 50	940 ± 30
A1	2740 ± 130	2870 ± 150
A2	2940 ± 170	3090 ± 180

study on the analysis of the so-called B1 region, in the blue lobe of the outflow (see Figure 4.1). This appellation refers to ISO observations and approximately corresponds to the A1 and A2 regions observed in molecular hydrogen (also see Figure 4.1), that were first referenced by Davis and Eisloeffel (1995).

We show on Figure 4.2 the excitation diagrams that we built based on the work of Caratti o Garatti et al. (2006) (rovibrational lines) and of Sylvie Cabrit (rotational lines, shown in Gusdorf et al. (2008b)). The left hand side panel shows the data uncorrected for reddening effects, whereas the right hand side one corresponds to the data corrected for reddening effects, using the maximum visual extinction $A_{\rm v} = 2$ supplied by Caratti o Garatti et al. (2006). To achieve this correction, we used the interstellar extinction law provided by Rieke and Lebofsky (1985). For the rotational part of the diagrams, two single-pixel points of observations are displayed, respectively called "pix1" and "pix2". Regarding the rovibrational part, two regions were observed by Caratti o Garatti et al. (2006), referred to as A1 and A2, both reported on the excitation diagrams.

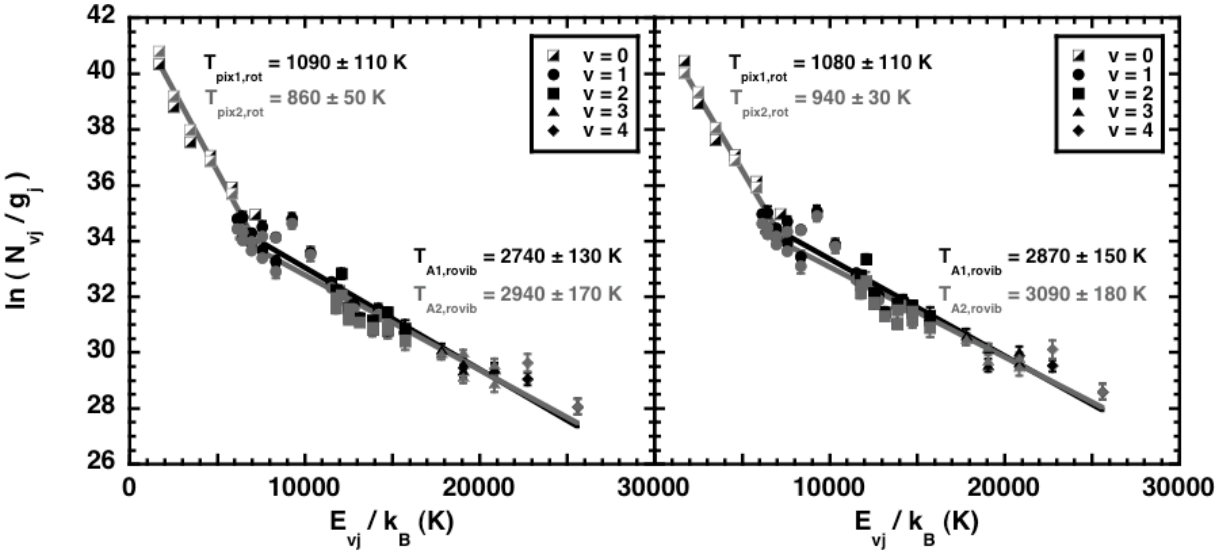

Figure 4.2 – Composite H_2 excitation diagrams, uncorrected (left hand side panel), and corrected (right hand side panel) for reddening with $A_{\rm V} = 2$; see text, Section 4.1.2. The excitation temperatures deduced from each set of observations are indicated.

Rotational and rovibrational temperatures were deduced from these diagrams for each set of data, and are compiled in Table 4.1. For both rotational and rovibrational sets of data, the similarity of the excitation diagrams and inferred excitation temperatures between the pixels or regions observed implies that the excitation conditions are the same for both pixels or regions, at least at the characteristic spatial resolution. Again in both cases, the correction for reddening effects slightly shifts the results but the error bars remain at least adjacent. We conclude that the reddening effects are of no significance here. Finally, we point out the presence of a component at ∼1000 K (traced by the purely rotational lines), and the one of a warmer one at ∼3000 K (traced by the rovibrational lines). Such conclusions were already reached in similar outflow regions such as the Orion Molecular Cloud Peak 1 (OMC-1) (Le Bourlot et al. (2002)), or more recently in various Herbig-Haro objects (Giannini et al. (2004), Giannini et al. (2006), Gredel (2007)).

4.2 C and J shocks grids comparisons and compact excitation diagrams

4.2.1 C and J shock models grid

We now compare the observed excitation diagrams to the modelled ones in order to constrain the physical parameters of the shocked gas, that is the pre-shock density $n_{\rm H}$, the shock velocity $v_{\rm s}$, and the magnetic field parameter b. To achieve such constraints, we have to compare the observations to a large grid of shock models for which all the above parameters are varied. Three pre-shock densities are investigated : $n_{\rm H} = 10^4, 10^5, 10^6$ cm^{-3}, in accordance with usual densities existing around proto-stellar objects. The magnetic field parameter choice is rather arbitrary, while the maximum shock velocities is imposed by the collisional dissociation of H_2, the main coolant, which leads to a thermal runaway and a J-type discontinuity (see Subsection 2.3.4). The initial chemical abundances are provided in Subsection 2.3.2, and the hydrogen-related assumptions that are made are presented in Subsection 3.2.2.

The grid of C and J-type shock models are consequently computed with the parameters detailed in respectively Tables 4.2 and 4.3.

4.2.2 Compact excitation diagrams

Given the size of the C-type shock model grid, specially for the pre-shock densities of $n_{\rm H} = 10^4, 10^5$ cm^{-3}, finding constraining parameters based on H_2 study by comparing every single modelled excitation diagram to the observed ones would be a very time-consuming task. We consequently use a necessary condition to discriminate among shock models that are likely to fit the observations. Indeed, excitation diagrams that do not reproduce at least the observed rotational emission of molecular hydrogen can be excluded from our study. We therefore use a synthetic representation based on this rotational part of the diagrams, focusing on the lines 0-0 S(2) to 0-0 S(7), observed by ISO.

On this compact rotational diagrams, the excitation of a single line is plotted against the mean excitation temperature of the pure rotational lines on the X-axis. We choose the

Tableau 4.2 – The C-type shock models grid. For each investigated density, initial shock velocities are shown on the first line of each tab (in km s^{-1}), whereas magnetic field parameter are given in the first column of each tab.

$n_H = 10^4$ cm^{-3}	10	15	20	22	25	28	30	32	35	45	50	55
b = 0.45	x	x	x	x	x	-	-	-	-	-	-	-
b = 0.60	x	x	x	x	x	x	x	x	x	-	-	-
b = 0.75	x	x	x	x	x	x	x	x	x	-	-	-
b = 1.00	x	x	x	-	x	-	x	-	x	x	x	x
b = 1.25	x	x	x	x	x	x	x	x	x	-	-	-
b = 1.50	x	x	x	x	x	x	x	x	x	-	-	-
b = 1.75	x	x	x	x	x	x	x	x	x	-	-	-
b = 2.00	x	x	x	x	x	x	x	x	x	-	-	-

$n_H = 10^5$ cm^{-3}	10	12	15	18	20	25	30	35	40	45	47
b = 0.30	x	x	x	x	-	-	-	-	-	-	-
b = 0.45	x	x	x	x	x	x	-	-	-	-	-
b = 0.60	x	x	x	x	x	-	-	x	-	-	-
b = 0.75	x	x	x	x	x	-	-	-	x	-	-
b = 1.00	x	-	x	-	x	x	x	x	x	x	x
b = 1.25	x	x	x	x	x	-	-	-	x	-	-
b = 1.50	x	x	x	x	x	-	-	-	x	-	-
b = 1.75	x	x	x	x	x	-	-	-	x	-	-
b = 2.00	x	x	x	x	x	-	-	-	x	-	-

$n_H = 10^5$ cm^{-3}	10	15	20	22	25	27	30	32	35
b = 1.00	x	x	x	x	x	x	x	x	x

Tableau 4.3 – The J-type shock models grid. The magnetic field is set $b = 0.1$; investigated initial shock velocities are given in km s^{-1} for pre-shock density of $n_H = 10^4, 10^5$ cm^{-3}.

$n_H = 10^4$ cm^{-3}	20	22	25	28	30	32	35	45	50
$n_H = 10^5$ cm^{-3}	10	11	12	15	18	20	-	-	-

$\ln(N_{vJ}/g_J)$ value of the 0-0 S(5) rotational line to be plotted on the Y-axis. This way, one point sums up the whole rotational part of the diagram, as a first approximation : as can be seen on the previous excitation diagrams, this part of the diagram indeed comprises the majority of the column density. The results of these comparisons for C-type shock models and density of $n_{\rm H} = 10^4, 10^5$ cm^{-3} are shown on Figure 4.3. On these panels, each colour corresponds to one magnetic field parameter value, and each point correspond to one initial shock velocity, with the following ranges being covered :

- $n_{\rm H} = 10^4$ cm^{-3} (lhs panel) : $b = 0.45, 0.60, 0.75, 1.00, 1.25, 1.50, 1.75, 2.00$, and $v_{\rm s} = 15, 20, 25, 30, 35, 45$ km s^{-1} ;
- $n_{\rm H} = 10^5$ cm^{-3} (rhs panel) : $b = 0.30, 0.45, 0.60, 0.75, 1.00, 1.25, 1.50, 1.75, 2.00$, and $v_{\rm s} = 10, 15, 20, 40$ km s^{-1} ;

The square data correspond to the L1157B1 knot as observed by ISO (pixel 1 and pixel 2), and the other points are the results of all the different models. As stated, this diagram allows to visualize the global comparison between all the models results and the observations in one sight.

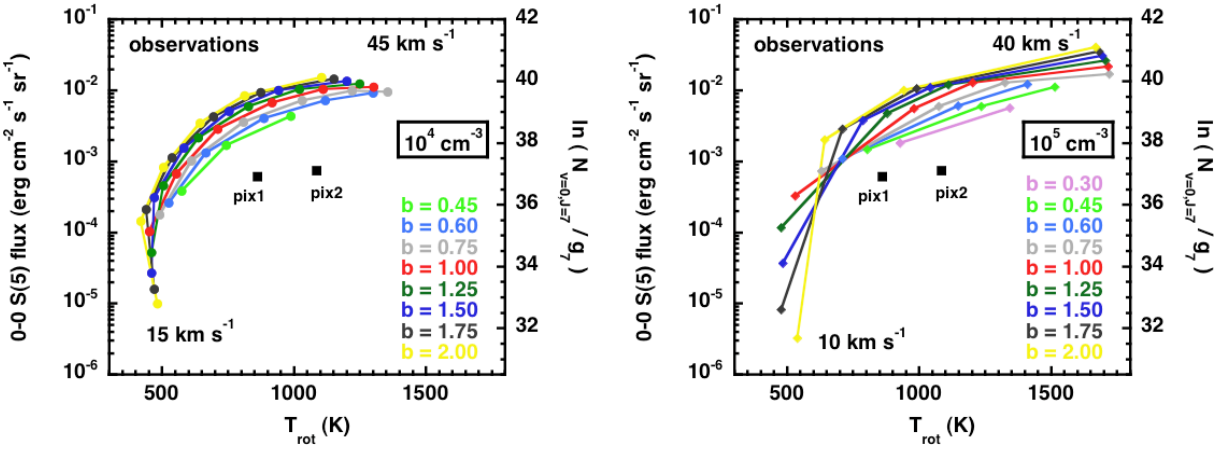

Figure 4.3 – Compact rotational diagrams for C-type shock models with $n_{\rm H} = 10^4, 10^5$ cm^{-3} (respectively left and right hand side panels). The corresponding magnetic field parameter is given on the panels. Each color corresponds to a pair of ($n_{\rm H}$, b) parameters, each point corresponds to a velocity, with different limits indicated on the panels for each pre-shock density. The list of velocities for each pre-shock density is given in Subsection 4.2.2. The black squares are the observed data.

The first comment on Figure 4.3 is that no stationary C-type shock model seems to be able to fit the observed data for the L1157B1 region, for the shown pre-shock densities. Denser C-type shock models ($n_{\rm H} = 10^6$ cm^{-3}) are not displayed but do not provide satisfying results either. For low magnetic field parameters, the critical velocities, that is the velocities above which no shock can propagate in the medium (see Flower and Pineau des Forêts (2003), Le Bourlot et al. (2002)), are very low and limit our range of investigation. For each density and each value of the magnetic field parameter, the rotational temperature of the slowest shock model is only indicative, and can not be fully trusted, as these models are too cold to exhibit a near-LTE behaviour (see for examples

the critical densities evolution with temperature in Table 3.1). Apart from this restriction, two general trends also emerge from this figure :

- when the shock velocity increases, the maximum temperature increases. This accounts for the rise of the rotational temperature with the shock velocity, and also generates a greater emission from molecular hydrogen, which explains the increase of the 0-0 S(5) line intensity ;
- when the magnetic field parameter increases, as can be seen on Figure 4.4 for $n_{\mathrm{H}} = 10^4$ cm^{-3}, and $v_{\mathrm{s}} = 20, 35$ km s^{-1} (respectively lhs and rhs panels), the maximum temperature decreases, which similarly explains the decrease of the rotational temperature and line intensity. However, this trend is fading at higher shock velocities. In fact, the high velocity ensures that the maximum shock temperature is high enough to excite molecular hydrogen whatever the magnetic field parameter value.

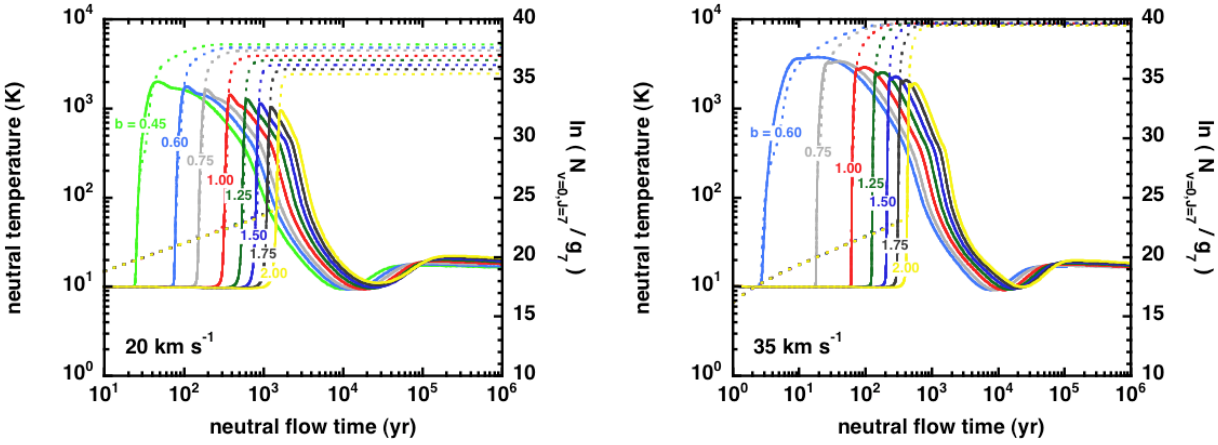

Figure 4.4 – Neutral temperature and $\ln(\mathrm{N}_{v=0,J=7}/\mathrm{g}_7)$ profiles for C-type shock models with $n_{\mathrm{H}} = 10^4$ cm^{-3} and $v_{\mathrm{s}} = 20, 35$ km s^{-1} (respectively left and right hand side panels, for various magnetic field parameters values).

Similarly, J-shock models do not produce satisfying levels of rotational emission, except in the case of $n_{\mathrm{H}} = 10^5$ cm^{-3}, and $v_{\mathrm{s}} = 12$ km s^{-1}. In the case of the J-type shock models, the rotational emission is not sufficient to account for the observations. To resolve this major discrepancy, we consequently have to consider the computation of a grid of CJ shock models.

4.3 CJ shocks grids comparisons

4.3.1 Non stationary models and molecular hydrogen emission

In fact, we have seen on Figures 2.4 and 3.3 that owing to the temperature profile of the different types of shock (and hence thanks to the different types of H_2 excitation temperatures), a CJ-type shock model can provide the appropriate answer to the rotational discrepancy : their rotational excitation is weaker than in stationary C-shock models,

but higher than the J-type ones, making them likely to fulfill the requirements raised by Figure 4.3.

Figure 4.5 illustrates the necessity to focus on CJ-type shock models. The C-type shock models are displayed for $n_{\rm H} = 10^4$ cm^{-3}, $b = 1$, and shock velocities from 10 to 55 km s^{-1}, with 5 km s^{-1} increments, and J-type shock models with $n_{\rm H} = 10^4$ cm^{-3}, $b = 0.1$, and shock velocities 20, 25, and 30 km s^{-1}. Also shown are the results for an evolutionary sequence of non-stationary CJ-type shock models for $n_{\rm H} = 10^4$ cm^{-3}, $b = 1$, and shock velocity of 25 km s^{-1}. The age of two non stationary models that were already used in the left hand side panels of template Figures 2.4 and 3.3 are indicated (175 and 500 yr), and the observational results are given for L1157 B1, as observed by ISO (two separate pixels, pix1 and pix2) under the form of the black square.

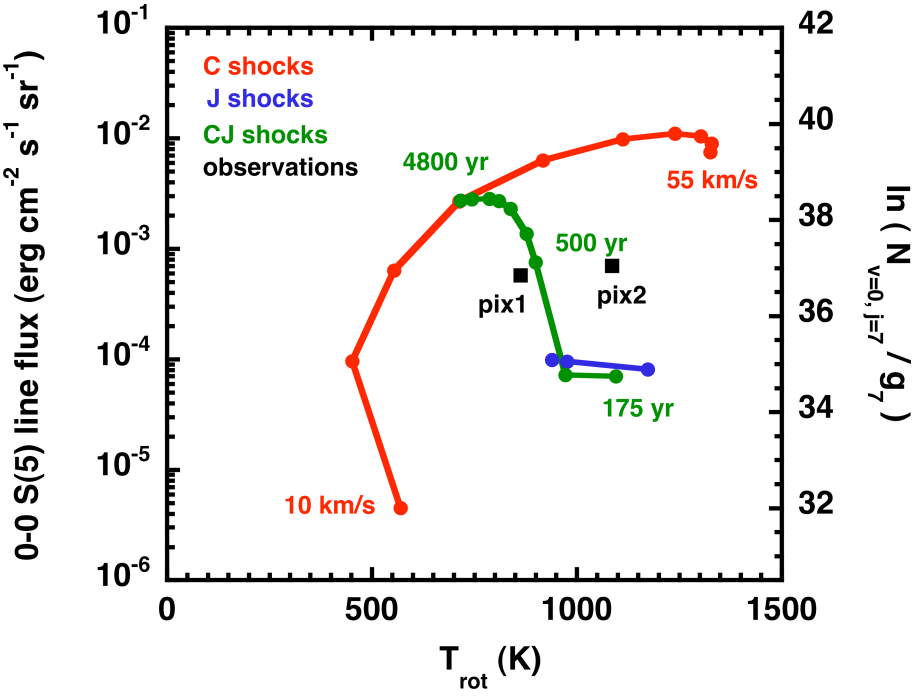

Figure 4.5 – Comparative compact excitation diagrams of C-, J-, and CJ-type shock models. The C-type shock models (red) are displayed for $n_{\rm H} = 10^4$ cm^{-3}, $b = 1$, and shock velocities from 10 to 55 km s^{-1}, with 5 km s^{-1} increments, and J-type shock models (blue) with $n_{\rm H} = 10^4$ cm^{-3}, $b = 0.1$, and shock velocities 20, 25, and 30 km s^{-1}. Also shown are the results for an evolutionary sequence (various ages) of non-stationary CJ-type shock models (green) for $n_{\rm H} = 10^4$ cm^{-3}, $b = 1$, and shock velocity of 25 km s^{-1}. The observed data are the black pixels.

The evolution of J-type models into C-type, through CJ-type of increasing ages, is well represented in this Figure. It is clear that only CJ-type models can provide a fit to the observations, a result which is consistent with earlier studies of ouflows, cited above, and which will receive further confirmation below. This figure is illustrative. Of course, the same work has been done for the whole grid of C-type shock models, that is for all the models displayed on Figure 4.3. The steady–state C-type models consistently overestimate

the intensity of the 0-0 S(5) transition, whatever value of b or $n_{\rm H}$ is adopted. Whilst the discrepancy might be resolved by assuming a small filling factor, this assumption would result in the intensities of lines from vibrational levels $v > 0$ being underestimated. When optimizing the values of the CJ-type model parameters, we shall make use of the entire H_2 excitation diagram, incorporating the emission observed from vibrationally excited levels. As previously stated, previous studies (Flower et al. (2003), Giannini et al. (2004), Giannini et al. (2006)) have already demonstrated the validity of this conclusion, extending it to the rovibrational part of the spectrum. Accordingly, we concentrate on CJ-type shock models for which the parameters to be varied include $n_{\rm H}$, $v_{\rm s}$, b, and the age of the shock wave.

A natural solution would be to run a grid of CJ shock models within the same parameters ranges as in the C shock models, and to add the shock age to the varied parameters list. Unfortunately, such an investigation is not sensible in computational time terms : the shock age range is too wide. As can be seen on Figure 4.5, the number of evolutionary ages investigated per ($n_{\rm H}$, $v_{\rm s}$, b) set makes a procedure which restricts the range of the search of parameters space is desirable, even essential. If the shock age is not pre-constrained, the numbers of CJ shock models to run would simply make the task impossible.

4.3.2 Our CJ shock model grid

On Figure 4.5, we see that from young CJ-type shock models (near the location of J-type shock models on the Figure) to older ones (asymptoting towards the C-type shock models), a wide range of rotational temperatures and 0-0 S(5) flux are covered, sweeping the observed values in the process. We consequently restrict our study to parameters sets for which the CJ-type shock models will be able to match the observed rotational excitation temperature (cf. Table 4.1) or 0-0 S(5) emission, to within a reasonable tolerance. On the example of the Figure 4.5, low velocity models are excluded because thay fail to generate enough 0-0 S(5) flux, and high velocity ones are excluded because the rotational temperature they generate is too high under the assumption of a filling factor of the unity. Following these principles, the parameters ranges restrict as :

- for $n_{\rm H} = 10^4$ cm^{-3}, 20 km s^{-1} $\leq v_{\rm s} \leq$ 35 km s^{-1}, and $0.45 \leq b \leq 2.00$;
- for $n_{\rm H} = 10^5$ cm^{-3}, 10 km s^{-1} $\leq v_{\rm s} \leq$ 20 km s^{-1}, and $0.30 \leq b \leq 2.00$.

In both cases, the magnetic field parameter is not well constrained. For $n_{\rm H} = 10^6$ cm^{-3}, even low velocity C-type shock models generate too high rotational temperatures and 0-0 S(5) flux, and this whole density value is excluded of our further studies. As seen in the previous Subsection, lower magnetic field parameters yield lower critical velocities, hence limiting our range of investigation.

The shock age still has to be constrained. As it is unrealistic to compute a blind grid of CJ shock models without guessing it, we have to get a first guess of its value. Again we use the compact excitation diagram. Indeed, considering the temperatures that are respectively reached in different kinds of shock models, we have seen on Figures 3.3 and 4.5 that the rotational $\ln(N_{vJ}/g_J)$ values are greater in a C-type shock than in a non stationary shock model. In fact, the H_2 rotational emission arising in a CJ shock model almost entirely comes from its magnetic precursor : the C-type contribution to this part of the spectrum emission is much larger than the J-type one. As previously stated, the

Tableau 4.4 – Best molecular hydrogen fits parameters for L1157 B1 : non stationary shock models.

	10^4 cm^{-3}			10^5 cm^{-3}	
	20 km s^{-1}	22 km s^{-1}	25 km s^{-1}	12 km s^{-1}	15 km s^{-1}
b = 0.30	-	-	-	50 yr	-
b = 0.45	600 yr	375 yr	225 yr	75 yr	-
b = 0.60	550 yr	450 yr	725yr	75 yr	-
b = 0.75	700 yr	625 yr	325 yr	100 yr	-
b = 1.00	850 yr	1000 yr	500 yr	235 yr	-
b = 1.25	1100 yr	625 yr	750 yr	305 yr	-
b = 1.50	1400 yr	1100 yr	850 yr	-	-
b = 1.75	1750 yr	1450 yr	825 yr	-	515
b = 2.00	2000 yr	1700 yr	1400 yr	-	515

$\ln(N_{vJ}/g_J)$ value is computed through the whole shock, and its value is calculated by our shock code at each point of the shock. To build a CJ shock model that reproduces the observational compact excitation diagram, we then have to add the J contribution to the C shock at the point where its contribution to the 0-0 S(5) $\ln(N_{vJ}/g_J)$ value is already close to that of the observational value. This provides a first guess of the computed shock age, whose surrounding values we also investigate to make sure we are not missing any eligible CJ shock model. This deduced shock age can then be compared to the dynamical age provided by the observations (around 2000 years for L1157B1, see Gueth et al. (1998)), providing another constraint.

We finally computed a grid of CJ (non stationary) shock models, using this criterion to get a first guess of the shock age for each of the above set of parameters, and then investigated the surrounding ages range to make sure we could not miss any satisfying fit of the H_2 observations. With $n_H = 10^6$ cm^{-3}, only models with evolutionary ages less than a few hundred years are able to fit the observed rotational temperature. We excluded such models on the grounds that the dynamical age deduced empirically is in the range 2000–3000 years Gueth et al. (1998).

4.4 Fitting molecular hydrogen observations for L1157B1

4.4.1 Best results

For each model of the shock grid (stationary and non stationary types), we generated a complete molecular excitation diagram similar as the ones introduced on Figure 3.3, that we the compared to the observational ones (Figure 4.2). We find numerous CJ-type shock models whose parameters are indicated on Table 4.4.We also found a J shock model that provides satisfying comparisons with the observations in terms of molecular hydrogen excitation diagram, for a pre-shock density of $n_H = 10^5$ cm^{-3}, and a shock velocity of

12 km s^{-1}.

4.4.2 Comments

In Figure 4.6, we compare the H_2 excitation diagram derived from the observations of L1157 B1 with the predictions of two representative satisfying CJ-type shock models with pre-shock densities $n_H = 10^4$ and 10^5 cm^{-3}. For the higher density, we also show the results from the J-type (stationary) shock model mentioned above. None of the models provides a completely satisfactory fit to the observations. As the shock evolves towards stationary C-type, i.e. as its age increases, the intensities of the rovibrational transitions decrease, relative to the pure rotational transitions within the vibrational ground state, $v = 0$. Thus, the J-type shock underestimates substantially the column densities of the $v = 0$ rotational levels. As these levels contribute most of the H_2 column density, we eliminate the J-type model from further consideration. On the other hand, the CJ-type shocks tend to underestimate the column densities of some of the vibrationally excited rotational levels.

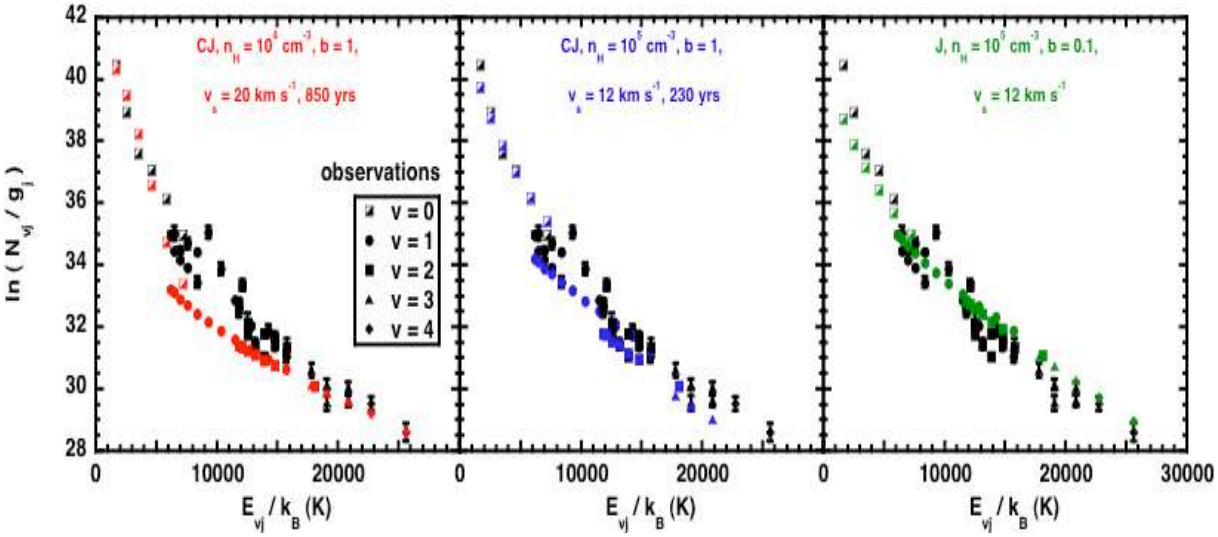

Figure 4.6 – Three models of the H_2 excitation diagram of the L1157 B1 : CJ-type $n_H = 10^4$ cm^{-3}, b = 1, $v_s = 20$ km s^{-1}, age 850 years old (left hand side panel) ; CJ-type $n_H = 10^5$ cm^{-3}, b = 1, $v_s = 12$ km s^{-1}, age 230 years old (middle panel) ; J-type $n_H = 10^5$ cm^{-3}, b = 0.1, $v_s = 12$ km s^{-1} (right hand side panel).

The partial conclusion associated to this molecular hydrogen study is that it corroborates that of Flower et al. (2003), Giannini et al. (2004), and Giannini et al. (2006) : non stationary shock models provide the most satisfactory fits to H_2 rotational and rovibrational emission. It is also interesting to mention that the first guess that we determined with the criterion described earlier in this section is generally providing the best fits, all other parameters remaining equal (n_H, v_s, and b).

Other molecular tracers for star formation : modelling aspects

5

Theoretical aspects

Ce chapitre présente et justifie la méthodologie utilisée pour modéliser l'émission de molécules caractéristiques telles CO et SiO dans les régions de formation stellaire. La présence de CO et SiO dans ces régions est d'abord commentée. Le concept de probabilité d'échappement est ensuite introduit, dans le cadre de l'approximation LVG. Le calcul du champ de radiation stellaire dans de telles conditions est alors présenté. Ce calcul est en effet indispensable à la résolution des équations de l'équilibre statistique, elles aussi décrites dans ce chapitre. Enfin le calcul de l'intensité intégrée associée à nos modèles de chocs, indispensable à la comparaison avec les observations disponibles, est réalisé.

5.1 CO and SiO in shock regions

5.1.1 The case of CO

Thanks to its strong binding energy, CO is widely distributed in the interstellar medium, with a roughly constant abundance (at least where most hydrogen is molecular). In fact, apart from molecular hydrogen, CO is the most abundant and thus observed molecule in the interstellar medium. Furthermore, CO is abundantly seen in shock regions : the first observed molecular outflows (see Snell et al. (1980)) was detected in the first rotational lines of CO, and CO is of major use to determine the wind dynamics and its interaction with the ambient gas (see for example Cabrit (2000)).

In addition to its large abundance, CO has many advantages over other molecules for studies matters of the shock regions :

- in such regions, CO exists in the gas phase (see Appendix C for the chain of reactions leading to the formation of gaseous CO). Furthermore CO also exists in the form of solid 'ice' in the grain mantles. These grain mantles are sputtered by the shock front, hence releasing extra CO in the gas phase ;
- CO has a small but finite (see Table 6.1) permanent dipole moment so that its pure rotational and rovibrational transitions are relatively strong ;
- its long wavelength transitions occur in reasonably good positions of the spectrum, i.e. in the near infrared and mm bands (J = 6 rotational level lies 116.2 K above the ground state). CO is widely observed also because its rotational transitions are

readily detectable with ground-based telescopes.

With all these advantages, CO is expected to be an efficient diagnostic and an important molecular coolant for cold clouds or regions with T $\simeq$ 10-100 K. Indeed, molecular outflows are often mapped in rotational transitions of CO. Figures 3.2 and 4.1 the map of L115 display the example of the L1157 region map, as seen thanks to the CO (2-1) transition.

5.1.2 The case of SiO

The silicon monoxide molecule SiO is the most widespread silicon-bearing molecule in the interstellar medium. It was first detected in the Galactic centre (Sgr B2, Wilson et al. (1971) and Ori A, Dickinson (1972)) at low fractional abundances of 2×10^{-12}. However, its fractional abundance largely depends on the differing physical conditions of interstellar object.

Its lowest fractional abundance $< 3 \times 10^{-12}$ was deduced from observations of dense clouds such as TMC1 and L183 (Ziurys et al. (1989), Martin-Pintado et al. (1992)). In these cold and quiescent surroundings, SiO is quickly generated by reaction between Si and O_2, before strong depletion on to grains takes place (as much as six orders of magnitude relative to the solar value). Silicon is thus believed to be present in the solid phase, in the form of refractory cores of silicate grains, or in the ice mantles around such grains.

In photodissociation regions, photodesorption, through UV radiation from nearby stars (Turner (1998), Walmsley et al. (1999)), brings silicon back in the gas phase, where its reaction with OH makes the SiO fractional abundance vary with the depth. Schilke et al. (2001) thus measured intermediate values of around 10^{-10}. Similar detections have been made in translucent molecular clouds (Turner (1998)) and spiral arm clouds (Greaves et al. (1996)).

SiO largest fractional abundances have been detected in dynamically active regions of the ISM, such as molecular outflows (around 10^{-7}, Gueth et al. (1998)), Supernovae remnants ($\leq 5\times10^{-9}$, van Dishoeck et al. (1993)). Even greater abundances were observed in star forming regions (2×10^{-6}, Martin-Pintado et al. (1992)), yielding the theory that in such dynamical regions, the grains are partially destroyed, releasing silicon in the gas phase. This assumption is also supported by the observation of large enhancements of elemental silicon in the gas phase in high velocity components of diffuse clouds (Sofia et al. (1993), Gry et al. (1998)). In favorable environments (as shocked regions), the silicon is later processed into SiO through reactions with OH and O_2.

It has been since firmly established that in regions of shocks, interstellar grains undergo destruction processes among which :

- sputtering of the grains mantles (Draine et al. (1983), Flower and Pineau des Forets (1994)), which arises through impacts with the most abundant neutral species (H, H_2, He). In fact, a majority of grains are charged and thus have a drift velocity with respect to such neutral molecules, which cause the impacts ;
- erosion of the grains cores, believed to be made of Si-bearing materials like forsterite (Mg_2SiO_4), fayalite (Fe_2SiO_4), or olivine ($MgFeSiO_4$), under the impact with neutral molecules such as He, C, N, O, H_2O, N_2, CO, and O_2. This erosion was stressed out by the works of Flower and Pineau des Forets (1995) and Flower et al. (1996). Field

et al. (1997) computed sputtering yields for carbonaceous grains, and May et al. (2000) provided sputtering probabilities for the above materials to determine the rate of erosion of Si by neutral particles.

A more complete description of grain processes in shock waves is given by Guillet et al. (2007).

Once released in the gas phase, silicon is then processed by the chemistry, undergoing sequences of reactions to form hydrosilicon bearing species, and, more interestingly, SiO (see Herbst et al. (1989), Langer and Glassgold (1990)). The detail of the reactions involving Si-bearing species, as well as a list of th Si-bearing species that are taken into account in our shock models can be found respectively in Appendix N and M. Of particular interest from the point of view of SiO creation are the two following reactions :

$$Si + O_2 \longrightarrow SiO + O \tag{5.1}$$

$$Si + OH \longrightarrow SiO + H \tag{5.2}$$

In the chemical models aiming to describe interstellar medium chemistry, reaction rates usually adopted for these reactions are respectively 2.7 $\times$ 10 $^{-10}$ exp (-111/T) and 1.7 $\times$ 10 $^{-10}$ exp (-111/T), the numerator 111 of the exponential argument standing for the difference in energy between the first two spin-orbit levels of the silicon ground state (see Langer and Glassgold (1990)). In this study, we preferentially use the reaction rates that were experimentally determined by Le Picard et al. (2001). The experimental value measured for the first reaction is 1.7 $\times$ 10^{-10} $(T/300)^{-0.53}$ exp (-17/T). The same expression is implemented for the second reaction rate. This choice and its consequences are further discussed and studied in Subsection 6.5.2.

Once SiO has been formed in the gas phase, numerous reactions are likely to destroy it (again, see the reactions list in Appendix N), among which :

$$SiO + OH \longrightarrow SiO_2 + H \tag{5.3}$$

whose importance relies on the large fractional abundance of OH in the post-shock gas. In the cooling phase of the shock, adsorption of SiO onto grains determines its abundance in the gas phase, even if it is not the most realistic fashion to model the post-shock regions. Its influence is studied in Appendix K.

Being specifically observed in shocked regions, SiO is the perfect tracer for shocked gas in the interstellar medium (see also Nisini et al. (2005), Schilke et al. (1997), Martin-Pintado et al. (1992),...). Figure 5.1 provides a map of the L1157 outflow in the (3-2) transition of SiO and methanol, which is another shock tracer, making the coincidence of their emission region with those of CO or H_2 (see Figure 4.1) clear.

5.2 The escape probability concept

In this section, we present the analytical considerations that allow to simplify the radiative transfer in the LVG (Large Velocity Gradient) approximation, which prevails for expanding medium with a large velocity gradient. By 'large' velocity gradient, one means a sufficient gradient so that the distance on which the considered matter is opaque is largely

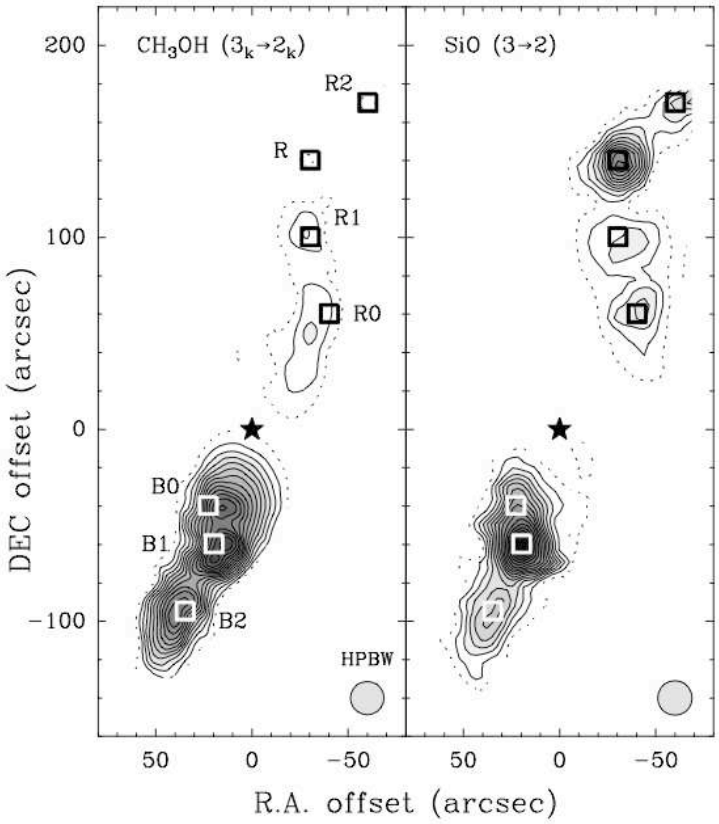

Figure 5.1 – The L1157 outflow as seen in the SiO and methanol (3-2) transition integrated intensity ; taken from Bachiller et al. (2001).

inferior to its typical dimensions. In fact, during its travel through the matter, the photon, emitted with a frequency ν, undergoes a strong Doppler effect on short distances, because of the large velocity gradient that exists within the shock region. When the Doppler shift is larger than the local width of the line in which it was emitted, the photon can no longer be absorbed by ambient atoms or molecules : the matter has become transparent for the photon.

5.2.1 Useful quantities

We start by introducing some useful quantities when it comes to radiative transfer problems. The absorption and emission coefficient per volume of emission unit for a spectral line corresponding to a $j \rightarrow i$ transition at the frequency ν_{ij} are respectively given by

$$\alpha_{ij} = \frac{n_i B_{ij} h\nu_{ij}}{4\pi}\left(1 - \frac{g_i n_j}{g_j n_i}\right) \tag{5.4}$$

$$\epsilon_{ij} = \frac{n_j A_{ji} h\nu_{ij}}{4\pi} \tag{5.5}$$

where n_i and n_j are the populations of levels i (inferior level) and j (superior level), g_i and g_j being their statistical weight. B_{ij} and A_{ij} denote the associated Einstein coefficients, and h is Planck's constant.

The source function S_{ij} of a line associated to the transition $j \rightarrow i$ in the frame of the atom is

$$S_{ij} = \frac{\epsilon_{ij}}{\alpha_{ij}} \tag{5.6}$$

Substituting α_{ij} and ϵ_{ij} by their value (equations 5.4 and 5.5), we then obtain

$$S_{ij} = \frac{2h\nu_{ij}^3}{c^2}\frac{1}{\frac{g_j n_i}{g_i n_j} - 1} \tag{5.7}$$

$$= \frac{2h\nu_{ij}^3}{c^2}\frac{1}{e^{\frac{h\nu_{ij}}{kT_{\rm exc}}} - 1} \tag{5.8}$$

$$= B_\nu(T_{\rm exc}) \tag{5.9}$$

where $B_\nu(T)$ is the Planck's function associated to the frequency ν, and where $T_{\rm exc}$ (defined by this relation) is called the excitation temperature associated to the transition $j \rightarrow i$.

5.2.2 Escape probability of a photon emitted at a given frequency ν, in a given direction

We now can introduce the concept of escape probability, first developed by Sobolev (1947, 1957, 1958) when studying the radiative transfer of a stellar envelope in fast and radial expansion. The assumption made by Sobolev is the following : a photon emitted at a point of the envelope can either be absorbed in the vicinity of this point, either escape because of the important Doppler shifts along the envelope. A necessary condition

is obviously that the expansion velocity must be much larger than the thermal velocity of the atoms. In this section, we present a way to estimate the escape probability for the photon via the Doppler shift, following the method presented in Surdej (1977).

We thus consider an expanding envelope, in which the level populations of the atoms have reached a stationary state. We also assume a complete redistribution over the frequency range and direction for the emitted photon, in the frame of the moving atom.

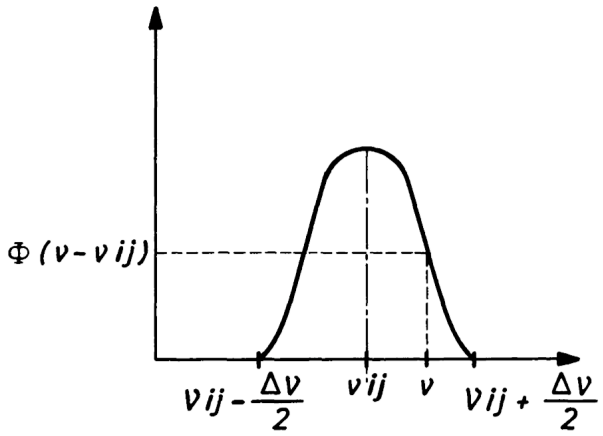

Figure 5.2 – Normalized line profile associated to the transition $j \rightarrow i$, in the frame of the atom. Taken from Surdej (1977).

Let $\Phi(\nu - \nu_{ij})$ be the arbitrary function that describes the local profile of a line, normalized to unity, equal to zero out of the range $[\nu_{ij} - (\Delta\nu/2), \nu_{ij} + (\Delta\nu/2)]$, where ν_{ij} is the central line frequency, and $\Delta\nu$ is the maximum width of the line profile due to chaotic movements of atoms. We assume

$$\frac{\Delta\nu}{\nu_{ij}} = \frac{2v_{\rm th}}{c} \tag{5.10}$$

where $v_{\rm th}$ is the thermal velocity of atoms, and c is the light velocity.

Because of the important velocity gradients along the envelope, the distance ΔS through which the Doppler shift of the frequency reaches the thermal width of the line is small compared to the typical scales of variations of the physical parameters of the envelope. Consequently, along such a distance, we can assume that the volumic coefficients of absorption α_{ij}, emission ϵ_{ij}, as well as the velocity gradient are constant, and that the local profile of the line remains the same. If $\partial v_{\rm s}/\partial s$ stands for the velocity gradient along a given direction and at a given point, we then have

$$\Delta S = \frac{2v_{\rm th}}{\partial v_{\rm s}/\partial s} \tag{5.11}$$

We now derive the expression for the escape probability β_{ij}, defined as the probability for a photon created through the transition $j \rightarrow i$ can escape the emission region in any direction. For more clarity, we'll forget the index 'ij' (and substitute it by '0' in the case of frequency) in the following developments.

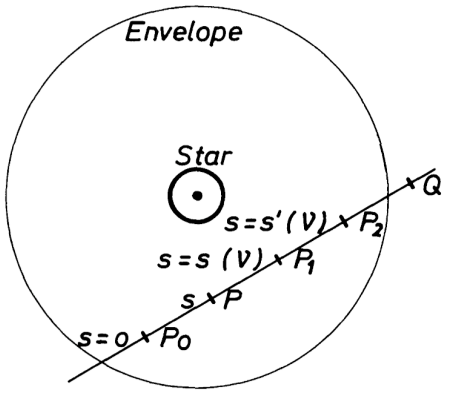

Figure 5.3 – Arbitrary direction in the envelope, along which the radiative transfer is considered. Taken from Surdej (1977).

Let P_0 be a given point in the expanding envelope, whose abscissa is $s = 0$ (see Figure 5.3). The abscissa axis s is positively oriented from P_0 towards Q. Let us assume that a photon is emitted at P_0 in this direction, at the frequency ν in the local frame. Because of the large velocity gradient $\partial v_{\rm s}/\partial s$, the photon has a probability $PR(P_0Q)$ to be absorbed between P_0 and P_1, whose respective abscissae are $s = 0$ and $s = s(\nu)$. Beyond P_1, the medium becomes totally transparent to photons at frequency ν because of the Doppler shift between P_0 and P_1.

Absorption probability for the photon, $PR(P_0Q)$ can then be expressed

$$PR_\nu(P_0Q) = \int_0^{s(\nu)} exp\left(-\int_0^s \alpha\Phi\left(\nu-\nu_0-\frac{\nu_0}{c}\frac{\partial v_{\rm s}}{\partial s}s'\right)ds'\right)\alpha\Phi\left(\nu-\nu_0-\frac{\nu_0}{c}\frac{\partial v_{\rm s}}{\partial s}s\right)ds \tag{5.12}$$

In this integral, the expression is the product of two terms whose physical interpretation is the following :

- $\alpha\Phi\left(\nu-\nu_0-\frac{\nu_0}{c}\frac{\partial v_{\rm s}}{\partial s}s\right)ds$ stands for the probability that a photon emitted at a frequency ν is absorbed in the vicinity of P, between abscissae s and $s+ds$;
- $-\frac{\nu_0}{c}\frac{\partial v_{\rm s}}{\partial s}s'$ accounts for the Doppler shift of the photon in the frame of $P(s)$, emitted at the frequency ν at P_0, due to the velocity difference between P_0 and $P(s)$;
- $exp\left(-\int_0^s \alpha\Phi\left(\nu-\nu_0-\frac{\nu_0}{c}\frac{\partial v_{\rm s}}{\partial s}s'\right)ds'\right)$ is the probability that the photon emitted at frequency ν is not absorbed between P_0 and $P(s)$;
- $\alpha\Phi\left(\nu-\nu_0-\frac{\nu_0}{c}\frac{\partial v_{\rm s}}{\partial s}s'\right)$ is the opaqueness of the medium for the considered photon.

We can simplify the equation 5.12 thanks to the following variables transformations

$$x = \nu-\nu_0-\frac{\nu_0}{c}\frac{\partial v_{\rm s}}{\partial s}s' \;;\; dx = \frac{\nu_0}{c}\frac{\partial v_{\rm s}}{\partial s}ds' \tag{5.13}$$

$$y = \nu-\nu_0-\frac{\nu_0}{c}\frac{\partial v_{\rm s}}{\partial s}s \;;\; dy = \frac{\nu_0}{c}\frac{\partial v_{\rm s}}{\partial s}ds \tag{5.14}$$

Equation 5.12 then writes

$$PR_\nu(P_0Q) = \int_{y(s(\nu))}^{\nu-\nu_0} exp\left(\int_{\nu-\nu_0}^{y}\frac{\alpha}{\nu_0}\frac{c}{\frac{\partial v_{\rm s}}{\partial s}}\Phi(x)dx\right)\frac{\alpha}{\nu_0}\frac{c}{\frac{\partial v_{\rm s}}{\partial s}}\Phi(y)dy \tag{5.15}$$

We have seen that under the LVG assumptions α and $\partial v_s/\partial s$ can be treated as constant in the integrates. We then can define the constant quantity

$$\tau_s = \frac{\alpha}{\nu_0}\frac{c}{\frac{\partial v_s}{\partial s}} \tag{5.16}$$

sometimes called Sobolev optical depth, thanks to which 5.15 simplifies

$$PR_\nu(P_0Q) = \int_{y(s(\nu))}^{\nu-\nu_0} \frac{d}{dy}\left(exp\left(\tau_s \int_{\nu-\nu_0}^{y} \Phi(x)dx\right)\right)dy \tag{5.17}$$

$$= 1 - exp\left(\tau_{ij}\int_{\nu-\nu_{ij}}^{y(s(\nu))}\Phi(x)dx\right) \tag{5.18}$$

5.2.3 Escape probability of a photon emitted at any frequency, in a given direction

The absorption probability $PR(P_0Q)$ of a photon emitted at any frequency of the line profile of the atom at P_0, in the direction P_0Q is given by

$$PR(P_0Q) = \int_{\nu_0-\frac{\Delta\nu}{2}}^{\nu_0+\frac{\Delta\nu}{2}} \Phi(\nu-\nu_0)PR_\nu(P_0Q)d\nu \tag{5.19}$$

Through th variable transformation : $l = \nu - \nu_0, dl = d\nu$ and thanks to equation 5.17, we obtain

$$PR(P_0Q) = \int_{-\frac{\Delta\nu}{2}}^{\frac{\Delta\nu}{2}} \Phi(l)\left(1 - exp\left(\tau_s\int_{l}^{y(s(\nu))}\Phi(x)dx\right)\right)dl \tag{5.20}$$

Then the normalization condition for $\Phi(\nu)$, $\int_{-\Delta\nu/2}^{\Delta\nu/2}\Phi(x)dx = 1$, allows us to write

$$PR(P_0Q) = 1 + \int_{-\frac{\Delta\nu}{2}}^{\frac{\Delta\nu}{2}} \frac{d}{dl}\left(exp\left(\tau_s\int_{l}^{y(s(\nu))}\Phi(x)dx\right)\right)\frac{1}{\tau_s}dl \tag{5.21}$$

$$= 1 + \left[\frac{exp\left(\tau_S\int_l^{y(s(\nu))}\Phi(y)dy\right)}{\tau_S}\right]_{-\Delta\nu/2}^{\Delta\nu/2} \tag{5.22}$$

If along P_0Q the velocity gradient $\partial v_s/\partial s$ is positive, the photon is reddened (at the local line frequency of $\nu_0-(\Delta\nu)/2$) at P_1. Similarly, if the velocity gradient is negative, the photon is bluened (at the local line frequency $\nu_0+(\Delta\nu)/2$) at P_1. The 5.14 transformation shows that

$$\text{if } \frac{\partial v_s}{\partial s} > 0 \qquad y(s(\nu)) = \nu - \nu_0 - \frac{\nu_0}{c}\frac{\partial v_s}{\partial s}s(\nu) \tag{5.23}$$

and since the Doppler shift between P_1 and P_0 is given by (see Figure 5.3)

$$\frac{\nu_0}{c}\frac{\partial v_s}{\partial s}s(\nu) = \nu - \left(\nu_0 - \frac{\Delta\nu}{2}\right) \tag{5.24}$$

Equation 5.23 writes

$$y(s(\nu)) = -\frac{\Delta\nu}{2} \tag{5.25}$$

Similarly

$$\text{if } \frac{\partial v_s}{\partial s} < 0 \qquad y(s(\nu)) = \frac{\Delta\nu}{2} \tag{5.26}$$

We can the simplify equation 5.21, using results obtained in 5.25 and 5.26

$$\text{if } \frac{\partial v_s}{\partial s} > 0 \qquad PR(P_0Q) = 1 - \left(exp\left(-\tau_s \int_{-\frac{\Delta\nu}{2}}^{\frac{\Delta\nu}{2}} \Phi(x)dx \right) - 1 \right) \frac{1}{\tau_s} \tag{5.27}$$

$$= 1 - \frac{exp(-\tau_S) - 1}{\tau_S} \tag{5.28}$$

$$\text{if } \frac{\partial v_s}{\partial s} < 0 \qquad PR(P_0Q) = 1 + \left(1 - exp\left(-\tau_s \int_{-\frac{\Delta\nu}{2}}^{\frac{\Delta\nu}{2}} \Phi(x)dx \right) \right) \frac{1}{\tau_s} \tag{5.29}$$

$$= 1 + \frac{1 - exp(-\tau_S)}{\tau_S} \tag{5.30}$$

that is, independently of the sign of $\partial v_s/\partial s$

$$PR(P_0Q) = 1 - (1 - exp(- \mid \tau_S \mid)) \frac{1}{\mid \tau_S \mid} \tag{5.31}$$

The probability β_0 for a photon created in the transition $j \rightarrow i$ to escape the medium in the given direction P_0Q is eventually given by

$$\beta_0(P_0Q) = 1 - PR(P_0Q) = \frac{1 - exp(- \mid \tau_S \mid)}{\mid \tau_S \mid} \tag{5.32}$$

5.2.4 Average over all directions

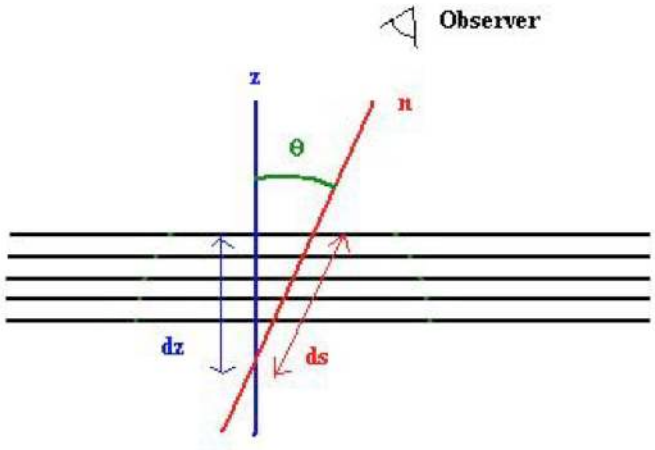

Figure 5.4 – The geometrical inclination parameter : θ.

Actually, optical depth τ_S depends on the escape direction of the considered photon. Indeed, we have seen that Sobolev optical depth is inversely proportional to the velocity gradient in the escape direction. Generally, this velocity gradient depends on the considered direction. We can express this dependence via a geometrical parameter, θ (see Figure 5.4 for an example of such a parameter in our geometry). Consequently, in the most general case, the escape probability depends on this parameter through the quantity $\mu = cos(\theta)$

$$\beta_0(P_0Q) = 1 - PR(P_0Q) = \frac{1 - exp(- \mid \tau_S(\mu) \mid)}{\mid \tau_S(\mu) \mid} \tag{5.33}$$

We now derive the average value of the escape probability over all directions, in two simple cases.

The situation of Surdej (1977). In the case of the stellar envelope studied by Surdej, the expansion is both radial and isotropic. In other terms, the velocity gradient is the same in all directions. Consequently, Sobolev optical depth is also identical, whatever the direction may be. The probability β for a photon created in the transition $j \rightarrow i$ to escape the medium in any direction is then given by

$$\beta_{ij} = \int_{\Omega=4\pi} (1 - PR(P_0Q)) \frac{d\omega}{4\pi} = \int_{\Omega=4\pi} \frac{1 - exp(- \mid \tau_s \mid)}{\tau_s} \frac{d\omega}{4\pi} \tag{5.34}$$

where the integration is done over all direction (solid angle $\Omega = 4\pi$). In this very specific case, the escape probability averaged on all directions is thus equal to the one in a given direction.

Our situation. The second case corresponds to our situation of a plane parallel shock. We have seen that the optical depth is inversely proportional to the velocity gradient in the considered direction. If one choose a reference direction z, for instance the perpendicular direction to the plane parallel shock, and if one name $\mu = cos\theta$ the geometrical parameter corresponding to the angle between this perpendicular direction and the escape direction of a given photon (see Figure 5.4), then $\tau(\mu) \propto \partial v_s / \partial s \propto \mu^2 / (dv_z/dz)$. In this case, the average of the escape probability over all directions writes

$$\beta_{ij} = \int_{\Omega=4\pi} \frac{1 - exp(- \mid \tau_s \mid / \mu^2)}{\mid \tau_s / \mu^2 \mid} \frac{d\omega}{4\pi} \tag{5.35}$$

where τ_S is defined with respect to the reference direction z. With such a coordinate system, one can write : $d\omega = 2\pi sin(\theta) d\theta = 2\pi d\mu$. Equation 5.35 then becomes

$$\beta_{ij} = \int_{\Omega=4\pi} \frac{1 - exp(- \mid \tau_s \mid / \mu^2)}{\mid \tau_s \mid} \mu^2 \frac{d\mu}{2} \tag{5.36}$$

In 1993, Neufeld and Kaufman have proposed an approximation of this expression averaged over all directions (see Neufeld and Kaufman (1993))

$$\beta_{ij} = \frac{1}{1 + 3 \mid \tau_S \mid} \tag{5.37}$$

This expression exhibits major advantages :

- the maximum discrepancy with exact expression (given in Hummer and Rybicki (1982)) is 15 % ;
- it is exact for large and small values of τ_S ;
- it doesn't introduce any singularity from a numerical point of view.

5.3 Calculation of radiation field

The mean intensity of the radiation field J_{ij} at a given point of the medium (for instance the point P_0 on Figure 5.3) is defined as the intensity of the radiation likely to interact with an atom at P_0 in all directions and on all the frequency range covered by the transition $j \rightarrow i$. This quantity is of major interest when one studies the statistical equilibrium equations, that allow to derive the populations of the rotational levels (see Section 5.4). Additionnally to a 'local contribution' J^1_{ij} caused by the radiation emitted by neighbour atoms in P_0, the mean intensity of the radiation field J_{ij} includes another contribution J^b_{ij}, due to the existence of a cosmic background, which behaves like a blackbody at a temperature of $\mathrm{T}_{BB} = 2.7$ K.

We start with the evaluation of the local contribution J^1_{ij}. To do so, let us consider the point P_0 and the direction QP_0 on Figure 5.3. The abscissa axis is now positively oriented from Q to P_0. The radiation intensity $I_{ij}(QP_0)$ at the local frequency ν at P_0 is given by

$$I^\nu_{ij}(QP_0) = \int_{s'(\nu)}^{0} \epsilon\Phi\left(\nu - \nu_0 - \frac{\nu_0}{c}\frac{\partial v_\mathrm{s}}{\partial s}s\right) exp\left(\int_s^0 -\alpha\Phi\left(\nu - \nu_0 - \frac{\nu_0}{c}\frac{\partial v_\mathrm{s}}{\partial s}s'\right)ds'\right)ds \tag{5.38}$$

In this integrate :

- $\epsilon\Phi(\nu - \nu_0 - (\nu_0/c)(\partial v_\mathrm{s}/\partial s)s)ds$ is the amount of energy emitted at the frequency ν at point P whose abscissa is s and by the length element ds towards the point P_0 ;
- $exp\left(\int_s^0 -\alpha\Phi\left(\nu - \nu_0 - \frac{\nu_0}{c}\frac{\partial v_\mathrm{s}}{\partial s}s'\right)ds'\right)$ stands for the attenuation undergone by the photons at frequency ν between points P and P_0 ;
- $s'(\nu)$ is the abscissa of the point P_2 beyond which the frequency of the radiation emitted in the transition is too much shifted to contribute to the local frequency ν at P_0.

The intensity of the radiation integrated over the line width in the frame of the atom in P_0 can be expressed

$$I_{ij}(QP_0) = \int_{\nu_{ij}-\frac{\Delta\nu}{2}}^{\nu_{ij}+\frac{\Delta\nu}{2}} \Phi(\nu - \nu_{ij})I^\nu_{ij}(QP_0)d\nu \tag{5.39}$$

Following the same way of thinking than in the previous section, we can simplify this expression. By substituting expression 5.38 in equation 5.39, and by using the variable transformations defined in Subsection 5.2.3, relations 5.25 and 5.26 respectively become

$$\text{if} \quad \frac{\partial v_\mathrm{s}}{\partial s} > 0 \qquad y(s(\nu)) = \frac{\Delta\nu}{2} \tag{5.40}$$

$$\text{if} \quad \frac{\partial v_\mathrm{s}}{\partial s} < 0 \qquad y(s(\nu)) = -\frac{\Delta\nu}{2} \tag{5.41}$$

and one obtain :

$$I_{ij}(QP_0) = S_{ij}\left(1 - \frac{1 - exp(-\mid \tau_{ij} \mid)}{\mid \tau_{ij} \mid}\right) = S_{ij}(1 - \beta_{ij(\mu)}) \tag{5.42}$$

where S_{ij} is the source function as defined by Equation 5.6.

Eventually, the local contribution J^1_{ij} to the mean intensity of the radiation field in P_0 is obtained by averaging equation 5.42 over all directions. Thanks to equation 5.34

$$J^1_{ij} = \int_{\Omega=4\pi} I_{ij}(QP_0)\frac{d\omega}{4\pi} \tag{5.43}$$

$$J^1_{ij} = S_{ij}(1 - \beta_{ij}) \tag{5.44}$$

In the case where the continuum comes from the cosmic background, radiated without attenuation and with an intensity of I_c constant over the frequency range of the transition, the radiation intensity $I_c(SP_0)$ emitted at any point S of the medium and appearing at the frequency ν to an atom at P_0 is given by

$$I^c_\nu(SP_0) = I_c exp\left(-\int_{s(\nu)}^{0} \alpha_{ij}\Phi\left(\nu - \nu_{ij} - \frac{\nu_{ij}}{c}\frac{\partial v_s}{\partial s}s'\right)ds'\right) \tag{5.45}$$

The exponential term expresses the radiation continuum extinction between points S_1 and P_0 , abscissa axis s being positively oriented from S to P_0. The atoms at points of abscissa $s < s(\nu)$ are too much distant of P_0 (that is, their Doppler shift is too large) to be able to absorb at the local frequency of the line ν defined at P_0. Integrating equation 5.45 over the line width in the frame bound to the atom at P_0, and using the variable transformations of Subsection 5.2.3, from the general expression

$$I^c(SP_0) = \int_{\nu_{ij}-\frac{\Delta\nu}{2}}^{\nu_{ij}+\frac{\Delta\nu}{2}} \Phi(\nu - \nu_{ij})I^c_\nu(SP_0)d\nu \tag{5.46}$$

we obtain the equation

$$I^c(SP_0) = I_c\frac{1 - exp(-\mid \tau_{ij} \mid)}{\mid \tau_{ij} \mid} \tag{5.47}$$

The contribution of the continuum caused by the cosmic background to the mean intensity of the radiation field at P_0 is then given by

$$J^b_{ij} = I_c\int_{\Omega=4\pi} \frac{1 - exp(-\mid \tau_{ij} \mid)}{\mid \tau_{ij} \mid}\frac{d\omega}{4\pi} \tag{5.48}$$

that is by

$$J^b_{ij} = I_c\beta_{ij} \tag{5.49}$$

where β_{ij} still corresponds to the averaged escape probability over all directions, which can be calculated ar approximated in both cases already studied (see 5.2.4).

One can now pay more attention to the continuum we have to take into account in the case of our study. The corresponding intensity is not due to the core of the star,

but to the ambient radiation field, that is to the cosmic background at 2.7 K. Because of its temperature value, this radiation belongs to the millimetric and submillimetric wave ranges. Consequently, it plays a major role in the equilibrium of rotational levels populations of the molecules (see section 5.4). For a line of central frequency ν_{ij}, the term I_c defined in the previous section then writes

$$I_c = B_{\nu_{ij}}(T_{BB}) \tag{5.50}$$

where $B_{\nu_{ij}}(T_{BB})$ is the Planck's function at the frequency ν_{ij} and blackbody temperature T_{BB} of the universe ($T_{BB} = 2.7$K)

$$B_{\nu_{ij}}(T_{BB}) = \frac{2h\nu_{ij}^3}{c^2} \frac{1}{e^{\frac{h\nu_{ij}}{kT_{BB}}} - 1} \tag{5.51}$$

where h is Planck's constant, k is Boltzmann's constant, and c is the light velocity in the vacuum.

Finally, the global radiation field can be expressed using both local and background contributions (Equations 5.44 and 5.49)

$$J_{ij} = S_{ij}(1 - \beta_{ij}) + I_c\beta_{ij} \tag{5.52}$$

5.4 Statistical equilibrium equations

In order to calculate the level populations n_i of a molecule, statistical equilibrium equations must be solved. In a stationary state, these equations are, for each level i

$$\frac{dn_i}{dt} = R_i + C_i = 0 \tag{5.53}$$

where R_i and C_i stand respectively for the volumic radiative and collisional rates of population for the level i. More explicitly

$$\frac{dn_i}{dt} = \sum_{j \neq i} [n_j A_{ji} + (n_j B_{ji} - n_i B_{ij}) J_{ij}] + \sum_{j \neq i} n_{H_2}(n_j C_{ji} - n_i C_{ij}) = 0 \tag{5.54}$$

where A_{ji}, B_{ji}, B_{ij} are respectively Einstein's coefficients for spontaneous emission, stimulated emission, and absorption, where C_{ij} denotes the collisional coefficient rate from level i to level j, and where J_{ij} is the mean radiation field intensity at a point where the calculation is done.

Moreover, in the case of rotational transitions of diatomic molecules with an electric dipolar moment, quantum mechanics selection rules only authorize transitions between i and j levels for which the difference between rotational quantum number verifies $\Delta J = \pm 1$, which allows us to write the evolution equation

$$\begin{aligned} \frac{dn_i}{dt} &= n_{i+1}A_{i+1,i} + (n_{i+1}B_{i+1,i} - n_i B_{i,i+1})J_{i,i+1} \\ &- n_i A_{i,i-1} + (n_{i-1}B_{i-1,i} - n_i B_{i,i-1})J_{i-1,i} \\ &+ \sum_{j \neq i} n_{H_2}(n_j C_{ji} - n_i C_{ij}) \end{aligned} \tag{5.55}$$

In addtion to this, we have shown in the previous section (5.3)

$$J_{ij} = S_{ij}(1 - \beta_{ij}) + I_c\beta_{ij} \tag{5.56}$$

where S_{ij} is the source function as defined by 5.6, β_{ij} is the escape probability of a photon created in the transition $j \rightarrow i$, and I_c is the mean intensity of the continuum radiation field.

Combining this expression with equation 5.55, and knowing that $g_iB_{ij} = g_jB_{ji}$ and $A_{ji}/B_{ji} = \sigma_{ij}$, and with $\sigma_{ij} = 2h\nu_{ij}^3/c^2$, we finally get

$$\begin{aligned} \frac{dn_i}{dt} &= \beta_{i,i+1}(n_{i+1}A_{i+1,i} + (n_{i+1}B_{i+1,i} - n_iB_{i,i+1})I_c) \\ &- \beta_{i-1,i}(n_iA_{i,i-1} + (n_iB_{i,i-1} - n_{i-1}B_{i-1,i})I_c) \\ &+ \sum_{j\neq i} n_{H_2}(n_jC_{ji} - n_iC_{ij}) \end{aligned} \tag{5.57}$$

Eventually, we obtain an equation very similar to 5.55, except that Einstein coefficients are multiplied by β_{ij}, and that J_{ij} has been substituted by I_c. In a matrix friendly formulation, this equation also writes

$$\begin{aligned} \frac{dn_i}{dt} = &- n_i\left(\beta_{i,i+1}B_{i,i+1}I_c + \beta_{i-1,i}A_{i,i-1} + \beta_{i-1,i}B_{i,i-1}I_c + \sum_{j\neq i} n_{H_2}C_{ij}\right) \\ &+ n_{i-1}(\beta_{i-1,i}B_{i-1,i}I_c + n_{H_2}C_{i-1,i}) \\ &+ n_{i+1}(\beta_{i,i+1}A_{i+1,i} + \beta_{i,i+1}B_{i+1,i}I_c + n_{H_2}C_{i+1,i} \\ &+ \sum_{j\neq i-1,i,i+1} n_{H_2}n_jC_{ji} \end{aligned} \tag{5.58}$$

In the statistical equilibrium equations, the photons generated in the transitions are likely to escape the medium in any direction. Consequently the escape probability formula must correspond to an average escape probability over all directions. Nevertheless in our shock model, the expansion is not radial nor isotropic : the geometry that we use is plane parallel. Consequently we use the formula 5.37 in this set of equations, that corresponds to Neufeld and Kaufman's approximation.

Eventually, we have a set of evolution equations for each level that we want to take into account. To calculate level populations is equivalent to resolve a set of equations. These equations clearly indicate the key role of the escape probability β_{ij}, which itself include superior and inferior levels via Sobolev optical depth (see 5.16). The set of equations to be solved is thus non linear, which raises a computer problem. We'll see how to resolve such a problem in section 6.1.

5.5 The final observable : integrated intensity

Once the statistical equilibrium equations are solved, it is possible to compute the integrated intensity of each transition, which is the observational quantity to which we'll

be able to compare the results of our models. In other terms, now that we know the level populations and the escape probabilities associated to the transitions between these levels, for each point of the shock, we can determine the radiated flux over all directions by the shock region for each considered line, given by

$$F_{j,j+1} = h\nu_{j,j+1} \sum_{\text{shock region}} n_{j+1} A_{j+1,j} \beta_{j,j+1} \Delta z \tag{5.59}$$

that is, by frequency and solid angle unit, we can now derive the integrated intensity

$$I_{j,j+1} = \frac{1}{4\pi} h\nu_{j,j+1} \sum_{\text{shock region}} n_{j+1} A_{j+1,j} \beta_{j,j+1}(\mu) \frac{\Delta z}{\Delta \nu} \tag{5.60}$$

for a given transition $j+1 \rightarrow j$, where n_{j+1} is the population of the level $j+1$, $\Delta\nu$ is the spectral width associated to the layer of spatial width Δz, $A_{j+1,j}$, $\nu_{j,j+1}$, $\beta_{j,j+1}$ respectively Einstein coefficient, frequency, and escape probability associated to the transition and h is Planck's constant. The sum is done over all the layers (or points) of the shock, and one must be aware of the fact that the escape probability formula used here is no longer averaged over all directions, but corresponds only to the escape probability in the observer's direction. We consequently use the following formula

$$\beta_{j,j+1} = \frac{1 - exp(- \mid \tau_{j,j+1} \mid)}{\tau_{j,j+1}} \tag{5.61}$$

From a rigorous point of view, dependance on μ of this expression should be included (see Formula 5.35, in which the integrate's argument corresponds to an escape probability in a given direction). We'll study later in the project how to overcome this geometrical difficulty and accurately model the shape of the flows (for a beginning of answer, see Appendix L). Nevertheless, the usual expression of $I_{j,j+1}$ is not this one, but the one that we are going to derive now in the case of pure rotational transitions $j+1 \rightarrow j$. In this case, the escape probability writes

$$\beta_{j,j+1} = \frac{1 - exp(- \mid \tau_{j,j+1} \mid)}{\tau_{j,j+1}} \tag{5.62}$$

where Sobolev optical depth can be written in terms of quantities of Subsection 5.2.1

$$\begin{aligned} \tau_{j,j+1} &= \frac{\alpha_{j,j+1}}{\nu_{j,j+1}} \frac{c}{\partial v_s / \partial s} \\ &= \frac{n_j B_{j,j+1} h\nu_{j,j+1}}{4\pi\nu_{j,j+1}} \left(1 - \frac{g_j n_{j+1}}{g_{j+1} n_j}\right) \frac{c}{\partial v_s / \partial s} \\ &= \frac{n_j B_{j,j+1} h}{4\pi} \left(1 - \frac{g_j n_{j+1}}{g_{j+1} n_j}\right) \frac{c}{\partial v_s / \partial s} \end{aligned} \tag{5.63}$$

This allows us to write

$$\begin{aligned} I_{j,j+1} &= \frac{1}{4\pi} h\nu_{j,j+1} \sum_{\text{shock region}} n_{j+1} A_{j+1,j} \frac{\Delta z}{\Delta \nu} (1 - e^{-|\tau_{j,j+1}|}) \frac{4\pi \mid \partial v_s / \partial s \mid}{hc n_j B_{j,j+1}} \frac{1}{1 - \frac{g_j n_{j+1}}{g_{j+1} n_j}} \\ &= \sum_{\text{shock region}} \frac{A_{j+1,j}}{B_{j,j+1}} \frac{n_{j+1}}{n_j} \frac{1}{1 - \frac{g_j n_{j+1}}{g_{j+1} n_j}} \frac{\mid \partial v_s / \partial s \mid}{c} \nu_{j,j+1} (1 - e^{-|\tau_{j,j+1}|}) \frac{\Delta z}{\Delta \nu} \end{aligned} \tag{5.64}$$

We can then use the Einstein coefficient's relations

$$A_{j+1,j} = \frac{16hB^3}{c^2}(j+1)^3 B_{j+1,j} \tag{5.65}$$

where B is the rotational constant, characteristic of the considered molecule, and

$$g_{j+1}B_{j+1,j} = g_j B_{j+1} \tag{5.66}$$

Furthermore, we know the expression of the frequency of the considered transition

$$h\nu_{j,j+1} = 2hB(j+1) \tag{5.67}$$

These last three relations allow us to write

$$\frac{A_{j+1,j}}{B_{j,j+1}} = \frac{g_j}{g_{j+1}} \frac{2h\nu_{j,j+1}^3}{c^2} \tag{5.68}$$

thanks to which we now can express

$$I_{j,j+1} = \sum_{\text{shock region}} \frac{2h\nu_{j,j+1}^3}{c^2} \frac{1}{\frac{g_{j+1}n_j}{g_j n_{j+1}} - 1} \frac{\nu_{j,j+1}}{c} \left| \frac{\partial v_\text{s}}{\partial s} \right| (1 - e^{-|\tau_{j+1,j}|}) \frac{\Delta z}{\Delta \nu} \tag{5.69}$$

Finally, we can re-write this equation, using the excitation temperature T_exc of the considered transition

$$\frac{g_{j+1}n_j}{g_j n_{j+1}} = exp\left(\frac{h\nu_{j,j+1}}{kT_\text{exc}}\right) \tag{5.70}$$

$$I_{j,j+1} = \sum_{\text{shock region}} B_\nu(T_\text{exc}) \frac{\nu_{j,j+1}}{c} \frac{\partial v_\text{s}}{\partial s} (1 - e^{-\tau_{j+1,j}}) \frac{\Delta z}{\Delta \nu} \tag{5.71}$$

where $B_\nu(T)$ is Planck's function at temperature T and frequency ν, given by

$$B_\nu(T) = \frac{2h\nu^3}{c^2} \frac{1}{e^{h\nu/kT} - 1} \tag{5.72}$$

In radioastronomy, the integrated intensity is often expressed in K km s^{-1}. The intensity-temperature conversion is based on the following relations

$$T = \frac{c^2}{2k\nu^2} I \tag{5.73}$$

with I in erg cm^{-2} Hz^{-1} sterad $^{-1}$ s^{-1}, and

$$\frac{\Delta\nu}{\nu} = \frac{\Delta v}{c} \tag{5.74}$$

which allow us to express the integrated flux over the transition

$$T_{j,j+1}\Delta v = \sum_{\text{shock region}} \frac{c^2}{2k\nu^2} B_\nu(T_\text{exc}) \frac{\partial v_\text{s}}{\partial s} (1 - e^{-\tau_{j+1,j}}) \Delta z \tag{5.75}$$

Eventually, for aims of comparisons with available observations, we must subtract the cosmic background contribution (at 2.7 K) to this quantity. We consequently calculate the previous quantity, corrected from this contribution

$$\begin{aligned} T_{j,j+1}\Delta v &= \sum_{\text{shock region}} \frac{c^2}{2k\nu^2} B_\nu(T_{\text{exc}}) \frac{\partial v_{\text{s}}}{\partial s} (1 - e^{-\tau_{j+1,j}}) \left(1 - \frac{B_\nu(T_{\text{Background}})}{B_\nu(T_{\text{exc}})}\right) \Delta z \\ &= \sum_{\text{shock region}} \frac{c^2}{2k\nu^2} \frac{\partial v_{\text{s}}}{\partial s} (1 - e^{-\tau_{j+1,j}}) \left(B_\nu(T_{\text{exc}}) - B_\nu(T_{\text{Background}})\right) \Delta z \end{aligned} \quad (5.76)$$

This quantity being likely to be compared to the observations, it is the one that we calculate in the LVG code.

6

Computational aspects

Ce chapitre est consacré à la présentation du code de transfert de rayonnement développé pour modéliser l'émission de SiO et CO. La programmation en elle-même est ainsi expliquée, ainsi que les tests basiques de validation effectués. Des tests un peu plus élaborés sont aussi présentés. La pertinence de l'utilisation de l'hypothèse LVG est testée. L'influence de certains paramètres liés au code de choc et au code de transfert de rayonnement est enfin étudiée.

6.1 Programming

In Chapters 2 and 3, the shock code that was used to simulate bipolar outflows and jets processes was presented. In Chapter 5, the way the radiative transfer is handled was introduced. The purpose of this chapter is to present the computational implementation of the LVG treatment, that runs as a independent program, using a series of molecular data that are made available in reference articles or appropriate databases, and also using a series of inputs that are provided by the output files of the shock code. The LVG program principles are described in the following Subsection, that also includes a schematic structure of the program.

6.1.1 The LVG code requirement and outputs

Various molecular data. Of crucial importance are two molecular parameters relative to their internal structure to compute their emission in the LVG context : the rotational

Molecule	CO	SiO
B (MHz)	57635.96828	21787.453
μ (debye)	3.0982	0.11011

Tableau 6.1 – Useful quantities for CO and SiO : B is the rotational constant, and μ is the dipolar moment. All values come from NIST. 1 debye = 10^{-18} cgs. Energetic diagrams for the twenty first rotational levels of these molecules can be found in Appendixes G and F, based on these data.

molecule	reference article	code
SiO	Turner et al. (1992)	T92
SiO	Schöier et al. (2005)	S05
SiO	Dayou and Balança (2006)	D06
CO	Flower (2001)	F01
CO	Balakrishnan et al. (2002)	B02
CO	Cecchi-Pestellini et al. (2002)	C02
CO	Schöier et al. (2005)	S05

Tableau 6.2 – Reference table for the various available sets of rate coefficients for the collisional excitation of CO and SiO in our LVG program.

constant B, and the dipolar moment μ, whose tabulated values are given in Table 6.1, as provided by the NIST database (www.nist.gov/data/). In fact, the energy separation between the rotational levels depends on the rotational constant, and appear in the expression of the optical depth, integrated intensity, and in the expression of the equations of statistical equilibrium. The dipolar moment is useful to compute the Einstein coefficients for the molecule.

In fact, regarding these coefficients, that also appear in the expression of the equations of statistical equilibrium and in the writing of the integrated intensity, an option is available for the user, who can choose to use the ones provided in the Leiden Atomic and Molecular Database (www.strw.leidenuniv.nl/moldata/), or let the LVG code calculate them by means of the following expressions :

$$A_{\mathrm{J+1,J}} = \frac{16hB^3}{c^2}(J+1)^3 B_{\mathrm{J+1,J}} \tag{6.1}$$

$$B_{\mathrm{J+1,J}} = \frac{32\pi^4\mu^2}{3h^2c}\frac{J+1}{2J+3} \tag{6.2}$$

$$g_{\mathrm{J}} B_{\mathrm{J,J+1}} = g_{J+1} B_{\mathrm{J+1,J}} \tag{6.3}$$

where $A_{J+1,J}$ is Einstein coefficient for spontaneous emission, $B_{\mathrm{J+1,J}}$ the one for stimulated emission, and $B_{\mathrm{J,J+1}}$ is the absorption coefficient between levels of quantum rotational number J and $J+1$. In these expressions, c is the light velocity in the vacuum, h is Planck's constant, and μ is the dipolar moment of the considered molecule (see Table 6.1).

Non less important are the set of rate coefficients data sets that are used to compute an accurate collisional excitation of the molecules. The Table 6.2 provides the references that provided the data set that we chose to implement in our LVG code. The Table 6.3 gives the corresponding input files characteristics for theses different data sets, referred to as their code in it. Our LVG program contains an option that allows for the user to choose the appropriate data set.

LVG input parameters. To compute molecular emission quantities at each point of the shock, the LVG code requires some physical quantities computed by the shock code at these points :

- necessary position parameters such as the arbitrary distance z (cm), the corresponding neutral and ionic flow times timeN and timeI (s) ;

Characteristics	$J_{\max}$	$T_{\min}$	$T_{\max}$	Number of T	Collision partners
SiO, T92	20	20	300	8	H_2
SiO, S05	40	20	2000	11	H_2
SiO, D06	20	10	300	30	H_2
CO, F01	30	5	400	41	o- and p- H_2
CO, B02	8	5	100	11	H
CO, B02	16	100	3000	11	H
CO, C02	14	5	500	10	He
CO, S05	40	5	2000	14	o- and p- H_2

Tableau 6.3 – Input files characteristics for the different collisional data. Details on extrapolation of these coefficients are given in Appendix J, as well as a computer program to compute such extrapolations.

- physical parameters essential for the computation of the equations of statistical equilibrium and for the calculation of molecular emission quantities : the neutral velocity $v_{\rm n}$ (cm s^{-1}), the neutral temperature $T_{\rm n}$ (K), and the velocity gradient $dv_{\rm n}/dz$ (s^{-1}) ;
- fractional abundance parameters for SiO and colliding species He and H_2 x(SiO), x(He), and x(H_2), and the associated density $n_{\rm H}$ (cm^{-3}).

For the purposes of the output files of the LVG code, some other useful parameters are also called by the LVG code :

- ionic flow parameters such as the ionic temperature $T_{\rm i}$ (K) and the ionic velocity $v_{\rm i}$ (cm s^{-1}) ;
- fractional abundances of other species related to SiO like OH, O_2 (that partner with Si to produce SiO), Si, SiO_2 and SiH_4.

LVG output quantities. Thanks to all these data, the LVG code is designed to compute every useful emission quantity at each point of the shock :

- the level population distribution, and the corresponding Boltzmann distribution for them ;
- the optical depth, given by :

$$\tau_{\rm J,J+1} = \frac{8\pi^3\mu^2}{3h} \times \frac{n(SiO)}{grad\_v} \times (J+1) \times \left(\frac{fp(J)}{2J+1} - \frac{fp(J+1)}{2J+3} \right) \qquad (6.4)$$

  where μ is the dipolar moment of the molecule, h is Planck's constant, $n(SiO)$ is the abundance of SiO, $grad\_v$ is the velocity gradient, and $fp(J)$ is the fractional population of the rotational level J.
- the excitation temperature, that writes :

$$T_{\rm exc}(J, J+1) = \frac{2hB}{k_{\rm B}} \times \frac{J+1}{ln\left(\frac{(2J+3)fp(J)}{(2J+1)fp(J+1)}\right)} \qquad (6.5)$$

  where $k_{\rm B}$ is Boltzmann's constant, and B is the molecular rotational constant ;

- the line temperature, that is computed in two different fashions :

$$I(J,J+1) = 2\frac{hB}{k}(J+1)(1-e^{-|\tau_{\mathrm{J,J+1}}|})(BOLE(J)-BOLB(J+1)) \quad (6.6)$$

$$I_2(J,J+1) = \frac{hc^3}{8k_{\mathrm{B}}\pi}A_{\mathrm{J+1,J}}\frac{n(SiO)fp(J+1)\beta_{\mathrm{J,J+1}}}{(2B(J+1))^2}\left(1-\frac{BOLB(J+1)}{BOLE(J)}\right) \quad (6.7)$$

where c is the vacuum speed of light, $\beta_{\mathrm{J,J+1}}$ is the escape probability in a given direction (see 5.61), $A_{\mathrm{J,J+1}}$ is the Einstein coefficient for spontaneous emission, and $BOLE(J)$ and $BOLB(J)$ are two convenient quantities expressed as :

$$BOLE(J) = \left(\frac{fp(J)/(2J+3)}{fp(J+1)/(2J+1)}-1\right)^{-1} \quad (6.8)$$

$$BOLB(J) = \left(\exp\left(\frac{2JhB}{k_{\mathrm{B}}T_{\mathrm{BB}}}\right)-1\right)^{-1} \quad (6.9)$$

$$(6.10)$$

where T_{BB} is the background temperature, set to 2.7 K.

Eventually the LVG program also computes integrated quantities through the whole shock, such as the integrated intensity, based on the two different calculations on the intensity, and the integrated intensity relative to that of the SiO (5-4) transition (for observational comparisons purposes).

6.1.2 Solving the statistical equilibrium equations

The whole complexity of the LVG program lies in the method used for the calculation of level populations, through the solving of the equations of statistical equilibrium. Various expressions for this set of equations have been introduced in Subsection 5.4, starting from 5.55 :

$$\begin{aligned}\frac{dn_i}{dt} = &- n_i(A_{i,i-1}+B_{i,i+1}J_{i,i+1}+B_{i,i-1}J_{i-1,i})\\ &+ n_{i-1}B_{i-1,i}J_{i-1,i}\\ &+ n_{i+1}(A_{i+1,i}+B_{i+1,i}J_{i,i+1})\\ &+ \sum_{\mathrm{coll}}\sum_{j\neq i}n_{\mathrm{coll}}(n_jC_{ji}-n_iC_{ij})\end{aligned} \quad (6.11)$$

leading to the final 5.58 formulation :

$$\begin{aligned}\frac{dn_i}{dt} = &- n_i\left(\beta_{i,i+1}B_{i,i+1}I_{\mathrm{c}}+\beta_{i-1,i}A_{i,i-1}+\beta_{i-1,i}B_{i,i-1}I_{\mathrm{c}}+\sum_{j\neq i}n_{\mathrm{H_2}}C_{ij}\right)\\ &+ n_{i-1}(\beta_{i-1,i}B_{i-1,i}I_{\mathrm{c}}+n_{\mathrm{H_2}}C_{i-1,i})\\ &+ n_{i+1}(\beta_{i,i+1}A_{i+1,i}+\beta_{i,i+1}B_{i+1,i}I_{\mathrm{c}}+n_{\mathrm{H_2}}C_{i+1,i}\\ &+ \sum_{j\neq i-1,i,i+1}n_{\mathrm{H_2}}n_jC_{ji}\end{aligned} \quad (6.12)$$

Two approaches to solving for the level populations may be taken :

- integrate the set of Equations 6.11 or 6.12 in parallel with the dynamical, thermal, and chemical rate equations of the shock wave, as is done currently for the H_2 molecule (Le Bourlot et al. (2002), see Section 3.2).
- assume local statistical equilibrium, i.e. set the lhs of Equations 6.11 or 6.12 to zero, and solve *a posteriori* the resulting algebraic equations by matrix inversion, using the physical structure provided by the MHD shock code. Since the radiative terms J depend indirectly on the level populations through the escape probabilities and excitation temperatures (Equation 5.56), the procedure must be iterated, updating J with values of β and $T_{\rm exc}$ obtained from the previous iteration.

The former approach is preferable, particularly when the molecule under consideration is an important shock coolant (e.g. H_2) – which is not the case of SiO. Furthermore, the flow time in the SiO emission zone is sufficiently long that the assumption of local statistical equilibrium is justified. Accordingly, we adopted the latter approach in the present work. It is common to most applications of the LVG method to astrophysical problems (e.g. Schilke et al. (1997), Neufeld and Kaufman (1993)) and has the advantage of being less demanding in CPU time. For more significant coolants, such as CO, ^{13}CO, and H_2O, the rate of cooling was computed in parallel with the shock dynamics, using the cooling functions calculated by Neufeld and Kaufman (1993), by means of the LVG method.

Although the two formulations are equivalent and converge to the same solution, we have found that inversion of the latter matrix encounters numerical instabilities and convergence problems at high optical depths, possibly due to round–off errors in the (vanishingly small) β terms. In the first formulation, the radiative elements of the matrix are never zero, even at high opacity, and we obtain much better convergence and accuracy. Hence we have adopted (6.11) in the present calculations. In our program, the convergence criterion is the following : the relative difference between successively computed level population must be less than 10^{-4}, for every computed level.

Eventually, the zero order estimate of the level populations (i.e. their first guess) at each point of the shock must be specified. Two cases are considered :

- at the first point of the shock, this first estimate is provided by Boltzman's distribution of the level populations (LTE situation) ;
- at any other point of the shock, the zero order is chosen equal to the result of the calculation at the previous point of the shock. Indeed, (for a reasonable choice of the step) physical conditions are quite continuous along the shock, and level populations of two neighbour points are expected not to be too different. The objective of this method is to gain CPU time.

6.1.3 Algorithm diagram

The program then runs the following way :

1. Declaration of the variables : the number of rotational levels taken into account is an input parameter of the program. J level has the energy

$$E_J = hBJ(J+1) \tag{6.13}$$

where B denotes the rotational constant of the considered molecule, whose value is given in Table 6.1.

2. Reading of the files paths : specification of the location of the directories where the input files (that is the output files of the MHD code) and the output files of the LVG code.
3. Opening of the input files, and of the output files where the results are about to be written.
4. Reading of the number of points taken into account in the MHD code.
5. Calls :
   - reading of the collisional coefficients : the number of levels and temperature for which the collisional coefficient rates are available, and the available collision partners depend on the sources, and are summarized in Table 6.3 ;
   - calculation (based on Equations 6.1, 6.2, and 6.3) or direct reading of the Einstein coefficients of the considered molecule ;
6. First point of the shock :
   - reading of the shock parameters (specified in Subsection 6.1.1)at this point ;
   - statistical initialization of the level populations of the considered molecule (Boltzman's distribution at the read temperature, see above) ;
   - writing of these values in the output files.
7. Entry in the loop on the number of points in the shock :
   - reading of the physical and chemical parameters at the given point ;
   - calculation of the collisional coefficient rates at the temperature of the considered point of the shock ; this calculation is done via a linear interpolation routine that uses the tabulated values. We can summarize the run of the routine the following sequence of steps :

     reading of the input temperature, and depending on the case :

     bracketting between two values of temperatures of the collisional excitation rate coefficients array, and linear interpolation of these coefficients ;

     attribution of the collision rate coefficients if the temperature belongs to the set of temperatures for which the data is tabulated ;

     attribution of the collision rate coefficient of the lowest temperature of the array, if the neutral temperature is inferior to this value, and attribution of the collision rate coefficients of the highest temperature of the array, if the neutral temperature is superior to this value ;

     calculation of the corresponding de-excitation rate coefficients via the detailed balance.
   - entry in the lambda iteration :

     first guess of the iteration : populations calculated at the previous point ;

     calculation of the escape probability (see Section 5.2) ;

     filling of the radiative and collisional matrixes (see Formula 6.11, on which appears the possibility to sum a collisional matrix added to a radiative matrix multiplied by the escape probability) ;

inversion of the total matrix, populations calculation ;

test of the convergence, and exit of the loop if the convergence criterion is verified, that is (see above), if the maximal relative difference between populations calculated in two successive iterations is not greater than 10^{-4}.

- calculation of intensity and excitation temperatures for the considered transitions by means of two formulas (both in kelvins) 6.6 and 6.7, and writing in the output files of $T_{\mathrm{exc}}, \tau_{\mathrm{J,J+1}}, intensity, populations, J, ...$; exit of the loop at the last point of the shock ;

8. Implementation of the integrated intensity in the output files until the truncation point (see Subsection 6.5.1).

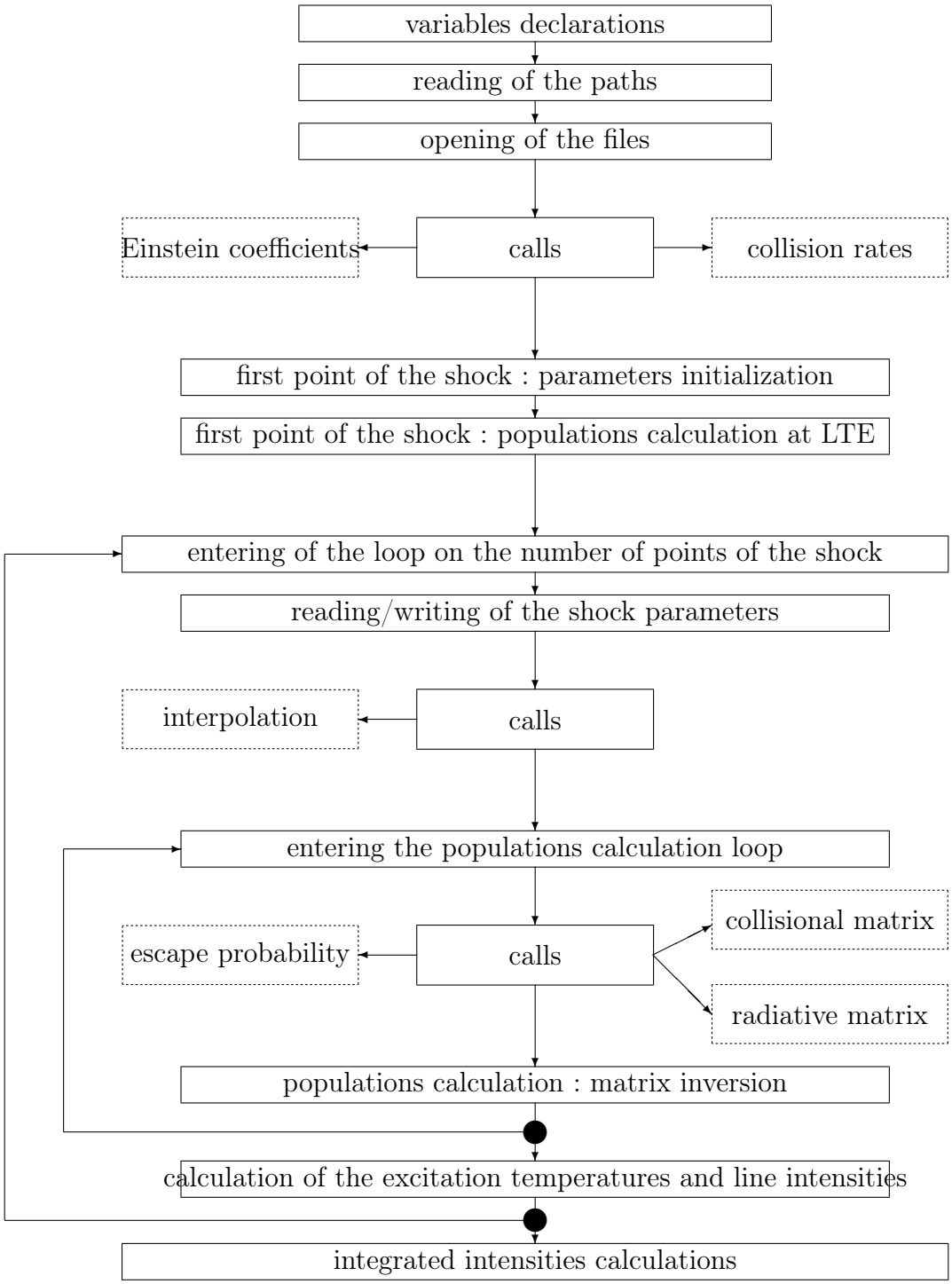
variables declarations
reading of the paths
opening of the files
Einstein coefficients
calls
collision rates
first point of the shock : parameters initialization
first point of the shock : populations calculation at LTE
entering of the loop on the number of points of the shock
reading/writing of the shock parameters
interpolation
calls
entering the populations calculation loop
escape probability
calls
collisional matrix
radiative matrix
populations calculation : matrix inversion
calculation of the excitation temperatures and line intensities
integrated intensities calculations

level	0	1	5	10	15
fracpop	4.12	11.38	12.94	0.87	5.59×10^{-3}
fracpop ETL	4.12	11.38	12.94	0.87	5.59×10^{-3}
err	0.01	0.005	0.02	0.04	0.001
Texc (K)	25.00	25.00	25.00	25.00	25.00
level	20	25	30	35	40
fracpop	3.97×10^{-9}	3.28×10^{-10}	3.22×10^{-15}	3.80×10^{-21}	5.42×10^{-28}
fracpop ETL	3.97×10^{-9}	3.28×10^{-10}	3.22×10^{-15}	3.80×10^{-21}	5.42×10^{-28}
err	0.009	0.006	0.004	0.01	0.007
Texc (K)	25.00	25.00	25.00	25.00	25.00

Tableau 6.4 – Comparisons of the fractional populations to the LTE situation, in the collision dominated medium case. 'err' stands for the relative uncertainties between the corresponding results. All results are in %, except the excitation temperatures (in K) : these ones are given for the transition for which 'level' is the lower state. For instance, the excitation temperature in the same column as the '0' level is the excitation temperature of the line 1 - 0.

6.2 Very basic tests

Before running our LVG code on the output files of the MHD code, we test in a few simple situations on single point conditions. In order to simplify, all the tests that are presented here are conducted with the SiO code. The CO code has been tested under exactly the same conditions, and the results of the comparisons are the same for both species.

6.2.1 Collision dominated medium

We first run the LVG code under the limit conditions of a collision dominated medium. In such an hypothetical medium, $n_{\mathrm{H}_2} = 10^6$ cm^{-3}, $n(SiO) = 10^{-2}$ cm^{-3}, the temperature $T_{\mathrm{n}} = 25$ K, and an arbitrary velocity gradient is chosen, corresponding to 30 km s^{-1} over 5 pc. To perfect the concept of a purely collisional medium, all the matrix elements of the radiative matrix are set to zero.

Under these assumptions, the Local Thermal Equilibrium conditions are expected to take place, generating a Boltzmann distribution for the level populations. Additionally, the excitation temperature of each transition are also expected to equal the kinetic temperature of the gas.

The Table 6.4 shows the results of such a computation. the fractional population and the equivalent LTE fractional population are provided on the first two lines for a samle of representative levels, showing no significant discrepancy : the maximum relative error is 0.04%. The excitation temperature is also displayed, and appear to perfectly meet our expectations, being equal to the value of the kinetic temperature of the gas for every transition, even at very low values of the fractional populations, for which computational uncertainties might have tainted the results.

level	0	1	5	10	15
Texc (K)	2.70	2.70	2.70	2.70	2.70
fracpop	33.97	46.97	3.36×10^{-3}	2.25×10^{-16}	4.54×10^{-38}
level	20	25	30	35	40
Texc (K)	2.70	2.70	2.70	2.70	2.70
fracpop	0.00	0.00	0.00	0.00	0.00

Tableau 6.5 – Excitation temperatures and fractional populations, in the case of a radiative dominated medium. fracpop are in %, and excitation temperatures in K : these ones are given for the transition for which 'level' is the lower state. For instance, the excitation temperature in the same column as the '0' level is the excitation temperature of the line 1 - 0.

6.2.2 Radiation dominated medium

We then consider the limit situation of a medium entirely dominated by radiation. The temperature and velocity gradient are the same as in the previous subsection. But the density of molecular hydrogen is $n_{\mathrm{H_2}} = 10^6$ cm^{-3}, and that of SiO $n(SiO) = 10^{-2}$ cm^{-3}. The medium lies in the radiation field of a blackbody at a temperature of 2.70 K. In order to make sure that no collisional process is possible, the collisional matrix elements are set to zero. Eventually the escape probability is set equal to one, ensuring the medium to be totally transparent to any emitted photon. Under such assumptions, the excitation of every transition is expected to match the value of the background temperature.

The results can be seen in Table 6.5 : every excitation temperature is perfectly equal to that of the background, even when the associated level populations are very low.

6.3 Other computational tests

The next step is to compare the results of our LVG code to previous calculations, available in reference articles such as the molecular clouds study of Goldreich and Kwan (1974). We also tested our program against codes available online, such as the RADEX one (www.sron.rug.nl/vdtak/radex/radex.php). Again, we only present SiO results, but such thorough examinations for CO were conducted, with similar levels of satisfying agreement.

6.3.1 Test of the level populations calculation

The third test that we run consists on a comparison with previously established results, provided by Goldreich and Kwan (1974). In this article, the authors consider a medium with the same characteristics as in the previous subsection : $n_{\mathrm{H_2}} = 10^6$ cm^{-3}, $n(SiO) = 10^{-2}$ cm^{-3}, the temperature $T_{\mathrm{n}} = 25$ K, and an arbitrary velocity gradient is chosen, corresponding to 30 km s^{-1} over 5 pc. Under these assumptions, the authors give a table of results,for the first six levels of SiO (and CO).

The authors also provide their own set of collisional de-excitation rate coefficient, that

level	0	1	2	3	4	5	6
n $_J$(GK)	0.1895	0.1316	0.0590	0.0148	0.0018	0.00012	0.000002
n $_J$	0.2158	0.1303	0.0554	0.0139	0.0018	0.00016	0.000004

Tableau 6.6 – Comparisons of level populations : results of Goldreich and Kwan (1974) are on the first line, ours on the second (no unit). n_J corresponds to the fractional population of the level divided by its statistical weight.

is the same for every considered rotational level, given by

$$C = n_{\mathrm{H_2}} < \sigma v_{\mathrm{T}} > \frac{hB}{kT} \tag{6.14}$$

where $< \sigma v_{\mathrm{T}} >$ is the so-called 'reduced rate coefficient' : $< \sigma v_{\mathrm{T}} >= 7 \times 10^{-12}\ \mathrm{T}^{1/2}\ \mathrm{cm}^3\ \mathrm{s}^{-1}$, and where h is Planck's constant, B is the rotational constant of SiO, and k is Boltzmann's constant. Excitation rate coefficients are calculated using the detailed balance. We have adopted the same collisional rate coefficients in order to produce efficient comparisons. The 'spherical' expression of the escape probability is also implemented, both for the solving of the equations of statistical equilibrium and for the derivation of the corresponding line temperatures (equation 5.61). The molecular data that are used are the same as the ones mentioned in the article.

Comparisons to Goldreich and Kwan's results are provided in the Tables 6.6 (level fractional populations divided by their statistical weight) and 6.7 (optical depth, excitation temperature, and line temperature). We can see that for every computed quantity the order of magnitude of the results are the same, and that the values do not differ very much. Still some discrepancies remain, which can be accounted for by a mixture of uncertainties : Goldreich and Kwan (1974) provide results for the 7 first rotational levels, but might have used more for the computation's purposes, and no details are given about the escape probability approximations that were used in limit cases, nor concerning the computational method that was used to solve the statistical equilibrium equations. A few decades of computer science progresses also might explain some differences in the results.

6.3.2 Test of the excitation temperature calculation

Eventually we compare our results in terms of excitation temperatures with those of similar LVG code. The first one is the code that was used in Schilke et al. (1997) article, nicely provided by Malcolm Walmsley, and which is based on the same matrix inversion routine. The second one is the RADEX online code (www.sron.rug.nl/vdtak/radex/radex.php).

When comparing our results to those computed with the same code that was used ten years ago, we proceed in the same fashion on the following questions :

- the Einstein coefficients are calculated inside the code, using the 6.1, 6.2, and 6.3 equations with the same values for the rotational constant and dipolar moment ;

transition	1-0	2-1	3-2	4-3	5-4	6-5
τ (GK)	7.16	17.95	16.40	6.44	1.01	0.07
τ	10.78	18.89	15.71	6.07	1.04	0.09
T $_{exc}$(GK)(K)	5.72	5.20	4.52	3.92	3.85	6.54
T $_{exc}$(K)	4.15	4.89	4.53	4.12	4.36	8.79
$\mathcal{J}$(GK)(K)	2.95	2.26	1.41	0.73	0.33	0.15
$\mathcal{J}$(K)	1.40	1.96	1.41	0.86	0.53	0.35

Tableau 6.7 – Comparisons of optical depths (no unit), excitation temperatures (K), and intensities (K) of the first transitions. 'GK' refers to the results of Goldreich and Kwan (1974). Data with no suscripts are our results.

physical parameter	1st point (a)	2nd point (b)	3rd point (c)
$T_{\rm b}$ (K)	2.7	2.7	2.7
$T_{\rm n}$ (K)	467.08	50	300
$n_{\rm H_2}$ (cm^{-3})	3.71×10^5	10^5	10^4
$n(SiO)$ (cm^{-3})	4.78	10^{-3}	10^{-3}
$dv_{\rm n}/dz$ (s^{-1})	9.1×10^{-11}	10^{-13}	10^{-12}

Tableau 6.8 – Physical parameters for our three reference points : background temperature, neutral gas temperature, density, SiO abundance, and velocity gradient.

- the collisional rate coefficients are implemented following Turner et al. (1992), to match this former program's treatment ;
- the 'spherical' expression of the escape probability, both for the solving of the equations of statistical equilibrium and for the derivation of the corresponding line temperatures (equation 5.61), in accordance with this former code. Particularly the same developments are used for limit values of the optical depth.

Similarly, when comparing our results to those computed with the RADEX code, we proceed in the same fashion on the following questions :

- the Einstein coefficients and collisional rate coefficients are directly taken from the Leiden Atomic and Molecular Database (www.strw.leidenuniv.nl/moldata/), as it is the case in the RADEX code ;
- the expression of the escape probability follows that of the RADEX code, that is

$$EP(\tau) = \frac{3}{2\tau}\left(1 - \frac{2}{\tau^2} + \left(\frac{2}{\tau} + \frac{2}{\tau^2}\right)e^{-\tau}\right) \tag{6.15}$$

  with simple maximum second order approximations in limit cases, although the ones used by RADEX remain unknown.

Three single point calculations, with parameters provided in the Table 6.8 : background temperature, neutral gas temperature, density, SiO abundance, and velocity gradient. Figure 6.1 presents the results in terms of excitation temperature at these three points. Comparisons were made between our LVG code (red data points, 'G08') and the code that

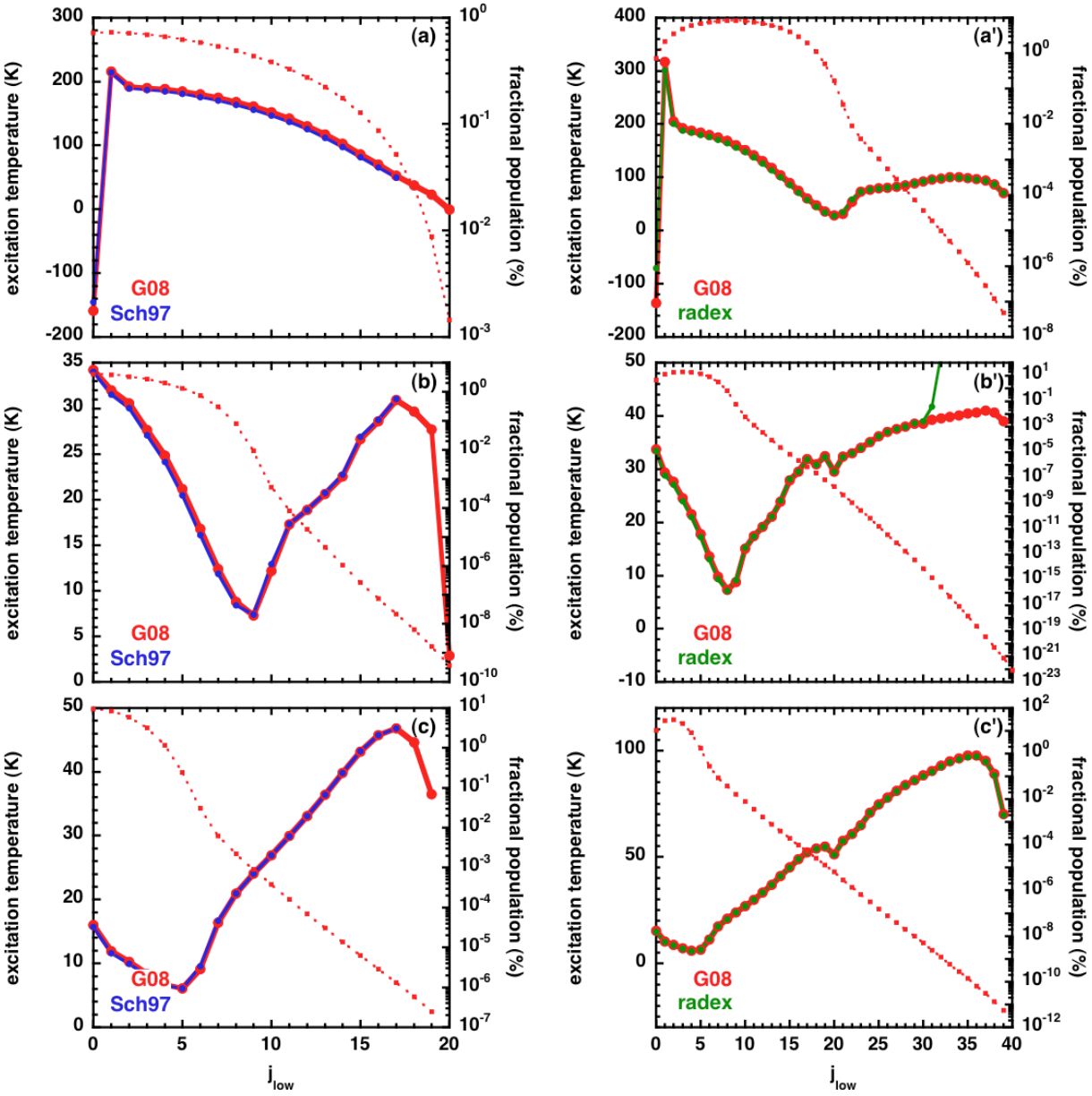

Figure 6.1 – Single point comparisons for the excitation temperature comparison at the three points specified in Table 6.8. Top, middle, and bottom panels respectively correspond to the 1st, 2nd and 3rd point of the table. The left hand side panels present comparisons with the LVG code that was used in Schilke et al. (1997), whereas the right hand side ones compare our results with RADEX ones.

was used by Schilke et al. (1997) (left hand side panel, blue data points, 'Schilke et al. (1997)'), and with the RADEX results (right hand side panels, green data points, 'radex'). The agreement between the results is very satisfying in both cases, and only exceeds a few percents in tough conditions (first transition excitation temperature for the first point), or on the '(b')' panel, for which the RADEX results show an unexpected behaviour for $j_{\rm low} > 30$. Nevertheless, such excitation temperature concern poorly populated levels that are not likely to significantely take part to the emission results.

6.4 Consistency of the LVG approach

A priori, the use of the LVG approach is justified by the values of the molecules critical densities, as presented in the tables of Appendixes H and I, with the different collision partners considered in the present study.

In this Section, we study the relevance *a posteriori* of the use of a LVG code to model the emission from the shock region. We make use of a C-type reference shock model with the following characteristics : the pre-shock density $n_{\rm H} = 10^5$ cm^{-3}, the shock velocity $v_{\rm s} = 30$ km s^{-1}, and the magnetic field parameter $b = 1$.

6.4.1 Optical depth evolution through the shock

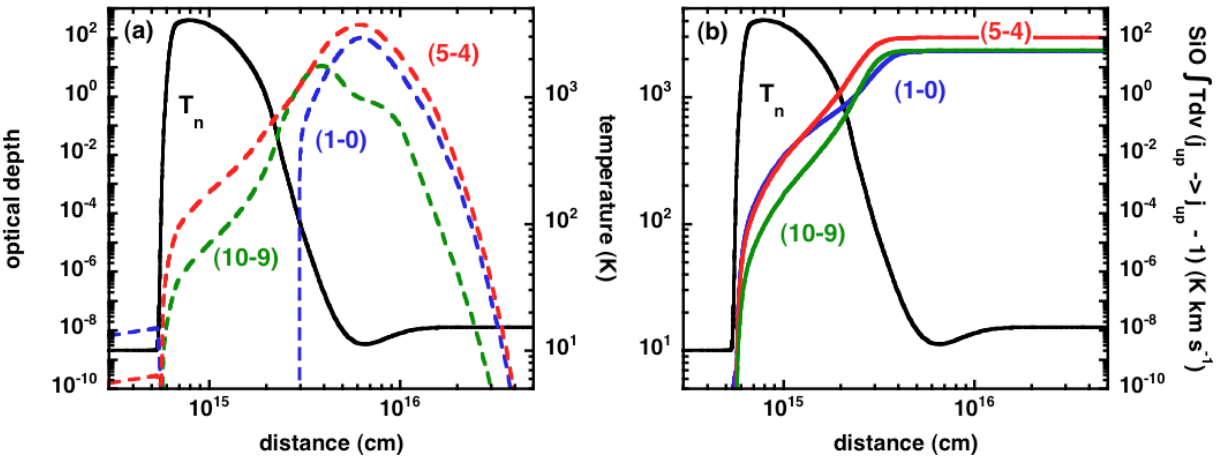

Figure 6.2 – Optical depth (left hand side panel, dashed curves) and integrated intensity (right hand side panel, continuous curves) evolution through the C-type reference shock model specified in Section 6.4, for the three representative rotational transitions (1-0), (5-4), and (10-9) of SiO. For each panel, the neutral temperature profile is also indicated in black.

The relevance of the use of an elaborate LVG method must be checked first. In fact, a simpler code with simpler assumptions and approximations might have been efficient enough to model the emission in the considered shocked regions.

The Figure 6.2 partially dispels this doubt, on the example of the above reference shock model. On the left hand side panel, the neutral temperature profile is plotted along

with the optical depth evolution of three representative rotational SiO transitions : (1-0), (5-4), and (10-9), against an arbitrary distance parameter. On the right hand side panel, the same neutral temperature profile is superposed with the integrated intensity profiles of the same transitions. The spread of the values range covered by the optical depth in the corresponding emission region confirms that no simpler code would have allowed for a better treatment of the radiative transfer. For example a program based on optically thin modelling only would have been irrelevant in this context.

6.4.2 LVG criterion

Another 'test of consistency' consists on the checking of the LVG criterion validity along the shock, as the LVG approximation has been done and the program has been built on it.

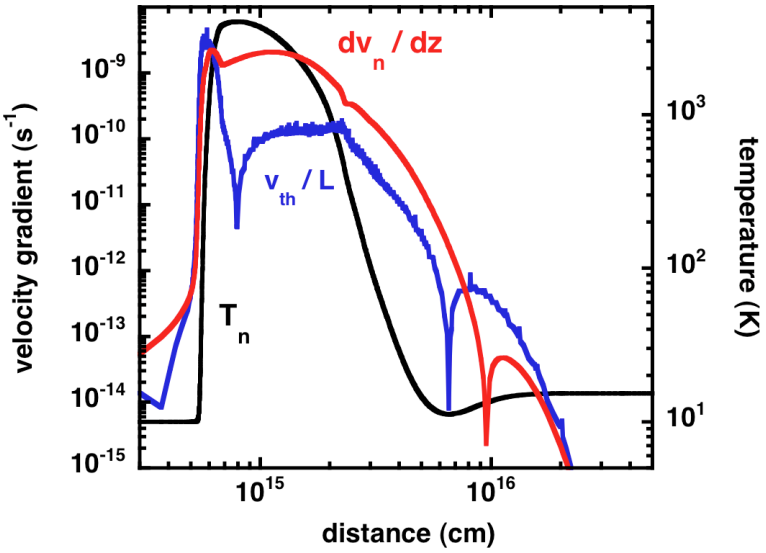

Figure 6.3 – Consistency of the LVG method for the C-type reference shock model indicated in Section 6.4.

We have seen in Section 5.2 that the LVG approximation is justified when the Doppler shift induced by the velocity gradient and estimated over a characteristic length of the shock, overcomes the thermal width of the considered line. Then, line photons are re-absorbed only within a region of size$< L$, where physical conditions and SiO excitation are uniform. This criterion may be rewritten as

$$\Delta v = \left(\frac{dv}{dz}\right) L > v_{\rm th} \tag{6.16}$$

where $v_{\rm th}$ is the thermal velocity (corresponding to half the FWHM of the considered line), and where Δv denotes the velocity variation (associated to the Doppler shift) over the characteristic length L. dv/dz stands for the velocity gradient. In terms of velocity gradients, this criterion writes

$$\left(\frac{dv}{dz}\right) > v_{\rm th}/L \tag{6.17}$$

$v_{\rm th}$ can be computed in each point of the shock thanks to its definition

$$v_{\rm th} = \sqrt{\frac{8k_{\rm B}T_{\rm n}}{\pi\mu m_{\rm H}}} \tag{6.18}$$

where $\mu m_{\rm H}$ is the mass of one SiO molecule, $k_{\rm B}$ is Boltzmann's constant, and $T_{\rm n}$ is the neutral temperature, evaluated in each point of the shock.

Finally the characteristic length that we use is the one of neutral temperature variations, and we calculate it in each point of the shock

$$L = \frac{T_{\rm n}}{dT_{\rm n}/dz} \tag{6.19}$$

Figure 6.3 shows the comparison of the quantities of equation 6.17 for each point of the shock. The LVG criterion may be seen to be verified throughout the cooling flow of the shock wave, where the bulk of the SiO emission arises. It is not verified in the far post-shock region, where the computed velocity gradient tends to zero ; but this region makes a negligible contribution to the line flux, owing to the low escape probabilities. On this figure, $v_{\rm th}/L$ is very simply estimated, since $dT_{\rm n}/dz$ is calculated between two successive points. This explains the non smooth aspect of the corresponding curve.

6.5 Influence of some parameters relative to LVG and MHD codes

For the purposes of this section, we make only use of the so-called reference model, already used by Schilke et al. (1997) for which : $n_{\rm H} = 10^5$ cm^{-3}, $v_{\rm s} = 30$ km s^{-1}, and $b = 0.63$, corresponding to $B = 200\mu$G. In this Section, we study the influence of important parameters on the SiO modelled emission. These parameters can appear either in the shock or in the LVG program.

6.5.1 Influence of the truncation of the calculation of integrated intensity

In the shock program, the post-shock processes are not taken into account a very realistic fashion. Because of the plane parallel geometry of the model, the species accumulate themselves in the post-shock region. In practice, such an accumulation is never observed, the shocked gas being able to flow along the shock. This problem raises the question of the point at which the LVG calculations are stopped in the post-shock regions. In other terms, the width of the shock, over which the integrated intensity is calculated has to be decided, which also means the influence of the shock age on the LVG calculations has to be reviewed.

In this Subsection, we investigate the influence of the choice of the truncation point, i.e. the point at which the LVG calculations are stopped in the post-shock, on the C-type reference model mentioned above. On the top panel of Figure 6.4, the neutral temperature

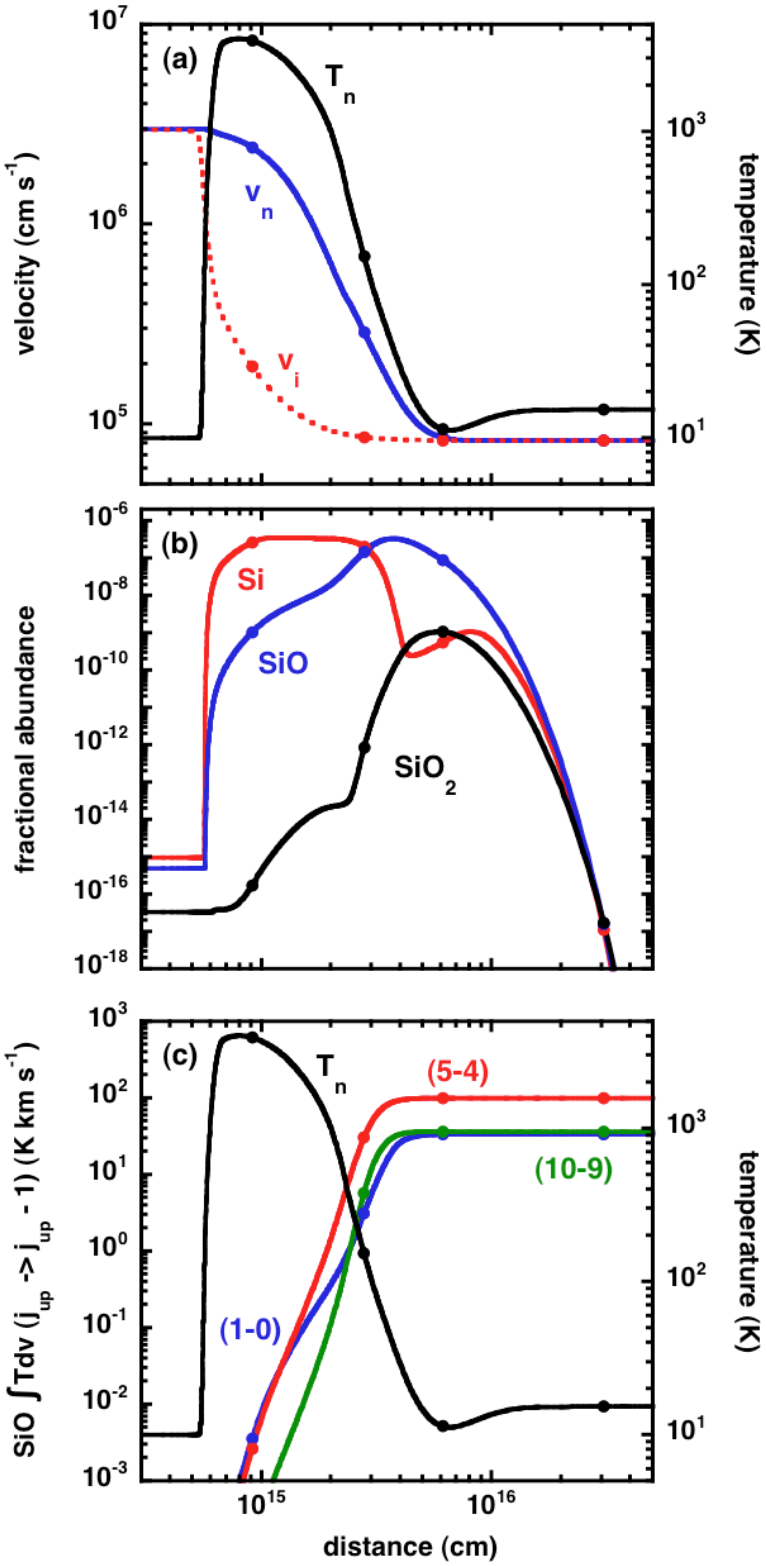

Figure 6.4 – Top panel : temperature (neutral) and (ionic and neutral) velocity profiles of the reference shock model specified in Section 6.5. Middle panel : corresponding Si-bearing species fractional abundance profiles. Bottom panel : corresponding integrated intensity evolution for three representative transitions (1-0), (5-4), and (10-9).

and fluid velocity profiles are plotted against the distance. The corresponding Si-bearing species fractional abundances profiles are plotted on the middle panel of the same Figure, whereas the bottom one shows the evolution of the integrated intensity of three representative SiO rotational transitions ((1-0), (5-4), (10-9)) through the shock. On all these curves, four points are highlighted, corresponding to evolutionary ages of 10, 100, 1000, and 10000 years in terms of neutral flow time.

The truncation effects on the integrated intensity can be seen on the bottom panel of Figure 6.4 :

- if the calculation is stopped after 1000 years, the integrated intensity has already reached a plateau, and the taking into account of further layers of the post-shock region won't modify its value ;
- before 1000 years, the integrated intensity value strongly depends on the truncation time, as SiO is still emitting in this part of the shock.

These trends can be interpreted by means of the top panel of the same Figure : after 1000 years, the medium is cold, and the velocity gradient tends to zero, thus generating no further SiO emission. SiO fractional abundance has no effect here, being almost the same at 100 and 1000 years, as can be seen on the middle panel. On the contrary, at 100 years, the temperature and velocity gradients are significant enough to account for SiO emission.

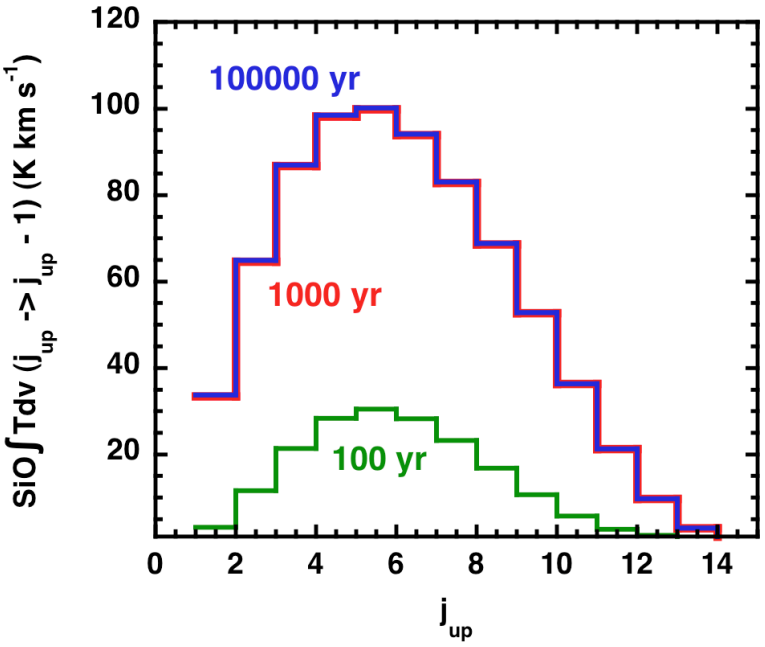

Figure 6.5 – Absolute integrated intensity diagram for the reference model, obtained with various truncation times : 100, 1000, and 10^5 years.

Nevertheless, the necessary time to reach its final integrated intensity value depends on the considered line, as can again be seen on the bottom panel of Figure 6.4 : the (10-9) transition seems to be the first line to reach its final value, soon followed by the (5-4) line, and the (1-0) transition. This is explained by the fact that the higher the transition is, the higher the temperature must be to generate its collisional excitation (see for example

the rotational levels diagram in Appendix F). At the temperatures existing between 100 and 1000 years, the (1-0) transition radiates more intensity than the (10-9) one.

This also explains why higher transitions are less affected by the truncation of the calculation of their integrated intensity, which can be seen on the integrated intensity diagram shown on Figure 6.5. The reaching of a plateau after 1000 years can also be seen on this Figure, as the diagrams corresponding to this value and to a truncation of 10000 years are exactly the same, whereas a shorter truncation generates lower emission.

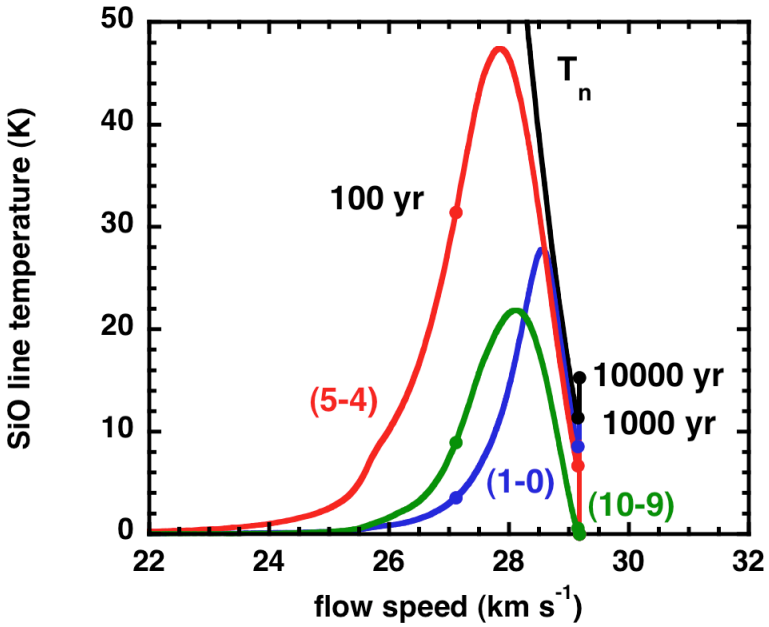

Figure 6.6 – Line profiles for the reference model, for three selected transitions (1-0), (5-4), and (10-9).

The line profiles corresponding to the transitions shown on Figure 6.5 are plotted on Figure 6.6, and also illustrate these results. On the X-axis of this Figure is the neutral velocity in the reference frame of the shock, whose lower values correspond to the pre-shock region. Through the shock, the neutral velocity in this frame increases, as can be seen thanks to the ages indication points on the curves. On the right hand side, the line temperature curve becomes a vertical line, corresponding to the accumulation of SiO in the post-shock gas phase at constant neutral velocity. This emission no longer contributes to the integrated intensity (there is no surface under the curve), and corresponds to the integrated intensity plateau. This Figure also shows the effects of the truncation on the shape of the considered profile, its influence decreasing for higher transitions that require higher temperatures to generate emission.

In the following studies, when investigating C-type shock models, the truncation time is the one necessary for the integrated intensity to reach the plateau. When simulating non-stationary shock models, the problem is simpler : the calculation time is taken equal as the evolutionary shock age.

6.5.2 SiO formation reaction rates

We have seen in Subsection 5.1.2 the importance of the reaction rates of formation of SiO from Si, which is released into the gas phase by the sputtering of the grains, namely

$$\mathrm{Si} + \mathrm{O_2} \longrightarrow \mathrm{SiO} + \mathrm{O} \tag{6.20}$$

$$\mathrm{Si} + \mathrm{OH} \longrightarrow \mathrm{SiO} + \mathrm{H} \tag{6.21}$$

for which the following rate coefficients ($\mathrm{cm^3\ s^{-1}}$)

$$k_1 = 2.7 \times 10^{-10} \exp(-111/T) \tag{6.22}$$

$$k_2 = 1.0 \times 10^{-10} \exp(-111/T) \tag{6.23}$$

were adopted by Schilke et al. (1997) from the compilation of Langer and Glassgold (1990). The exponential factor in equation 6.22 derives from the argument Graff (1989) that the reactions proceed only with the fine–structure states of Si ($3p^2\ ^3P_J$) with $J > 0$, of which $J = 1$, which lies 111 K above the $J = 0$ ground state, is the more significantly populated at low temperatures. More recently, the rate coefficient for reaction (6.20) has been measured at low temperatures ($15 \leq T \leq 300$ K) by Le Picard et al. (2001) and found to be given by

$$k_1 = 1.72 \times 10^{-10} (T/300)^{-0.53} \exp(-17/T). \tag{6.24}$$

We have adopted (6.24) and the same expression for k_2. Evidently, the differences between the present and previous values of these rate coefficients are most significant for temperatures $T \lesssim 100$ K, i.e. in the cooling flow of the shocked gas.

In this Subsection, we study the influence of the choice of the reaction rates for reactions 6.20 and 6.21 on the results in terms of SiO emission, thanks to the reference model specified above. We investigate two different implementations, the first one corresponding to the compilation og Langer and Glassgold (1990), as expressed in Equations 6.22 and 6.23, the second one to that of Le Picard et al. (2001) measurements (6.24 for both reactions).

Th Figure 6.7 shows the characteristic shock profiles obtained with both scenarios. As SiO is not very abundant in the gas phase, the molecular cooling it generates is not significant, and does not modify the temperature profile of the shock, which is the same in both situations (top panel). On the contrary, Si-bearing species fractional abundance profiles are different in the two considered cases : before 3×10^{15} cm, more SiO is produced with Langer and Glassgold (1990) reaction rates, before the situation inverts itself. After this arbitrary distance, not only Le Picard et al. (2001) reaction rates generate more SiO production in the gas phase, the maximum is reached for both SiO fractional abundances shortly after, which means that the maximum value obtained with Le Picard et al. (2001) is slightly higher than the one obtained with Langer and Glassgold (1990) ones.

The bottom panel of Figure 6.7 shows the integrated intensity evolution in both cases for three representative rotational transitions (1-0), (5-4), and (10-9). With Langer and Glassgold (1990) rates, the integrated intensity is clearly greater than with Le Picard et al. (2001) ones until 3×10^{15} cm because of the higher abundance of SiO mentioned

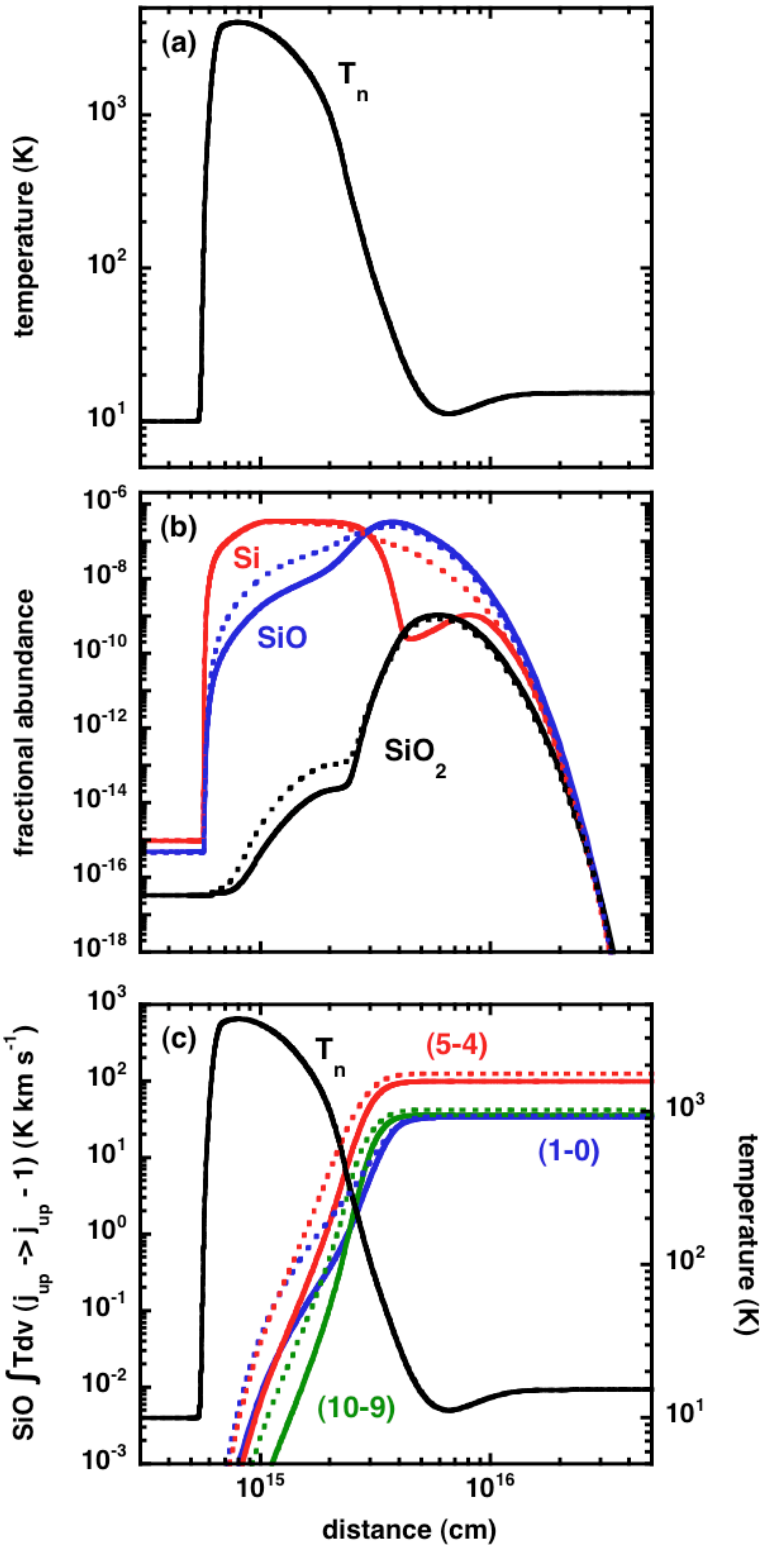

Figure 6.7 – Top panel : temperature profile of the reference shock model. Middle panel : corresponding Si-bearing species fractional abundance profiles, obtained with respectively Le Picard et al. (2001) (continuous curves) and Langer and Glassgold (1990) (dotted curves) SiO formation reaction rates. Bottom panel : corresponding integrated intensity evolution for three representative transitions (1-0), (5-4), and (10-9).

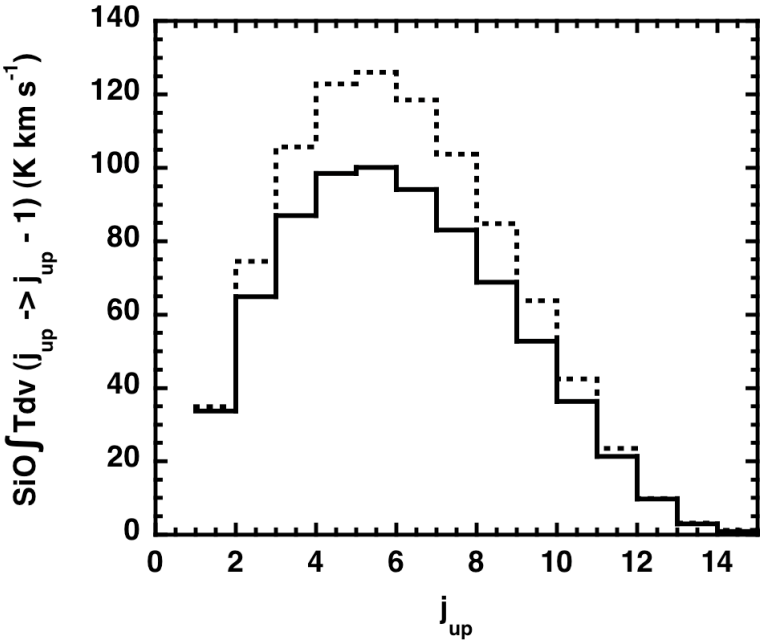

Figure 6.8 – Absolute integrated intensity diagram for the reference model, obtained with respectively Le Picard et al. (2001) (continuous curves) and Langer and Glassgold (1990) (dotted curves) SiO formation reaction rates.

above. After this arbitrary distance, the difference between the two integrated intensities decreases when the SiO fractional abundance and the velocity gradients are still high enough to generate a significant emission, without vanishing. In fact, the plateau is reached soon after for the integrated intensity, due to the physical conditions : the temperature, fractional abundance and velocity gradients are not sufficient to generate significant emission for the two scenarios to tend towards the same values. This is less true for the lower transitions, that still can be excited despite low temperatures conditions (see for example the rotational levels diagram in Appendix F), and for higher transitions, whose excitation remain low anyway, as can be seen on the integrated intensity diagram on Figure 6.8.

Again, line profiles also illustrate these conclusions, on Figure 6.9. In the case of Langer and Glassgold (1990) reaction rates, the profiles are broader towards the beginning of the shock, because more SiO is produced earlier, hence excited in this case. This is not true though for the (1-0) transition owing to the high temperatures at which SiO is produced, which tend to favor higher transitions. The maximum line temperatures that are reached are slightly larger with Le Picard et al. (2001) rates, owing to the fact that SiO maximum fractional abundances are also slightly higher in this case. Complementary parameters, both concerning the shock code and the LVG code, are investigated in Appendix K.

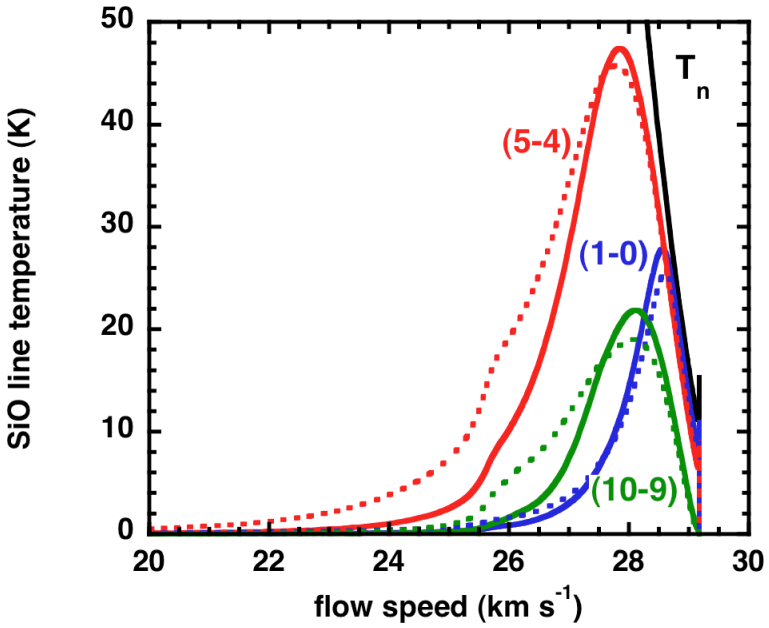

Figure 6.9 – Line profiles for the reference model, obtained with respectively Le Picard et al. (2001) (continuous curves) and Langer and Glassgold (1990) (dotted curves) SiO formation reaction rates, for three selected transitions (1-0), (5-4), and (10-9).

Other molecular tracers for star formation : SiO results

7

Schilke et al's reference model studies

Dans ce chapitre, les différences notables de notre étude avec les résultats des travaux antérieurs réalisée par Schilke et al. (1997) sont énumérées, dans le cas de l'émission de la molécule de SiO dans les chocs stationnaires de type C. Les différences en termes de modélisation sont d'abord présentées, tant pour le code de choc que pour le transfert de rayonnement. Les divergences de résultat sur l'exemple d'un modèle de référence sont ensuite analysées. L'influence de paramètres physiques tels le champ magnétique et l'inclinaison du flot observé par rapport à la ligne de visée est enfin décrite.

7.1 Differences with Schilke et al.'s methods

7.1.1 Differences in the shock code

The ways the physics of shocks are handled and general processes are taken into account by the shock code are described in the Chapter 2, with some extensions in Appendixes A and B. The fashion in which the processes related to molecular hydrogen are treated is detailed in Section 3.2.

In these Chapters, the way the shocks are treated (Section 2.1) and their equations are written down (Section 2.2), as well as the handling of the source terms for these equations (Appendixes A and B) are common to the version of the shock code that was used by Schilke et al. (1997). Similarly, their version of the shock code already made use of an extensive chemical network including about a hundred species bound by approximately a thousand reactions (see for example Subsection 2.3.1.

On the contrary, the treatment of molecular hydrogen as presented in Section 3.2 is the result of revisions that have taken place since Schilke et al. (1997)'s article (see the references listed in this Section). In addition to this, the present work uses the state-of-the-art calculation of Wrathmall et al. (2007) for the H–H_2 collisional rate coefficients set (see Section 3.4). Another important update of the shock code concerns the treatment of the charge and of the dynamical effects of the grains, as introduced in Subsection 2.3.2. The problem of critical velocities has also been investigated (following the references cited in Subsections 2.3.3 and 2.3.4), leading to the settings of new upper limits for the possible C-type shock velocities.

7.1.2 Differences in the LVG code

The implementation of the radiative transfer is presented in Chapter 6. In particular, the choice of the molecular constants (rotational constant and dipolar moment) for SiO is given in Table 6.1, and is fairly the same as that of Schilke et al. (1997)'s study. The choice of two additional sets of molecular data differs between our study and the one of Schilke et al. (1997), leading to minor discrepancies (a few percents) in the results of the LVG code (for example in terms of excitation temperatures) :

- in Schilke et al. (1997)'s investigation, the Einstein coefficients were calculated *in situ* by the LVG code, using the expressions 6.1, 6.2, and 6.3, whereas we use the list recently provided by the Leiden Atomic and Molecular Database (www.strw.leidenuniv.nl/moldata/) ;
- in Schilke et al. (1997)'s investigation, the Turner et al. (1992) set of collisional rate coefficients with H_2 as a unique collision partner were implemented, for $j_{\rm up} \leq 20$, and for eight given temperatures between 20 and 300 K. We use the more recent work of Dayou and Balança (2006), with the same number of rotational levels being taken into account, but with more working temperatures available (30) between fairly the same limits (10 to 300 K). Again the influence of this choice is not significant in terms of excitation temperatures for example. Furthermore, we included collisions with Helium thanks to the work of Dayou and Balança (2006) in our equations of statistical equilibrium (see 6.2 and 6.3 for the details of these references).

More important is the choice of the escape probability expression that is used in the solving of the set of equations of statistical equilibrium. We favored the use of the approximation of Neufeld and Kaufman (1993) (Expression 5.37), simpler and more convenient in our plane parallel geometry, whereas Expression 5.61 was used by Schilke et al. (1997). The influence of such a choice has been studied thoroughly, and is presented in Subection 6.5.1.

7.1.3 Other differences : chemistry

This Subsection can be found in Gusdorf et al. (2008a).

SiO formation. As specified in Subsection 6.5.2, the two reactions 6.20 and 6.21 are of crucial importance for the formation of SiO. While Schilke et al. (1997) implemented Langer and Glassgold (1990) rate for those, we take benefit from the experimental work of Le Picard et al. (2001) that has taken place in the meantime. The influence and consequences of such a choice are studied in Subsection 6.5.2.

SiO destruction. The abundance of SiO is limited by its conversion to SiO_2 in the reaction with OH

$$\mathrm{SiO + OH \longrightarrow SiO_2 + H} \tag{7.1}$$

whose rate coefficient remains subject to considerable uncertainty. We adopt the same expression as Schilke et al. (1997), viz.

$$k_6 = 1.0 \times 10^{-11} (T/300)^{-0.7} \tag{7.2}$$

in units of $\mathrm{cm^3\ s^{-1}}$. However, we note that Zachariah and Tsang (1995) calculated a barrier of 433 K to reaction (7.1), and a rate coefficient

$$k_6 = 2.5 \times 10^{-12} (T/300)^{0.78} \exp(-613/T);$$

see the discussion of Le Picard et al. (2001). At $T = 300$ K, the latter rate coefficient is 30 times smaller than the former. In the ambient (pre-shock) and the post-shock gas, where $T \approx 10$ K, the existence of an activation energy of several hundred kelvin would prevent the oxidation of SiO in reaction (7.1) from occurring. The rate coefficient for reaction (7.1) in the UMIST data base (Le Teuff et al. (2000)) is

$$k_6 = 2.0 \times 10^{-12}$$

in $\mathrm{cm^3\ s^{-1}}$, which is 50 times smaller than (7.2) at $T = 10$ K. Fortunately, the conversion of SiO into SiO_2 occurs in a region which is too cold and optically thick to contribute to the SiO line intensities, and so the uncertainty in the rate coefficient for reaction 7.1 is not significant in the present context.

The oxygen scenario. Schilke et al. (1997) made the implicit assumption of a chemical equilibrium to simulate the initial state of the gas. In such an equilibrium, the initial fractional abundance of O_2 is approximately 10^{-5}, whereas observations with the Odin satellite (Pagani et al. (2003), Larsson et al. (2007)) have placed upper limits of $n(O_2)/n(H_2) \lesssim 10^{-7}$. In view of these measurements, we have considered two scenarios, both with an initial gas–phase fractional abundance $n(O_2)/n_{\mathrm{H}} = 1.0 \times 10^{-7}$, as a consequence of the freeze–out of oxygen on to grains, but with differing assumptions regarding its chemical form in the grain mantles.

- the molecular oxygen which formed in the gas phase was adsorbed on to the grains, where it remained as O_2 ice in the pre-shock medium, with a fractional abundance of 1.3×10^{-5}, relative to n_{H}. The initial fractional abundance of H_2O ice is an order of magnitude larger than that the fractional abundance of O_2 ice;
- atomic oxygen was adsorbed on to the grains before O_2 was synthesized and subsequently hydrogenated to H_2O ice in the grain mantles of the cold pre-shock medium. The fractional abundance of H_2O ice increases by only 25% as a consequence, to 1.3×10^{-4}.

7.2 Reference model

This Section can be found in Gusdorf et al. (2008a).

7.2.1 The shock structure

First, we compare the computed shock structure with that of Schilke et al. (1997), for a reference C-type shock model, in which the pre-shock density $n_{\mathrm{H}} = 10^5\ \mathrm{cm^{-3}}$ and the magnetic field strength $B = 200\ \mu$G, and the shock velocity $v_{\mathrm{s}} = 30\ \mathrm{km\ s^{-1}}$. The most striking difference between the current and the previous model is that the width of the

shock wave decreases by a factor of approximately 4, to 5×10^{15} cm, from 2×10^{16} cm in the study of Schilke et al. (1997) ; see Figure 7.1a. This difference is attributable to the more accurate treatment of the coupling between the neutral fluid and the charged grains in the current model and is an indication of the significance of the inertia of the (negatively) charged grains in dark clouds, in which the degree of ionization is low. With the narrower shock wave is associated a higher maximum temperature of the neutral fluid, as there is less time for the initial energy flux, $\rho_{\rm n}v_{\rm s}^3/2$, associated with the bulk flow, to be converted into internal energy of the H_2 molecules or to be radiated away. Thus, $T_{\rm n} \approx 4000$ K here, compared with $T_{\rm n} \approx 2000$ K in the model of Schilke et al. (1997).

There are chemical differences between the models also, which are related in part to the changes in the shock structure ; these differences may be summarized as follows :

- the fraction of the Si in the grain cores which is released into the gas phase by sputtering is approximately ten times smaller in the current model than in the model of Schilke et al. (1997). This reduction is attributable partly to the sputtering yields, which have higher thresholds and are smaller for olivine ($MgFeSiO_4$) than for the amorphous silica (SiO_2) considered by Schilke et al. (1997) ; but the main reason for the decrease is the enhanced coupling between the neutral fluid and the charged grains, which reduces the shock width and hence the time available to erode the grains. On the other hand, the magnitude of the ion–neutral drift speed is similar in both calculations. As a consequence of the reduction in the shock width, the integrated SiO line intensities predicted by the current model are smaller, in general, than calculated by Schilke et al. (1997) ; see the following Sections ;
- the displacement of the maximum fractional abundance of SiO, which forms in the gas–phase reactions 6.20 and 6.21, from that of Si, which is eroded from the grains, is a more significant fraction of the shock width in the current model ; cf. Figure 7.1b. The initial fractional abundance of O_2 in the pre-shock medium is lower here, by a factor of approximately 10, than in the model of Schilke et al. (1997), delaying the initial formation of SiO. The O_2 is assumed to be predominantly in the form of ice, which is sputtered rapidly from the grains in the early stages of development of the shock wave, as may be seen from the two orders of magnitude increase in the fractional abundance of gas–phase O_2, apparent in Figure 7.1c. The fractional abundances of O_2 and OH decrease subsequently, at high kinetic temperatures, owing to their dissociation by H in the chemical reactions O_2(H, O)OH and OH(H, O)H_2. The former reaction, which is endothermic by over 8000 K, proves to be less effective in destroying O_2 over the smaller width of the current shock model (see Figure 7.1c) than was the case in the calculations of Schilke et al. (1997). On the other hand, the lower energy threshold of 17 K in reaction (6.24) allows oxidation reactions to proceed further into the post-shock region, compared with Schilke et al. (1997), whose adopted threshold was 111 K. As a consequence, conversion of Si into SiO is slower initially but more complete eventually than predicted by Schilke et al. (1997) ;
- SiO_2 is removed more rapidly from the gas phase in the current model. The compression is more rapid than in the model of Schilke et al. (1997), and so the rate of adsorption of molecules to grains ("freeze–out") is higher. If the oxidation of SiO in the reaction SiO(OH, H)SiO_2 has an activation energy of several hundred kel-

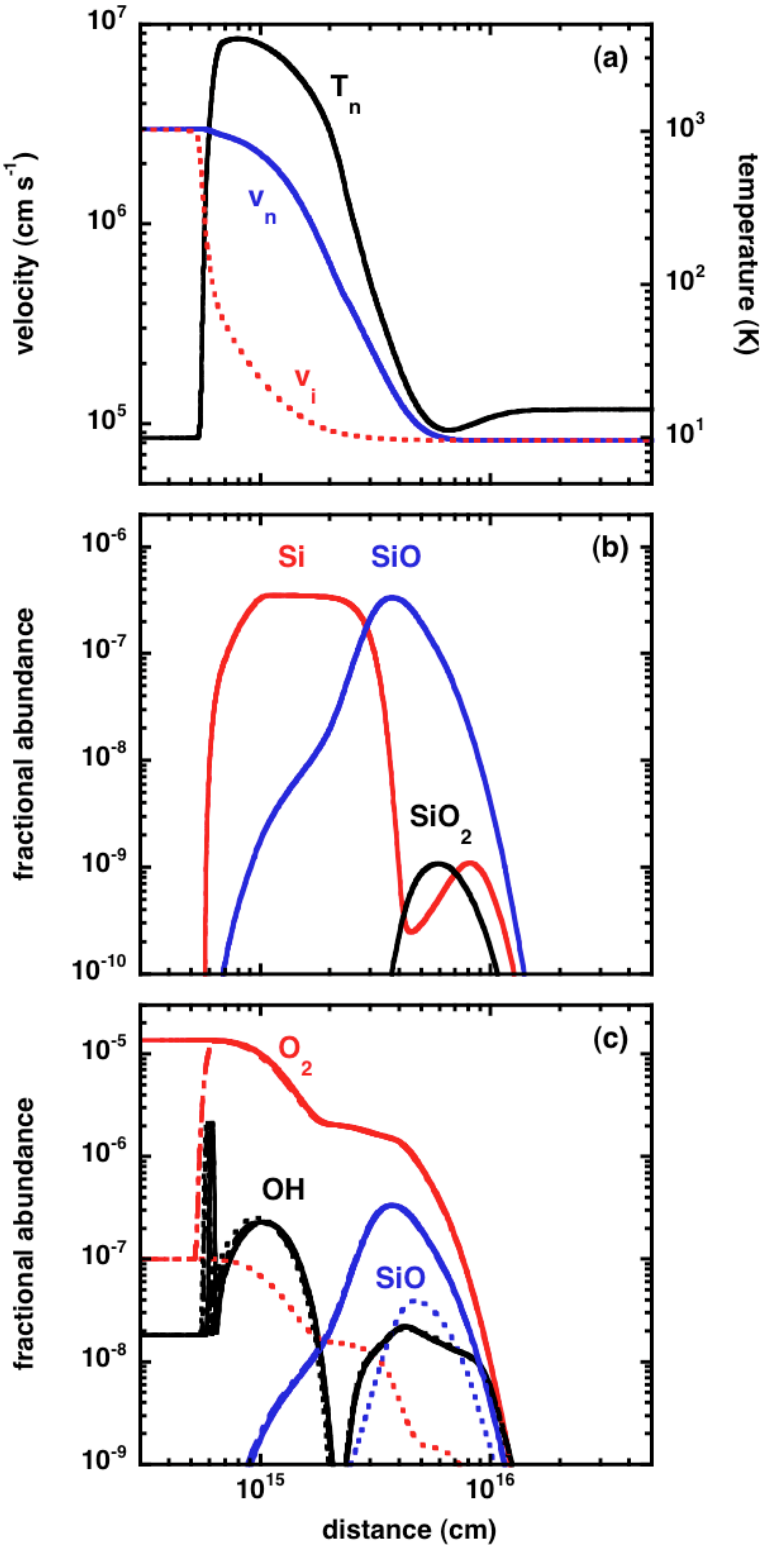

Figure 7.1 – (a) Temperature of the neutral fluid and velocity profiles of the neutral and charged fluids, predicted by the present C-type shock model. The shock parameters are $n_{\rm H} = 10^5$ cm^{-3} and $B = 200$ μG in the pre-shock gas, and $v_{\rm s} = 30$ km s^{-1}, $\zeta = 5 \times 10^{-17}$ s^{-1}. The fractional abundances of selected (b) Si-bearing and (c) O-bearing species are plotted also (cf. Schilke et al. (1997), fig. 2). On the bottom figure, the dotted line corresponds to the ice H_2O scenario, and the semi-dotted ones to the O_2 scenario.

vin (Zachariah and Tsang (1995) ; see Subsection 6.5.2), the maximum fractional abundance of SiO_2 would be reduced still further.

Regarding the initial O_2 scenario, it turns out that the first scenario (in which O_2 is initially adsorbed on to grains) is practically equivalent to assuming that the O_2 is initially in the gas–phase (see Figure 7.1c), as its release from the grain mantles occurs early and rapidly (on a timescale of a few years for the model in Figure 7.1) in the shock wave. On the other hand, the second scenario can result in reduced levels of oxidation of Si to SiO in the gas–phase (cf. Fig. 7.1), depending on the relative importance of reactions 6.20 and 6.21 in the oxidation process. In what follows, we present results corresponding principally to the first scenario, with the second being considered mainly in Section 8.3.

The observable quantities are the intensities of the rotational transitions of SiO and the velocity–profiles of these emission lines. Having computed the shock structure, we evaluate the line intensities and profiles as described in Chapters 5 and 6, assuming that the shock is viewed face–on.

7.2.2 Physical conditions in the SiO emission region

Figure 7.2 illustrates the variation of physical conditions throughout the formation region of the SiO 5–4 rotational line for our reference model with $n_{\rm H} = 10^5$ cm^{-3}, $v_{\rm s} =$ 30 km s^{-1}, and $b = 0.63$. It may be seen that the line is optically thin through most of the hot precursor (where the flow speeds of the charged and neutral fluids differ), due to both the low SiO abundance and the large velocity gradient there. Therefore the line intensity is low despite a high kinetic temperature. At the rear of the shock wave, approaching maximum compression, the synthesis of SiO and the steady decrease in velocity gradient eventually raise the optical depth in the line, and the 5–4 intensity peaks, with the line temperature attaining values close to the local kinetic temperature of the neutral fluid, $T_{\rm n}$; that is, the line approaches LTE. The intensity then declines rapidly as the gas cools ; the decline occurs in 500 years for the model shown here. This behaviour is insensitive to the rate of re-adsorption of SiO on to the grains, which occurs over much longer timescales.

7.2.3 The reference model's line profiles

In Figure 7.3, we compare the intensity profiles of various rotational lines, as functions of the flow speed of the neutral fluid, expressed in the frame of the pre-shock gas, for our reference model : $n_{\rm H} = 10^5$ cm^{-3}, $v_{\rm s} = 30$ km s^{-1}, and $b = 0.63$. The profiles are seen to be narrow (widths of 1–2 km s^{-1}), with similar shapes and peaking within 2 km s^{-1} of $v_{\rm s}$, as expected for compressed material at the rear of the shock wave.[1] Note that the transition 2–1 peaks further into the cooling flow, because the lower j–levels are repopulated from the higher levels as the temperature falls.

[1]The maximum compression of the post-shock relative to the pre-shock gas, $\sqrt{2}v_{\rm s}/v_{\rm A}$, where $v_{\rm s}$ is the shock speed and $v_{\rm A}$ is the Alfvén speed in the pre-shock gas, occurs when the magnetic pressure in the post-shock gas is equal to the initial ram pressure. It follows that the flow speed in the post-shock gas cannot fall below $v_{\rm min} = v_{\rm A}/\sqrt{2} = 1.3b$ km s^{-1} *in the shock frame*, where b is the scaling parameter of the magnetic field, defined in Subsection 2.1.3.

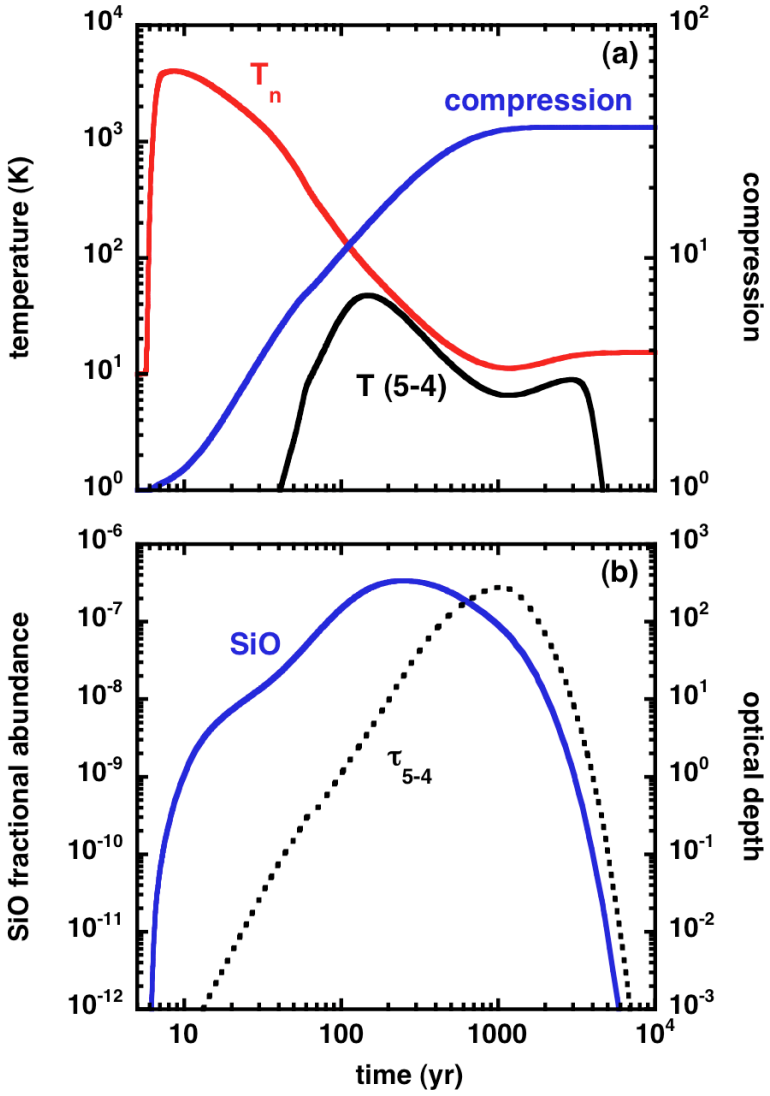

Figure 7.2 – (a) The temperature of the neutral fluid, $T_{\rm n}$, the brightness temperature, $T(5-4)$, in the $j = 5$–4 line, and the compression factor, $n_{\rm H}/n_{\rm H}({\rm initial})$; (b) the the optical depth, τ_{5-4} in the 5–4 transition and the fractional abundance of SiO, $n({\rm SiO})/n_{\rm H}$, as functions of the flow time of the neutral fluid, $t_{\rm n}$. The model parameters are $n_{\rm H} = 10^5$ cm^{-3}, $v_{\rm s} = 30$ km s^{-1}, and $b = 0.63$.

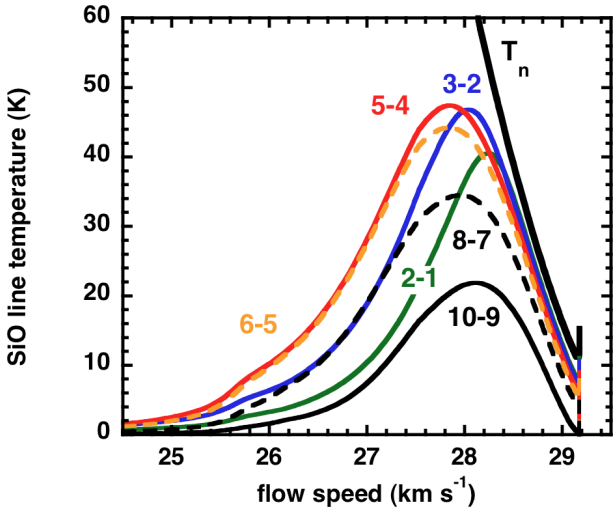

Figure 7.3 – The velocity profiles of transitions from rotational levels $j \rightarrow j-1$ of SiO, computed for our refeence model, viewed face–on. Only those lines detectable from the ground are shown. The model parameters are $n_{\rm H} = 10^5$ cm^{-3}, $B = 200$ μG, and $v_{\rm s} = 30$ km s^{-1}. The flow speed is in the reference frame of the pre-shock gas. The neutral temperature profile, $T_{\rm n}$, is shown also, as are indicative values of the flow time of the neutral fluid.

The general shape and centroid velocities are globally similar to those found by Schilke et al. (1997) (their Figure 3b where the profiles were plotted *in the shock frame*), although the differences between the various lines are less significant in the present calculations. Also, the emission wing from the fast precursor, at the start of the shock wave, is weaker in the current models, owing to the delay in SiO formation (see Subsection 7.2.1), making our line profiles narrower than in Schilke et al. (1997). Note that including local thermal broadening in our profile calculations would not significantly change our predicted SiO line width of 1–2 km s−1, because the SiO emission peaks at low temperatures, $T_{\rm n} \lesssim 100$ K, where the Doppler width is $\sqrt{kT/44m_{\rm H}} \leq 0.1$ km s^{-1}.

7.3 Influence of physical parameters

The results of this Section can be found in Gusdorf et al. (2008a).

7.3.1 Influence of the transverse magnetic field strength

The existence of a magnetic field transverse to the direction of propagation is a necessary condition for a C-type shock wave to form, and it is instructive to consider the variation of the structure of the shock wave with the strength of the magnetic field. Energy equipartition arguments, applied to the magnetic and thermal energy densities in the pre-shock molecular gas, of particle density $n({\rm H}_2) + n({\rm He}) = 0.6 n_{\rm H}$ and kinetic temperature T, suggest that $B^2/(8\pi) \approx n_{\rm H} k_{\rm B} T$ and hence that $B = b n_{\rm H}^{0.5}$, where b is a scaling parameter (cf. Subsection 2.1.3) such that B is in μG when $n_{\rm H}$ is in cm^{-3}. In gas of $T = 10$ K,

equipartition with the thermal energy implies $b = 0.18$. However, we note that such a low value of b is inconsistent with the existence of a steady–state C-type shock wave when $n_{\rm H} = 10^5$ cm^{-3} and $v_{\rm s} \geq 10$ km s^{-1}, as the corresponding ion magnetosonic speed in the pre-shock gas (9.7 km s^{-1}) is lower than the shock speed.

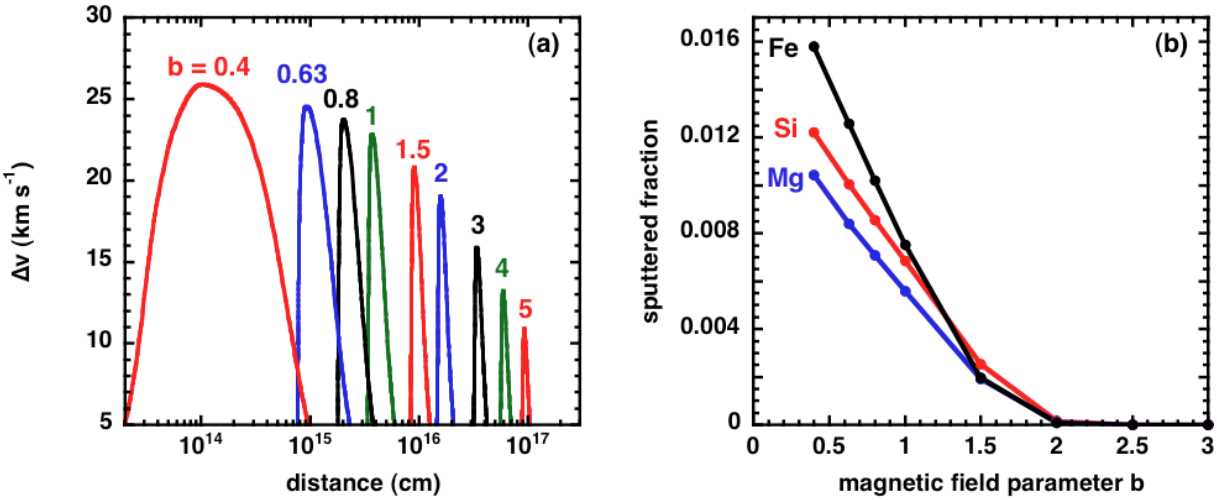

Figure 7.4 – (a) The ion–neutral velocity difference, $\Delta v = |v_{\rm i} - v_{\rm n}|$, and (b) the fractions of Mg, Si and Fe eroded from olivine ($MgFeSiO_4$) grains, computed as functions of the transverse magnetic field strength, B, in the pre-shock gas; $n_{\rm H} = 10^5$ cm^{-3} and $v_{\rm s} = 30$ km s^{-1}.

In Figure 7.4, we present results as a function of the transverse magnetic field strength, for the parameters of the model of Schilke et al. (1997) : $n_{\rm H} = 10^5$ cm^{-3}, $v_{\rm s} = 30$ km s^{-1}, and a magnetic field scaling parameter b in the range $0.5 \leq b \leq 5$. We recall that Schilke et al. (1997) adopted $B = 200$ μG, corresponding to $b = 0.63$. This value of b is consistent with the analysis of Zeeman measurements by Crutcher (1999), who concluded that there was an approximate equipartition of the magnetic and kinetic energy densities in the molecular clouds that he had observed. It may be seen from Figure 7.4 that increasing the magnetic field inhibits the release of Si from refractory grain cores in the shock wave, owing to the reduction in the maximum ion–neutral velocity difference, Δv.

The effect of varying the scaling parameter, b, on the emergent SiO line intensities is shown in Figure 7.5, for our reference model.

In panels (a) and (b) of Figure 7.5 are plotted the predicted line profiles, peak temperatures, and integrated intensities of the SiO 5–4 line, for various values of b. It may be seen that the maximum intensity is reached for intermediate values of $0.63 \lesssim b \lesssim 1$. At smaller b, SiO is less abundant : the shock wave is narrower and hotter, and so O_2 is more readily destroyed by H, resulting in incomplete oxidation of Si into SiO. At larger b, the SiO emission decreases owing to less efficient sputtering of Si (see Figure 7.4b) at the lower ion–neutral drift speeds. In particular, the predicted intensity drops from $T_{\rm peak} = 10$ K at $b = 2$ to practically zero at $b = 3$.

Panels (c) and (d) of Figure 7.5 show the relative peak and integrated line temperatures, as functions of $j_{\rm up}$, for various values of $b \leq 2$ (curves for $b > 2$ are not shown as they lead to negligible SiO emission). It may be seen that the values $0.63 \lesssim b \lesssim 1$, which

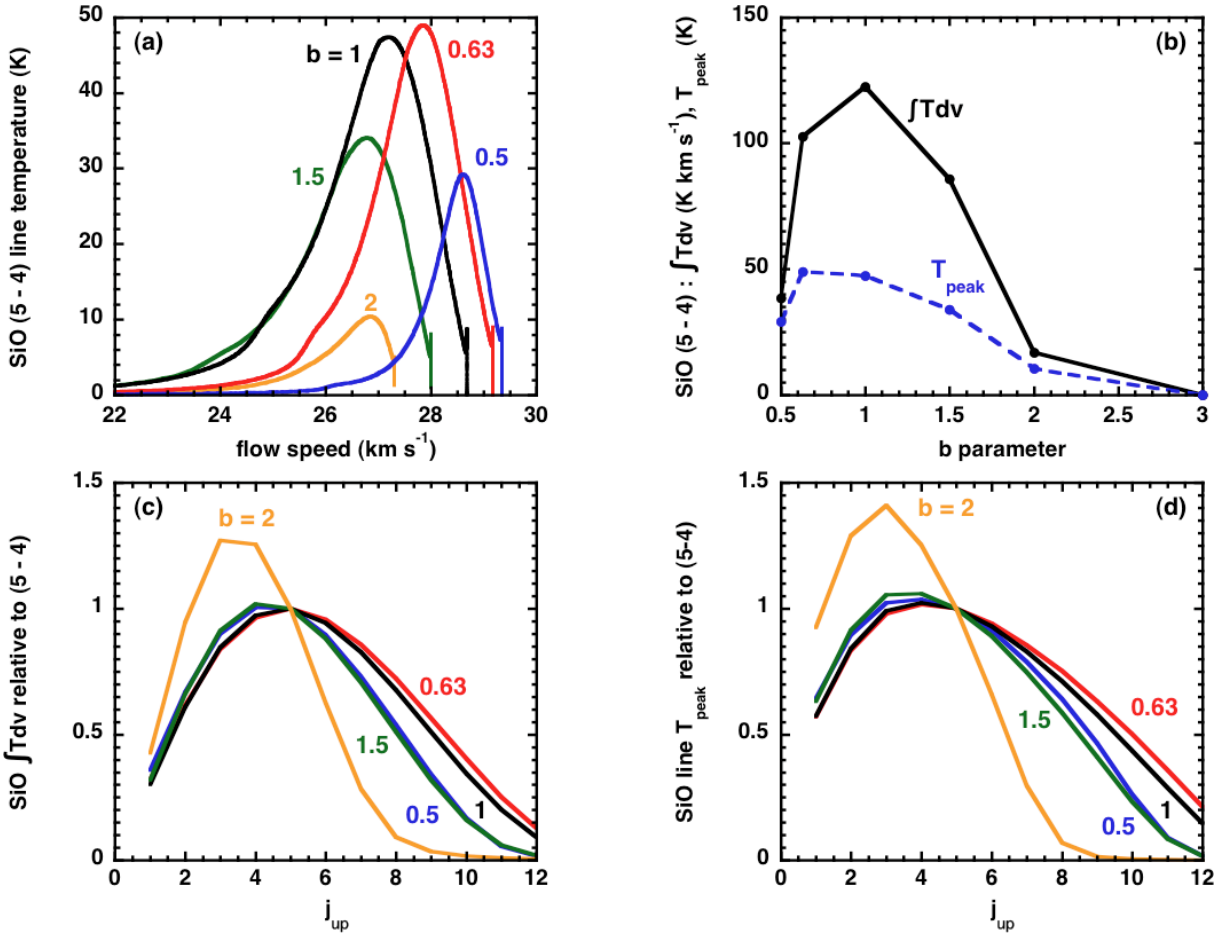

Figure 7.5 – (a) The SiO 5–4 line temperature, as a function of the flow speed of the neutral fluid, in the reference frame of the pre-shock gas, for the specified values of the magnetic field parameter, b; (b) the peak and integrated intensities of the 5–4 line, as functions of b; (c) the integrated and (d) the peak intensities of rotational emission lines $j_{\rm up} \rightarrow j_{\rm up} - 1$ of SiO, relative to the 5–4 transition, for the specified values of b. All calculations for $v_{\rm s} = 30$ km s^{-1} and $n_{\rm H} = 10^5$ cm^{-3}.

give rise to the strongest 5–4 emission, also yield the highest relative intensities of lines from $j_{\rm up} \geq 7$. For example, the intensity of the 11–10 line, relative to 5–4, is 3 to 4 times larger than when $b = 0.5$ or $b = 1.5$. Comparison with Figure 8.5 will suggest that this dependence on b may be difficult to distinguish observationally from variations in shock speed. A less ambiguous indication of the value of b might be obtained from the width of the cooling zone, which increases as b^2, from 10^{15} cm for $b = 0.4$ to 2×10^{16} cm for $b = 2$ and for the parameters of our reference model (see Figure 7.4a).

7.3.2 Influence of the viewing angle

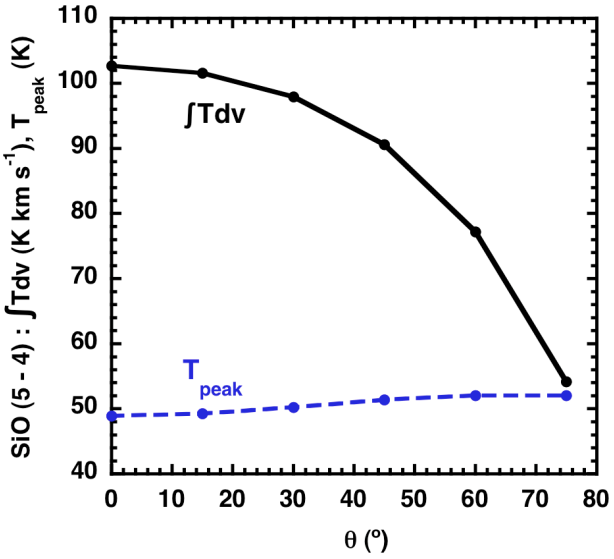

Figure 7.6 – Effect of the inclination angle, θ, on the integrated and peak intensities of the 5–4 line.

Statistically, there is a low probability that a planar shock should happen to be viewed face–on. Accordingly, we have explored the effects on the SiO rotational line intensities of varying the viewing angle, for the case of our reference model, using the formula L.53, derived in Appendix L.

The variations of $T_{\rm peak}(5-4)$ and $T{\rm d}V(5-4)$ with viewing angle, θ, are plotted in Figure 7.6. The peak intensity is almost unaffected by the inclination, as the line is already optically thick for a face–on view (see Equation L.53). On the other hand, the velocity projection reduces the line width, and the integrated intensity, $T{\rm d}V$, declines steadily with increasing viewing angle – by up to a factor of 2 at 75^o. However, such a variation would be difficult to deduce from observations, given the typical uncertainties in beam filling factors.

Panels (a) and (b) of Figure 7.7 illustrate the changes in the (relative to 5–4) peak and integrated SiO line temperatures. Significant changes, compared with viewing face–on, are seen only for inclinations greater than 60^o from the normal, and they affect only the optically thin lines $j_{\rm up} \leq 3$ and $j_{\rm up} \geq 12$. The main change in the curves for the relative integrated line temperatures (panel (b) of Figure 7.7) is that the maximum occurs at lower

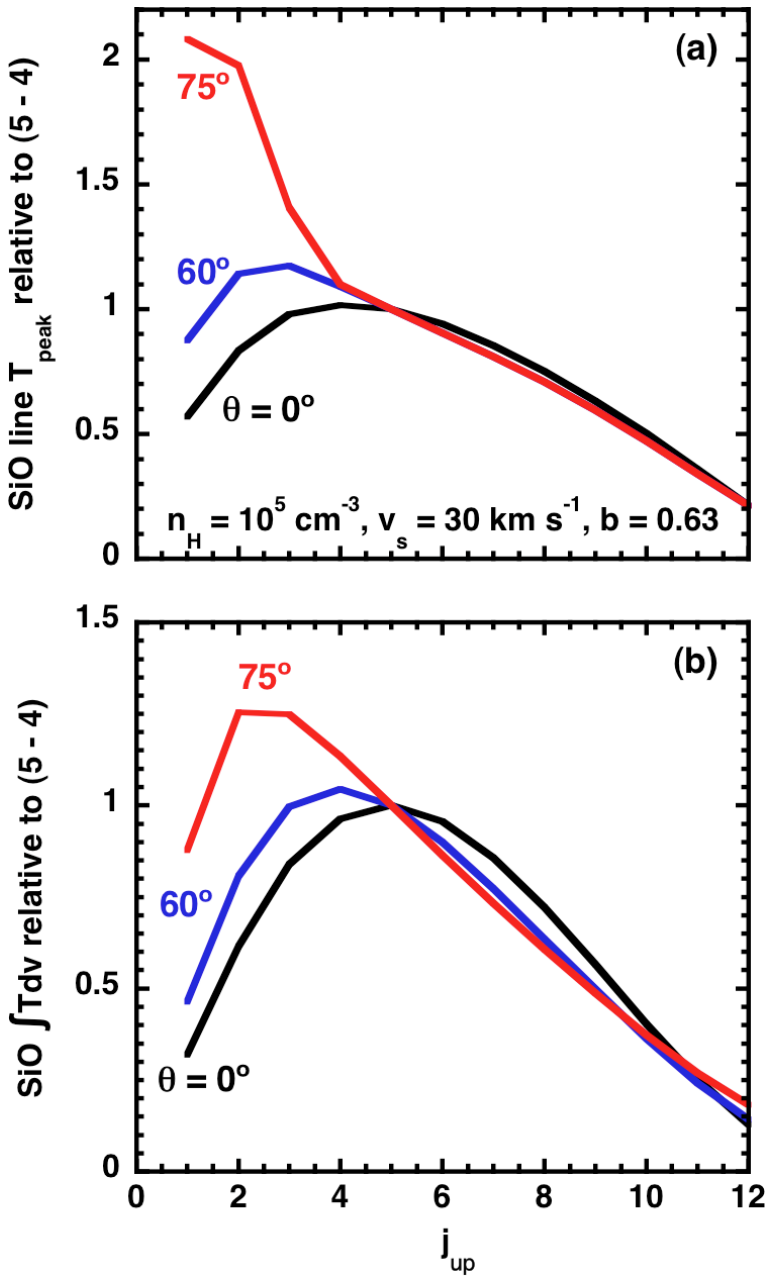

Figure 7.7 – Effect of the inclination angle, θ, on (a) the peak, and (b) the integrated intensities of the rotational emission lines of SiO, relative to the 5–4 line.

$j_{\rm up}$ as θ increases ; this effect could be easily confused with a face–on shock of slightly lower pre-shock density (cf. Figure 8.5). The relative peak temperature (panel (a)) is even more strongly modified, with an upward turn of the curve at $j_{\rm up} \leq 4$. The latter characteristic appears to be the only unambiguous signature of a viewing angle $> 60^o$ in the context of our one–dimensional models.

8

Comparisons with observations

Dans ce chapitre, l'émission de la molécule de SiO dans les chocs stationnaires de type C est étudiée et comparée aux observations disponibles pour le flot bipolaire L1157, dans la continuité du travail de Schilke et al. (1997). Les modèles d'une large grille de chocs sont comparés aux données observationnelles sous diverses hypothèses d'abondance initiale de dioxygène. Les conditions physiques associées à ces modèles de chocs sont ensuite systématiquement fournies, toujours à des fins de comparaison avec des observations.

The results of this Chapter are presented in Gusdorf et al. (2008a).

8.1 A grid of C-type shock models

8.1.1 SiO production in C-type shock models

We have computed a grid of shock models with the following parameters :

- $n_{\rm H} = 10^4$ cm^{-3}, $v_{\rm s} = 20, 25, 30, 35, 40, 45, 50$ km s^{-1} ;
- $n_{\rm H} = 10^5$ cm^{-3}, $v_{\rm s} = 20, 25, 30, 35, 40, 45$ km s^{-1} ;
- $n_{\rm H} = 10^6$ cm^{-3}, $v_{\rm s} = 20, 25, 27, 30, 32, 34$ km s^{-1}.

The maximum shock speed for $n_{\rm H} \gtrsim 10^4$ cm^{-3} is determined by the collisional dissociation of H_2, the main coolant, which leads to a thermal runaway and a J-discontinuity (Le Bourlot et al. (2002), Flower et al. (2003)).

In fact, we computed two grids, one for each of the scenarios concerning the initial distribution of oxygen between O_2 and H_2O ices, as specified towards the end of Subsection 7.1.3. We concentrate on the first of these two scenarios, but some additional Figures for the second scenario are given in Section 8.3.

Because of the sharply defined sputtering threshold energy of approximately 50 eV, there is negligible sputtering of Si from the olivine ($MgFeSiO_4$) for shock speeds of 20 km s^{-1} or less. The fractions of the Mg, Si and Fe which are released from the olivine into the gas phase are shown in Figure 8.1. Comparing Figure 8.1 with the corresponding Figure 4 of May et al. (2000), whose sputtering yields are used in the present calculations, shows that the fractions of Mg, Si and Fe which are sputtered from olivine have decreased by an order of magnitude. As the same sputtering yields have been used in both studies, this change is attributable to the reduction in the shock width, resulting from the

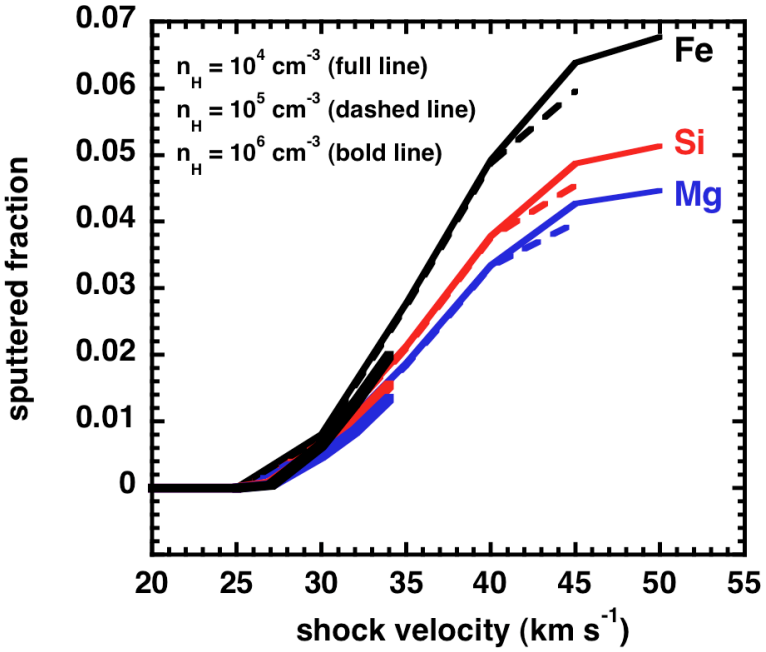

Figure 8.1 – The fractions of Mg, Si and Fe, initially in the form of olivine ($MgFeSiO_4$), which are released into the gas phase by sputtering within a steady–state C-type shock wave.

improved treatment of grain–neutral coupling. We note that CO is the principal eroding partner (cf. May et al. (2000)).

Figure 8.1 shows that the degree of sputtering is, in fact, insensitive to the pre-shock gas density (cf. Caselli et al. (1997)) ; it depends essentially on the shock speed. Polynomial fits of the sputtered fractions of Fe, Si and Mg, as functions of the shock speed, are given in the article Gusdorf et al. (2008a), itself available in Appendix O.

In Figure 8.2, we display the fractional gas–phase abundances of Si and SiO, as functions of the relevant flow time. Silicon is produced by erosion of the charged grains by collisions, principally with molecules, at the ion–neutral drift speed. Once the drift speed exceeds the sputtering threshold velocity, the erosion of Si occurs rapidly, as Figure 8.2 shows. Thus, the flow time which is directly relevant to the release of Si into the gas phase is that of the *charged* fluid, rather than that of the neutrals, which is the appropriate measure of the total time for formation of SiO. As noted in the second point of the comparison in Subsection 7.2.1, there is an additional, chemical delay to the conversion of Si into SiO, in reactions (6.20) and (6.21), which is apparent in our Figure 8.2, owing to the low abundance and partial destruction of O_2. The magnitude of this delay depends on the parameters of the model, notably the shock speed, v_s, and the pre-shock gas density, n_H. Conversion is almost instantaneous for $v_s \geq 30$ km s^{-1}, $n_H = 10^6$ cm^{-3}, when OH is formed abundantly at the start of the shock and reaction (6.21) dominates the oxidation process.

Figure 8.3 shows the variation with shock speed and pre-shock gas density of the fractional abundance of SiO, computed through the entire shock wave. It is evident from Figure 8.3 that the duration of the C-type shock wave, as measured by the temperature

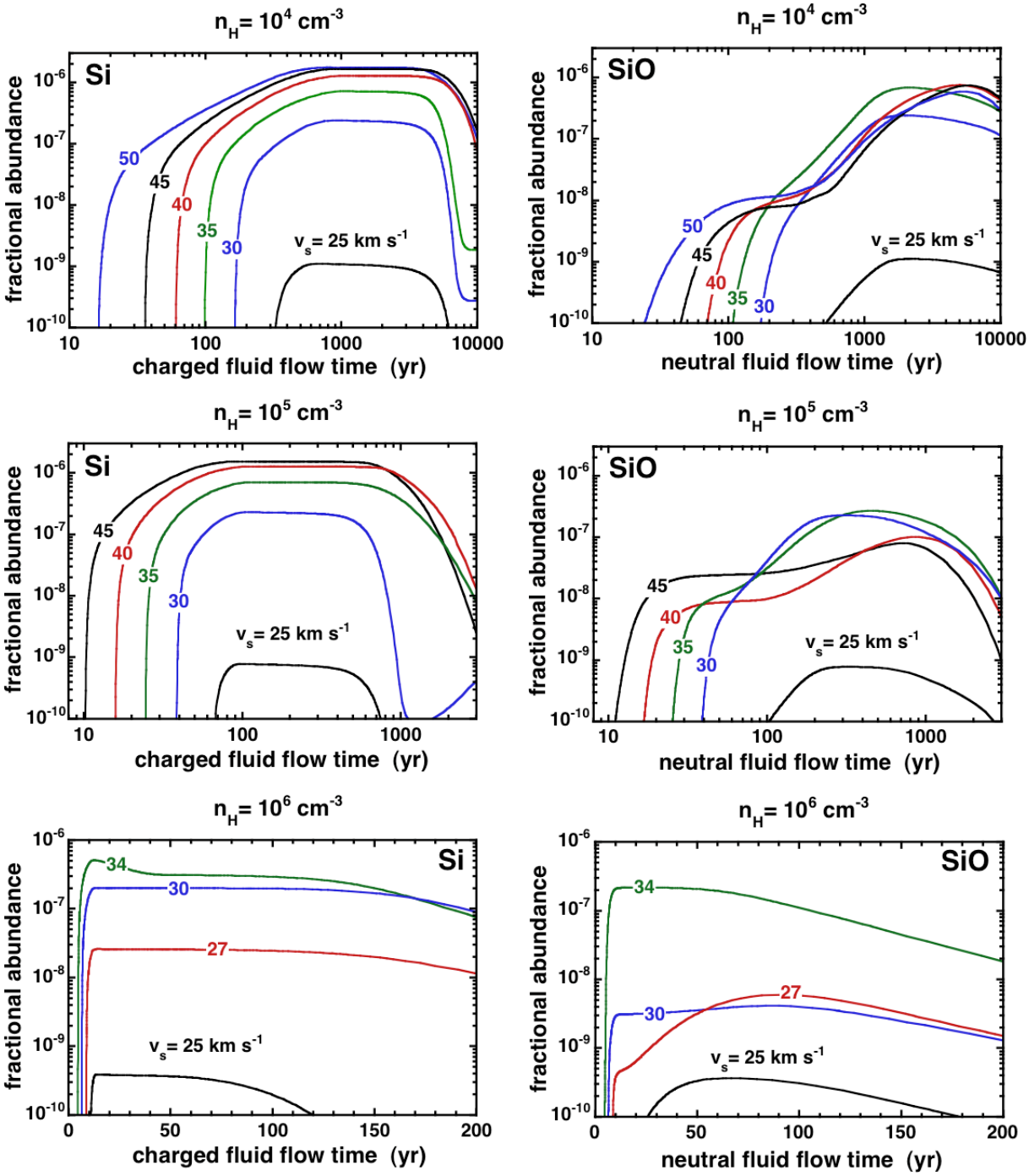

Figure 8.2 – The fractional abundances of Si, released into the gas phase by the sputtering of olivine ($MgFeSiO_4$), and of SiO, which subsequently forms in reactions 6.20 and 6.21. In *the left-hand panels*, the independent variable (abscissa) is the flow time of the charged fluid : see text, 8.1.1.

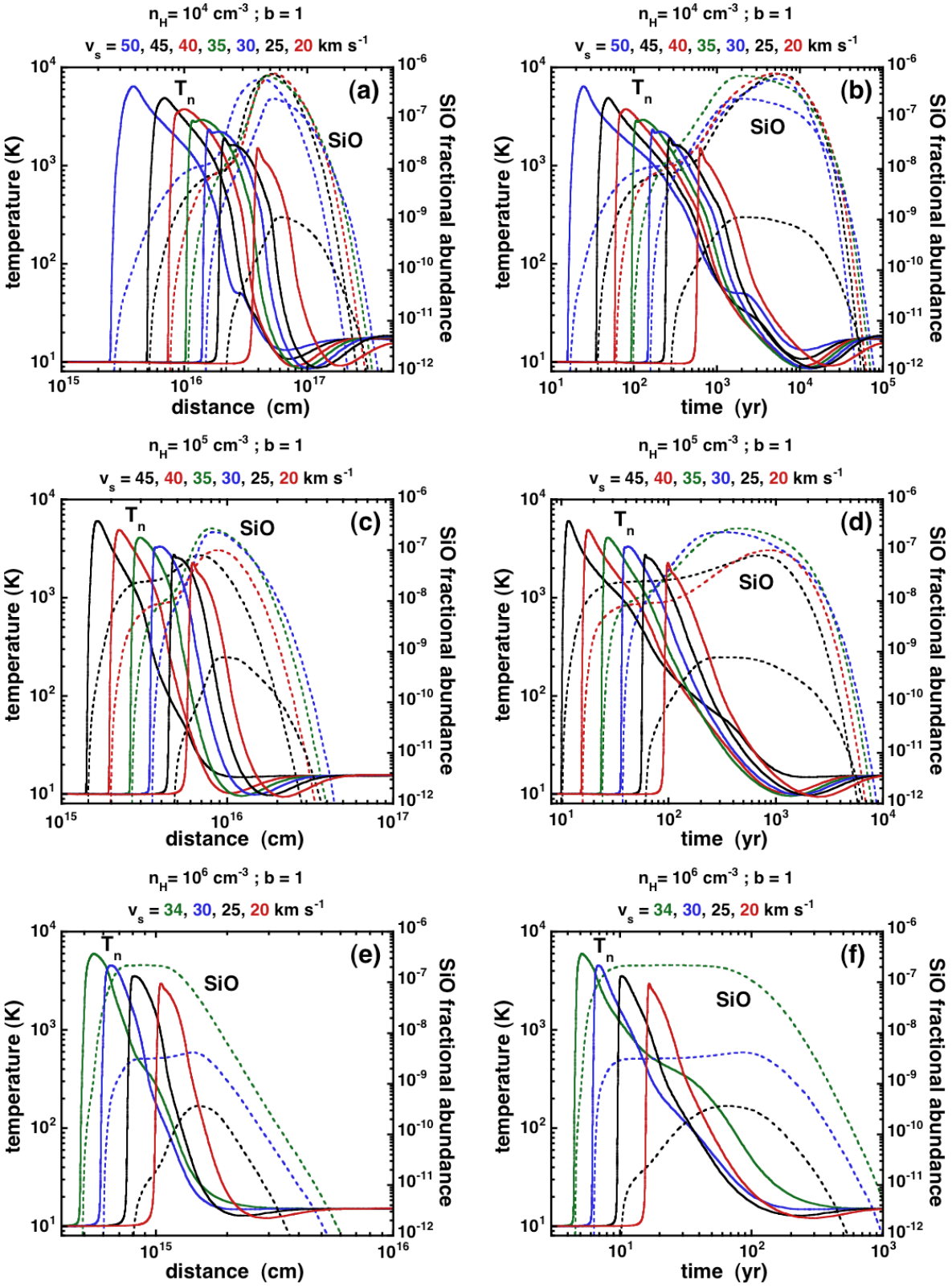

Figure 8.3 – The fractional abundance of SiO, $n(\mathrm{SiO})/n_{\mathrm{H}}$, computed for the grid of shock models and plotted as a function of distance (left) and neutral flow time (right) ; $n(\mathrm{SiO})/n_{\mathrm{H}}$ is negligible for $v_{\mathrm{s}} \lesssim 20$ km s^{-1}. In addition, the temperature of the neutral fluid is plotted also.

profile, is of the order of 10^4, 10^3 and 10^2 years for pre-shock gas densities $n_{\rm H} = 10^4$, 10^5 and 10^6 cm^{-3}, respectively. The peak SiO abundance is reached over similar timescales. It may be seen that the highest fractional abundances of SiO are attained for the lowest pre-shock density, $n_{\rm H} = 10^4$ cm^{-3}. At higher densities, both O_2 and OH, which are reactants in (6.20) and (6.21), are destroyed by the atomic hydrogen which is produced in the shock wave. Thus, the conversion of Si into SiO becomes incomplete at high density, and the gas–phase SiO abundance depends on $n_{\rm H}$ even though the Si sputtered fraction does not (cf. Figure 8.1).

8.1.2 Physical conditions studies in the SiO emission region

Physical conditions. In order to illustrate the dependence of conditions in the SiO emission region on the shock parameters, we present, in Figure 8.4, the important physical quantities, evaluated *at the peak of the SiO 5–4 line*, for all models in our grid. We have verified that this is equivalent to computing intensity–weighted geometric means of the same quantities over the region where the 5–4 line intensity is more than 50% of its maximum value.[2] Hence, it provides a good indication of the mean characteristics of the region producing the peak of the emission.

Figure 8.4 shows that the SiO emission peak always occurs in the cool and dense post-shock region : $T_{\rm n} \approx 50$ K (Figure 8.4a) and a density of 10–40 times the pre-shock value, close to maximum compression (Figure 8.4b). The SiO fractional abundance, $n({\rm SiO})/n_{\rm H}$, is also approximately equal to its maximum value in the shock wave (compare Figure 8.4c with Figure 8.3). The trend to lower SiO abundance at higher $n_{\rm H}$, noted in Subsection 8.1.1, is clearly visible here. Finally, the "LVG parameter", $n({\rm SiO})/({\rm d}v_z/{\rm d}z)$, lies typically in the range $10^{14} - 10^{16}$ cm^{-2} km^{-1} s, implying that the 5–4 line is optically thick at its peak for most models of our grid.

Peak line temperatures. In the left column of Figure 8.5, we show the predicted peak temperature of the SiO 5–4 line for the grid of models considered in Subsection 8.1.1, as well as the variation with $j_{\rm up}$ of the peak brightness temperatures of various lines, relative to that of 5–4. The *relative* intensities have the advantage of being independent of the beam filling factor, and thus they are comparable directly to observations, without prior knowledge of the source size.

The relative peak intensities are within 20% of unity for $j_{\rm up} \leq 7$ over a broad range of model parameters ($v_{\rm s} \geq 30$ km s^{-1} and $n_{\rm H} < 10^6$ cm^{-3}), owing to the large opacity and near–LTE excitation conditions. For larger values of $j_{\rm up}$, the relative intensities are more dependent on the shock speed and ≈ 1 only when the limiting speed is approached. The absolute peak brightness temperature in the 5–4 line is typically 10–50 K for $v_{\rm s} \geq 30$ km s^{-1}, similar to the kinetic temperature in the emission region, but drops sharply at lower shock speeds, for which the SiO abundance (and opacity) is small. The broken curves in Figs. 8.5d and h are the results obtained assuming that the initial abundance of O_2 ice is negligible, i.e. the second of the two scenarios described in Subsection 7.1.3.

[2]Values evaluated at the peak also differ by less than a factor 2 from the same parameters evaluated at the "median" point where the integrated line intensity, $T{\rm d}V(5-4)$, reaches half of its total.

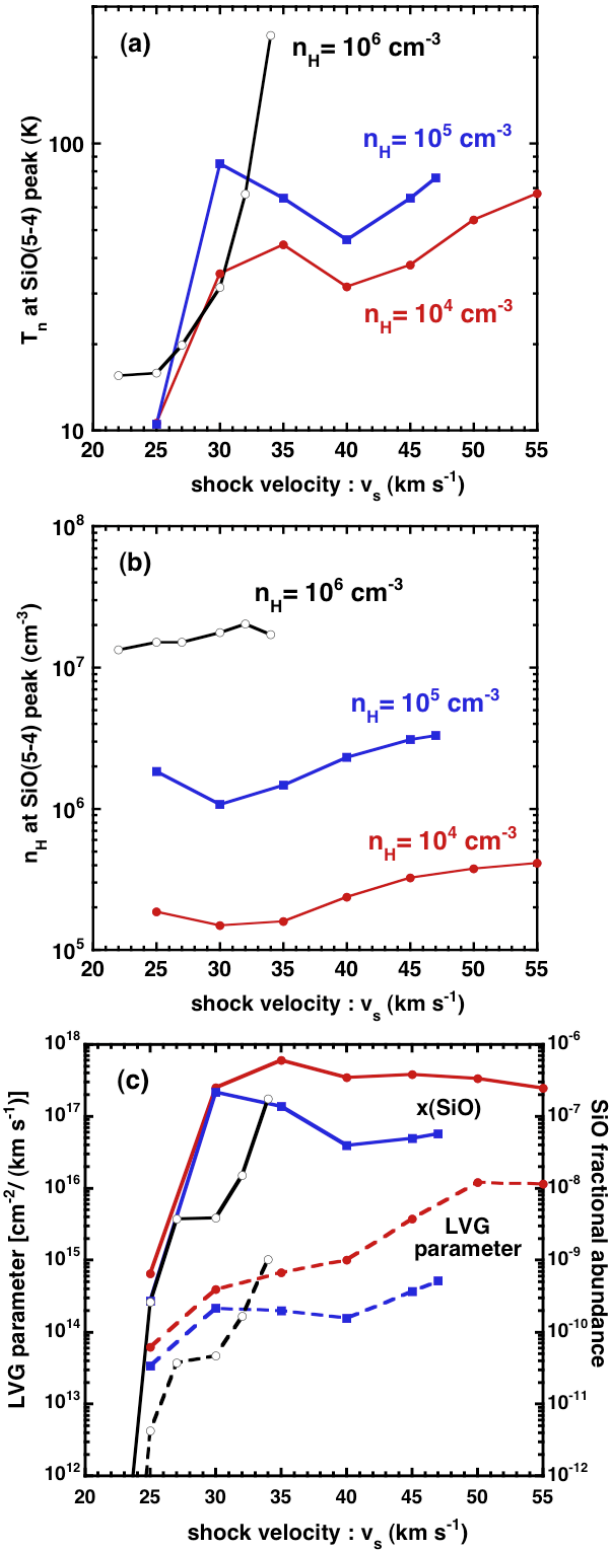

Figure 8.4 – Physical conditions at the position of the peak in the SiO 5–4 line intensity $[T_{\rm peak}(5-4)]$ as functions of the shock speed, $v_{\rm s}$, for all models of the grid : (a) neutral temperature, $T_{\rm n}$; (b) total density, $n_{\rm H}$; (c) the LVG parameter, $n({\rm SiO})/({\rm d}v_z/{\rm d}z)$, and the fractional abundance of SiO, $x({\rm SiO}) \equiv n({\rm SiO})/n_{\rm H}$.

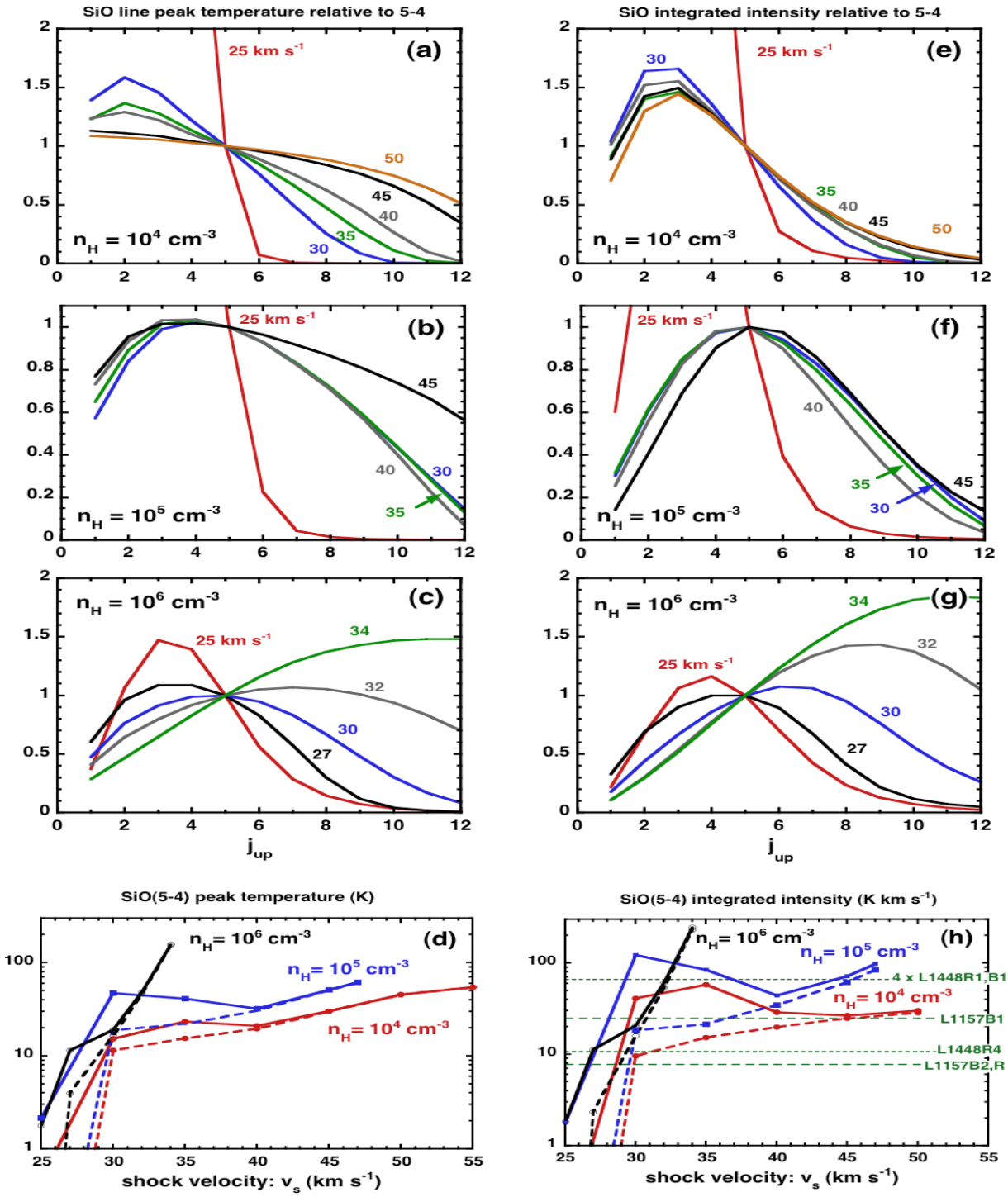

Figure 8.5 – **a–c)** The peak line temperatures, $T_{\rm peak}$, of the rotational emission lines of SiO, relative to the 5–4 line, as functions of the rotational quantum number of the upper level of the transition, $j_{\rm up}$, for the grid of models in Section 8.1. The value of density, $n_{\rm H}$, of the pre-shock gas is indicated in each panel. **d)** The *absolute* peak brightness temperature of the 5–4 line, $T_{\rm peak}(5-4)$, as a function of shock speed, $v_{\rm s}$, for all three values of the pre-shock gas density, $n_{\rm H}$. Shock speeds in excess of 34 km s^{-1} are absent when $n_{\rm H} = 10^6$ cm^{-3}, as they give rise to a J-type discontinuity, and the shock wave is no longer C-type; see Section 8.1. The right–hand panels **e)–h)** show the corresponding values of the integrated line intensities, $T{\rm d}V$. The values of $T{\rm d}V(5-4)$ observed in L1157 and L1448 are indicated. In panels **d)** and **h)**, the broken curves show the results obtained assuming that the initial abundance of O_2 ice is negligible, i.e. the second scenario described in Subection 7.1.3.

Integrated line intensities. In the right column of Figure 8.5 are presented the integrated intensities (denoted $T\mathrm{d}V$) of the rotational emission lines of SiO, relative to the 5–4 line, computed for the grid of models considered in Subsection 8.1.1. There are significant differences between the relative integrated and peak ($T_{\rm peak}$) line temperatures (right and left columns, respectively, of Figure 8.5), owing to systematic variations in linewidth with $j_{\rm up}$, i.e. in the extent of the region where the line is significantly excited. The relative integrated intensities of lines with $j_{\rm up} \geq 7$ remain the most sensitive to the shock speed. As may be seen in Schilke et al. (1997), the maximum value of $T\mathrm{d}V$ occurs at higher values of the rotational quantum number, $j_{\rm up}$, for higher $n_{\rm H}$. Although the shock temperature varies only weakly with $n_{\rm H}$ (see Figure 8.3), a higher density enhances the rates of collisional excitation of the high–j levels, for any given value of the shock speed, $v_{\rm s}$. In Section 8.2, we explore the usefulness of this effect for constraining the pre-shock density, based on a comparison with actual observations.

The variation of the *absolute* integrated intensity of the 5–4 rotational emission line with the shock parameters is shown also in Figure 8.5h. The bump in $T\mathrm{d}V$ of the 5–4 transition, for $30 \leq v_{\rm s} \leq 40$ km s^{-1} and $10^4 \leq n_{\rm H} \leq 10^5$ cm^{-3} is caused by incomplete O_2 destruction in the shock wave, resulting in more rapid SiO formation and warmer emission zones (cf. Figure 8.4). As the broken curves in Figure 8.5d and h show, this "bump" is absent in our second scenario, where O_2 is never abundant in the gas phase. At higher shock speeds, the results from the two scenarios become identical, as OH dominates the oxidation of Si in both cases.

8.2 Comparisons with observations

8.2.1 Line profiles

Rotational line profiles. As Schilke et al. (1997) first noted, the generic SiO line profile predicted by steady planar C-type shock waves, with a peak at high velocity (in the post-shock gas) and a tail at lower velocity (in the accelerating precursor), is reminiscent of the SiO line profiles in the L1448 molecular jet (Bachiller et al. (1991)). Similarly, we note that the reversed shape of SiO profiles in the L1157 bowshocks, with a peak at low velocity and a high velocity tail (Zhang et al. (1995)), could arise if the post-shock gas is stationary in the cloud frame, i.e. if one observes the reverse shock, in which the jet is being decelerated. However, in either case, the SiO profiles predicted by our models remain narrower than those observed, with widths of 0.5–2 km s^{-1}, as compared to the observed widths of 5–20 km s^{-1} in 3"–10" beams.

Broader line profiles from steady C-type shocks could arise if Si was sputtered not only from grain cores, as assumed here, but also from SiO–containing grain mantles, with lower binding energy. Then, the SiO abundance would be much enhanced at intermediate velocities, in the precursor (see Schilke et al. (1997)). However, owing to the steep temperature decline across the shock wave, this situation results in large variations of the line widths and velocity centroids with the emitting rotational level, $j_{\rm up}$ (cf. Figure 5 of Schilke et al. (1997)). Indeed, the observed profiles are very similar from line to line, with the (8–7)/(2–1) intensity ratio showing only modest variations with velocity (see, for example,

fig. 9 of Nisini et al. (2007)). These observations suggest that the broad SiO lines are not attributable entirely to intrinsic velocity gradients through a single, planar C-type shock wave. There may be several shock–cooling zones inside the beam, each with a narrow intrinsic profile, which appear spread out in radial velocity owing to a range of inclination angles or propagation speeds, in the observer's frame. This conclusion is supported by interferometric observations of L1157 and L1448 (Guilloteau et al. (1992), Gueth et al. (1998), Benedettini et al. (2007)), which reveal systematic velocity gradients across the SiO emitting knots (reminiscent, in some cases, of a bowshock geometry ; Dutrey et al. (1997)) down to 2"–3" resolution ; at the distances of L1157 and L1448, the angular dimensions of the SiO emitting regions in Figure 7.3, for example, are a few tenths of an arcsec. Such complex two–dimensional modelling lies outside the scope of the present paper. However, we argue in Subsection 8.2.2 that we may still perform a meaningful comparison of our predicted SiO line intensities with observations of knots in outflows, without reproducing in detail the line profiles, provided that the shock conditions do not vary too much across the beam.

Narrow SiO lines near ambient velocity. In addition to the typically broad SiO line profiles mentioned above, some outflow regions such as NGC1333 and L1448 exhibit extremely narrow SiO emission lines, with $\Delta v \approx 0.5$ km s^{-1}, near rest velocity (Lefloch et al. (1998), Codella et al. (1999) ; Jiménez-Serra et al. (2004), Jiménez-Serra et al. (2005)). The corresponding SiO abundance of 10^{-11}–10^{-10} is two to three orders of magnitude smaller than in the broad SiO components (Codella et al. (1999) ; Jiménez-Serra et al. (2005)). Jiménez-Serra et al. (2005) proposed that this feature in L1448 traces a magnetic precursor, where neutral gas is just beginning to accelerate and grain species are starting to be released into the gas phase. However, as we now explain, detailed multifluid shock models do not support this interpretation.

Our SiO line profile calculations show that emission from a magnetic precursor does not give rise to a narrow feature near the speed of the pre-shock gas. The line intensity increases as the neutral fluid is accelerated, heated, and enriched in SiO – by orders of magnitude by the time that grain–sputtering is complete. In fact, this deduction could have been made already, on the basis of Figures 3 and 5 of Schilke et al. (1997), which cover the entire velocity range relevant to predicting the SiO line profiles. Truncation of the precursor when the neutral fluid has been accelerated to only $v_{\rm n} = 0.5$ km s^{-1} would imply a very finely–tuned shock age, a circumstance which appears to us to be improbable. Furthermore, an ion–neutral drift speed of at least 5 km s^{-1} is needed to start releasing species from grain mantles, where binding energies are a few tenths of an eV (Flower and Pineau des Forets (1994)), and of at least 20 km s^{-1} to start sputtering grain cores (May et al. (2000)). However, the $H^{13}CO^+$ line does not show evidence of this predicted acceleration : its emission peak is shifted by only +0.5 km s^{-1} from the velocity of the ambient gas, like the narrow SiO feature (Jiménez-Serra et al. (2004)).

We believe that a more likely explanation of the narrow SiO feature in L1448 is that it traces Si–enriched post-shock material that has been decelerated by and mixed with the ambient gas, as proposed originally by Lefloch et al. (1998) and Codella et al. (1999) in connection with other regions. Given a shock speed $v_{\rm s} \leq 30$ km s^{-1} and the high ambient

density characteristic of Class 0 protostellar envelopes, deceleration could be achieved readily within the L1448 flow age of approximately 3500 years. The low SiO fractional abundance would then be a consequence of mixing with SiO–poor ambient gas. Alternatively, the narrow feature might arise in a reverse C-type shock, where outflow material at $v < 20$ km s^{-1} is brought almost to rest by the much denser ambient medium, and the shock speed is too low to produce abundant SiO. Both interpretations are consistent with NH_3 observations of dense gas in the envelope of the L1448 protostar, with radial velocity and spatial extent similar to that of the narrow SiO feature and signs of heating near the path of the fast L1448 jet (Curiel et al. (1999)).

8.2.2 Integrated line intensities

If our explanation of SiO profile broadening is correct, one could in principle recover the parameters of *each* individual emission zone in the beam by analysing the relative intensity ratios *as functions of velocity*. Unfortunately, such data are currently quite noisy and not yet available for a wide range of values of $j_{\rm up}$. Furthermore, knowledge of the beam–filling factor as a function of velocity would be necessary to obtain absolute intensities and remove ambiguity in the shock parameters ; but this would require sub-arcsecond angular resolution, which is not yet available. Nevertheless, one may still derive some approximate *beam–averaged* shock properties, if all of the shock components have similar excitation conditions, as is suggested by single–dish data, which show the line ratios to be insensitive to velocity, v. In this case, the observed profile will be simply a convolution of the individual, narrow shock profiles with the (unknown) filling–factor, $\phi(v)$. The observed absolute $T{\rm d}V$ is simply that for a single shock, multiplied by the total beam filling factor of the SiO–emitting region in the beam, $f = \int \phi(v){\rm d}v$, as inferred from its overall size in single–dish maps. The values of $T{\rm d}V$ for different $j_{\rm up}$, relative to the 5–4 transition, remain unchanged compared to a single shock, because f cancels out in the ratios, thereby enabling direct comparison with our models. In the following, we assume that this situation prevails.

By way of illustration of the applicability of the shock models, we show in Figure 8.6 the relative integrated intensities of the rotational transitions of SiO observed in the outflow sources L1157 and L1448 (Nisini et al. (2007)) and predicted by the grid of models, whose parameters are specified ; in all cases, the magnetic field scaling parameter $b = 1$. As noted in Subsection 7.3.1, this value of b yields the largest relative intensities of the high–j lines and hence will yield a *lower limit* to the shock speed required to reproduce the observations (except at $n_{\rm H} = 10^5$ cm^{-3}, where high–j excitation is a non-monotonic function of $v_{\rm s}$; see Figure 8.5f). We assume also that the shock wave is viewed face–on ; if the true inclination exceeds 60^o, this assumption results in the pre-shock density being slightly underestimated (see Subsection 7.3.2). The models shown as the full curves are those which provide the best fits to the observations. In order to illustrate how well the shock parameters are constrained, we plot as dashed curves "near–miss" models that fit most of the data points, or fit all points but do not reproduce the absolute intensity of the 5–4 line (see below).

Figure 8.6 demonstrates that steady–state C-type shocks with Si–sputtering from grain cores can reproduce successfully the relative integrated intensities of SiO lines in these

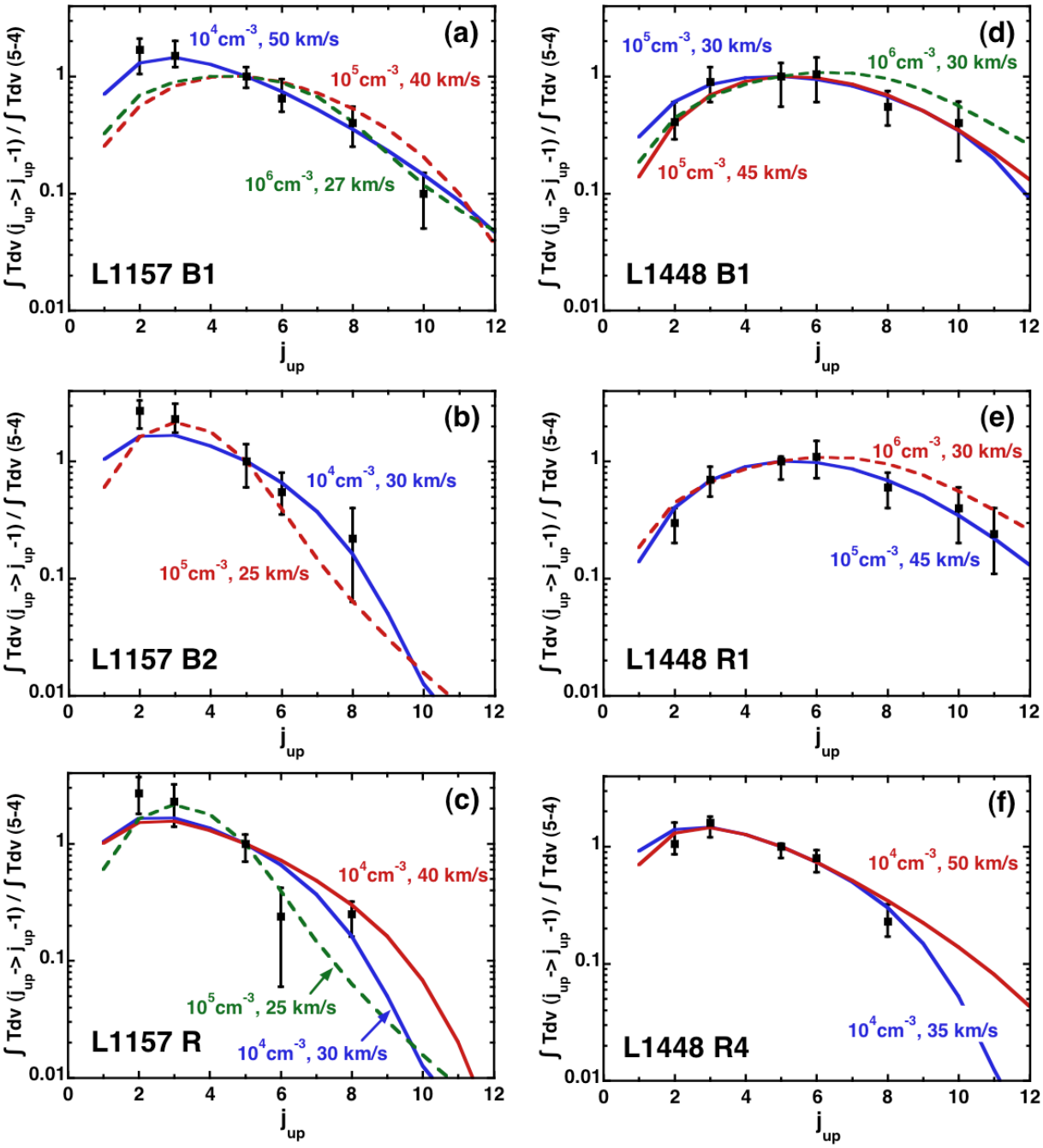

Figure 8.6 – The relative intensities of the rotational emission lines of SiO observed in the outflow sources L1157 and L1448 (Nisini et al. (2007) : points with error bars) and predicted by the C-type shock models (curves) with the parameters ($n_{\rm H}$, $v_{\rm s}$) indicated ; see text, Subsection 8.2.2. The data points which are plotted include a correction for differing beam sizes, which is significant for low–j lines. Full curves denote the best–fitting models of our grid. Broken curves show "near–miss" models with a different value of $n_{\rm H}$, which either yield a worse fit to the data points or do not reproduce the absolute $T{\rm d}V$ of the 5–4 line.

	Face–on C–type shock models[a,b]						Slab LVG models[a,c]			
SiO knot	$n_{\rm H}^{\rm init}$	$v_{\rm s}$	$T_{\rm kin}$	$n_{\rm H}$	LVG	$x_{\rm SiO}$	$T_{\rm kin}$	$n_{\rm H}$	LVG	$x_{\rm SiO}$
L1448B1	1(5)	30,45	90–70	10–30	2–4	0.5–2	>500	8	0.1	1
L1448 R1	1(5)	45	70	30	4	0.5	>500	10	0.1	1
L1448 R4	1(4)	35–50	45–55	1.5–4	7–100	3–7	200	2.5	0.03	0.3
L1157 B1	1(4)	50	55	4	100	3	150–300	3	0.08	0.8
L1157 B2	1(4)	30	35	1.5	4	2	200–300	2	0.05	
L1157 R	1(4)	30–40	35–30	1.5–2	4–10	2–3	50–100	1–5	0.02	0.6

[a]Units : $n_{\rm H}^{\rm init}$ is the pre-shock density, in cm^{-3} ; $v_{\rm s}$ the shock speed, in km s^{-1} ; $T_{\rm kin}$ is the local gas kinetic temperature, in K ; $n_{\rm H}$ is the local gas density, **in 10^5 cm^{-3} ; "LVG" is the local LVG parameter, n(SiO)$/(dv_{\rm n}/dz)$, in 10^{14} cm^{-2} km^{-1} s ; and $x_{\rm SiO}$ is the local fractional abundance, in units of 10^{-7}.**

[b]Best grid model from Fig. 8.6 and physical parameters at the SiO 5–4 line peak from Fig. 8.4.

[c]Values taken from Tables 4 and 5 of Nisini et al. (2007). The LVG parameter is given by $N({\rm SiO})/\Delta V$, with $\Delta V = 10$ km s^{-1}.

Tableau 8.1 – Properties of SiO–emission regions deduced from face–on C-type shock models or homogeneous–slab LVG models.

molecular outflows. Furthermore, Fig. 8.5h shows that the models can reproduce also the *absolute* integrated intensity of SiO 5–4 with the estimated beam filling factors $f \approx 1$ in L1157 and L1448-R4 and $f \simeq 1/4$ in L1448 R1 and B1 (cf. Nisini et al. (2007)). Alternative fits with higher density and lower shock speeds ($n_{\rm H} = 10^6$ cm^{-3} and $27 \lesssim v_{\rm s} \lesssim 30$ km s^{-1} ; $n_{\rm H} = 10^5$ cm^{-3} and $v_{\rm s} = 25$ km s^{-1}) underestimate $T{\rm d}V(5-4)$ and are thus ruled out. The shock speed, $v_{\rm s}$, is constrained to within 15 km s^{-1} and the pre-shock density to within a factor of 10, with one of our grid values of $n_{\rm H}$ yielding a clear best fit in all cases.

It is instructive to compare the physical parameters at the SiO peak of our best–fit, steady–state C-type shock models to those previously inferred from an LVG analysis, assuming a slab of constant density, temperature, and velocity gradient along the line of sight (Nisini et al. (2007)). From Table 8.1, it may be seen that the 'slab LVG' approach yields similar values of the density to our shock models but overestimates by a factor 5–10 the kinetic temperature and underestimates by several orders of magnitude the Sobolev LVG opacity parameter. The cool post-shock layer emits over a narrow velocity range and needs to be more optically thick in SiO to produce the same $T{\rm d}V$ as a hot slab with a large velocity gradient along the line of sight. On the other hand, similar SiO abundances are deduced using both approaches, to within typically a factor of 3.

8.3 An alternate O_2 scenario

We now consider equivalent results as in Sections 8.1 and 8.2, only under the alternate O_2 assumption described in Section 7.1.3, where atomic oxygen was adsorbed on to the grains before O_2 was synthesized and subsequently hydrogenated to H_2O ice in the grain mantles of the cold pre-shock medium.

8.3.1 A grid of C-type shock models

Figure 8.7 shows the equivalent of Figure 8.2. H_2O ice undergoes immedaite and quick sputtering from the grain mantles due to collisions H, H_2 and He, as O_2 did in the first scenario described in Section 7.1.3. Once in the gas phase, and again similarly to O_2 , H_2O is available to generate erosion of the silicon material of the grain cores. The difference in efficacy of this process as generated by these two different species is only noticeable at the lowest displayed velocities (25 km s^{-1}). At these temperatures, the sputtering rates have yet to reach a plateau and the weight difference between O_2 and H_2O makes the sputtering generated by the former more efficient than the latter.

Once in the gas phase, Si combines with either O_2 or OH to form SiO (Reactions 6.20 and 6.21). In the scenario where ice water is sputtered from the grains instead of molecular oxygen, much less O_2 is present in the gas phase, and OH combines with Si to form SiO. In the present scenario, OH is less abundant than O_2 is in the first case scenario, hence the slight shift of the SiO peak fractional abundance towards the post-shock region compared to the first case oxygen scenario, where O_2 is abundant enough through the whole width of the shock in the gas phase. This also explains the very slighter values for the SiO peak fractional abundance in the present case. At high shock velocities, both these effects are limited by the dissociation of O_2 that arise in the first case scenario. Again at 25 km s^{-1}, the SiO abundance is low due to the poor amount of Si that is sputtered from the grain cores.

These effects can also be seen On Figure 8.8, which is the equivalent of Figure 8.3, only for the assumptions made under the pressent O_2 scenario.

Figure 8.9 shows similar results as its equivalent for the first case oxygen scenario, that is the Figure 8.4. The most important difference is the absence or the less important breaks of the monotony of the curves, that can be accounted for by the fact that in the present oxygen scenario, the results are not dependent on the abundance of O_2, that can undergo dissociation from 35 km s^{-1} in the previously studied scenario.

8.3.2 Comparisons with observations

The variation of the peak temperature and the *absolute* integrated intensity of the 5–4 rotational emission line with the shock parameters is shown also in Figure 8.5 d and h. As already explained, the bumps that are observed in the first case scenario disappear in the second case, as O_2 is never abundant in the gas phase. At higher shock speeds, the results from the two scenarios become identical, as OH dominates the oxidation of Si in both cases.

Figure 8.10 is the equivalent of Figure 8.6 for the current O_2 scenario considered. Again, the relative intensities can be well reproduced by steady–state C-type shocks. The absolute SiO $T\mathrm{d}V(5-4)$ favour the low n_{H}, high v_{s} cases (cf. the dashed curved in Fig. 8.5h). The best–fit shock parameters and the inferred physical conditions at the (5–4) line peak are almost unchanged, as the range of shock speeds is such that oxidation of Si by OH is dominant.

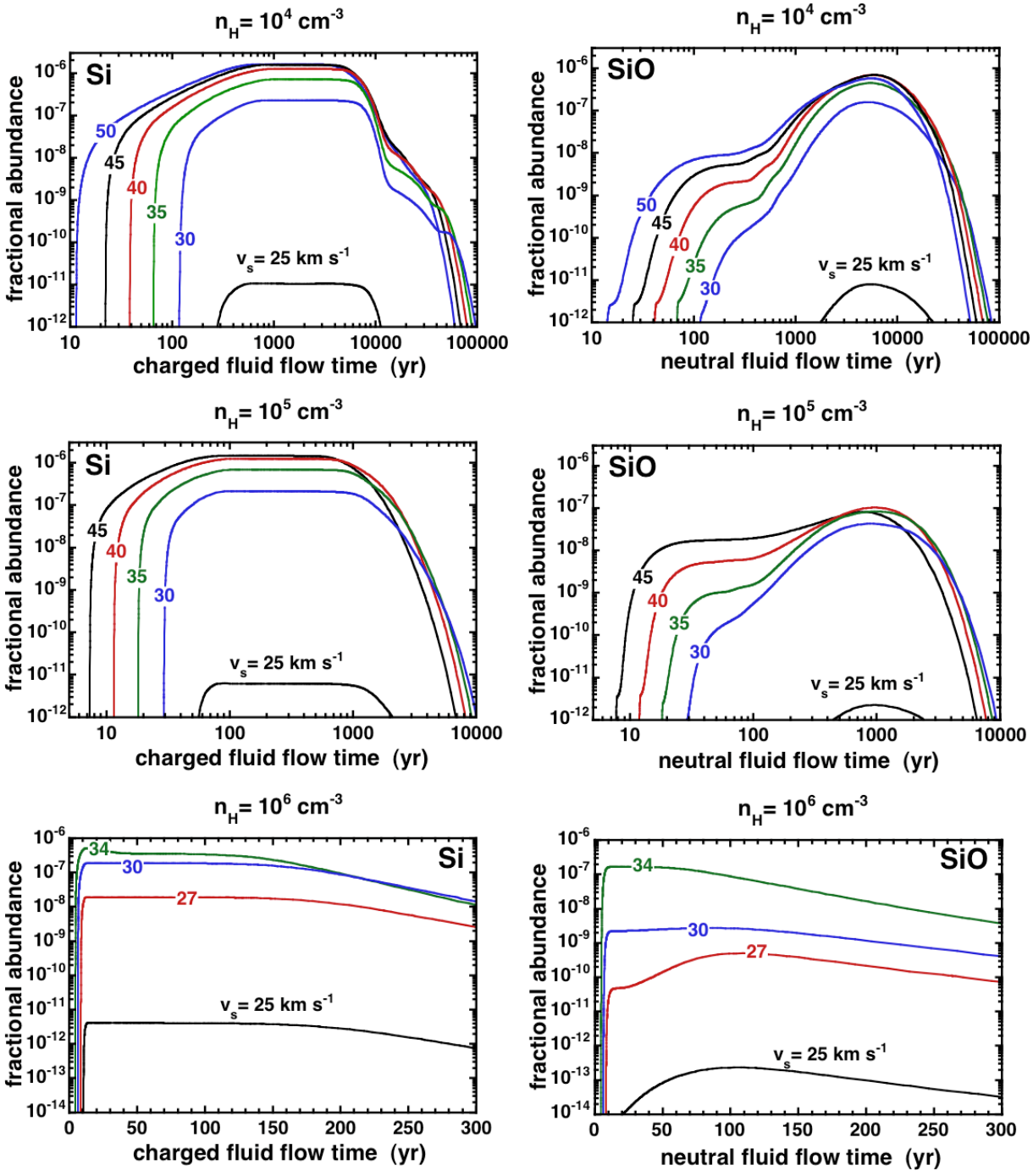

Figure 8.7 – As Figure 8.2, but assuming that the initial abundance of O_2 ice is negligible (the second scenario described in Subsection 7.1.3).

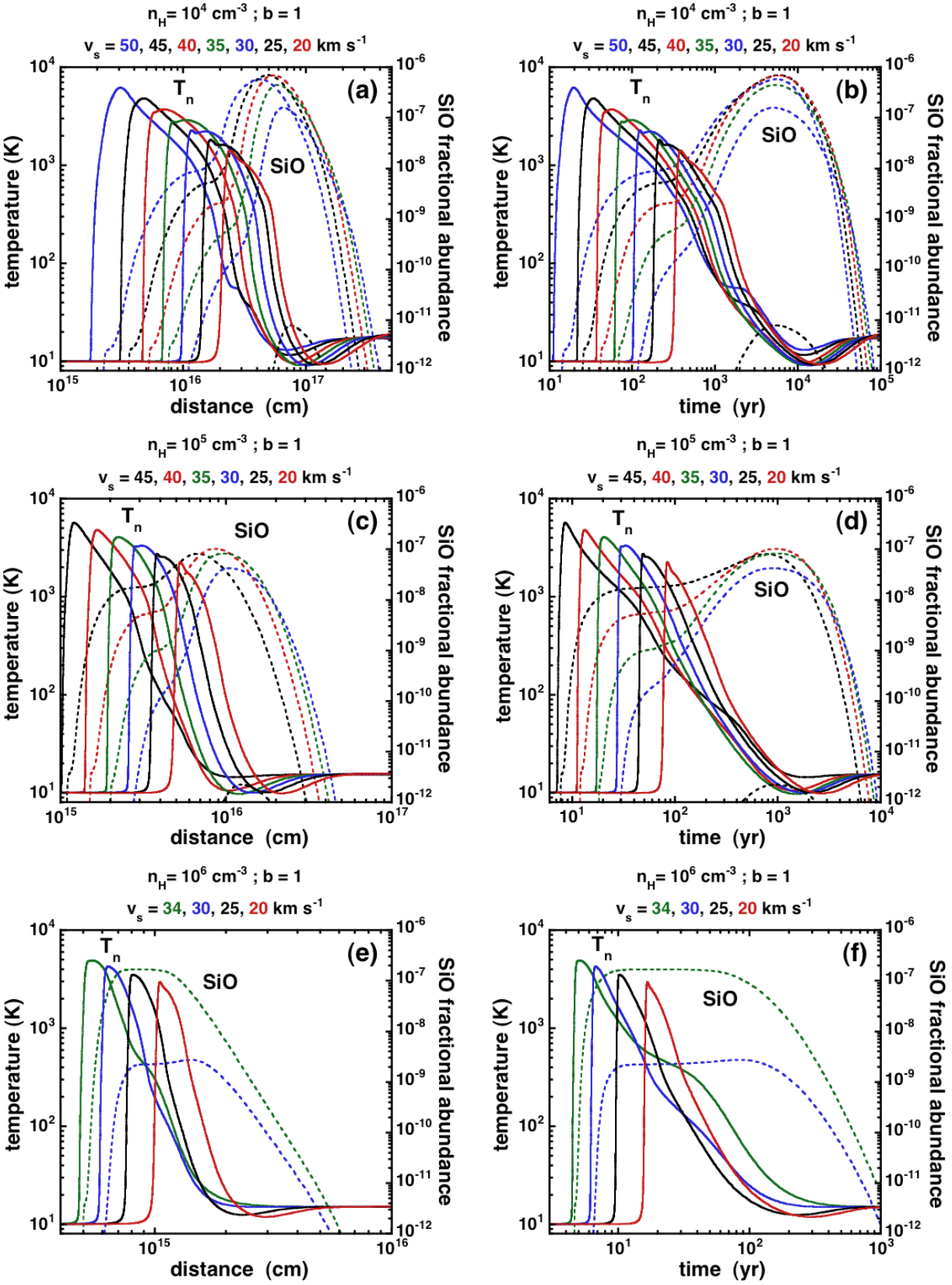

Figure 8.8 – As Figure 8.3, but assuming that the initial abundance of O_2 ice is negligible (the second scenario described in Subsection 7.1.3).

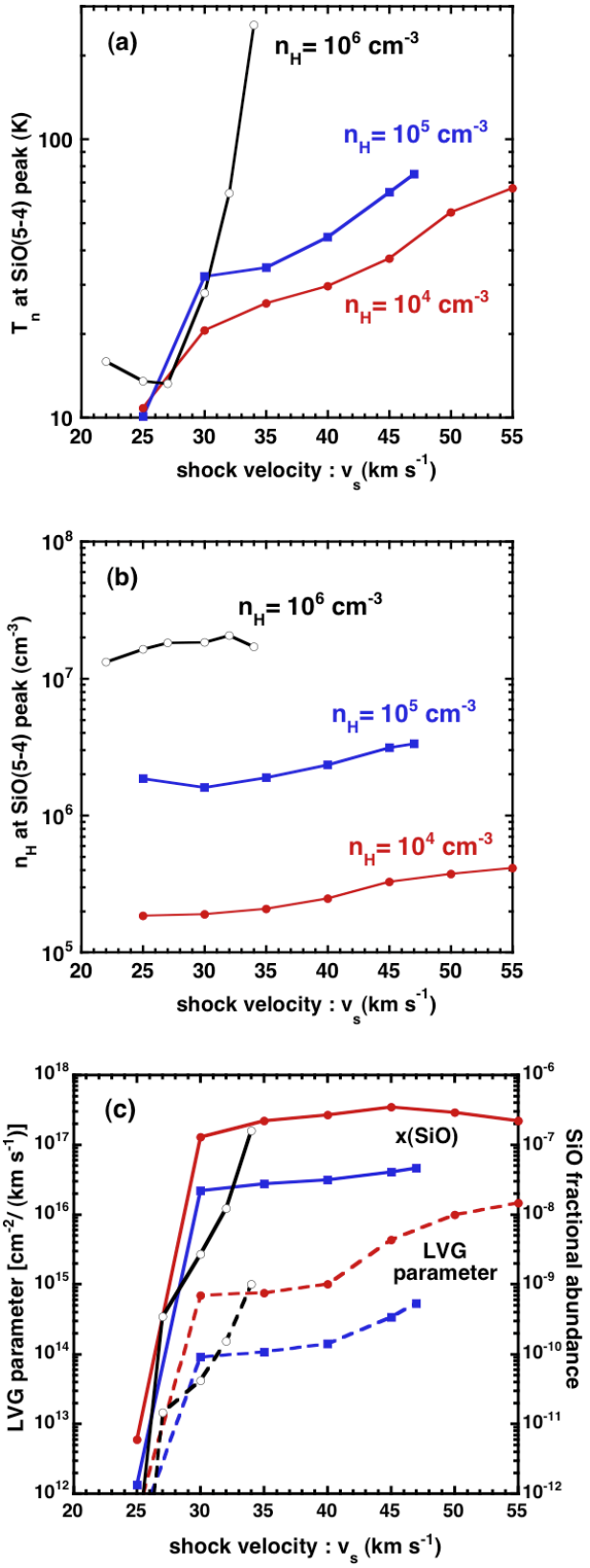

Figure 8.9 – As Figure 8.4, but assuming that the initial abundance of O_2 ice is negligible (the second scenario described in Subsection 7.1.3).

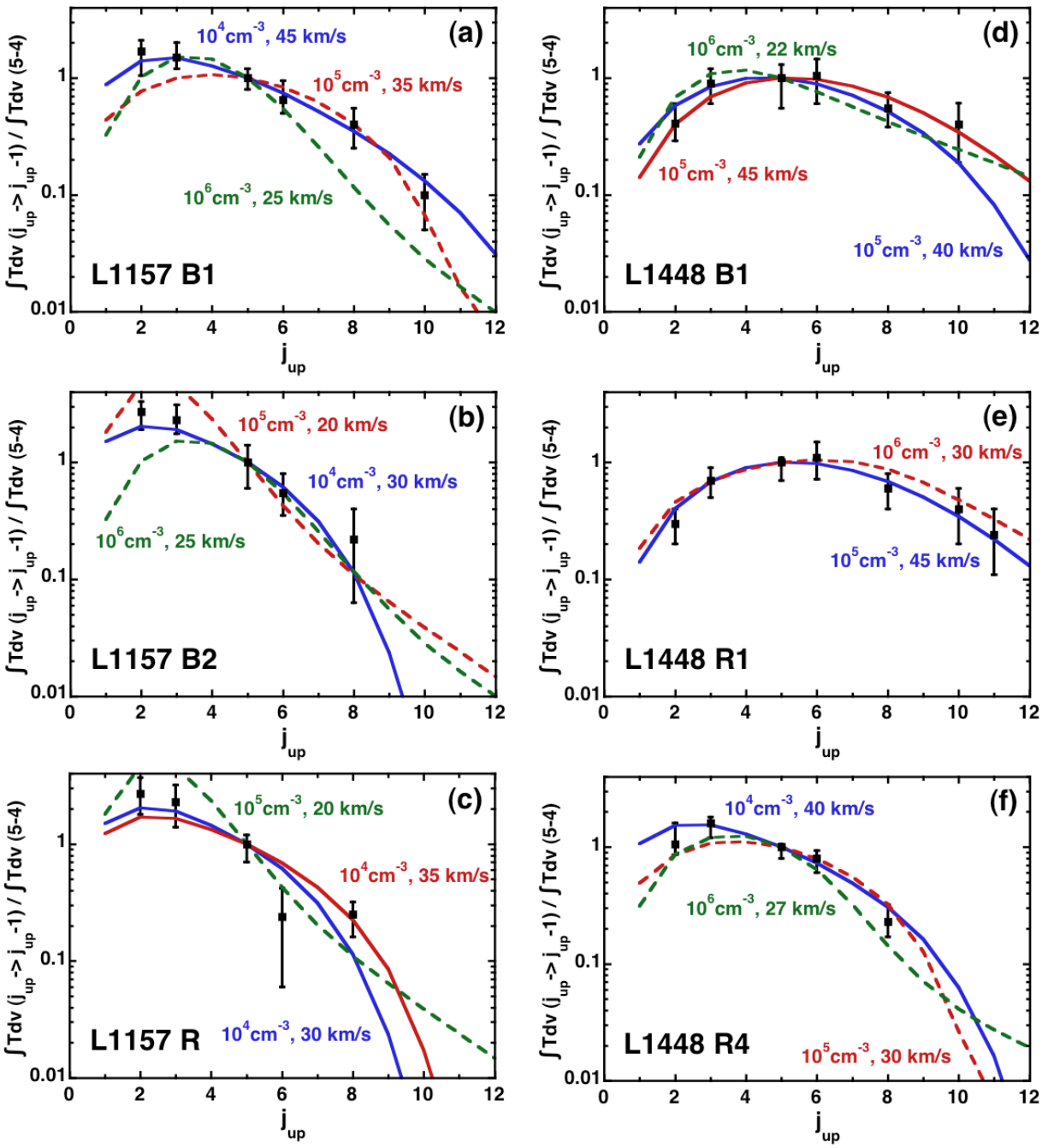

Figure 8.10 – As Figure 8.6, but assuming that the initial abundance of O_2 ice is negligible (the second scenario described in Subsection 7.1.3).

9

Alternate Si initial repartition scenarios

Dans ce chapitre, l'étude de l'émission de la molécule de SiO dans les chocs stationnaires de type C se poursuit, avec de nouvelles hypothèses inédites de répartition du silicium dans les grains de poussières du milieu interstellaire. La présence de SiO, puis de Si neutre dans les manteaux des grains, et son influence sur la production et l'émission de SiO dans les flots bipolaires sont ensuite étudiées.

In the previous chapter, a grid of C-type shock models are computed and the calculated SiO line intensities and profiles are compared with observations. With respect to the line intensities, the agreement with the observations is satisfactory, for rotational transitions up to SiO(11–10). However, the line profiles predicted under these assumptions were narrower than observed, with predicted widths of 0.5–2 km s^{-1}, as compared with the observed widths of 5–20 km s^{-1}, in 3"–10" beams. Partly with this discrepancy in mind, we consider now the possibility that elemental Si may be present in the grain mantles, where the corresponding binding energy is much lower than that of the Si in the silicate grain cores.

9.1 SiO in the grains mantles

This Section can be found in Gusdorf et al. (2008b).

In this Section, we consider the presence of Si in the grain mantles in the form of SiO, and hence transfer a small percentage (1%, 5%, or 10%) of the Si, and the corresponding amounts of oxygen, from the cores to the mantles. If this process is mediated by the passage of shock waves, our calculations indicate that the dominant form of silicon in the mantle is likely to be SiO ; see, for example, Figure 1 of Gusdorf et al. (2008a) or Figure 7.1. The SiO is then released directly into the gas phase, through sputtering by the most abundant neutrals, H, H_2 and He in a subsequent shock wave. Such sputtering processes were incorporated already for known mantle constituents, such as water and carbon monoxide. The sputtering rate of SiO was calculated using the same parameters as for CO. Adopting the parameters appropriate to a more polar species, such as H_2O, has no significant influence on the results, as the mantle species are, in either case, sputtered rapidly (in the magnetic precursor). In addition to this, the study of C-type shocks presented in the previous chapter shows that the results are not sensitive to the molecular

oxygen scenario (discussed in Subsection 7.1.3), particularly at high shock speeds, as Si can be oxidized in the gas phase by both O_2 and OH. The infuence of the O_2 scenario is all the more reduced in this section as an important part of the gas phase SiO is directly released as such from the grain mantles.

9.1.1 SiO production

In the previous chapter, Si is assumed to be present in grains in the form of silicates, contained in the cores, with an initial fractional abundance of 3.37×10^{-5}, relative to elemental H. We consider now two particular C-type shock models, for which the pre-shock density $n_{\rm H} = 10^4$ cm^{-3}, the shock velocity $v_{\rm s} = 25$ and 50 km s^{-1}, respectively, and $b = 1$. At 25 km s^{-1}, the velocity of the C-type shock model is inadequate for significant erosion of the grain cores to take place, and this model failed to produce enough SiO to account for the observations. On the other hand, the higher velocity (50 km s^{-1}) shock yielded good agreement with the SiO observations of L1157 B1, in terms of the integrated line intensities. In both cases, Si is released into the gas phase through erosion of the grain cores. Because of the time required to oxidize Si in the gas phase, the SiO emission peaks in the post-shock region. When $v_{\rm s} = 50$ km s^{-1}, the fractional abundance of SiO attains 7×10^{-7}, before decreasing, owing to adsorption on to the grains. We introduce now an alternative scenario, in which 5% of the silicon is initially in the mantles, in the form of SiO.

Figure 9.1 shows the neutral temperature profiles and the fractional abundances of Si–containing species, for the models with $v_{\rm s} = 25$ and 50 km s^{-1}. In both cases, essentially all of the SiO which is initially in the mantles is released into the gas phase by sputtering, subsequently freezing back on to grains in the cold, post-shock gas. The more SiO is initially present in the grain mantles, the higher is the maximum fractional abundance of SiO in the gas phase. At the lower shock speed, the SiO produced following erosion of Si from the grain cores is negligible, compared with SiO sputtered directly from the mantles. Even at the higher shock speed of $v_{\rm s} = 50$ km s^{-1}, only about 5% of the silicon is released from the grain cores : see Gusdorf et al. (2008a), Figure 2 (or 8.1).

9.1.2 SiO emission

When comparing the models with the observations of SiO, we consider first the integrated intensity of the SiO(5–4) line, $\int T{\rm d}v(5-4)$ K km s^{-1}, and then the integrated intensities of rotational transitions up to (11–10), expressed relative to SiO(5–4).

The variation of the integrated intensity of the SiO(5–4) line with the percentage of SiO initially in the mantles is shown in Figure 9.2. Observational data relating to L1448 and L1157, compiled by Nisini et al. (2007), are displayed also. Our calculations show that the observed line intensities can be reproduced when only of the order of 1% of the elemental silicon is initially in the grain mantles, as SiO. Core erosion alone is sufficient only at the higher shock speed, 50 km s^{-1} ; Figure 9.2 confirms the efficacy of mantle sputtering at lower speeds.

Figure 9.3 presents the integrated intensities of other rotational transitions, relative to the (5–4) line ; observational data relating to L1157 B1 are shown also. At the lower

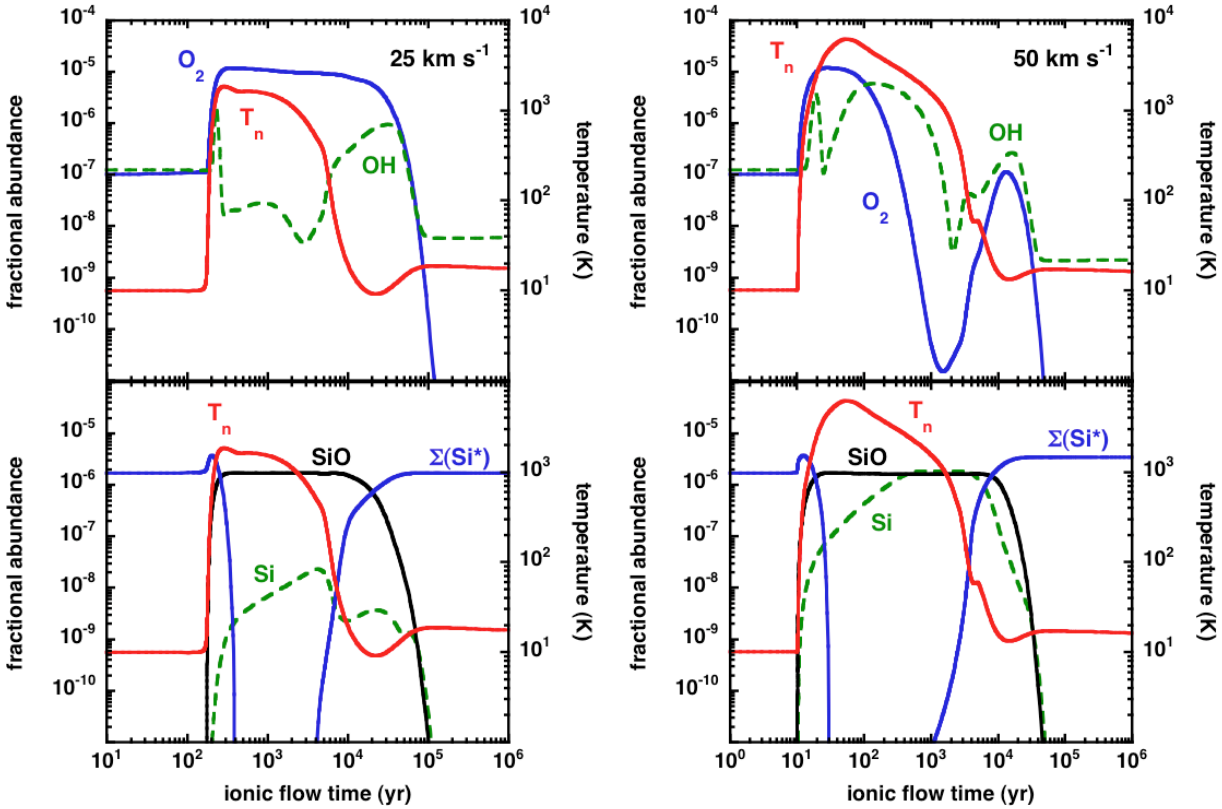

Figure 9.1 – The temperature of the neutral fluid, $T_{\rm n}$, and the fractional abundances of OH and O_2 (top panels) and of Si, SiO, and total amount of silicon in the grain mantles, Σ Si* (bottom panels), as functions of the flow time of the charged fluid, for two reference C-type shock models : $n_{\rm H} = 10^4$ cm^{-3}, $b = 1$, $v_{\rm s} = 25$ km s^{-1} (left–hand panels) and 50 km s^{-1} (right–hand panels). In both models, it is assumed that 5% of the elemental silicon is initially in the mantles, in the form of SiO.

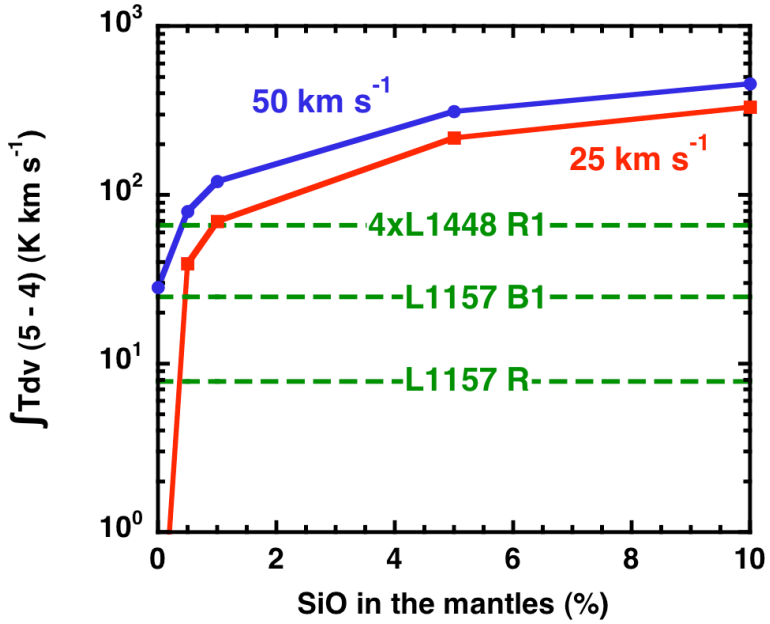

Figure 9.2 – The integrated intensity of the SiO(5–4) line, $\int T\mathrm{d}v(5-4)$, as a function of the percentage of SiO initially in the grain mantles, for both of the C-type shock models : $n_{\mathrm{H}} = 10^4$ cm^{-3}, $b = 1$, $v_{\mathrm{s}} = 25$ km s^{-1} (lower curve) and 50 km s^{-1} (upper curve). At the lower shock speed, the erosion of Si from the grain cores is negligible compared with the release of SiO from the mantles. The SiO(5–4) intensities observed in L1157 and L1448 are indicated by the horizontal lines.

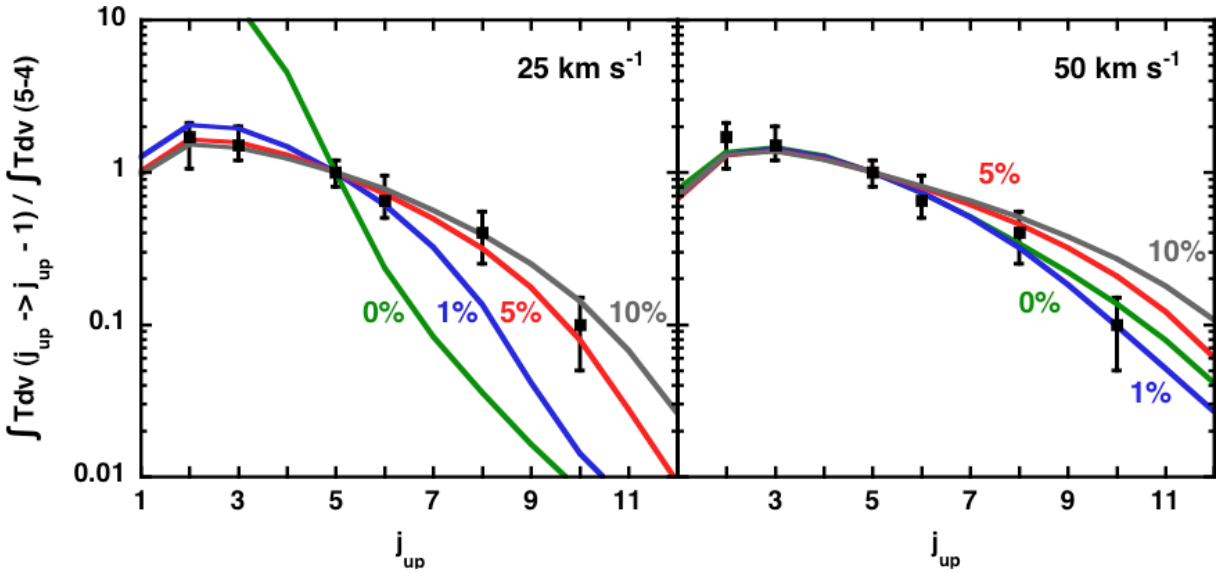

Figure 9.3 – The integrated intensities of rotational transitions of SiO, relative to the (5–4) line : $n_{\mathrm{H}} = 10^4$ cm^{-3}, $b = 1$, $v_{\mathrm{s}} = 25$ km s^{-1} (upper panel) and 50 km s^{-1} (lower panel). The observational data relate to L1157 B1. The initial fraction of silicon in the form of SiO in the grain mantles varies from 0% to 10%, as indicated.

shock speed, only the SiO sputtered from the mantles contributes significantly to the line emission. Furthermore, as the SiO is released into regions of high temperature, the emission in the high rotational transitions becomes stronger as the amount of SiO in the mantles increases. At the lower shock speed, 5% seems adequate to fit the relative line intensities ; but this model predicts a value of the (5–4) line intensity which is 3–10 times higher than observed in L1448–L1157 (cf. Figure 9.2). A low effective surface filling factor of 0.3–0.1 would then be required to reconcile this model with the observations, and this is incompatible with the typical sizes of the SiO knots observed by Nisini et al. (2007), which are comparable with the thickness of the SiO emitting layer in the model. On the other hand, at the higher speed, models with less than 1% of silicon in the mantles fit satisfactorily both the relative and the absolute line intensities.

9.1.3 line profiles

The motivation for considering SiO being present in grain mantles was its possible consequences for the widths of the emission lines. Figure 9.4 displays the line profiles obtained when 5% of elemental silicon is initially in the mantles. As SiO is now present in the gas phase over the full width of the shock wave, the lines are much broader than predicted when assuming that Si is released by erosion of the grain cores only ; cf. Gusdorf et al. (2008a), Figure 8 (or 7.3). However, the computed profiles vary considerably from line to line, whereas they are observed to be similar (see, for example, Figure 9 of Nisini et al. (2007)).

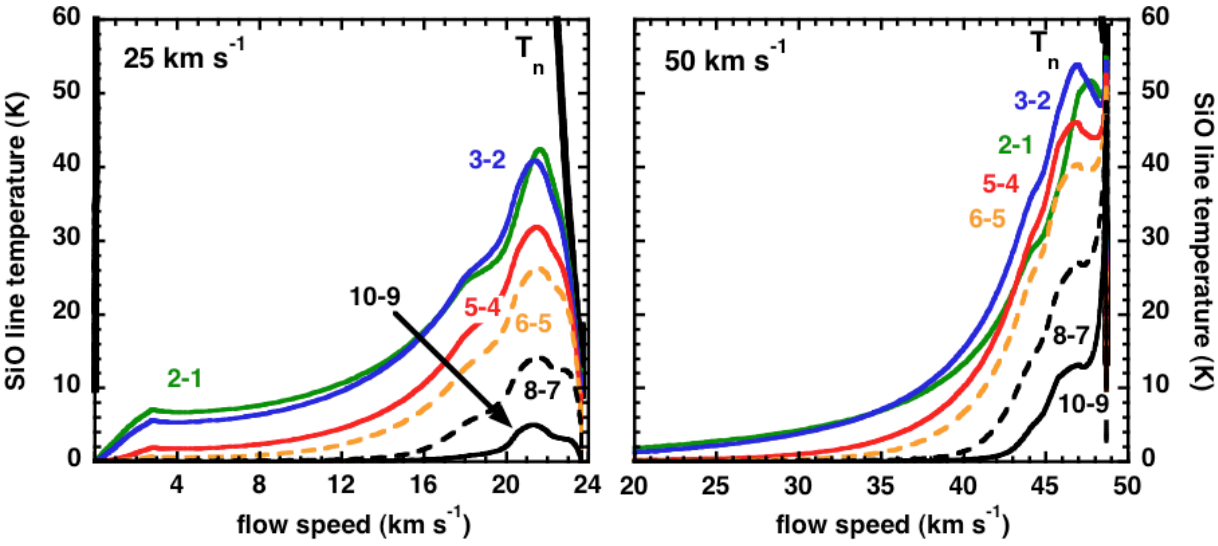

Figure 9.4 – Profiles of the SiO rotational transitions (2–1), (3–2), (5–4), (6–5), (8–7), and (10–9) computed for $n_{\rm H} = 10^4$ cm^{-3}, $b = 1$, $v_{\rm s} = 25$ km s^{-1} (left panel) and 50 km s^{-1} (right panel). 5% of the elemental silicon is assumed to be initially in the grain mantles, in the form of SiO.

9.2 Neutral Si in the grains mantles

In this section, we investigate the possibility for elemental Si to be sputtered from the grain mantles. To do so, we transfer the same amount of Si from the initial grain cores repartition to the initial grain mantles repartition. Unlike what is done in the previous Section, we don't have to correct the elemental oxygen initial repartition, as only Si is initially transferred from the cores to the mantles.

9.2.1 SiO production

Respective amounts of 0, 1, 5, and 10% of the initial silicon present in the cores are transferred to the mantles, where the sputtering occurs at rates equal to the ones of CO, with H, H_2 and He as collisions partners. As the sputtering is quick and very efficient, this assumption is not of crucial importance in the context of our study. As Si is released in the gas phase, instead of SiO, we expect the O_2 scenario (as described in Subsection 7.1.3) to play a role, and decide to investigate it. We stick with the reference C-type shock models used in the previous Section, that is the ones for which $n_{\rm H} = 10^4$ cm^{-3}, $b = 1$, $v_{\rm s} = 25$ km s^{-1} and 50 km s^{-1}.

Figures 9.5 and 9.6 are the equivalent Figures as Figure 9.1, obtained with the present initial repartition scenario for Si, and respectively for each of the oxygen scenarios as introduced in Subsection 7.1.3. On the left panels of these Figures are the results obtained for the low-velocity model (at 25 km s^{-1}), whereas the right panels show the results of the higher velocity model, (at 50 km s^{-1}). In these Figures, 5% of the silicon is assumed to be initially in the form of Si in the mantles.

When most of the oxygen is initially located on the grain mantles under the form of O_2 (Figure 9.5), the conversion of Si into SiO is more efficient at 25 km s^{-1} than at 50 km s^{-1}. In fact, molecular oxygen is destroyed by dissociation at higher velocities, whereas it remains under the form of O_2 through the whole shock at lower shock velocities. On the contrary, in the case of an initial repartition of the oxygen on the grains mantles under the forma of water ice (Figure 9.6), the conversion of Si into SiO is given a boost by the higher abundance of OH through the shock at high velocity. Thanks to the reaction with gas phase molecular hydrogen, the SiO fractional abundance profiles are slightly wider than in the second oxygen scenario. At high velocity, this difference is only noticeable in the warmest part of the shock when O_2 is not yet dissociated.

9.2.2 SiO emission

We compare our reference models to observations in the same fashion as in Subsection 9.1.2, considering first the integrated intensity of the SiO(5-4) line, $\int T dv$(5 - 4) K km s^{-1} (Figure 9.7, as equivalent to the Figure 9.2), and then the integrated intensities of rotational transitions up to (11-10), expressed relative to SiO(5-4) (Figures 9.8 and 9.9, equivalent to 9.3).

The variation of the integrated intensity of the SiO(5–4) line with the percentage of SiO initially in the mantles is shown in Figure 9.7. Observational data relating to L1448 and L1157, compiled by Nisini et al. (2007), are displayed again. Our calculations show

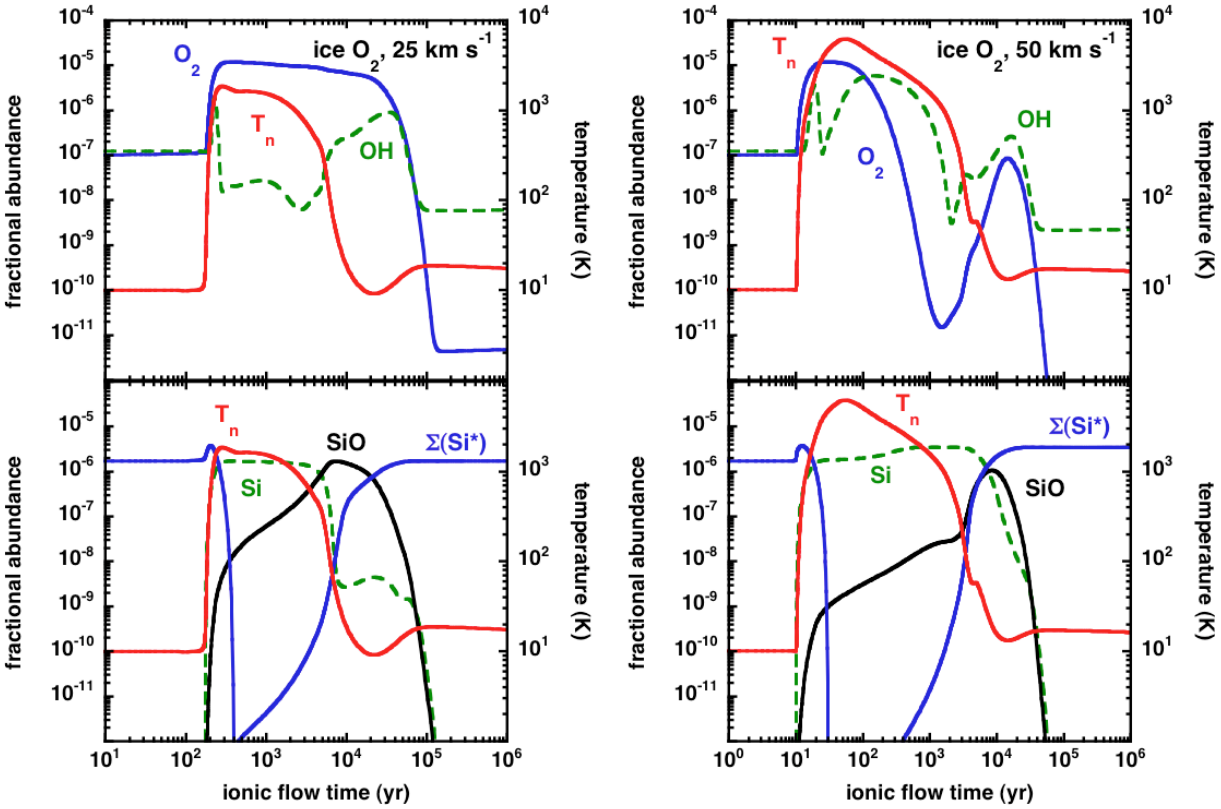

Figure 9.5 – As Figure 9.1, assuming 5% of the elemental silicon is initially in the mantles in its neutral form.

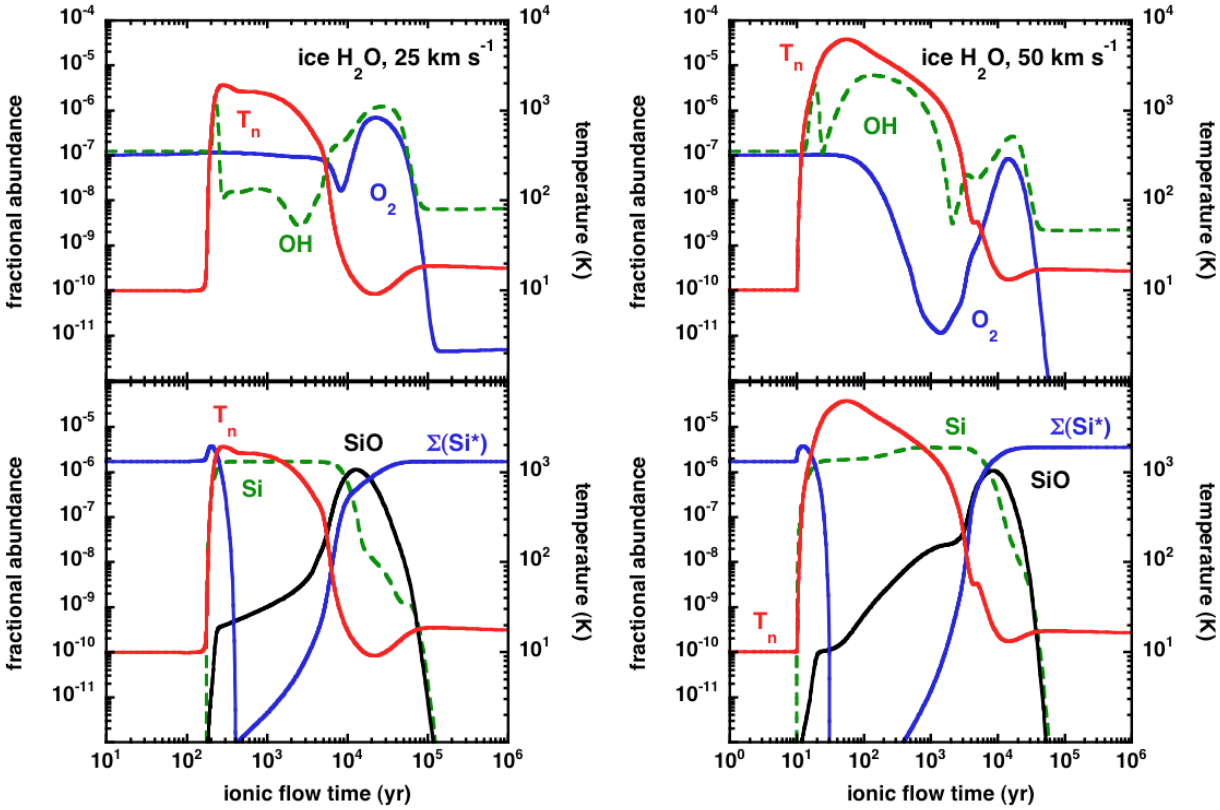

Figure 9.6 – As Figure 9.1, assuming 5% of the elemental silicon is initially in the mantles in its neutral form, and assuming that the initial abundance of O_2 ice is negligible (the second scenario described in Subsection 7.1.3).

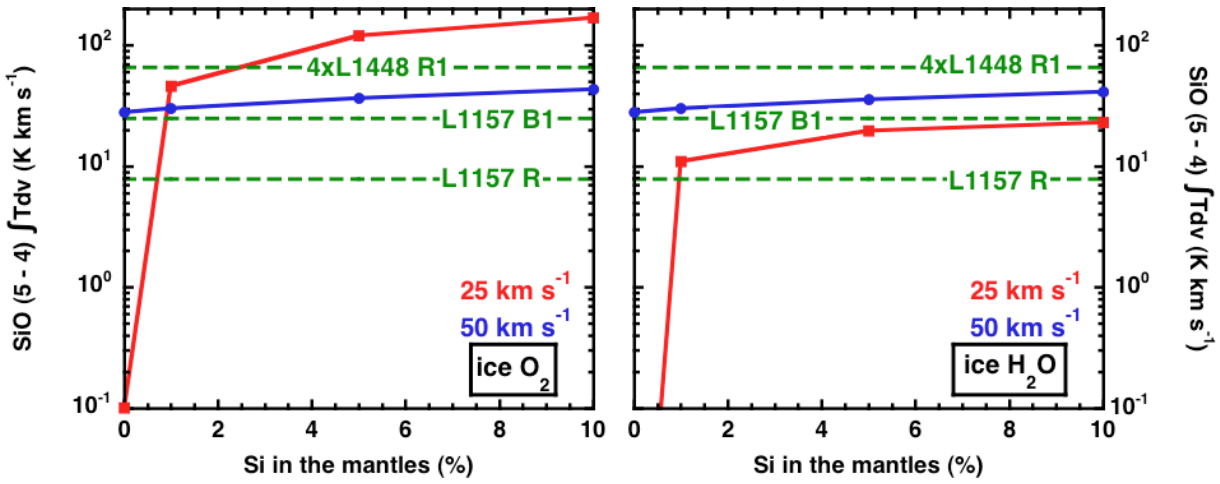

Figure 9.7 – As Figure 9.2, assuming the elemental silicon is initially in the mantles in its neutral form. Left : assuming a high initial fractional abundance of O_2 ice, and right : assuming that the initial abundance of O_2 ice is negligible (the second scenario described in Subsection 7.1.3).

that the observed line intensities can be reproduced when some elemental silicon is initially in the grain mantles, whatever the oxygen initial repartition scenario. The exact initial Si proportion determination remains subject to that of the observational filling factor. As previously stated, core erosion alone is sufficient only at the higher shock speed, 50 km s^{-1}, and the Figure confirms the efficacy of mantle sputtering at lower shock velocities.

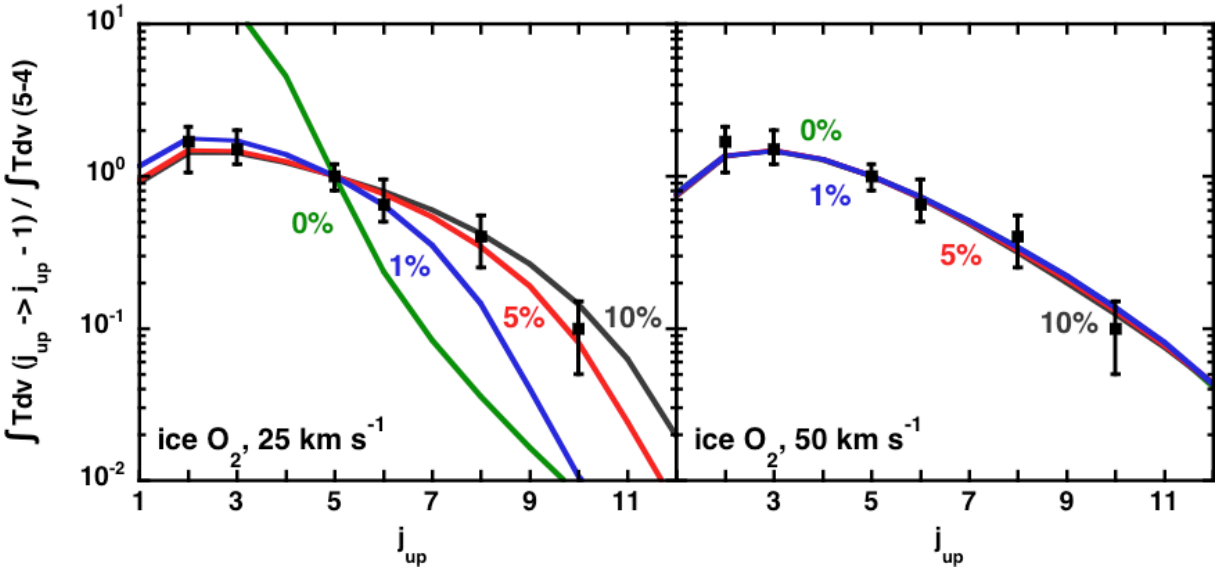

Figure 9.8 – As Figure 9.3, assuming 5% of the elemental silicon is initially in the mantles in its neutral form.

Figures 9.8 and 9.9 present the integrated intensities of other rotational transitions, relative to the (5–4) line, respectively in the case of the first and second initial oxygen repartition scenario presented in Subsection 7.1.3 ; observational data relating to L1157 B1 are shown also.

On Figure 9.8, the case where oxygen is initially present on the grain mantles under the form of molecular oxygen is considered. At the lower shock speed, only the Si sputtered from the mantles generate the SiO that contributes significantly to the line emission. Furthermore, as the SiO is formed into regions of high temperature, the emission in the high rotational transitions becomes stronger as the amount of SiO in the mantles increases. At the lower shock speed, 5 and 10% seem adequate to fit the relative line intensities ; but these models would imply a low effective surface filling factor of 0.05–0.6 to reconcile this model with the observations, and this is incompatible with the typical sizes of the SiO knots observed by Nisini et al. (2007), which are comparable with the thickness of the SiO emitting layer in the model. On the other hand, at the higher speed, models with less than 1% of silicon in the mantles fit satisfactorily both the relative and the absolute line intensities.

The same study is shown on the case where oxygen is initially present on the grain mantles under the form of ice water. At the lower shock speed, only the Si sputtered from the mantles generate the SiO that contributes significantly to the line emission. Furthermore, as the SiO is formed into regions of high temperature, the emission in the high rotational transitions becomes stronger as the amount of SiO in the mantles increases.

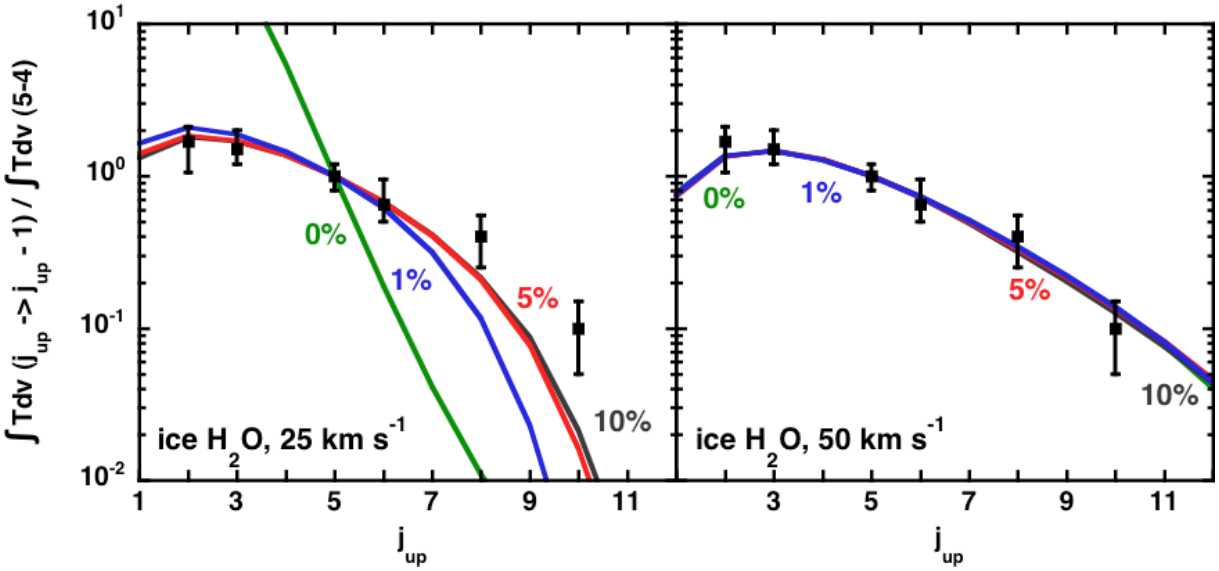

Figure 9.9 – As Figure 9.3, assuming 5% of the elemental silicon is initially in the mantles in its neutral form, assuming that the initial abundance of O_2 ice is negligible (the second scenario described in Subsection 7.1.3).

However, no match seems to be found with the observations from the point of view of relative line integrated intensities. Again, at the higher speed, models with less than 1% of silicon in the mantles fit satisfactorily both the relative and the absolute line intensities.

9.2.3 line profiles

As in the previous Section, the motivation for investigating the presence of Si in grain mantles was its possible consequences for the widths of the emission lines. Figures 9.10 and 9.11 display the line profiles obtained when 5% of elemental silicon is initially in the mantles, respectively in the case of the first and second initial oxygen repartition scenario presented in Subsection 7.1.3.

The most successful model in terms of broadening of the line profiles is the low velocity one combined with the oxygen scenario where oxygen exists on grain mantles under the form of molecular oxygen ice. Indeed, as can be seen on Figures 9.5 and 9.6, the SiO abundance profile is the broadest in this case : SiO forms significantly owing to the presence of OH and mainly O_2 over the whole width of the shock. This is less true at low velocity in the other case of oxygen initial repartition scenario, as there is not as much as O_2 in the gas phase. Eventually at higher shock velocities, SiO is only significantly formed in the cooling region of the shock, where the neutral velocity tends to zero. The line profiles at high shock velocity are consequently narrower than the ones obtained at lower shock velocities. However, the computed profiles vary considerably from line to line, whereas they are observed to be similar (see, for example, Figure 9 of Nisini et al. (2007)).

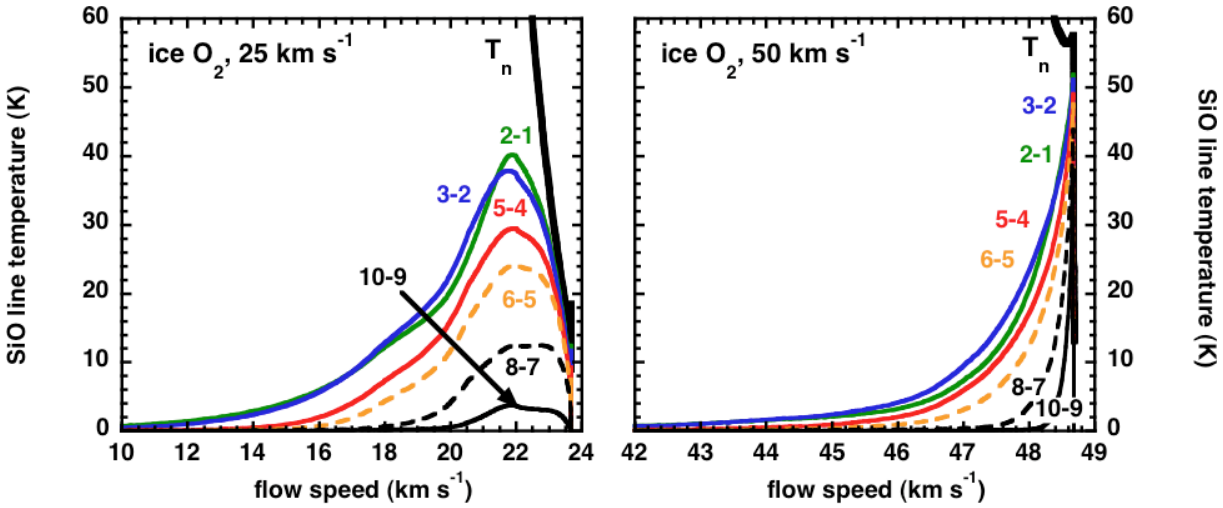

Figure 9.10 – As Figure 9.4, assuming 5% of the elemental silicon is initially in the mantles in its neutral form.

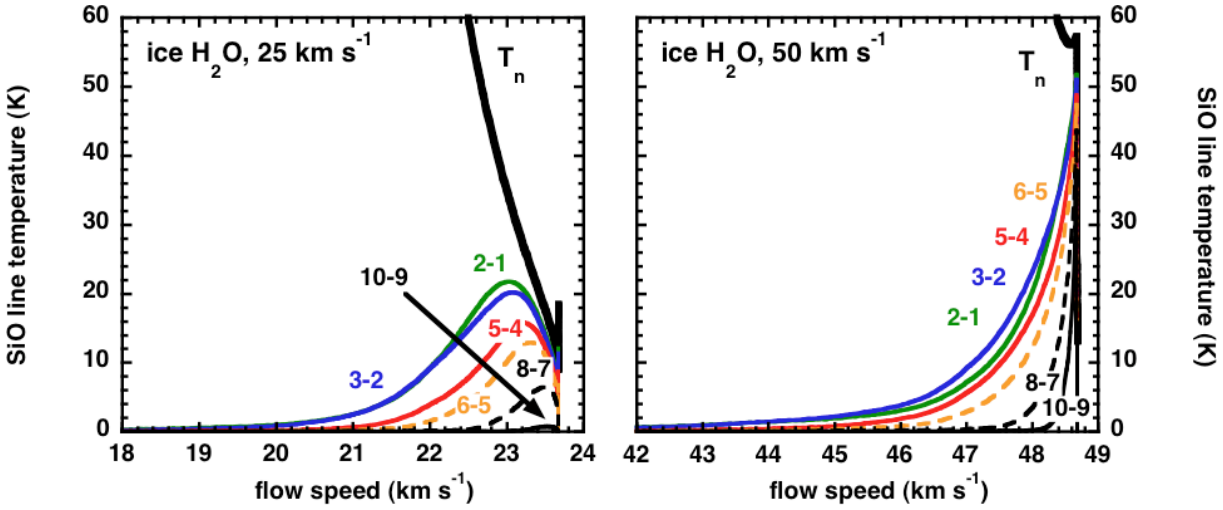

Figure 9.11 – As Figure 9.4, assuming 5% of the elemental silicon is initially in the mantles in its neutral form, and assuming that the initial abundance of O_2 ice is negligible (the second scenario described in Subsection 7.1.3).

Other molecular tracers for star formation : a broader view

10

Simultaneous fitting with molecular hydrogen observations

Les diagrammes d'observation obtenus pour la molécule de dihydrogène peuvent être reproduits de façon convenable par des modèles de chocs non stationnaires, comme l'a confirmé le chapitre 4. D'autre part, les deux chapitres précédents ont montré l'efficacité des modèles de chocs stationnaires de type C pour reproduire les données observationnelles relatives au SiO. Le présent chapitre est une tentative d'ajustement simultané des données H_2 et SiO, c'est-à-dire par un même modèle de choc, non stationnaire en l'occurrence. L'émission de SiO dans les chocs stationnaires de type J est brièvement décrite, en préambule à l'étude relative aux chocs non stationnaires, qui suit. Le recours aux répartitions 'originales' du matériel silicaté dans les grains de poussières est nécessaire afin de reproduire de façon satisfaisante l'émission observée de SiO dans L1157B1 par un modèle de choc non stationnaire.

In the case of the SiO emission, stationary C-type shock waves have been shown to be able to account for the observed rotational line intensities in the previous chapters (see also Gusdorf et al. (2008a), Gusdorf et al. (2008b)). In this Section, we investigate the possibility for other kinds of shocks to account for these observations, in an attempt to simultaneously fit SiO and H_2 observations. Indeed, the successful fitting of H_2 by J-type, and also by CJ-type of shock models has been demonstrated in Subsection 4.4.1.

10.1 SiO emission in J-type shocks

In this section, we consider two particular J-type shock models, for which the pre-shock density $n_{\rm H} = 10^4$ cm^{-3}, the shock velocity $v_{\rm s} = 25$ and 50 km s^{-1}, respectively, and $b = 0.1$. We do not make any *a priori* assumption about the O_2 initial repartition scenario.

10.1.1 No silicon material in the grain mantles

In a J-type shock model, as stated in Subsection 2.1.2, there is no magnetic field component, and all the particles hence belong to the same fluid. A crucial consequence of

this single fluid state is the absence of drift velocity between neutral and charged species, and the much reduced probability of collisions between those two kinds of species. In particular, large neutral molecules or atoms do not collide with charged grains, and only negligible sputtering of the grain mantles and erosion of the grain cores occur.

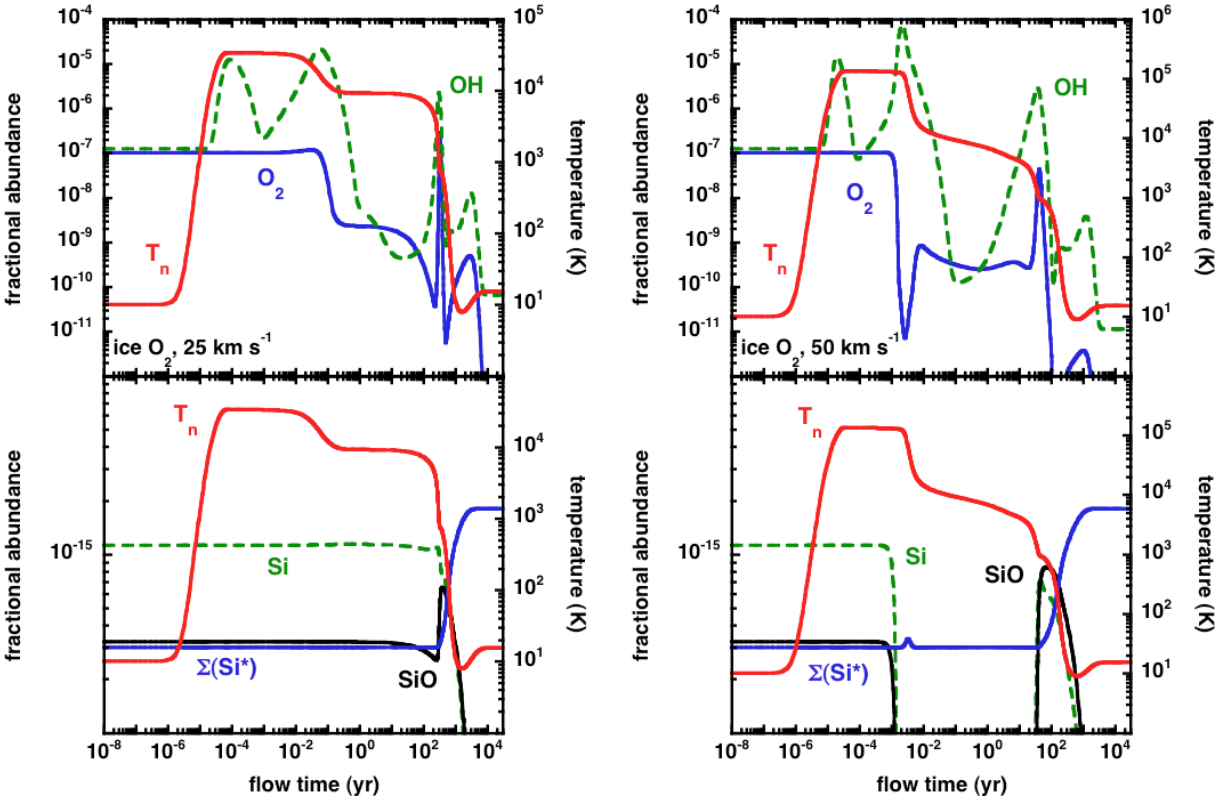

Figure 10.1 – The temperature of the neutral fluid, $T_{\rm n}$, and the fractional abundances of OH and O_2 (top panels) and of Si, SiO, and total amount of silicon in the grain mantles, Σ Si* (bottom panels), as functions of the flow time of the fluid, for two reference J-type shock models : $n_{\rm H} = 10^4$ cm^{-3}, $b = 1$, $v_{\rm s} = 25$ km s^{-1} (left–hand panels) and 50 km s^{-1} (right–hand panels). In both models, it is assumed that no elemental silicon is initially in the mantles ; the oxygen scenario is the first one of those described in the Subsection 7.1.3, in which part of the oxygen is initially in the grain mantles under the form of O_2.

The direct consequence is that no silicon material is stripped from the grains nor released in the gas phase, leading to a much lower expected fractional abundance for Si-bearing species, specially SiO. The Figure 10.1 shows the production of SiO from the two J-type shock models. Whatever the velocity, the SiO fractional abundance does not exceed 10^{-15}. Indeed in those shock conditions, even when SiO is likely to be formed in the gas phase, the gas temperature is so high that it undergoes dissociation.

The first conclusion from Figure 10.1 is that this low production of SiO is not dependent on the considered O_2 scenario. In fact, O_2 and OH are always available in the medium in much larger amounts than Si, to form SiO through Reactions 6.20 and 6.21. Whatever the assumption on the initial repartition of O_2, the amount of Si in the gas phase is not sufficient to generate relevant formation of SiO. In addition to this, the levels of SiO

Tableau 10.1 – Predicted SiO (5 - 4) line integrated intensity for the two reference J-type shock models mentioned in Section 10.1, for each O_2 scenario described in Subsection 7.1.3.

$\int Tdv(5-4)[\mathrm{K\,km\,s^{-1}}]$	ice O_2	ice H_2O
25 km s^{-1}	7.1×10^{-8}	6.7×10^{-8}
50 km s^{-1}	9.6×10^{-9}	9.7×10^{-9}

emission are nowhere near the observations made for example around L1157 B1. Table 10.1 provides the predicted SiO (5 - 4) line integrated intensity for the two reference J-type shock models, showing a huge discrepancies with the values shown in Subsections 9.1.2 or 9.2.2. To make up for these discrepancies, we study the inclusion of silicon in the grain mantles, in a similar fashion as what is done in Sections 9.1 and 9.2 for the C-type shock models. As such, J-type shock models are no good candidate to match SiO observations.

10.1.2 SiO in the grain mantles

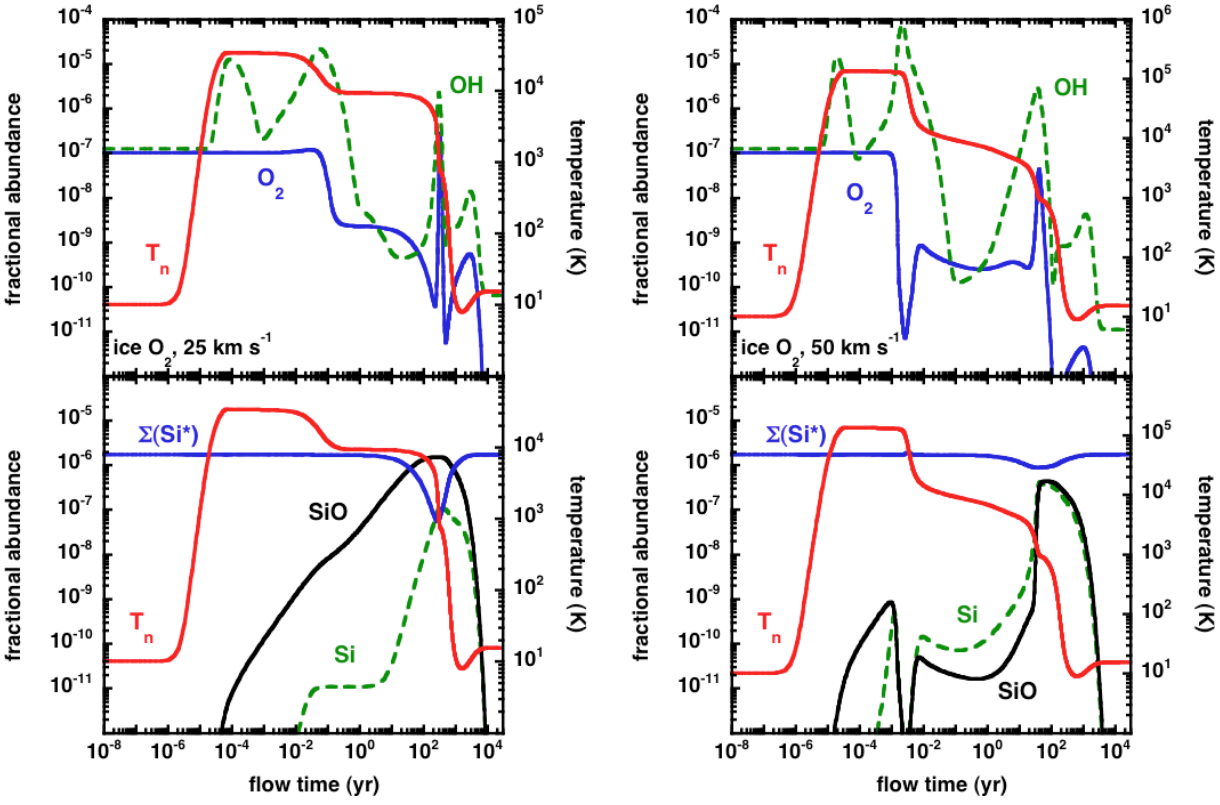

Figure 10.2 – As Figure 10.1, assuming 5% of the elemental silicon is initially in the mantles under the form of SiO. The oxygen scenario is the first one of those described in the Subsection 7.1.3.

In fact, in a J-type shock, the absence of drift velocity between neutral and charged

particles prevents the erosion of the grain core through collisions between those species. Nevertheless, some thermal sputtering of the grain mantles does occur owing to the very high temperatures that are reached in the single considered fluid. This sputtering is the only grain process taken into account in our version of the code, though Guillet et al. (2007) demonstrated other grain reactions could be of non negligible influence in J-type shock modelling.

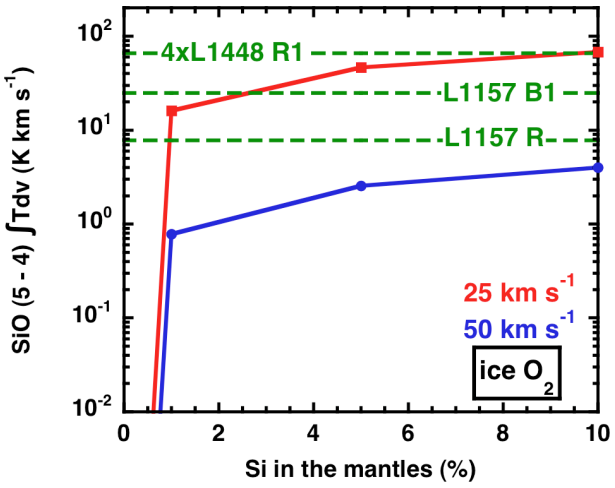

Figure 10.3 – The integrated intensity of the SiO(5–4) line, $\int T\mathrm{d}v(5-4)$, as a function of the percentage of SiO initially in the grain mantles, for both of the J-type shock models : $n_{\mathrm{H}} = 10^4$ cm^{-3}, $b = 1$, $v_{\mathrm{s}} = 25$ km s^{-1} (lower curve) and 50 km s^{-1} (upper curve). The SiO(5–4) intensities observed in L1157 and L1448 are indicated by the horizontal lines. The oxygen scenario is the first one of those described in the Subsection 7.1.3.

Such a sputtering can be visualized on Figure 10.2 : on the bottom panels, the fractional abundance of Si and SiO are displayed against the flow time. The blue curve corresponds almost exactly to that of the SiO that belongs to the grain mantles (whose initial repartition is 5% the initial equilibrium repartition of Si in the grain cores), and is progressively depleted to be released in the gas phase through the sputtering, whatever the shock velocity. However, at high velocity, the high temperatures that are reached also generate dissociation and ionization of the species, which complicates their fractional abundance profiles. The comparison of these panels with those of the Figure 10.1 shows that the gas phase SiO is here solely and directly generated by the sputtering of the mantles. The choice of the oxygen scenario (initially partly present in the grain mantles under the form of O_2) as described in Subsection 7.1.3 has consequently no influence on the results.

Similarly to what was done in Subsections 9.1.2 and 9.2.2, we compare our models with observations, considering first the integrated intensity of the SiO(5–4) line, $\int T\mathrm{d}v(5-4)$ K km s^{-1}. The variation of the integrated intensity of the SiO(5–4) line with the percentage of SiO initially in the mantles is shown in Figure 10.3, along with observational data relating to L1448 and L1157, compiled by Nisini et al. (2007). Our calculations show that the observed line intensities can be reproduced when only of the order of 1 to 10% of the elemental silicon is initially in the grain mantles, as SiO, in the case of the low velocity reference model. At the higher shock speed, the dissociation of SiO and

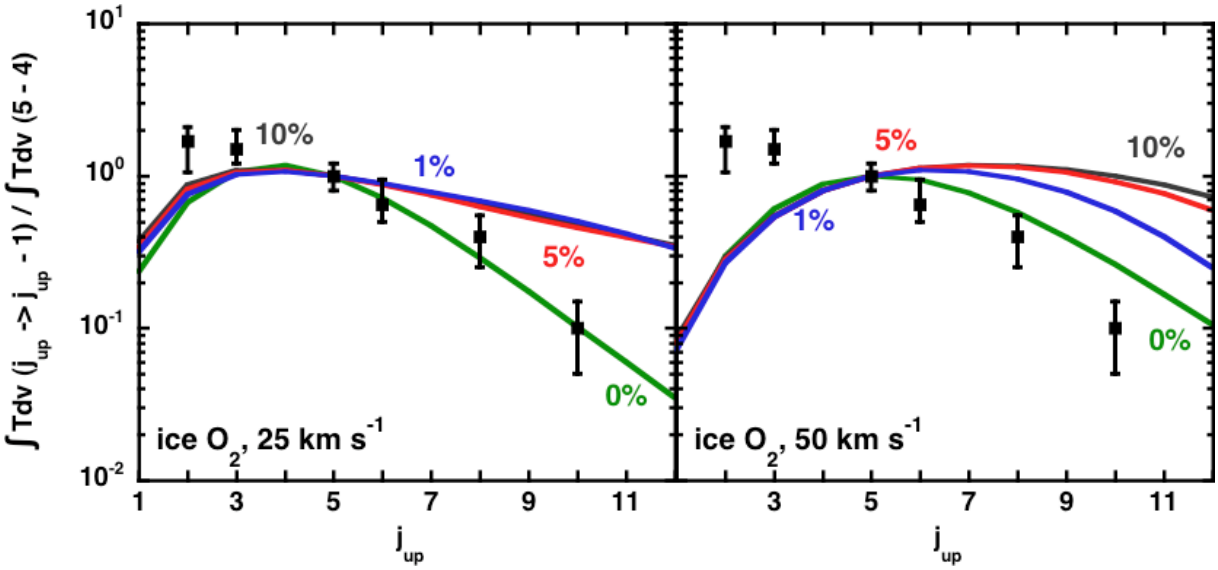

Figure 10.4 – The integrated intensities of rotational transitions of SiO, relative to the (5–4) line : $n_{\rm H} = 10^4$ cm^{-3}, $b = 1$, $v_{\rm s} = 25$ km s^{-1} (upper panel) and 50 km s^{-1} (lower panel). The observational data relate to L1157 B1. The initial fraction of silicon in the form of SiO in the grain mantles varies from 0% to 10%, as indicated. The oxygen scenario is the first one of those described in the Subsection 7.1.3.

subsequent ionization of its component (see Figure 10.2) prevents an efficient emission whatever the initial amount of SiO placed in the grain mantles.

Still following our previous way of comparing model results to observations, Figure 10.4 is displayed, presenting the integrated intensities of other rotational transitions, relative to the (5–4) line ; observational data relating to L1157 B1 are shown also. The very high temperatures at which SiO is released in the gas phase in both cases (see Figure 10.3) generates a much higher relative emission in the highest rotational transitions, making them unlikely to fit the observational data, whatever the amount of SiO in the grain mantles. Again under these assumptions, J-type shock models do not account for the observations.

10.1.3 Neutral Si in the grain mantles

We consequently study the possibility for Si to be present under its neutral form in the grain mantles, as was done for the C-type shock models in Section 9.2. Again, Figure 10.5 shows the production of SiO through our reference J-type models, when initially including 5% of Si in the grain mantles. In both models, Si is released from these mantles exactly the same way as SiO was in the previous Subsection, confirming the lack of influence of the sputtering rates at these very high temperatures. Once in the gas phase, Si then reacts with O_2 but mostly OH to form SiO. As the most abundant formation reaction partner is OH, there is once again no dependence on the choice of the O_2 scenario as presented in Subsection 7.1.3. In addition to this, the temperature is so high in both cases that the conversion of Si into SiO is almost immediate. Combined with the fractional abundance

profile of Si, this explains why SiO fractional abundance profile then closely follows that of OH. This dependence on the OH abundance leads to very narrow fractional abundance profiles for SiO, yielding consequently narrow emission zone for this molecule.

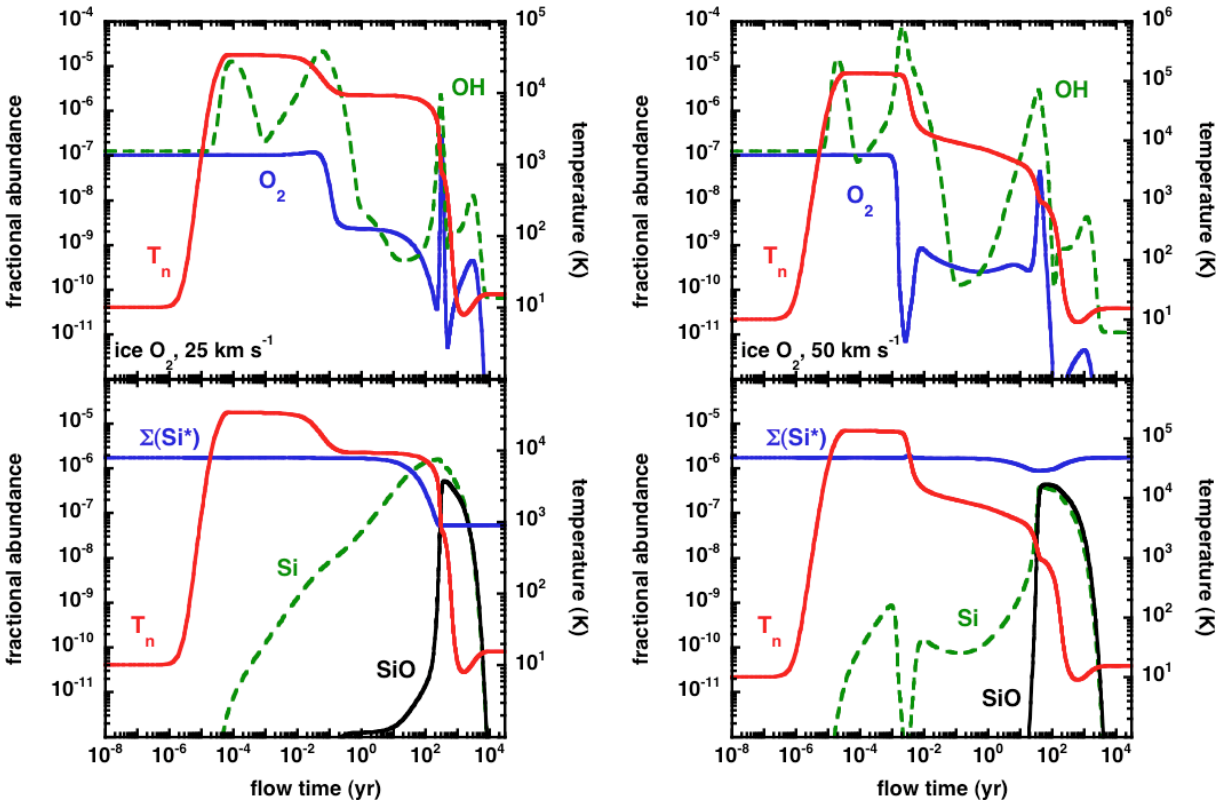

Figure 10.5 – As Figure 10.1, assuming 5% of the elemental silicon is initially in the mantles under the form of neutral Si. The oxygen scenario is the first one of those described in the Subsection 7.1.3.

The effect of such small emission region can be seen on Figure 10.6, which shows the integrated intensity of the SiO(5–4) line, $\int T\mathrm{d}v(5-4)$ K km s^{-1}. The variation of the integrated intensity of the SiO(5–4) line with the percentage of Si initially in the mantles is shown in Figure 10.3, along with observational data relating to L1448 and L1157, compiled by Nisini et al. (2007). Under the current assumptions of this Subsection, our reference models need a large amount of Si to be placed in the mantles to account for the observational data, at low shock velocity. At the higher shock speed, the dissociation of SiO and subsequent ionization of its component (see Figure 10.5) prevents an efficient emission whatever the initial amount of Si placed in the grain mantles. Only the lowest shock velocity model combined with the scenario where a maximum amount of Si (10%) is placed in the mantles seems to be likely to fit the data in terms of absolute SiO(5–4) integrated intensity for L1157 B1.

Unfortunately, the Figure 10.7 shows the impossibility to account for the observational data in terms of integrated intensities of other rotational transitions, relative to the (5–4) line. Again, the very high temperatures at which SiO is formed in the gas phase in both cases (see Figure 10.5) generates too much relative emission in the highest rotational

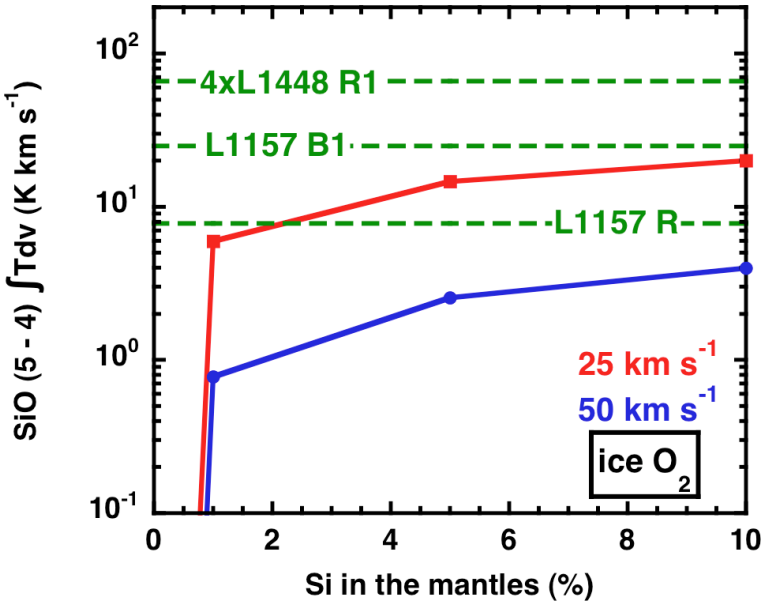

Figure 10.6 – As Figure 10.3, assuming a small fraction (1 to 10 %) of the elemental silicon is initially in the mantles under the form of neutral Si. The oxygen scenario is the first one of those described in the Subsection 7.1.3.

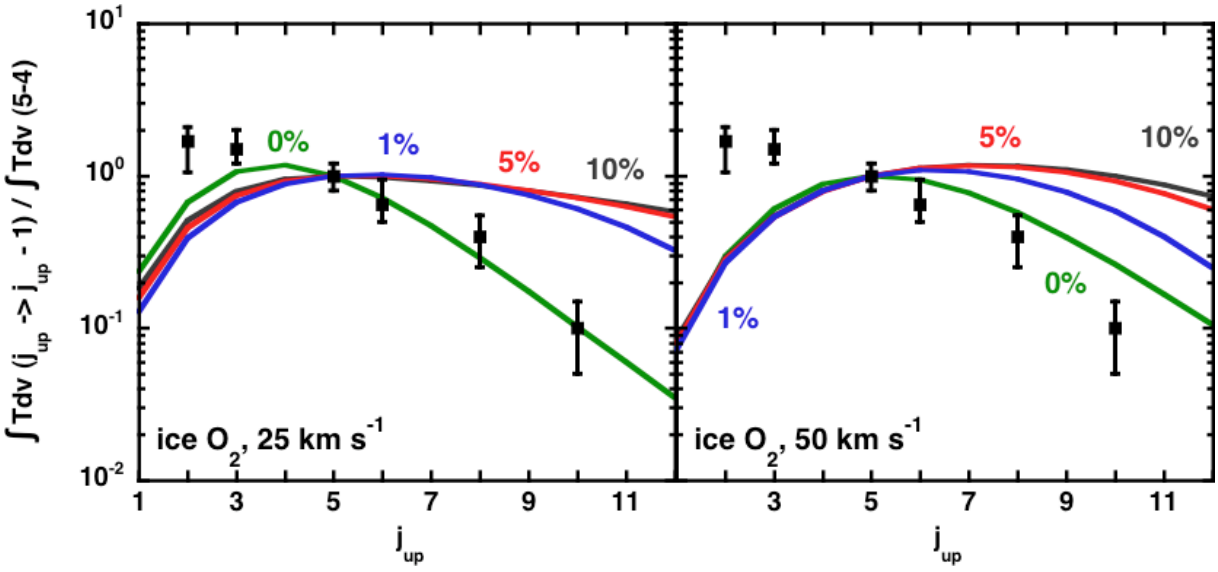

Figure 10.7 – As Figure 10.4, assuming a small fraction (1 to 10 %) of the elemental silicon is initially in the mantles under the form of neutral Si. The oxygen scenario is the first one of those described in the Subsection 7.1.3.

transitions, making them unlikely to fit the observational data, whatever the amount of Si in the grain mantles. Again under these assumptions, J-type shock models do not account for the observations.

10.2 SiO emission in non stationary shock models

The results of this Section are presented in Gusdorf et al. (2008b).

In the case of the SiO emission, stationary C-type shock waves have then been shown to be able to account for the observed rotational line intensities in Chapters 8 and 9 (see also Gusdorf et al. (2008a), Gusdorf et al. (2008b)), whereas J-type shock waves seem not to be able to reproduce the observations (see the previous Section). However, the dynamical age of the blue lobe of the L1157 outflow, inferred from observations (see Gueth et al. (1998)), is 2000–3000 years, which is less than the time (of the order of 10^4 years) required for a typical C-type shock wave to attain a steady state. Furthermore, previous studies (see, for example, Flower et al. (2003), Giannini et al. (2004) and Giannini et al. (2006)) have demonstrated the necessity of considering non-stationary shock waves in order to account successfully for both the pure rotational and the rovibrational emission of molecular hydrogen observed in molecular outflows. In the case of L1157 B1, such non stationary shock waves have been shown to provide the best rovibrational emission fits for molecular hydrogen in Chapter 4. Accordingly, we proceed to consider SiO emission in non-stationary shock waves in order to investigate the possibility for our models to simultaneously simulate both SiO and molecular hydrogen observations. As presented in Section 2.4, we simulate such shock waves by introducing a discontinuity into the flow at a given value of the fluid flow time, which becomes a parameter of the model. In practice, we introduce the discontinuity at one half the age of the shock wave, taken to be the flow time of the *charged* fluid at the point at which the flow is terminated. We refer to such models as "CJ-type", as they possess both C- and J-type characteristics.

10.2.1 No silicon material in the grain mantles

Our aim is to find a model that accounts for the observational data pertaining to both SiO and H_2, on the assumption that their emission is generated by the same non-stationary shock wave(s). The predictions of the SiO line intensities are not affected by our choice of shock termination point, which is taken to be twice the flow time at the J-discontinuity. The highly compressed gas behind the J-discontinuity does not contribute significantly to the line intensities. We discuss first the emission from SiO which occurs following the erosion of Si from the grain cores.

SiO production and the Influence of the O_2 scenario. The erosion of Si from the grain cores occurs in the magnetic precursor of the CJ-type shock, where there is a non-zero drift velocity between charged and neutral species. We have noted already in Section 9.1 that core erosion is significant only in the case of the high–velocity shock, $v_s = 50$ km s^{-1}, and so this is the model which we consider. In order to enhance the extent of the region in which the flow velocities of the charged and the neutral fluids are

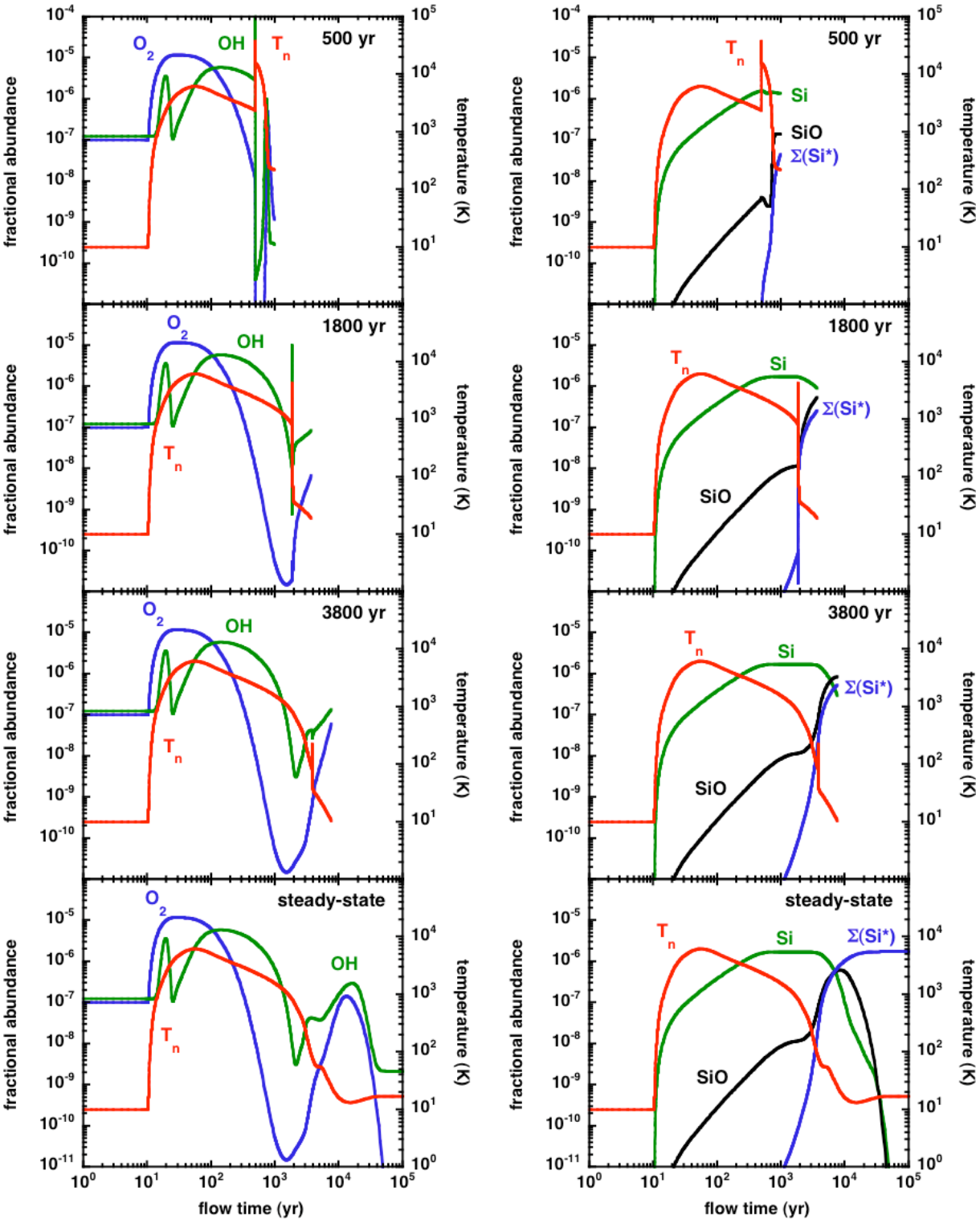

Figure 10.8 – The temperature of the neutral fluid, T_n, and the fractional abundances of OH and O_2 (left–hand panels) and of Si, SiO, and silicon in the grain mantles, Σ Si* (right–hand panels), as functions of the flow time of the charged fluid, for the CJ-type shock model in which $n_H = 10^4$ cm^{-3}, $b = 1$, and $v_s = 50$ km s^{-1}. The shock age increases from top to bottom : 500, 1800, 3800 years, and steady–state. In these calculations, there is no SiO in the grain mantles, and the gas–phase silicon is produced solely by erosion of the silicate grain cores.

decoupled, we consider evolved shock waves, with ages $\geq$ 500 years. We recall that the pre-shock parameters are $n_{\rm H} = 10^4$ cm^{-3} and $b = 1$.

Figure 10.8 illustrates the production of SiO in CJ-type shock waves with ages of 500, 1800 and 3800 years ; the corresponding stationary shock is shown also. There is a chemical delay to the formation of SiO, following the release of Si into the gas phase, due to the time required for oxidation to take place ; this delay is significant in the case of non-stationary models, as it is comparable with the evolutionary ages being considered, i.e. of the order of 10^3 years. Consequently, the maximum fractional abundance of SiO tends to increase with the shock age. In the CJ-type models, the flow speed becomes almost constant behind the J-discontinuity ; this has consequences for the predicted SiO emission, as will be seen below.

Figure 10.8 has been generated under the first assumption described in Subsection 7.1.3, in which the oxygen exists under its molecular form on the grain mantles in the pre-shock medium. In our shock models, O_2 is quickly sputtered from these grain mantles in the magnetic part of the shock, as can be seen on the left panels of the Figure 10.8. These panels also show the strong dissociation undergone by molecular oxygen in the shock, that occurs because of the high shock velocity and the high temperatures generated. OH is consequently more abundant than O_2 in the region where Si is available to react to form SiO, and is then the preferential partner for this reaction. The choice of the initial repartition of O_2 is hence of no importance in this case : under the second assumption introduced in Subsection 7.1.3, the abundance of molecular oxygen in the gas phase is also lower than that of OH, which is again the preferential reaction partner in the formation reaction of SiO.

SiO emission and comparisons with observations. Figure 10.9 shows the contributions to the intensities of three lines of SiO, (2–1), (5–4), and (10–9), as functions of the flow time of the charged fluid, for the CJ-type model specified above. In the magnetic precursor, Si is eroded from the grain cores and then oxidized to SiO in the gas phase, resulting in rotational line emission whose intensity increases through the shock wave. The emission saturates behind the discontinuity, owing to the low fluid velocity gradient. In the CJ-type models (top three panels of Figure 10.9), the populations of excited rotational levels, and the intensity of, in particular, the (10–9) line, are given a boost whose significance increases with the temperature jump at the J-discontinuity, i.e. towards lower evolutionary ages ; this explains the variations of the relative line intensities with the shock age, seen in Figure 10.10. The younger the CJ-type shock, the larger is the temperature jump and the stronger are the lines from high rotational levels, relative to low levels.

In the case of the stationary (C-type) shock model, emission arises over almost the full width of the shock wave, including the SiO fractional abundance peak ; this explains why all the lines have higher final integrated intensities. In addition, as the $j = 10$ level lies only 115 K above the ground state, it can be excited right through to the point where the fluid velocity reaches its (constant) post-shock value, which accounts for the high relative integrated intensity of the (10–9) transition in the stationary shock model.

Figure 10.10 shows that either a stationary C-type shock or young CJ-type shocks provide the best fits to the observations of L1157 B1. However, the lower panel of Fi-

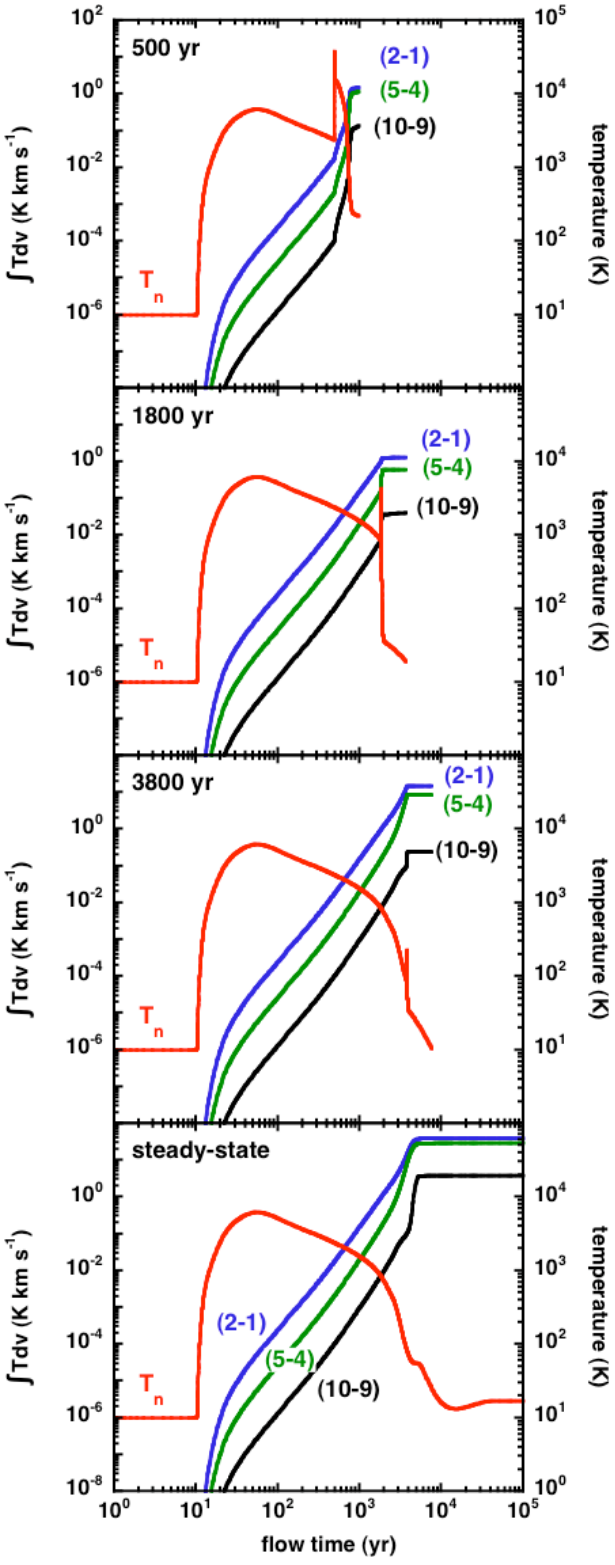

Figure 10.9 – The integrated intensities, $\int T \mathrm{d}v$, of the SiO (2–1), (5–4) and (10–9) rotational transitions, as functions of the flow time of the charged fluid, for the CJ-type shock model in which $n_{\mathrm{H}} = 10^4$ cm^{-3}, $b = 1$, and $v_{\mathrm{s}} = 50$ km s^{-1}. The shock age increases from top to bottom : 500, 1800, 3800 years, and steady–state. The temperature of the neutral fluid, T_{n}, is plotted also. In these calculations, there is no SiO in the grain mantles, and the gas–phase silicon is produced solely by erosion of the silicate grain cores.

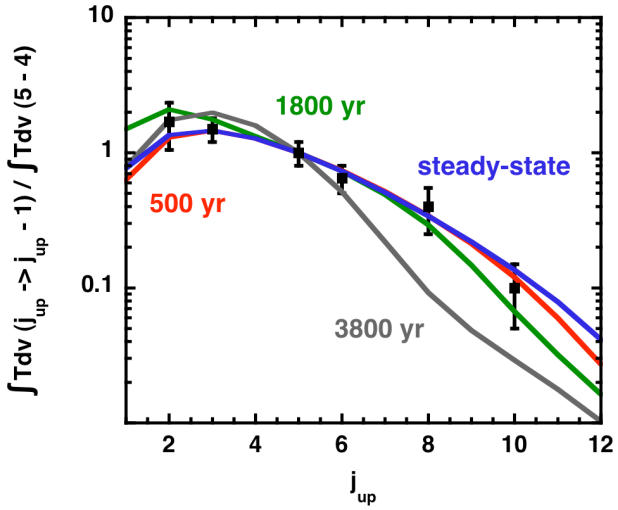

Figure 10.10 – Integrated SiO line intensities, relative to the (5–4) transition, for the CJ-type shock model in which $n_{\rm H} = 10^4$ cm^{-3}, $b = 1$, and $v_{\rm s} = 50$ km s^{-1}. The shock ages are 500, 1800, 3800 years, and the corresponding steady–state results are plotted also. In these calculations, there is no SiO in the grain mantles, and the gas–phase silicon is produced solely by erosion of the silicate grain cores. The observed points, with error bars, relate to L1157 B1.

gure 10.12 shows that the absolute SiO(5–4) line intensity is substantially underestimated by the young CJ-type shock models, if it is assumed that there is no SiO in the grain mantles and the gas–phase silicon is produced exclusively by erosion of the silicate grain cores. In this case, only the stationary shock model is a good candidate to fit the SiO observations.

10.2.2 SiO in the grains mantles

SiO production and the influence of the O_2 scenario. Still looking for non stationary shock models likely to fit the SiO observations, we now turn to non-stationary shock models in which SiO is supposed to be present in the grain mantles; the fraction of the elemental silicon which is initially in the mantles is varied from 0% to 10%[3]. As in Section 9.1, we consider the following model parameters : $n_{\rm H} = 10^4$ cm^{-3}, $b = 1$, $v_{\rm s} = 25$ and 50 km s^{-1}.

The production of SiO in such shock models under such assumptions is shown on Figure 10.11. On both panels, it appears that the amount of SiO released from the grain mantles is higher than the one generated following the grain cores erosion, except in one case, for the higher shock velocity, when only 1% of the Si is initially placed in the grain mantles. At such high velocity, molecular oxygen is dissociated, and SiO forms through the reaction of Si with OH, making the influence of the oxygen scenario negligible. For all the other cases presented on the panels of Figure 10.11, the emitting SiO is originating

[3]The possibility that solid SiO at the higher concentrations might be detectable in the infrared needs careful evaluation.

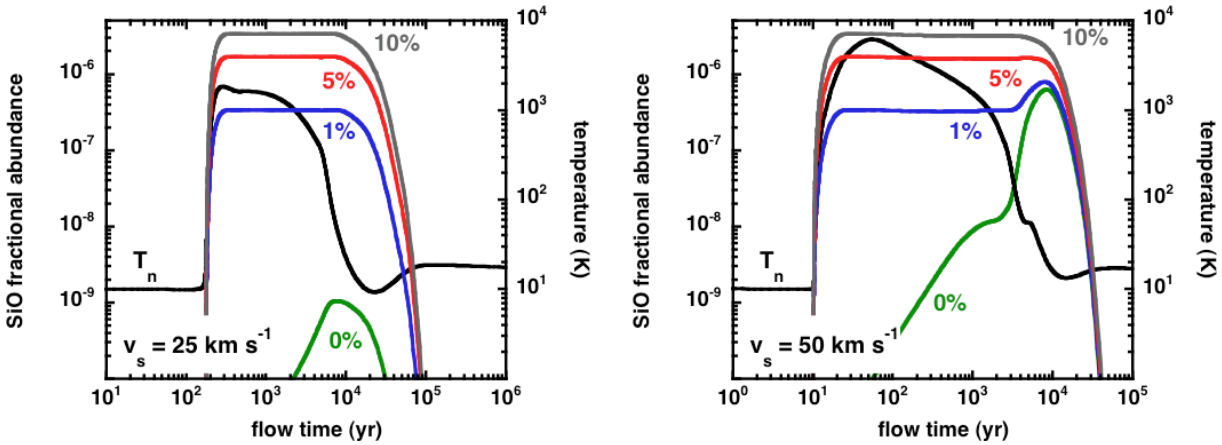

Figure 10.11 – SiO fractional abundance when directly released from the grain mantles in C-type shock reference models ($n_{\rm H} = 10^4$ cm^{-3}, $b = 1$, $v_{\rm s} = 25$ and 50 km s^{-1}, respectively left and right panel. Various amounts of SiO are initially placed in the grain mantles.

from the direct sputtering of the grain mantles, and the choice of the oxygen scenario has consequently no influence on this emission.

SiO emission and comparisons with observations. First, we compare the computed values of the integrated SiO(5–4) line intensity with those observed in L1157 and L1448 ; see Figure 10.12. As expected, the line emission increases with the amount of SiO in the grains mantles. We see also that the line intensity tends to increase with the evolutionary age of the shock, owing to the greater velocity extent of the emitting region. Exceptions to this general trend are young, high–velocity CJ-type shocks (cf. lower panel of Figure 10.12), for which the temperature rise at the J-discontinuity is sufficient to cause partial dissociation of molecular hydrogen. Consequent to the reduction in the efficiency of H_2 cooling, the width of the cooling zone, behind the discontinuity, is greater and the SiO line intensity is enhanced.

Figure 10.12 shows that agreement can be found between the observed and calculated (5–4) line intensity for almost every model in which there is some SiO in the grain mantles. With a view to finding a means of discriminating between the models, we plot, in Figure 10.13, the integrated SiO line intensities, relative to the (5–4) transition. In the calculations shown in this Figure, it was assumed that 5% of the elemental silicon was initially in the form of SiO in the grain mantles.

At the lower shock speed, the populations of the high rotational levels are greater when the shock is young, owing to the larger jump in temperature at the J-discontinuity. The oldest shock (4000 years) remains far from the steady–state limit. On the other hand, at the higher shock speed, the 3800 years–old CJ-type shock has almost attained steady state. The cooling efficiency behind the J-discontinuity in the youngest shock (with an age of 500 years) is reduced by the partial dissociation of molecular hydrogen. Reasonable agreement with the observations is found for evolutionary ages of a few thousand years.

Owing to the presence of the embedded J-discontinuity, the profiles of the SiO lines predicted by CJ-type models are compressed in velocity space, as compared with the

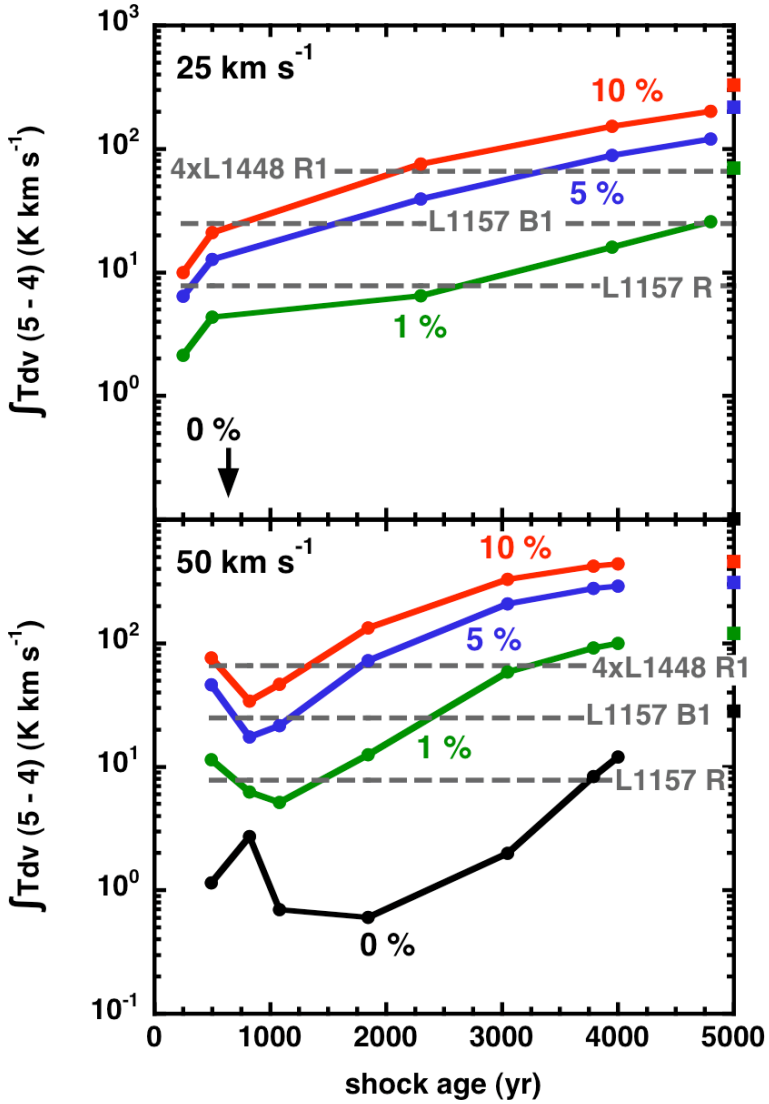

Figure 10.12 – The integrated intensity of the SiO(5–4) line, $\int T\mathrm{d}v(5-4)$, as a function of the age of the shock wave and the percentage of silicon initially in the form of SiO in the grain mantles ; $n_{\mathrm{H}} = 10^4$ cm^{-3}, $b = 1$, $v_{\mathrm{s}} = 25$ km s^{-1} (upper panel) and 50 km s^{-1} (lower panel). The points corresponding to the limit of steady–state are plotted on the right–hand y-axis. The SiO(5–4) intensities observed in L1157 and L1448 are indicated by the horizontal lines.

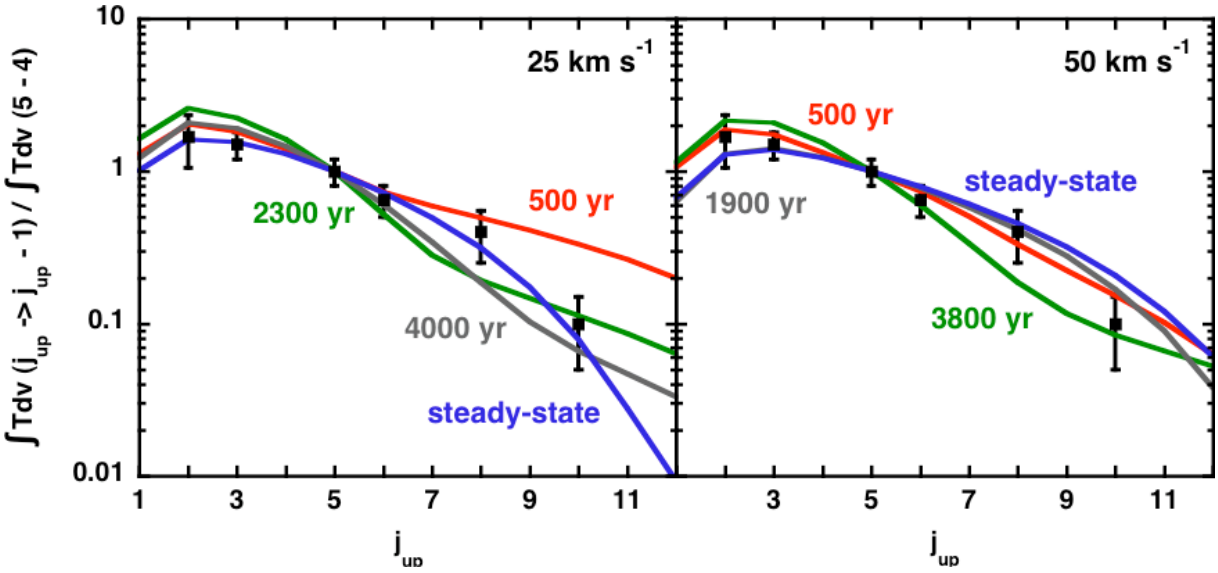

Figure 10.13 – Integrated SiO line intensities, relative to the (5–4) transition, for the CJ-type shock models in which $n_{\rm H} = 10^4$ cm^{-3}, $b = 1$, and $v_{\rm s} = 25$ km s^{-1} (upper panel) and $v_{\rm s} = 50$ km s^{-1} (lower panel). The evolutionary ages of the shocks are indicated, and the corresponding steady–state results are plotted also. In these calculations, 5% of the elemental silicon is assumed to be initially in the grain mantles, in the form of SiO. The observed points, with error bars, relate to L1157 B1. The highest rotational level for which observations are available, $j_{\rm up} = 10$, lies 115 K above the ground state.

steady–state C-type models discussed in Section 9.1. The younger the shock wave, the greater is the fraction of the emission that is contributed by the gas immediately behind the discontinuity. As the flow velocity of this gas becomes approximately constant, the lines become much narrower than in the steady–state limit : the predicted widths decrease to 0.1–0.2 km s^{-1}, which is much smaller than the observed widths of 5–20 km s^{-1}, in 3"–10" beams. In this respect, the CJ-type models face a problem which is analogous to that encountered by Gusdorf et al. (2008a), and for which, in the concluding remarks Section of Gusdorf et al. (2008b), we advance the same tentative explanation.

10.2.3 Neutral Si in the grains mantles

In this section, we investigate the possibility for CJ-type shock models to fit the observations when Si is placed in the grain mantles in various amounts ranging from 1 to 10%. To do so, we study different evolutionary ages for two non stationary shock models whose steady-state C-type models have already been used along with the same Si and O_2 repartition in Section 9.2.

SiO production and influence of the O_2 scenario. Figure 9.5 and 9.6 show the production of SiO in two reference C-type shock models for which : $n_H = 10^4$ cm^{-3}, $b = 1$, $v_s = 25$ and 50 km s^{-1}, 5% of Si being initially placed in the grain mantles, within the two initial repartition of oxygen scenarios introduced in Subsection 7.1.3. Unlike the low velocity reference shock model, the high velocity is insensitive to the choice of the oxygen scenario, owing to the dissociation of molecular oxygen that occurs because of the high temperatures that are reached. We then study the production of SiO and the influence of the choice of the oxygen scenario on the example the non stationary shock models corresponding to the lowest velocity one.

Figure 10.14 hence shows the production of SiO for CJ-type shock models of varying evolutionary stages (500, 2300, and 4000 years), with the following parameters : $n_H = 10^4$ cm^{-3}, $b = 1$, $v_s = 25$ km s^{-1}, 5% of Si being initially placed in the grain mantles. The left-hand side panels show the results under the assumption that the oxygen is initially frozen on to the grain mantles under the form of O_2, whereas the right-hand side ones show the same results when the oxygen is present under the form of ice water on the surface of these grains. The production of SiO follows the same progression in every case :

- Si is first sputtered from the grain mantles in the C part of the shock, and is released in the gas phase where it reaches a constant abundance (in a similar fashion as SiO in Figure 10.11) ;
- Si then reacts in the C part of the shock to form SiO. In the first case of oxygen scenario (left panels), O_2 is the preferential reaction partner, and its high abundance in the gas phase guarantees a more efficient production of SiO than in the second case (right panels) where OH is the less abundant preferential reaction partner for the formation of SiO ;
- the higher temperatures reached in the J contribution largely enhance SiO production in every case ;
- SiO production goes on in the post-shock region if the temperature conditions allow for it.

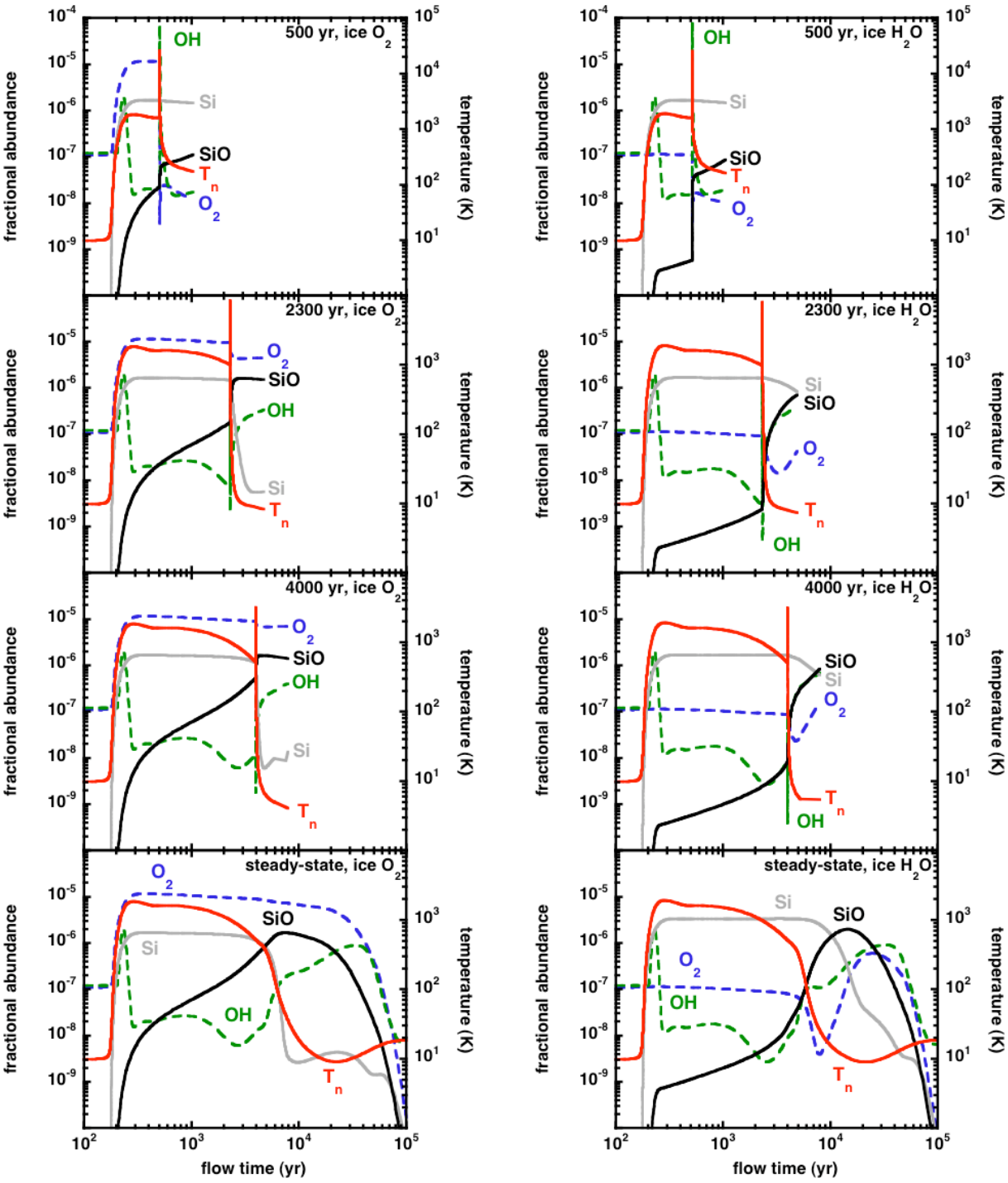

Figure 10.14 – Production of SiO in a CJ-type reference shock model for which $n_{\rm H} = 10^4$ cm^{-3}, $b = 1$, $v_{\rm s} = 25$ km s^{-1}, for different evolutionary ages (500, 2300, and 4000 years), and associated steady-state C-type shock model. 5% of Si is initially placed in the grain mantles. Left : with the first oxygen scenario as described in Subsection 7.1.3. Right : with the second assumption regarding the oxygen scenario.

Figure 10.14 consequently shows the dependence of SiO formation for this reference model on the choice of the oxygen scenario.

SiO emission and comparisons with observations. As already done in Subsections 9.1.2, 9.2.2, 10.2.1, and 10.2.2, we now study the SiO emission in our reference CJ-type shock models (various amounts of Si initially in the grain mantles for various evolutionary stages of shocks with $n_{\rm H} = 10^4$ cm^{-3}, $b = 1$, $v_{\rm s} = 25$ and 50 km s^{-1}) through the computed values of the integrated SiO(5–4) line intensity with those observed in L1157 and L1448. The results are shown on Figures 10.15 and 10.16, respectively assuming that oxygen is initially present in the grain mantles under the form of molecular oxygen or water.

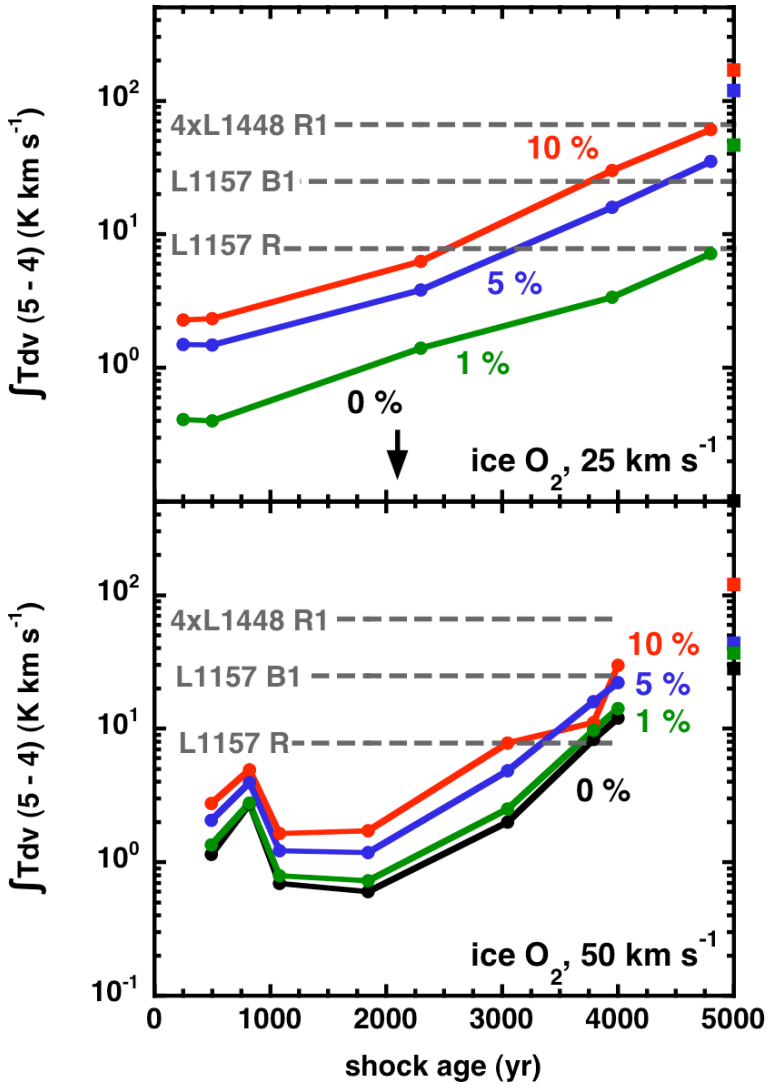

Figure 10.15 – As Figure 10.12, assuming the elemental silicon is initially in the mantles in its neutral form.

As expected, whatever the choice of the oxygen scenario, the line emission globally

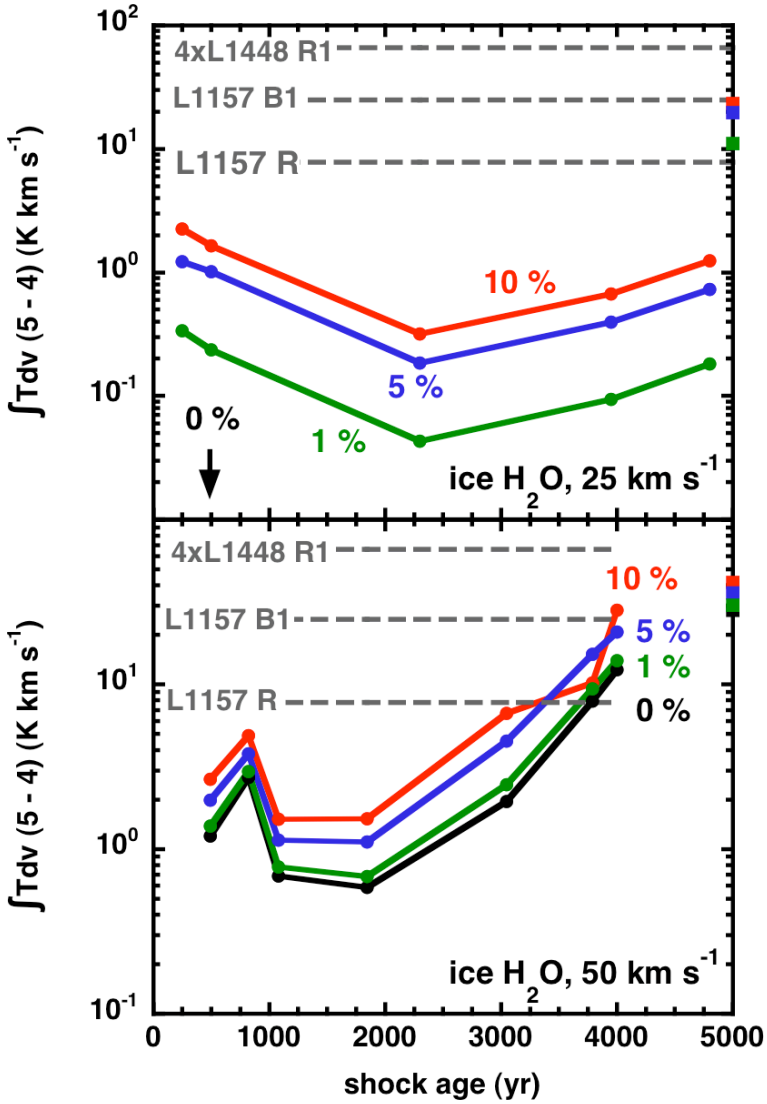

Figure 10.16 – As Figure 10.12, assuming the elemental silicon is initially in the mantles in its neutral form, and assuming that the initial abundance of O_2 ice is negligible (the second scenario described in Subsection 7.1.3).

increases with the amount of Si in the grains mantles. More delicate is the interpretation of the variation of the emission of SiO with the evolutionary age of the shock. This emission depends on the abundance of SiO in the gas phase, as well as on the corresponding gas temperature, and also on the velocity gradient. As an example, the low velocity reference shock model can be analyzed under the assumption that oxygen is initially present in the grain mantles under the form of water ice (top panel of Figure 10.16), and for example when 5% of Si is initially placed in the grain mantles. The drop of the integrated SiO(5–4) line value from the youngest shock to the oldest ones can be interpreted thanks to the Figure 10.14. For the 500 years old shock, the amount of SiO that is formed is less important than in the wider 2300 years old one. Nevertheless, in the former case, the temperature at which SiO is present in the gas phase is much larger, and in the post-shock region SiO is still emitting because the velocity gradient are still important. On the contrary the highest temperature generated in the latter case is much smaller, and the velocity gradient quickly decrease towards zero in the post-shock region. The difference in temperature with older shock models is less important, whereas more SiO is generated in the larger, older CJ-type shock models. This explains why the emission increases again after 2300 years.

Figures 10.15 and 10.16 also confirm the independence of the results to the choice of the initial repartition of oxygen for the high velocity shock models, and that agreement can be found between observations and models when large amounts (5-10%) of Si are initially present in the grain mantles, and for large evolutionary ages (except for the low velocity case when O_2 initially exists under the form of water ice in the grain mantles).

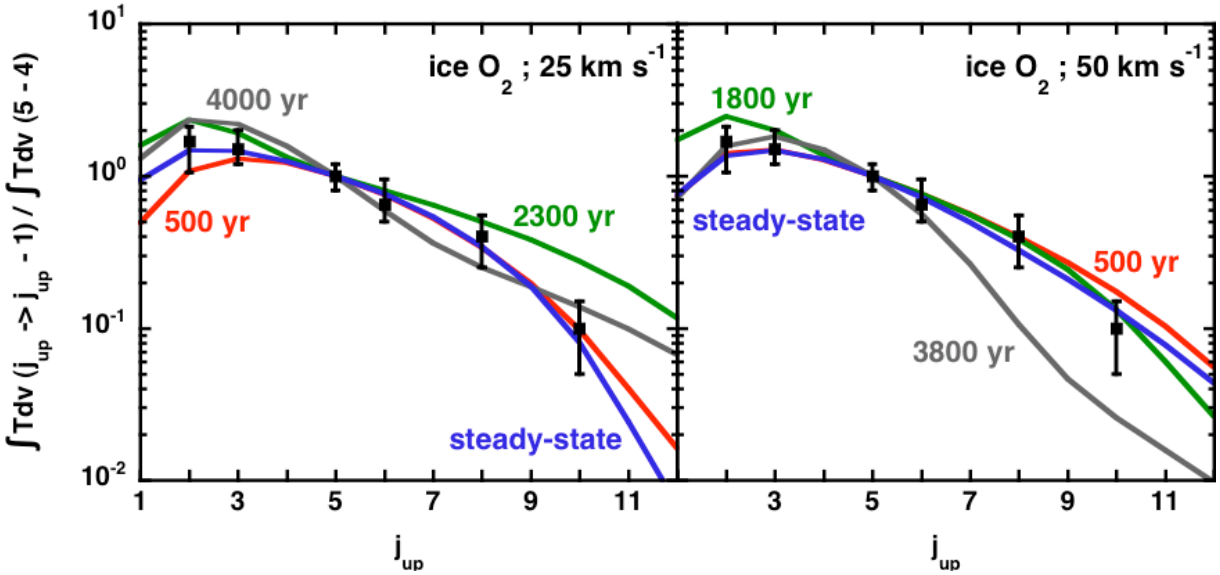

Figure 10.17 – As Figure 10.13, assuming the elemental silicon is initially in the mantles in its neutral form.

With a view to finding a means of discriminating between the models, we plot, in Figure 10.17, the integrated SiO line intensities, relative to the (5–4) transition. In the calculations shown in this Figure, it was assumed that 5% of the elemental silicon was initially in the form of SiO in the grain mantles. We interpret the right panel of this Figure

with the help of Figure 10.14. The youngest shock presents weak low lying lines emission due to the high temperatures that are reached through the J-discontinuity and in the post-shock. For the 2300 years old shock, the peak temperature is very high and the C-type part of the shock is rather wide and warm, which explains the emission spreading towards the high energy levels. The oldest shock has a wide and warm C-type part, but its peak temperature is not as high as the previous one. The high energy emission consequently drops compared to that of the 2300 years old, though still far from the steady state case.

At the lower shock speed, satisfying agreement can be found with the observations for older shocks (4000-4800 years old) when a large amount of Si is initially placed in the grain mantles (5-10%) in terms of integrated intensities relative to the SiO(5–4) line, in accordance with the results of Figure 10.15. Unfortunately, these ages do not range in the observational values of 2000-3000 years inferred by Gueth et al. (1998). At the highest shock velocity, Figure 10.15 also indicates a good fit of the observational data for old shocks with large amounts of Si in the grain mantles, but this good agreement is not confirmed in terms of integrated intensities relative to the SiO(5–4) line, as can be seen on the left panel of Figure 10.17.

10.3 The case of L1157 B1

After an initial selection of model parameters, based on H_2 observations, and detailed in Chapter 4, we proceed to comparisons with the observed SiO rotational line intensities. There is now an additional parameter, namely, the fraction of silicon present as SiO in the grain mantles.

10.3.1 SiO in the grains mantles

The result of this Subsection are introduced in Gusdorf et al. (2008b).

As in Sections 10.1 and 10.2, we consider first the integrated intensity of the SiO(5–4) line. It is clear that, for the low shock speeds which were derived from the analysis of the H_2 rovibrational spectrum, some silicon must be present in the grain mantles : grain–core erosion alone would not give rise to a sufficient amount of gas–phase SiO to account for the observations of its rotational lines. We assume that either 1% or 10% of the silicon is SiO in the mantles.

In Figure 10.18 is plotted the SiO(5–4) integrated line intensity against the magnetic field parameter, b, for CJ-type shocks with a pre-shock density $n_{\rm H} = 10^4$ cm^{-3}, shock velocities $v_{\rm s} = 20$, 22, and 25 km s^{-1} (in the left-hand side panel), and $n_{\rm H} = 10^5$ cm^{-3}, $v_{\rm s} = 12$ and 15 km s^{-1} (in the right-hand side panel). We recall that these models were found to give acceptable fits to the H_2 observations. We note that the evolutionary age was varied simultaneously with b, in order to optimize the fits to the observed H_2 excitation diagram, giving rise to the variations which are seen in the (5–4) line intensity. This variation is particularly striking in the results for a pre-shock density of 10^5 cm^{-3} and shock velocity of 12 km s^{-1} : the model for which $b = 0.45$ (age 75 years) incorporates a significant magnetic precursor, whereas, when $b = 0.6$ (age 75 years), the precursor is negligible. In the latter case, there is much less sputtering of SiO from the grain mantles,

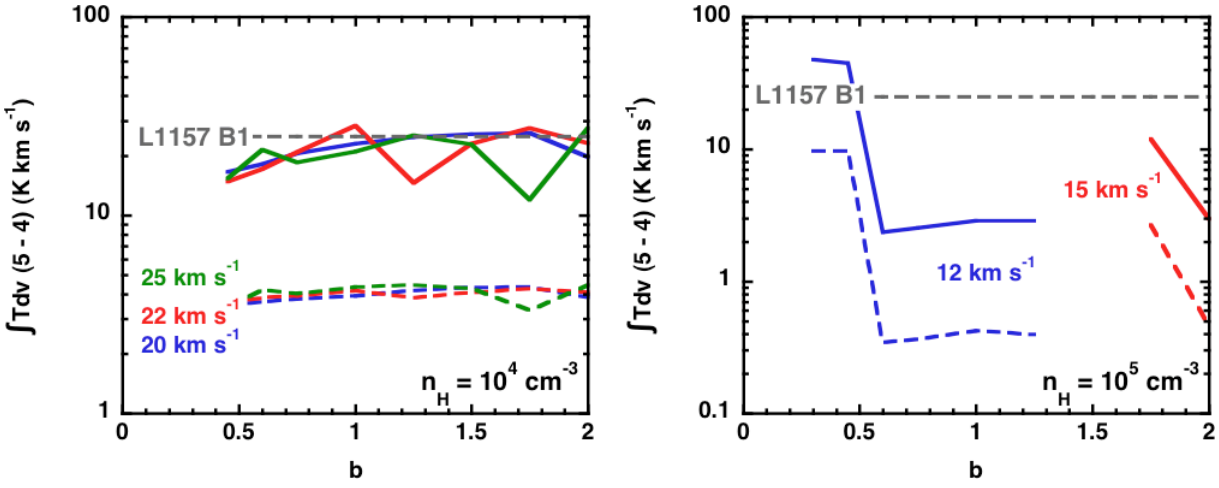

Figure 10.18 – The integrated intensity of the SiO(5–4) line, $\int T\mathrm{d}v(5-4)$, against the magnetic field parameter, b, for models in which the pre-shock density $n_{\mathrm{H}} = 10^4$ cm^{-3}, the shock velocity $v_{\mathrm{s}} = 20$, 22, and 25 km s^{-1} (upper panel), and $n_{\mathrm{H}} = 10^5$ cm^{-3}, $v_{\mathrm{s}} = 12$ and 15 km s^{-1} (lower panel). Results were obtained assuming either 10% (full curves) or 1% (broken curves) of the silicon is initially SiO in the grain mantles.

and the SiO emission is correspondingly weaker. The results in Figure 10.11 may be seen to support the higher percentage (10%) of silicon being present in the mantles.

Finally, we compare the integrated line intensities, relative to the (5–4) transition, with the observations. This comparison eliminates the models with $n_{\mathrm{H}} = 10^5$ cm^{-3}, which are found to overestimate the intensities of the lines from high rotational levels. On the other hand, as may be seen from Figure 10.19, a range of combinations of b and the shock age remains compatible with the relative line intensities for $n_{\mathrm{H}} = 10^4$ cm^{-3} and the optimal shock speed is $v_{\mathrm{s}} = 20$ km s^{-1}. The only observational point that is not well fitted by the models (the (10–9) transition) could be more closely approached by reducing the amount of SiO assumed to be initially in the mantles. The evolutionary ages of the models in Figure 10.19 lie in the range 500–2000 years, as compared with the dynamical age estimate of 2000–3000 years, derived empirically (Gueth et al. (1998)).

10.3.2 Neutral Si in the grains mantles

We now proceed to comparisons with the observed SiO rotational line intensities with the grid of models that were selected based on H_2 observations (and detailed in Chapter 4). The additional parameter is now the fraction of silicon present as Si in the grain mantles.

One more time, we consider first the integrated intensity of the SiO(5–4) line. Similarly to the previous Subsection, for the low shock speeds which were derived from the analysis of the H_2 rovibrational spectrum, some silicon must be present in the grain mantles : grain–core erosion alone would not give rise to a sufficient amount of gas–phase SiO to account for the observations of its rotational lines. We assume that either 1% or 10% of the silicon is initially in the mantles. In accordance with the results of Subsection 10.2.3, and given the low shock speeds models that we study, we have to consider the influence

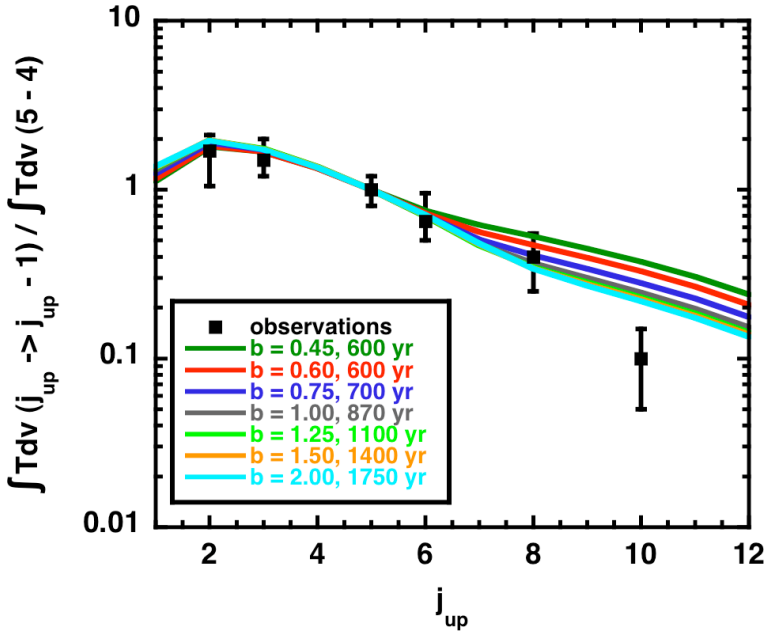

Figure 10.19 – The best–fitting models of the H_2 and SiO observations of L1157 B1 : CJ-type shocks for which $n_H = 10^4$ cm^{-3} and $v_s = 20$ km s^{-1} ; the magnetic field parameter, b and the evolutionary age are varied simultaneously. 10% of the silicon is initially SiO in the grain mantles.

of the oxygen scenario on the results.

In Figures 10.20 and 10.21 are plotted the SiO(5–4) integrated line intensity against the magnetic field parameter, b, for CJ-type shocks with a pre-shock density $n_H = 10^4$ cm^{-3}, shock velocities $v_s = 20$, 22, and 25 km s^{-1} (in the left-hand side panel), and $n_H = 10^5$ cm^{-3}, $v_s = 12$ and 15 km s^{-1} (in the right-hand side panel), respectively for each oxygen initial repartition presented in Subsection 7.1.3.

As already stated in the previous section, these models were found to give acceptable fits to the H_2 observations, and their evolutionary age was varied simultaneously with b in order to optimize the fits to the observed H_2 excitation diagram. Similarly as in the previous section, this age variation generates that of the SiO (5–4) line integrated intensity, and this variation spectacularly shows in the results for a pre-shock density of 10^5 cm^{-3} and shock velocity of 12 km s^{-1} : the model for which $b = 0.45$ (age 75 years) incorporates a significant magnetic precursor, whereas, when $b = 0.6$ (age 75 years), the precursor is negligible. In the latter case, there is much less sputtering of Si and consequent formation of SiO, whose emission is correspondingly weaker.

The main difference with the results of the previous section also shows on Figures 10.20 and 10.21 : no model with elemental Si in the grain mantles seems to be able to fit the SiO observations in terms of absolute integrated SiO line intensities. The origin of these discrepancies can be found on Figures 10.15 and 10.16 : with models with Si initially included in the grain mantles instead of SiO, the formation of SiO is delayed with respect to the sputtering of Si thanks to the reaction rates of Equations 6.20 and 6.21. To generate enough SiO to account for the observations, a sufficiently wide C-type part is necessary,

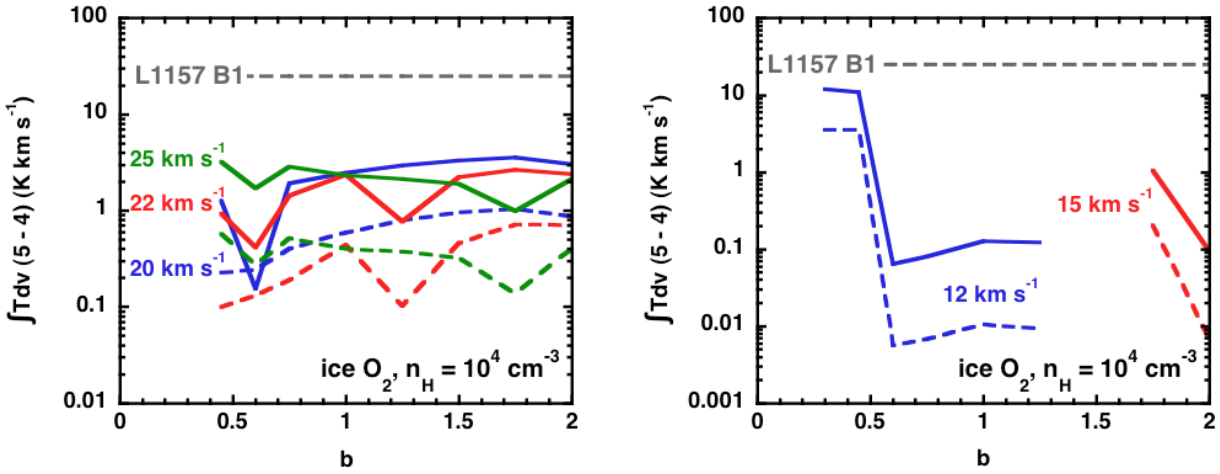

Figure 10.20 – As Figure 10.18, assuming the elemental silicon is initially in the mantles in its neutral form.

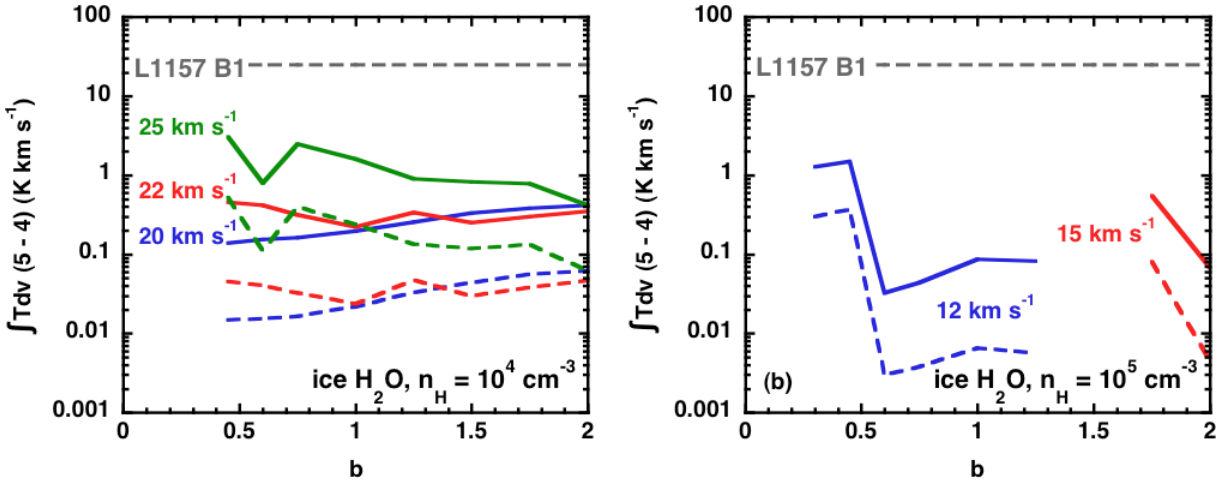

Figure 10.21 – As Figure 10.18, assuming the elemental silicon is initially in the mantles in its neutral form, and assuming that the initial abundance of O_2 ice is negligible (the second scenario described in Subsection 7.1.3).

that is an old CJ-type shock models, at least older than the ones selected to match H_2 observational data in the case of L1157 B1 region. CJ-type shock models that fit molecular hydrogen observations, combined with the inclusion of Si in the grain mantles, are not eligible to fit the SiO observations, at least in the range of Si amount that we consider in this study.

11

Simultaneous fitting with CO

Dans ce chapitre, la production et l'émission de la molécule de CO est étudiée dans les différents types de modèles de chocs utilisés tout au long de cette thèse, stationnaires comme non stationnaires. Enfin, CO est ajoutée à la liste des molécules dont l'émission est ajustée simultanément à celle de SiO et H_2, c'est-à-dire par le même modèle de choc que ces deux molécules.

In this chapter, we present the CO production and emission in all different kinds of shocks : stationary (C- and J-type), and non stationary (CJ-type). We study the emission of CO with th same means as for SiO, although a comparative article is in the submission process, focused on the significance of the departures from an equilibrium state when solving the CO rotational level population within the shock code or externally, as it has been done during this study (Flower and Gusdorf (2008)). We compare our results to the observations compiled by Giannini et al. (2001) in the case of the L1157 B1 region. As anticipated, the initial distribution of elemental oxygen (see Subsection 7.1.3), and of elemental silicon have no influence on the CO emission from the shock wave.

11.1 CO emission in stationary shocks

11.1.1 CO emission in C-type shocks

We begin with the interpretation of CO emission in C-type shock models through the examples of two reference models already studied in terms of SiO emission, for which : $n_{\rm H} = 10^4$ cm^{-3}, $b = 1$, $v_{\rm s} = 25$ and 50 km s^{-1}.

CO production in those reference shock models can be visualized on Figure 11.1. The rise in temperature characteristic of the compression is accompanied with the sputtering of the grain mantles, that initially contain CO. CO is then released in the gas phase, where its stability makes its fractional abundance constant until the post-shock region, where the cold temperatures generate the adsorption on to the grains. This balance between the release of CO in the gas phase and re-adsorption on to the grain mantles is the same whatever the shock velocity.

Figure 11.2 shows the emission of CO in those reference shock models, through the CO lines integrated intensity diagram. The results as obtained by Giannini et al. (2001)

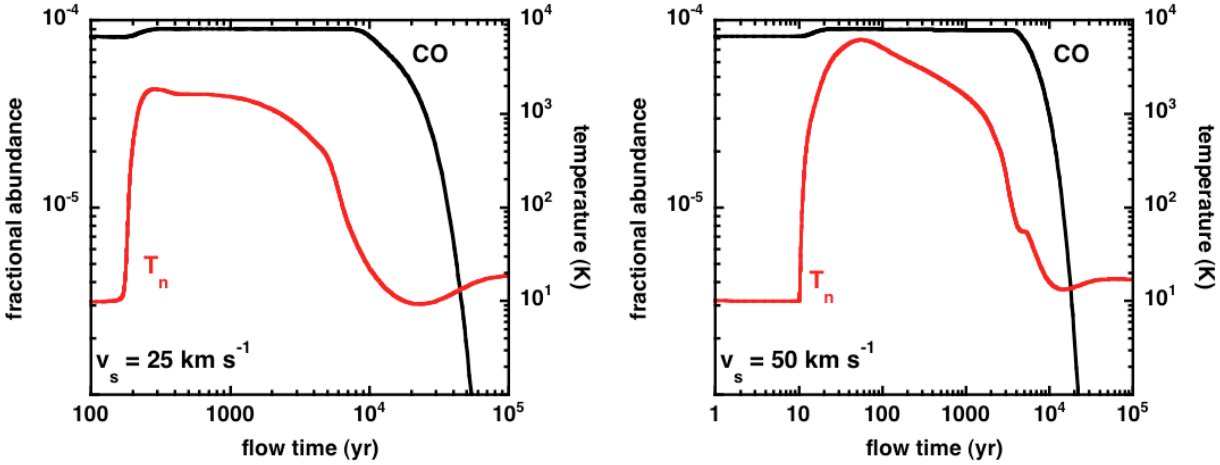

Figure 11.1 – CO production in C-type reference shock models : $n_{\rm H} = 10^4$ cm^{-3}, $b = 1$, $v_{\rm s} = 25$ (left panel) and 50 km s^{-1} (right panel). CO fractional abundance and temperature profiles.

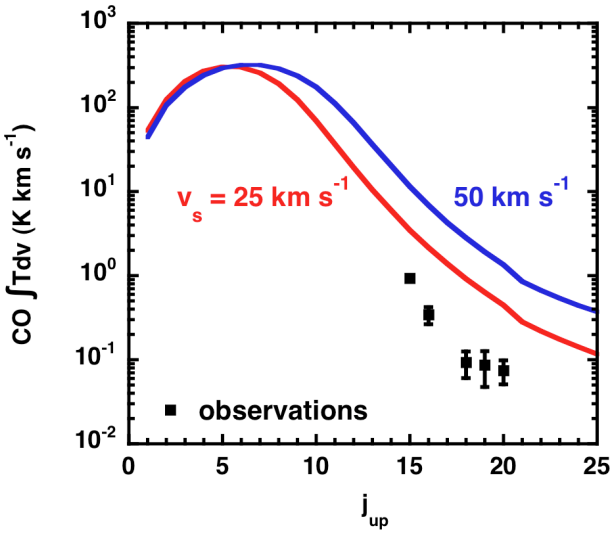

Figure 11.2 – CO emission in C-type reference shock models : $n_{\rm H} = 10^4$ cm^{-3}, $b = 1$, $v_{\rm s} = 25$ (red curve) and 50 km s^{-1} (blue curve) : absolute integrated intensity diagram.

are displayed also for the L1157 B1 region. Direct comparison between models and observations tend to indicate the necessity of an observational filling factor in order to obtain a satisfying match, although the shape of the observational curve seems to be well reproduced by our models. At higher shock velocity, the temperatures that are reached are higher than in the low velocity case, as can be seen on Figure 11.1, hence a wider integrated intensity diagram profile, and higher excitation for higher lying rotational levels.

11.1.2 CO emission in J-type shocks

In the case of J-type shock models, the production of SiO is shown on Figure 11.3, for two reference shock models with the following parameters : $n_{\mathrm{H}} = 10^4$ cm^{-3}, $b = 0.1$, $v_{\mathrm{s}} = 25$ and 50 km s^{-1}.

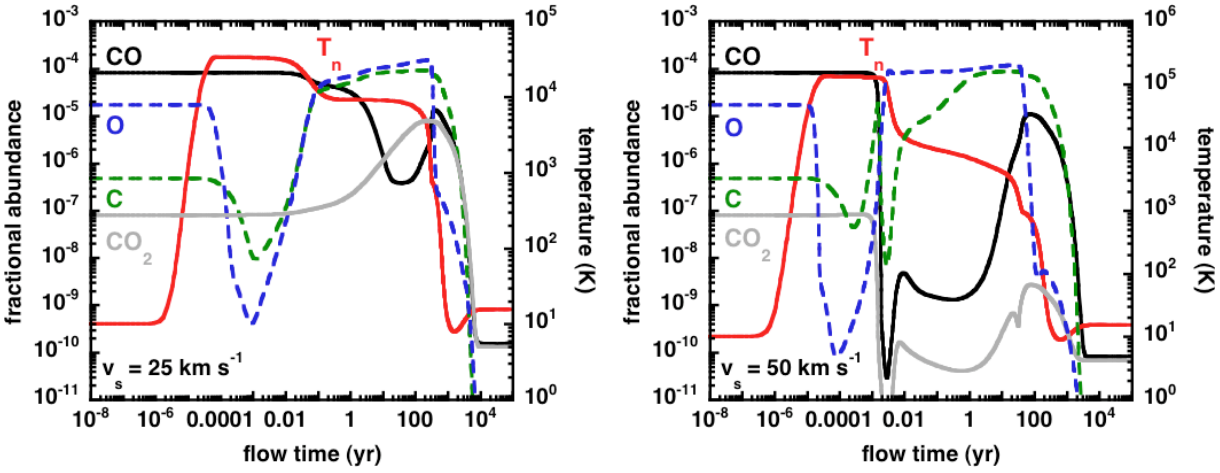

Figure 11.3 – CO production in J-type reference shock models : $n_{\mathrm{H}} = 10^4$ cm^{-3}, $b = 1$, $v_{\mathrm{s}} = 25$ (left panel) and 50 km s^{-1} (right panel). C, O, CO, CO_2 fractional abundance and temperature profiles.

Unlike in the case of C-type shock models, the sputtering of the grain mantles is negligible. Indeed, there is no drift velocity between the neutral and charged fluid (all the species belong to the same fluid, as there is no magnetic field), and hence no possibility of collision between the generally charged grains and the abundant neutral species such as H_2 likely to generate this sputtering. The carbon monoxide that is available in the gas phase comes integrally from its initial repartition in this gas phase.

The other striking difference with C-type shock cases comes from the higher temperatures that are reached in J-type shock models. As can be seen on Figure 11.3, the temperatures that are reached are greater than 10^4 K whatever the shock velocity. Such temperatures trigger the dissociation of molecular hydrogen. Elemental hydrogen is consequently present in the gas phase, and is likely to provoke CO dissociation through the reaction :

$$\mathrm{CO} + \mathrm{H} \longrightarrow \mathrm{OH} + \mathrm{C} \tag{11.1}$$

whose activation barrier is of 77700 K, and which is consequently favored by these high temperatures. In the post-shock regions, where the temperature drops, CO reforms and is then re-adsorbed on to the grain mantles.

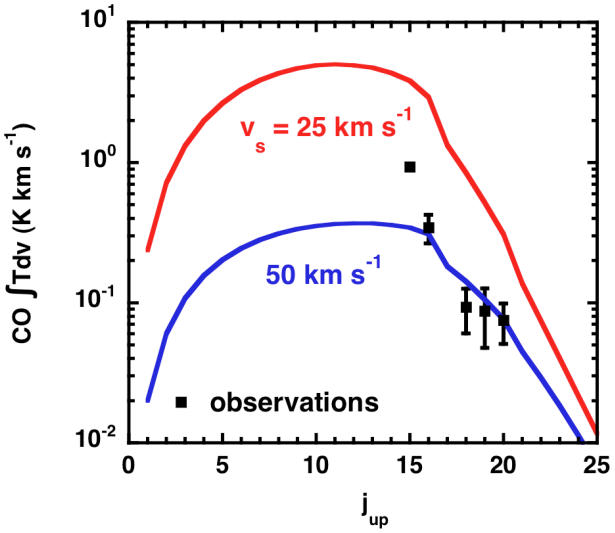

Figure 11.4 – CO emission in J-type reference shock models : $n_{\rm H} = 10^4$ cm^{-3}, $b = 1$, $v_{\rm s} = 25$ (red curve) and 50 km s^{-1} (blue curve) : absolute integrated intensity diagram.

The CO lines integrated intensity diagrams can be interpreted accordingly, and is plotted on Figure 11.4. Because of its dissociation, the CO emission is less important than in the C-type shock cases. However, when it is present in the gas phase, the temperature conditions are much warmer in the J-type case, which generates broader line integrated intensity diagram profiles. The dissociation being more important at higher velocity, the integrated intensity is even smaller in this case, and excludes this model from being a possible fit for the observations. Again, the low velocity model shape of the diagram seems to be a satisfying match to that of the observed one, though a definitive conclusion could only be reached through the knowledge of the exact filling factor. A possible discrimination between C-type and J-type shock models could also be achieved through the comparison of the low lying levels emission with the observations that have yet to be done.

11.2 CO emission in non stationary shocks

We finally consider the production and emission of SiO in CJ-type shock models, again based on the analysis of two reference shock parameters sets, to which we now add another parameter : the evolutionary shock age. Our selection of reference CJ-type shock models is the same as during the SiO analysis, namely :

- $n_{\rm H} = 10^4$ cm^{-3}, $b = 1$, $v_{\rm s} = 25$ km s^{-1} at 500, 2300, and 4000 years ;
- $n_{\rm H} = 10^4$ cm^{-3}, $b = 1$, $v_{\rm s} = 50$ km s^{-1} at 500, 1800, and 3800 years.

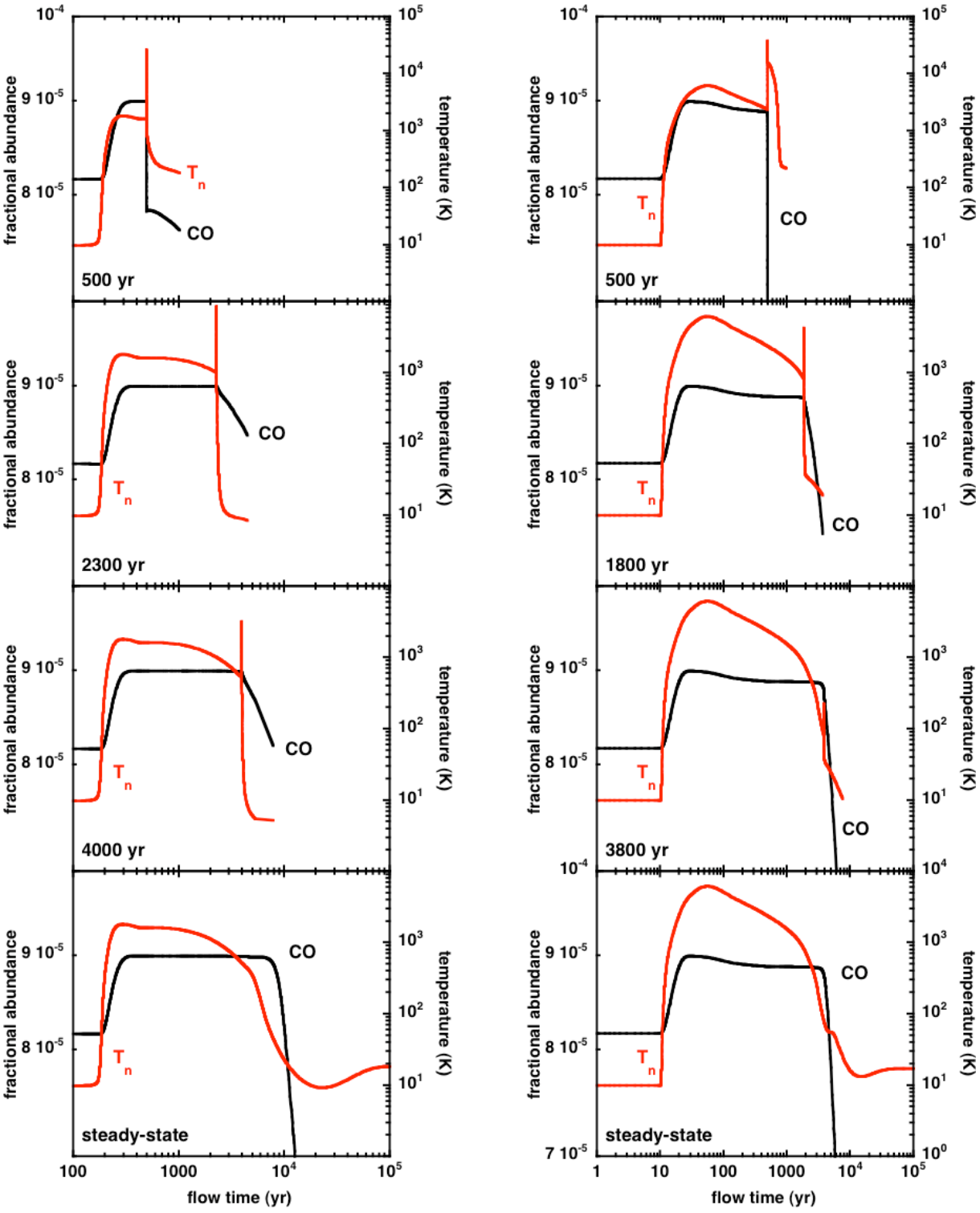

Figure 11.5 – CO production in CJ-type reference shock models : $n_{\rm H} = 10^4$ cm^{-3}, $b = 1$, $v_{\rm s} = 25$ (left panel, evolutionary ages 500, 2300, and 4000 years) and 50 km s^{-1} (right panel, evolutionary ages 500, 1800, 3800 years), and corresponding steady-state C-type shock models. CO fractional abundance and temperature profiles.

11.2.1 CO production in non stationary shock models

CO production is shown for these reference models on Figure 11.6, for the respective low and high velocity (left and right panels), and for the corresponding C-type shock models. In every case, the shock starts with its magnetic, C-type part, in which CO is sputtered from the grain mantles and released in the gas phase. Except in the youngest shock models for each velocity, the temperature that are reached are not high enough to generate H_2 dissociation, and the consequent CO one through Reaction 11.1. Apart from these young cases, in the cold, post-shock gas, CO get adsorbed on the grain mantles again, which explains the relatively slow decrease of its gas phase abundance. On the other hand, when the temperature is sufficient, H_2 gets dissociated, and so can be CO through the reaction 11.1. This is what happens for the youngest low and high velocity shock models, which accounts for the fast decrease of the gas phase CO abundance.

11.2.2 CO emission in non stationary shock models

The CO emission trends can be visualized on Figure 11.6 that shows the absolute CO lines integrated intensity diagram in each case, low velocity (left hand side panels) or faster one (right hand side), for the already considered evolutionary ages.

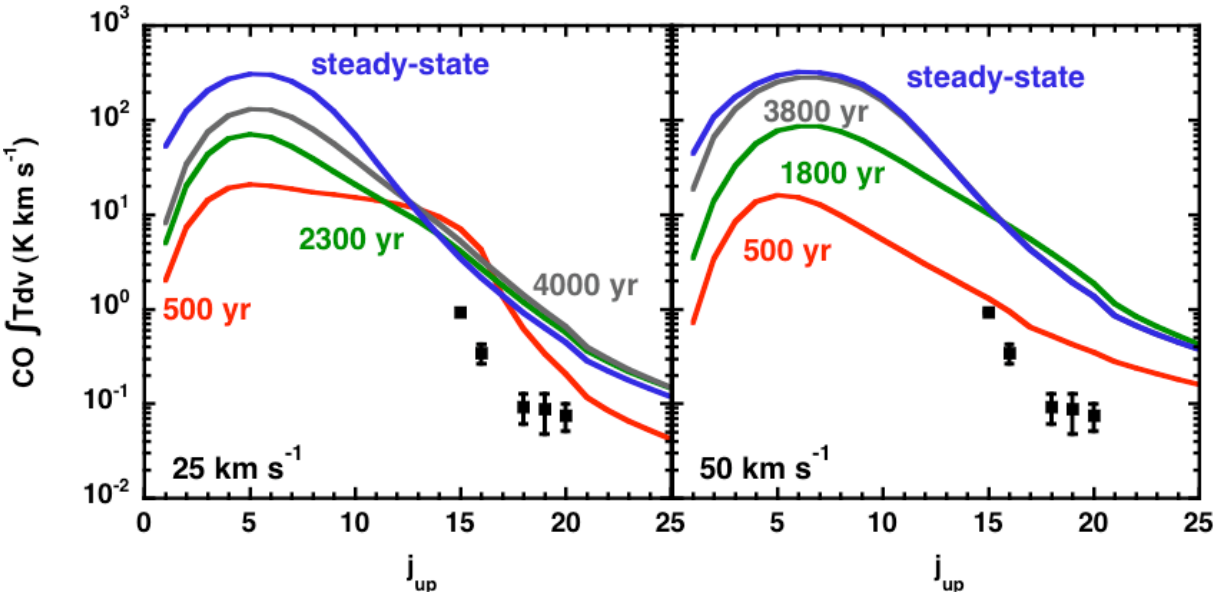

Figure 11.6 – CO emission in CJ-type reference shock models : $n_{\rm H} = 10^4$ cm^{-3}, $b = 1$, $v_{\rm s} = 25$ (left panel, evolutionary ages 500, 2300, and 4000 years) and 50 km s^{-1} (right panel, evolutionary ages 500, 1800, 3800 years), and corresponding steady-state C-type shock models : absolute integrated intensity diagram.

Both diagrams present a mixture of C- and J-type emission characteristics :

- high integrated intensity values, owing to the C-type component in which CO undergoes no dissociation or adsorption and can consequently emit :
- broad integrated intensity diagram profiles because of the high temperatures reached in the J-type contribution of the non stationary shock models.

The older the shock, the wider the magnetic component, and hence the higher the excitation at low temperature is, which explains the evolution of the emission value with the shock age for the low lying rotational levels. For the older shock model at high velocity, the results are almost identical to that of the steady-state C-type shock models, as the difference in the temperature profiles between those two models is minimal. The younger the shock, the higher the temperature in the J-type contribution, and the broader the integrated intensity diagram profile becomes. Eventually, the comparison with observations seem to exclude high velocity models. Concerning the low shock speed ones, the shock age does not seem to be strongly constrained by the comparison with observations, due to the lack of information we have about the filling factor value. All ages seem to provide decent shape comparison with the observational data, but it appears again that constraining efficacy could be gained from comparisons with low lying levels observations.

11.3 The case of L1157 B1

The result of this Section are introduced in Gusdorf et al. (2008b).

As in the case of SiO, we computed the CO integrated line intensities for all models which simulated the H_2 emission satisfactorily. Models for which $n_{\rm H} = 10^5$ cm^{-3} generated too much emission from the high rotational levels, relative to the low levels. CJ-type shock models with a pre-shock density $n_{\rm H} = 10^4$ cm^{-3} provided better fits to the observations. Figure 11.7 shows a comparison between observed and calculated (absolute) integrated line intensities ; the observations were compiled by Giannini et al. (2001). The model for which results are displayed is the same as in Figure 10.12 and corresponds to $n_{\rm H} = 10^4$ cm^{-3} and $v_{\rm s} = 20$ km s^{-1} ; there are various combinations of the magnetic field strength parameter, b, and the shock age. The shape of the theoretical curves in this Figure 11.7 is in good agreement with that observed, although there remains a discrepancy in the absolute values which may indicate an overestimation of the beam filling factor, for which we adopted a value of 1/16, corresponding to a beam diameter of 80" and a source diameter of 20" . Figure 11.7 shows that the rotational transitions which are observed are not ideal discriminants of the models : observations of lines from lower or higher rotational levels would be desirable, in this regard.

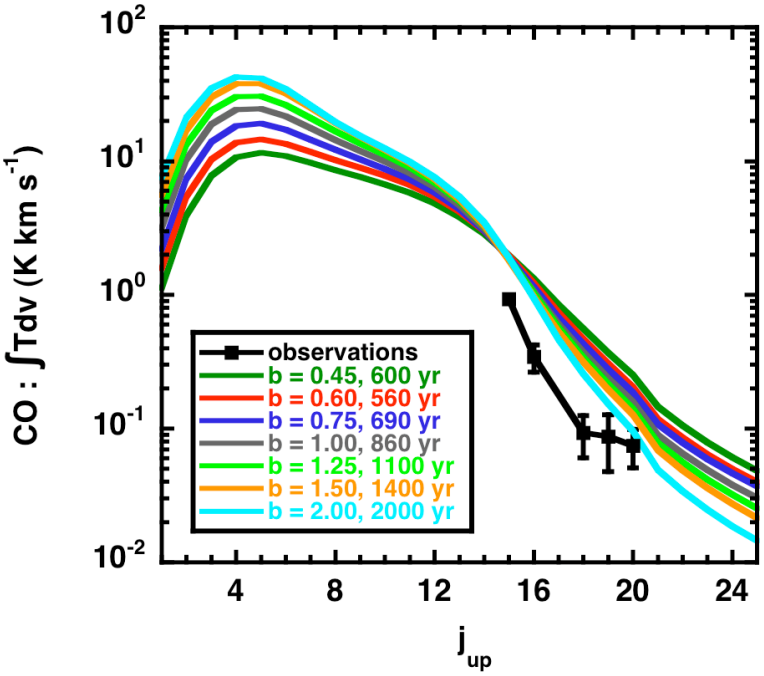

Figure 11.7 – The integrated intensities of the CO rotational lines, $\int T\mathrm{d}v$, for CJ-type shocks for which $n_{\mathrm{H}} = 10^4$ cm^{-3} and $v_{\mathrm{s}} = 20$ km s^{-1} ; the magnetic field parameter, b and the evolutionary age are varied simultaneously.

Conclusions and perspectives

12

Improving our methods of exploration

De nombreuses pistes restent à explorer pour développer plus avant le travail réalisé au cours de cette thèse. Les outils utilisés peuvent ainsi toujours être améliorés. Les entrées et sorties du code de transfert de rayonnement peuvent ainsi être perfectionnées en vue de comparaisons toujours plus précises avec les observations. Le code de choc peut lui aussi faire l'objet d'optimisations substantielles, concernant le traitement des grains par exemple. Enfin, une prise en compte plus précise de la structure spatiale des chocs étudiés doit absolument être implémentée, et pourra peut-être permettre à terme une comparaison satisfaisante entre les profils de raie observés et modélisés.

12.1 Improving the inputs of the LVG code

Precise radiative and collisional data are of crucial importance when it comes to radiative transfer modelling. In fact, equations of statistical equilibrium must be solved to determine the integrated intensities of each transition. Thanks to progress in terms of computation time and manpower, more precise or complete sets of data are regularly published.

Such computations are one of the work aims of the Molecular Universe Research and Training Network. We can cite for example the obtention of rotational and rovibrational cross section of H_2O+H/He/H_2, or the ones of CH^++H_2, or N_2H^++H_2/He. The collisions of SiO with H_2 are also being accurately studied. Such data are then compiled on internet databases such as the Paris Observatory one (http ://basecol.obspm.fr/).

Available data can also be extended by means of approximations (like the Infinite Order Sudden Approximation, see Schöier et al. (2005)), and allow to benefit from data that are adapted to the physical parameters of our studies in terms of range temperatures or quantum numbers. These data are also compiled on internet databases, among which the Leiden one (http ://www.strw.leidenuniv.nl/ moldata/). The Appendix J provides the full description of an extrapolation code based on the IOS approximation.

12.2 Improving our computational methods

Implementing more reliable LVG techniques. Another computational challenge and update of the LVG code consists of the implementation of new techniques to solve the equations of statistical equilibrium. Indeed, in certain cases, robust routines are required to avoid some computational instabilities that can easily arise in such conditions of temperatures and densities.

Among the techniques that have already proved to be more efficient than a simple Λ-iteration, one can cite :

- the accelerated Λ-iteration, based on the use of an approximate lambda operator combined with the preconditioning of the equations of statistical equilibirum (see Rybicki and Hummer (1991)) ;
- the Coupled Escape Probability for exact calculation of line emission from multi-level systems, solving only algebraic equations for the level populations (see Elitzur and Asensio Ramos (2006)).

Improving the shock code's accuracy. Following the recent works(Guillet et al. (2007)), a more accurate treatment of grains processing is always possible, though the cost in CPU time of these refined treatment make them a target for a non immediate future.

Another refinement of the shock code could be simply to include a LVG module in it, thus benefiting from the strong VODE method of solving non linear multiple differential equations. Attempts have been made to do so during this study, without success yet.

12.3 Improving the outputs of the LVG code

Extending the models grid. To perform accurate comparisons with observations, the number of models can be extended, by widening the ranges of various parameters, and by reducing the steps between the grids values for these parameters. Shock velocities range can be extended to the limits set by the different critical velocities in the pre-shock regions. The magnetic field parameter can be varied to the limits of the known situations (although there is a lack of observations for magnetic field strength). The density range cannot be extended, but smaller grid steps can be considered. In the case of CJ shocks, the age of the shock can be wider varied as well. Finally the angle of view of the shock or the flow has never been extensively investigated yet. The method to include this new parameter has been presented in Gusdorf et al. (2008a), and a brief study of its effects was also made available.

Implementing precise comparisons procedures. Once all these grids improvements are performed, it will be necessary for us to implement a rigorous procedure to compare observations to models results. This can be achieved by means of statistical tools, such as χ^2 methods over the sample of observations/models.

12.4 Modelling the spatial structure of the shock

Until now, the shocks have been considered as planar parallel, and viewed face on. A more accurate description requires to take the effects of inclination into account (in the escape probability and in the integrated intensity formula), which has already been done in our LVG code. In addition to this, the spatial structure of the shock could also be modelled more precisely.

In fact, the structure of the outflows are far from being planar parallel, but present an ellipsoidal shape : such objects are called bow-shocks. An extensive 3D modelling of such a structure would be impossible to perform in terms of CPU time, but it could be approximated by a continuous sum of planar parallel shocks, with shock velocities corresponding to the projection of the bow-shock velocity along the direction perpendicular to the structure. Once again, the effects of inclination of the shock with respect to the line of sight or the axis of the bow-shock must be taken into account : the surface brightness, brilliance temperature, and integrated intensity formula must be re-written.

These modifications have been made, and relations between those characteristic quantity for different inclinations (face on or with an inclination angle θ with $\mu = cos(\theta)$) have been calculated, obtained for brilliance temperature and integrated intensity, following the derivations presented in Appendix L. The code to actually compute the sum of plane parallel shocks and its inferred emission quantity such as the integrated intensity remains to be written, but the method has already been tested by Kristensen et al. (2008) for H_2 simulations.

13

Towards new fields of exploration

Une fois les améliorations méthodologiques décrites dans le chapitre précédent réalisées, de nouvelles pistes d'exploration seront possibles en termes d'utilisation du présent travail. De nouvelles raies moléculaires pourront être inclues dans l'études, d'autres flots bipolaires pourront aussi faire l'objet d'études similaires, grâce notamment à l'utilisation de nouveaux moyens d'observation (Herschel, ALMA). Enfin, d'autres objets astrophysiques pourront aussi être décrits à l'aide du même traitement, parmi lesquels les restes de supernovae, ou les galaxies brillantes en H_2.

13.1 Predicting other molecules emission

L1157 is the best example of a chemically active outflow, many observations being available, in other molecular lines than CO, SiO, or H_2. Generally speaking, objects of interest are often been observed in various molecular species, whether they are related to star formation or to supernovae remnants. Amongst these observations, some molecules present a modelling interest, as their importance as a probe for interstellar shock regions has been demonstrated, and also because their collisional rate coefficients have already been computed. These two last conditions ensure that their emission can be computed over a grid of models, and that the comparison between models and observations will provide further constraints on the physical conditions of the shocked region.

The case of H_2O, HDO and CO. From these points of view, H_2O is the most interesting molecule. It plays an important role in the thermal balance of the gas, and is the main repository of oxygen not to be locked up in CO. But even more important is its correlation with temperature. Indeed, it is frozen onto grains mantles at low temperatures (< 100 K), and is mostly in the gas phase at high temperatures ($> 100 - 300$ K), thanks to the sputtering the mantles undergo in such physical conditions. Its emission comparison with other shock tracers is stressed in Nisini et al. (2007). In addition to this, the existence of collisional data with He (Green et al. (1993)) and H_2 (Phillips et al. (1996), Dubernet and Grosjean (2002), and Grosjean et al. (2003)) made its modelling possible by Faure et al. (2007). Thanks to the work engaged in the Molecular Universe Network, improved data sets should soon be available. ISO observations have been made, only for a couple of lines,

by Giannini et al. (2001). H_2O has been made a priority target for Herschel observations, with specific emphasis in star formation and Supernovae Remnants programs, and also in the extra-galactic key project. Similarly, HDO should be studied extensively by Herschel, as well as CO, for which ground obtained data are already available, and the LVG code ready.

The shock tracers aimed at by Herschel. Other than SiO, one can cite CH^+ and H_2S, for which collisional data have yet to be calculated.

Other shock tracers in Star forming regions. To a smaller extent, being similarly attached to grains mantles at low temperatures, ammonia can also be studied. Regarding L1157, observations were compiled in Bachiller et al. (1993), and collisional data with collision partners He (Machin and Roueff (2005)) and H_2 (Danby et al. (1986)) are available. Another candidate for models-observations comparisons is OH. Although not systematically observed in outflow regions, this radical is known to be widespread in molecular clouds and to thermalize at densities lower than CO. It is thus expected to provide informations on the possible presence of low density gas in the outflow, difficult to detect even in CO. Again, concerning L1157, bservational data are available in Giannini et al. (2001) and collisional data have been computed with H_2 as a collision partner by Offer and van Dishoeck (1992). Similarly, HCN is a tracer of dense regions, as it has a high critical density. It has been observed in L1157 by Bachiller and Perez Gutierrez (1997), and its collisional rate coefficients have been computed by Green and Thaddeus (1974). SO and HCO^+ have also been known as a tracer of shocks. SO has been known as a tracer of shocks since Pineau des Forets et al. (1993). Consequently it is also a good target for models-observations comparisons, since its collisional rate coefficients were published by Green (1994), and because of its detection in L1157 (see Bachiller and Perez Gutierrez (1997)). Of similar interest is HCO^+, as its emission excess in bipolar outflows has been modelled by Rawlings et al. (2004), and as both collisional (Flower (1999)) and observational data (Bachiller and Perez Gutierrez (1997)) are available. For all these species, both collisional and observational data are available, and they have been rated as "prioritary" by the Herschel program (except for OH).

The list of potential molecules is much longer than the one that is suggested here. In the future, observations of numerous molecules such as SO_2, CH_3OH, H_2CO, CS, CN, HNC, and C_3H_2 will be available, as well as their collisional rate coefficients (some of them being already published).

13.2 Investigating more star forming regions

The comparison protocole can also be extended to new outflows regions, before or after adapting it to new molecular species.

The most logical candidate for such an extension of the study is L1448. Indeed, its SiO emission has been investigated as accurately as it has been for L1157 (see Nisini et al. (2007)). Unfortunately, no extensive excitation diagram for H_2 has been published to date. However, rotational transitions were observed by Nisini et al. (2000), and two rovibrational

lines were also studied by Davis and Eisloeffel (1995). CO and H_2O measurements have also been performed on this outflow, and made available by Nisini et al. (2000). SWAS measurements for the water transition at 557 GHz are also being published in Franklin et al. (2008).

Unfortunately, rare are the outflows to have been placed under such a meticulous scrutiny as L1157 and L1448 in terms of SiO line measurements. Nevertheless, articles such as Caratti o Garatti et al. (2006) and Giannini et al. (2001) provide enough observational data to perform cross comparisons between H_2, CO, H_2O and OH observations on NGC1333 IRAS 4, HH211, and IRAS18273+0113.

Larger samples with focuses on H_2 only for example can also be examined, using the available rotational or rovibrational data such as the ones compiled in Caratti o Garatti et al. (2006) over a large number of active jets. Such statistical sampling would provide a wider view on physical conditions in regions of molecular outflows, and hence on star formation.

13.3 Using the new generation's instruments

In a longer term future, the new generation of instruments will also play an important role in the surveys of spectral lines whose emission can already be predicted by models, aiming for the above molecules and/or regions. Among these future instruments, two are of particular importance :

- Herschel (under development, due for launch in 2008) is the fourth cornerstone mission in the horizon 2000 ESA science program : it's a 3.5 m class satellite telescope, with high angular resolution (11".3 at 157μm), and high signal to noise. The embarked HIFI spectrometer is expected to yield very high ($R = \lambda/\Delta\lambda \sim 10^6 - 10^7$) spectral resolution in the range 0.48-1.25THz and 1.41-1.91 THz, making HIFI the perfect instrument dedicated to the study of molecular emission. For example, this range covers 14 transitions of ortho-H_2O, when considering the first 25 energy levels ranging from 34 K to $\sim$ 1090 K above the ground state ;
- the Attacama Large Millimeter Array (ALMA), which consists of 64 12-m diameter antennas, with a surface accuracy of 20 μm, fo a total collecting area of 7238 m^2 with an angular resolution of 0.2". The receivers are designed to operate in 4 bands ranging from 86 to 720 GHz. ALMA should be able of achieving good brightness sensitivity for protostellar outflows, that are usually generated at a distance of several hundreds of pc, on scales smaller than 10 UA, allowing to study the detailed spatial distribution of the gas and dust. It should thus provide images in molecular lines at very high spatial and spectral resolution that are needed to disentangle the detailed velocity field within the envelopes, or to separate the disk/infall structure of the protostar. Thanks to multiline observations with such angular resolution and sensitivity, steps will thus be made forward detailed physical conditions and chemical structure of the shocks. Finally, ALMA will also be used through polarization measurements contributing to resolve the magnetic field structure, which is believed to play a fundamental role in the generation of bipolar outflows.

In the meantime, of course, the classical instruments can still be used to produce quality molecular emission observations, such as the JCMT, the 30-m antenna of IRAM, or APEX.

13.4 Broadening the field of applications

Beyond star-forming regions, various regions in the interstellar medium can be modelled by means of a shock code similar to the one that was made use of during this study.

Supernovae remnants. The MHD code can also be used to study supernovae remnants. From this point of view, IC 443 is the prime example of a SN blast wave with an ambient molecular cloud. Its interaction with this surrounding gas can be studied, and lead to useful information on the state of the shocked gas, also providing support for investigations of the chemistry across the shocked gas layer. Large amounts of H_2 observational data, both rotational and rovibrational are already available and can immediately lead to preliminary constraints on the physical conditions of the pre-shock region. Such a study has been initiated in the past by Cesarsky et al. (1999). CO observations are also available. Finally IC443 is a target for OH and H_2O studies which will help completing and refining the obtained constraints (see also Snell et al. (2005)).

w28 and w44 are other interesting candidates for models/observations comparisons. Integrated intensities values for a few CO lines are already available, some atomic lines have also been measured, and OH and H_2O future observations should also be likely to help a better modelling and understanding of their interaction with the surrounding gas.

Bright H_2 emitting galaxies. A new field of investigation has been recently opened with the discovery of strong mid-infrared emission lines of molecular hydrogen in extragalactic objects. Added to the lack of PAH features and low excitation gas tracers, the observers suggested that the H_2 emission could be generated by the shock wave caused by galactic interactions and collisions. Investigations are ongoing at the Institut d'Astrophysique Spatiale in an attempt to model these episodes using the very same shock code as ran to study bipolar outflows.

A

Source terms : chemistry

For further details concerning these equations, the interested reader can refer to Flower et al. (1985), Flower et al. (1986), Flower and Pineau-Des-Forets (1986).

A.1 Number and mass of created particles

We note $\mathcal{C}_\alpha$ the production rate of atomic and molecular species per unit of volume and time. Consequently, the total number of neutral and ionized particles created through chemical processes per unit of volume and time can be written

$$\mathcal{N}_\alpha = \sum_{\substack{\alpha, \\ \text{neutral} \\ \text{species}}} \mathcal{C}_\alpha \quad \text{and} \quad \mathcal{N}_\text{i} = \sum_{\substack{\alpha, \\ \text{ionized} \\ \text{species}}} \mathcal{C}_\alpha \tag{A.1}$$

Similarly we present the equations of mass transfer from the ionized fluid to the neutral fluid, and from the neutral fluid to the ionized fluid

$$\mathcal{S}_\alpha = \sum_{\substack{\alpha, \\ \text{neutral} \\ \text{species}}} \mathcal{C}_\alpha m_\alpha \quad \text{and} \quad \mathcal{S}_\text{i} = \sum_{\substack{\alpha, \\ \text{ionized} \\ \text{species}}} \mathcal{C}_\alpha m_\alpha \tag{A.2}$$

The condition $\mathcal{S}_i = -\mathcal{S}_n$ provides a check up of the consistency of the program.

A.2 Momentum

We note $\mathcal{C}_{\alpha\beta}$ the creation ($\mathcal{C}_{\alpha\beta} \geq 0$) or destruction ($\mathcal{C}_{\alpha\beta} \leq 0$) rate of the α species through the β reaction. Thus we have

$$\mathcal{C}_\alpha = \sum_\beta \mathcal{C}_{\alpha\beta} \tag{A.3}$$

The momentum transfer between neutral and ionized fluid can be the result of three different processes.

(i) Reactive (inelastic) collisions between ions and neutrals. The momentum transfer rate towards the neutral fluid per unit of volume and time is

$$\mathcal{A}_n^{(i)} = \sum_{\substack{\alpha, \\ \text{neutral} \\ \text{species}}} \sum_{\beta} \mathcal{C}_{\alpha\beta} m_\alpha v_\beta \tag{A.4}$$

where we assume that the α species is created with the velocity of the center of mass of the reaction β, v_β. If all the reactants are neutrals, $v_\beta = v_\mathrm{n}$, whereas if there are all ions, $v_\beta = v_\mathrm{i}$. For a reaction between a neutral and an ion, $v_\beta = (m_i v_\mathrm{i} + m_n v_\mathrm{n})/(m_i + m_n)$. Again, the condition

$$\sum_{\substack{\alpha, \\ \text{neutral} \\ \text{species}}} \sum_{\beta} \mathcal{C}_{\alpha\beta} m_\alpha v_\beta = \sum_{\substack{\alpha, \\ \text{ionized} \\ \text{species}}} \sum_{\beta} \mathcal{C}_{\alpha\beta} m_\alpha v_\beta \tag{A.5}$$

provides a checkup of the execution of the program.

(ii) Elastic collisions between ions and neutrals (ambipolar diffusion). The cross section of this process is

$$\sigma_{in} = 2.41\pi \left(\frac{e^2 \alpha_n}{\mu_{in} v_{in}^2} \right)^{1/2} \tag{A.6}$$

where e is the charge of the electron, α_n is the polarisability of neutrals, $\mu_{in} = \mu_i \mu_n/(\mu_i + \mu_n)$ is the reduced mass of the ion-neutral system, and v_{in} is their relative velocity. The corresponding rate coefficient is

$$< \sigma v >_{in} = 2.41\pi \left(\frac{e^2 \alpha_n}{\mu_{in}} \right)^{1/2} \tag{A.7}$$

and the momentum is transfered from ions to neutrals at the rate of

$$\mathcal{A}_n^{(ii)} = \frac{\rho_n \rho_i}{\mu_n + \mu_i} < \sigma v >_{in} (v_\mathrm{i} - v_\mathrm{n}) \tag{A.8}$$

We can notice that electron-neutral scattering is negligible with respect to the ion-neutral scattering.

(iii) Elastic collisions between grains and neutrals (ambipolar diffusion). Because they belong to the charged fluid, grains also play a role in momentum transfer, and they have a drift velocity with respect to the neutrals. A good approximate of the corresponding momentum transfer is

$$\mathcal{A}_n^{(iii)} = \pi a^2 |v_\mathrm{i} - v_\mathrm{n}| (v_\mathrm{i} - v_\mathrm{n}) \mu_{in} \tag{A.9}$$

where a is the radius of the grain, and $\mu_{in} = \mu_i \mu_n/(\mu_i + \mu_n)$ is the reduced mass of the grain-neutral system.

A.3 Energy

Energy transfers also exist between neutral and charged fluids, through chemical, collisional, or radiative processes. In this section, we interest ourselves to chemical ((i) to (iii)) and collisional ((iv) to (vi)) processes. We also mention one consequence of the photophysic activity of the interstellar medium (vii).

(i) Reactive collisions between ions and ions, neutrals and neutrals, ions and neutrals. Chemical reactions generate a transfer of kinetic energy because the product of the reaction has an actual velocity in the frame of the fluid. The corresponding rates for the neutral and ionized fluids are

$$\mathcal{B}_n^{(i)} = \sum_{\substack{\alpha, \\ \text{neutral} \\ \text{species}}} \sum_{\beta} \mathcal{C}_{\alpha\beta} \frac{1}{2} m_\alpha v_\beta^2 \quad \text{and} \mathcal{B}_i^{(i)} = \sum_{\substack{\alpha, \\ \text{ionized} \\ \text{species}}} \sum_{\beta} \mathcal{C}_{\alpha\beta} \frac{1}{2} m_\alpha v_\beta^2 \tag{A.10}$$

The corresponding term for electrons can be neglected.

(ii) Energy transfer between reactants (ions, electrons and neutrals). If we do take into account the enthalpy transfer between ionized and charged fluids, formation ($\mathcal{C}_{\alpha\beta} > 0$) and destruction ($\mathcal{C}_{\alpha\beta} < 0$) must be treated separately. If the reactions generating more than two products (like molecular dissociation, for example) are of no importance, as we assumed in the previous model, then neutrals are created via the recombination of an ion with an electron, with respective kinetic temperatures T_i et T_e, and are destructed through ionization at temperature T_n. Consequently, the rate at which enthalpy is added to the neutral fluid can be written

$$\mathcal{B}_n^{(ii)} = \sum_{\substack{\alpha, \\ \text{neutral} \\ \text{species}}} \left[\sum_{\substack{\beta, \\ \mathcal{C}_{\alpha\beta}>0}} \mathcal{C}_{\alpha\beta} \frac{3}{2} k \frac{T_\mathrm{i} + T_e}{2} + \sum_{\substack{\beta, \\ \mathcal{C}_{\alpha\beta}<0}} \mathcal{C}_{\alpha\beta} \frac{3}{2} k T_\mathrm{n} \right] \tag{A.11}$$

We can proceed similarly for ions

$$\mathcal{B}_i^{(ii)} = \sum_{\substack{\alpha, \\ \text{ionized} \\ \text{species}}} \left[\sum_{\substack{\beta, \\ \mathcal{C}_{\alpha\beta}>0}} \mathcal{C}_{\alpha\beta} \frac{3}{2} k T_\mathrm{n} + \sum_{\substack{\beta, \\ \mathcal{C}_{\alpha\beta}<0}} \mathcal{C}_{\alpha\beta} \frac{3}{2} k T_\mathrm{i} \right] \tag{A.12}$$

and eventually for electrons

$$\mathcal{B}_e^{(ii)} = \sum_{\substack{\alpha, \\ \text{ionized} \\ \text{species}}} \sum_{\substack{\beta, \\ \mathcal{C}_{\alpha\beta}<0}} \mathcal{C}_{\alpha\beta} \frac{3}{2} k T_e \tag{A.13}$$

(iii) Endothermicity and exothermicity of chemical reactions. This contribution can take part in the heating or to the cooling of the medium. Consequently, ΔE, the energy

default of chemical reactions can influence the thermal balance, with a heating (or cooling) rate of the neutral fluid per unit of volume and time equal to

$$\mathcal{B}_n^{(iii)} = \sum_{\substack{\alpha, \\ \text{neutral} \\ \text{species}}} \sum_{\substack{\beta, \\ \mathcal{C}_{\alpha\beta}>0}} \mathcal{C}_{\alpha\beta} \frac{M_\beta - m_\alpha}{M_\beta} \Delta E_\alpha \tag{A.14}$$

where M_β is the total mass of the products of the reaction β. Similarly we have for the ionized fluid

$$\mathcal{B}_i^{(iii)} = \sum_{\substack{\alpha, \\ \text{ionized} \\ \text{species}}} \sum_{\substack{\beta, \\ \mathcal{C}_{\alpha\beta}>0}} \mathcal{C}_{\alpha\beta} \frac{M_\beta - m_\alpha}{M_\beta} \Delta E_\alpha \tag{A.15}$$

(iv) Elastic collisions between ions and neutrals. Heat is also exchanged between the different fluids through ion-neutral scattering. The heating rate of the neutrals generated by this process is given by

$$\mathcal{B}_n^{(iv)} = \frac{\rho_n \rho_i}{\mu_n \mu_i} < \sigma v >_{in} \frac{2\mu_n \mu_i}{(\mu_n + \mu_i)^2} \left[\frac{3}{2} k (T_\mathrm{i} - T_\mathrm{n}) + \frac{1}{2} (v_\mathrm{i} - v_\mathrm{n})(\mu_i vi + \mu_n v_\mathrm{n}) \right] \tag{A.16}$$

(v) Elastic collisions between electronic and neutrals. A similar expression is still valid for electron-neutral scattering, and simplifies thanks to the fact that $m_e \ll \mu_n$

$$\mathcal{B}_n^{(v)} = \frac{\rho_n \rho_i}{\mu_n \mu_i} < \sigma v >_{en} \frac{2m_e}{\mu_n} \left[\frac{4}{2} k (T_e - T_\mathrm{n}) + \frac{1}{2} (v_\mathrm{i} - v_\mathrm{n}) \mu_n v_\mathrm{n} \right] \tag{A.17}$$

where the scattering cross section is considered as independent on the energy, with

$$< \sigma v >_{en} = 10^{-19} \left(\frac{8kT_e}{\pi m_e} \right)^{1/2} \mathrm{m}^3 \ \mathrm{s}^{-1} \tag{A.18}$$

(vi) Elastic collisions between electrons and ions. The heating rate of the fluid of electrons through coulombian scattering on ions can be estimated with the following expression

$$\mathcal{B}_e^{(vi)} = \frac{4e^4}{\mu_i k T_e} \left(\frac{2\pi m_e}{k T_e} \right)^{1/2} \ln \Lambda \left(\frac{\rho_i}{\mu_i} \right)^2 k (T_\mathrm{i} - T_e) \tag{A.19}$$

with $\mathcal{B}_i^{(vi)} = -\mathcal{B}_e^{(vi)}$, and where

$$\Lambda = \frac{3}{2e^3} \left(\frac{k^3 T_e^3 \mu_i}{\pi \rho_i} \right)^{1/2} \tag{A.20}$$

(vii) Other source terms for electrons. Non thermal electrons are also injected through ionization of the atoms and molecules of the gas by cosmic rays, and significantly thermalized (heating via photoelectric effect on grains can also be significant, but is subjected to considerable uncertainties on the physical properties of the grains). The injection rate of energy (in the grains fluid) through this process is $\delta E \zeta \rho_\mathrm{n} / \mu_n$, where δE

is the average energy transfered to the electron gas via ionization by cosmic rays, and ζ is the ionization rate by cosmic rays. Ideally, the heating rate through photoionization should be given by

$$\mathcal{B}_e^{(vii)} = \sum_\alpha n_\alpha \int_{\nu_\alpha}^{\nu_H} \frac{4\pi J_\nu}{h\nu} a_\nu(\alpha)(h\nu - h\nu_\alpha) d\nu \tag{A.21}$$

where J_ν is the mean intensity at frequency ν, $a_\nu(\alpha)$ is the photoionization cross section for the species α (depending on the frequency), and ν_α is the threshold frequency of photoionization. The integrate should be calculated until the Lyman limit of hydrogen (given by $h\nu_H = 13.598\text{eV}$). In practice, one often has to consider an estimate of the value of the integrate of the equation A.21, because of the uncertainties on the mean radiation intensity and on the frequency dependance of the photoionization cross section. We use the formula

$$\delta E(\text{eV}) \;=\; \max\left\{5.7, \left[32 - 7\log\left(\frac{\rho_n}{\rho_i}\frac{\mu_i}{\mu_n}\right)\right]\right\} \tag{A.22}$$

The corresponding photoionization rate for the electrons fluid then writes

$$\mathcal{B}_e^{(vii)} = \sum_\alpha \delta E_\alpha \gamma_\alpha n_\alpha \tag{A.23}$$

where δE_γ stands for the average energy of the photoelectron produced by the photoionization of the α species, with a density n_α, and which photoionization rate is γ_α.

B

Source terms : molecular cooling

B.1 Molecular vibrations and rotations

The atoms of a molecule are never in a steady state, whatever value the temperature could be reaching. In fact, even in a solid which temperature approaches the absolute zero, atoms constantly oscillate around their equilibrium position. Two kinds of movements can be characterised in this oscillation : vibration and rotation.

Rotational movements of a molecule can be described by means of a model of rigid rotator. The resolution of the Schrodinger equation for a molecule in free three-dimensional rotation shows that the rotational energy of a diatomic rigid rotator is quantized. In other terms, the energy of two atoms bound by a rigid bond can only have well defined values. However, the description of molecule with a rigid rotator model is only an approximation, because the nuclei also vibrate. In addition to this, centrifugal forces due to the rotation of the molecule generate a slight distorsion which itself provokes a modification of its inertia momentum. Taking the effects into account, the rotational energy levels (in joules) are given by

$$E_r = hcBJ(J+1) - hcDJ^2(J+1)^2 \tag{B.1}$$

where B is the rotational constant, expressed in cm^{-1}, related to the inertia momentum I via

$$B = h/8\pi^2 cI \tag{B.2}$$

and where D is the centrifugal distorsion constant, related to the vibration frequency ω of the molecule through the equation

$$D = 4B^3/\omega^2 \tag{B.3}$$

J is the rotational quantum number of the molecule ($J = 0, 1, 2, ...$), which gives the value of the rotational kinetic moment (equal to $\sqrt{J(J+1)}h/2\pi$), c is the light velocity in the vacuum, and h is Planck's constant. The order of magnitude of the rotational energy is typically 1 J mol^{-1}.

The vibrational movements of a molecule can be described by means of the harmonic oscillator model. Once again, the resolution of the equation of Schrödinger for a unidimensional oscillator shows that the vibrational energy of a molecule is also quantized.

Nevertheless, nuclei vibrations are never simple harmonic vibrations. The stretch of the oscillator is never perfectly elastic, and the vibrations are anharmonic. Taking this effect into account, the possible values of the vibrational energy of a diatomic molecule (in joules) are given by

$$E_v = (v + \frac{1}{2})hc\omega_e - (v + \frac{1}{2})^2 hcx_e\omega_e + (v + \frac{1}{2})^3 hcy_e\omega_e + \dots \tag{B.4}$$

where v is the vibrational quantum number ($v = 0, 1, 2, ...$), ω_e is the hypothetical frequency of the small amplitude vibrations around the equilibrium position of the nuclei, and x_e and y_e are the anharmonic constants. The typical value of the vibrational energy is around 10^3 J mol^{-1}.

To these values of rotational and vibrational energy correspond several populated levels, between which quantum mechanics allows us to determine every permitted transition. Precisely, these transitions can be provoked by collisions likely to occur in interstellar shocks. These transitions accompany emission of photons, which can contribute to the cooling or heating of the interstellar gas. In the following calculations, we won't take distorsion or anharmonicity into account (that is, all the terms following the '-' in the expressions of rotational and vibrational energies). We will study only the case of molecular hydrogen, keeping in mind that rotational and/or vibrational de-excitation of other molecules such as CO, OH, NH_3, ou H_2O are also taken into account in the model.

B.2 The case of molecular hydrogen

Molecular hydrogen is of particular interest because of its important fractional abundance in the interstellar medium. Indeed, even if coefficient rates of the reactions in which molecular hydrogen is involved are rather low, they occur so many times that they have to be taken into account as major processes.

Molecular hydrogen being an homonuclear molecule, its mass centre is the same as the electric charge's barycentre. Consequently, molecular hydrogen has no permanent electric dipolar moment, and radiative transitions associated to an electronic transition are of quadrupolar kind. Nevertheless, molecular hydrogen being by far the most abundant molecule of the interstellar medium, its contribution to the heating or cooling of the ambiant gas is prevailing.

The lack of permanent electric dipolar moment has two important consequences for molecular hydrogen :

- molecular hydrogen exists in two forms, called ortho- or para- H_2. In the ortho-H_2, nuclear spins are aligned, thus $I = 1$, whereas for para-H_2, nuclear spins are anti-parallel, and consequently $I = 0$. Nuclei being made of identical fermions, the nuclear wave function that includes vibrational, rotational, and spin effects, must be antisymmetric with respect to the swap of photons. The wave function describing the fundamental state for vibration is invariant through this operation, whereas the rotational part of the wave function is multiplied by (-1)^J, where J is the rotational quantum number. The spin function of the triplet, $I = 1$, is symmetric with respect to proton swap, whereas the spin function of the singulet, $I = 0$, is antisymmetric.

The state $I = 1$ (ortho-H_2) then corresponds to odd values of J, and the state $J = 0$ (para-H_2) is associated to even J values ;

- quadrupolar transitions don't allow the transition to one form from another.

Nevertheless, transitions remain possible between rovibrational levels of molecular hydrogen, which can play an important role in the energy transfers along the shock. This contribution must be taken into account in the source terms of the equations of conservation. Consequently, the populations of all the levels of molecular hydrogen must be computed.

B.3 Molecular hydrogen cooling

The method of evaluation of the contribution to the cooling by molecular hydrogen is presented in Flower et al. (1986). We call n_J the population density of the rotational level J of molecular hydrogen. The total density of molecular hydrogen is thus

$$n(H_2) = \sum_J n_J \tag{B.5}$$

and the total density of hydrogen nuclei is

$$n(H) = n(H^0) + 2n(H_2) \tag{B.6}$$

$A(J \longrightarrow J-2)$ is the rate of spontaneous radiative decay of the level $J \geq 2$ (in s^{-1}). The corresponding collisional de-excitation rate is

$$C(J \rightarrow J-2) = n_J \left[n(H^0) + n(H_2)\right] < \sigma v >_{J \rightarrow J-2} \tag{B.7}$$

where $< \sigma v >_{J \longrightarrow J-2}$ is the coefficient rate of collisional de-excitation, which we assume identical for molecular or atomic hydrogen. The collisional excitation rate is related to B.7 through the 'detailed balance'

$$(2J-3)C(J-2 \rightarrow J) = (2J+1)C(J \rightarrow J-2)\exp(-x) \tag{B.8}$$

with

$$x = 2(2J-1)B/kT_{\rm n} \tag{B.9}$$

In equation B.9, B is the rotational constant of H_2 in his fundamental vibrational state, and k is Boltzmann's constant. In our calculations, we use the expression

$$\begin{aligned} < \sigma v >_{J \rightarrow J-2} &= 4.6 \times 10^{-12}(2J-3)T_{\rm n}^{1/2}(1+x)^{1/2} \\ &\times \exp\left[\frac{-5.01x}{1+BJ(J+1)/kT_{\rm n}} - 0.1187(4J-2)\right] \end{aligned} \tag{B.10}$$

If we only consider radiative and collisional transitions between rotational levels, the gradient of the population flux of the state J in a stationary state writes

$$\begin{aligned} \frac{d}{dz}(v_{\rm n} n_J) &= \left[C(J+2 \rightarrow J) + A(J+2 \rightarrow J)\right] n_{J+2} \\ &- \left[C(J \rightarrow J+2) + C(J \rightarrow J-2) + A(J \rightarrow J-2)\right] n_J \\ &+ C(J-2 \rightarrow J) n_{J-2} \end{aligned} \tag{B.11}$$

where $v_{\rm n}$ is the neutral fluid velocity in the z direction. At the static limit, $v_{\rm n} = 0$, and left's part of the equation B.11 vanishes.

In practice, the population flux of the J level can also evolve because of the chemical reactions that create or destroy molecular hydrogen. If we assume that chemical reactions populate (and de-populate) the levels proportionally to their local density, then the equation B.11 can be generalized

$$\begin{aligned}\frac{d}{dz}(v_{\rm n} n_J) &= \left[C(J+2\rightarrow J)+A(J+2\rightarrow J)\right] n_{J+2} \\ &- \left[C(J\rightarrow J+2)+C(J\rightarrow J-2)+A(J\rightarrow J-2)\right] n_J \\ &+ C(J-2\rightarrow J) n_{J-2} \\ &+ \frac{n_J}{n(H_2)}\frac{d}{dz}\left[u_n n(H_2)\right] \end{aligned} \tag{B.12}$$

where $u_n n(H_2)$ is the molecular flux of molecular hydrogen.

The radiative cooling rate of the gas via rotational transitions for molecular hydrogen can then write

$$\left[\mathcal{B}_n(H_2)\right]_{radiative} = -\sum_{J\geq 2} n_J A(J\rightarrow J-2) 2(2J-1) B \tag{B.13}$$

As the populations of the excited states of molecular hydrogen are likely to grow a lot along the shocks, their contribution to the internal energy of the fluid must also be taken into account. The internal energy of neutral gas per volume unit is

$$\frac{\rho_n}{\mu_n} U_n = \sum_{v,J} n(v,J) E(v,J) \tag{B.14}$$

where $n(v,J)$ is the density of molecular hydrogen in the rovibrational state (v,J), and where $E(v,J)$ is the corresponding excitation energy. We don't take the excited vibrational states into account, and we then obtained

$$\frac{\rho_n}{\mu_n} U_n = \sum_{v,J} n_J B J(J+1) \tag{B.15}$$

Among the necessary conditions to seal the neutral particles energy conservation, we thus have

$$\frac{d}{dz}\left(\frac{\rho_n v_{\rm n} U_n}{\mu_n}\right) = \sum_J B J(J+1)\frac{d}{dz}(u_n n_J) \tag{B.16}$$

where $d(u_n n_J)/dz$ is provided by equation B.12.

Previously, we have assumed that the de-excitation coefficients for atomic and molecular hydrogen were identical. The key point is that molecular hydrogen requires a special treatment because of its important abundance in the interstellar medium, and in spite of its symmetry that prevents the existence of a permanent electric dipolar moment.

C

The influence of chemical processes on the structure of the shock

By allowing the interstellar medium to reach unusual temperatures, interstellar shocks also initiate chemical reactions that are not likely to occur under 'normal' conditions. Through these chemical processes, species are formed or destroyed, ions or neutrals added to the corresponding fluids, that then play a role in the thermal balance of the shock, which has an influence on the number of reactions the shock can initiate, and so on. Our interest in this Chapter is to study the influence of those chemical processes on the structure of the shock, through the examples of carbon- and oxygen-bearing species (see Flower (1987)).

C.1 Carbon-bearing species

There is a history of mutually beneficial interaction between 'classical' interstellar chemistry and the study of interstellar shocks. For example, the old question of explaining the amount of CH^+ has perhaps found its solution with the study of interstellar shocks. Early studies showed that radiative association

$$C^+ + H \longrightarrow CH^+ + h\nu$$

was too slow a process, in comparison with dissociative recombination,

$$CH^+ + e^- \longrightarrow C + H$$

to account for the observed column density of CH^+. The ion-molecule reaction

$$C^+ \ + \ H_2 \ \longrightarrow \ C\,H^+ \ + \ H \qquad \text{(C.1)}$$

was mentioned as an alternative, but the endothermicity of this reaction (0.4 eV) is much larger than the thermal energy ($\simeq$ 0.01 eV) available in the cold interstellar gas, and so the reaction C.1 was discounted. It was years later that it was realized that shocks might provide the energy required to overcome the endothermicity of this reaction.

In quantitative terms, the energy required is provided when the ion-neutral drift speed, (v_i - v_n) $\geq$ 7 km s^{-1}, and reaction C.1 then proceeds with a rate constant k$\approx 10^{-10}$cm^3

s^{-1}. Once formed, CH^+ can be destroyed in two principal reactions. The first one is a ion-molecule reaction

$$CH^+ \ + \ H_2 \ \longrightarrow \ CH_2^+ \ + \ H \tag{C.2}$$

whose rate coefficient has the Langevin value, $k = 1.2 \times 10^{-9}$ cm^3 s^{-1}, independent of the temperature. Alternatively, dissociative recombination may occur,

$$CH^+ \ + \ e^- \ \longrightarrow \ C \ + \ H \tag{C.3}$$

whose rate coefficient depends on the temperature, and is about 2.9 $\times 10^{-7}$ cm^3 s^{-1} at $T = 300$ K. In shocks, reaction C.2 proceeds more rapidly than C.3 if the ratio of the electron and molecular hydrogen densities is such as $n_e/n(H_2) \leq 5 \times 10^{-3}$, which is generally the case in diffuse clouds.

The formation of CH_2^+ is followed rapidly by

$$CH_2^+ \ + \ H_2 \ \longrightarrow \ CH_3^+ \ + \ H \tag{C.4}$$

but this particular chain effectively ends here, because the reactions that would be likely to follow have a too large endothermicity (and are consequently too slow). Instead, CH_3^+ undergoes dissociative recombination,

$$CH_3^+ \ + \ e^- \ \longrightarrow \ CH_2 \ + \ H_2 \tag{C.5}$$

The net effect of this sequence of reactions is to neutralize the C^+ ions. When these are a major component of the ionized gas, the interaction with the magnetic field and hence the structure of the shock (via the length of the magnetic precursor, for example, see Subsection 2.1.2 or Draine (1980)) can be greatly affected by this chemical sequence.

In diffuse clouds, the sequence of reactions does not end with C.5. Photodissociation can occur

$$CH_2 \ + \ h\nu \longrightarrow CH \ + \ H \tag{C.6}$$

and

$$CH \ + \ h\nu \longrightarrow C \ + \ H \tag{C.7}$$

as well as photoionization,

$$CH \ + \ h\nu \longrightarrow CH^+ \ + \ e^- \tag{C.8}$$

reactions C.7 and C.8 proceeding with comparable rates. Reaction C.8 may be followed by C.2, recycling the CH^+, or by photodissociation

$$CH^+ \ + h\nu \ \longrightarrow C \ + \ H^+ \tag{C.9}$$

The neutral atomic carbon produced in C.7 and C.9 may be ionized by the radiation field,

$$C \ + \ h\nu \longrightarrow C^+ \ + \ e^- \tag{C.10}$$

One can easily understand that these last two reactions are crucially important to the degree of ionization of the gas. The width of a MHD shock is inversely proportional to

the ion density, and changes in the shock profile are reflected in the column densities of species such as CH^+, which are formed preferentially within the shock.

Shocks are also a possible source of interstellar C_3H_2. The CH, which is produced, for example, in C.6 above can react with C^+,

$$C^+ \ + \ CH \ \longrightarrow \ C_2^+ \ + \ H \tag{C.11}$$

initiating the hydrogen-abstraction sequence :

$$\begin{array}{rcl} C_2^+ + H_2 & \longrightarrow & C_2H^+ + H \\ C_2H^+ + H_2 & \longrightarrow & C_2H_2^+ + H \\ C_2H_2^+ + H_2 & \longrightarrow & C_2H_3^+ + H - 800K \end{array} \tag{C.12}$$

The following reaction of the chain is too endothermic to have to be taken into account. The neutral hydrocarbons C_2H and C_2H_2 may then be produced by dissociative recombination of $C_2H_2^+$ and $C_2H_3^+$. Then another reactions chain can occur, likely to produce more complex species, like cyclic carbon-bearing molecules, which may themselves modify the structure of the shock.

C.2 Oxygen-bearing species

Unlike carbon, atomic oxygen has an ionization potential which exceeds that of hydrogen and is consequently not ionized by the background radiation field. In the ambient medium, the oxygen chemistry is initiated either by the charge exchange process

$$H^+ \ + \ O \ \longrightarrow \ H \ + \ O^+ \ - \ 227 \ K \tag{C.13}$$

followed by hydrogen abstraction and dissociative recombination reactions analogous to those considered above, or by

$$H_3^+ \ + \ O \ \longrightarrow \ O \, H^+ \ + \ H_2 \tag{C.14}$$

followed by

$$\begin{array}{rcl} OH^+ + H_2 & \longrightarrow & H_2O^+ + H \\ H_2O^+ + H_2 & \longrightarrow & H_3O^+ + H \end{array}$$

and dissociative recombination of the product ions. In either case, the initial ion (H^+ in C.13 or H_3^+ in C.14) is produced directly by cosmic ray ionization (CR)

$$H \ + \ CR \ \longrightarrow \ H^+ \ + \ e^- + \ CR \tag{C.15}$$

$$H_2 \ + \ CR \ \longrightarrow \ H_2^+ \ + \ e^- + \ CR \tag{C.16}$$

followed by

$$H_2^+ \ + \ H_2 \ \longrightarrow \ H_3^+ \ + \ H \tag{C.17}$$

Cosmic rays with energy of a few MeV are believed to be responsible for C.15 and C.16, but the rates of cosmic-ray ionization have to be deduced indirectly.

Within shocks, on the other hand, the temperature of the neutral gas can be sufficiently high to drive the neutral-neutral reactions

$$O + H_2 \longrightarrow O H + H \tag{C.18}$$

and

$$OH + H_2 \longrightarrow H_2 O + H \tag{C.19}$$

In diffuse clouds, OH and H_2O may be removed by photodissociation,

$$OH + h\nu \longrightarrow O + H \tag{C.20}$$

and

$$H_2 O + h\nu \longrightarrow OH + H \tag{C.21}$$

but can also react with C^+,

$$C^+ + OH \longrightarrow CO^+ + H \tag{C.22}$$

and

$$C^+ + H_2O \longrightarrow HCO^+ + H \tag{C.23}$$

The CO^+ which is produced in C.23 reacts with H_2, yielding HCO^+,

$$CO^+ + H_2 \longrightarrow HCO^+ + H \tag{C.24}$$

which dissociatively recombines,

$$HCO^+ + e^- \longrightarrow CO + H \tag{C.25}$$

Reactions C.23-C.25 are sufficiently rapid to ensure that substantial amounts of CO are produced in shocks which propagate in diffuse interstellar clouds. And again, the shocks initiate reactions that form species which react with other species and which modify the structure of the shock.

These two examples show the influence of the chemical processes, and the importance of the interaction between chemistry and hydrodynamics.

D

H_2 rovibrational levels

Tableau D.1 – H_2 rovibrational levels energy table for v = 0, 1, 2.

v=0, J	Energy (K)	v=1, J	Energy (K)	v=2, J	Energy (K)
0	000.00	0	5987.1	0	11636
1	170.50	1	6149.2	1	11790
2	509.85	2	6471.6	2	12095
3	1015.2	3	6951.6	3	12551
4	1681.7	4	7584.6	4	13151
5	2503.9	5	8365.3	5	13891
6	3474.4	6	9286.6	6	14764
7	4586.4	7	10342	7	15763
8	5829.8	8	11522	8	16881
9	7197.0	9	12818	9	18107
10	8677.3	10	14221	10	19435
11	10262	11	15722	11	20854
12	11940	12	17311	12	22355
13	13703	13	18980	13	23931
14	15540	14	20718	14	25571
15	17444	15	22517	15	27266
16	19403	16	24368	16	29009
17	21412	17	26264	17	30792
18	23460	18	28195	18	32606
19	25540	19	30155	19	34445
20	27645	20	32135	20	36300
21	29767	21	34130	21	38165
22	31900	22	36131		
23	34038	23	38134		
24	36175				
25	38305				

Tableau D.2 – H_2 rovibrational levels energy table for v = 3, 4, 5.

v=3, J	Energy (K)	v=4, J	Energy (K)	v=5, J	Energy (K)
0	16953	0	21943	0	26607
1	17098	1	22080	1	26736
2	17388	2	22353	2	26993
3	17819	3	22760	3	27375
4	18387	4	23296	4	27879
5	19086	5	23956	5	28499
6	19912	6	24734	6	29230
7	20857	7	25624	7	30064
8	21912	8	26617	8	30996
9	23070	9	27707	9	32016
10	24323	10	28884	10	33116
11	25660	11	30140	11	34290
12	27074	12	31467	12	35527
13	28557	13	32855	13	36820
14	30098	14	34297	14	38160
15	31690	15	35784		
16	33325	16	37308		
17	34994	17	38861		
18	36690				
19	38405				

Tableau D.3 – H_2 rovibrational levels energy table for v = 6, 7, 8.

v=6, J	Energy (K)	v=7, J	Energy (K)	v=8, J	Energy (K)
0	30943	0	34946	0	38606
1	31064	1	35059	1	38709
2	31305	2	35282	2	38915
3	31662	3	35615	3	39221
4	32133	4	36052		
5	32713	5	36590		
6	33395	6	37222		
7	34174	7	37943		
8	35041	8	38744		
9	35990				
10	37013				
11	38101				

E

H_2 critical densities

Tableau E.1 – Critical densities (cm^{-3}), n_{crit}, at which the probabilities of collisional and radiative de-excitation are equal, for the first transitions of H_2. The collisional partner is He, and the transition wavelengths are also indicated in μm. Numbers in parentheses are powers of 10.

Jup	λ (μm)	n_{crit} (100 K)	n_{crit} (500 K)	n_{crit} (1000 K)	n_{crit} (2000 K)
0-0 S(0)	28.2	3.0(+01)	5.5(+00)	2.1(+00)	9.0(-01)
0-0 S(1)	17.0	8.3(+02)	1.2(+02)	3.6(+01)	1.3(+01)
0-0 S(2)	12.3	1.7(+04)	1.3(+03)	3.1(+02)	9.0(+01)
0-0 S(3)	9.66	1.7(+05)	9.5(+03)	1.8(+03)	4.3(+02)
0-0 S(4)	8.02	1.7(+06)	5.5(+04)	7.9(+03)	1.5(+03)
0-0 S(5)	6.91	7.4(+06)	2.3(+05)	2.9(+04)	4.9(+03)
0-0 S(6)	6.11	2.7(+07)	7.5(+05)	8.7(+04)	1.3(+04)
0-0 S(7)	5.51	9.4(+07)	2.3(+06)	2.4(+05)	3.1(+04)
1-0 S(1)	2.12	1.7(+13)	6.1(+10)	1.7(+09)	6.0(+07)
1-0 S(2)	2.03	1.3(+13)	5.2(+10)	1.5(+09)	5.0(+07)
2-1 S(1)	2.25	3.3(+12)	1.8(+10)	6.5(+08)	3.0(+07)

Tableau E.2 – Critical densities (cm^{-3}), n_{crit}, at which the probabilities of collisional and radiative de-excitation are equal, for the first transitions of H_2. The collisional partner is H_2, and the transition wavelengths are also indicated in μm. Numbers in parentheses are powers of 10.

Jup	λ (μm)	n_{crit} (100 K)	n_{crit} (500 K)	n_{crit} (1000 K)	n_{crit} (2000 K)
0-0 S(0)	28.2	4.9(+01)	1.3(+01)	5.1(+00)	1.9(+00)
0-0 S(1)	17.0	9.3(+02)	2.2(+02)	8.0(+01)	2.7(+01)
0-0 S(2)	12.3	1.8(+04)	2.4(+03)	6.4(+02)	1.8(+02)
0-0 S(3)	9.66	3.0(+05)	1.9(+04)	3.6(+03)	8.2(+02)
0-0 S(4)	8.02	2.6(+06)	1.1(+05)	1.6(+04)	3.0(+03)
0-0 S(5)	6.91	1.2(+07)	4.4(+05)	5.7(+04)	9.2(+03)
0-0 S(6)	6.11	3.9(+07)	1.4(+06)	1.8(+05)	2.5(+04)
0-0 S(7)	5.51	1.0(+08)	3.9(+06)	4.7(+05)	6.2(+04)
1-0 S(1)	2.12	2.6(+12)	2.0(+11)	1.4(+10)	5.1(+08)
1-0 S(2)	2.03	4.0(+12)	2.4(+11)	1.6(+10)	5.5(+08)
2-1 S(1)	2.25	4.3(+12)	8.1(+10)	3.9(+09)	1.4(+08)

F

SiO rotational levels

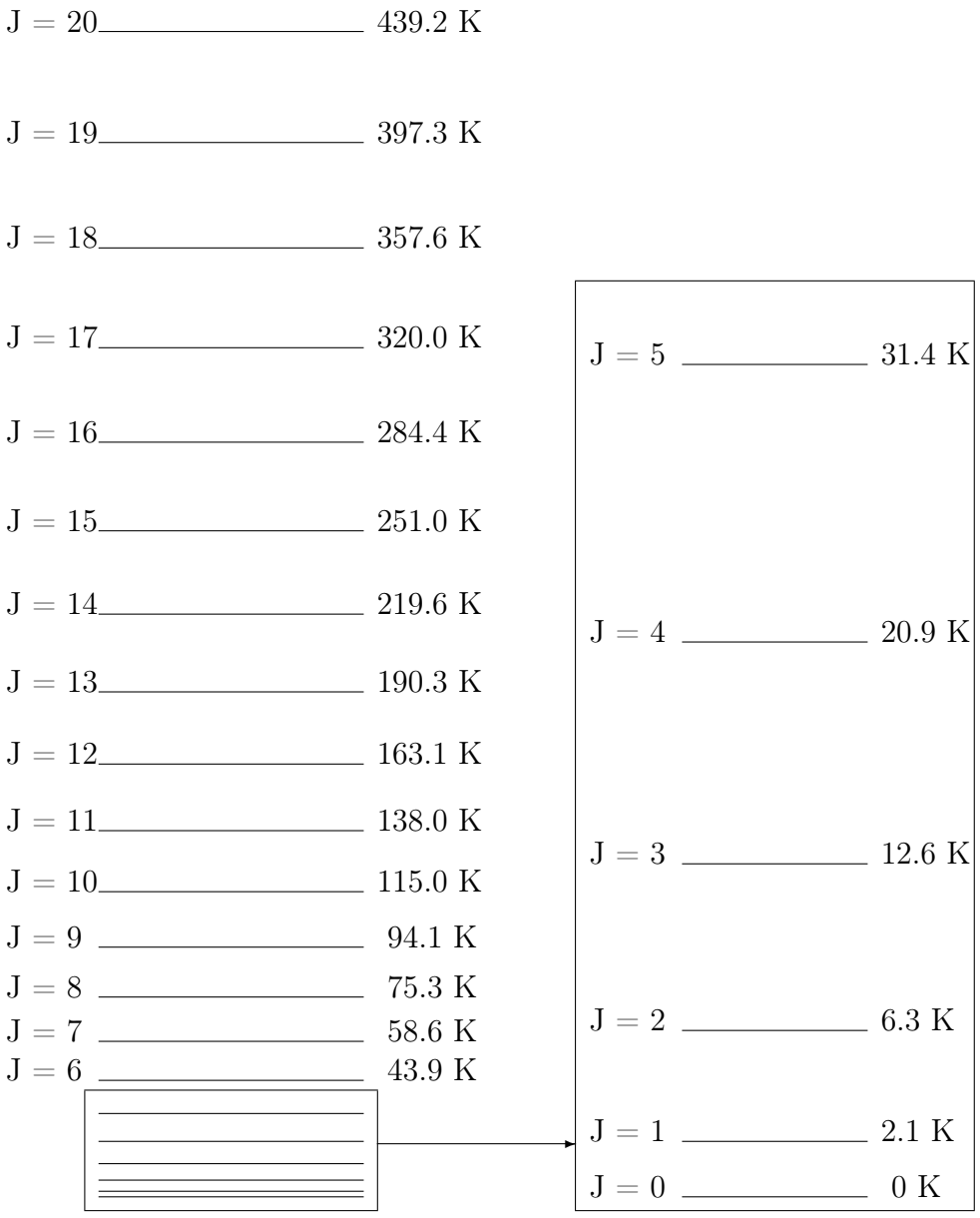

G

CO rotational levels

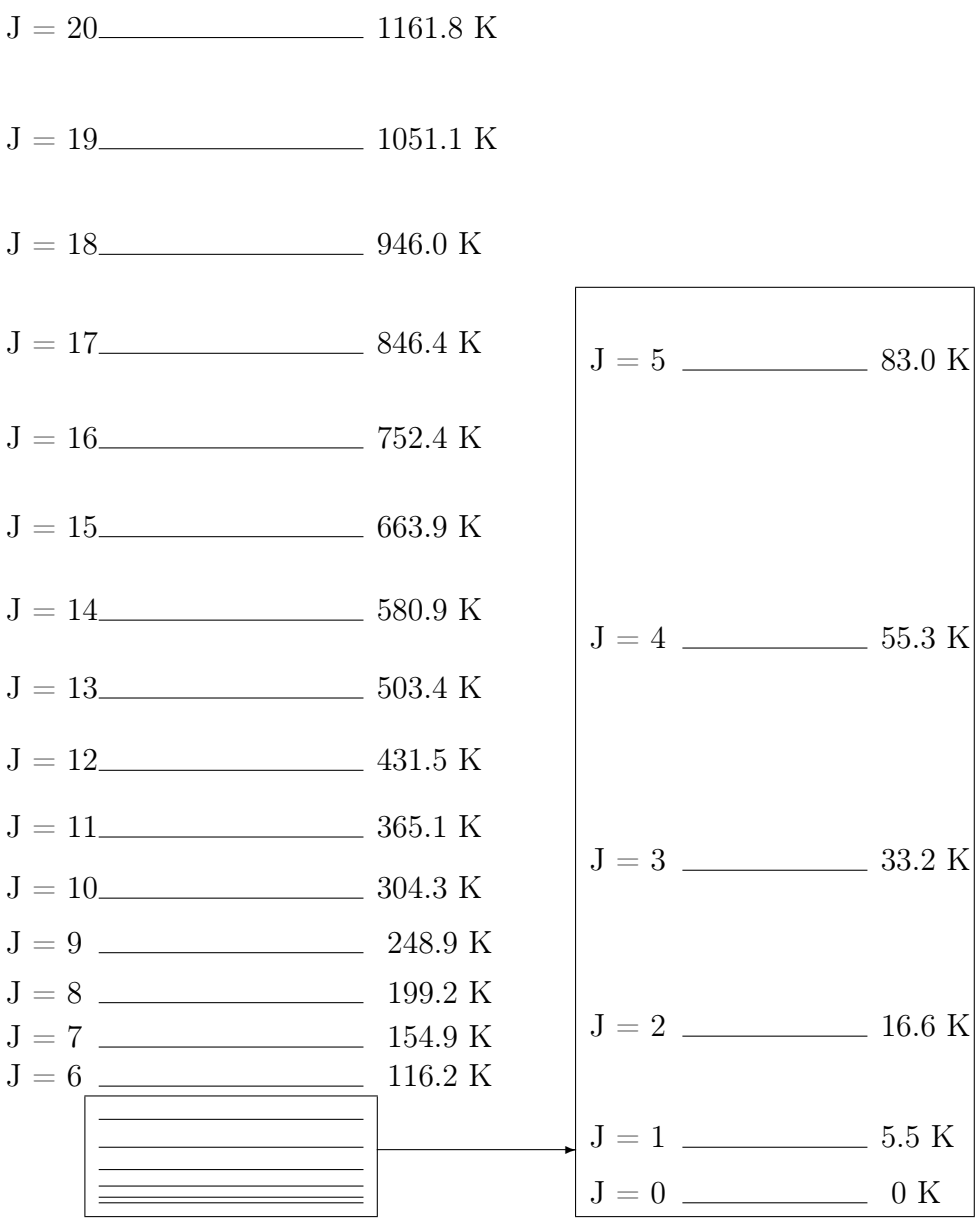

H

SiO critical densities

Tableau H.1 – Critical densities (cm^{-3}), n_{crit}, at which the probabilities of collisional and radiative de-excitation are equal, for the first transitions of SiO. The collisional partner is He, and the energy of the upper level is also given in K. Numbers in parentheses are powers of 10.

Jup	Energy (K)	n_{crit} (10 K)	n_{crit} (50 K)	n_{crit} (100 K)	n_{crit} (300 K)
1	2.1	5.2(+04)	6.8(+04)	7.8(+04)	9.3(+04)
2	6.3	3.5(+05)	4.0(+05)	4.2(+05)	4.5(+05)
3	12.6	1.2(+06)	1.4(+06)	1.4(+06)	1.3(+06)
4	20.9	2.9(+06)	3.3(+06)	3.3(+06)	3.1(+06)
5	31.4	6.1(+06)	6.6(+06)	6.6(+06)	6.1(+06)
6	43.9	1.1(+07)	1.2(+07)	1.2(+07)	1.1(+07)
7	58.6	1.8(+07)	1.9(+07)	1.9(+07)	1.8(+07)
8	75.3	2.8(+07)	2.8(+07)	2.8(+07)	2.7(+07)
9	94.1	4.0(+07)	4.0(+07)	4.0(+07)	3.8(+07)
10	115.0	5.6(+07)	5.5(+07)	5.5(+07)	5.2(+07)
11	138.0	7.4(+07)	7.4(+07)	7.3(+07)	7.0(+07)
12	163.1	9.5(+07)	9.5(+07)	9.5(+07)	9.0(+07)
13	190.3	1.2(+08)	1.2(+08)	1.2(+08)	1.1(+08)
14	219.6	1.5(+08)	1.5(+08)	1.5(+08)	1.4(+08)
15	251.0	1.8(+08)	1.9(+08)	1.8(+08)	1.8(+08)
16	284.4	2.2(+08)	2.2(+08)	2.2(+08)	2.1(+08)
17	320.0	2.7(+08)	2.7(+08)	2.7(+08)	2.5(+08)
18	357.6	3.1(+08)	3.2(+08)	3.1(+08)	3.0(+08)
19	397.3	3.7(+08)	3.7(+08)	3.7(+08)	3.5(+08)
20	439.2	4.3(+08)	4.3(+08)	4.2(+08)	4.1(+08)

Tableau H.2 – Critical densities (cm^{-3}), n_{crit}, at which the probabilities of collisional and radiative de-excitation are equal, for the first transitions of SiO. The collisional partner is para-H_2, and the energy of the upper level is also given in K. Numbers in parentheses are powers of 10.

Jup	Energy (K)	n_{crit} (10 K)	n_{crit} (50 K)	n_{crit} (100 K)	n_{crit} (300 K)
1	2.1	5.1(+04)	6.0(+04)	6.2(+04)	6.7(+04)
2	6.3	3.6(+05)	3.8(+05)	3.5(+05)	3.2(+05)
3	12.6	1.2(+06)	1.3(+06)	1.2(+06)	9.8(+05)
4	20.9	3.0(+06)	3.1(+06)	2.9(+06)	2.3(+06)
5	31.4	6.0(+06)	6.2(+06)	5.7(+06)	4.7(+06)
6	43.9	1.0(+07)	1.1(+07)	9.9(+06)	8.2(+06)
7	58.6	1.7(+07)	1.7(+07)	1.6(+07)	1.3(+07)
8	75.3	2.5(+07)	2.5(+07)	2.4(+07)	2.0(+07)
9	94.1	3.6(+07)	3.6(+07)	3.3(+07)	2.8(+07)
10	115.0	4.9(+07)	4.9(+07)	4.6(+07)	3.9(+07)
11	138.0	6.5(+07)	6.5(+07)	6.1(+07)	5.2(+07)
12	163.1	8.4(+07)	8.4(+07)	7.9(+07)	6.7(+07)
13	190.3	1.1(+08)	1.1(+08)	1.0(+08)	8.6(+07)
14	219.6	1.3(+08)	1.3(+08)	1.2(+08)	1.1(+08)
15	251.0	1.6(+08)	1.6(+08)	1.5(+08)	1.3(+08)
16	284.4	1.9(+08)	2.0(+08)	1.8(+08)	1.6(+08)
17	320.0	2.4(+08)	2.3(+08)	2.2(+08)	1.9(+08)
18	357.6	2.7(+08)	2.8(+08)	2.6(+08)	2.2(+08)
19	397.3	3.3(+08)	3.2(+08)	3.0(+08)	2.6(+08)

I

CO critical densities

Tableau I.1 – Critical densities (cm^{-3}), n_{crit}, at which the probabilities of collisional and radiative de-excitation are equal, for the first transitions of CO. The collisional partner is H, and the energy of the upper level is also given in K. Numbers in parentheses are powers of 10.

Jup	Energy (K)	n_{crit} (10 K)	n_{crit} (50 K)	n_{crit} (100 K)	n_{crit} (300 K)
1	5.5	6.4(+02)	8.8(+02)	8.6(+02)	8.6(+02)
2	16.6	1.1(+03)	3.0(+03)	3.2(+03)	3.3(+03)
3	33.2	1.8(+03)	7.1(+03)	8.4(+03)	9.3(+03)
4	55.3	2.6(+03)	1.4(+04)	1.8(+04)	2.0(+04)
5	83.0	3.3(+03)	2.5(+04)	3.2(+04)	3.7(+04)
6	116.2	3.6(+03)	4.1(+04)	5.3(+04)	6.3(+04)
7	154.9	3.7(+03)	6.1(+04)	8.2(+04)	9.8(+04)
8	199.2	2.3(+03)	7.8(+04)	1.2(+05)	1.5(+05)
9	249.0	2.0(+03)	1.1(+05)	1.7(+05)	2.1(+05)
10	304.3	1.6(+03)	1.4(+05)	2.4(+05)	2.9(+05)
11	365.1	1.3(+03)	1.7(+05)	3.2(+05)	3.9(+05)
12	431.5	1.1(+03)	2.2(+05)	4.2(+05)	5.2(+05)
13	503.4	8.4(+02)	2.6(+05)	5.4(+05)	6.7(+05)
14	580.9	6.6(+02)	3.2(+05)	7.0(+05)	8.7(+05)
15	663.9	5.1(+02)	3.9(+05)	8.9(+05)	1.1(+06)
16	752.4	4.0(+02)	4.7(+05)	1.1(+06)	1.4(+06)

Tableau I.2 – Critical densities (cm^{-3}), n_{crit}, at which the probabilities of collisional and radiative de-excitation are equal, for the first transitions of CO. The collisional partner is He, and the energy of the upper level is also given in K. Numbers in parentheses are powers of 10.

Jup	Energy (K)	n_{crit} (10 K)	n_{crit} (50 K)	n_{crit} (100 K)	n_{crit} (300 K)
1	5.5	3.9(+03)	7.0(+03)	7.9(+03)	8.5(+03)
2	16.6	8.5(+03)	2.0(+04)	2.1(+04)	2.1(+04)
3	33.2	1.4(+04)	4.9(+04)	5.5(+04)	5.4(+04)
4	55.3	1.6(+04)	9.4(+04)	1.1(+05)	1.1(+05)
5	83.0	1.7(+04)	1.5(+05)	2.0(+05)	2.1(+05)
6	116.2	1.4(+04)	2.1(+05)	3.0(+05)	3.4(+05)
7	154.9	1.2(+04)	2.9(+05)	4.3(+05)	5.1(+05)
8	199.2	9.7(+03)	3.6(+05)	5.7(+05)	7.2(+05)
9	249.0	7.7(+03)	4.4(+05)	7.3(+05)	9.6(+05)
10	304.3	4.8(+03)	5.0(+05)	8.9(+05)	1.2(+06)
11	365.1	4.2(+03)	5.8(+05)	1.1(+06)	1.5(+06)
12	431.5	3.5(+03)	6.6(+05)	1.3(+06)	1.8(+06)
13	503.4	2.6(+03)	7.5(+05)	1.6(+06)	2.3(+06)
14	580.9	1.5(+03)	6.4(+05)	1.2(+06)	1.5(+06)

Tableau I.3 – Critical densities (cm^{-3}), n_{crit}, at which the probabilities of collisional and radiative de-excitation are equal, for the first transitions of CO. The collisional partner is para-H_2, and the energy of the upper level is also given in K. Numbers in parentheses are powers of 10.

Jup	Energy (K)	n_{crit} (10 K)	n_{crit} (50 K)	n_{crit} (100 K)	n_{crit} (300 K)
1	5.5	2.6(+03)	2.3(+03)	2.1(+03)	2.1(+03)
2	16.6	9.9(+03)	1.1(+04)	1.1(+04)	9.3(+03)
3	33.2	3.1(+04)	3.7(+04)	3.5(+04)	2.9(+04)
4	55.3	6.9(+04)	8.7(+04)	8.4(+04)	7.0(+04)
5	83.0	1.3(+05)	1.6(+05)	1.6(+05)	1.4(+05)
6	116.2	3.0(+05)	2.8(+05)	2.7(+05)	2.4(+05)
7	154.9	5.8(+05)	4.5(+05)	4.4(+05)	3.8(+05)
8	199.2	8.7(+05)	6.5(+05)	6.2(+05)	5.6(+05)
9	249.0	1.2(+06)	9.3(+05)	9.0(+05)	8.0(+05)
10	304.3	1.7(+06)	1.2(+06)	1.2(+06)	1.1(+06)
11	365.1	1.3(+06)	1.3(+06)	1.4(+06)	1.4(+06)
12	431.5	2.0(+06)	1.7(+06)	1.8(+06)	1.8(+06)
13	503.4	3.9(+06)	2.3(+06)	2.3(+06)	2.2(+06)
14	580.9	3.1(+06)	2.5(+06)	2.6(+06)	2.6(+06)
15	663.9	3.3(+06)	3.2(+06)	3.2(+06)	3.2(+06)
16	752.4	7.0(+06)	3.8(+06)	3.8(+06)	3.8(+06)
17	846.4	4.2(+06)	4.1(+06)	4.3(+06)	4.3(+06)
18	946.0	4.7(+06)	4.6(+06)	4.7(+06)	4.9(+06)
19	1051.1	1.6(+07)	6.4(+06)	5.9(+06)	5.7(+06)
20	1161.8	2.4(+07)	6.5(+06)	6.3(+06)	6.4(+06)

J

Extrapolation of collisional rate coefficients

J.1 Theoretical treatment

J.1.1 Temperature extrapolation

We use an 'usual' method to extrapolate the coefficient rates of collisional de-excitation ($\Delta J = J_u \rightarrow J_l$, with $J_u > J_l$) in the case of a linear molecule

$$\gamma_{J,J'} = A(\Delta J) y \exp\left[-B(\Delta J) y^{1/4}\right] \times \exp\left[-C(\Delta J) y^{1/2}\right] \tag{J.1}$$

where $y = \Delta E/kT$ and where the three parameters A, B, C are determined by fits obtained via a 'smallest squares' method, done on the set of initial data for each ΔJ. This method provides most of the coefficient rates with an errorbar of 50%, and generally typically 20 %.

This approximation is based on the fact that cross sections in quantum mechanics usually include a λ^2 factor (λ is the De Broglie wavelength), and a tunneling factor $e^{-d/\lambda}$ (the original formula was empirically proposed by de Jong et al. (1975), and motivated by Albrecht (1983)). The additional term in the exponential $\exp\left[-B(\Delta J) y^{1/4}\right]$ allows to spread the fit on a wider range of kinetic temperatures (also see Larsson et al. (2002)).

When the kinetic temperature falls outside the range of temperature for which the collisional coefficient rates are known, that is between T_{low} and T_{high}, the LVG code no longer does any extrapolation, and uses the values of the rate coefficients respectively for T_{low} and T_{high}.

J.1.2 Rotational quantum number extrapolation

Extrapolation of $\gamma_{J,0}$ coefficient rates. Before the extrapolation of the $\gamma_{J',J}$ coefficient rates, one must fit the coefficient rates that link quantum rotational number j level to the rotational ground state, at a given temperature. To achieve this, we use the following fit

$$\gamma_{J,0} = \exp\left(a + bJ + cJ^2\right) \tag{J.2}$$

where a, b, and c are the coefficients determined by the fit (see the computational details of this determination in section J.2.1. Nevertheless, not all the known coefficient rates are taken into account to realise the fit. For example, in the case of collisions between CO and p-H_2, only the levels whose rotational quantum number is superior to 7 are used (see Larsson et al. (2002),Schöier et al. (2005)).

Extrapolation of $\gamma_{J',J}$ coefficient rates. The method that we use to extrapolate the coefficient rates $\gamma_{J',J}$ is based on the IOS approximation (Infinite Order Sudden Approximation, see DePristo et al. (1979) and Goldflam et al. (1977)), thanks to which the matrix of coefficient rates can be entirely determined with the $\gamma_{J,0}$ coefficients, themselves determined through the previous method. The formula is the following

$$\gamma_{J,J'} = (2J'+1) \sum_{L=|J-J'|}^{J+J'} (2L+1) \begin{pmatrix} J & J' & L \\ 0 & 0 & 0 \end{pmatrix} \gamma_{L,0} \tag{J.3}$$

where

$$\begin{pmatrix} J & J' & L \\ 0 & 0 & 0 \end{pmatrix} \tag{J.4}$$

stands for the Wigner 3-j symbol. This expression remains valid as long as the energy of the colliding molecules is bigger than the difference of energy between successive rotational levels. The latter increases with J (see Equation 6.13), this expression can be questioned at higher rotational quantum numbers. DePristo et al. (1979) have shown that multiplying this expression (within the sum symbol) by

$$A(L,J) = \frac{6+\Omega(L)^2}{6+\Omega(J)^2} \tag{J.5}$$

with

$$\Omega(J') = 0.13 J' B_0 l \left(\frac{\mu}{T}\right)^{1/2} \tag{J.6}$$

one can approximately correct this problem. In this formula, B_0 is the rotational constant (expressed in cm^{-1}), μ is the reduced mass of the system in atomic mass units, and T is the kinetic temperature. l is a parameter called scattering length (expressed in Å), which is given the fixed value of 3 Å.

J.2 Computational treatment

J.2.1 The routine of extrapolation of the coefficient rates γ_{J0} (IDL)

Opening of the file of incomplete set of γ_{J0} coeffcient rate We present here the example of the collisions between CO and p-H_2. The incomplete data file is called : 'J0_pH2_inc.txt'. The subroutine that we use is an IDL one.

```
PRO gamma_J0_p
      openr, 1, 'J0_pH2_inc.txt'
      data = fltarr(42,29)
      readf, 1, data
      Jup = extrac(data, 0, 0, 1, 29)
      schoier1 = extrac(data, 1, 0, 41, 29)
      schoier2 = alog(schoier1)
      A = [-25, -0.2, +0.005]
      weights = replicate(1, 29, 1)
      save, /variables, filename='myvariables.sav'
      print, data
      close, 1
END
```

Calculation of the coefficients of the fit of the incomplete set of γ_{J0} coefficient rates We now determine the fit coefficients. The fit is done with the levels which rotational quantum number is between 7 and 29. We use the following sequence of IDL commands (for the case of collisional data between CO and p-H_2, at T = 5 K) :

```
    .run gamma_J0_p
gamma_J0_p
restore, 'myvariables.sav'
fit = CURVEFIT(Jup[6 :*], schoier2[0,6 :*], weights[6 :*], A, sigma, function_name =
'mon_poly')
print, A
```

Eventually we use the routine 'mon_poly.pro' : this function represents the second degree polynome with which we fit the 'incomplete' set of collisional data γ_{J0}.

```
PRO mon_poly, Jup, a, Y, pder
      Y = a[0] + a[1]*Jup + a[2]*Jup^2
      IF n_params() ge 4 THEN pder = [[replicate(1.0,n_elements(Jup))],[Jup],[Jup^2]]
END
```

J.2.2 The program of extrapolation of the coefficient rates (Fortran90)

```
    PROGRAM EXTRA_CO_oH2
IMPLICIT NONE
!-------------------------------------------------------------------------------
! precision parameters
!-------------------------------------------------------------------------------
INTEGER, PARAMETER : : DP=selected_real_kind(P=15) ! real kind
INTEGER, PARAMETER : : LONG=KIND(1) ! integer kind
```

```
!-----------------------------------------------------------------------
! parameters relative to CO
!-----------------------------------------------------------------------
INTEGER(KIND=LONG), PARAMETER : : Jmax_CO_oH2 = 40
REAL(KIND=DP), PARAMETER : : Brot_CO = 57635.9682D6 / 299792458D2
! rotational constant (MHz)
REAL(KIND=DP), PARAMETER : : Moment_CO = 0.10980_DP
! dipolar moment (Debye ;1debye=1.e-18 CGS)
REAL(KIND=DP) : : sl
! scattering length

!-----------------------------------------------------------------------
! parameters relative to the opening and reading files subroutine
!-----------------------------------------------------------------------
CHARACTER(LEN=75) : : name_file_coeff_CO_oH2
CHARACTER(LEN=*), PARAMETER : : format_header_out1 = '(2X,A2,2X,A2)'
CHARACTER(LEN=*), PARAMETER : : format_header_out2 = '(41F14.1)'
CHARACTER(LEN=*), PARAMETER : : format_out1 = '(2x,I2,2x,I2)'
CHARACTER(LEN=*), PARAMETER : : format_out2 = '(ES14.4E3)'
INTEGER : : file_coeff_CO_oH2
INTEGER : : error

!-----------------------------------------------------------------------
! parameters relative to the writing of the output
!-----------------------------------------------------------------------
CHARACTER(LEN=75) : : filein$
INTEGER : : nchar

!-----------------------------------------------------------------------
! parameters relative to the data
!-----------------------------------------------------------------------
REAL(KIND=DP), DIMENSION(1 :41) : : temp_CO_oH2
REAL(KIND=DP), DIMENSION(0 :Jmax_CO_oH2,0 :Jmax_CO_oH2,41) : : Rate_CO_oH2

!-----------------------------------------------------------------------
! parameters relative to the extrapolation
!-----------------------------------------------------------------------
INTEGER : : i,j,k,l,l1,l2
REAL(KIND=DP) : : A,sum,om1,om2,wig

WRITE(*,*) 'Which value of l do you wish to use ?'
WRITE(*,*) 'l is the scattering length, in angstroms'
WRITE(*,*) 'Typically l = 3 A'
WRITE(*,*) 'Example : if your input scattering length is 3 A,'
WRITE(*,*) 'first write the value of l'
READ(*,*) sl
WRITE(*,*) 'then write the name of the output directory : l3'
READ(*,*) filein$



DO i = 1,LEN(filein$)
    IF (filein$(i :i) /= '') THEN
```

```
        nchar = i
    END IF
ENDDO


filein$ = filein$(1 :nchar)

CALL READ_CO_oH2_incomplet
CALL READ_gamma_j_0_oH2
CALL OPEN_FILES


DO i = 1,41
    DO j = 20,40
        DO k = 1,j-1
            l1 = abs(j - k)
            l2 = j + k
              DO l = l1,l2
                  wig = wigner(j,k,l)
                  om1 = func(l,temp_CO_oH2(i))
                  om2 = func(j,temp_CO_oH2(i))
                  A = (6 + om1 ** 2) / (6 + om2 ** 2)
                  sum = (2 * DBLE(l) + 1._DP) * (wig ** 2) * A * Rate_CO_oH2(l,0,i)
                  Rate_CO_oH2(j,k,i) = Rate_CO_oH2(j,k,i) + (2 * DBLE(k) + 1._DP) * sum
              ENDDO
        ENDDO
    ENDDO
ENDDO
DO i = 1, Jmax_CO_oH2
    DO j = 0,i-1
        WRITE(file_coeff_CO_oH2,format_out1,ADVANCE='NO') i,j
            DO k = 1,41
              WRITE(file_coeff_CO_oH2,format_out2,ADVANCE='NO') RATE_CO_oH2(i,j,k)
            ENDDO
        WRITE(file_coeff_CO_oH2,*)
    ENDDO
ENDDO


CLOSE(file_coeff_CO_oH2)

CONTAINS

SUBROUTINE OPEN_FILES
!-------------------------------------------------------------------------------
! purpose : open the input and output files, write relevant informations in the output header
! subroutine/function needed :
! input variables :
! output variables :
! results :
!-------------------------------------------------------------------------------
IMPLICIT NONE

name_file_coeff_CO_oH2 =
'/export/home/dph3ag1/mhd_gr/input/'//filein$(1 :nchar)//'/coeff_CO_oH2.in'
```

```
file_coeff_CO_oH2 = get_file_number()

open(file_coeff_CO_oH2,file = name_file_coeff_CO_oH2)
WRITE(file_coeff_CO_oH2,*) 'In this file you can find the collision coefficient rates of CO with ortho-H2'
WRITE(file_coeff_CO_oH2,*) 'For 5 K ≤ T ≤ 400 k and for J = 1 to 21, the values are tabulated (Flower 2001).'
WRITE(file_coeff_CO_oH2,*) 'For 5 K ≤ T ≤ 400 K and for the J-0 levels (J = 21 to 40), the values are computed following the extrapolation procedure provided by Schoier, Van der Tak, Van Dishoeck and Black, AA 2005 (polynomial exponential extrapolation).'
WRITE(file_coeff_CO_oH2,*) 'For 5 K ≤ T ≤ 400 K, the other missing values are computed following the IOS approximation procedure provided by Schoier, Van der Tak, Van Dishoeck and Black, AA 2005.'
WRITE(file_coeff_CO_oH2,*)
WRITE(file_coeff_CO_oH2,format_header_out1,ADVANCE='NO') 'Up','Lo'

DO i = 1,41
    WRITE(file_coeff_CO_oH2,format_header_out2,ADVANCE='NO') temp_CO_oH2(i)
END DO

WRITE(file_coeff_CO_oH2,*)

END SUBROUTINE OPEN_FILES

SUBROUTINE READ_CO_oH2_incomplet

!-------------------------------------------------------------------------------
! purpose : reads the datas in the input file coeff_CO_oH2_incomplet
! subroutine/function needed :
! input variables :
! output variables :
! results :
!-------------------------------------------------------------------------------

IMPLICIT NONE

INTEGER(KIND=LONG) : : i,Ji,Jf,error
CHARACTER(LEN=*), PARAMETER : : name_file_coeff_CO_oH2_incomplet =
'/export/home/dph3ag1/fit_CO/coeff_CO_oH2_incomplet.in'
CHARACTER(LEN=*), PARAMETER : : format_CO_oH2_incomplet_temp = '(5X,41F10.1)'
INTEGER : : file_coeff_CO_oH2_incomplet

file_coeff_CO_oH2_incomplet = get_file_number()
open(file_coeff_CO_oH2_incomplet,file = name_file_coeff_CO_oH2_incomplet, status = 'OLD',
access = 'SEQUENTIAL',form='FORMATTED', action='READ')

Rate_CO_oH2= 0._DP
temp_CO_oH2 = 0._DP


! skip the comments
DO i = 1,6
    READ(file_coeff_CO_oH2_incomplet,*)
ENDDO
```

```
! read the temperatures
READ(file_coeff_CO_oH2_incomplet,format_CO_oH2_incomplet_temp) temp_CO_oH2
! skip the comments


DO i = 1,3
      READ(file_coeff_CO_oH2_incomplet,*)
ENDDO
DO i = 1,441
      READ(file_coeff_CO_oH2_incomplet,*,iostat=error)Ji,Jf,Rate_CO_oH2(Ji-1,Jf-1, :)
      IF (error>0) STOP "*** WARNING, error in READ_CO_oH2_incomplet"
ENDDO


END SUBROUTINE READ_CO_oH2_incomplet

SUBROUTINE READ_gamma_j_0_oH2

!-------------------------------------------------------------------------------
! purpose : reads the datas in the input file gamma_j_0_oH2
! subroutine/function needed :
! input variables :
! output variables :
! results :
!-------------------------------------------------------------------------------

IMPLICIT NONE

INTEGER(KIND=LONG) : : i,Ji,Jf,error,Nrates
CHARACTER(LEN=*), PARAMETER : : name_file_gamma_j_0_oH2 =
'/export/home/dph3ag1/fit_CO/gamma_j_0_oH2.in'
CHARACTER(LEN=*), PARAMETER : : format_gamma_j_0_oH2_temp = '(8X,41F16.1)'
INTEGER : : file_gamma_j_0_oH2

file_gamma_j_0_oH2 = get_file_number()
open(file_gamma_j_0_oH2,file = name_file_gamma_j_0_oH2, status = 'OLD',
access = 'SEQUENTIAL',form='FORMATTED', action='READ')

! skip the comments


DO i = 1,7
      READ(file_gamma_j_0_oH2,*)
ENDDO


! read the temperatures
READ(file_gamma_j_0_oH2,format_gamma_j_0_oH2_temp) temp_CO_oH2
! skip the comments
READ(file_gamma_j_0_oH2,*)
! read the collision rates
error = 0


DO i = 1,40
```

```
      READ(file_gamma_j_0_oH2,*,iostat=error) j,k,Rate_CO_oH2(j,0, :)
      IF (error>0) STOP "*** WARNING, error in READ_gamma_j_0_oH2"
ENDDO


END SUBROUTINE READ_gamma_j_0_oH2

FUNCTION func(j,T)

!-------------------------------------------------------------------------------
! purpose : calculate a useful factor for IOS expression
! subroutine/function needed :
! input variables :
! output variables :
! results :
!-------------------------------------------------------------------------------

IMPLICIT NONE

INTEGER(KIND=LONG), INTENT(in) : : j
REAL(KIND=DP), INTENT(in) : : T
REAL(KIND=DP) : : func

func = 0.13 * DBLE(j) * Brot_CO * sl * sqrt(18._DP/(19._DP * T))

END FUNCTION func

FUNCTION wigner(j1,j2,l)

!-------------------------------------------------------------------------------
! purpose : calculate the Wigner matrix for IOS expression
! subroutine/function needed :
! input variables :
! output variables :
! results :
!-------------------------------------------------------------------------------

IMPLICIT NONE

INTEGER(KIND=LONG), INTENT(in) : : j1,j2,l
INTEGER(KIND=LONG) : : j,g,i
REAL(KIND=DP) : : f2j1,f2j2,f2l,f2g,fg,fj1,fj2,fl
REAL(KIND=DP) : : wigner

f2j1 = 1
f2j2 = 1
f2l = 1
f2g = 1
fg = 1
fj1 = 1
fj2 = 1
fl = 1


j = j1 + j2 + l
```

```
    IF (MOD(j,2) /= 0) THEN
       wigner = 0._DP
    ELSE IF (MOD(j,2) == 0) THEN
          g = j / 2
          DO i = 1,j - 2 * j1
              f2j1 = i * f2j1
          ENDDO
          DO i = 1,j - 2 * j2
              f2j2 = i * f2j2
          ENDDO
          DO i = 1,j - 2 * l
              f2l = i * f2l
          ENDDO
          DO i = 1,j + 1
              f2g = i * f2g
          ENDDO
          DO i = 1,g
              fg = i * fg
          ENDDO
          DO i = 1,g - j1
              fj1 = i * fj1
          ENDDO
          DO i = 1,g - j2
              fj2 = i * fj2
          ENDDO
          DO i = 1,g - l
              fl = i * fl
          ENDDO
          wigner = ((-1) ** g) * sqrt(DBLE(f2j1) * DBLE(f2j2) * DBLE(f2l) / DBLE(f2g))
                   * DBLE(fg) / (DBLE(fj1) * DBLE(fj2) * DBLE(fl))
    END IF


END FUNCTION wigner

FUNCTION GET_FILE_NUMBER() RESULT (num)

!-----------------------------------------------------------------------
! purpose :
! gives a file number available for opening, i.e. a free logical unit
! example :
! n=GET_FILE_NUMBER()
! OPEN(n,file='sample.txt')
! subroutine/function needed :
! input variables :
! output variables :
! results :
! num -> 'LONG' integer : the first free logical unit
!-----------------------------------------------------------------------

IMPLICIT NONE
INTEGER(KIND=LONG) : : num
LOGICAL : : opened
```

```
opened = .TRUE.
num = 9 ! start file number after 10


DO WHILE (opened .AND. num < 50)
    num = num + 1
    INQUIRE(UNIT=num, opened=opened)
END DO
IF (num == 50 .and. opened) STOP "*** WARNING : no file number available ***"


END FUNCTION GET_FILE_NUMBER
END PROGRAM EXTRA_CO_oH2
```

K

Influence of other parameters on integrated intensity diagrams

For the purposes of this section, we make only use of the so-called reference model, already used by Schilke et al. (1997), and in Section 7.2 of this report, for which : $n_{\rm H} = 10^5$ cm^{-3}, $v_{\rm s} = 30$ km s^{-1}, and $b = 0.63$. In Chapters 2 and 3, the shock code that was used to simulate bipolar outflows and jets processes was presented. In Chapters 5 and 6, the way the radiative transfer is handled was introduced. In the Section 7.1, the updates of these respective treatments against the ones used by Schilke et al. (1997) were stressed out, and the influence of some of some updated parameters on the results were already investigated in Section 6.5. In this Chapter, we study the influence of complementary parameters on the SiO modelled emission.

K.1 Influence of some parameters relative to the SiO code : choice of the escape probability formula

We first present the influence of the choice of the escape probability formula that was used in our radiative transfer program (see Section 5.2). We compare the two ways that we have to compute the escape probability in the calculation of level populations at the statistical equilibrium state :

- the first expression (that we shall call 'plane parallel', or 'ep1') is the approximate of the average of the escape probability on all the space : $ep1 = 1/(1 + 3 \mid \tau_S \mid)$, as introduced by Neufeld and Kaufman (1993) ;
- the second expression (that we will call 'spherical', or 'ep2') is the average of the escape probability, calculated in the case where the velocity gradient is the same in all directions (see Subsection 5.2.4 or Section 5.2) : $ep2 = (1 - exp(- \mid \tau_S \mid))/ \mid \tau_S \mid$.

For such a shock, the velocity and temperature profiles are provided on Figure 7.1, as well as the Si-bearing species fractional abundances evolution.

Focus is made on the representative (1-0), (5-4), and (10-9) rotational transitions. The corresponding optical depth and escape probability evolution through the reference shock model are plotted on Figure K.1. The optical depth is not significantly dependent on the choice of the escape probability formula, whereas the escape probability shows larger and systematic discrepancies : the 'spherical' formula always leads to smaller escape probabilities.

The greater the escape probability, the smaller the excitation temperature. The excitation temperature is consequently smaller in every point of the shock in the case of the 'spherical' escape probability formula, itself generating a larger integrated intensity. This effect shows on Figure K.2 that displays the corresponding integrated intensity diagrams in both cases. In addition to this, it appears that the difference between the two cases decreases for transitions between levels for which $j_{\rm up} > 10$.

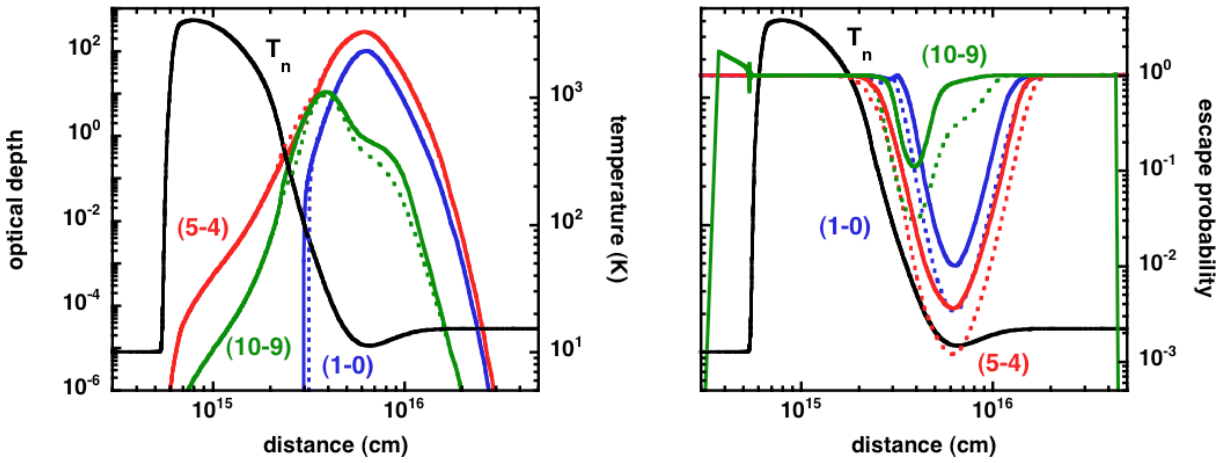

Figure K.1 – Left : neutral temperature and optical depth profile through the shock, for three given transitions (1-0), (5-4), and (10-9). The continuous curves correspond to the plane parallel formula for escape probability, while the dotted curves were obtained with the spherical formula. Right : neutral temperature and escape probability profiles for the same transition, computed with the plane parallel (continuous curves) and spherical (dotted curves) of the escape probability. The corresponding model is the reference shock model as presented in the beginning of this Appendix.

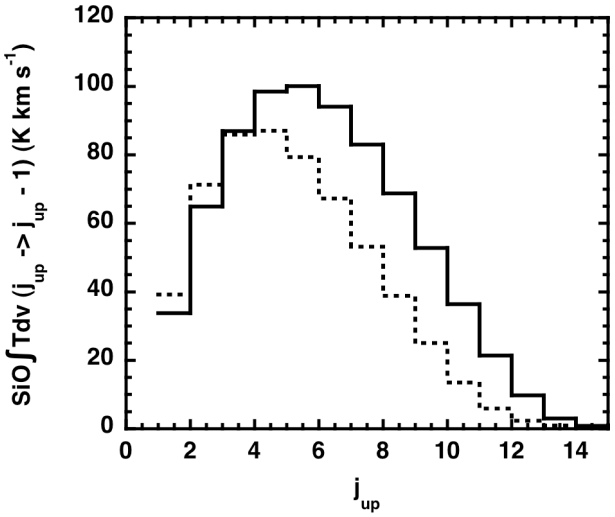

Figure K.2 – Absolute integrated intensity diagram for the reference model, obtained with plane parallel (continuous curve) or spherical (dotted curve) expression of the escape probability.

The explanation of this effect lies in the examination of the associated escape probability (right panel of Figure K.1). In the region of emission of the shock, the high-j_{up} transitions are optically thin whatever the choice of the escape probability formula : the emission of these lines are weak in both cases, and the difference between the integrated intensity is also weaker.

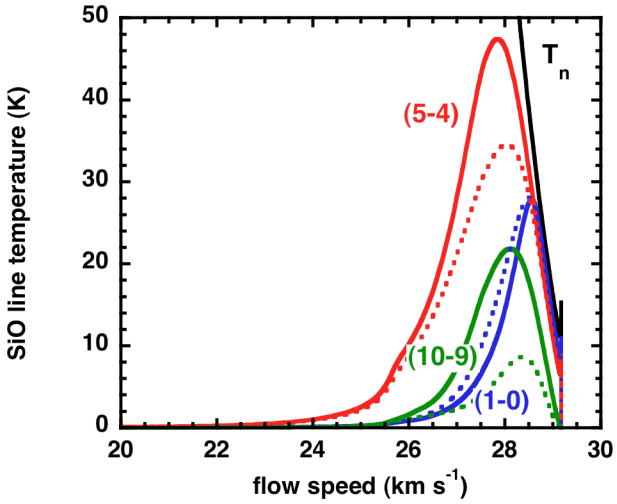

Figure K.3 – Line profiles for the reference model, obtained with plane parallel (continuous curve) or spherical (dotted curve) expression of the escape probability, for three selected transitions (1-0), (5-4), and (10-9).

The Figure K.3 shows the line profiles corresponding to these chosen transitions. The similarity of the (1-0) profiles seem to contradict the escape probability profiles, that show discrepancies. In fact, the corresponding rotational levels are more populated, and collisions dominate radiative excitation : the state approaches LTE, and the excitation temperature is dominated by this collisional effect that doesn't depend on the escape probability. Regarding the (5-4) transition different line profiles, the different escape probabilities in the emission region and the importance of the radiative excitation account for these discrepancies. As the escape probability is smaller in the case of a 'plane parallel' geometry, the excitation temperature is larger in this case, and so is the integrated intensity.

The MHD shock models plane parallel shocks, we consequently implement the Neufeld and Kaufman (1993) formula for the escape probability in the following developments.

K.2 Influence of some parameters relative to the shock code.

In this Subsection, we study the influence of chosen parameters of the shock program on the results for the SiO emission, such as :

- the modelling of some molecules cooling ;
- the adsorption of molecules on to grains in the cold, post-shock region.

The model that we use to do so is still the reference model taht was introduced at the beginning of this Section.

K.2.1 Cooling modeling

In the list of the shock inputs that were omitted in Subsection 2.1.3, one particular feature is an option that allows for the choice of the modelling of the cooling by CO and H_2O.

First option 'KN = 0' corresponds to a very simple treatment where :

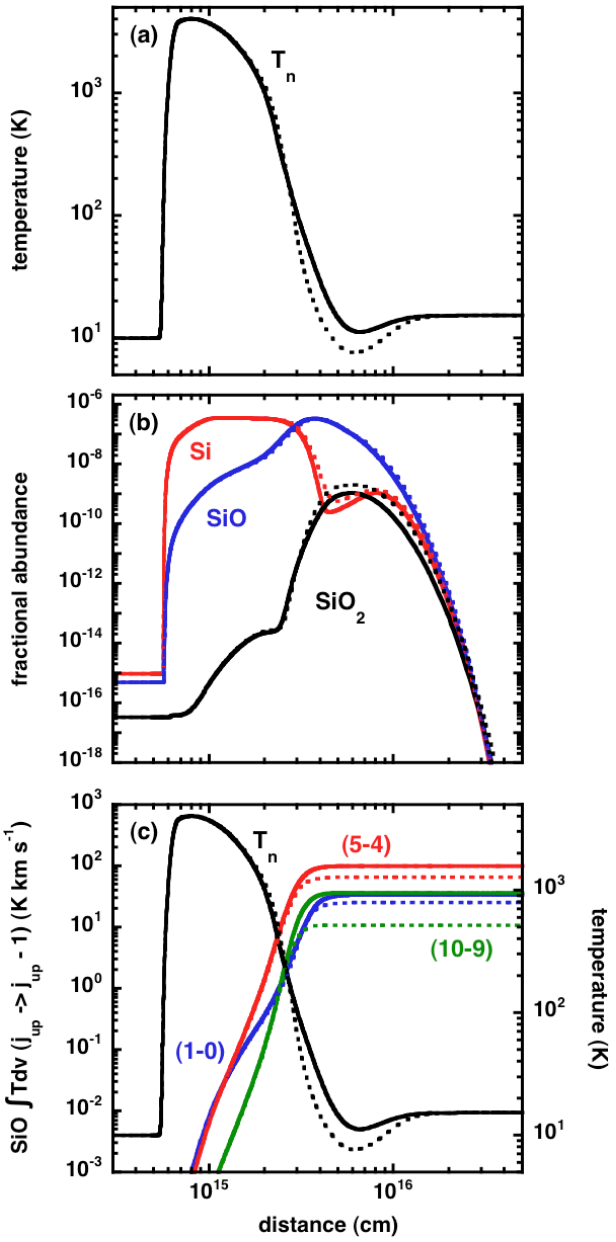

Figure K.4 – Top panel : temperature profile of the reference shock model, for a simple (dotted line, 'KN = 0') or elaborate (continuous lines, 'KN = 1') molecular cooling treatment. Middle panel : corresponding Si-bearing species fractional abundance profiles. Bottom panel : corresponding integrated intensity evolution for three representative transitions (1-0), (5-4), and (10-9).

- the only excited transition is the one between the ground state and the first excited level ;
- the following de-excitation is radiative, and the emitted photon escapes from the medium anyway ;
- the cooling by CO molecule is due to ^{13}CO, ^{12}CO transitions being considered as optically thick.

Cooling rates (erg cm^{-3}s^{-1}) deduced from these considerations are the following

$$\Gamma_{H_2O} = 1.0 \times 10^{-26} T_{\rm n}[n(H) + n(H_2)/2^{1/2}]n(H_2O)exp(-35/T_{\rm n}) \quad \text{(K.1)}$$

$$\Gamma_{CO} = 1.1 \times 10^{-28} T_{\rm n}[n(H) + n(H_2)/2^{1/2}]n(^{13}CO)exp(-5/T_{\rm n}) \quad \text{(K.2)}$$

If one chooses the second option, 'KN = 1', the cooling is taken into account through the interpolation of the results of a grid obtained via an escape probability method. In this option, respectively 179 and 170 rotational levels are taken into account for ortho-H_2O and para-H_2O. The 75 first rotational transitions of the first vibrational level of CO are considered.

The top panel of Figure K.4 shows the difference generated on the temperature profiles in the two cases. When the molecular cooling is described in a simpler manner, the cooling is more efficient when the distance exceeds 3×10^{15} cm. In fact, the underlying assumption is that all photons escape from the medium, taking away a lot of energy. For the regions closer to the origin, the best efficiency of the elaborate method may be explained by the influence of higher transitions of CO and H_2O, which are not taken into account in the simpler method. Indeed, at such temperatures, these transitions are likely to be excited, hence contribute to the cooling, owing to their optical thinness.

On the contrary, fractional abundance of SiO (same Figure, middle panel) is not significantly modified by the temperature structure of the shock : most of the SiO is formed when the distance is less than 3×10^{15} cm, where the temperature profiles only slightly differ. Reaction rates of formation of SiO depending mostly on temperature, abundances of SiO are quite the same in this region. Temperature discrepancies beyond this distance are not sufficient then to modify the chemistry of SiO.

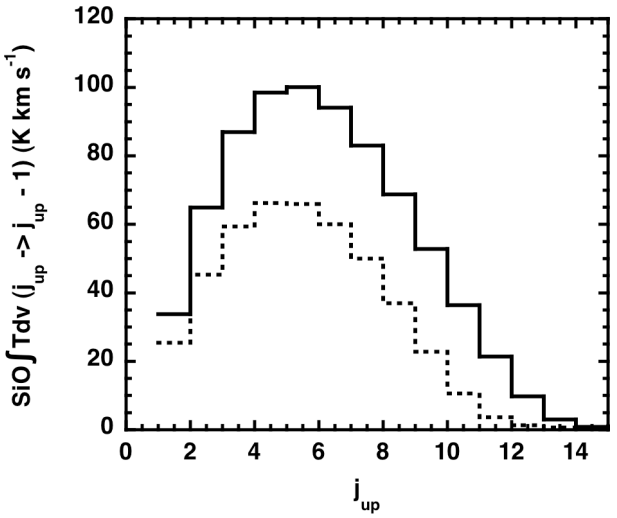

Figure K.5 – Absolute integrated intensity diagram for the reference model, obtained with an elaborate (continuous curve) or simple (dotted curve) treatment of the cooling generated by CO and H_2O.

Consequently, the possible difference of the integrated intensity diagram in both cases won't be caused by an effect of SiO abundance. The bottom panel confirms this trend, showing that the totality of the integrated intensity is emitted between 3 and 5×10^{15} cm, that is in a region where :

- the temperature is high enough for the SiO transitions to be excited ;
- the difference of temperature in both models allows to understand the differences of integrated intensities, on the left curve.

The bottom panel confirms the temperature's influence : where the temperature profiles differ, so does the integrated intensity, which is larger in the elaborate scenario than in the simple one, leading to the integrated intensity diagram in Figure K.5.

The line profiles can be interpretated with similar arguments : they significantly differ only in the region where the temperature profiles are different, that is on the right hand side of a 26-27 km s^{-1} limit of the Figure K.6, which exactly correspond to the right hand side of a 3×10^{15} cm limit on Figure K.4. The emission of SiO transitions is more important in the elaborate cooling scenario owing to the higher temperatures, which explains their higher maximum integrate intensity, and also the slight shift of the intensity peak towards higher flow speeds.

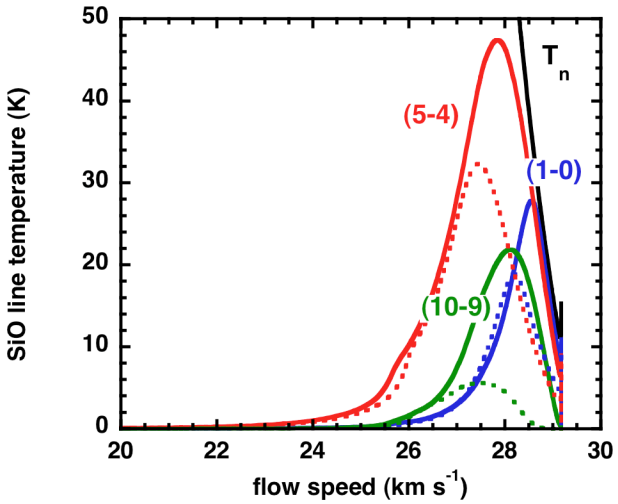

Figure K.6 – Line profiles for the reference model, obtained with an elaborate (continuous curve) or simple (dotted curve) treatment of the cooling generated by CO and H_2O, for three selected transitions (1-0), (5-4), and (10-9).

In the following studies, we use the option 'KN = 1' which models the molecular cooling from CO and H_2O in a more accurate fashion.

K.2.2 Adsorption on grains

We study the influence of the adsorption of the gas phase molecules on to grains in the cold regions of the shock, by means of the reference shock model used in the previous Subsections.

When adsorption on to grains is taken into account, all gas phase molecules are ultimately adsorbed in the post-shock region. The final neutral temperature is consequently that of the grains, which play the role of thermostat of the medium. This explains the increase of temperature observed on the shock profile after $4 - 5 \times 10^{15}$ cm that can be seen on the top panel of Figure K.7. The neutral temperature is also plotted on the same Figure in absence of adsorption, and decreases to finally reach the gas temperature.

The corresponding Si-bearing species fractional abundance profiles are also plotted on the bottom panel of this Figure. The timescale for freeze-out is sufficiently large that the chemical profiles are modified only in the cold post-shock gas. The main difference when dropping the adsorption also occurs around $4 - 5 \times 10^{15}$ cm : instead of decreasing due to the adsorption on grains, the fractional abundance of SiO decrease because of its chemical conversion in SiO_2.

Consequently, more SiO remains in the gas phase in an adsorption free scenario, but at a temperature that is less than the one necessary to generate its significant excitation. In the scenario where adsorption is taken into account, the neutral temperature is slightly greater in the post-shock region, which accounts for the slightly higher values of the integrated intensity in this case. This effect can be viewed on Figure K.8, that shows the integrated intensity diagram corresponding to both scenarios.

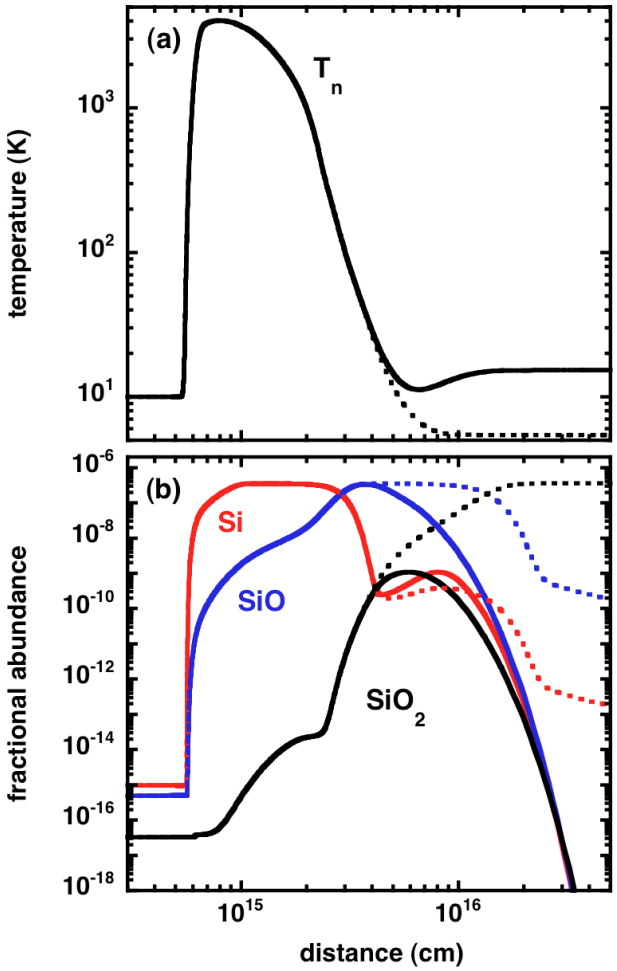

Figure K.7 – Top panel : temperature profile of the reference shock model, including (continuous curves) or not including (dotted curves) the adsorption on to grains in the post-shock region.. Middle panel : corresponding Si-bearing species fractional abundance profiles.

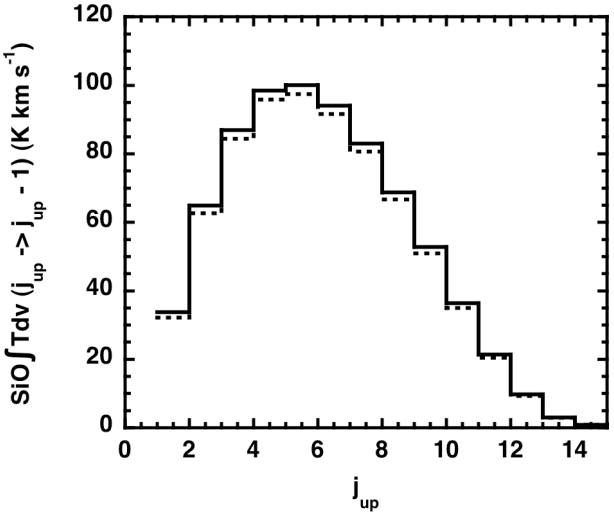

Figure K.8 – Absolute integrated intensity diagram for the reference model, including (continuous curves) or not including (dotted curves) the adsorption on to grains in the post-shock region.

L

Bowshocks modelling

L.1 Modelling : geometrical aspects

L.1.1 Calculation of the $(\vec{u_{perp}}, \vec{u_{obs}})$ angle

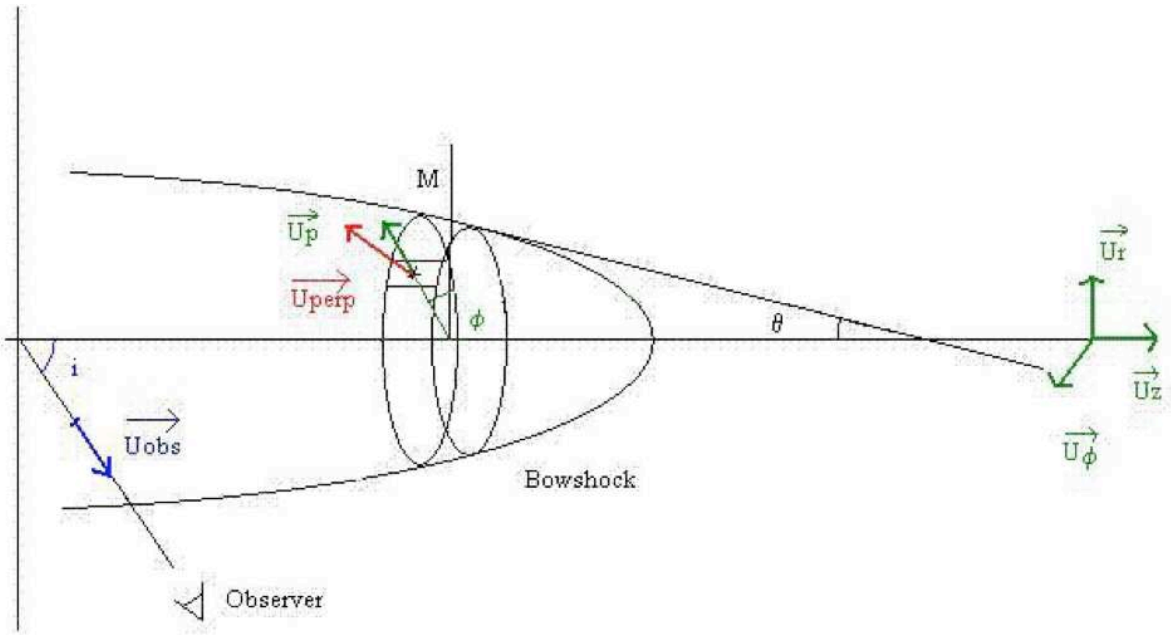

Figure L.1 – Bowshock modeling : notations.

In this section we try to determine the angle between the perpendicular vector to the surface, $\vec{u_{perp}}$, and the vector giving the direction of the observer (i.e. the unit vector in the direction of the line of sight), $\vec{u_{obs}}$. As we can see on Figure L.1, it is always possible to find a plan containing these two vectors, thanks to the revolution symmetry of the bowshock structure. Consequently, we can read directly the coordinates of this vector on this figure in terms of vectors $\vec{u_r}$, $\vec{u_\phi}$, $\vec{u_z}$

$$\vec{u_{obs}} = \vec{u_z} \cos i - \vec{u_r} \sin i \tag{L.1}$$

Now, we aim to find the coordinates of the vector $\vec{u_{perp}}$ in the same referential. We define the vector $\vec{u_p}$, which direction is given by OM (see Figure L.1). In consequence of this, we can express $\vec{u_{perp}}$ as a function of $\vec{u_p}$ and $\vec{u_z}$

$$\vec{u_{perp}} = \vec{u_p}\cos\theta + \vec{u_z}\sin\theta \tag{L.2}$$

According to its definition, we can also express $\vec{u_p}$ as a function of $\vec{u_r}$ and $\vec{u_\phi}$

$$\vec{u_p} = \vec{u_r}\cos\phi + \vec{u_\phi}\sin\phi \tag{L.3}$$

Finally, we obtain for $\vec{u_{perp}}$

$$\vec{u_{perp}} = \vec{u_r}\cos\theta\cos\phi + \vec{u_\phi}\cos\theta\sin\phi + \vec{u_z}\sin\theta \tag{L.4}$$

which allows us to express the scalar product between $\vec{u_{obs}}$ and $\vec{u_{perp}}$, and thus finally the cosinus of the angle between these vectors

$$\begin{aligned} \vec{u_{perp}}.\vec{u_{obs}} &= -\cos\theta\cos\phi\sin i + \sin\theta\cos i & \text{(L.5)} \\ &= \cos(\vec{u_{perp}}, \vec{u_{obs}}) & \text{(L.6)} \end{aligned}$$

L.1.2 Ring surface

In this section we determine the surface of a ring cut in the structure of the bowshock (exactly similar to the surface of the external ring of a slice of bread, for instance ; see Figure L.2). To do that, we define the angle θ, which sinus is the only known quantity of this problem

$$\sin\theta = \frac{v_1}{v_{bow}} \tag{L.7}$$

We then need to determine the radiuses r_1 and r_2 in function of this quantity to be able to calculate the surface. We use the general equation of the tangent y(x) to a function f(x) in a point of abscissa x_0

$$y = f'(x_0)(x - x_0) + f(x_0) \tag{L.8}$$

In our situation, we can model the profile of the bowshock structure by the equation

$$z = r^s \tag{L.9}$$

Consequently we have

$$\frac{dz}{dr} = sr^{s-1} \tag{L.10}$$

The equation of the tangent is then given by

$$z = sr_1^{s-1}(r - r_1) + z_1 = sr_1^{s-1}(r - r_1) + r_1^s \tag{L.11}$$

As a consequence, the value of the z coordinate of the point where $r = 0$ is

$$z(r = 0) = -sr_1^s + r_1^s = r_1^s(1 - s) \tag{L.12}$$

We now can evaluate the tangent of the θ angle

$$\tan\theta = \frac{r_1}{z_1 - z(r = 0)} = \frac{r_1}{r_1^s + r_1^s(s - 1)} = \frac{r_1}{sr_1^s} \tag{L.13}$$

which directly provides the value of r_1 in function of s and i_1 :

$$r_1 = (s\tan(a\sin(\sin i_1)))^{\frac{1}{1-s}} \tag{L.14}$$

The method we use is only an approximation : indeed, we calculate the surface of a rectangle, which length is half the sum of r_1 and r_2, and which width is the quantity l (see Figure L.2). To do this, we need to know the angle ψ, defined by

$$\tan\psi = \frac{r_1 - r_2}{z_1 - z_2} \qquad \sin\psi = \frac{r_1 - r_2}{l} \tag{L.15}$$

Finally we obtain the simple expression

$$dS = 2\pi\frac{1}{2}(r_1 + r_2)l = 2\pi\frac{1}{2}(r_1 + r_2)\frac{r_1 - r_2}{\sin\psi} \tag{L.16}$$

where all the quantities are expressed in function of s and i_1.

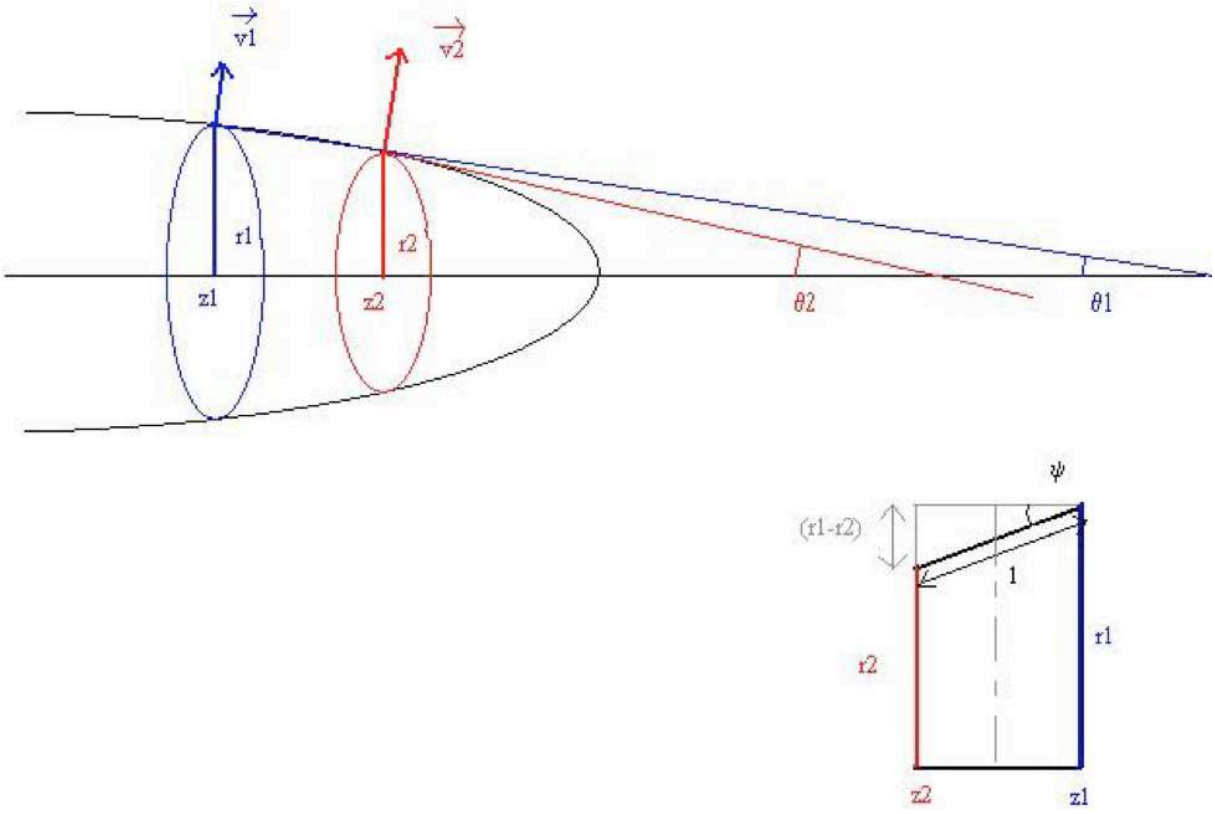

Figure L.2 – Bowshock modeling : ring surface estimate.

L.2 Temperature correction

L.2.1 Velocity in the frame of the observer

We now aim to establish the expression of the velocity in the frame of the observer, since this quantity will be used in the computer program. To do this, we first define the vector $\vec{v_0}$, which represents the velocity at which the motionless matter 'sees' the arrival of the shock. As we can see on Figure L.3, it is possible to break up the initial vector $\vec{v_0}$ in the frame of the bow-shock in terms of vectors $\vec{u_{perp}}$ (see Subsection L.1.1) and $\vec{u_{paral}}$ (tangent to the surface of the bow-shock)

$$\vec{v_0} = v_0\cos\theta\vec{u_{par}} - v_0\sin\theta\vec{u_{perp}} \tag{L.17}$$

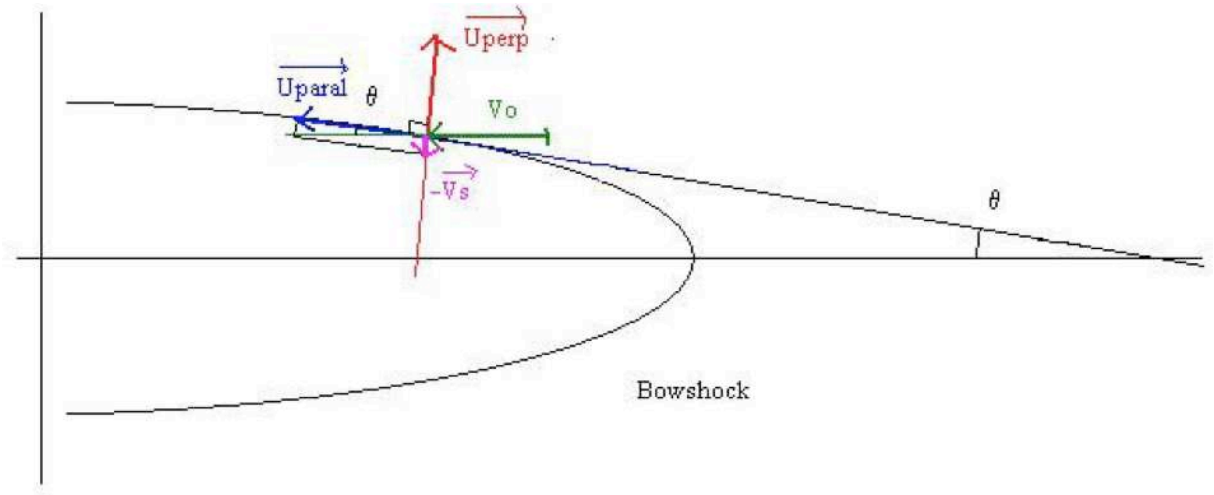

Figure L.3 – Bowshock modeling : notations.

In this expression, the component along the vector $u_{paral}^{\rightarrow}$ is conserved, and the shock velocity can thus be expressed through the perpendicular component

$$\vec{v_{\rm s}} = v_0 \sin\theta \vec{u_{perp}} \quad \text{(L.18)}$$
$$v_{\rm s} = v_0 \sin\theta \quad \text{(L.19)}$$

The temporal evolution of the propagation velocity of the bow-shock in the frame of the bow-shock is then given by

$$\vec{v(t)} = v_0 \cos\theta \vec{u_{par}} - v_{\rm n}(t)\vec{u_{perp}} \quad \text{(L.20)}$$

where $\vec{v_{\rm n}}$ is the velocity in the frame of the shock.

Eventually, we can express the propagation velocity of the bow-shock in the frame of the observer

$$\vec{v_{obs}(t)} = \vec{v(t)} - \vec{v_0} \quad \text{(L.21)}$$
$$= (-v_{\rm n}(t) + v_{\rm s})\vec{u_{perp}} \quad \text{(L.22)}$$
$$= (-v_{\rm n}(t) + v_0 \sin\theta)\vec{u_{perp}} \quad \text{(L.23)}$$

L.2.2 Relation between gradients : in the perpendicular direction of the shock, or along the line of sight

On the Figure L.4, the component of the velocity along the direction $\vec{u_z}$ is given by

$$\vec{v} = \vec{v(z)} = v_z(z)\vec{u_z} \quad \text{(L.24)}$$

In consequence of this, we can express the scalar product between $\vec{v}$ and the unit vector defining the direction of the observer (i.e. the direction of the line of sight)

$$\vec{v}.\vec{n} = v_z(z)\vec{u_z}.\vec{n} = v_z(z)\cos\theta \quad \text{(L.25)}$$

We then define the curvilinear abscissa in the direction of the observer, and we can express it as well in terms of z coordinate thanks to the angle θ

$$\vec{s} = s\vec{n} \qquad s = \frac{z}{\cos\theta} \qquad ds = \frac{dz}{\cos\theta} \quad \text{(L.26)}$$

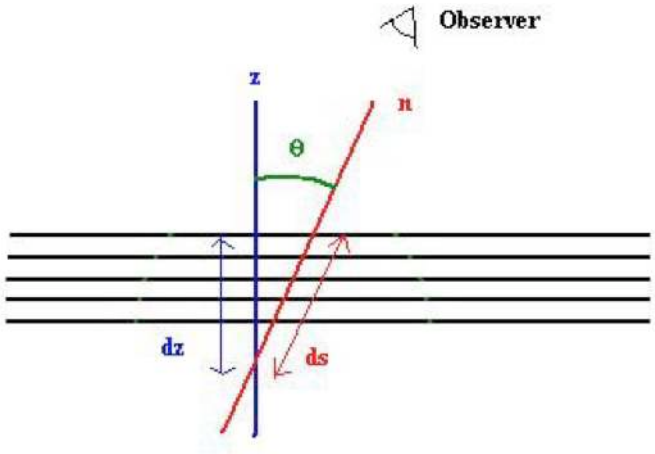

Figure L.4 – Bow-shock modelling : relations between gradients.

Finally, we obtain

$$\frac{d(\vec{v}\vec{n})}{ds} = \frac{d(v_z \cos\theta)}{ds} = \cos^2\theta \frac{dv_z}{dz} = \mu^2 \frac{dv_z}{dz} \tag{L.27}$$

that can also be written

$$\frac{\partial v_\mathrm{s}}{\partial s} = \mu^2 \frac{dv_z}{dz} \tag{L.28}$$

L.2.3 Temperature correction

So far, the emissivity radiated by the shock has been estimated under the assumption that the shock was seen face on by the observer, which is obviously not always the case. In this section, we determine this emissivity when the angle between the line of sight and the perpendicular direction to the shock is θ. We use the notation $\mu = \cos\theta$ (see Figure L.4).

First case : $\mu = 1$. We define the energy emitted or radiated by an elementary volume $\Delta V = \Delta S \Delta z$ per unit of solid angle by

$$\frac{dE_j}{d\omega}(\mu = 1) = \frac{h\nu}{4\pi} n_{j+1} A_{j+1,j} \beta_{j,j+1} \Delta z \Delta S \tag{L.29}$$

$$= \frac{h\nu}{4\pi} n_{j+1} A_{j+1,j} \frac{1 - \exp\tau_{j,j+1}}{\tau_{j,j+1}} \Delta z \Delta S \tag{L.30}$$

Taking into account the following relations

$$B_\nu(T_\mathrm{exc}) = \frac{2h\nu^3}{c^2} \frac{1}{\frac{g_{j+1} n_j}{g_j n_{j+1}} - 1} \tag{L.31}$$

$$\tau_{j,j+1} = \frac{hc}{4\pi} n_j B_{j,j+1} \left(1 - \frac{g_j n_{j+1}}{g_{j+1} n_j}\right) \frac{1}{\partial v_\mathrm{s}/\partial s} \tag{L.32}$$

$$B_{j,j+1} = \frac{g_{j+1}}{g_j} B_{j+1,j} \tag{L.33}$$

$$\frac{A_{j+1,j}}{B_{j+1,j}} = \frac{16h}{c^2} B^3 (j+1)^3 = \frac{2h\nu^3}{c^2} \tag{L.34}$$

We can derive the other expression for this energy

$$\frac{dE_j}{d\omega}(\mu = 1) = \frac{h\nu}{4\pi} n_{j+1} A_{j+1,j} \beta_{j,j+1} \Delta z \Delta S \tag{L.35}$$

$$= B_\nu(T_\mathrm{exc})(1 - \exp^{-\tau}) \Delta z \Delta S \tag{L.36}$$

We then define the surface brilliance by the relation

$$SB(\mu=1) = \frac{dE_j}{d\omega}(\mu=1) \times \frac{1}{\Delta\nu_z \Delta S} \tag{L.37}$$

which can also be expressed by

$$\begin{aligned} SB(\mu=1) &= \frac{h\nu}{4\pi} n_{j+1} A_{j+1,j} \beta_{j,j+1} \frac{\Delta z}{\Delta\nu_z} && \text{(L.38)} \\ &= B_\nu(T_{\rm exc})(1-\exp^{-\tau}) && \text{(L.39)} \end{aligned}$$

The definition and expression of the surface brilliance allows us to obtain the following expressions for the brilliance temperature

$$\begin{aligned} T_b(\mu=1) &= \frac{c^2}{2k\nu^2} SB(\mu=1) && \text{(L.40)} \\ &= \frac{c^2}{2k\nu^2} \frac{h\nu}{4\pi} n_{j+1} A_{j+1,j} \beta_{j,j+1} \frac{\Delta z}{\Delta\nu_z} && \text{(L.41)} \\ &= \frac{c^2}{2k\nu^2} B_\nu(T_{\rm exc})(1-\exp^{-\tau}) && \text{(L.42)} \end{aligned}$$

Finally, using the Doppler shift expression

$$\Delta\nu_z = \frac{\nu}{c}\Delta v_z \tag{L.43}$$

we obtain the quantity that is used in the code to evaluate the emissivity of the shock

$$\begin{aligned} (T_b \Delta v_z)(\mu=1) &= \frac{c^2}{2k\nu^2} \frac{h\nu}{4\pi} n_{j+1} A_{j+1,j} \beta_{j,j+1} \frac{c}{\nu_z} \Delta z && \text{(L.44)} \\ &= \frac{c^2}{2k\nu^2} B_\nu(T_{\rm exc})(1-\exp^{-\tau}) \frac{c}{\nu} \Delta\nu_z && \text{(L.45)} \end{aligned}$$

Second case : any μ. In the case of any μ, the energy emitted by an elementary volume of the shock per unit of solid angle becomes

$$\frac{dE_j}{d\omega}(\mu) = \frac{h\nu}{4\pi} n_{j+1} A_{j+1,j} \beta_{j,j+1}(\mu) \Delta z \Delta S \tag{L.46}$$

The only difference with the case $\mu = 1$ is that now, the escape probability depends on the μ factor. Again, we can define the surface brilliance by

$$\begin{aligned} SB(\mu) &= \frac{h\nu}{4\pi} n_{j+1} A_{j+1,j} \beta_{j,j+1}(\mu) \frac{\Delta z \Delta S}{\Delta\nu_{obs} \Delta S_{obs}} && \text{(L.47)} \\ &= \frac{h\nu}{4\pi} n_{j+1} A_{j+1,j} \frac{1-\exp^(-\tau/\mu^2)}{\tau/\mu^2} \frac{\Delta z \Delta S}{\Delta\nu_{obs} \Delta S_{obs}} && \text{(L.48)} \end{aligned}$$

We can read on the Figure L.4 and use the expresssion of the Doppler shift to derive the following relations

$$\begin{aligned} \Delta S_{obs} &= \mu \Delta S && \text{(L.49)} \\ \Delta\nu_{obs} &= \Delta v_{rad} \frac{\nu}{c} = \Delta v_z \frac{\nu}{c} && \text{(L.50)} \end{aligned}$$

Which eventually provides the relation

$$\begin{aligned} SB(\mu) &= \frac{h\nu}{4\pi} n_{j+1} A_{j+1,j} \beta_{j,j+1}(\mu=1) \frac{1-\exp^(-\tau/\mu^2)}{1-\exp^(-\tau)} \frac{\Delta z}{\Delta\nu_z} && \text{(L.51)} \\ &= \frac{1-\exp^(-\tau/\mu^2)}{1-\exp^(-\tau)} SB(\mu=1) && \text{(L.52)} \end{aligned}$$

In this case, the brilliance temperature then writes

$$T_b(\mu) = \frac{c^2}{2k\nu^2} SB(\mu) = \frac{c^2}{2k\nu^2} \frac{1-\exp^{(}-\tau/\mu^2)}{1-\exp^{(}-\tau)} SB(\mu=1) \tag{L.53}$$

$$= \frac{1-\exp^{(}-\tau/\mu^2)}{1-\exp^{(}-\tau)} T_b(\mu=1) \tag{L.54}$$

In addition to this we can express the elementary variation of v_{rad} along the line of sight in terms of the variation of v_z along the perpendicular direction to the shock

$$\Delta v_{rad} = \mu^2 \frac{\Delta v_z}{\Delta z} \Delta s = \mu^2 \frac{\Delta v_z}{\Delta z} \frac{\Delta z}{\mu} = \mu \Delta v_z \tag{L.55}$$

The emissivity of the shock can eventually be estimated by means of

$$T_b(\mu) \Delta v_{rad} = \mu \frac{1-\exp^{(}-\tau/\mu^2)}{1-\exp^{(}-\tau)} T_b(\mu=1) \Delta v_z \tag{L.56}$$

M

The chemical species included in the MHD code

Taken from the initial species file 'species.in_1e4".

```
!————————— list of chemical species — Steady state at T = 19.67 K —————————
!———— WARNING : order = neutrals, species on mantles, ions >0, ions <0 ————
!——— name, composition, initial density(cm-3), formation enthalpy (kCal/mol) ———
!—-————————————————————————————————————————————————————————————————————
1   H       01000000000000   2.033D-04   051.634
2   H2      02000000000000   4.999D-01   000.000
3   He      00000010000000   1.000D-01   000.000
4   C       00010000000000   4.769D-07   169.980 –> C/H = 8.27e-5
5   CH      01010000000000   9.254D-09   141.600     A&G : 3.55e-4
6   CH2     02010000000000   3.342D-08   093.900
7   CH3     03010000000000   1.097D-09   034.800
8   CH4     04010000000000   3.644D-08   -15.970
9   O       00000100000000   1.732D-05   058.980 –> O/H = 1.24e-4
10  O2      00000200000000   1.181D-05   000.000     A&G : 7.41e-4
11  OH      01000100000000   1.230D-07   009.250
12  H2O     02000100000000   4.638D-07   -57.100
13  CO      00010100000000   8.166D-05   -27.200
14  CO2     00010200000000   8.027D-07   -93.965
15  C2      00020000000000   1.663D-09   198.200
16  C2H     01020000000000   7.773D-09   113.300
17  C2H2    02020000000000   8.667D-11   056.320
18  C3      00030000000000   6.924D-14   194.000
19  C3H     01030000000000   3.891D-13   177.000 ***
20  C3H2    02030000000000   2.850D-12   114.000 ***
39  CH3OH   04010100000000   1.000D-16   -99.999
42  H2CO    02010100000000   1.000D-16   -99.999
42  HCO2H   02010200000000   1.000D-16   -99.999
21  N       00001000000000   8.136D-06   112.530 –> N/H = 6.39e-5
22  NH      01001000000000   6.002D-08   090.000     A&G : 9.33e-5
23  NH2     02001000000000   1.004D-06   046.200
24  NH3     03001000000000   3.492D-07   -09.299
25  CN      00011000000000   5.552D-08   103.200
26  HCN     01011000000000   7.974D-08   032.390
27  HNC     01011000000000   8.993D-08   048.000
28  N2      00002000000000   2.704D-05   000.000
29  NO      00001100000000   3.072D-08   021.460
32  S       00000000010000   1.413D-05   065.600     A&G : 1.86e-5
33  SH      01000000010000   2.613D-08   032.600
34  H2S     02000000010000   2.996D-08   -04.230
35  CS      00010000010000   1.396D-07   063.000
36  SO      00000100010000   5.980D-08   001.200
37  SO2     00000200010000   2.475D-07   -70.300
38  OCS     00010100010000   2.036D-10   -34.000
```

37	Si	00000000001000	1.126D-15	106.700	A&G : 3.55e-5
38	SiH	01000000001000	7.402D-20	089.690	
39	SiH2	02000000001000	7.267D-22	069.140 *	
40	SiH3	03000000001000	4.825D-24	048.540 *	
41	SiH4	04000000001000	3.171D-22	011.000	
42	SiO	00000100001000	3.242D-16	-24.300	
43	SiO2	00000200001000	2.114D-17	-73.000	
44	Mg	00000000100000	1.000D-16	035.000	
39	Fe	00000000000010	1.451D-08	098.700	
38	C54H18	18540000000000	8.701D-07	-99.999	PAH/nH =1(-8)
63	G	00600000000000	4.027D-11	-99.999	Ngrain = 8.30(-11)
41	H2O*	02000100000001	1.029D-04	H2O*/nH =1.03(-4)	
42	O2*	00000200000001	1.000D-16		
42	CO*	00010100000001	8.271D-06		CO*/nH =8.27(-6)
43	CO2*	00010200000001	1.339D-05		CO2*/nH =1.34(-5)
39	CH4*	04010000000001	1.549D-06		CH4*/nH =1.55(-6)
44	NH3*	03001000000001	1.549D-05		NH3*/nH =1.55(-5)
44	N2*	00002000000001	1.000D-16		
39	CH3OH*	04010100000001	1.859D-05		CH3OH*/nH =1.86(-6)
42	H2CO*	02010100000001	6.199D-06		H2CO*/nH =6.20(-6)
42	HCO2H*	02010200000001	7.240D-06		HCO2H*/nH =7.24(-6)
42	OCS*	00010100010001	2.069D-07		OCS*/nH =2.07(-7)
55	H2S*	02000000010001	3.720D-06		H2S*/nH =3.72(-6)
62	Fe*	00000000000011	3.245D-15		
41	SiH4*	04000000001001	1.000D-16		
42	SiO*	00000100001001	1.000D-16		
43	SiO2*	00000200001001	1.000D-16		
59	O**	00000100000002	1.399D-04		Noyaux = 4*3.50(-5)
60	Si**	00000000001002	3.370D-05		Noyaux = 3.370(-5)
61	Mg**	00000000100002	3.230D-05		Noyaux = 3.700(-5)
62	Fe**	00000000000012	3.230D-05		Noyaux = 3.230(-5)
63	C**	00010000000002	1.629D-04		Noyaux = 1.630(-4)
48	H+	01000001000000	2.756D-09	365.200	
49	H2+	02000001000000	2.285D-12	355.700	
50	H3+	03000001000000	8.939D-09	265.000	
51	He+	00000011000000	8.213D-10	567.000	
52	C+	00010001000000	1.906D-09	429.700	A&G : 3.55e-4
53	CH+	01010001000000	4.907D-14	387.000	
54	CH2+	02010001000000	8.715D-14	331.000	
55	CH3+	03010001000000	6.897D-10	262.000	
56	CH4+	04010001000000	8.658D-15	272.000 **	
57	CH5+	05010001000000	2.494D-11	216.000 *	
58	O+	00000101000000	3.618D-14	373.000	
59	O2+	00000201000000	1.577D-09	278.400	
60	OH+	01000101000000	2.924D-13	309.310	
61	H2O+	02000101000000	3.851D-13	233.700	
62	H3O+	03000101000000	2.982D-09	143.000	
63	CO+	00010101000000	2.717D-14	295.970	
64	HCO+	01010101000000	3.936D-08	197.300	
65	HCO2+	01010201000000	5.660D-11	141.000 *	
66	C2+	00020001000000	3.510D-17	476.000	
67	C2H+	01020001000000	7.229D-17	404.000	
68	C2H2+	02020001000000	7.053D-12	317.500	
69	C2H3+	03020001000000	4.930D-12	267.900	
70	C3+	00030001000000	9.910D-18	479.000 *	
71	C3H+	01030001000000	7.503D-16	381.000 *	
72	C3H2+	02030001000000	3.081D-15	330.000 * **	
73	C3H3+	03030001000000	1.388D-13	282.000 * **	
74	N+	00001001000000	1.481D-10	447.690	
75	NH+	01001001000000	9.212D-15	401.100	
76	NH2+	02001001000000	4.136D-13	302.700	
77	NH3+	03001001000000	1.240D-10	224.900	
78	NH4+	04001001000000	2.439D-09	151.000 *	
79	CN+	00011001000000	5.987D-16	429.300	
80	C2N+	00021001000000	7.071D-11	410.000 *	
81	HCN+	01011001000000	1.190D-14	346.000	
83	H2CN+	02011001000000	2.813D-09	226.000 *	
84	H2NC+	02011001000000	2.954D-11	265.000 *	

85	N2+	00002001000000	1.777D-14	359.298		
86	N2H+	01002001000000	2.603D-09	247.500		
87	NO+	00001101000000	2.896D-10	235.330		
88	HNO+	01001101000000	8.150D-12	256.800		
92	S+	00000001010000	5.319D-08	304.000	–>	S/H = 1.47e-5
93	SH+	01000001010000	9.585D-09	271.800		A&G : 1.86e-5
94	H2S+	02000001010000	5.897D-11	237.000		
95	H3S+	03000001010000	1.970D-10	190.000	*	
96	CS+	00010001010000	2.834D-14	324.000		
97	HCS+	01010001010000	5.237D-10	243.000		
98	SO+	00000101010000	7.732D-09	239.200		
99	HSO+	01000101010000	2.774D-10	210.000		
100	HSO2+	01000201010000	2.872D-10	143.000		
101	HOCS+	01010101010000	2.565D-12	181.000		
51	Si+	00000001001000	2.650D-17	295.000		
109	SiH+	01000001001000	2.769D-19	271.820		
110	SiH2+	02000001001000	6.140D-20	276.360	*	
111	SiH3+	03000001001000	4.275D-22	237.320	*	
112	SiH4+	04000001001000	2.794D-30	279.900		
113	SiH5+	05000001001000	1.596D-24	219.380	*	
114	SiO+	00000101001000	4.486D-23	239.520		
115	SiOH+	01000101001000	2.715D-18	-99.999		
102	Fe+	00000001000010	4.853D-10	280.240		LM : Fe/nH=1.5(-8)
103	C54H18+	18540001000000	1.143D-09	-99.999		
63	G+	00600001000000	2.420D-12	-99.999		
104	C54H18-	18540000000100	1.288D-07	-99.999		PAH/nH = 1(-8)
63	G-	00600000000100	3.599D-12	-99.999		Ngrain = 8.30(-11)

N

The chemical network of the MHD code

```
!-------------------------------------------------------------------------------
!
! update :
! --------
!
!   29/08/01 : ajout de C** (meme taux d'erosion que Si**)
!
!   12/01/01 : ajout des reactions d'erosion pour les especes Si**, Mg**, Fe**, O**
!              attention : les alpha,beta, gamma d'ont plus le meme sens
!
!   24/08/00 :
!              * creation from the file Chemistry.dat
!              * suppression of one reaction that appears twice :
!                ADSOR C3 +GRAIN =CH4* CH4* CH4*
!              * suppression of the column 'DE' :
!                the excess of energy is computed in the shock code.
!              Remark : The old format is unchanged, if there is a value
!                for DE, it is not read in the code.
!              * change in one reaction (problem of conservation)
!                SiOH+ +PHOTON =SiO+ O --> SiOH+ +PHOTON =SiO+ H
!              * change 17 reactions : -> new specy=SECPHO (secondary photon)
!                first reaction : 56 88 C +CRP =C+ ELECTR
!                last reaction : 56 88 CO +CRP =C O
!                changes are (idem for the 17 reactions) :
!                CRP -> SECPHO in reactants
!                beta = 140000.0 -> beta = 0.0
!   31/08/00 :
!              * change 23 reactions : same as last change of 24/08/00
!                first reaction : 56 88 C54H18 +SECPHO =C54H18+ ELECTR
!                last reaction : 13 87 SiH4 +SECPHO =SiH3 H
!                changes are (idem for the 22 reactions) :
!                CRP -> SECPHO in reactants
!                beta = 0.0 or 140000.0 -> beta = 0.0
!
!
! columns :
! --------
!              * reference or comment
!              * R1, R2, P1, P2, P3, P4 : reactants and product of the reaction
!                R1 + R2 -> P1 + P2 + P3 + P4
!              * gamma(cm3.s-1), beta(K), alpha : Ahrrenius coefficients
!                in general  :
!                          rate = gamma*EXP(-beta/T)*(T/300)**alpha
!                special cases :
!                          * photo-reactions
!                                  rate = gamma*EXP(-beta*Av)*RAD
!                          * CR induced desorption from grains
!                                  rate = gamma*sigma(grain)*N(grains)/N(species on grains)
!                          * CR ionisation or dissociation
```

```
!                              rate = gamma*EXP(-beta/T)*(T/300)**alpha + other terms...
!                          * H2 and HD formation
!                              rate = gamma*(T/300)**alpha*nH/n(H)
!                          * three body reactions on grains surface
!                              rate = gamma*<sigma.v>(grain)*N(grains)/N(species on grains)
!                              /(Teff/beta+1)Ó
!                          * sputtering of grain mantle
!                              complicated !
!                          * erosion of grain cores
!                              rate = gamma*EXP(-beta/T)*(T/300)**alpha * <sigma.v>(grain)
!                          * adsorption on grains
!                              rate = gamma*<sigma.v>(grain)
!-------------------------------------------------------------------------------
```

!	R1	R2	P1	P2	P3	P4	gamma	alpha	beta
87 88	H	+H	=H2				8.14D-17	0.5	
IONIZ	H	+ELECTR	=H+	ELECTR	ELECTR		9.20D-10	0.5	157890.0
IONIZ	H2	+ELECTR	=H2+	ELECTR	ELECTR		1.40D-09	0.5	179160.0
IONIZ	H	+H+	=H+	H+	ELECTR		1.30D-13	0.5	157890.0
IONIZ	H	+H3+	=H3+	H+	ELECTR		1.30D-13	0.5	157890.0
IONIZ	H	+He+	=He+	H+	ELECTR		1.30D-13	0.5	157890.0
IONIZ	H	+H3O+	=H3O+	H+	ELECTR		1.30D-13	0.5	157890.0
IONIZ	H	+H3S+	=H3S+	H+	ELECTR		1.30D-13	0.5	157890.0
IONIZ	H	+HCO+	=HCO+	H+	ELECTR		1.30D-13	0.5	157890.0
IONIZ	H	+Fe+	=Fe+	H+	ELECTR		1.30D-13	0.5	157890.0
IONIZ	H	+NH3+	=NH3+	H+	ELECTR		1.30D-13	0.5	157890.0
IONIZ	H	+NH4+	=NH4+	H+	ELECTR		1.30D-13	0.5	157890.0
IONIZ	H	+S+	=S+	H+	ELECTR		1.30D-13	0.5	157890.0
IONIZ	H	+SiOH+	=SiOH+	H+	ELECTR		1.30D-13	0.5	157890.0
IONIZ	H	+O2+	=O2+	H+	ELECTR		1.30D-13	0.5	157890.0
IONIZ	H2	+H+	=H+	H2+	ELECTR		1.10D-13	0.5	179160.0
IONIZ	H2	+H3+	=H3+	H2+	ELECTR		1.10D-13	0.5	179160.0
IONIZ	H2	+He+	=He+	H2+	ELECTR		1.10D-13	0.5	179160.0
IONIZ	H2	+H3O+	=H3O+	H2+	ELECTR		1.10D-13	0.5	179160.0
IONIZ	H2	+H3S+	=H3S+	H2+	ELECTR		1.10D-13	0.5	179160.0
IONIZ	H2	+HCO+	=HCO+	H2+	ELECTR		1.10D-13	0.5	179160.0
IONIZ	H2	+Fe+	=Fe+	H2+	ELECTR		1.10D-13	0.5	179160.0
IONIZ	H2	+NH3+	=NH3+	H2+	ELECTR		1.10D-13	0.5	179160.0
IONIZ	H2	+NH4+	=NH4+	H2+	ELECTR		1.10D-13	0.5	179160.0
IONIZ	H2	+S+	=S+	H2+	ELECTR		1.10D-13	0.5	179160.0
IONIZ	H2	+SiOH+	=SiOH+	H2+	ELECTR		1.10D-13	0.5	179160.0
IONIZ	H2	+O2+	=O2+	H2+	ELECTR		1.10D-13	0.5	179160.0
IONIZ	He	+H+	=H+	He+	ELECTR		1.10D-13	0.5	285328.0
IONIZ	He	+H3+	=H3+	He+	ELECTR		1.10D-13	0.5	285328.0
IONIZ	He	+He+	=He+	He+	ELECTR		1.10D-13	0.5	285328.0
IONIZ	He	+H3O+	=H3O+	He+	ELECTR		1.10D-13	0.5	285328.0
IONIZ	He	+H3S+	=H3S+	He+	ELECTR		1.10D-13	0.5	285328.0
IONIZ	He	+HCO+	=HCO+	He+	ELECTR		1.10D-13	0.5	285328.0
IONIZ	He	+Fe+	=Fe+	He+	ELECTR		1.10D-13	0.5	285328.0
IONIZ	He	+NH3+	=NH3+	He+	ELECTR		1.10D-13	0.5	285328.0
IONIZ	He	+NH4+	=NH4+	He+	ELECTR		1.10D-13	0.5	285328.0
IONIZ	He	+S+	=S+	He+	ELECTR		1.10D-13	0.5	285328.0
IONIZ	He	+SiOH+	=SiOH+	He+	ELECTR		1.10D-13	0.5	285328.0
IONIZ	He	+O2+	=O2+	He+	ELECTR		1.10D-13	0.5	285328.0
DISSO	H2	+ELECTR	=ELECTR	H	H		2.00D-09	0.5	116300.0
DISSO	H2	+H	=H	H	H		1.00D-10	0.0	052000.0
DISSO	H2	+He	=He	H	H		1.00D-11	0.0	052000.0
DISSO	H2	+H2	=H2	H	H		1.25D-11	0.0	052000.0
DISSO	H2	+H+	=H+	H	H		3.00D-11	0.5	052000.0
DISSO	H2	+H3+	=H3+	H	H		3.00D-11	0.5	052000.0
DISSO	H2	+He+	=He+	H	H		3.00D-11	0.5	052000.0
DISSO	H2	+H3O+	=H3O+	H	H		3.00D-11	0.5	052000.0
DISSO	H2	+H3S+	=H3S+	H	H		3.00D-11	0.5	052000.0
DISSO	H2	+HCO+	=HCO+	H	H		3.00D-11	0.5	052000.0
DISSO	H2	+Fe+	=Fe+	H	H		3.00D-11	0.5	052000.0

DISSO	H2	+NH3+	=NH3+	H	H			3.00D-11	0.5	052000.0
DISSO	H2	+NH4+	=NH4+	H	H			3.00D-11	0.5	052000.0
DISSO	H2	+S+	=S+	H	H			3.00D-11	0.5	052000.0
DISSO	H2	+SiOH+	=SiOH+	H	H			3.00D-11	0.5	052000.0
DISSO	H2	+O2+	=O2+	H	H			3.00D-11	0.5	052000.0
	C54H18	+ELECTR	=C54H18-	PHOTON				1.00D-07	0.00	000000.0
	C54H18+	+ELECTR	=C54H18	PHOTON				3.30D-06	-.50	000000.0
	C54H18+	+C54H18-	=C54H18	C54H18				3.00D-09	-.50	000000.0
	C54H18-	+H+	=C54H18	H				7.50D-08	-.50	000000.0
	C54H18-	+H3+	=C54H18	H2	H			2.20D-08	-.50	000000.0
	C54H18-	+H3+	=C54H18	H	H		H	2.20D-08	-.50	000000.0
	C54H18-	+He+	=C54H18	He				3.80D-08	-.50	000000.0
	C54H18-	+C+	=C54H18	C				2.20D-08	-.50	000000.0
	C54H18-	+H3O+	=C54H18	H2O	H			1.70D-08	-.50	000000.0
	C54H18-	+H3S+	=C54H18	H2S	H			1.30D-08	-.50	000000.0
	C54H18-	+NH4+	=C54H18	NH3	H			1.80D-08	-.50	000000.0
	C54H18-	+HCO+	=C54H18	CO	H			1.40D-08	-.50	000000.0
	C54H18-	+HCS+	=C54H18	CS	H			1.10D-08	-.50	000000.0
	C54H18-	+Si+	=C54H18	Si				1.40D-08	-.50	000000.0
	C54H18-	+Fe+	=C54H18	Fe				1.00D-08	-.50	000000.0
	C54H18-	+S+	=C54H18	S				1.30D-08	-.50	000000.0
	C54H18	+H+	=C54H18+	H				4.40D-09	0.00	000000.0
	C54H18	+H3+	=C54H18+	H2	H			1.30D-09	0.00	000000.0
	C54H18	+H3+	=C54H18+	H	H		H	1.30D-09	0.00	000000.0
	C54H18	+He+	=C54H18+	He				2.20D-09	0.00	000000.0
	C54H18	+C+	=C54H18+	C				1.30D-09	0.00	000000.0
	C54H18	+H3O+	=C54H18+	H2O	H			1.00D-09	0.00	000000.0
	C54H18	+H3S+	=C54H18+	H2S	H			7.40D-10	0.00	000000.0
	C54H18	+NH4+	=C54H18+	NH3	H			1.00D-09	0.00	000000.0
	C54H18	+HCO+	=C54H18+	CO	H			8.20D-10	0.00	000000.0
	C54H18	+HCS+	=C54H18+	CS	H			6.50D-10	0.00	000000.0
	C54H18	+Si+	=C54H18+	Si				8.30D-10	0.00	000000.0
	C54H18	+Fe+	=C54H18+	Fe				5.90D-10	0.00	000000.0
	C54H18	+S+	=C54H18+	S				7.80D-10	0.00	000000.0
	C54H18-	+H	=C54H18	H	ELECTR			3.30D-09	0.00	005500.0
	C54H18-	+C	=C54H18	C	ELECTR			9.60D-10	0.00	005500.0
	C54H18-	+CH	=C54H18	CH	ELECTR			9.60D-10	0.00	005500.0
	C54H18-	+O	=C54H18	O	ELECTR			8.30D-10	0.00	005500.0
	C54H18-	+OH	=C54H18	OH	ELECTR			8.30D-10	0.00	005500.0
56 88	C54H18	+SECPHO	=C54H18+	ELECTR				2.00D+04	0.00	140000.0
56 88	C54H18-	+SECPHO	=C54H18	ELECTR				2.00D+04	0.00	140000.0
	G	+ELECTR	=G-	PHOTON				6.90D-05	0.50	000000.0
	G-	+H+	=G	H				1.60D-06	0.50	000000.0
	G-	+H3+	=G	H2	H			4.61D-07	0.50	000000.0
	G-	+H3+	=G	H	H		H	4.61D-07	0.50	000000.0
	G-	+He+	=G	He				8.00D-07	0.50	000000.0
	G-	+C+	=G	C				4.61D-07	0.50	000000.0
	G-	+H3O+	=G	H2O	H			3.66D-07	0.50	000000.0
	G-	+H3S+	=G	H2S	H			2.70D-07	0.50	000000.0
	G-	+NH4+	=G	NH3	H			3.76D-07	0.50	000000.0
	G-	+HCO+	=G	CO	H			2.96D-07	0.50	000000.0
	G-	+HCS+	=G	CS	H			2.38D-07	0.50	000000.0
	G-	+Si+	=G	Si				3.01D-07	0.50	000000.0
	G-	+Fe+	=G	Fe				2.13D-07	0.50	000000.0
	G-	+S+	=G	S				2.82D-07	0.50	000000.0
	G	+H+	=G+	H				1.60D-06	0.50	000000.0
	G	+H3+	=G+	H2	H			4.61D-07	0.50	000000.0
	G	+H3+	=G+	H	H		H	4.61D-07	0.50	000000.0
	G	+He+	=G+	He				8.00D-07	0.50	000000.0
	G	+C+	=G+	C				4.61D-07	0.50	000000.0
	G	+H3O+	=G+	H2O	H			3.66D-07	0.50	000000.0
	G	+H3S+	=G+	H2S	H			2.70D-07	0.50	000000.0
	G	+NH4+	=G+	NH3	H			3.76D-07	0.50	000000.0
	G	+HCO+	=G+	CO	H			2.96D-07	0.50	000000.0
	G	+HCS+	=G+	CS	H			2.38D-07	0.50	000000.0
	G	+Si+	=G+	Si				3.01D-07	0.50	000000.0
	G	+Fe+	=G+	Fe				2.13D-07	0.50	000000.0
	G	+S+	=G+	S				2.82D-07	0.50	000000.0

	G+	+ELECTR	=G	PHOTON		6.90D-05	0.50	000000.0
	G	+SECPHO	=G+	ELECTR		0.63D+08	0.00	140000.0
	G-	+SECPHO	=G	ELECTR		0.41D+09	0.00	140000.0
P& H	H	+CRP	=H+	ELECTR		4.60D-01	0.00	000000.0
P& H	He	+CRP	=He+	ELECTR		5.00D-01	0.00	000000.0
P& H	H2	+CRP	=H+	H	ELECTR	4.00D-02	0.00	000000.0
P& H	H2	+CRP	=H	H		1.50D+00	0.00	000000.0
P& H	H2	+CRP	=H2+	ELECTR		9.60D-01	0.00	000000.0
P& H	C	+CRP	=C+	ELECTR		1.80D+00	0.00	000000.0
P& H	O	+CRP	=O+	ELECTR		2.80D+00	0.00	000000.0
56 88	C	+SECPHO	=C+	ELECTR		1.02D+03	0.00	140000.0
2Z89	CH	+SECPHO	=C	H		1.46D+03	0.00	140000.0
13 87	CH4	+SECPHO	=CH3	H		4.68D+03	0.00	140000.0
2Z89	CH+	+SECPHO	=C	H+		3.52D+02	0.00	140000.0
2Z89	OH	+SECPHO	=O	H		1.02D+03	0.00	140000.0
2Z89	H2O	+SECPHO	=OH	H		1.94D+03	0.00	140000.0
2Z89	O2	+SECPHO	=O2+	ELECTR		2.34D+02	0.00	140000.0
2Z89	O2	+SECPHO	=O	O		1.50D+03	0.00	140000.0
2Z89	CO2	+SECPHO	=CO	O		3.42D+03	0.00	140000.0
2Z89	C2	+SECPHO	=C	C		4.74D+02	0.00	140000.0
77 87	C2H	+SECPHO	=C2	H		8.16D+03	0.00	140000.0
2Z89	C2H2	+SECPHO	=C2H	H		1.03D+04	0.00	140000.0
2Z89	C2H2	+SECPHO	=C2H2+	ELECTR		2.62D+03	0.00	140000.0
2Z88	C3	+SECPHO	=C2	C		2.24D+03	0.00	140000.0
13 87	C3H	+SECPHO	=C3	H		8.16D+03	0.00	140000.0
13 87	C3H2	+SECPHO	=C3H	H		8.16D+03	0.00	140000.0
56 88	CO	+SECPHO	=C	O		6.80D+02	1.20	140000.0
16B83	O	+H2	=OH	H		1.55D-13	2.80	002980.0
UMIST	CO	+H	=OH	C		1.10D-10	0.50	077700.0
72 83	O2	+H	=OH	O		1.63D-09	-.90	008750.0
16B83	OH	+H	=O	H2		7.00D-14	2.80	001950.0
16B83	OH	+H2	=H2O	H		9.54D-13	2.00	001490.0
16B83	H2O	+H	=OH	H2		5.24D-12	1.90	009265.0
17B73	C	+H2	=CH	H		1.16D-09	0.50	014100.0
P& H	C	+H	=CH	PHOTON		1.00D-17	0.00	000000.0
22 86	CH	+H2	=CH2	H		2.38D-10	0.00	001760.0
17B73	CH2	+H2	=CH3	H		5.18D-11	0.17	006400.0
23B83	CH3	+H2	=CH4	H		3.00D-10	0.00	005460.0
59 82	C2	+H2	=C2H	H		1.60D-10	0.00	001419.0
S88	C2H	+H2	=C2H2	H		1.14D-11	0.00	000950.0
17B73	CH	+H	=C	H2		1.16D-09	0.50	002200.0
22 86	CH2	+H	=CH	H2		4.70D-10	0.00	000370.0
17B73	CH3	+H	=CH2	H2		5.18D-11	0.17	005600.0
23B83	CH4	+H	=CH3	H2		3.00D-10	0.00	006560.0
P& H	O2	+C	=CO	O		3.30D-11	0.50	000000.0
93 88	OH	+CO	=CO2	H		4.40D-13	-1.15	000390.0
95 88	OH	+C	=CO	H		3.10D-11	-.36	000000.0
94 88	OH	+O	=O2	H		3.10D-11	-.36	000000.0
61 81	CH	+O	=HCO+	ELECTR		2.40D-14	0.50	000000.0
61 81	CH	+O	=CO	H		9.50D-11	0.50	000000.0
P& H	CH2	+O	=CO	H	H	2.00D-11	0.50	000000.0
X	CH3	+O	=CO	H2	H	1.80D-10	0.50	000000.0
P& H	C2	+O	=CO	C		5.00D-11	0.50	000000.0
P& H	C2H	+O	=CO	CH		1.00D-10	0.00	000250.0
X	C3	+O	=CO	C2		5.00D-11	0.50	000000.0
13 87	C3H	+O	=C2H	CO		5.00D-11	0.50	000000.0
13 87	C3H2	+O	=C2H2	CO		5.00D-11	0.50	000000.0
24Y83	C+	+H	=CH+	PHOTON		7.00D-17	0.00	000000.0
GRE92	C+	+H2	=CH2+	PHOTON		5.00D-16	0.00	000000.0
14 87	C+	+H2	=CH+	H		1.50D-10	0.00	004640.0
14 87	CH+	+H	=C+	H2		1.50D-10	0.00	000000.0
27B77	CH+	+H2	=CH2+	H		1.20D-09	0.00	000000.0
27B77	CH2+	+H	=CH+	H2		1.20D-09	0.00	002700.0
28B75	CH2+	+H2	=CH3+	H		7.00D-10	0.00	000000.0
28B75	CH3+	+H	=CH2+	H2		7.00D-10	0.00	010560.0
4Z89	CH3+	+H2	=CH5+	PHOTON		6.00D-15	0.00	000000.0
28B75	CH3+	+H2	=CH4+	H		2.00D-10	0.00	032500.0
28B75	CH4+	+H	=CH3+	H2		2.00D-10	0.00	000000.0

28B75	CH4+	+H2	=CH5+	H		4.00D-11	0.00	000000.0
28B75	CH5+	+H	=CH4+	H2		4.00D-11	0.00	002200.0
	H+	+ELECTR	=H	PHOTON		2.90D-12	-.74	000000.0
22Z90	H2+	+ELECTR	=H	H		1.60D-08	-.43	000000.0
P& H	He+	+ELECTR	=He	PHOTON		4.50D-12	-.67	000000.0
McC03	H3+	ELECTR	H	H	H	5.10d-08	-.52	000000.0
McC03	H3+	ELECTR	H2	H		1.70d-08	-.52	000000.0
P& H	C+	+ELECTR	=C	PHOTON		4.40D-12	-.61	000000.0
22Z90	CH+	+ELECTR	=C	H		1.50D-07	-.42	000000.0
22Z90	CH2+	+ELECTR	=C	H2		1.25D-07	-.50	000000.0
22Z90	CH2+	+ELECTR	=CH	H		1.25D-07	-.50	000000.0
22Z90	CH3+	+ELECTR	=CH2	H		1.75D-07	-.50	000000.0
22Z90	CH3+	+ELECTR	=CH	H2		1.75D-07	-.50	000000.0
P& H	CH4+	+ELECTR	=CH3	H		3.00D-07	-.50	
P& H	CH4+	+ELECTR	=CH2	H	H	3.00D-07	-.50	
22Z90	CH5+	+ELECTR	=CH	H2	H2	8.75D-08	-.30	000000.0
22Z90	CH5+	+ELECTR	=CH2	H2	H	8.75D-08	-.30	000000.0
22Z90	CH5+	+ELECTR	=CH3	H2		8.75D-08	-.30	000000.0
22Z90	CH5+	+ELECTR	=CH4	H		8.75D-08	-.30	000000.0
79 79	H+	+H2	=H2+	H		6.40D-10	0.00	021300.0
01R79	H2+	+H	=H+	H2		6.40D-10	0.00	000000.0
P& H	H2+	+H2	=H3+	H		2.10D-09	0.00	000000.0
P& H	H3+	+H	=H2+	H2		2.10D-09	0.00	020000.0
52R84	H+	+O	=O+	H		6.00D-10	0.00	000227.0
P& H	H+	+OH	=OH+	H		2.10D-09	0.00	000000.0
80R74	H+	+O2	=O2+	H		1.20D-09	0.00	000000.0
80R74	H+	+H2O	=H2O+	H		8.20D-09	0.00	000000.0
P& H	H+	+CH	=CH+	H		1.90D-09	0.00	000000.0
P& H	H+	+CH2	=CH+	H2		1.40D-09	0.00	000000.0
P& H	H+	+CH2	=CH2+	H		1.40D-09	0.00	000000.0
P& H	H+	+CH3	=CH3+	H		3.40D-09	0.00	000000.0
80R74	H+	+CH4	=CH3+	H2		2.28D-09	0.00	000000.0
80R74	H+	+CH4	=CH4+	H		1.52D-09	0.00	000000.0
18R80	H+	+CO2	=HCO+	O		4.20D-09	0.00	000000.0
P& H	H2+	+C	=CH+	H		2.40D-09	0.00	000000.0
P& H	H2+	+O	=OH+	H		1.50D-09	0.00	000000.0
38R75	H2+	+CO	=HCO+	H		2.16D-09	0.00	000000.0
38R75	H2+	+CO	=CO+	H2		6.44D-10	0.00	000000.0
P& H	H2+	+OH	=OH+	H2		7.60D-10	0.00	000000.0
38R75	H2+	+H2O	=H2O+	H2		3.90D-09	0.00	000000.0
38R75	H2+	+H2O	=H3O+	H		3.40D-09	0.00	000000.0
P& H	H2+	+CH	=CH+	H2		7.10D-10	0.00	000000.0
P& H	H2+	+CH	=CH2+	H		7.10D-10	0.00	000000.0
P& H	H2+	+CH2	=CH3+	H		1.00D-09	0.00	000000.0
P& H	H2+	+CH2	=CH2+	H2		1.00D-09	0.00	000000.0
P& H	H3+	+O	=OH+	H2		8.00D-10	0.00	000000.0
P& H	H3+	+OH	=H2O+	H2		1.30D-09	0.00	000000.0
5Z89	H3+	+CO	=HCO+	H2		1.70D-09	0.00	000000.0
39R82	H3+	+CO2	=HCO2+	H2		2.00D-09	0.00	000000.0
40R75	H3+	+H2O	=H3O+	H2		4.30D-09	0.00	000000.0
P& H	H3+	+C	=CH+	H2		2.00D-09	0.00	000000.0
P& H	H3+	+CH	=CH2+	H2		1.20D-09	0.00	000000.0
P& H	H3+	+CH2	=CH3+	H2		1.70D-09	0.00	000000.0
P& H	H3+	+CH3	=CH4+	H2		2.10D-09	0.00	000000.0
5Z89	H3+	+CH4	=CH5+	H2		1.90D-09	0.00	000000.0
85 86	He+	+H2	=H+	H	He	1.10D-13	-.24	000000.0
P& H	He+	+OH	=OH+	He		5.50D-10	0.00	000000.0
P& H	He+	+OH	=O+	H	He	5.50D-10	0.00	000000.0
74 85	He+	+H2O	=OH+	H	He	2.30D-10	-.94	000000.0
74 85	He+	+H2O	=H2O+	He		4.86D-11	-.94	000000.0
74 85	He+	+H2O	=H+	OH	He	1.64D-10	-.94	000000.0
42R85	He+	+CO	=C+	O	He	1.50D-09	0.00	000000.0
42R85	He+	+O2	=O+	O	He	1.00D-09	0.00	000000.0
81R77	He+	+CO2	=CO+	O	He	7.70D-10	0.00	000000.0
81R77	He+	+CO2	=O+	CO	He	1.80D-10	0.00	000000.0
81R77	He+	+CO2	=C+	O2	He	4.00D-11	0.00	000000.0
P& H	He+	+CH	=C+	H	He	1.10D-09	0.00	000000.0
P& H	He+	+CH2	=C+	H2	He	7.50D-10	0.00	000000.0

P& H	He+	+CH2	=CH+	H	He		7.50D-10	0.00	000000.0
P& H	He+	+CH3	=CH+	H2	He		9.00D-10	0.00	000000.0
P& H	He+	+CH3	=CH2+	H	He		9.00D-10	0.00	000000.0
43R76	He+	+CH4	=H+	CH3	He		4.00D-10	0.00	000000.0
43R76	He+	+CH4	=CH+	H2	H	He	2.56D-10	0.00	000000.0
43R76	He+	+CH4	=CH2+	H2	He		8.48D-10	0.00	000000.0
43R76	He+	+CH4	=CH3+	H	He		8.00D-11	0.00	000000.0
43R76	He+	+CH4	=CH4+	He			1.60D-11	0.00	000000.0
88 85	C+	+OH	=CO+	H			8.00D-10	0.00	000000.0
88 85	C+	+OH	=H+	CO			8.00D-10	0.00	000000.0
74 85	C+	+H2O	=HCO+	H			2.43D-09	-.63	000000.0
73R84	C+	+O2	=O+	CO			5.15D-10	0.00	000000.0
73R84	C+	+O2	=CO+	O			3.15D-10	0.00	000000.0
82R81	C+	+CO2	=CO+	CO			1.10D-09	0.00	000000.0
78 83	C+	+CH	=C2+	H			3.80D-10	0.00	000000.0
78 83	C+	+CH	=CH+	C			3.80D-10	0.00	000000.0
P& H	C+	+CH2	=CH2+	C			5.20D-10	0.00	000000.0
P& H	C+	+CH2	=C2H+	H			5.20D-10	0.00	000000.0
7R82	C+	+CH4	=C2H2+	H2			3.25D-10	0.00	000000.0
7R82	C+	+CH4	=C2H3+	H			9.75D-10	0.00	000000.0
52R84	O+	+H	=H+	O			6.00D-10	0.00	000000.0
52R84	O+	+H2	=OH+	H			1.20D-09	0.00	000000.0
P& H	O2+	+C	=CO+	O			5.20D-11	0.00	000000.0
P& H	O2+	+C	=C+	O2			5.20D-11	0.00	000000.0
44R81	OH+	+H2	=H2O+	H			1.01D-09	0.00	000000.0
44R81	H2O+	+H2	=H3O+	H			8.30D-10	0.00	000000.0
P& H	H3O+	+H	=H2O+	H2			6.10D-10	0.00	020500.0
P& H	H3O+	+C	=HCO+	H2			1.00D-11	0.00	000000.0
P& H	H3O+	+CH	=CH2+	H2O			6.80D-10	0.00	000000.0
P& H	H3O+	+CH2	=CH3+	H2O			9.40D-10	0.00	000000.0
P& H	O+	+ELECTR	=O	PHOTON			3.40D-12	-.64	000000.0
1Z83	O2+	+ELECTR	=O	O			1.95D-07	-.70	000000.0
22Z90	OH+	+ELECTR	=O	H			3.75D-08	-.50	000000.0
22Z90	H2O+	+ELECTR	=OH	H			3.15D-07	-.50	000000.0
90 88	H3O+	+ELECTR	=OH	H2			8.45D-07	-.50	000000.0
90 88	H3O+	+ELECTR	=H2O	H			4.55D-07	-.50	000000.0
49R76	CH3+	+O	=HCO+	H2			3.10D-10	0.00	000000.0
49R76	CH3+	+O	=H3+	CO			1.30D-11	0.00	000000.0
8R80	CH5+	+O	=H3O+	CH2			2.16D-10	0.00	000000.0
51R80	CH5+	+CO	=HCO+	CH4			9.90D-10	0.00	000000.0
40R75	CH5+	+H2O	=H3O+	CH4			3.70D-09	0.00	000000.0
52R84	CO+	+H2	=HCO+	H			1.30D-09	0.00	000000.0
52R84	CO+	+H	=H+	CO			7.50D-10	0.00	000000.0
52R84	HCO+	+H	=CO+	H2			1.30D-09	0.00	024500.0
P& H	HCO+	+C	=CH+	CO			1.10D-09	0.00	000000.0
P& H	HCO+	+CH	=CH2+	CO			6.30D-10	0.00	000000.0
P& H	HCO+	+CH2	=CH3+	CO			8.60D-10	0.00	000000.0
27R77	HCO+	+CH3	=CH4+	CO			1.40D-09	0.00	009060.0
51R80	HCO+	+CH4	=CH5+	CO			9.90D-10	0.00	004920.0
65R78	HCO+	+H2O	=H3O+	CO			2.50D-09	0.00	000000.0
15	HCO+	+O2	=HCO2+	O			1.00D-09	0.00	001450.0
15	HCO2+	+O	=HCO+	O2			1.00D-09	0.00	000000.0
15	HCO+	+OH	=HCO2+	H			1.00D-09	0.00	000000.0
15	HCO2+	+H	=HCO+	OH			1.00D-09	0.00	007500.0
15	HCO2+	+CO	=HCO+	CO2			1.00D-09	0.00	000000.0
15	HCO+	+CO2	=HCO2+	CO			1.00D-09	0.00	005000.0
6R80	HCO2+	+CH4	=CH5+	CO2			7.80D-10	0.00	000000.0
22Z90	CO+	+ELECTR	=C	O			1.00D-07	-.46	000000.0
22Z90	HCO+	+ELECTR	=CO	H			2.40D-07	-.69	000000.0
6Z88	HCO2+	+ELECTR	=CO2	H			2.24D-07	-.50	000000.0
6Z88	HCO2+	+ELECTR	=CO	OH			1.16D-07	-.50	000000.0
27C77	C2+	+H2	=C2H+	H			1.40D-09	0.00	000000.0
45C77	C2+	+H2	=H+	C2H			1.50D-09	0.00	001260.0
45C77	C2H+	+H2	=C2H2+	H			1.70D-09	0.00	000000.0
46C84	C2H2+	+H2	=C2H3+	H			5.00D-10	0.00	000800.0
22Z90	C2+	+ELECTR	=C	C			3.00D-07	-.50	000000.0
22Z90	C2H+	+ELECTR	=C2	H			1.35D-07	-.50	000000.0
22Z90	C2H+	+ELECTR	=CH	C			1.35D-07	-.50	000000.0

75 88	C2H2+	+ELECTR	=C2H	H		1.50D-07	-.50	000000.0
75 88	C2H2+	+ELECTR	=CH	CH		1.50D-07	-.50	000000.0
75 88	C2H3+	+ELECTR	=C2H	H2		1.35D-07	-.50	000000.0
75 88	C2H3+	+ELECTR	=CH2	CH		1.35D-07	-.50	000000.0
75 88	C2H3+	+ELECTR	=C2H2	H		3.00D-08	-.50	000000.0
58 83	C3+	+H2	=C3H+	H		3.00D-10	0.00	000000.0
46C84	C3H+	+H2	=C3H2+	H		1.00D-09	0.00	000500.0
62 86	C3H+	+H2	=C3H3+	PHOTON		3.00D-13	-1.0	000000.0
46C84	C3H2+	+H2	=C3H3+	H		1.00D-10	0.00	002000.0
27C77	C2+	+H2	=C2H+	H		1.40D-09	0.00	000000.0
45C77	C2+	+H2	=H+	C2H		1.50D-09	0.00	001260.0
45C77	C2H+	+H2	=C2H2+	H		1.70D-09	0.00	000000.0
46C84	C2H2+	+H2	=C2H3+	H		5.00D-10	0.00	000800.0
22Z90	C2+	+ELECTR	=C	C		3.00D-07	-.50	000000.0
22Z90	C2H+	+ELECTR	=C2	H		1.35D-07	-.50	000000.0
22Z90	C2H+	+ELECTR	=CH	C		1.35D-07	-.50	000000.0
75 88	C2H2+	+ELECTR	=C2H	H		1.50D-07	-.50	000000.0
75 88	C2H2+	+ELECTR	=CH	CH		1.50D-07	-.50	000000.0
75 88	C2H3+	+ELECTR	=C2H	H2		1.35D-07	-.50	000000.0
75 88	C2H3+	+ELECTR	=CH2	CH		1.35D-07	-.50	000000.0
75 88	C2H3+	+ELECTR	=C2H2	H		3.00D-08	-.50	000000.0
58 83	C3+	+H2	=C3H+	H		3.00D-10	0.00	000000.0
46C84	C3H+	+H2	=C3H2+	H		1.00D-09	0.00	000500.0
62 86	C3H+	+H2	=C3H3+	PHOTON		3.00D-13	-1.0	000000.0
46C84	C3H2+	+H2	=C3H3+	H		1.00D-10	0.00	002000.0
P& H	C3+	+ELECTR	=C2	C		3.00D-07	-.50	000000.0
P& H	C3H+	+ELECTR	=C2	CH		1.50D-07	-.50	000000.0
P& H	C3H+	+ELECTR	=C2H	C		1.50D-07	-.50	000000.0
75 88	C3H2+	+ELECTR	=C3H	H		1.50D-07	-.50	000000.0
75 88	C3H2+	+ELECTR	=C2H	CH		1.50D-07	-.50	000000.0
75 88	C3H3+	+ELECTR	=C3H2	H		1.50D-07	-.50	000000.0
75 88	C3H3+	+ELECTR	=C2H2	CH		1.50D-07	-.50	000000.0
P& H	H+	+C2	=C2+	H		3.10D-09	0.00	000000.0
P& H	H+	+C2H	=C2+	H2		1.50D-09	0.00	000000.0
P& H	H+	+C2H	=C2H+	H		1.50D-09	0.00	000000.0
78 83	H+	+C2H2	=C2H+	H2		2.00D-09	0.00	000000.0
78 83	H+	+C2H2	=C2H2+	H		2.00D-09	0.00	000000.0
4 84	H+	+C3H	=C3+	H2		2.00D-09	0.00	000000.0
4 84	H+	+C3H	=C3H+	H		2.00D-09	0.00	000000.0
4 84	H+	+C3H2	=C3H+	H2		2.00D-09	0.00	000000.0
4 84	H+	+C3H2	=C3H2+	H		2.00D-09	0.00	000000.0
P& H	He+	+C2H	=C+	CH	He	5.10D-10	0.00	000000.0
P& H	He+	+C2H	=CH+	C	He	5.10D-10	0.00	000000.0
P& H	He+	+C2H	=C2+	H	He	5.10D-10	0.00	000000.0
3R75	He+	+C2H2	=CH+	CH	He	7.70D-10	0.00	000000.0
3R75	He+	+C2H2	=C2+	H2	He	1.61D-09	0.00	000000.0
3R75	He+	+C2H2	=C2H+	H	He	8.75D-10	0.00	000000.0
3R75	He+	+C2H2	=C2H2+	He		2.45D-10	0.00	000000.0
4 84	He+	+C3H	=C3+	H	He	2.00D-09	0.00	000000.0
4 84	He+	+C3H2	=C3H+	H	He	1.00D-09	0.00	000000.0
4 84	He+	+C3H2	=C3+	H2	He	1.00D-09	0.00	000000.0
P& H	H3+	+C2H	=C2H2+	H2		1.70D-09	0.00	000000.0
2R77	H3+	+C2H2	=C2H3+	H2		2.90D-09	0.00	000000.0
4 84	H3+	+C3H	=C3H2+	H2		2.00D-09	0.00	000000.0
4 84	H3+	+C3H2	=C3H3+	H2		2.00D-09	0.00	000000.0
P& H	C+	+C2H	=C3+	H		1.00D-09	0.00	000000.0
7R82	C+	+C2H2	=C3H+	H		2.20D-09	0.00	000000.0
P& H	HCO+	+C2H	=C2H2+	CO		7.80D-10	0.00	000000.0
54R77	HCO+	+C2H2	=C2H3+	CO		1.36D-09	0.00	000000.0
4 84	HCO+	+C3H	=C3H2+	CO		1.40D-09	0.00	000000.0
4 84	HCO+	+C3H2	=C3H3+	CO		1.40D-09	0.00	000000.0
10R86	H3O+	+C2H	=C2H2+	H2O		2.20D-10	0.00	004100.0
15	H3O+	+C2H2	=C2H3+	H2O		1.00D-09	0.00	007330.0
75 88	H3O+	+C3H	=C3H2+	H2O		2.00D-09	0.00	000000.0
75 88	H3O+	+C3H2	=C3H3+	H2O		3.00D-09	0.00	000000.0
10R86	C2H2+	+H2O	=H3O+	C2H		2.20D-10	0.00	000000.0
10R86	C2H3+	+H2O	=H3O+	C2H2		1.11D-09	0.00	000000.0
83R83	C3H+	+H2O	=HCO+	C2H2		2.48D-10	0.00	000000.0

83R83	C3H+	+H2O	=C2H3+	CO		2.02D-10	0.00	000000.0
P& H	H+	+Fe	=Fe+	H		7.40D-09	0.00	000000.0
P& H	H3+	+Fe	=Fe+	H2	H	4.90D-09	0.00	000000.0
P& H	C+	+Fe	=Fe+	C		2.60D-09	0.00	000000.0
P& H	HCO+	+Fe	=Fe+	CO	H	1.90D-09	0.00	000000.0
P& H	H3O+	+Fe	=Fe+	H2O	H	3.10D-09	0.00	000000.0
P& H	O2+	+Fe	=Fe+	O2		1.10D-09	0.00	000000.0
P& H	Fe+	+ELECTR	=Fe	PHOTON		3.70D-12	-.65	000000.0
P& H	N	CRP	N+	ELECTR		2.10E+00	0.00	000000.0
2Z89	CN	+SECPHO	=C	N		2.12D+04	0.00	140000.0
2Z89	HCN	+SECPHO	=CN	H		6.23D+03	0.00	140000.0
2Z89	HNC	+SECPHO	=CN	H		6.23D+03	0.00	140000.0
2Z89	NH2	+SECPHO	=NH	H		1.60D+02	0.00	140000.0
2Z89	NH2	+SECPHO	=NH2+	ELECTR		1.30D+03	0.00	140000.0
2Z89	NH3	+SECPHO	=NH2	H		2.63D+03	0.00	140000.0
2Z89	NH3	+SECPHO	=NH	H2		1.08D+03	0.00	140000.0
2Z89	NH3	+SECPHO	=NH3+	ELECTR		1.15D+03	0.00	140000.0
2Z89	NO	+SECPHO	=N	O		9.64D+02	0.00	140000.0
2Z89	NO	+SECPHO	=NO+	ELECTR		9.88D+02	0.00	140000.0
97 83	N	H2	NH	H		8.66D-10	0.50	014600.0
97 83	NH	H2	NH2	H		5.25D-12	0.79	006700.0
97 83	NH2	H2	NH3	H		6.22D-11	0.50	006300.0
14Z90	CN	H2	HCN	H		3.53D-13	3.31	000756.0
97 83	NH	H	N	H2		8.66D-10	0.50	002400.0
97 83	NH2	H	NH	H2		5.25D-12	0.79	002200.0
97 83	NH3	H	NH2	H2		6.22D-11	0.50	005700.0
P& H	NH	O	OH	N		2.90D-11	0.50	000000.0
P& H	NH2	O	NH	OH		3.50D-12	0.50	000000.0
97 83	NH3	O	NH2	OH		2.50D-12	0.00	003020.0
P& H	CN	O	CO	N		1.80D-11	0.50	000050.0
97 83	NH3	OH	NH2	H2O		2.30D-12	0.00	000800.0
P& H	NH	C	CN	H		1.10D-10	0.50	000000.0
94 88	CH	N	CN	H		2.10D-11	0.00	000000.0
97 83	CN	N	N2	C		7.30D-10	0.00	004500.0
P& H	NH	N	N2	H		5.00D-11	0.50	000000.0
94E88	OH	N	NO	H		5.30D-11	0.00	000050.0
97 83	O2	N	NO	O		3.30D-12	1.00	003150.0
P& H	NO	C	CN	O		1.10D-10	0.50	000000.0
94E88	NO	N	N2	O		3.40D-11	0.00	000050.0
97 83	NO	O	O2	N		7.50D-13	1.00	016000.0
GUESS	HNC	H	HCN	H		1.00D-10	0.50	000200.0
GUESS	HNC	O	CO	NH		2.00D-10	0.50	000200.0
GUESS	HNC	OH	H2O	CN		2.00D-10	0.50	000200.0
GUESS	HNC	O2	CO2	NH		2.00D-11	0.50	002000.0
3Z82	NH2	C	HNC	H		2.00D-11	0.50	000000.0
P& H	CH2	N	HCN	H		2.00D-11	0.50	000000.0
P& H	CH3	N	HCN	H2		2.00D-11	0.50	000000.0
GUESS	CH5+	HNC	C2H3+	NH3		1.00D-09	0.00	000000.0
GUESS	CH5+	HCN	C2H3+	NH3		1.00D-09	0.00	005120.0
13R85	N+	H2	NH+	H		8.40D-10	0.00	000168.5
10R80	NH+	H2	NH2+	H		1.27D-09	0.00	000000.0
10R80	NH+	H2	H3+	N		2.25D-10	0.00	000000.0
10R80	NH2+	H2	NH3+	H		2.70D-10	0.00	000000.0
07R83	NH3+	H2	NH4+	H		2.40D-12	0.00	000000.0
13R85	NH+	H	N+	H2		6.52D-10	0.00	000000.0
10R80	NH2+	H	NH+	H2		1.27D-09	0.00	024000.0
10R80	NH3+	H	NH2+	H2		2.25D-10	0.00	012800.0
15	NH4+	H	NH3+	H2		1.00D-09	0.00	011000.0
04R84	CN+	H2	HCN+	H		1.00D-09	0.00	000000.0
04R84	HCN+	H	CN+	H2		1.00D-09	0.00	015800.0
01R79	HCN+	H2	H2CN+	H		9.80D-10	0.00	000000.0
01R79	H2CN+	H	HCN+	H2		9.80D-10	0.00	034400.0
9Z89	N2+	H2	N2H+	H		2.00D-09	0.24	000000.0
10R80	N2H+	H	N2+	H2		2.10D-09	0.00	030300.0
08R82	N2H+	H2	H3+	N2		1.80D-09	0.00	008300.0
52	H+	HNC	H+	HCN		1.00D-09	0.00	000000.0
15	H+	HCN	H+	HNC		1.00D-09	0.00	007850.0
P& H	H+	NH	NH+	H		2.10D-09	0.00	000000.0

P& H	H+	NH2	NH2+	H		2.90D-09	0.00	000000.0
12R85	H+	NH3	NH3+	H		5.20D-09	0.00	000000.0
15	H+	CN	CN+	H		2.10D-09	0.00	006150.0
12R85	H+	HCN	HCN+	H		1.10D-08	0.00	000000.0
01R72	H+	NO	NO+	H		1.90D-09	0.00	000000.0
P& H	He+	NH	N+	H	He	1.10D-09	0.00	000000.0
P& H	He+	NH2	NH+	H	He	8.00D-10	0.00	000000.0
P& H	He+	NH2	N+	H2	He	8.00D-10	0.00	000000.0
02R75	He+	NH3	NH3+	He		2.64D-10	0.00	000000.0
02R75	He+	NH3	NH2+	H	He	1.76D-09	0.00	000000.0
02R75	He+	NH3	NH+	H2	He	1.76D-10	0.00	000000.0
P& H	He+	CN	C+	N	He	8.80D-10	0.00	000000.0
P& H	He+	CN	N+	C	He	8.80D-10	0.00	000000.0
01R77	He+	HCN	CN+	H	He	1.46D-09	0.00	000000.0
01R77	He+	HCN	CH+	N	He	6.20D-10	0.00	000000.0
01R77	He+	HCN	C+	NH	He	7.75D-10	0.00	000000.0
01R77	He+	HCN	N+	CH	He	2.48D-10	0.00	000000.0
01R77	He+	HNC	CN+	H	He	1.55D-09	0.00	000000.0
01R77	He+	HNC	C+	NH	He	1.55D-09	0.00	000000.0
02R77	He+	N2	N+	N	He	7.92D-10	0.00	000000.0
02R77	He+	N2	N2+	He		4.08D-10	0.00	000000.0
02R77	He+	NO	N+	O	He	1.38D-09	0.00	000000.0
02R77	He+	NO	O+	N	He	2.24D-10	0.00	000000.0
P& H	H3+	NH	NH2+	H2		1.30D-09	0.00	000000.0
P& H	H3+	NH2	NH3+	H2		1.80D-09	0.00	000000.0
5Z89	H3+	NH3	NH4+	H2		9.10D-09	0.00	000000.0
	H3+	N	NH2+	H		4.50D-20	0.00	000000.0
P& H	H3+	CN	HCN+	H2		1.00D-09	0.00	000000.0
P& H	H3+	CN	H2CN+	H		1.00D-09	0.00	000000.0
12R85	H3+	HCN	H2CN+	H2		9.50D-09	0.00	000000.0
12R85	H3+	HNC	H2CN+	H2		9.50D-09	0.00	000000.0
5Z89	H3+	N2	N2H+	H2		1.30D-09	0.00	000000.0
08R82	H3+	NO	HNO+	H2		1.10D-09	0.00	000000.0
19R80	H3O+	NH3	NH4+	H2O		2.20D-09	0.00	000000.0
	H3O+	CN	H2CN+	OH		4.50D-09	0.00	000000.0
19R78	H3O+	HCN	H2CN+	H2O		4.50D-09	0.00	000000.0
19R78	H2CN+	H2O	H3O+	HCN		4.50D-09	0.00	002460.0
19R78	H3O+	HNC	H2CN+	H2O		4.50D-09	0.00	000000.0
19R78	H2CN+	H2O	H3O+	HNC		4.50D-09	0.00	010300.0
P& H	HCO+	NH	NH2+	CO		6.40D-10	0.00	000000.0
P& H	NH2+	CO	HCO+	NH		6.40D-10	0.00	006100.0
P& H	HCO+	NH2	NH3+	CO		8.90D-10	0.00	000000.0
05R78	HCO+	NH3	NH4+	CO		1.90D-09	0.00	000000.0
12R85	HCO+	HCN	H2CN+	CO		3.70D-09	0.00	000000.0
12R85	HCO+	HNC	H2CN+	CO		3.70D-09	0.00	000000.0
04R71	HCO2+	NO	HNO+	CO2		1.00D-10	0.00	000000.0
P& H	C+	NH	CN+	H		7.80D-10	0.00	000000.0
P& H	C+	NH2	HCN+	H		1.10D-09	0.00	000000.0
05R79	C+	NH3	NH3+	C		5.29D-10	0.00	000000.0
05R79	C+	NH3	H2NC+	H		7.80D-10	0.00	000000.0
05R79	C+	NH3	H2CN+	H		7.80D-10	0.00	000000.0
05R79	C+	NH3	HCN+	H2		2.08D-10	0.00	000000.0
12R85	C+	HCN	C2N+	H		3.40D-09	0.00	000000.0
12R85	C+	HNC	C2N+	H		3.40D-09	0.00	000000.0
09R84	C+	NO	NO+	C		3.40D-09	0.00	000000.0
09R84	C+	NO	N+	CO		9.02D-10	0.00	000000.0
09R84	N+	CO	C+	NO		9.02D-10	0.00	015400.0
17R77	O2+	N	NO+	O		7.84D-11	0.00	000000.0
18R83	O2+	NH3	NH3+	O2		2.00D-09	0.00	000000.0
08R78	O2+	NO	NO+	O2		4.40D-10	0.00	000000.0
P& H	CH2+	N	HCN+	H		9.40D-10	0.00	000000.0
P& H	C2H+	N	C2N+	H		8.30D-10	0.00	000000.0
P& H	CH3+	N	HCN+	H2		6.70D-11	0.00	000000.0
M88	CH3+	N	H2CN+	H		6.70D-11	0.00	000000.0
M88	C2H2+	N	CH+	HCN		2.50D-11	0.00	000000.0
M88	C2H2+	N	CH+	HNC		2.50D-11	0.00	002600.0
M88	C2H2+	N	C2N+	H2		2.25D-10	0.00	000000.0
17R80	N+	O2	O2+	N		2.81D-10	0.00	000000.0

17R80	N+	O2	NO+	O		2.37D-10	0.00	000000.0
17R80	N+	O2	O+	NO		3.30D-11	0.00	000000.0
09R84	N+	CO	CO+	N		8.25D-10	0.00	000000.0
09R84	N+	CO	NO+	C		1.46D-10	0.00	000000.0
10R80	N+	NO	NO+	N		4.51D-10	0.00	000000.0
10R80	N+	NO	N2+	O		7.95D-11	0.00	000000.0
13R83	NH3+	H2O	NH4+	OH		2.50D-10	0.00	000000.0
13R83	NH4+	OH	NH3+	H2O		2.50D-10	0.00	003400.0
06R80	N2H+	O	OH+	N2		1.40D-10	0.00	003400.0
08R82	N2H+	H2O	H3O+	N2		2.60D-09	0.00	000000.0
06R80	N2H+	CO	HCO+	N2		8.80D-10	0.00	000000.0
06R80	HCO+	N2	N2H+	CO		8.80D-10	0.00	011200.0
08R82	N2H+	CO2	HCO2+	N2		1.40D-09	0.00	000000.0
08R82	HCO2+	N2	N2H+	CO2		1.40D-09	0.00	006400.0
15R74	N2H+	NH3	NH4+	N2		2.30D-09	0.00	000000.0
15R74	NH4+	N2	N2H+	NH3		2.30D-09	0.00	044000.0
08R82	N2H+	NO	HNO+	N2		3.40D-10	0.00	000000.0
01R83	C2N+	NH3	N2H+	C2H2		1.90D-10	0.00	000000.0
01R83	C2N+	NH3	H2CN+	HCN		1.70D-09	0.00	000000.0
P& H	HNO+	C	CH+	NO		1.00D-09	0.00	000000.0
04R71	HNO+	CO	HCO+	NO		1.00D-10	0.00	000000.0
04R71	HNO+	CO2	HCO2+	NO		1.00D-10	0.00	000000.0
P& H	HNO+	OH	H2O+	NO		6.20D-10	0.00	000000.0
08R82	HNO+	H2O	H3O+	NO		2.30D-09	0.00	000000.0
P& H	NO+	Fe	Fe+	NO		1.00D-09	0.00	000000.0
P& H	N+	ELECTR	N	PHOTON		3.80D-12	-0.62	000000.0
P& H	NH+	ELECTR	N	H		2.00D-07	-0.50	000000.0
P& H	NH2+	ELECTR	NH	H		1.50D-07	-0.50	000000.0
P& H	NH2+	ELECTR	N	H	H	1.50D-07	-0.50	000000.0
22Z90	NH3+	ELECTR	NH2	H		3.00D-07	-0.50	000000.0
22Z90	NH4+	ELECTR	NH2	H2		7.60D-07	-0.50	000000.0
22Z90	NH4+	ELECTR	NH3	H		7.60D-07	-0.50	000000.0
P& H	CN+	ELECTR	C	N		1.80D-07	-0.50	000000.0
75 88	C2N+	ELECTR	C2	N		1.00D-07	-0.50	000000.0
75 88	C2N+	ELECTR	CN	C		2.00D-07	-0.50	000000.0
75 88	HCN+	ELECTR	CN	H		1.50D-07	-0.50	000000.0
75 88	HCN+	ELECTR	CH	N		1.50D-07	-0.50	000000.0
22Z90	N2+	ELECTR	N	N		3.60D-08	-0.42	000000.0
6Z88	N2H+	ELECTR	N2	H		1.70D-07	-1.00	000000.0
7Z88	H2CN+	ELECTR	HCN	H		1.75D-07	-0.50	000000.0
7Z88	H2CN+	ELECTR	HNC	H		1.75D-07	-0.50	000000.0
7Z88	H2NC+	ELECTR	HNC	H		1.75D-07	-0.50	000000.0
7Z88	H2NC+	ELECTR	NH2	C		1.75D-07	-0.50	000000.0
22Z90	NO+	ELECTR	N	O		4.30D-07	-0.37	000000.0
P& H	HNO+	ELECTR	NO	H		3.00D-07	-0.50	000000.0
15	SO	+SECPHO	=S	O		9.64D+02	0.00	140000.0
15	CS	+SECPHO	=S	C		2.12D+04	0.00	140000.0
15	SH	+SECPHO	=S	H		1.46D+03	0.00	140000.0
2Z89	OCS	+SECPHO	=CO	S		1.07D+04	0.00	140000.0
2Z89	H2S	+SECPHO	=S	H2		1.03D+04	0.00	140000.0
2Z89	H2S	+SECPHO	=H2S+	ELECTR		3.39D+03	0.00	140000.0
2Z89	SO2	+SECPHO	=SO	O		1.77D+03	0.00	140000.0
16Z88	S	+H2	=SH	H		1.04D-10	.132	009620.0
16Z88	SH	+H2	=H2S	H		6.41D-12	.087	008050.0
16Z88	SH	+H	=S	H2		2.50D-11	0.00	000000.0
16Z88	H2S	+H	=SH	H2		1.29D-11	0.00	000860.0
16Z88	SO	+H	=OH	S		5.90D-10	-.31	011100.0
16Z88	SO2	+H	=SO	OH		9.25D-09	-.74	014700.0
16Z88	OCS	+H	=SH	CO		1.70D-11	0.00	002000.0
UMIST	SH	+O	=SO	H		1.60D-10	0.00	000100.0
17Z88	SH	+O	=OH	S		1.70D-11	0.67	000950.0
16Z88	H2S	+O	=SH	OH		1.40D-11	0.00	001920.0
16Z88	H2S	+OH	=SH	H2O		6.30D-12	0.00	000080.0
16Z88	CS	+O	=CO	S		2.70D-10	0.00	000760.0
16Z88	CS	+OH	=OCS	H		1.55D-13	1.12	000800.0
24Z87	S	+O2	=SO	O		5.19D-12	0.00	000265.0
16Z88	SO	+O	=S	O2		6.60D-13	0.00	002760.0
16Z88	SO	+O2	=SO2	O		1.40D-12	0.00	002820.0

23Z90	SO	+OH	=SO2	H		1.96D-10	-.17	000000.0
UMIST	SO	+N	=NO	S		1.73D-11	0.50	000750.0
16Z88	SO	+C	=CO	S		7.20D-11	0.00	000000.0
16Z88	SO	+C	=CS	O		1.70D-10	0.00	000000.0
16Z88	SO2	+O	=SO	O2		9.27D-11	-.46	009140.0
16Z88	OCS	+O	=SO	CO		2.60D-11	0.00	002250.0
16Z88	CH	+S	=CS	H		1.10D-12	0.00	000000.0
16Z88	CH	+S	=SH	C		1.73D-11	0.50	004000.0
16Z88	OH	+S	=SO	H		1.00D-10	0.00	000100.0
16Z88	SH	+C	=CS	H		2.00D-11	0.00	000000.0
16Z88	SH	+C	=CH	S		1.20D-11	0.58	005880.0
16Z88	SH	+CO	=OCS	H		5.95D-14	1.12	008330.0
18Z86	S+	+H2	=SH+	H		2.20D-10	0.00	009860.0
18Z86	SH+	+H2	=H2S+	H		1.90D-10	0.00	008500.0
P& H	SH+	+H2	=H3S+	PHOTON		1.00D-15	0.00	000000.0
18Z86	H2S+	+H2	=H3S+	H		1.40D-11	0.00	002300.0
1R84	CS+	+H2	=HCS+	H		4.80D-10	0.00	000000.0
18Z86	SH+	+H	=S+	H2		1.10D-10	0.00	000000.0
18Z86	H2S+	+H	=SH+	H2		2.00D-10	0.00	000000.0
18Z86	H3S+	+H	=H2S+	H2		6.00D-11	0.00	000000.0
P& H	SO+	+H	=S+	0H		6.10D-10	0.00	011385.0
GUESS	H+	+S	=S+	H		1.00D-15	0.00	000000.0
P& H	H+	+SH	=SH+	H		1.60D-09	0.00	000000.0
P& H	H+	+SH	=S+	H2		1.60D-09	0.00	000000.0
P& H	H+	+H2S	=H2S+	H		7.60D-09	0.00	000000.0
P& H	H+	+CS	=CS+	H		4.90D-09	0.00	000000.0
P& H	H+	+SO	=SO+	H		3.20D-09	0.00	000000.0
P& H	H+	+OCS	=SH+	CO		5.90D-09	0.00	000000.0
P& H	H3+	+S	=SH+	H2		2.60D-09	0.00	000000.0
P& H	H3+	+SH	=H2S+	H2		1.90D-09	0.00	000000.0
P& H	H3+	+H2S	=H3S+	H2		3.70D-09	0.00	000000.0
P& H	H3+	+CS	=HCS+	H2		2.90D-09	0.00	000000.0
P& H	H3+	+SO	=HSO+	H2		1.90D-09	0.00	000000.0
8R82	H3+	+SO2	=HSO2+	H2		1.30D-09	0.00	000000.0
8R82	H3+	+OCS	=HOCS+	H2		1.90D-09	0.00	000000.0
P& H	He+	+SH	=S+	H	He	1.70D-09	0.00	000000.0
P& H	He+	+H2S	=S+	H2	He	3.60D-09	0.00	000000.0
P& H	He+	+H2S	=SH+	H	He	4.80D-10	0.00	000000.0
P& H	He+	+H2S	=H2S+	He		3.10D-10	0.00	000000.0
P& H	He+	+CS	=C+	S	He	1.30D-09	0.00	000000.0
P& H	He+	+CS	=S+	C	He	1.30D-09	0.00	000000.0
P& H	He+	+SO	=O+	S	He	8.30D-10	0.00	000000.0
P& H	He+	+SO	=S+	0	He	8.30D-10	0.00	000000.0
P& H	He+	+OCS	=CS+	0	He	7.60D-10	0.00	000000.0
P& H	He+	+OCS	=S+	CO	He	7.60D-10	0.00	000000.0
P& H	He+	+OCS	=CO+	S	He	7.60D-10	0.00	000000.0
P& H	He+	+OCS	=O+	CS	He	7.60D-11	0.00	000000.0
2R73	He+	+SO2	=S+	02	He	8.60D-10	0.00	000000.0
2R73	He+	+SO2	=SO+	0	He	3.44D-09	0.00	000000.0
P& H	C+	+S	=S+	C		1.50D-09	0.00	000000.0
P& H	C+	+SH	=CS+	H		1.10D-09	0.00	000000.0
3R78	C+	+H2S	=HCS+	H		1.28D-09	0.00	000000.0
3R78	C+	+H2S	=H2S+	C		4.25D-10	0.00	000000.0
P& H	C+	+CS	=CS+	C		1.60D-09	0.00	000700.0
P& H	C+	+SO	=S+	CO		2.60D-10	0.00	000000.0
P& H	C+	+SO	=CS+	0		2.60D-10	0.00	000000.0
P& H	C+	+SO	=SO+	C		2.60D-10	0.00	000000.0
P& H	C+	+SO	=CO+	S		2.60D-10	0.00	000000.0
P& H	C+	+OCS	=CS+	CO		1.60D-09	0.00	000000.0
P& H	C+	+SO2	=SO+	CO		2.30D-09	0.00	000000.0
P& H	CH+	+S	=S+	CH		4.70D-10	0.00	000000.0
P& H	CH+	+S	=SH+	C		4.70D-10	0.00	000000.0
P& H	CH+	+S	=CS+	H		4.70D-10	0.00	000000.0
19Z82	CH+	+SO	=OH+	CS		1.00D-09	0.00	000000.0
19Z82	CH+	+SO	=SH+	CO		1.00D-09	0.00	000000.0
P& H	CH3+	+S	=HCS+	H2		1.40D-09	0.00	000000.0
P& H	CH3+	+SO	=HOCS+	H2		9.50D-10	0.00	000000.0
P& H	CH5+	+S	=SH+	CH4		1.30D-09	0.00	000000.0

P& H	H3O+	+S	=SH+	H2O		3.20D-10	0.00	004930.0
4R79	H3O+	+H2S	=H3S+	H2O		1.90D-09	0.00	000000.0
P& H	HCO+	+S	=SH+	CO		3.30D-10	0.00	000000.0
P& H	HCO+	+SH	=H2S+	CO		8.20D-10	0.00	000000.0
P& H	HCO+	+CS	=HCS+	CO		1.20D-09	0.00	000000.0
P& H	HCO+	+SO	=HSO+	CO		7.50D-10	0.00	000000.0
7R75	HCO+	+H2S	=H3S+	CO		1.60D-09	0.00	000000.0
5R78	HCO+	+OCS	=HOCS+	CO		1.10D-09	0.00	000000.0
P& H	O2+	+S	=SO+	O		5.40D-10	0.00	000000.0
P& H	O2+	+S	=S+	O2		5.40D-10	0.00	000000.0
P& H	O2+	+H2S	=H2S+	O2		1.40D-09	0.00	000000.0
P& H	S+	+CH	=CS+	H		6.20D-10	0.00	000000.0
P& H	S+	+CH2	=HCS+	H		1.00D-11	0.00	000000.0
P& H	S+	+OH	=SO+	H		6.10D-10	0.00	000000.0
P& H	S+	+OH	=SH+	O		2.90D-10	0.00	008820.0
P& H	S+	+SH	=SH+	S		9.70D-10	0.00	000350.0
1R84	S+	+NO	=NO+	S		3.20D-10	0.00	000000.0
10R81	S+	+NH3	=NH3+	S		1.60D-09	0.00	000000.0
1R84	S+	+O2	=SO+	O		2.30D-11	0.00	000000.0
5R84	NH3+	+H2S	=NH4+	SH		6.00D-10	0.00	000000.0
P& H	HNO+	+S	=SH+	NO		1.10D-09	0.00	000000.0
P& H	N2H+	+S	=SH+	N2		1.10D-09	0.00	000000.0
P& H	SH+	+O	=SO+	H		2.90D-10	0.00	000000.0
P& H	SH+	+O	=S+	OH		2.90D-10	0.00	000000.0
P& H	SH+	+S	=S+	SH		9.70D-10	0.00	000000.0
P& H	SH+	+C	=CS+	H		9.90D-10	0.00	000000.0
P& H	SH+	+CH	=CH2+	S		5.80D-10	0.00	000000.0
P& H	SH+	+OH	=H2S+	O		3.10D-10	0.00	007500.0
P& H	SH+	+OH	=H2O+	S		4.30D-10	0.00	009200.0
10R81	SH+	+H2O	=H3O+	S		6.30D-10	0.00	000000.0
10R81	SH+	+H2S	=H2S+	SH		5.00D-10	0.00	001000.0
10R81	SH+	+H2S	=H3S+	S		5.00D-10	0.00	000000.0
1R84	SH+	+NO	=NO+	SH		3.30D-10	0.00	000000.0
10R81	SH+	+NH3	=NH3+	SH		5.25D-10	0.00	000000.0
10R81	SH+	+NH3	=NH4+	S		9.75D-10	0.00	000000.0
P& H	H2S+	+O	=SH+	OH		3.10D-10	0.00	000000.0
P& H	H2S+	+O	=SO+	H2		3.10D-10	0.00	000000.0
P& H	H2S+	+C	=HCS+	H		1.00D-09	0.00	000000.0
P& H	H2S+	+S	=S+	H2S		1.10D-09	0.00	000000.0
10R81	H2S+	+SH	=SH+	H2S		5.00D-10	0.00	000000.0
10R81	H2S+	+NO	=NO+	H2S		3.70D-10	0.00	000000.0
10R81	H2S+	+H2O	=H3O+	SH		8.10D-10	0.00	000000.0
10R81	H2S+	+NH3	=NH4+	SH		1.36D-09	0.00	000000.0
10R81	H2S+	+NH3	=NH3+	H2S		3.40D-10	0.00	000000.0
10R81	H3S+	+NH3	=NH4+	H2S		1.90D-09	0.00	000000.0
13R78	H3S+	+HCN	=H2CN+	H2S		1.90D-09	0.00	000000.0
19Z82	HCS+	+O	=HCO+	S		1.00D-09	0.00	000000.0
P& H	SO+	+NH3	=NH3+	SO		1.30D-09	0.00	000000.0
P& H	S+	+Fe	=Fe+	S		1.80D-10	0.00	000000.0
P& H	SH+	+Fe	=Fe+	SH		1.60D-09	0.00	000000.0
P& H	SO+	+Fe	=Fe+	SO		1.60D-09	0.00	000000.0
P& H	H2S+	+Fe	=Fe+	H2S		1.80D-09	0.00	000000.0
P& H	S+	+ELECTR	=S	PHOTON		3.90D-12	-.63	000000.0
P& H	SH+	+ELECTR	=S	H		2.00D-07	-.50	000000.0
P& H	H2S+	+ELECTR	=SH	H		1.50D-07	-.50	000000.0
P& H	H2S+	+ELECTR	=S	H	H	1.50D-07	-.50	000000.0
P& H	H2S+	+ELECTR	=H2S	PHOTON		1.10D-10	-.70	000000.0
P& H	H3S+	+ELECTR	=H2S	H		3.00D-07	-.50	000000.0
P& H	H3S+	+ELECTR	=SH	H2		1.00D-07	-.50	000000.0
P& H	CS+	+ELECTR	=C	S		2.00D-07	-.50	000000.0
P& H	CS+	+ELECTR	=C	S		2.00D-07	-.50	000000.0
21Z91	HCS+	+ELECTR	=CS	H		7.00D-07	-.50	000000.0
P& H	SO+	+ELECTR	=S	O		2.00D-07	-.50	000000.0
P& H	HSO+	+ELECTR	=SO	H		2.00D-07	-.50	000000.0
UMIST	HSO2+	ELECTR	SO	H	O	1.00E-07	-.50	000000.0
UMIST	HSO2+	ELECTR	SO	OH		1.00E-07	-.50	000000.0
P& H	HOCS+	+ELECTR	=OH	CS		2.00D-07	-.50	000000.0
P& H	HOCS+	+ELECTR	=OCS	H		2.00D-07	-.50	000000.0

L&G90	Si	+SECPHO	=Si+	ELECTR		3.00D+03	0.00	140000.0
L&G90	SiO	+SECPHO	=Si	O		3.00D+03	0.00	140000.0
L&G90	SiO2	+SECPHO	=SiO	O		3.00D+03	0.00	140000.0
2Z89	SiH	+SECPHO	=Si	H		1.46D+03	0.00	140000.0
13 87	SiH4	+SECPHO	=SiH3	H		4.68D+03	0.00	140000.0
McKay	SiH4	H	SiH3	H2		2.60D-11	0.00	001400.0
McKay	SiH3	H	SiH2	H2		2.00D-11	0.00	000000.0
McKay	SiH2	H	SiH	H2		2.00D-11	0.00	000000.0
McKay	SiH	H	Si	H2		2.00D-11	0.00	000000.0
McKay	SiH2	O2	SiO	H2O		7.50D-12	0.00	000000.0
McKay	SiH	O2	SiO	OH		1.70D-10	0.00	000000.0
UMIST	SiH2	O	SiO	H	H	5.00D-11	0.50	000000.0
UMIST	SiH	O	SiO	H		4.00D-11	0.50	000000.0
ROW01	Si	O2	SiO	O		1.72D-10	-0.53	000017.0
ROW01	Si	OH	SiO	H		1.72D-10	-0.53	000017.0
HRBST	SiO	OH	SiO2	H		1.00D-12	-0.70	000000.0
2063	Si+	H2	SiH2+	PHOTON		3.00D-18	0.00	000000.0
2227	SiH+	H2	SiH3+	PHOTON		3.00D-17	-1.00	000000.0
2459	SiH3+	H2	SiH5+	PHOTON		1.00D-18	-0.50	000000.0
1724	Si+	H2	SiH+	H		1.50D-10	0.00	014310.0
27B77	SiH+	H2	SiH2+	H		1.20D-09	0.00	028250.0
28B75	SiH2+	H2	SiH3+	H		7.00D-10	0.00	006335.0
28B75	SiH3+	H2	SiH4+	H		2.00D-10	0.00	047390.0
2570	SiH4+	H2	SiH5+	H		1.00D-09	0.00	000000.0
2223	SiH+	H	Si+	H2		1.90D-09	0.00	000000.0
27B77	SiH2+	H	SiH+	H2		1.20D-09	0.00	000000.0
28B75	SiH3+	H	SiH2+	H2		7.00D-10	0.00	000000.0
28B75	SiH4+	H	SiH3+	H2		2.00D-10	0.00	000000.0
28B75	SiH5+	H	SiH4+	H2		4.00D-11	0.00	004470.0
2791	SiO+	H2	SiOH+	H		3.20D-10	0.00	000000.0
383	H+	Si	Si+	H		9.90E-10	0.00	000000.0
411	H+	SiH	SiH+	H		1.70E-09	0.00	000000.0
412	H+	SiH	Si+	H2		1.70E-09	0.00	000000.0
419	H+	SiH2	SiH2+	H		1.50E-09	0.00	000000.0
420	H+	SiH2	SiH+	H2		1.50E-09	0.00	000000.0
425	H+	SiH3	SiH3+	H		1.50E-09	0.00	000000.0
426	H+	SiH3	SiH2+	H2		1.50E-09	0.00	000000.0
429	H+	SiH4	SiH4+	H		1.50E-09	0.00	000000.0
430	H+	SiH4	SiH3+	H2		1.50E-09	0.00	000000.0
461	H+	SiO	SiO+	H		3.30E-09	0.00	000000.0
759	He+	Si	Si+	He		3.30E-09	0.00	000000.0
812	He+	SiH	Si+	H	He	1.80E-09	0.00	000000.0
821	He+	SiH2	SiH+	H	He	1.00E-09	0.00	000000.0
822	He+	SiH2	Si+	H2	He	1.00E-09	0.00	000000.0
829	He+	SiH3	SiH2+	H	He	1.00E-09	0.00	000000.0
830	He+	SiH3	SiH+	H2	He	1.00E-09	0.00	000000.0
834	He+	SiH4	SiH3+	H	He	1.00E-09	0.00	000000.0
835	He+	SiH4	SiH2+	H2	He	1.00E-09	0.00	000000.0
879	He+	SiO	Si+	O	He	8.60E-10	0.00	000000.0
880	He+	SiO	O+	Si	He	8.60E-10	0.00	000000.0
L&G90	He+	SiO2	SiO+	O	He	5.00E-10	0.00	000000.0
L&G90	He+	SiO2	Si+	O2	He	5.00E-10	0.00	000000.0
1033	C+	Si	Si+	C		2.10E-09	0.00	000000.0
1072	C+	SiH2	SiH2+	C		1.00E-09	0.00	000000.0
1078	C+	SiH3	SiH3+	C		1.00E-09	0.00	000000.0
1125	C+	SiO	Si+	CO		5.40E-10	0.00	000000.0
L&G90	C+	SiO2	SiO+	CO		1.00E-09	-0.60	000000.0
2471	S+	Si	Si+	S		1.60E-09	0.00	000000.0
2489	S+	SiH	SiH+	S		4.20E-10	0.00	000000.0
618	H3+	Si	SiH+	H2		2.00E-09	0.00	000000.0
644	H3+	SiH	SiH2+	H2		2.00E-09	0.00	000000.0
	H3+	Si	SiH2+	H		1.70E-09	0.00	000000.0
648	H3+	SiH2	SiH3+	H2		2.00E-09	0.00	000000.0
652	H3+	SiH3	SiH4+	H2		2.00E-09	0.00	000000.0
654	H3+	SiH4	SiH5+	H2		2.00E-09	0.00	000000.0
680	H3+	SiO	SiOH+	H2		2.00E-09	0.00	000000.0
1731	H3O+	Si	SiH+	H2O		1.80E-09	0.00	000000.0
1745	H3O+	SiH	SiH2+	H2O		9.70E-10	0.00	000000.0

1746	H3O+	SiH2	SiH3+	H2O		2.00E-09	0.00	000000.0
1764	H3O+	SiO	SiOH+	H2O		2.00E-09	0.00	000000.0
2258	HCO+	Si	SiH+	CO		1.60E-09	0.00	000000.0
2279	HCO+	SiH	SiH2+	CO		8.70E-10	0.00	000000.0
2283	HCO+	SiH2	SiH3+	CO		2.00E-09	0.00	000000.0
2286	HCO+	SiH4	SiH5+	CO		1.40E-09	0.00	000000.0
2305	HCO+	SiO	SiOH+	CO		7.90E-10	0.00	000000.0
2071	Si+	OH	SiO+	H		6.30E-10	0.00	000000.0
L&G90	Si+	H2O	SiOH+	H		2.30E-10	-0.60	000000.0
2082	Si+	O2	SiO+	O		1.00E-13	0.00	000000.0
2226	SiH+	O	SiO+	H		4.00E-10	0.00	000000.0
2229	SiH+	NH3	NH4+	Si		1.00E-09	0.00	000000.0
2230	SiH+	H2O	H3O+	Si		8.00E-10	0.00	000000.0
2391	SiH2+	O	SiOH+	H		6.30E-10	0.00	000000.0
2393	SiH2+	O2	SiOH+	OH		2.40E-11	0.00	000000.0
2458	SiH3+	O	SiOH+	H2		2.00E-10	0.00	000000.0
2571	SiH4+	H2O	H3O+	SiH3		2.00E-09	0.00	000000.0
2572	SiH4+	CO	HCO+	SiH3		1.00E-09	0.00	000000.0
2623	SiH5+	H2O	H3O+	SiH4		2.00E-09	0.00	000000.0
3116	Si+	ELECTR	Si	PHOTON		4.90E-12	-0.60	000000.0
3125	SiH+	ELECTR	Si	H		2.00E-07	-0.50	000000.0
3135	SiH2+	ELECTR	Si	H	H	2.00E-07	-0.50	000000.0
3136	SiH2+	ELECTR	SiH	H		1.50E-07	-0.50	000000.0
3137	SiH2+	ELECTR	Si	H2		1.50E-07	-0.50	000000.0
3146	SiH3+	ELECTR	SiH2	H		1.50E-07	-0.50	000000.0
3147	SiH3+	ELECTR	SiH	H2		1.50E-07	-0.50	000000.0
3156	SiH4+	ELECTR	SiH3	H		1.50E-07	-0.50	000000.0
3157	SiH4+	ELECTR	SiH2	H2		1.50E-07	-0.50	000000.0
3163	SiH5+	ELECTR	SiH4	H		1.50E-07	-0.50	000000.0
3164	SiH5+	ELECTR	SiH3	H2		1.50E-07	-0.50	000000.0
3227	SiO+	ELECTR	Si	O		2.00E-07	-0.50	000000.0
3247	SiOH+	ELECTR	SiO	H		1.50E-07	-0.50	000000.0
3248	SiOH+	ELECTR	Si	OH		1.50E-07	-0.50	000000.0
EROSI	Mg**	+He	=GRAIN	He	Mg	1.221D-2	73.0	0041.187
EROSI	Fe**	+He	=GRAIN	He	Fe	1.151D-2	73.0	0040.976
EROSI	Si**	+He	=GRAIN	He	Si	1.224D-2	73.0	0042.175
EROSI	C**	+He	=GRAIN	He	C	1.224D-2	73.0	0042.175
EROSI	O**	+He	=GRAIN	He	O	5.348D-2	73.0	0036.030
EROSI	Mg**	+C	=GRAIN	C	Mg	2.935D-2	48.0	0036.740
EROSI	Fe**	+C	=GRAIN	C	Fe	2.386D-2	47.0	0042.794
EROSI	Si**	+C	=GRAIN	C	Si	2.698D-2	48.0	0036.502
EROSI	C**	+C	=GRAIN	C	C	2.698D-2	48.0	0036.502
EROSI	O**	+C	=GRAIN	C	O	1.054D-1	48.0	0030.812
EROSI	Mg**	+N	=GRAIN	N	Mg	2.935D-2	48.0	0036.740
EROSI	Fe**	+N	=GRAIN	N	Fe	2.386D-2	47.0	0042.794
EROSI	Si**	+N	=GRAIN	N	Si	2.698D-2	48.0	0036.502
EROSI	C**	+N	=GRAIN	N	C	2.698D-2	48.0	0036.502
EROSI	O**	+N	=GRAIN	N	O	1.054D-1	48.0	0030.812
EROSI	Mg**	+O	=GRAIN	O	Mg	2.884D-2	48.0	0030.238
EROSI	Fe**	+O	=GRAIN	O	Fe	4.116D-2	44.0	0059.438
EROSI	Si**	+O	=GRAIN	O	Si	3.373D-2	47.0	0037.810
EROSI	C**	+O	=GRAIN	O	C	3.373D-2	47.0	0037.810
EROSI	O**	+O	=GRAIN	O	O	1.006D-1	47.0	0031.588
EROSI	Mg**	+H2O	=GRAIN	H2O	Mg	2.884D-2	48.0	0030.238
EROSI	Fe**	+H2O	=GRAIN	H2O	Fe	4.116D-2	44.0	0059.438
EROSI	Si**	+H2O	=GRAIN	H2O	Si	3.373D-2	47.0	0037.810
EROSI	C**	+H2O	=GRAIN	H2O	C	3.373D-2	47.0	0037.810
EROSI	O**	+H2O	=GRAIN	H2O	O	1.006D-1	47.0	0031.588
EROSI	Mg**	+N2	=GRAIN	N2	Mg	2.093D-2	48.0	0027.730
EROSI	Fe**	+N2	=GRAIN	N2	Fe	4.324D-2	47.0	0042.335
EROSI	Si**	+N2	=GRAIN	N2	Si	2.217D-2	47.0	0028.013
EROSI	C**	+N2	=GRAIN	N2	C	2.217D-2	47.0	0028.013
EROSI	O**	+N2	=GRAIN	N2	O	1.149D-1	46.0	0046.018
EROSI	Mg**	+CO	=GRAIN	CO	Mg	2.093D-2	48.0	0027.730
EROSI	Fe**	+CO	=GRAIN	CO	Fe	4.324D-2	47.0	0042.335
EROSI	Si**	+CO	=GRAIN	CO	Si	2.217D-2	47.0	0028.013
EROSI	C**	+CO	=GRAIN	CO	C	2.217D-2	47.0	0028.013
EROSI	O**	+CO	=GRAIN	CO	O	1.149D-1	46.0	0046.018

EROSI	Mg**	+O2	=GRAIN	O2	Mg	2.093D-2	48.0	0027.730
EROSI	Fe**	+O2	=GRAIN	O2	Fe	4.324D-2	47.0	0042.335
EROSI	Si**	+O2	=GRAIN	O2	Si	2.217D-2	47.0	0028.013
EROSI	C**	+O2	=GRAIN	O2	C	2.217D-2	47.0	0028.013
EROSI	O**	+O2	=GRAIN	O2	O	1.149D-1	46.0	0046.018
ADSOR	C	+GRAIN	=CH4*			1.00D+00		0000102.
ADSOR	CH	+GRAIN	=CH4*			1.00D+00		0000102.
ADSOR	CH2	+GRAIN	=CH4*			1.00D+00		0000102.
ADSOR	CH3	+GRAIN	=CH4*			1.00D+00		0000102.
ADSOR	CH4	+GRAIN	=CH4*			1.00D+00		0000102.
ADSOR	O	+GRAIN	=H2O*			1.00D+00		0000102.
ADSOR	O2	+GRAIN	=O2*			1.00D+00		0000102.
ADSOR	OH	+GRAIN	=H2O*			1.00D+00		0000102.
ADSOR	H2O	+GRAIN	=H2O*			1.00D+00		0000102.
ADSOR	CO	+GRAIN	=CO*			1.00D+00		0000102.
ADSOR	CO2	+GRAIN	=CO2*			1.00D+00		0000102.
ADSOR	C2	+GRAIN	=CH4*	CH4*		1.00D+00		0000102.
ADSOR	C2H	+GRAIN	=CH4*	CH4*		1.00D+00		0000102.
ADSOR	C2H2	+GRAIN	=CH4*	CH4*		1.00D+00		0000102.
ADSOR	C3	+GRAIN	=CH4*	CH4*	CH4*	1.00D+00		0000102.
ADSOR	C3H	+GRAIN	=CH4*	CH4*	CH4*	1.00D+00		0000102.
ADSOR	C3H2	+GRAIN	=CH4*	CH4*	CH4*	1.00D+00		0000102.
ADSOR	N	+GRAIN	=NH3*			1.00D+00		0000102.
ADSOR	NH	+GRAIN	=NH3*			1.00D+00		0000102.
ADSOR	NH2	+GRAIN	=NH3*			1.00D+00		0000102.
ADSOR	NH3	+GRAIN	=NH3*			1.00D+00		0000102.
ADSOR	CN	+GRAIN	=CH4*	NH3*		1.00D+00		0000102.
ADSOR	HCN	+GRAIN	=CH4*	NH3*		1.00D+00		0000102.
ADSOR	HNC	+GRAIN	=CH4*	NH3*		1.00D+00		0000102.
ADSOR	N2	+GRAIN	=N2*			1.00D+00		0000102.
ADSOR	NO	+GRAIN	=H2O*	NH3*		1.00D+00		0000102.
ADSOR	S	+GRAIN	=H2S*			1.00D+00		0000102.
ADSOR	SH	+GRAIN	=H2S*			1.00D+00		0000102.
ADSOR	H2S	+GRAIN	=H2S*			1.00D+00		0000102.
ADSOR	CS	+GRAIN	=CH4*	H2S*		1.00D+00		0000102.
ADSOR	SO	+GRAIN	=H2O*	H2S*		1.00D+00		0000102.
ADSOR	SO2	+GRAIN	=H2O*	H2O*	H2S*	1.00D+00		0000102.
ADSOR	OCS	+GRAIN	=OCS*			1.00D+00		0000102.
ADSOR	Fe	+GRAIN	=Fe*			1.00D+00		0000102.
ADSOR	Si	+GRAIN	=SiH4*			1.00D+00		0000102.
ADSOR	SiH	+GRAIN	=SiH4*			1.00D+00		0000102.
ADSOR	SiH2	+GRAIN	=SiH4*			1.00D+00		0000102.
ADSOR	SiH3	+GRAIN	=SiH4*			1.00D+00		0000102.
ADSOR	SiH4	+GRAIN	=SiH4*			1.00D+00		0000102.
ADSOR	SiO	+GRAIN	=SiO*			1.00D+00		0000102.
ADSOR	SiO2	+GRAIN	=SiO2*			1.00D+00		0000102.
SPUTT	CH4*	+H	=CH4	H	GRAIN	4.00D-05	0.00	002000.0
SPUTT	CH4*	+H2	=CH4	H2	GRAIN	1.00D-04	0.00	002000.0
SPUTT	CH4*	+He	=CH4	He	GRAIN	8.00D-04	0.00	002000.0
SPUTT	H2O*	+H	=H2O	H	GRAIN	4.00D-05	0.00	006000.0
SPUTT	H2O*	+H2	=H2O	H2	GRAIN	1.00D-04	0.00	006000.0
SPUTT	H2O*	+He	=H2O	He	GRAIN	8.00D-04	0.00	006000.0
SPUTT	CO*	+H	=CO	H	GRAIN	4.00D-05	0.00	001900.0
SPUTT	CO*	+H2	=CO	H2	GRAIN	1.00D-04	0.00	001900.0
SPUTT	CO*	+He	=CO	He	GRAIN	8.00D-04	0.00	001900.0
SPUTT	CO2*	+H	=CO2	H	GRAIN	4.00D-05	0.00	003100.0
SPUTT	CO2*	+H2	=CO2	H2	GRAIN	1.00D-04	0.00	003100.0
SPUTT	CO2*	+He	=CO2	He	GRAIN	8.00D-04	0.00	003100.0
SPUTT	NH3*	+H	=NH3	H	GRAIN	4.00D-05	0.00	003600.0
SPUTT	NH3*	+H2	=NH3	H2	GRAIN	1.00D-04	0.00	003600.0
SPUTT	NH3*	+He	=NH3	He	GRAIN	8.00D-04	0.00	003600.0
SPUTT	CH3OH*	+H	=CH3OH	H	GRAIN	4.00D-05	0.00	006000.0
SPUTT	CH3OH*	+H2	=CH3OH	H2	GRAIN	1.00D-04	0.00	006000.0
SPUTT	CH3OH*	+He	=CH3OH	He	GRAIN	8.00D-04	0.00	006000.0
SPUTT	H2CO*	+H	=H2CO	H	GRAIN	4.00D-05	0.00	006000.0
SPUTT	H2CO*	+H2	=H2CO	H2	GRAIN	1.00D-04	0.00	006000.0
SPUTT	H2CO*	+He	=H2CO	He	GRAIN	8.00D-04	0.00	006000.0
SPUTT	HCO2H*	+H	=HCO2H	H	GRAIN	4.00D-05	0.00	006000.0

SPUTT HCO2H*	+H2	=HCO2H	H2	GRAIN	1.00D-04	0.00	006000.0
SPUTT HCO2H*	+He	=HCO2H	He	GRAIN	8.00D-04	0.00	006000.0
SPUTT OCS*	+H	=OCS	H	GRAIN	4.00D-05	0.00	006000.0
SPUTT OCS*	+H2	=OCS	H2	GRAIN	1.00D-04	0.00	006000.0
SPUTT OCS*	+He	=OCS	He	GRAIN	8.00D-04	0.00	006000.0
SPUTT H2S*	+H	=H2S	H	GRAIN	4.00D-05	0.00	006000.0
SPUTT H2S*	+H2	=H2S	H2	GRAIN	1.00D-04	0.00	006000.0
SPUTT H2S*	+He	=H2S	He	GRAIN	8.00D-04	0.00	006000.0
DESOR CH4*	+CRP	=CH4	GRAIN		7.00D+01	0.00	000000.0
DESOR H2O*	+CRP	=H2O	GRAIN		7.00D+01	0.00	000000.0
DESOR CO*	+CRP	=CO	GRAIN		7.00D+01	0.00	000000.0
DESOR CO2*	+CRP	=CO2	GRAIN		7.00D+01	0.00	000000.0
DESOR NH3*	+CRP	=NH3	GRAIN		7.00D+01	0.00	000000.0
DESOR CH3OH*	+CRP	=CH3OH	GRAIN		7.00D+01	0.00	000000.0
DESOR H2CO*	+CRP	=H2CO	GRAIN		7.00D+01	0.00	000000.0
DESOR HCO2H*	+CRP	=HCO2H	GRAIN		7.00D+01	0.00	000000.0
DESOR OCS*	+CRP	=OCS	GRAIN		7.00D+01	0.00	000000.0
DESOR H2S*	+CRP	=H2S	GRAIN		7.00D+01	0.00	000000.0

END

O

Articles

A&A 482, 809–829 (2008)
DOI: 10.1051/0004-6361:20078900

Astronomy & Astrophysics

SiO line emission from C-type shock waves: interstellar jets and outflows

A. Gusdorf[1,2], S. Cabrit[3], D. R. Flower[1], and G. Pineau des Forêts[2,3,4]

[1] Physics Department, The University, Durham DH1 3LE, UK
e-mail: david.flower@durham.ac.uk
[2] Institut d'Astrophysique Spatiale (IAS), Bâtiment 121, 91405 Orsay, France
[3] LERMA (UMR 8112 du CNRS), Observatoire de Paris, 61 avenue de l'Observatoire, 75014 Paris, France
[4] Université Paris-Sud 11 and CNRS (UMR 8617), France

Received 23 October 2007 / Accepted 12 February 2008

ABSTRACT

We study the production of SiO in the gas phase of molecular outflows, through the sputtering of Si-bearing material in refractory grain cores, which are taken to be olivine. We calculate also the rotational line spectrum of the SiO. The sputtering is driven by neutral particle impact on charged grains, in steady-state C-type shock waves, at the speed of ambipolar diffusion. The emission of the SiO molecule is calculated by means of an LVG code. A grid of models, with shock speeds in the range $20 < v_s < 50$ km s^{-1} and preshock gas densities $10^4 < n_H < 10^6$ cm^{-3}, has been generated. We compare our results with those of an earlier study (Schilke et al. 1997). Improvements in the treatment of the coupling between the charged grains and the neutral fluid lead to narrower shock waves and lower fractions of Si ($\lesssim$10%) being released into the gas phase. Erosion of grain cores is significant ($\gtrsim$1%) only for C-type shock speeds $v_s > 25$ km s^{-1}, given the adopted properties of olivine. More realistic assumptions concerning the initial fractional abundance of O_2 lead to SiO formation being delayed, so that it occurs in the cool, dense postshock flow. Good agreement is obtained with recent observations of SiO line intensities in the L1157 and L1448 molecular outflows. The inferred temperature, opacity, and SiO column density in the emission region differ significantly from those estimated by means of LVG "slab" models. The fractional abundance of SiO is deduced and found to be in the range $4 \times 10^{-8} \lesssim n(\mathrm{SiO})/n_H \lesssim 3 \times 10^{-7}$. Observed line profiles are wider than predicted and imply multiple, unresolved shock regions within the beam.

Key words. astrochemistry – atomic processes – magnetohydrodynamics (MHD) – molecular processes – radiative transfer – shock waves

1. Introduction

Unlike CO, which is observed extensively in the interstellar medium of our own and other galaxies, its homologue SiO is observed principally in outflows associated with regions of star formation. This striking difference in behaviour is a consequence of the lower elemental abundance and the more complete depletion of silicon from the gas phase during grain formation. Both carbon and silicon form refractory materials – graphite and silicates – of which the cores of interstellar grains are believed to be composed; but the much higher elemental abundance of carbon, $n_C/n_H = 3.55 \times 10^{-4}$, compared with silicon, $n_{Si}/n_H = 3.37 \times 10^{-5}$ (Anders & Grevesse 1989), leads to some of the carbon remaining in the gas phase.

The SiO molecule was first detected in the Galactic centre (Sgr B2) by Wilson et al. (1971) and subsequently in Ori A by Dickinson (1972). More recent observations of SiO in jets (see, for example, Bachiller et al. 1991; Martín-Pintado et al. 1992; Codella et al. 1999; Nisini et al. 2007) imply that, in these objects, at least some of the silicon has been restored to the gas phase; this can be achieved through sputtering of the grain material, probably in shock waves, which are features of the outflows. It has been known since the study by Draine et al. (1983) that grain ice-mantles can be eroded in C-type shock waves, owing to impact of neutral particles on charged grains at the ion-neutral drift speed, which is the speed of ambipolar diffusion. More recent work (Flower & Pineau des Forêts 1995; Flower et al. 1996; Field et al. 1997; May et al. 2000) has shown that this process might result also in the partial erosion of the refractory grain cores. The simulations undertaken by May et al. of the sputtering of various silicates (forsterite, fayalite and olivine) by neutral atoms showed that C-shock speeds in excess of 30 km s^{-1} are necessary to erode a significant fraction (more than a few per cent) of these materials. On the other hand, it has since been recognized (Le Bourlot et al. 2002; Ciolek et al. 2004) that the speeds at which C-type shock waves can propagate are limited, both by the collisional dissociation of molecular hydrogen, which leads to a thermal runaway and the formation of a J-type shock wave, and by the ion magnetosonic speed, whose value is constrained by the inertia of the charged grains. Consequently, the efficacy of the erosion of silicates in C-type shock waves is restricted by the maximum C-shock speed, which depends on the preshock density and transverse magnetic field strength, and on the fraction of charged grains (Flower & Pineau des Forêts 2003).

In a previous study of SiO production in the interstellar medium, Schilke et al. (1997, henceforth Sch97) considered in detail the erosion of silicon from grain cores and from their mantles by C-type shock waves and the resulting SiO emission spectrum; this study remains the only one of its kind that has been published to date. In the intervening decade, there has been progress in our understanding of the sputtering process

(May et al. 2000), the gas-phase chemistry of silicon (Le Picard et al. 2001), and the grain dynamics (Flower & Pineau des Forêts 2003), and so it seems timely to revisit this topic. Recent observations of SiO in jets (Nisini et al. 2007) extend to higher rotational levels than previously and provide a further motivation for such an study. Accordingly, we have reconsidered the chemistry of silicon in steady-state, planar MHD shock waves, with a view to providing a grid of models which may serve in the analysis of current and future observations of rotational transitions of SiO in outflows. These models yield additional results relating to rovibrational transitions of H_2 and rotational lines of CO, as well as forbidden lines of atoms and atomic ions, including [Fe II] (cf. Giannini et al. 2006).

Grain-grain collisions and the sputtering of silicon in oblique C-type shock waves, in which the preshock magnetic field direction is inclined to the plane of the shock front, have been considered by Caselli et al. (1997). However, such simulations have yet to incorporate the gas-phase chemistry and the radiative cooling processes, in order to enable quantitative analyses of the spectral line observations to be made.

2. The model

We summarize below those developments, in both the MHD code and the data used and produced by the code, which are relevant to the modelling of the intensities and the profiles of the rotational lines of SiO. We take as our baseline the study by Sch97. The reader is referred to the more recent papers cited below for details of the modifications.

2.1. The dynamics of charged grains

The main revision of the code itself concerns the treatment of the charge and of the dynamical effects of the grains. The charge distribution of both the grains and the "very small grains" (VSG), represented by polycyclic aromatic hydrocarbons in our model, are calculated, assuming that collisions with gas-phase particles (electrons, ions and neutrals) determine the charge; see Flower & Pineau des Forêts (2003). As was mentioned in the Introduction, allowance for the mass density of the (mainly negatively) charged grains can reduce significantly the magnetosonic speed in the charged fluid

$$c_{\rm m}^2 = \frac{5k_{\rm B}(T_+ + T_-)}{3(\mu_+ + \mu_-)} + \frac{B^2}{4\pi(\rho_+ + \rho_-)}$$

where $T_\pm$ are the temperatures, $\mu_\pm$ are the mean masses and $\rho_\pm$ are the mass densities of the positively and negatively charged fluids; B is the magnetic field strength in the preshock gas. The magnetosonic speed is the maximum speed at which a C-type shock can propagate in the medium. Furthermore, the momentum transfer between the charged grains and the neutral fluid affects the ion-neutral drift speed and has consequences for the degree of sputtering of the grains within a C-type shock wave.

2.2. Radiative cooling by H_2

The thermal balance of the medium, particularly the radiative cooling by H_2, is treated more exactly in the current model. Rovibrational excitation of H_2, principally by H, H_2 itself, and He, followed by radiative decay, is the principal mechanism of cooling the shock-heated gas. Following Le Bourlot et al. (2002), the populations of the rovibrational levels of H_2 are calculated in parallel with the hydrodynamical and chemical rate equations, yielding the most accurate determination of the rate of cooling by H_2 that is achievable within the framework of a time-independent (steady-state) model of the shock structure. The rate coefficients for the collisional excitation by H of rovibrational transitions of H_2 are from the recent work of Wrathmall et al. (2007). Collisional dissociation and ionization of H_2, as well as ionization of H, are taken into account. Collisional dissociation of H_2 is a particularly important process, as the removal of H_2 can lead to a thermal runaway. The associated increase in the kinetic temperature, $T_{\rm n}$, of the neutral fluid, and hence of the adiabatic sound speed

$$c_{\rm s}^2 = \frac{5k_{\rm B}T_{\rm n}}{3\mu_{\rm n}}$$

where $\mu_{\rm n}$ is the mean mass of the neutral fluid, can give rise to a sonic point in the flow and hence to a J-type discontinuity. This phenomenon imposes an additional constraint on the maximum speed of a C-type shock wave in a molecular medium.

In the compressed gas of the postshock region where most of SiO forms, cooling by ^{12}CO, ^{13}CO, and H_2O starts to dominate that by H_2. In order to predict accurately the emitted SiO emission spectrum, an LVG treatment of the cooling by these species has been introduced, following the procedures of Neufeld & Kaufman (1993). A "thermal gradient" $c_{\rm s}/z'$, where $z' = z + 1.0 \times 10^{13}$ cm and z is the independent integration variable, is added quadratically to the macroscopic velocity gradient, in order to simulate photon escape through thermal line broadening.

2.3. The sputtering of grains

The sputtering probabilities computed by May et al. (2000) for olivine ($MgFeSiO_4$) are used to determine the rate of erosion of Si from (charged) silicate grains by neutral particles. We include also the sputtering of carbonaceous (amorphous carbon) grains, using the sputtering yields of Field et al. (1997). Impacts (at the ion-neutral drift speed) of abundant heavy neutral species are the most effective in eroding the grain cores. For collisions with CO, for example, we adopted the sputtering probabilities calculated for impacts of Si atoms, which have the same mass as CO and hence the same impact energy. As May et al. (2000) have shown, similar yields of Si are obtained from the three types of silicate: fayalite, Fe_2SiO_4; forsterite, Mg_2SiO_4; and olivine, $MgFeSiO_4$.

The grain mantles are eroded first, through impacts with the most abundant neutral species, H, H_2 and He, at ion-neutral drift speeds which are below the threshold for erosion of the cores (Draine et al. 1983; Flower & Pineau des Forêts 1994). The initial composition of the gas is calculated in chemical equilibrium, whilst that of the grain mantles, and the elemental depletion into the grain cores, is based on observations (cf. Flower & Pineau des Forêts 2003, Table 1). We incorporated a representative polycyclic aromatic hydrocarbon (PAH), with a fractional abundance $n_{\rm PAH}/n_{\rm H} = 10^{-6}$, an upper limit which is consistent with estimates of the fraction of elemental carbon likely to be present in the form of very small grains (Li & Draine 2001; Weingartner & Draine 2001). The state of charge of this species was computed following Flower & Pineau des Forêts (2003), who showed that increasing the fractional abundance of the PAH results in higher values of the magnetosonic speed in the preshock gas, thereby enabling C-type shock waves to propagate at higher speeds. In their turn, the higher speed shocks erode the silicate grains more effectively. However, the adopted PAH abundance has little effect on the internal structure of the shock wave, as the grains become negatively charged in the shock wave and dominate grain-neutral momentum transfer.

The total number density of the grains was computed

- from the total mass of the refractory cores, which is 0.78×10^{-2} times the mass of the gas for the adopted composition of the cores;
- assuming a bulk mass density of 3 g cm^{-3}; and
- taking a size distribution of the grain cores

$$\mathrm{d}n_\mathrm{g}(a_\mathrm{g})/\mathrm{d}a_\mathrm{g} \propto a_\mathrm{g}^{-3.5},$$

following Mathis et al. (1977), where $n_\mathrm{g}(a_\mathrm{g})$ is the number density of grains with radius a_g, assumed to have upper and lower limits of 0.3 μm and 0.01 μm, respectively.

The thickness of the grain mantles was determined from their molecular composition (Flower & Pineau des Forêts 2003, Table 2), assuming a mean number of 5×10^4 molecular binding sites per layer of the mantle and a thickness of 2×10^{-4} μm for each layer, independent of the size of the grain core; there are no Si-containing species in the mantles. This procedure yields an initial mantle thickness of 0.015 μm on the grain cores, whose mean radius is $a_\mathrm{g} = 0.02$ μm. However, the erosion of the grain mantles occurs sufficiently rapidly, as the ion and neutral flow velocities begin to decouple in the shock wave, that the existence of thick ice-mantles on the grains in the preshock gas has little effect on the shock dynamics (see Fig. 6 of Guillet et al. 2007).

2.4. Chemistry

The chemical reaction network comprises over 900 reactions connecting the abundances of more than 100 species, in both the gas and the solid phases. The complete list of species and reactions is available from http://massey.dur.ac.uk/drf/outflows_test/species_chemistry_shock/. In the context of the present study, we emphasize the gas-phase chemistry of silicon and the formation of SiO, in particular. The total rate of cosmic ray ionization of hydrogen, ζ, was taken to be 5×10^{-17} s^{-1}.

Two reactions are important for the formation of SiO from Si, which is released into the gas phase by the sputtering of the grains, namely

$$\mathrm{Si} + \mathrm{O_2} \longrightarrow \mathrm{SiO} + \mathrm{O} \quad (1)$$

$$\mathrm{Si} + \mathrm{OH} \longrightarrow \mathrm{SiO} + \mathrm{H} \quad (2)$$

for which the following rate coefficients (cm^3 s^{-1})

$$k_1 = 2.7 \times 10^{-10} \exp(-111/T) \quad (3)$$

$$k_2 = 1.0 \times 10^{-10} \exp(-111/T) \quad (4)$$

were adopted by Sch97 from the compilation of Langer & Glassgold (1990). The exponential factor in Eq. (3) derives from the argument (Graff 1989) that the reactions proceed only with the fine-structure states of Si ($3p^2\ ^3P_J$) with $J > 0$, of which $J = 1$, which lies 111 K above the $J = 0$ ground state, is the more significantly populated at low temperatures. More recently, the rate coefficient for reaction (1) has been measured at low temperatures ($15 \leq T \leq 300$ K) by Le Picard et al. (2001) and found to be given by

$$k_1 = 1.72 \times 10^{-10} (T/300)^{-0.53} \exp(-17/T). \quad (5)$$

We have adopted (5) and the same expression for k_2. Evidently, the differences between the present and previous values of these rate coefficients are most significant for temperatures $T \lesssim 100$ K, i.e. in the cooling flow of the shocked gas.

The abundance of SiO is limited by its conversion to SiO_2 in the reaction with OH

$$\mathrm{SiO} + \mathrm{OH} \longrightarrow \mathrm{SiO_2} + \mathrm{H} \quad (6)$$

whose rate coefficient remains subject to considerable uncertainty. We adopt the same expression as Sch97, viz.

$$k_6 = 1.0 \times 10^{-11} (T/300)^{-0.7} \quad (7)$$

in units of cm^3 s^{-1}. However, we note that Zachariah & Tsang (1995) calculated a barrier of 433 K to reaction (6), and a rate coefficient

$$k_6 = 2.5 \times 10^{-12} (T/300)^{0.78} \exp(-613/T);$$

see the discussion of Le Picard et al. (2001). At $T = 300$ K, the latter rate coefficient is 30 times smaller than the former. In the ambient (preshock) and the postshock gas, where $T \approx 10$ K, the existence of an activation energy of several hundred kelvin would prevent the oxidation of SiO in reaction (6) from occurring. The rate coefficient for reaction (6) in the UMIST data base (Le Teuff et al. 2000) is

$$k_6 = 2.0 \times 10^{-12}$$

in cm^3 s^{-1}, which is 50 times smaller than (7) at $T = 10$ K. Fortunately, the conversion of SiO into SiO_2 occurs in a region which is too cold and optically thick to contribute to the SiO line intensities, and so the uncertainty in the rate coefficient for reaction (6) is not significant in the present context.

Re-adsorption of molecules on to grains ("freeze-out") in the postshock gas is included, as in Sch97. The effects of freeze-out on the abundance of SiO and its spectrum are considered below.

2.5. Line transfer

The physical and chemical profiles which derive from the shock model summarized above are used in a large velocity gradient (LVG) calculation of the intensities of the emission lines of SiO and of CO. Our implementation of this technique is described in Appendix A, where we note that an expression for the escape probability which differs from that of Sch97 has been adopted.

3. Results

3.1. Comparison with the calculations of Schilke et al. (1997)

First, we compare the computed shock structure with that of Sch97, for a reference C-type shock model, in which the preshock density $n_\mathrm{H} = 10^5$ cm^{-3} and the magnetic field strength $B = 200$ μG, and the shock velocity $v_\mathrm{s} = 30$ km s^{-1}. The most striking difference between the current and the previous model is that the width of the shock wave decreases by a factor of approximately 4, to 5×10^{15} cm, from 2×10^{16} cm in the study of Sch97; see Fig. 1a. This difference is attributable to the more accurate treatment of the coupling between the neutral fluid and the charged grains in the current model and is an indication of the significance of the inertia of the (negatively) charged grains in dark clouds, in which the degree of ionization is low. With the narrower shock wave is associated a higher maximum temperature of the neutral fluid, as there is less time for the initial energy flux, $\rho_\mathrm{n} v_\mathrm{s}^3/2$, associated with the bulk flow, to be converted into internal energy of the H_2 molecules or to be radiated

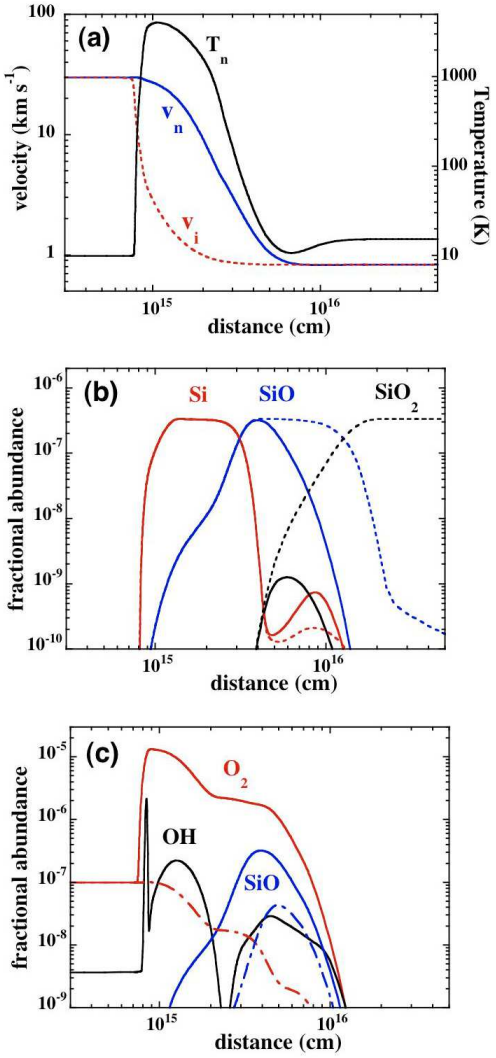

Fig. 1. a) Temperature of the neutral fluid and velocity profiles of the neutral and charged fluids, predicted by the present C-type shock model. The shock parameters are $n_{\rm H} = 10^5$ cm^{-3} and $B = 200$ μG in the preshock gas, and $v_{\rm s} = 30$ km s^{-1}, $\zeta = 5 \times 10^{-17}$ s^{-1}. The fractional gas-phase abundances of selected Si-and O-bearing species are plotted in panels **b)** and **c)**; cf. Sch97, Fig. 2. The broken curves in panel **b)** are the corresponding results obtained when re-adsorption on to grains is neglected. The discontinuous curves in panel **c)** show the effects of assuming the initial abundance of O_2 ice to be negligible, i.e. the second of the two scenarios described in Sect. 3.1.

away. Thus, $T_{\rm n} \approx 4000$ K here, compared with $T_{\rm n} \approx 2000$ K in the model of Sch97.

There are chemical differences between the models also, which are related in part to the changes in the shock structure; these differences may be summarized as follows.

(i) The fraction of the Si in the grain cores which is released into the gas phase by sputtering is approximately ten times smaller in the current model than in the model of Sch97. This reduction is attributable partly to the sputtering yields, which have higher thresholds and are smaller for olivine ($MgFeSiO_4$) than for the amorphous silica (SiO_2) considered by Sch97; but the main reason for the decrease is the enhanced coupling between the neutral fluid and the charged grains, which reduces the shock width and hence the time available to erode the grains. On the other hand, the magnitude of the ion-neutral drift speed is similar in both calculations. As a consequence of the reduction in the shock width, the integrated SiO line intensities predicted by the current model are smaller, in general, than calculated by Sch97; see Sect. 4.

(ii) The displacement of the maximum fractional abundance of SiO, which forms in the gas-phase reactions (1) and (2), from that of Si, which is eroded from the grains, is a more significant fraction of the shock width in the current model; cf. Fig. 1b. The initial fractional abundance of O_2 in the preshock medium is lower here, by a factor of approximately 10, than in the model of Sch97, delaying the initial formation of SiO. The O_2 is assumed to be predominantly in the form of ice, which is sputtered rapidly from the grains in the early stages of development of the shock wave, as may be seen from the two orders of magnitude increase in the fractional abundance of gas-phase O_2, apparent in Fig. 1c. The fractional abundances of O_2 and OH decrease subsequently, at high kinetic temperatures, owing to their dissociation by H in the chemical reactions O_2(H, O)OH and OH(H, O)H_2. The former reaction, which is endothermic by over 8000 K, proves to be less effective in destroying O_2 over the smaller width of the current shock model (see Fig. 1c) than was the case in the calculations of Sch97. On the other hand, the lower energy threshold of 17 K in reaction (5) allows oxidation reactions to proceed further into the postshock region, compared with Sch97, whose adopted threshold was 111 K. As a consequence, conversion of Si into SiO is slower initially but more complete eventually than predicted by Sch97.

(iii) SiO_2 is removed more rapidly from the gas phase in the current model. The compression is more rapid than in the model of Sch97, and so the rate of adsorption of molecules to grains ("freeze-out") is higher. If the oxidation of SiO in the reaction SiO(OH, H)SiO_2 has an activation energy of several hundred kelvin (Zachariah & Tsang 1995; see Sect. 2.4), the maximum fractional abundance of SiO_2 would be reduced still further.

Also shown in Fig. 1b are the fractional abundances which are obtained neglecting re-adsorption on to the grains. The timescale for freeze-out is sufficiently large that the chemical profiles are modified only in the cold postshock gas, where the flow speed is practically constant and the optical depths in the SiO lines are large. Consequently, whilst the effects re-adsorption on the composition of the postshock gas are dramatic, the freeze-out of SiO has no effect on the predicted line intensities.

In chemical equilibrium, the initial fractional abundance of O_2 is approximately 10^{-5}, whereas observations with the Odin satellite (Pagani et al. 2003; Larsson et al. 2007) have placed upper limits of $n(O_2)/n(H_2) \lesssim 10^{-7}$. In view of these measurements, we have considered two scenarios, both with an initial gas-phase fractional abundance $n(O_2)/n_{\rm H} = 1.0 \times 10^{-7}$, as a consequence of the freeze-out of oxygen on to grains, but with differing assumptions regarding its chemical form in the grain mantles.

– The molecular oxygen which formed in the gas phase was adsorbed on to the grains, where it remained as O_2 ice in the preshock medium, with a fractional abundance of 1.3×10^{-5}, relative to $n_{\rm H}$. The initial fractional abundance of H_2O ice is an order of magnitude larger than that the fractional abundance of O_2 ice.
– Atomic oxygen was adsorbed on to the grains before O_2 was synthesized and subsequently hydrogenated to H_2O ice in the grain mantles of the cold preshock medium. The

fractional abundance of H_2O ice increases by only 25% as a consequence, to 1.3×10^{-4}.

It turns out that the first scenario is practically equivalent to assuming that the O_2 is initially in the gas-phase (see Fig. 1c), as its release from the grain mantles occurs early and rapidly (on a timescale of a few years for the model in Fig. 1) in the shock wave. On the other hand, the second scenario can result in reduced levels of oxidation of Si to SiO in the gas-phase (cf. Fig. 1), depending on the relative importance of reactions 1 and 2 in the oxidation process. In what follows, we present results corresponding principally to the first scenario, with the second being considered mainly in Appendix C.

3.2. A grid of models

We have computed a grid of shock models with the following parameters:

- $n_H = 10^4$ cm^{-3}, $v_s = 20, 25, 30, 35, 40, 45, 50$ km s^{-1};
- $n_H = 10^5$ cm^{-3}, $v_s = 20, 25, 30, 35, 40, 45$ km s^{-1};
- $n_H = 10^6$ cm^{-3}, $v_s = 20, 25, 27, 30, 32, 34$ km s^{-1}.

In all of these models, we characterized the preshock magnetic field strength by

$$B = bn_H^{0.5},$$

where n_H is in cm^{-3} and B is in μG; the scaling parameter b was taken equal to 1. (The effect on Si sputtering of varying b is discussed in Sect. 3.3.) The maximum shock speed for $n_H \gtrsim 10^4$ cm^{-3} is determined by the collisional dissociation of H_2, the main coolant, which leads to a thermal runaway and a J-discontinuity (Le Bourlot et al. 2002; Flower & Pineau des Forêts 2003).

In fact, we computed two grids, one for each of the scenarios concerning the initial distribution of oxygen between O_2 and H_2O ices, as specified towards the end of the previous Sect. 3.1. We concentrate on the first of these two scenarios, but some additional figures for the second scenario are given in Appendix C as online material. (Our results are available in digital tabular format on request to the authors.)

Because of the sharply defined sputtering threshold energy of approximately 50 eV, there is negligible sputtering of Si from the olivine ($MgFeSiO_4$) for shock speeds of 20 km s^{-1} or less. The fractions of the Mg, Si and Fe which are released from the olivine into the gas phase are shown in Fig. 2. Comparing Fig. 2 with the corresponding Fig. 4 of May et al. (2000), whose sputtering yields are used in the present calculations, shows that the fractions of Mg, Si and Fe which are sputtered from olivine have decreased by an order of magnitude. As the same sputtering yields have been used in both studies, this change is attributable to the reduction in the shock width, resulting from the improved treatment of grain-neutral coupling. We note that CO is the principal eroding partner (cf. May et al. 2000).

Figure 2 shows that the degree of sputtering is, in fact, insensitive to the preshock gas density (cf. Caselli et al. 1997); it depends essentially on the shock speed. Polynomial fits of the sputtered fractions of Fe, Si and Mg, as functions of the shock speed, are given in Appendix B.

In Fig. 3, we display the fractional gas-phase abundances of Si and SiO, as functions of the relevant flow time. Silicon is produced by erosion of the charged grains by collisions, principally with molecules, at the ion-neutral drift speed. Once the drift speed exceeds the sputtering threshold velocity, the erosion

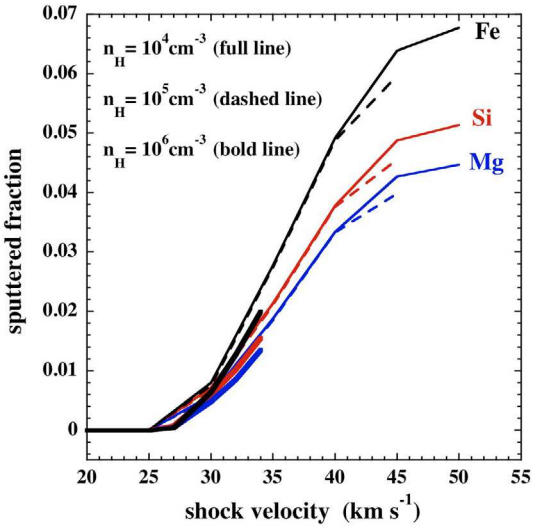

Fig. 2. The fractions of Mg, Si and Fe, initially in the form of olivine ($MgFeSiO_4$), which are released into the gas phase by sputtering within a steady-state C-type shock wave.

of Si occurs rapidly, as Fig. 3 shows. Thus, the flow time which is directly relevant to the release of Si into the gas phase is that of the *charged* fluid, rather than that of the neutrals, which is the appropriate measure of the total time for formation of SiO. As noted in item (ii) of Sect. 3.1, there is an additional, chemical delay to the conversion of Si into SiO, in reactions (1) and (2), which is apparent in our Fig. 3, owing to the low abundance and partial destruction of O_2. The magnitude of this delay depends on the parameters of the model, notably the shock speed, v_s, and the preshock gas density, n_H. Conversion is almost instantaneous for $v_s \geq 30$ km s^{-1}, $n_H = 10^6$ cm^{-3}, when OH is formed abundantly at the start of the shock and reaction (2) dominates the oxidation process.

Figure 4 shows the variation with shock speed and preshock gas density of the fractional abundance of SiO, computed through the entire shock wave. It is evident from Fig. 4 that the duration of the C-type shock wave, as measured by the temperature profile, is of the order of 10^4, 10^3 and 10^2 yr for preshock gas densities $n_H = 10^4$, 10^5 and 10^6 cm^{-3}, respectively. The peak SiO abundance is reached over similar timescales. It may be seen that the highest fractional abundances of SiO are attained for the lowest preshock density, $n_H = 10^4$ cm^{-3}. At higher densities, both O_2 and OH, which are reactants in (1) and (2), are destroyed by the atomic hydrogen which is produced in the shock wave. Thus, the conversion of Si into SiO becomes incomplete at high density, and the gas-phase SiO abundance depends on n_H even though the Si sputtered fraction does not (cf. Fig. 2).

3.3. Dependence on the transverse magnetic field strength

The existence of a magnetic field transverse to the direction of propagation is a necessary condition for a C-type shock wave to form, and it is instructive to consider the variation of the structure of the shock wave with the strength of the magnetic field. Energy equipartition arguments, applied to the magnetic and thermal energy densities in the preshock molecular gas, of particle density $n(H_2) + n(He) = 0.6n_H$ and kinetic temperature T, suggest that $B^2/(8\pi) \approx n_H k_B T$ and hence that $B = bn_H^{0.5}$, where b is a scaling parameter (cf. Sect. 3.2) such that B is in μG when n_H is in cm^{-3}; this is the proportionality adopted in the grid of models presented in Sect. 3.2. In gas of $T = 10$ K,

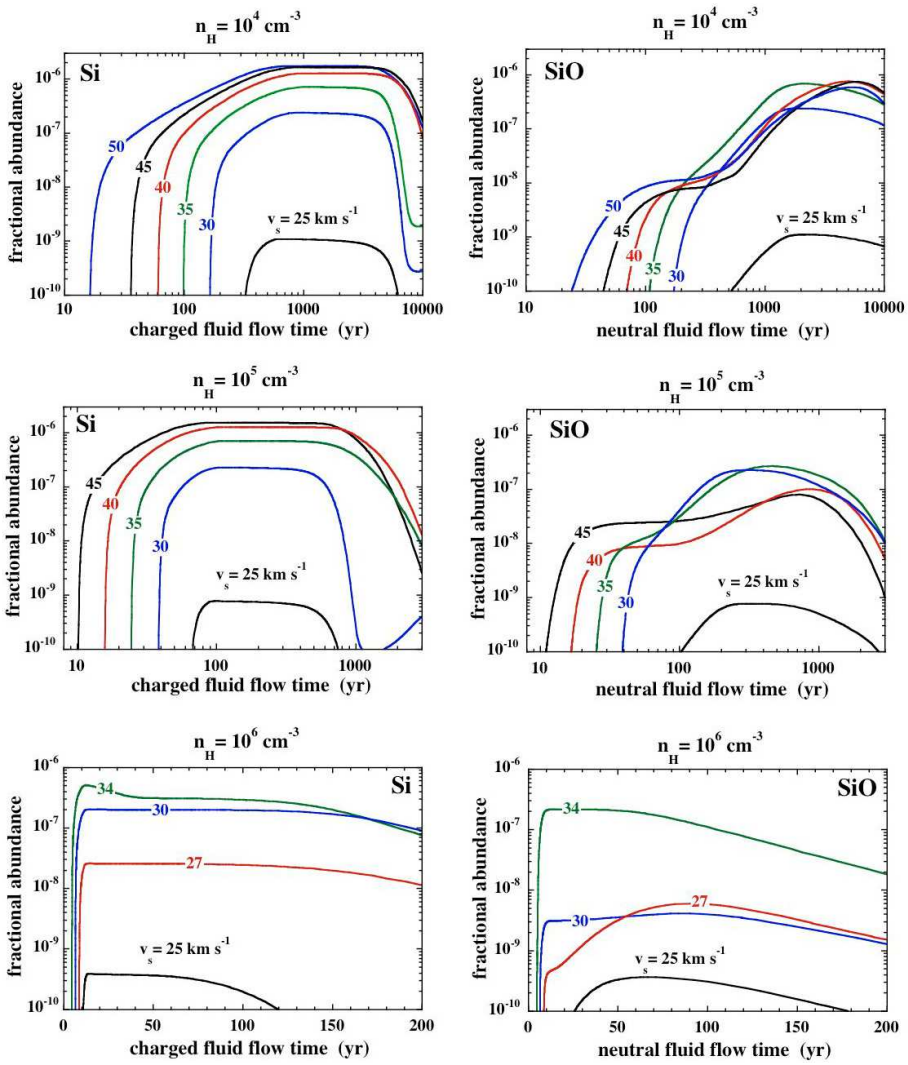

Fig. 3. The fractional abundances of Si, released into the gas phase by the sputtering of olivine ($MgFeSiO_4$), and of SiO, which subsequently forms in reactions (1) and (2). In *the left-hand panels*, the independent variable (abscissa) is the flow time of the charged fluid: see text, Sect. 3.2.

equipartition with the thermal energy implies $b = 0.18$. However, we note that such a low value of b is inconsistent with the existence of a steady-state C-type shock wave when $n_H = 10^5$ cm^{-3} and $v_s \geq 10$ km s^{-1}, as the corresponding ion magnetosonic speed in the preshock gas (9.7 km s^{-1}) is lower than the shock speed.

In Fig. 5, we present results as a function of the transverse magnetic field strength, for the parameters of the model of Sch97: $n_H = 10^5$ cm^{-3}, $v_s = 30$ km s^{-1}, and a magnetic field scaling parameter b in the range $0.5 \leq b \leq 5$. We recall that Sch97 adopted $B = 200$ μG, corresponding to $b = 0.63$. This value of b is consistent with the analysis of Zeeman measurements by Crutcher (1999), who concluded that there was an approximate equipartition of the magnetic and kinetic energy densities in the molecular clouds that he had observed. It may be seen from Fig. 5 that increasing the magnetic field inhibits the release of Si from refractory grain cores in the shock wave, owing to the reduction in the maximum ion-neutral velocity difference, Δv. In Sect. 4.5, we consider how the magnetic field strength affects the relative intensities of the rotational transitions of SiO.

4. SiO rotational emission lines

The observable quantities are the intensities of the rotational transitions of SiO and the velocity-profiles of these emission lines. Having computed the shock structure, we evaluate the line intensities and profiles as described in Appendix A, assuming that the shock is viewed face-on.

4.1. Physical conditions in the SiO emission region

Figure 6 illustrates the variation of physical conditions throughout the formation region of the SiO 5−4 rotational line for our reference model with $n_H = 10^5$ cm^{-3}, $v_s = 30$ km s^{-1}, and $b = 0.63$. It may be seen that the line is optically thin through most of the hot precursor (where the flow speeds of the charged and neutral fluids differ), due to both the low SiO abundance and the large velocity gradient there. Therefore the line intensity is low despite a high kinetic temperature. At the rear of the shock wave, approaching maximum compression, the synthesis of SiO and the steady decrease in velocity gradient eventually raise the optical depth in the line, and the 5−4 intensity peaks, with the line temperature attaining values close to the local kinetic temperature of the neutral fluid, T_n; that is, the line approaches LTE. The intensity then declines rapidly as the gas cools; the decline occurs in 500 yr for the model shown here. This behaviour is insensitive to the rate of re-adsorption of SiO on to the grains, which occurs over much longer timescales.

In order to illustrate the dependence of conditions in the SiO emission region on the shock parameters, we present, in Fig. 7, the important physical quantities, evaluated *at the peak of the SiO 5−4 line*, for all models in our grid. We have verified

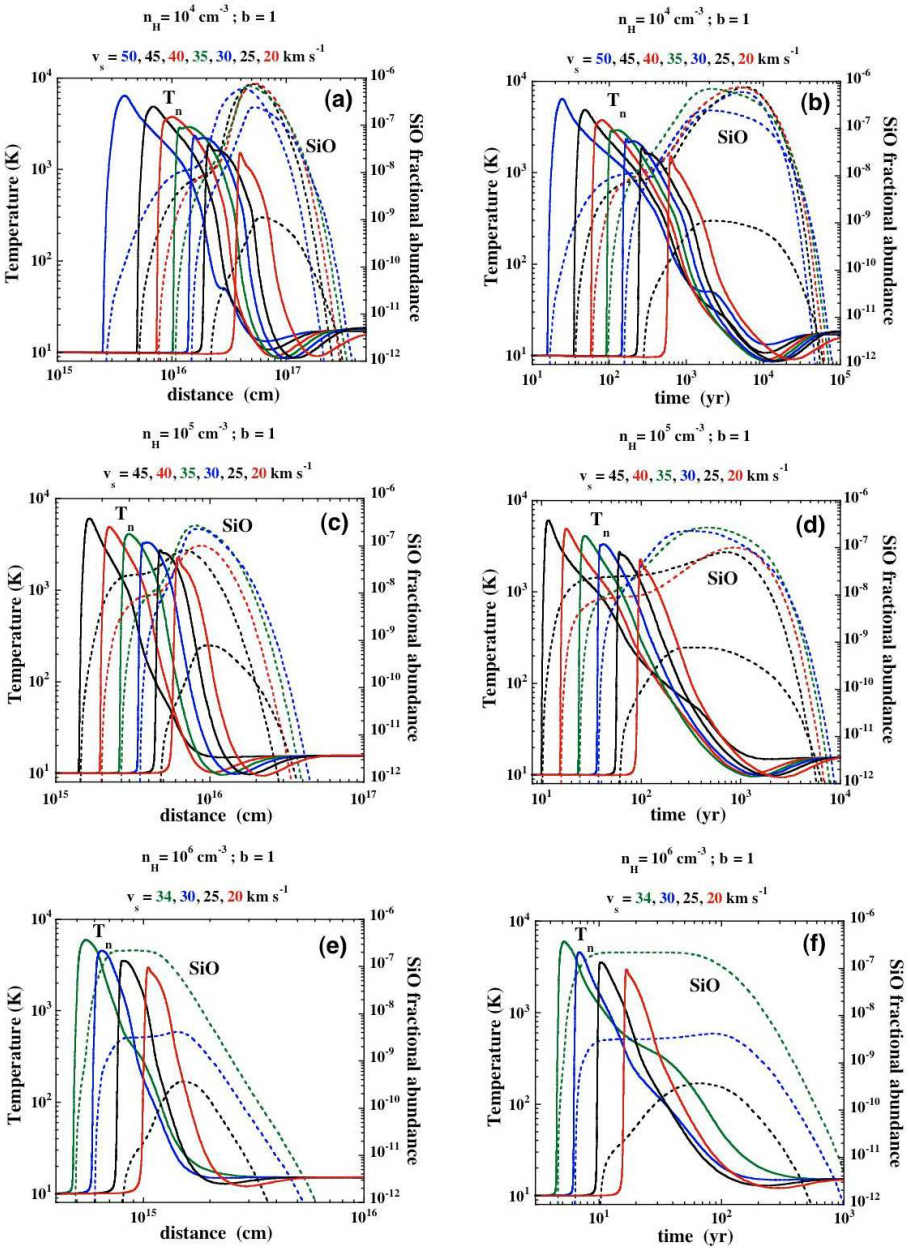

Fig. 4. The fractional abundance of SiO, $n(\mathrm{SiO})/n_\mathrm{H}$, computed for the grid of shock models and plotted as a function of distance (*left*) and neutral flow time (*right*); $n(\mathrm{SiO})/n_\mathrm{H}$ is negligible for $v_\mathrm{s} \lesssim 20$ km s^{-1}. In addition, the temperature of the neutral fluid is plotted. (See also Fig. C.1 of Appendix C.)

that this is equivalent to computing intensity-weighted geometric means of the same quantities over the region where the 5−4 line intensity is more than 50% of its maximum value[1]. Hence, it provides a good indication of the mean characteristics of the region producing the peak of the emission.

Figure 7 shows that the SiO emission peak always occurs in the cool and dense postshock region: $T_\mathrm{n} \approx 50$ K (Fig. 7a) and a density of 10−40 times the preshock value, close to maximum compression (Fig. 7b). The SiO fractional abundance, $n(\mathrm{SiO})/n_\mathrm{H}$, is also approximately equal to its maximum value in the shock wave (compare Figs. 7c with 4). The trend to lower SiO abundance at higher n_H, noted in Sect. 3.2, is clearly visible here. Finally, the "LVG parameter", $n(\mathrm{SiO})/(\mathrm{d}v_z/\mathrm{d}z)$, lies typically in the range 10^{14}−10^{16} cm^{-2} km^{-1} s, implying that the 5−4 line is optically thick at its peak for most models of our grid. In Sect. 4.5, we compare these physical parameters to values inferred previously from LVG analyses of observations, assuming a uniform slab which fills the beam.

4.2. Line profiles and peak line temperatures

In Fig. 8, we compare the intensity profiles of various rotational lines, as functions of the flow speed of the neutral fluid, expressed in the frame of the preshock gas, for our reference model: $n_\mathrm{H} = 10^5$ cm^{-3}, $v_\mathrm{s} = 30$ km s^{-1}, and $b = 0.63$. The profiles are seen to be narrow (widths of 1−2 km s^{-1}), with similar shapes and peaking within 2 km s^{-1} of v_s, as expected for compressed material at the rear of the shock wave[2]. Note that

[1] Values evaluated at the peak also differ by less than a factor 2 from the same parameters evaluated at the "median" point where the integrated line intensity, $T\mathrm{d}V(5{-}4)$, reaches half of its total.

[2] The maximum compression of the postshock relative to the preshock gas, $\sqrt{2}v_\mathrm{s}/v_\mathrm{A}$, where v_s is the shock speed and v_A is the Alfvén speed in the preshock gas, occurs when the magnetic pressure in the postshock gas is equal to the initial ram pressure. It follows that the flow speed in the postshock gas cannot fall below $v_\mathrm{min} = v_\mathrm{A}/\sqrt{2} = 1.3b$ km s^{-1} *in the shock frame*, where b is the scaling parameter of the magnetic field, defined in Sect. 3.2.

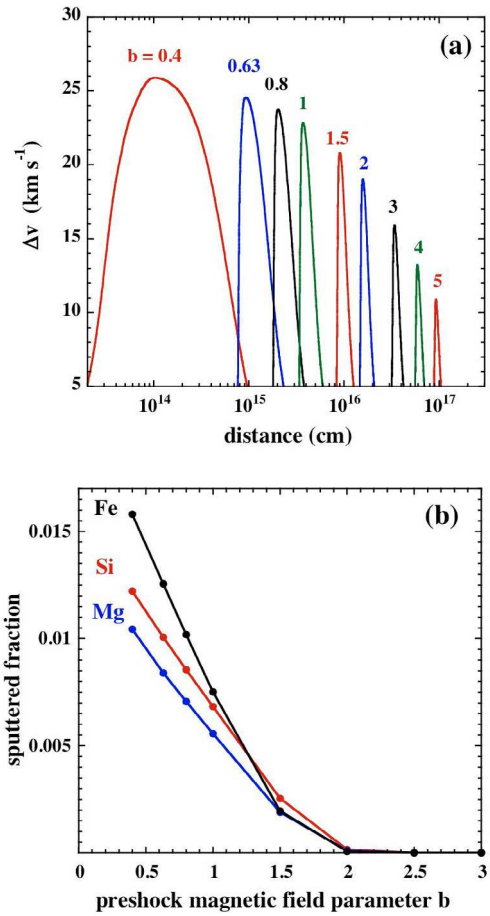

Fig. 5. **a)** The ion-neutral velocity difference, $\Delta v = |v_i - v_n|$, and **b)** the fractions of Mg, Si and Fe eroded from olivine ($MgFeSiO_4$) grains, computed as functions of the transverse magnetic field strength, B, in the preshock gas; $n_H = 10^5$ cm^{-3} and $v_s = 30$ km s^{-1}. Note that $B = bn_H^{0.5}$, where b is a scaling parameter (cf. Sect. 3.2) such that B is in μG when n_H is in cm^{-3}.

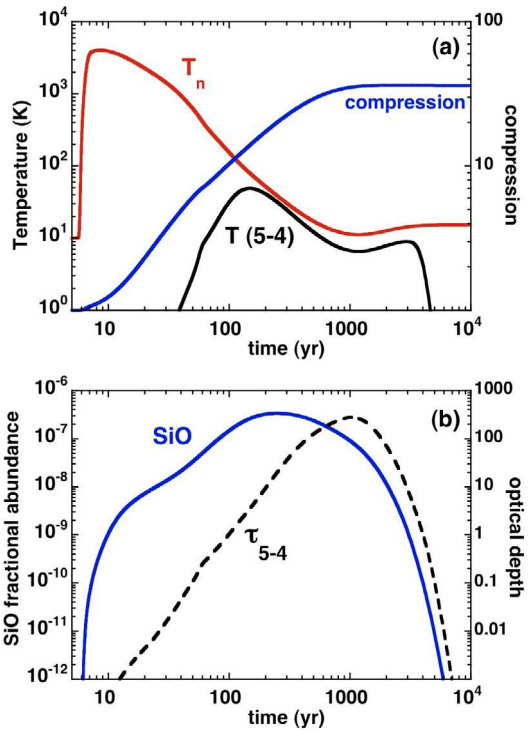

Fig. 6. **a)** The temperature of the neutral fluid, T_n, the brightness temperature, $T(5-4)$, in the $j = 5-4$ line, and the compression factor, n_H/n_H(initial); **b)** the optical depth, τ_{5-4} in the 5−4 transition and the fractional abundance of SiO, $n(SiO)/n_H$, as functions of the flow time of the neutral fluid, t_n. The model parameters are $n_H = 10^5$ cm^{-3}, $v_s = 30$ km s^{-1}, and $b = 0.63$.

the transition 2−1 peaks further into the cooling flow, because the lower j-levels are repopulated from the higher levels as the temperature falls.

The general shape and centroid velocities are globally similar to those found by Sch97 (their Fig. 3b where the profiles were plotted *in the shock frame*), although the differences between the various lines are less significant in the present calculations. Also, the emission wing from the fast precursor, at the start of the shock wave, is weaker in the current models, owing to the delay in SiO formation (see Sect. 3.1), making our line profiles narrower than in Sch97. Note that including local thermal broadening in our profile calculations would not significantly change our predicted SiO line width of 1−2 km s^{-1}, because the SiO emission peaks at low temperatures, $T_n \lesssim 100$ K, where the Doppler width is $\sqrt{kT/44m_H} \leq 0.1$ km s^{-1}.

In the left column of Fig. 9, we show the predicted peak temperature of the SiO 5−4 line for the grid of models considered in Sect. 3.2, as well as the variation with j_{up} of the peak brightness temperatures of various lines, relative to that of 5−4. The *relative* intensities have the advantage of being independent of the beam filling factor, and thus they are comparable directly to observations, without prior knowledge of the source size.

The relative peak intensities are within 20% of unity for $j_{up} \leq 7$ over a broad range of model parameters ($v_s \geq 30$ km s^{-1} and $n_H < 10^6$ cm^{-3}), owing to the large opacity and near-LTE excitation conditions. For larger values of j_{up}, the relative intensities are more dependent on the shock speed and ≈1 only when the limiting speed is approached. The absolute peak brightness temperature in the 5−4 line is typically 10−50 K for $v_s \geq 30$ km s^{-1}, similar to the kinetic temperature in the emission region, but drops sharply at lower shock speeds, for which the SiO abundance (and opacity) is small. The broken curves in Figs. 9d and h are the results obtained assuming that the initial abundance of O_2 ice is negligible, i.e. the second of the two scenarios described in Sect. 3.1.

4.3. Integrated line intensities

In the right column of Fig. 9 are presented the integrated intensities (denoted TdV) of the rotational emission lines of SiO, relative to the 5−4 line, computed for the grid of models considered in Sect. 3.2. There are significant differences between the relative integrated and peak (T_{peak}) line temperatures (right and left columns, respectively, of Fig. 9), owing to systematic variations in linewidth with j_{up}, i.e. in the extent of the region where the line is significantly excited. The relative integrated intensities of lines with $j_{up} \geq 7$ remain the most sensitive to the shock speed. As may be seen in Sch97, the maximum value of TdV occurs at higher values of the rotational quantum number, j_{up}, for higher n_H. Although the shock temperature varies only weakly with n_H (see Fig. 4), a higher density enhances the rates of collisional excitation of the high-j levels, for any given value of the shock speed, v_s. In Sect. 5, we explore the usefulness of this effect for constraining the preshock density, based on a comparison with actual observations.

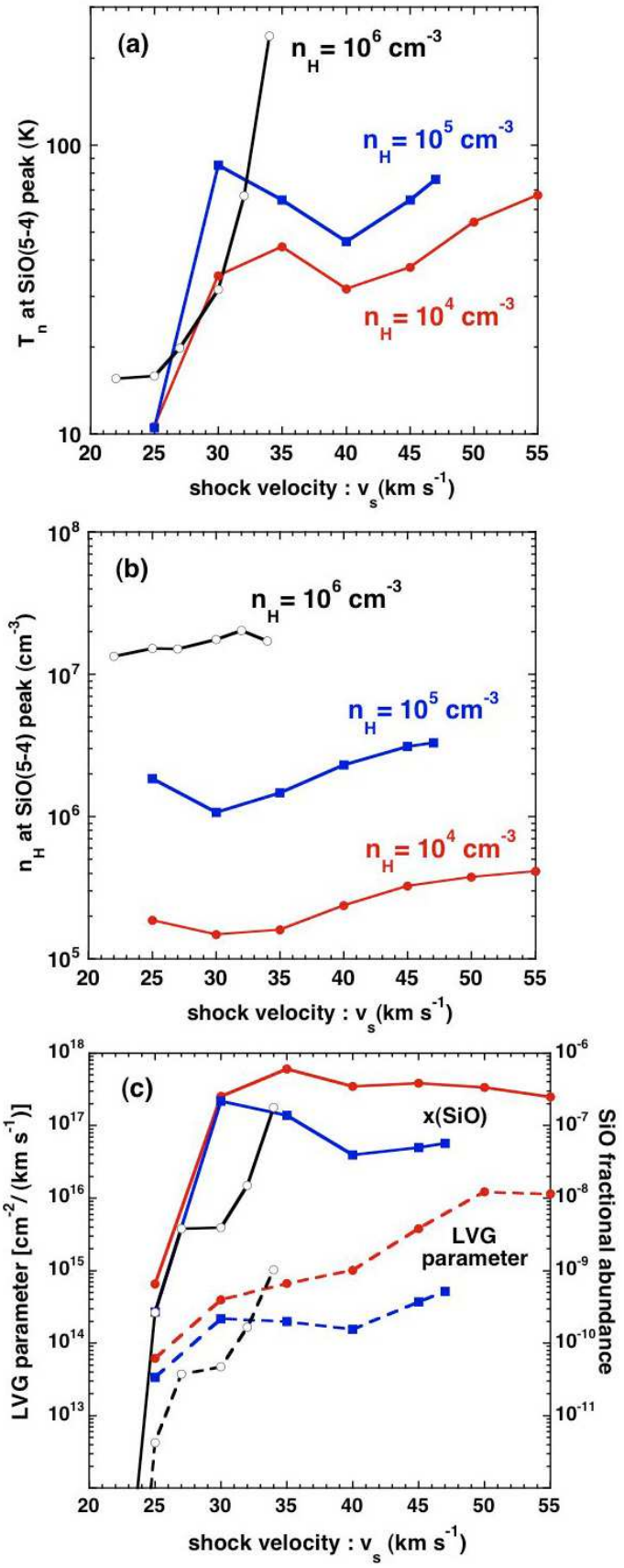

Fig. 7. Physical conditions at the position of the peak in the SiO 5−4 line intensity [$T_{\rm peak}(5{-}4)$] as functions of the shock speed, $v_{\rm s}$, for all models of the grid: **a)** neutral temperature, $T_{\rm n}$; **b)** preshock density, $n_{\rm H}$; **c)** the LVG parameter, $n({\rm SiO})/({\rm d}v_z/{\rm d}z)$, and the fractional abundance of SiO, $x({\rm SiO}) \equiv n({\rm SiO})/n_{\rm H}$. (See also Fig. C.2 of Appendix C.)

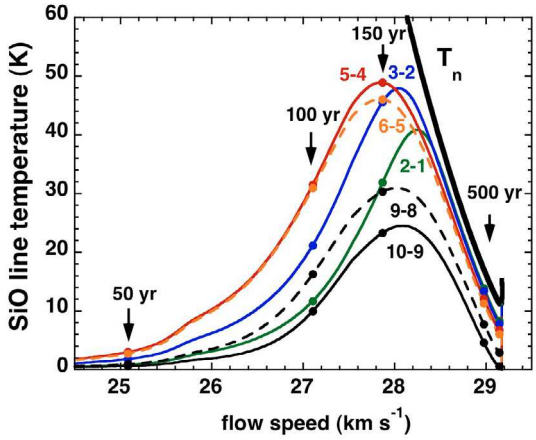

Fig. 8. The velocity profiles of transitions from rotational levels $j \rightarrow j-1$ of SiO, computed for our reference model, viewed face-on. Only those lines detectable from the ground are shown. The model parameters are $n_{\rm H} = 10^5$ cm^{-3}, $B = 200$ μG, and $v_{\rm s} = 30$ km s^{-1}. The flow speed is in the reference frame of the preshock gas. The neutral temperature profile, $T_{\rm n}$, is shown also, as are indicative values of the flow time of the neutral fluid. (See also Fig. C.3 of Appendix C.)

The variation of the *absolute* integrated intensity of the 5−4 rotational emission line with the shock parameters is shown also in Fig. 9h. The bump in $T{\rm d}V$ of the 5−4 transition, for $30 \leq v_{\rm s} \leq 40$ km s^{-1} and $10^4 \leq n_{\rm H} \leq 10^5$ cm^{-3} is caused by incomplete O_2 destruction in the shock wave, resulting in more rapid SiO formation and warmer emission zones (cf. Fig. 7). As the broken curves in Figs. 9d and h show, this "bump" is absent in our second scenario, where O_2 is never abundant in the gas phase. At higher shock speeds, the results from the two scenarios become identical, as OH dominates the oxidation of Si in both cases.

4.4. Influence of viewing angle

Statistically, there is a low probability that a planar shock should happen to be viewed face-on. Accordingly, we have explored the effects on the SiO rotational line intensities of varying the viewing angle, for the case of our reference model, using the formula (A.16), derived in Appendix A.

The variations of $T_{\rm peak}(5{-}4)$ and $T{\rm d}V(5{-}4)$ with viewing angle, θ, are plotted in the bottom panel of Fig. 10. The peak intensity is almost unaffected by the inclination, as the line is already optically thick for a face-on view (see Eq. (A.16)). On the other hand, the velocity projection reduces the line width, and the integrated intensity, $T{\rm d}V$, declines steadily with increasing viewing angle – by up to a factor of 2 at 75°. However, such a variation would be difficult to deduce from observations, given the typical uncertainties in beam filling factors.

Panels (a) and (b) of Fig. 10 illustrate the changes in the (relative to 5−4) peak and integrated SiO line temperatures. Significant changes, compared with viewing face-on, are seen only for inclinations greater than 60° from the normal, and they affect only the optically thin lines $j_{\rm up} \leq 3$ and $j_{\rm up} \geq 12$. The main change in the curves for the relative integrated line temperatures (panel (b) of Fig. 10) is that the maximum occurs at lower $j_{\rm up}$ as θ increases; this effect could be easily confused with a face-on shock of slightly lower preshock density (cf. Fig. 9). The relative peak temperature (panel (a)) is even more strongly modified, with an upward turn of the curve at $j_{\rm up} \leq 4$. The latter characteristic appears to be the only unambiguous signature of a

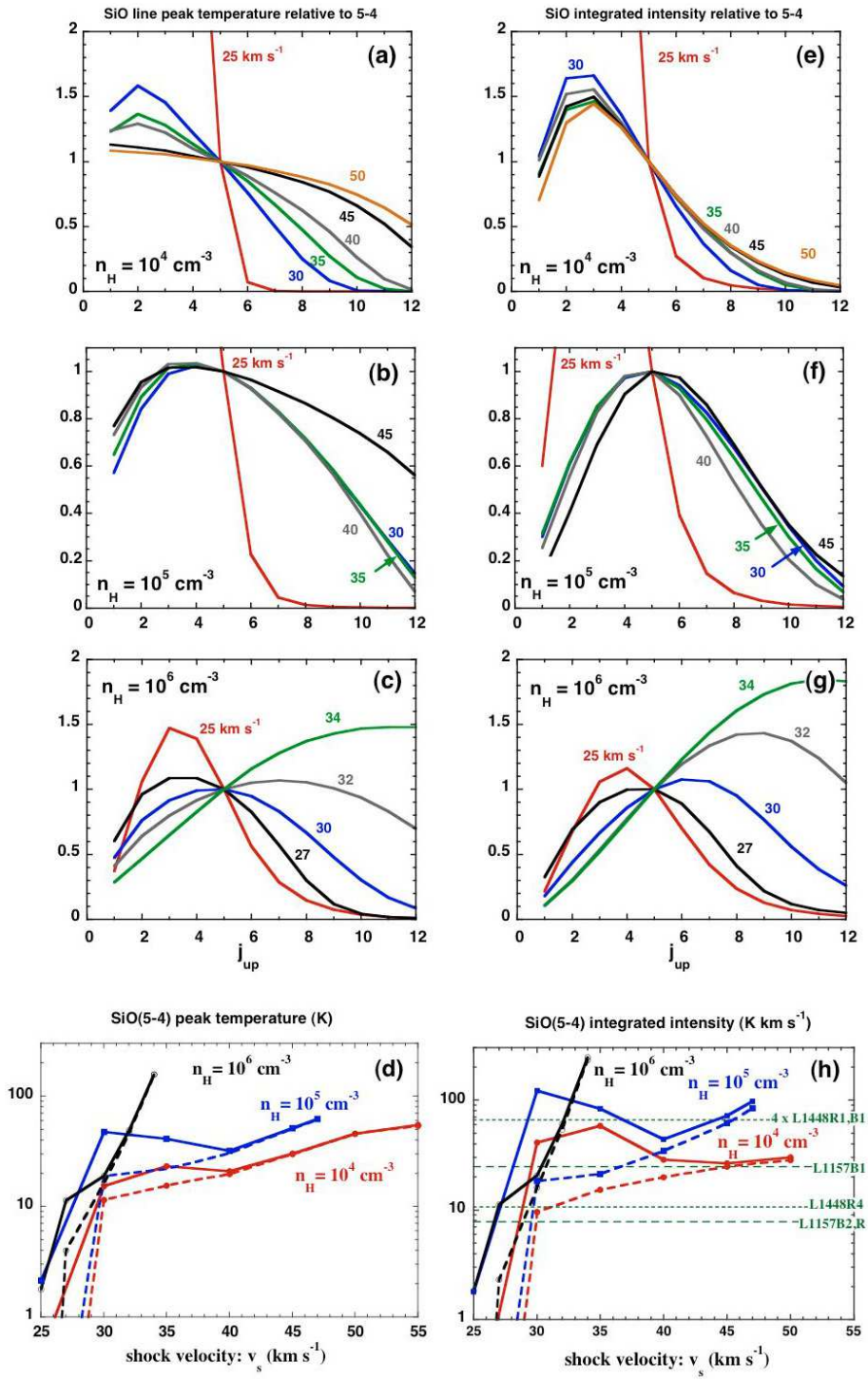

Fig. 9. a)–c) The peak line temperatures, $T_{\rm peak}$, of the rotational emission lines of SiO, relative to the 5−4 line, as functions of the rotational quantum number of the upper level of the transition, $j_{\rm up}$, for the grid of models in Sect. 3.2. The value of density, $n_{\rm H}$, of the preshock gas is indicated in each panel. **d)** The *absolute* peak brightness temperature of the 5−4 line, $T_{\rm peak}(5{-}4)$, as a function of shock speed, $v_{\rm s}$, for all three values of the preshock gas density, $n_{\rm H}$. Shock speeds in excess of 34 km s^{-1} are absent when $n_{\rm H} = 10^6$ cm^{-3}, as they give rise to a J-type discontinuity, and the shock wave is no longer C-type; see Sect. 3.2. The right-hand panels **e)–h)** show the corresponding values of the integrated line intensities, $T{\rm d}V$. The values of $T{\rm d}V(5{-}4)$ observed in L1157 and L1448 are indicated. In panels **d)** and **h)**, the broken curves show the results obtained assuming that the initial abundance of O_2 ice is negligible, i.e. the second of the two scenarios described in Sect. 3.1.

viewing angle >60° in the context of our one-dimensional models.

4.5. Influence of the transverse magnetic field strength

In Sect. 3.3, we have seen that the efficiency of sputtering Si from grains decreases monotonically with increasing magnetic field strength. The effect of varying the scaling parameter, b, on the emergent SiO line intensities is shown in Fig. 11, for our reference model.

In panels a and b of Fig. 11 are plotted the predicted line profiles, peak temperatures, and integrated intensities of the SiO 5−4 line, for various values of b. It may be seen that the maximum intensity is reached for intermediate values of $0.63 \lesssim b \lesssim 1$. At smaller b, SiO is less abundant: the shock wave is narrower and hotter, and so O_2 is more readily destroyed by H, resulting in incomplete oxidation of Si into SiO. At larger b, the SiO emission decreases owing to less efficient sputtering of Si (see Fig. 5b) at the lower ion-neutral drift speeds. In particular, the predicted intensity drops from $T_{\rm peak} = 10$ K at $b = 2$ to practically zero at $b = 3$.

Panels c and d of Fig. 11 show the relative peak and integrated line temperatures, as functions of $j_{\rm up}$, for various values of $b \leq 2$ (curves for $b > 2$ are not shown as they lead to negligible SiO emission). It may be seen that the values $0.63 \lesssim b \lesssim 1$,

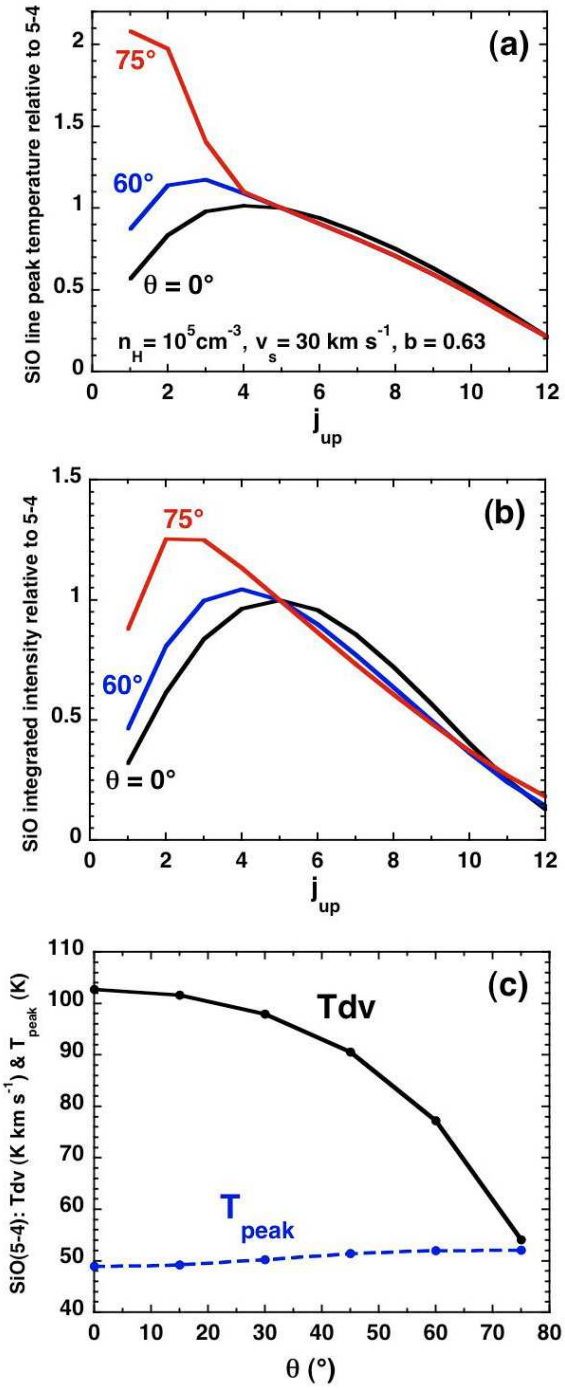

Fig. 10. Effect of the inclination angle, θ, on **a)** the peak, and **b)** the integrated intensities of the rotational emission lines of SiO, relative to the 5−4 line; **c)** the integrated and peak intensities of the 5−4 line.

which give rise to the strongest 5−4 emission, also yield the highest relative intensities of lines from $j_{\rm up} \geq 7$. For example, the intensity of the 11−10 line, relative to 5−4, is 3 to 4 times larger than when $b = 0.5$ or $b = 1.5$. Comparison with Fig. 9 suggests that this dependence on b may be difficult to distinguish observationally from variations in shock speed. A less ambiguous indication of the value of b might be obtained from the width of the cooling zone, which increases as b^2, from 10^{15} cm for $b = 0.4$ to 2×10^{16} cm for $b = 2$ and for the parameters of our reference model (see Fig. 5a).

5. Comparisons with observations

5.1. Rotational line profiles

As Sch97 first noted, the generic SiO line profile predicted by steady planar C-type shock waves, with a peak at high velocity (in the postshock gas) and a tail at lower velocity (in the accelerating precursor), is reminiscent of the SiO line profiles in the L1448 molecular jet (Bachiller et al. 1991). Similarly, we note that the reversed shape of SiO profiles in the L1157 bowshocks, with a peak at low velocity and a high velocity tail (Zhang et al. 1995), could arise if the postshock gas is stationary in the cloud frame, i.e. if one observes the reverse shock, in which the jet is being decelerated. However, in either case, the SiO profiles predicted by our models remain narrower than those observed, with widths of 0.5−2 km s^{-1}, as compared to the observed widths of 5−20 km s^{-1} in 3″−10″ beams.

Broader line profiles from steady C-type shocks could arise if Si was sputtered not only from grain cores, as assumed here, but also from SiO-containing grain mantles, with lower binding energy. Then, the SiO abundance would be much enhanced at intermediate velocities, in the precursor (see Sch97). However, owing to the steep temperature decline across the shock wave, this situation results in large variations of the line widths and velocity centroids with the emitting rotational level, $j_{\rm up}$ (cf. Fig. 5 of Sch97). In fact, the observed profiles are very similar from line to line, with the (8−7)/(2−1) intensity ratio showing only modest variations with velocity (see, for example, Fig. 9 of Nisini et al. 2007). These observations suggest that the broad SiO lines are not attributable entirely to intrinsic velocity gradients through a single, planar C-type shock wave. There may be several shock-cooling zones inside the beam, each with a narrow intrinsic profile, which appear spread out in radial velocity owing to a range of inclination angles or propagation speeds, in the observer's frame. This conclusion is supported by interferometric observations of L1157 and L1448 (Guilloteau et al. 1992; Gueth et al. 1998; Benedettini et al. 2007), which reveal systematic velocity gradients across the SiO emitting knots (reminiscent, in some cases, of a bowshock geometry; Dutrey et al. 1997) down to 2″−3″ resolution; at the distances of L1157 and L1448, the angular dimensions of the SiO emitting regions in Fig. 8, for example, are a few tenths of an arcsec. Such complex two-dimensional modelling lies outside the scope of the present paper. However, we argue in Sect. 5.3 that we may still perform a meaningful comparison of our predicted SiO line intensities with observations of knots in outflows, without reproducing in detail the line profiles, provided that the shock conditions do not vary too much across the beam.

5.2. Narrow SiO lines near ambient velocity

In addition to the typically broad SiO line profiles mentioned above, some outflow regions such as NGC 1333 and L1448 exhibit extremely narrow SiO emission lines, with $\Delta v \approx$ 0.5 km s^{-1}, near rest velocity (Lefloch et al. 1998; Codella et al. 1999; Jiménez-Serra et al. 2004, 2005). The corresponding SiO abundance of 10^{-11}−10^{-10} is two to three orders of magnitude smaller than in the broad SiO components (Codella et al. 1999; Jiménez-Serra et al. 2005). Jiménez-Serra et al. proposed that this feature in L1448 traces a magnetic precursor, where neutral gas is just beginning to accelerate and grain species are starting to be released into the gas phase. However, as we now explain, detailed multifluid shock models do not support this interpretation.

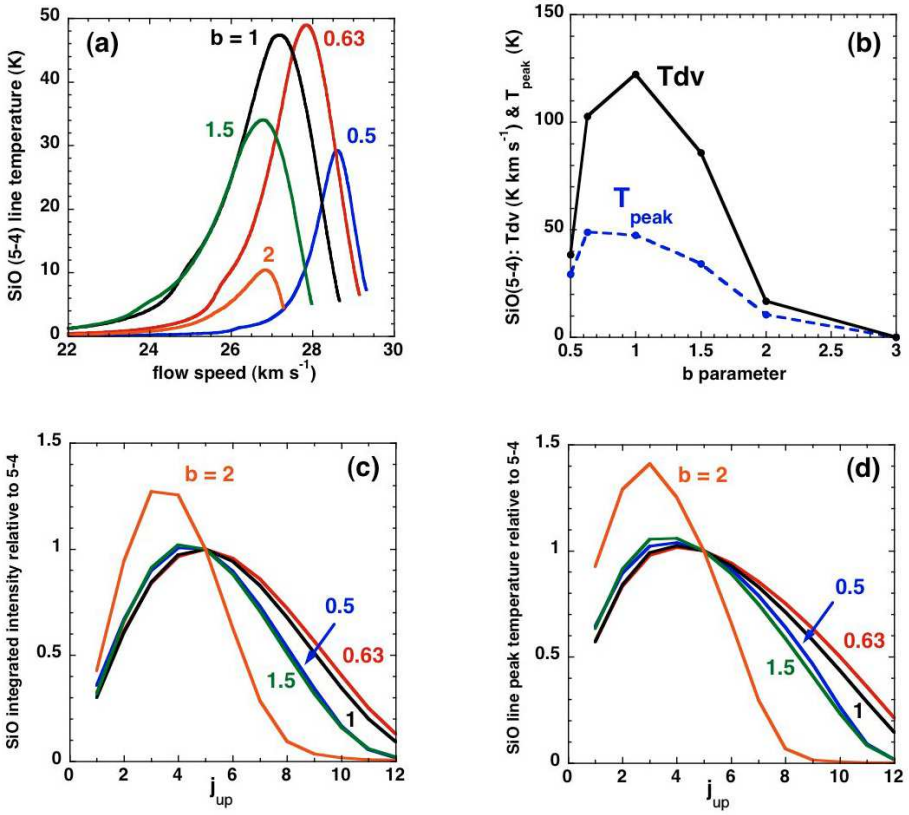

Fig. 11. a) The SiO 5–4 line temperature, as a function of the flow speed of the neutral fluid, in the reference frame of the preshock gas, for the specified values of the magnetic field parameter, b; **b)** the peak and integrated intensities of the 5–4 line, as functions of b; **c)** the integrated and **d)** the peak intensities of rotational emission lines $j_{\rm up} \rightarrow j_{\rm up} - 1$ of SiO, relative to the 5–4 transition, for the specified values of b. All calculations for $v_{\rm s} = 30$ km s^{-1} and $n_{\rm H} = 10^5$ cm^{-3}.

Our SiO line profile calculations show that emission from a magnetic precursor does not give rise to a narrow feature near the speed of the preshock gas. The line intensity increases as the neutral fluid is accelerated, heated, and enriched in SiO – by orders of magnitude by the time that grain-sputtering is complete. Indeed, this deduction could have been made already, on the basis of Figs. 3 and 5 of Sch97, which cover the entire velocity range relevant to predicting the SiO line profiles. Truncation of the precursor when the neutral fluid has been accelerated to only $v_{\rm n} = 0.5$ km s^{-1} would imply a very finely-tuned shock age, a circumstance which appears to us to be improbable. Furthermore, an ion-neutral drift speed of at least 5 km s^{-1} is needed to start releasing species from grain mantles, where binding energies are a few tenths of an eV (Flower & Pineau des Forêts 1994), and of at least 20 km s^{-1} to start sputtering grain cores (May et al. 2000). However, the $H^{13}CO^+$ line does not show evidence of this predicted acceleration: its emission peak is shifted by only +0.5 km s^{-1} from the velocity of the ambient gas, like the narrow SiO feature (Jiménez-Serra et al. 2004).

We believe that a more likely explanation of the narrow SiO feature in L1448 is that it traces Si-enriched postshock material that has been decelerated by and mixed with the ambient gas, as proposed originally by Lefloch et al. (1998) and Codella et al. (1999) in connection with other regions. Given a shock speed $v_{\rm s} \leq 30$ km s^{-1} and the high ambient density characteristic of Class 0 protostellar envelopes, deceleration could be achieved readily within the L1448 flow age of approximately 3500 yr. The low SiO fractional abundance would then be a consequence of mixing with SiO-poor ambient gas. Alternatively, the narrow feature might arise in a reverse C-type shock, where outflow material at $v < 20$ km s^{-1} is brought almost to rest by the much denser ambient medium, and the shock speed is too low to produce abundant SiO. Both interpretations are consistent with NH_3 observations of dense gas in the envelope of the L1448 protostar, with radial velocity and spatial extent similar to that of the narrow SiO feature and signs of heating near the path of the fast L1448 jet (Curiel et al. 1999).

5.3. SiO line intensities

If our explanation of SiO profile broadening is correct, one could in principle recover the parameters of *each* individual emission zone in the beam by analysing the relative intensity ratios *as functions of velocity*. Unfortunately, such data are currently quite noisy and not yet available for a wide range of values of $j_{\rm up}$. Furthermore, knowledge of the beam-filling factor as a function of velocity would be necessary to obtain absolute intensities and remove ambiguity in the shock parameters; but this would require sub-arcsecond angular resolution, which is not yet available. Nevertheless, one may still derive some approximate *beam-averaged* shock properties, if all of the shock components have similar excitation conditions, as is suggested by single-dish data, which show the line ratios to be insensitive to velocity, v. In this case, the observed profile will be simply a convolution of the individual, narrow shock profiles with the (unknown) filling-factor, $\phi(v)$. The observed absolute $T{\rm d}V$ is simply that for a single shock, multiplied by the total beam filling factor of the SiO-emitting region in the beam, $f = \int \phi(v){\rm d}v$, as inferred from its overall size in single-dish maps. The values of $T{\rm d}V$ for different $j_{\rm up}$, relative to the 5–4 transition, remain unchanged compared to a single shock, because f cancels out in the ratios, thereby enabling direct comparison with our models. In the following, we assume that this situation prevails.

By way of illustration of the applicability of the shock models, we show in Fig. 12 the relative integrated intensities of the

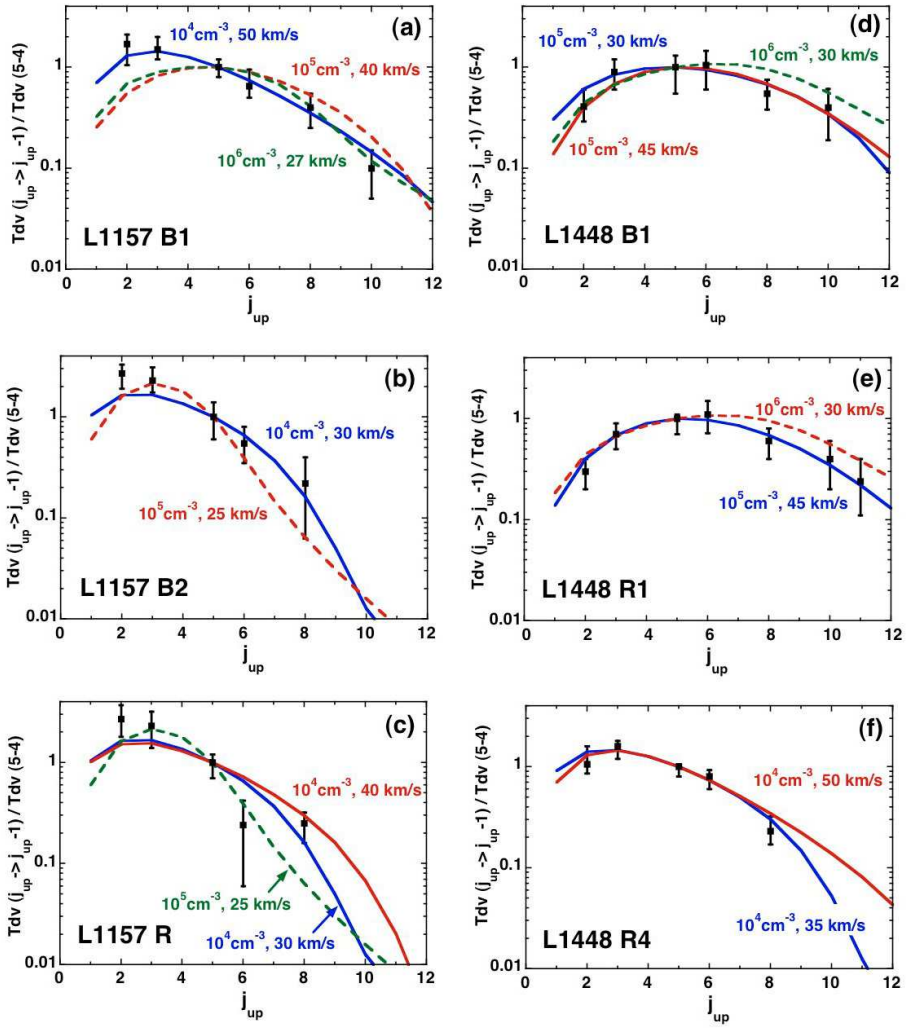

Fig. 12. The relative intensities of the rotational emission lines of SiO observed in the outflow sources L1157 and L1448 (Nisini et al. 2007: points with error bars) and predicted by the C-type shock models (curves) with the parameters ($n_{\rm H}$, $v_{\rm s}$) indicated; see text, Sect. 5. The data points which are plotted include a correction for differing beam sizes, which is significant for low-j lines. Full curves denote the best-fitting models of our grid. Broken curves show "near-miss" models with a different value of $n_{\rm H}$, which either yield a worse fit to the data points or do not reproduce the absolute $T{\rm d}V$ of the 5−4 line. (See also Fig C.4 of Appendix C.)

rotational transitions of SiO observed in the outflow sources L1157 and L1448 (Nisini et al. 2007) and predicted by the grid of models, whose parameters are specified; in all cases, the magnetic field scaling parameter $b = 1$. As noted in Sect. 4.5, this value of b yields the largest relative intensities of the high-j lines and hence will yield a *lower limit* to the shock speed required to reproduce the observations (except at $n_{\rm H} = 10^5$ cm^{-3}, where high-j excitation is a non-monotonic function of $v_{\rm s}$; see Fig. 9f). We assume also that the shock wave is viewed face-on; if the true inclination exceeds 60°, this assumption results in the preshock density being slightly underestimated (see Sect. 4.4). The models shown as the full curves are those which provide the best fits to the observations. In order to illustrate how well the shock parameters are constrained, we plot as dashed curves "near-miss" models that fit most of the data points, or fit all points but do not reproduce the absolute intensity of the 5−4 line (see below).

Figure 12 demonstrates that steady-state C-type shocks with Si-sputtering from grain cores can reproduce successfully the relative integrated intensities of SiO lines in these molecular outflows. Furthermore, Fig. 9h shows that the models can reproduce also the *absolute* integrated intensity of SiO 5−4 with the estimated beam filling factors $f \approx 1$ in L1157 and L1448-R4 and $f \simeq 1/4$ in L1448 R1 and B1 (cf. Nisini et al. 2007). Alternative fits with higher density and lower shock speeds ($n_{\rm H} = 10^6$ cm^{-3} and $27 \lesssim v_{\rm s} \lesssim 30$ km s^{-1}; $n_{\rm H} = 10^5$ cm^{-3} and $v_{\rm s} = 25$ km s^{-1}) underestimate $T{\rm d}V(5{-}4)$ and are thus ruled out. The shock speed, $v_{\rm s}$, is constrained to within 15 km s^{-1} and the preshock density to within a factor of 10, with one of our grid values of $n_{\rm H}$ yielding a clear best fit in all cases.

In Appendix C, we present, in Fig. C.4 results equivalent to those in Fig. 12, but for the secondary grid of models, in which oxygen is initially in the form of H_2O ice rather than O_2 ice. Again, the relative intensities can be well reproduced by steady-state C-type shocks. The absolute SiO $T{\rm d}V(5{-}4)$ favour the low $n_{\rm H}$, high $v_{\rm s}$ cases (cf. the dashed curved in Fig. 9h). The best-fit shock parameters and the inferred physical conditions at the (5−4) line peak are almost unchanged, as the range of shock speeds is such that oxidation of Si by OH is dominant.

It is instructive to compare the physical parameters at the SiO peak of our best-fit, steady-state C-type shock models to those previously inferred from an LVG analysis, assuming a slab of constant density, temperature, and velocity gradient along the line of sight (Nisini et al. 2007). From Table 1, it may be seen that the "slab LVG" approach yields similar values of the density to our shock models but overestimates by a factor 5−10 the kinetic temperature and underestimates by several orders of magnitude the Sobolev LVG opacity parameter. The cool post-shock layer emits over a narrow velocity range and needs to be more optically thick in SiO to produce the same $T{\rm d}V$ as a hot slab with a large velocity gradient along the line of sight. On the other hand, similar SiO abundances are deduced using both approaches, to within typically a factor of 3.

We note that the models should be able to simulate also the other spectral observations of the sources, notably the H_2 line

Table 1. Properties of SiO-emission regions deduced from face-on C-type shock models or homogeneous-slab LVG models.

	Face-on C-type shock models[a,b]						Slab LVG models[a,c]			
SiO knot	n_H^{init}	v_s	T_{kin}	n_H	LVG	x_{SiO}	T_{kin}	n_H	LVG	x_{SiO}
L1448 B1	1(5)	30,45	90–70	10–30	2–4	0.5–2	>500	8	0.1	1
L1448 R1	1(5)	45	70	30	4	0.5	>500	10	0.1	1
L1448 R4	1(4)	35–50	45–55	1.5–4	7–100	3–7	200	2.5	0.03	0.3
L1157 B1	1(4)	50	55	4	100	3	150–300	3	0.08	0.8
L1157 B2	1(4)	30	35	1.5	4	2	200–300	2	0.05	
L1157 R	1(4)	30–40	35–30	1.5–2	4–10	2–3	50–100	1–5	0.02	0.6

[a] Units: n_H^{init} is the preshock density, in cm^{-3}; v_s the shock speed, in km s^{-1}; T_{kin} is the local gas kinetic temperature, in K; n_H is the local gas density, in 10^5 cm^{-3}; "LVG" is the local LVG parameter, n(SiO)/(dv_n/dz), in 10^{14} cm^{-2} km^{-1} s; and x_{SiO} is the local fractional abundance, in units of 10^{-7}.
[b] Best grid model from Fig. 12 and physical parameters at the SiO 5−4 line peak from Fig. 7.
[c] Values taken from Tables 4 and 5 of Nisini et al. (2007). The LVG parameter is given by N(SiO)/ΔV, with ΔV = 10 km s^{-1}.

intensities. In a forthcoming publication, we shall consider in detail the outflow L1157 and make a more comprehensive comparison of its observed spectrum with the predictions of shock models.

6. Concluding remarks

We have considered the structure of C-type shock waves propagating into molecular gas containing amorphous carbon and silicate grains; olivine ($MgFeSiO_4$) was chosen as the representative silicate-grain material. We find that the degree of sputtering of silicon from the grains is smaller, by about an order of magnitude, than was predicted by the calculations of Sch97, owing partly to higher sputtering thresholds and lower sputtering yields but principally to the reduced width of the shock wave in the present calculations. The reduction in the shock width is a consequence of a more accurate treatment of the coupling between the neutral fluid and the charged grains in the current model.

A grid of C-type shock models has been computed, for values of the preshock gas density and the shock speed which are believed to span the ranges of these parameters in molecular outflows; two scenarios were considered regarding the initial distribution of oxygen in the gas and solid phases. The maximum speed of a C-type shock is limited by the inertia of the (charged) grains in the preshock gas and by the collisional dissociation of molecular hydrogen within the shock wave, which can lead to a J-type discontinuity (Le Bourlot et al. 2002; Flower & Pineau des Forêts 2003). We find that significant sputtering of the grain cores occurs only for shock speeds $v_s \geq 25$ km s^{-1} and moderate magnetic field strengths close to equipartition with the cloud kinetic energy (magnetic field parameter $0.5 \leq b \leq 2$). However, we note that the sputtering threshold energy is determined principally by the so-called "displacement energy", E_D, of the material, whose value for the silicates of relevance here remains uncertain (May et al. 2000). The sputtering yields increase rapidly from threshold, and a reduction in the threshold energy would enable significant sputtering to occur at lower shock speeds or higher magnetic field strengths.

We find that, in the absence of silicon-containing grain mantles, SiO line emission in steady-state planar C-type shock waves arises predominantly from cool postshock gas, close to maximum compression, with negligible emission from the precursor. Except at the lowest shock speeds, the SiO emission is optically thick and close to LTE for $4 \leq j_{up} \leq 7$. The relative line intensities, as functions of j_{up}, together with the absolute 5−4 line intensity, provide good diagnostics of the shock parameters, n_H and v_s. The influence of the viewing angle and transverse magnetic field strength is found to be relatively minor over the typical ranges of their values.

Our shock models provide good fits to both the relative and absolute SiO intensities in the molecular outflows L1157 and L1448; the SiO fractional abundance is deduced to be in the range $4 \times 10^{-8} \lesssim n(\mathrm{SiO})/n_H \lesssim 3 \times 10^{-7}$. The emission regions of the shock wave are much colder, more optically thick, and have 10 to 100 times greater SiO column density than estimated previously from optically thin LVG slab models (Nisini et al. 2007). Our results are in line with a recent analysis of interferometric maps of the HH212 jet (Cabrit et al. 2007), demonstrating that the SiO emission is optically thick and close to LTE, with an intrinsic peak brightness temperature of approximately 50 K. On the other hand, the line profiles predicted by our planar C-type shocks are typically 10 times narrower than observed in L1157 and L1448, suggesting that the single-dish beam includes shocks with various inclinations and speeds, and/or mixing layers. Detailed modelling of the line ratios as functions of velocity, with a careful correction for differing beam widths, would be needed to clarify this issue.

Whilst the grid of models presented here is intended to provide a guide to interpreting observations of outflow sources, it should be recalled that the dynamical timescales which characterize these regions are often too short to enable C-type shock waves to attain their steady-state structure (Chièze et al. 1998; Lesaffre et al. 2004). The presence of an embedded J-type discontinuity has then to be considered when modelling specific sources. Studies of the outflow source in Orion (Le Bourlot et al. 2002), of jets associated with low-mass star formation (Giannini et al. 2004, 2006; McCoey et al. 2004), and of the supernova remnant IC 443 (Cesarsky et al. 1999) have shown that the rovibrational line spectrum of H_2 can be reproduced successfully by hybrid shock waves, but not by pure C- or J-type shocks. The influence of the discontinuity on the C-component (magnetic precursor), and hence on the formation of SiO and its emission line spectrum, becomes important for ages smaller than the flow time to maximum compression.

The existence of Si-containing grain mantles is another circumstance that would significantly modify the intensities of SiO lines and their profiles. The fractional abundance of SiO in the warm shock precursor would be enhanced, compared with the models considered here, in which Si is sputtered exclusively from olivine grain cores. The effects of non-steady C-type

shocks and Si-containing mantles will be considered in a forthcoming paper.

Acknowledgements. Antoine Gusdorf and the University of Durham acknowledge the support of the European Commission under the Marie Curie Research Training Network "The Molecular Universe" MRTN-CT-2004-512302. We thank Brunella Nisini for helpful correspondence relating to the SiO observations of Nisini et al. (2007). We thank also Paul Goldsmith and Laurent Pagani for information regarding SWAS and Odin observations of O_2.

References

Anders, E., & Grevesse, N. 1989, Geochim. Cosmochim. Act., 53, 197
Bachiller, R., Martín-Pintado, J., & Fuente, A. 1991, A&A, 243, L21
Benedettini, M., Viti, S., Codella, C., et al. 2007, MNRAS, 381, 1127
Cabrit, S., Codella, C., Gueth, F., et al. 2007, A&A, 468, L29
Caselli, P., Hartquist, T. W., & Havnes, O. 1997, A&A, 322, 296
Cesarsky, D., Cox, P., Pineau des Forêts, G., et al. 1999, A&A, 348, 945
Chièze, J.-P., Pineau des Forêts, G., & Flower, D. R. 1998, MNRAS, 295, 672
Ciolek, G. E., Roberge, W. G., & Mouschovias, T. Ch. 2004, ApJ, 610, 781
Codella, C., Bachiller, R., & Reipurth, B. 1999, A&A, 343, 585
Crutcher, R. M. 1999, ApJ, 520, 706
Curiel, S., Torrelles, J. M., Rodríguez, L. F., Gómez, J. F., & Anglaga, G. 1999, ApJ, 527, 310
Dayou, F., & Balança, C. 2006, A&A, 459, 297
Dickinson, D. F. 1972, ApJ, 175, L43
Draine, B. T., Roberge, W. G., & Dalgarno, A. 1983, ApJ, 264, 485
Dutrey, A., Guilloteau, S., & Bachiller, R. 1997, A&A, 325, 758
Field, D., May, P. W., Pineau des Forêts, G., & Flower, D. R. 1997, MNRAS, 285, 839
Flower, D. R., & Pineau des Forêts, G. 1994, MNRAS, 268, 724
Flower, D. R., & Pineau des Forêts, G. 1995, MNRAS, 275, 1049
Flower, D. R., & Pineau des Forêts, G. 2003, MNRAS, 343, 390
Flower, D. R., Pineau des Forêts, G., Field, D., & May, P. W. 1996, MNRAS, 280, 447
Flower, D. R., Le Bourlot, J., Pineau des Forêts, G., & Cabrit, S. 2003, Ap&SS, 287, 183
Giannini, T., McCoey, C., Caratti o Garatti, A., et al. 2004, A&A, 419, 999
Giannini, T., McCoey, C., Nisini, B., et al. 2006, A&A, 459, 821
Goldreich, P., & Kwan, J. 1974, ApJ, 189, 441
Graff, M. M. 1989, ApJ, 339, 239
Gueth, F., Guilloteau, S., & Bachiller, R. 1998, A&A, 333, 287
Guillet, V., Pineau des Forêts, G., & Jones, A. 2007, A&A, 476, 263
Guilloteau, S., Bachiller, R., Fuente, A., & Lucas, R. 1992, A&A, 265, L49
Hummer, D. G., & Rybicki, G. B. 1982, ApJ, 254, 767
Jiménez-Serra, I., Martín-Pintado, J., Rodríguez-Franco, A., & Marcelino, N. 2004, ApJ, 603, L49
Jiménez-Serra, I., Martín-Pintado, J., Rodríguez-Franco, A., & Martín, S. 2005, ApJ, 627, L121
Langer, W. D., & Glassgold, A. E. 1990, ApJ, 352, 123
Larsson, B., Liseau, R., Pagani, L., et al. 2007, A&A, 466, 999
Le Bourlot, J., Pineau des Forêts, G., Flower, D. R., & Cabrit, S. 2002, MNRAS, 332, 985
Lefloch, B., Castets, A., Cernicharo, J., & Loinard, L. 1998, ApJ, 504, L109
Le Picard, S. D., Canosa, A., Pineau des Forêts, G., Rebrion-Rowe, C., & Rowe, B. R. 2001, A&A, 372, 1064
Lesaffre, P., Chièze, J.-P., Cabrit, S., & Pineau des Forêts, G. 2004, A&A, 427, 157
Le Teuff, Y. H., Millar, T. J., & Markwick, A. J. 2000, A&AS, 146, 157
Li, A., & Draine, B. T. 2001, ApJ, 554, 778
Martín-Pintado, J., Bachiller, R., & Fuente, A. 1992, A&A, 254, 315
Mathis, J. S., Rumpl, W., & Nordsieck, K. H. 1977, ApJ, 217, 425
May, P. W., Pineau des Forêts, G., Flower, D. R., et al. 2000, MNRAS, 318, 809
McCoey, C., Giannini, T., Flower, D. R., & Caratti o Garatti, A. 2004, MNRAS, 353, 813
Neufeld, D. A., & Kaufman, M. J. 1993, ApJ, 418, 263
Nisini, B., Codella, C., Giannini, T., et al. 2007, A&A, 462, 163
Pagani, L., Olofsson, A. O. H., Bergman, P., et al. 2003, A&A, 402, L77
Schilke, P., Walmsley, C. M., Pineau des Forêts, G., & Flower, D. R. 1997, A&A, 321, 293 (Sch97)
Schoier, F. L., Van der Tak, F. F. S., Van Dishoeck, E. F., & Black, J. H. 2005, A&A, 432, 369
Surdej, J. 1977, A&A, 60, 303
Turner, B. E., Chan, K., Green, S., & Lubowich, D. A. 1992, ApJ, 321, 293
Van der Tak, F. F. S., Black, J. H., Schöier, F. L., Jansen, D. J., & van Dishoeck, E. F. 2007, A&A, 468, 627
Weingartner, J. C., & Draine, B. T. 2001, ApJS, 134, 263
Wilson, R. W., Penzias, A. A., Jefferts, K. B., Kutner, M., & Thaddeus, P. 1971, ApJ, 167, L97
Wrathmall, S. A., Gusdorf, A., & Flower, D. R. 2007, MNRAS, 382, 133
Zachariah, M. R., & Tsang, W. 1995, J. Phys. Chem., 99, 5308
Zhang, Q., Ho, P. T. P., Wright, M. C. H., & Wilner, D. J. 1995, ApJ, 451, L71

Appendix A: SiO radiative transfer

A.1. Photon escape probabilities

The SiO rotational level populations and excitation temperatures in our planar shock models are calculated by means of a large velocity gradient (LVG) method. This approximate treatment assumes that, owing to the macroscopic velocity field and resulting Doppler shifts, emitted line photons are either re-absorbed locally or escape to infinity. The escape probability of a line photon in a given direction $\hat{\boldsymbol{s}}$ is then (see Surdej 1977, for a pedagogical derivation):

$$\beta_s = \frac{1 - \mathrm{e}^{-\tau_s}}{\tau_s} \tag{A.1}$$

where the "LVG optical depth" τ_s is defined as

$$\tau_s = \frac{hc}{4\pi} \frac{n_\mathrm{l}}{\partial(\boldsymbol{v} \cdot \hat{\boldsymbol{s}})/\partial s} B_\mathrm{lu} \left(1 - \frac{g_\mathrm{l} n_\mathrm{u}}{g_\mathrm{u} n_\mathrm{l}}\right), \tag{A.2}$$

with $\partial(\boldsymbol{v} \cdot \hat{\boldsymbol{s}})/\partial s$ the radial velocity gradient along direction $\hat{\boldsymbol{s}}$, n_l and n_u the number density of molecules in the lower and upper levels of the transition, respectively, g_l and g_u the corresponding statistical weights, and B_lu the Einstein coefficient for stimulated absorption. The mean intensity of the radiation field at the local frequency ν of the transition, averaged over all angles, may then be expressed in terms of local quantities only as

$$\bar{J}_\nu = S_\nu(1 - \bar{\beta}) + I_\mathrm{c}\bar{\beta}, \tag{A.3}$$

where $\bar{\beta} = \int \beta_s \mathrm{d}\Omega/4\pi$ is the escape probability averaged over all solid angles; I_c is the mean intensity of the continuum radiation field, taken to be a blackbody (Planck) function $B_\nu(T)$ at the temperature of the cosmic background, $T_\mathrm{bg} = 2.73$ K; and $S_\nu = B_\nu(T_\mathrm{ex})$ is the local source function, where the excitation temperature T_ex of the transition is defined through $n_\mathrm{u}/n_\mathrm{l} \equiv g_\mathrm{u}/g_\mathrm{l} \exp(-h\nu/k_\mathrm{B}T_\mathrm{ex})$. Two expressions have been used for the average escape probability $\bar{\beta}$:

- that of Neufeld & Kaufman (1993):

$$\bar{\beta}_\mathrm{plane} = \frac{1}{1 + 3\tau_\perp}, \tag{A.4}$$

  where $\tau_\perp$ is the LVG opacity in the z-direction, normal to the shock front. This approximation to $\bar{\beta}$ is accurate for a plane-parallel flow, where $\partial(\boldsymbol{v} \cdot \hat{\boldsymbol{s}})/\partial s = \mu^2(\mathrm{d}v_z/\mathrm{d}z)$ and $\tau_s = \tau_\perp/\mu^2$ (with the usual notation $\mu = \cos\theta = \hat{\boldsymbol{s}} \cdot \hat{\boldsymbol{z}}$).
- an isotropic approximation:

$$\bar{\beta}_\mathrm{isotropic} = \beta_\perp = \frac{1 - \mathrm{e}^{-\tau_\perp}}{\tau_\perp} \cdot \tag{A.5}$$

The first expression was ultimately adopted in the present study for consistency with our one-dimensional shock geometry, whereas the second was used by Sch97. Since $\bar{\beta}$ is always smaller in the plane-parallel case (owing to the reduced velocity gradients at small μ), photon trapping is more efficient and the excitation temperatures are increased compared to the isotropic approximation. Thus, adopting the expression of

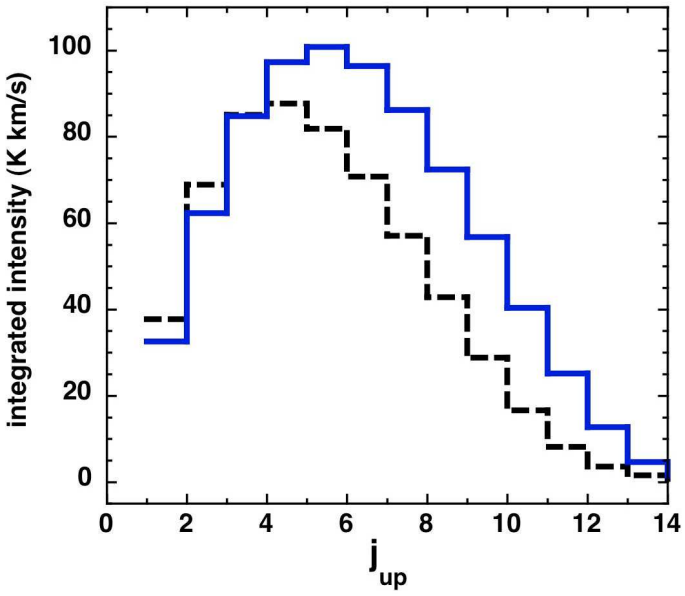

Fig. A.1. The integrated intensities of the rotational transitions of SiO. Full curves correspond to the Neufeld & Kaufman (1993) expression (A.4) for the escape probability in a plane-parallel flow, dashed curves to the isotropic case, Eq. (A.5). The model parameters are $n_{\rm H} = 10^5$ cm^{-3}, $B = 200$ μG, and $v_{\rm s} = 30$ km s^{-1}.

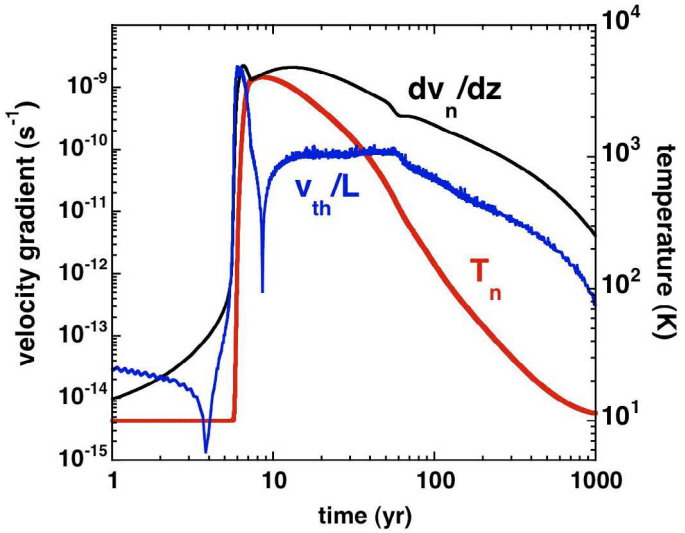

Fig. A.2. Consistency of the LVG method: velocity gradient criterion (A.6). The model parameters are $n_{\rm H} = 10^5$ cm^{-3}, $B = 200$ μG, and $v_{\rm s} = 30$ km s^{-1}.

Neufeld & Kaufman (1993) leads to larger integrated SiO line intensities; this effect is illustrated in Fig. A.1 for our reference shock model. It is marginally significant for small and large values of the rotational quantum number but reaches a factor 3 for $j_{\rm up} \approx 12$.

A necessary condition for the local LVG approximation to be valid is that, over the characteristic distance L where physical conditions vary, the velocity shift Δv arising from the velocity gradient should be larger than the local line thermal width $v_{\rm th}$. Then, line photons are re-absorbed only within a region of size $<L$, where physical conditions and SiO excitation are uniform. This criterion can be rewritten as

$$|{\rm d}v_z/{\rm d}z| > v_{\rm th}/L, \qquad \text{(A.6)}$$

where

$$v_{\rm th} = \sqrt{\frac{8k_{\rm B}T_{\rm n}}{\pi m}},$$

$T_{\rm n}$ is the temperature of the neutral fluid, and m is the mass of the molecule.

In Fig. A.2 we compare the left and right hand sides of (A.6) for our reference shock model, using $L \approx T_{\rm n}/|{\rm d}T_{\rm n}/{\rm d}z|$ as a characteristic distance. The LVG criterion may be seen to be verified throughout the cooling flow of the shock wave, where the bulk of SiO emission arises. It is not verified in the far postshock region, where the computed velocity gradient tends to zero; but this region makes a negligible contribution to the line flux, owing to the low escape probabilities.

A.2. Numerical implementation

In the diatomic SiO molecule, electric dipole transitions take place only between adjacent rotational levels of the ground vibrational state ($\Delta j = \pm 1$ with j the rotational quantum number), while collisionally induced transitions can, in principle, connect any pair of levels (in practice they become less probable with increasing level separation). The evolution of the population density n_i of level i may thus be written in the following matrix form:

$$\begin{aligned}\frac{{\rm d}n_i}{{\rm d}t} &= n_{i+1}(A_{i+1,i} + B_{i+1,i}\bar{J}_{i,i+1}) \\ &\quad -n_i(A_{i,i-1} + B_{i,i+1}\bar{J}_{i,i+1} + B_{i,i-1}\bar{J}_{i-1,i}) \\ &\quad +n_{i-1}B_{i-1,i}\bar{J}_{i-1,i} \\ &\quad +\sum_{\rm coll}\sum_{j\neq i} n_{\rm coll}(n_j C_{ji} - n_i C_{ij}), \qquad \text{(A.7)}\end{aligned}$$

where $n_{\rm coll}$ is the number density of each collisional partner (here H_2 and He), C_{ij} is the collisional rate coefficient from level i to level j, and A and B denote the Einstein coefficients for spontaneous and induced radiative transitions. Two approaches to solving for the level populations may be taken:

- Integrate the set of Eqs. (A.7) in parallel with the dynamical, thermal, and chemical rate equations of the shock wave, as is done currently for the H_2 molecule (Le Bourlot et al. 2002).
- Assume local statistical equilibrium, i.e. set the lhs of Eqs. (A.7) to zero, and solve a posteriori the resulting algebraic equations by matrix inversion, using the physical structure provided by the MHD shock code. Since the radiative terms $\bar{J}$ depend indirectly on the level populations through the escape probabilities and excitation temperatures (Eq. (A.3)), the procedure must be iterated, updating $\bar{J}$ with values of $\bar{\beta}$ and $T_{\rm ex}$ obtained from the previous iteration.

The former approach is preferable, particularly when the molecule under consideration is an important shock coolant (e.g. H_2) – which is not the case of SiO. Furthermore, the flow time in the SiO emission zone is sufficiently long that the assumption of local statistical equilibrium is justified. Accordingly, we adopted the latter approach in the present work. It is common to most applications of the LVG method to astrophysical problems (e.g. Sch97, Neufeld & Kaufman 1993) and has the advantage of being less demanding in CPU time. For more significant coolants, such as CO, ^{13}CO, and H_2O, the rate of cooling was computed in parallel with the shock dynamics, using the cooling

functions calculated by Neufeld & Kaufman (1993), by means of the LVG method.

Note that Eqs. (A.7) may be put in a different (matrix) form by expressing explicitly $\bar{J}$ as a function of $B_\nu(T_{\rm ex})$ and $I_{\rm c}$. Using the standard relationships between Einstein coefficients, and the definition of $T_{\rm ex}$ in terms of n_j and n_{j+1}, all terms involving $T_{\rm ex}$ cancel from the equations, leaving radiative terms which are proportional to the $\bar{\beta}$'s (see Goldreich & Kwan 1974):

$$\begin{aligned}\frac{{\rm d}n_i}{{\rm d}t} = &+ n_{i+1}\bar{\beta}_{i,i+1}\left(A_{i+1,i} + B_{i+1,i}I_{\rm c}\right)\\ &- n_i\left(\bar{\beta}_{i-1,i}A_{i,i-1} + \bar{\beta}_{i,i+1}B_{i,i+1}I_{\rm c} + \bar{\beta}_{i-1,i}B_{i,i-1}I_{\rm c}\right)\\ &+ n_{i-1}\bar{\beta}_{i-1,i}B_{i-1,i}I_{\rm c}\\ &+ \sum_{\rm coll}\sum_{j\neq i} n_{\rm coll}(n_j C_{ji} - n_i C_{ij}). \end{aligned} \quad (A.8)$$

Although the two formulations are equivalent and converge to the same solution, we have found that inversion of the latter matrix encounters numerical instabilities and convergence problems at high optical depths, possibly due to round-off errors in the (vanishingly small) $\bar{\beta}$ terms. In the first formulation, the radiative elements of the matrix are never zero, even at high opacity, and we obtain much better convergence and accuracy. Hence we have adopted (A.7) in the present calculations. The "lambda-iteration" is terminated when we reach convergence of the level populations to 1 part in 10^4.

Our code was tested thoroughly against the routine used by Sch97, in the case $\bar{\beta} = \beta_\perp$, and against the web-based online version of RADEX (`www.sron.rug.nl/vdtak/radex/radex.php`), which uses yet another expression for the escape probability, valid for a turbulent homogeneous sphere (Van der Tak et al. 2007). Discrepancies never exceeded a few percent.

The MHD shock code provides the physical and chemical profiles (of the temperatures, densities, velocities, and abundances) which are required in order to apply the LVG technique. For SiO, we used the rate coefficients for collisional de-excitation published by Turner et al. (1992), for which the collision partner is ground state para-H_2. These data are available for rotational quantum numbers $0 \leq J \leq 20$ and for kinetic temperatures T = 20, 40, 70, 100, 150, 200, 250, 300 K and are interpolated to intermediate values of T. We made use also of the extrapolated data of Schöier et al. (2005), which extend to J = 40 and T = 2000 K. Subsequent calculations, using the rate coefficients of Dayou & Balança (2006) for collisions of SiO with para-H_2, have shown that the rotational line intensities are insensitive to these collision rates because the lines are formed under conditions which approach LTE. For collisions of SiO with He, we used the rate coefficients of Dayou & Balança (2006), for $J \leq 26$ and kinetic temperatures in the range $10 \leq T \leq 300$ K. At temperatures higher than the maximum for which the rate coefficients were calculated, we assumed that they remain constant. Upwards (excitation) rate coefficients were obtained from detailed balance.

The Einstein A-values, and the rotational constant B_0 = 21711.967 MHz (corresponding to $hB_0/k_{\rm B}$ = 1.042 K) for the ground vibrational state of $^{28}Si^{16}O$ were taken from the NIST database (`www.nist.gov/data/`).

A.3. Emergent line intensities and radiation temperatures

Each layer of the shock wave, of thickness $|\Delta z|$, elementary surface ΔS, and velocity v_z, emits the following luminosity (in erg s^{-1}) over all directions in a given transition $j+1 \rightarrow j$ of frequency $\nu = 2B_0(j+1)$:

$$F_\nu(v_z) = \bar{\beta}\, h\nu\, n_{j+1}A_{j+1,j}\ |\,\Delta z\,|\ \Delta S. \quad (A.9)$$

In order to compute line profiles, however, we need to evaluate the *specific intensity* per unit solid angle, frequency interval, and projected emitting area (in erg cm^{-2} s^{-1} Hz^{-1} sr^{-1}). Following Sch97, we assume that the shock is viewed face-on, i.e. in the z-direction, normal to the shock front. The intensity is

$$I_\perp(v_z) = \frac{\beta_\perp}{4\pi}\, h\nu\, n_{j+1}A_{j+1,j}\frac{|\,\Delta z\,|}{|\Delta v_z|}, \quad (A.10)$$

where $|\Delta v_z|$ is the Doppler width of the layer, viewed along the z-axis:

$$|\Delta v_z| = \frac{\nu}{c}|\Delta v_z| = \frac{\nu}{c}|\Delta z| \times |{\rm d}v_z/{\rm d}z|. \quad (A.11)$$

Consequently the intensity becomes

$$I_\perp(v_z) = \frac{hc}{4\pi}\frac{\beta_\perp}{|\,{\rm d}v_z/{\rm d}z\,|}n_{j+1}A_{j+1,j}. \quad (A.12)$$

Noting that $\beta_\perp = (1 - {\rm e}^{-\tau_\perp})/\tau_\perp$ and using the definition of τ in Eq. (A.2) as well as the relationships between A and B-Einstein coefficients, one obtains the alternative, simpler expression

$$I_\perp(v_z) = B_\nu(T_{\rm ex})\,(1 - {\rm e}^{-\tau_\perp}) \quad (A.13)$$

which corresponds to the well-known radiative transfer result for a uniform slab of excitation temperature $T_{\rm ex}$ and opacity $\tau_\perp$.

In order to compare with actual observed SiO spectra, one needs to add the cosmic background, and take into account the `ON-OFF` subtraction applied to radio spectra (to remove atmospheric noise). The cosmic background at the `ON` position and velocity v_z is $B_\nu(T_{\rm bg})\exp(-\tau_\perp)$, due to attenuation by the layer, while at the `OFF` position it is simply $B_\nu(T_{\rm bg})$. The observed intensity is thus

$$\begin{aligned} I_\perp^{\rm obs}(v_z) = \texttt{ON} - \texttt{OFF} &= \left[B_\nu(T_{\rm ex}) - B_\nu(T_{\rm bg})\right](1 - {\rm e}^{-\tau_\perp})\\ &= I_\perp(v_z) \times \left[1 - B_\nu(T_{\rm bg})/B_\nu(T_{\rm ex})\right]. \end{aligned} \quad (A.14)$$

Finally, we convert the observed specific intensity of the layer to a *line radiation temperature* $T_{\rm R}$ (in kelvin) using the definition

$$T_{\rm R} \equiv \frac{I^{\rm obs}c^2}{2k_B\nu^2} \quad (A.15)$$

which is standard in radioastronomy. Once radiation temperatures are calculated for each shock layer, and thus each v_z, the line profile is integrated over v_z to yield integrated line intensities, $T{\rm d}V$, in K km s^{-1}. Note that the specific intensities, radiation temperatures and $T{\rm d}V$ are valid for a shock that entirely fills the observing beam. Otherwise, the observed brightness temperature has to be reduced by an appropriate "surface filling factor", $f \approx \Delta S/(\text{beam area})$.

A.4. Line profile at arbitrary inclinations

In the general case of an arbitrary viewing angle, $\mu = \cos\theta$, the term $\tau_\perp$ in Eq. (A.13) is replaced by the LVG opacity in the chosen direction, $\tau(\mu) = \tau_\perp/\mu^2$. Therefore

$$T_{\rm R}(\mu) = T_{\rm R\perp}\frac{\left(1 - {\rm e}^{-\tau_\perp/\mu^2}\right)}{(1 - {\rm e}^{-\tau_\perp})}\,. \quad (A.16)$$

Table B.1. The numerical values of the coefficients, $a_i(X)$, of the polynomial fits to the fractions of $X \equiv$ Fe, Si and Mg sputtered from olivine grains. Numbers in parentheses are powers of 10.

X	a_0	a_1	a_2	a_3	a_4	a_5
Mg	–0.5322	0.09172	–0.006035	0.0001879	–2.746(-06)	1.522(–08)
Si	–0.4147	0.07364	–0.004953	0.0001560	–2.279(-06)	1.250(–08)
Fe	–0.8579	0.14681	–0.009607	0.0002979	–4.349(-06)	2.413(–08)

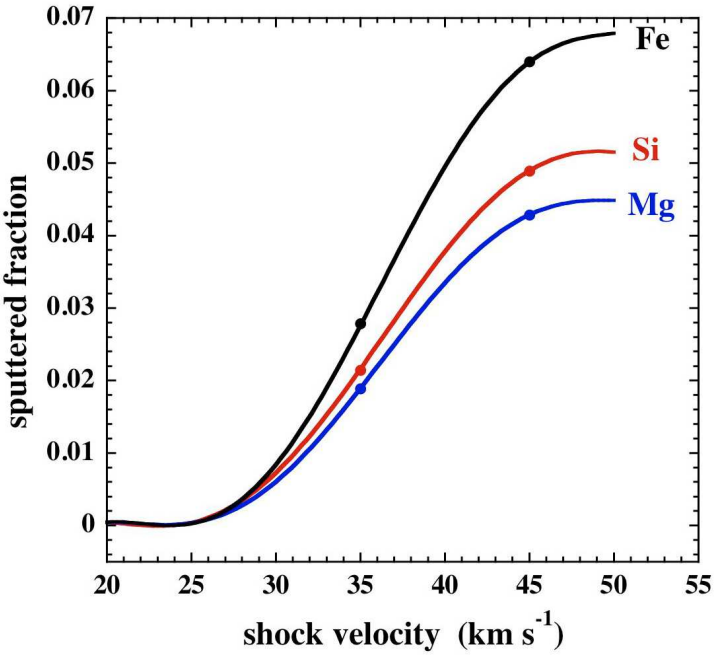

Fig. B.1. Fits of the fractions of Fe, Si and Mg sputtered from olivine grains, as functions of the shock speed. The points on the curves indicate the limiting speeds of steady-state C-type shock waves, for preshock gas densities $n_H = 10^5$ and 10^6 cm^{-3}, with the lower speed corresponding to the higher density. The parameters of the fits to the curves are given in Table B.1.

Thus, T_R will be multiplied by $1/\mu^2$ in the optically thin regime and will be unchanged in the optically thick regime. At the same time, the velocity of the layer, v_z, is replaced by its projection along the photon path, μv_z, so the line profile becomes narrower. A view which is not face-on will leads to a larger $T\mathrm{d}V$ for optically thin lines, and to a smaller $T\mathrm{d}V$ for optically thick lines (assuming that the source still fills the beam entirely). A quantitative evaluation of this effect, for our reference shock model, is presented in Sect. 4.4.

Appendix B: Fractions of Fe, Si and Mg sputtered from olivine

In Sect. 3.2, we presented and discussed the sputtering of Fe, Si and Mg from grains composed of olivine ($MgFeSiO_4$). In Fig. B.1, we show the numerical fits to these results, as functions of the shock speed; they are practically independent of the preshock gas density. Also shown in this figure are the limiting speeds of steady-state C-type shock waves for preshock densities $n_H = 10^5$ and 10^6 cm^{-3}; the limiting speed is lower for the higher density. The limit is associated with the thermal runaway which occurs, owing to the collisional dissociation of H_2 within the shock wave. The numerical values of the coefficients of the polynomial fits, of the form

$$y(\mathrm{X}) = \sum_{i=0}^{5} a_i(\mathrm{X}) v_s^i,$$

are given in Table B.1; the shock speed, v_s, is in km s^{-1}. We have assumed that the magnetic field parameter $b = 1$.

Appendix C: Initial gas-phase abundance of O_2

We present, in Figs. C.1–C.4, the results corresponding to those in Figs. 4, 7, 8 and 12, respectively, of the main text, but derived from our secondary grid of models, in which $n(O_2)/n_H = 1.0 \times 10^{-7}$ initially in the gas phase but the excess oxygen is in form of H_2O ice, rather than O_2 ice as in our primary grid. We recall that the initial fractional abundance of O_2 in chemical equilibrium is $n(O_2)/n_H \approx 10^{-5}$.

In these models, O_2 is never abundant in the gas phase, and Si oxidation occurs only in reaction 2, with OH. Thus, SiO formation is less efficient at intermediate shock speeds and not significant at $v_s = 25$ km s^{-1}.

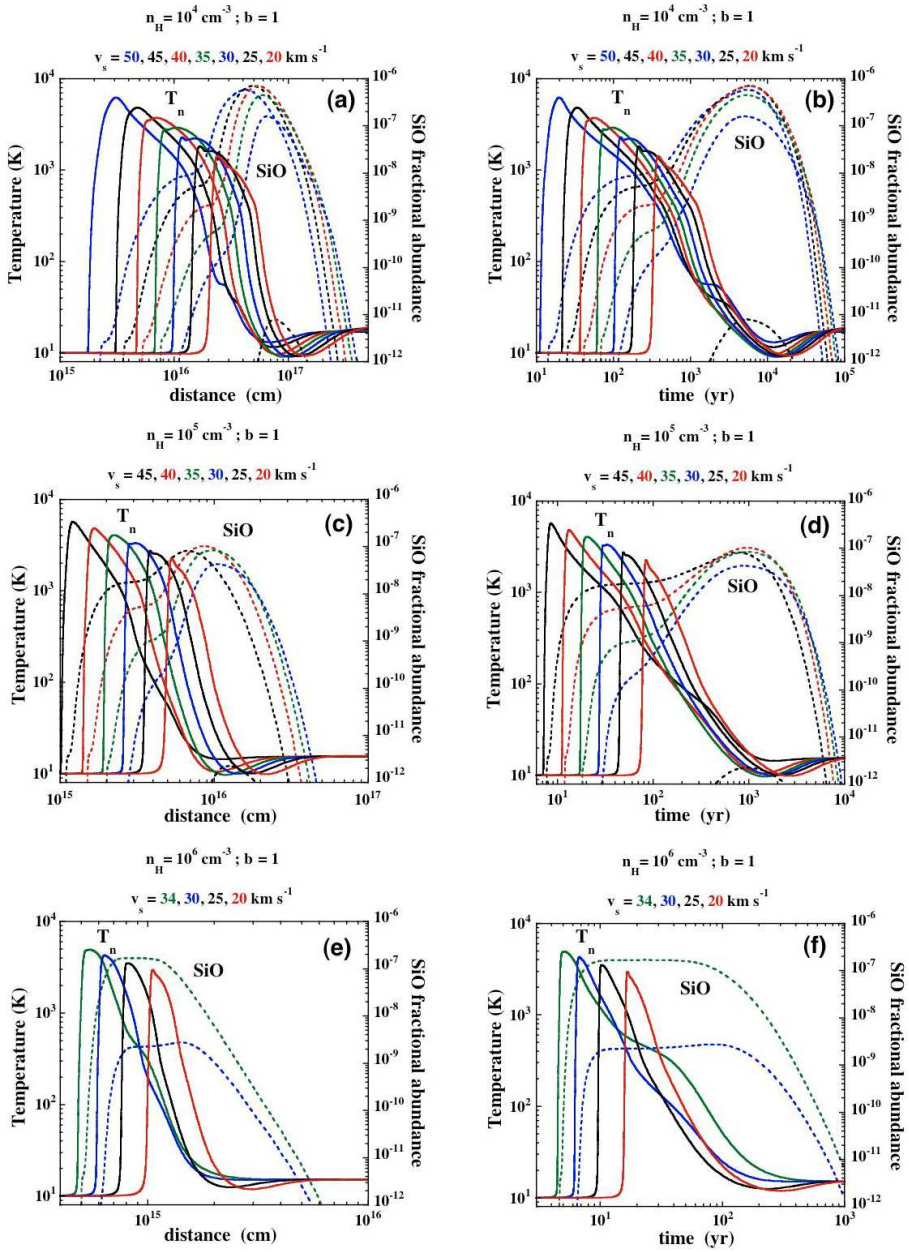

Fig. C.1. As Fig. 4, but assuming that the initial abundance of O_2 ice is negligible (the second of the two scenarios described in Sect. 3.1).

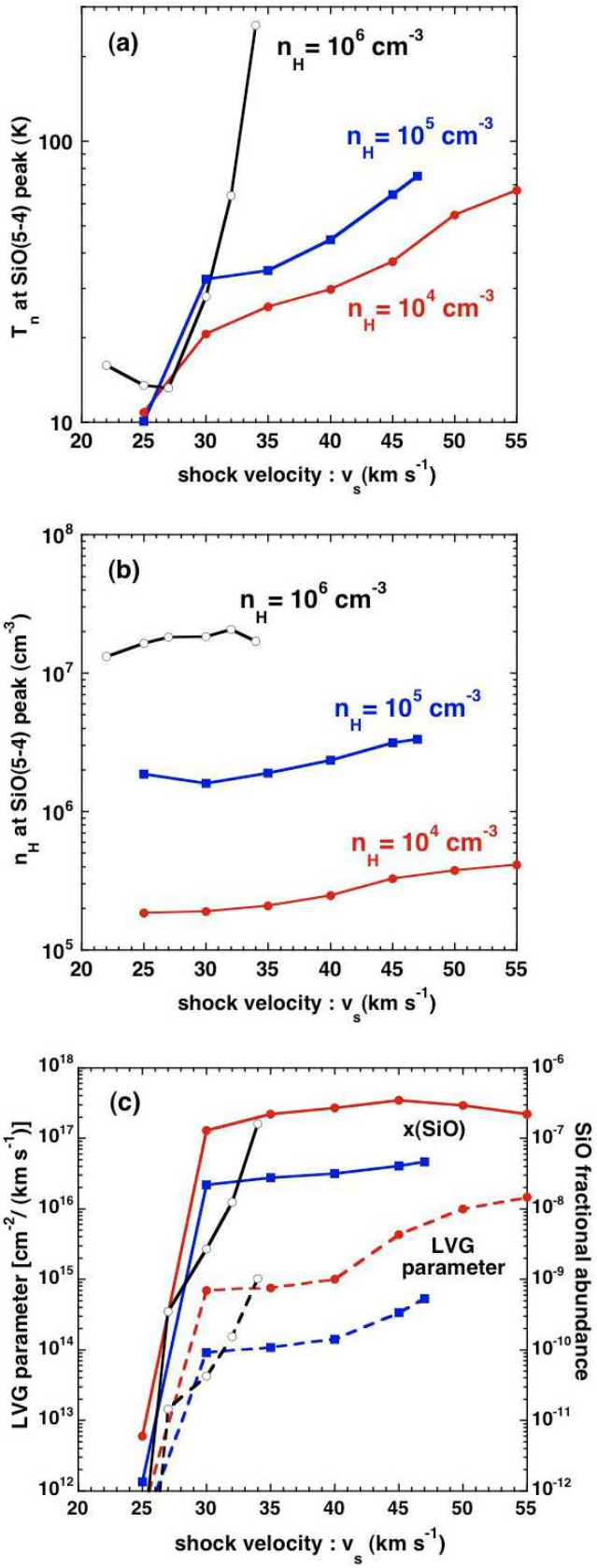

Fig. C.2. As Fig. 7, but assuming that the initial abundance of O_2 ice is negligible (the second of the two scenarios described in Sect. 3.1).

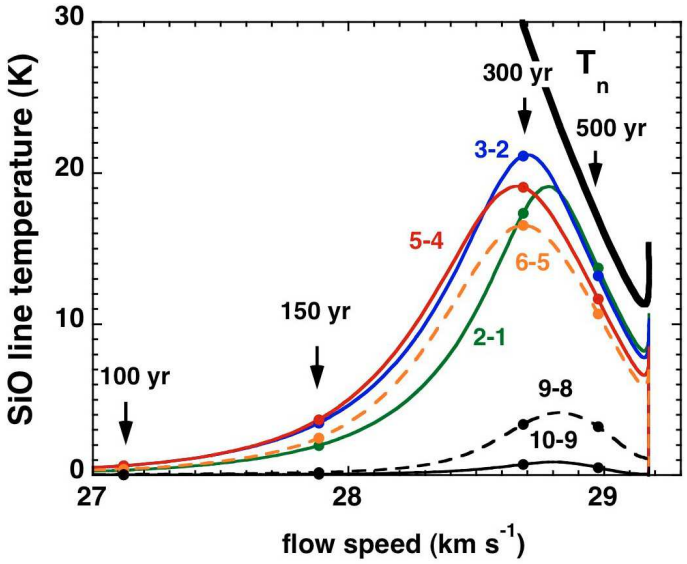

Fig. C.3. As Fig. 8, but assuming that the initial abundance of O_2 ice is negligible (the second of the two scenarios described in Sect. 3.1).

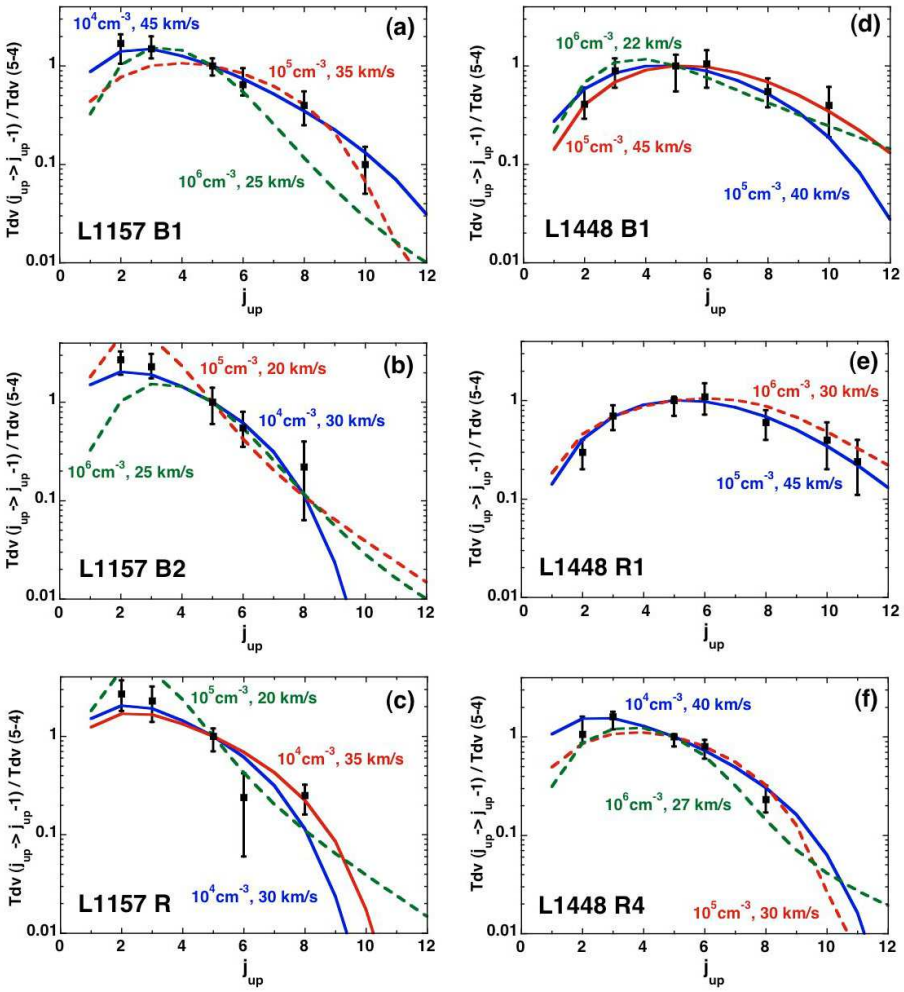

Fig. C.4. As Fig. 12, but assuming that the initial abundance of O_2 ice is negligible (the second of the two scenarios described in Sect. 3.1).

A&A 490, 695–706 (2008)
DOI: 10.1051/0004-6361:200810443

Astronomy & Astrophysics

SiO line emission from interstellar jets and outflows: silicon-containing mantles and non-stationary shock waves⋆

A. Gusdorf[1,2], G. Pineau des Forêts[2,3,4], S. Cabrit[3], and D. R. Flower[1]

[1] Physics Department, The University, Durham DH1 3LE, UK
e-mail: antoine.gusdorf@durham.ac.uk
[2] Institut d'Astrophysique Spatiale (IAS), Bâtiment 121, 91405 Orsay, France
[3] LERMA (UMR 8112 du CNRS), Observatoire de Paris, 61 Avenue de l'Observatoire, 75014 Paris, France
[4] Université Paris-Sud 11 and CNRS (UMR 8617), France

Received 23 June 2008 / Accepted 29 August 2008

ABSTRACT

Context. We study the production and emission of SiO and H_2 in the gas phase of molecular outflows, extending previous work in which we considered steady-state C-type shock waves and assumed the silicon to be present only in the cores of silicate grains.
Aims. We place constraints on the physical parameters of the pre-shock region, using recent observations of SiO and observations of molecular hydrogen. We show the effects of introducing SiO-containing mantles and of varying the age of the shock wave. We consider simultaneously the emission of SiO and H_2 from the young L1157 outflow.
Methods. The molecular outflows are studied by means of a code that can generate stationary C- and J-type shock models and approximate non-stationary solutions, which combine these two types of shock wave. The emission of molecular hydrogen is computed by this code, whereas the SiO emission is computed by means of a separate LVG model, which uses the calculated physical and chemical profiles. A grid of models has been computed, with shock speeds in the range $10 \leq v_s \leq 35$ km s^{-1} and pre-shock gas densities $10^4 \leq n_H \leq 10^6$ cm^{-3}. A wide range of magnetic field strengths has been investigated, from 45 μG to about 600 μG.
Results. We illustrate our results by means of observational data obtained on the blue lobe of the L1157 outflow. Given the combinations of pre-shock densities and shock velocities necessary to fit the H_2 observations, we find that the erosion only of the silicate material in the grains cores cannot account for the observed SiO line intensities. We investigate the possiblity that a fraction of the SiO is present initially in the grain mantles, and we succeed in constraining this fraction. Introducing even a few percent of the silicon (as SiO) into the mantles is sufficient to increase the SiO line widths and fluxes by an order of magnitude. With this assumption, it is possible to find a non-stationary shock model that provides a reasonable fit of the observations of both H_2 and SiO.
Conclusions. With a few percent of the silicon present initially in the grain mantles, good agreement is obtained with recent observations of SiO line integrated line intensities for a pre-shock density $n_H = 10^4$ cm^{-3} and a shock speed $v_s = 20$ km s^{-1}. The magnetic field strength and the shock age are not well constrained by the observations of either H_2 or SiO. We show that CO observations (in particular, with the Herschel satellite) could provide further discrimination between the models.

Key words. astrochemistry – magnetohydrodynamics (MHD) – molecular processes – ISM: jets and outflows – infrared: ISM – radio lines: ISM

1. Introduction

In a previous article (Gusdorf et al. 2008, henceforth G08), we investigated the SiO emission from steady-state C-type shock waves, in an attempt at accounting for recent observations of SiO emission lines in the L1157 and L1448 molecular outflows. Simulations of stationary shocks were performed by means of a one-dimensional dynamical and chemical code, whose outputs were used in an LVG model, in order to calculate the SiO emission. In this stationary C-type shock model, grain erosion is a consequence of ambipolar diffusion: the grains are predominantly negatively charged in the shock wave and are impacted by the neutrals at the ion-neutral drift velocity. When the shock speed is sufficiently high, this process releases Si into the gas phase, where oxidation reactions lead to the formation and thence the emission of SiO. G08 made the assumption that elemental silicon was solely in the form of silicates (in practice, olivine) in the grain cores. The code and its recent updates, as well as our implementation of the LVG technique, are described in G08. We use rate coefficients for rotational transitions in SiO, induced by He and by para-H_2, from the recent work of Dayou & Balança (2006).

The gas-phase reactions leading to the formation of SiO were discussed by G08. Neutral Si reacts either with OH or O_2 to form SiO, and so the fractional abundance of O_2 in the pre-shock gas is an important parameter. In our previous study, we considered two scenarios, relating to the initial distribution of oxygen:

- molecular oxygen formed in the gas phase was adsorbed subsequently on to the grains, where it remained as O_2 ice in the pre-shock medium, with a fractional abundance which was taken to be of 1.3×10^{-5}, relative to elemental hydrogen. (We note that the initial abundance of water ice is an order of magnitude larger than that of O_2 ice.)
- atomic oxygen was adsorbed on to the grains before O_2 was synthesized in the gas phase and was hydrogenated to water ice in the mantles of the grains in the cold pre-shock medium. As a consequence, the fractional abundance of H_2O ice increases by 25%, to 1.3×10^{-4}.

⋆ Appendices are only available in electronic form via http://www.aanda.org

In both cases, the initial gas-phase fractional abundance of molecular oxygen is $n(O_2)/n(H_2) = 10^{-7}$, consistent with satellite observations by Pagani et al. (2003) and Larsson et al. (2007). In our previous study (of C-type shocks), we found that the results were not sensitive to the scenario which was adopted, particularly at high shock speeds, as Si can be oxidized in the gas phase by both O_2 and OH. Accordingly, we make the first assumption in the present work.

G08 computed a grid of C-type shock models and compared the calculated SiO line intensities and profiles with observations. With respect to the line intensities, the agreement with the observations was satisfactory, for rotational transitions up to SiO(11–10). However, the line profiles predicted under these assumptions were narrower than observed, with predicted widths of 0.5–2 km s^{-1}, as compared with the observed widths of 5–20 km s^{-1}, in 3″–10″ beams. Partly with this discrepancy in mind, we consider now the possibility that SiO may be present in the grain mantles[1], where the corresponding binding energy is much lower than that of the Si in the silicate grain cores. We transfer a small percentage (1%, 5%, or 10%) of the Si, and the corresponding amounts of oxygen, from the cores to the mantles. If this process is mediated by the passage of shock waves, our calculations indicate that the dominant form of silicon in the mantle is likely to be SiO; see, for example, Fig. 1 of G08. The SiO is then released directly into the gas phase, through sputtering by the most abundant neutrals, H, H_2 and He in a subsequent shock wave. Such sputtering processes were incorporated already for known mantle constituents, such as water and carbon monoxide. The sputtering rate of SiO was calculated using the same parameters as for CO. Adopting the parameters appropriate to a more polar species, such as H_2O, has no significant influence on the results, as the mantle species are, in either case, sputtered rapidly (in the magnetic precursor).

In steady-state C-type shock waves, the SiO emission peaks in the post-shock gas, owing to the chemical delay introduced by the oxidation of Si to SiO and also to the larger line optical depths at low velocity gradients. In view of the small dynamical ages (<5000 yr) of several outflows and jets, we consider how the SiO emission is affected when the C-type shock wave has not yet reached steady-state, and its precursor is truncated by an embedded *J*-discontinuity.

It has been shown previously (Flower et al. 2003; Giannini et al. 2004, 2006) that non-stationary shock waves are favoured by observations of rovibrational emission lines of H_2 in outflows. Stationary C-type models are unable to fit simultaneously the column densities of both the vibrationally excited levels and the rotational levels of the vibrational ground state. It is conceivable that a combination of C-type shock models with appropriate parameters, including filling factors, could be found which fits the observations of H_2; but it is not possible for single or even multiple C-type shock models to reproduce also the observations of SiO, if it is assumed that the only source of Si in the gas phase is the erosion of the grain cores.

In the following Sect. 2, we summarize the results obtained for stationary C-type shock waves. Section 3 contains an initial discussion of non-stationary (CJ-type) models and is followed, in Sect. 4, by more detailed considerations of using such models to interpret the H_2 and SiO emission line observations of the L1157 B1 outflow. Our concluding remarks are made in Sect. 5.

[1] The possibility that silicon may be present in grain mantles has been considered previously by Walmsley et al. (1999) and Schilke et al. (2001), in the context of photon-dominated regions.

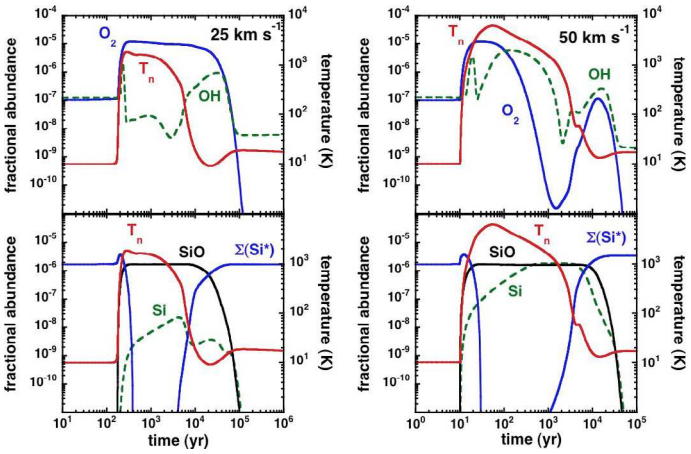

Fig. 1. The temperature of the neutral fluid, T_n, and the fractional abundances of OH and O_2 (*top panels*) and of Si, SiO, and silicon in the grain mantles, Σ Si* (*bottom panels*), as functions of the flow time of the charged fluid, for two reference C-type shock models: $n_H = 10^4$ cm^{-3}, $b = 1$, $v_s = 25$ km s^{-1} (*left-hand panels*) and 50 km s^{-1} (*right-hand panels*). In both models, it is assumed that 5% of the elemental silicon is initially in the mantles, in the form of SiO.

2. Stationary C-type shock waves with SiO present in the grain mantles

G08 assumed that Si was present in grains in the form of silicates, contained in the cores, with an initial fractional abundance of 3.37×10^{-5}, relative to elemental H. We consider now two particular C-type shock models, for which the pre-shock density $n_H = 10^4$ cm^{-3}, the shock velocity $v_s = 25$ and 50 km s^{-1}, respectively, and $b = 1$; in our models, b is a parameter that scales the transverse magnetic field, B, such that $B = b\sqrt{n_H}$, where B is in μG and n_H in cm^{-3}. At 25 km s^{-1}, the velocity of the C-type shock model is inadequate for significant erosion of the grain cores to take place, and this model failed to produce enough SiO to account for the observations. On the other hand, the higher velocity (50 km s^{-1}) shock yielded good agreement with the SiO observations of L1157 B1, in terms of the integrated line intensities. In both cases, Si is released into the gas phase through erosion of the grain cores. Because of the time required to oxidize Si in the gas phase, the SiO emission peaks in the post-shock region. When $v_s = 50$ km s^{-1}, the fractional abundance of SiO attains 7×10^{-7}, before decreasing, owing to adsorption on to the grains.

We introduce now an alternative scenario, in which the silicon is initially in the mantles, in the form of SiO. If the silicon in the mantles was assumed to be in atomic form instead, we found that the SiO line intensities were underestimated (because of the chemical delay in oxidizing the atomic silicon to SiO in the gas phase) in the lower speed shock wave models which fit satisfactorily the observations of H_2; see Sect. 4 below. Owing to the rapidity with which the mantles are eroded during the passage of a shock wave, another possibility – that the atomic silicon is already present in the gas phase, following its release from the grains by an earlier shock – gave very similar results. Accordingly, we consider now an example in which 5% of the silicon is assumed to be initially in the form of SiO in the mantles.

Figure 1 shows the neutral temperature profiles and the fractional abundances of Si-containing species, for the models with $v_s = 25$ and 50 km s^{-1}. In both cases, essentially all of the SiO which is initially in the mantles is released into the gas phase by

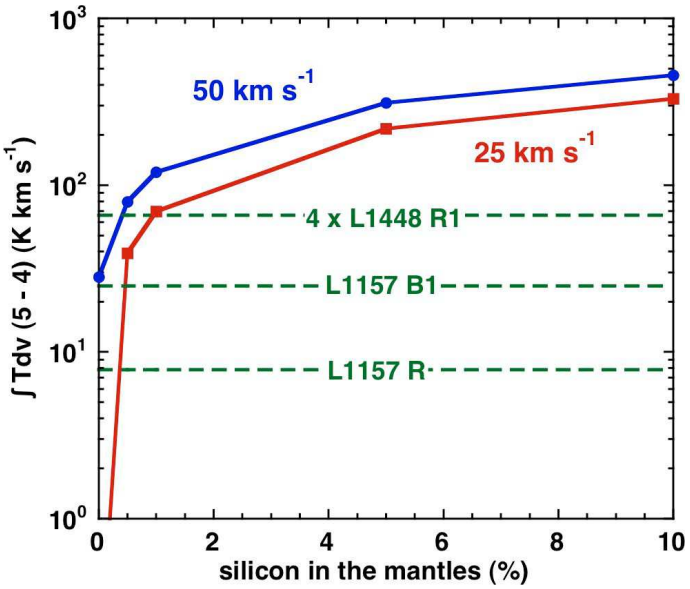

Fig. 2. The integrated intensity of the SiO(5–4) line, $\int T\mathrm{d}v(5-4)$, as a function of the percentage of SiO initially in the grain mantles, for both of the C-type shock models: $n_{\mathrm{H}} = 10^4$ cm^{-3}, $b = 1$, $v_{\mathrm{s}} = 25$ km s^{-1} (*lower curve*) and 50 km s^{-1} (*upper curve*). At the lower shock speed, the erosion of Si from the grain cores is negligible compared with the release of SiO from the mantles. The SiO(5–4) intensities observed in L1157 and L1448 are indicated by the horizontal lines.

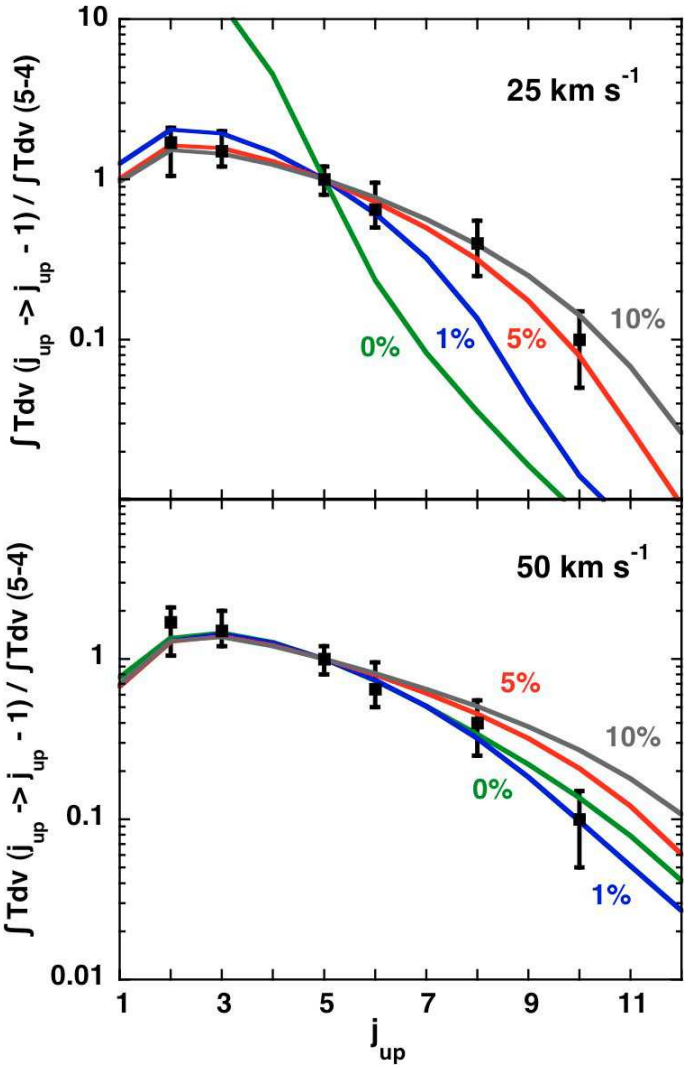

Fig. 3. The integrated intensities of rotational transitions of SiO, relative to the (5–4) line, in stationary C-type shock waves: $n_{\mathrm{H}} = 10^4$ cm^{-3}, $b = 1$, $v_{\mathrm{s}} = 25$ km s^{-1} (*upper panel*) and 50 km s^{-1} (*lower panel*). The observational data relate to L1157 B1. The initial fraction of silicon in the form of SiO in the grain mantles varies from 0% to 10%, as indicated. In the lower limit, the SiO which is seen in this figure arises from the erosion of silicates in the grain cores.

sputtering, subsequently freezing back on to grains in the cold, post-shock gas. The more SiO is initially present in the grain mantles, the higher is the maximum fractional abundance of SiO in the gas phase. At the lower shock speed, the SiO produced following erosion of Si from the grain cores is negligible, compared with SiO sputtered directly from the mantles. Even at the higher shock speed of $v_{\mathrm{s}} = 50$ km s^{-1}, only about 5% of the silicon is released from the grain cores: see G08, Fig. 2, and the curve marked Si in the lower right hand panel of Fig. 1 of the present paper.

When comparing the models with the observations of SiO, we consider first the integrated intensity of the SiO(5–4) line, $\int T\mathrm{d}v(5-4)$ K km s^{-1}, and then the integrated intensities of rotational transitions up to (11–10), expressed relative to SiO(5–4).

- The variation of the integrated intensity of the SiO(5–4) line with the percentage of SiO initially in the mantles is shown in Fig. 2. Observational data relating to L1448 and L1157, compiled by Nisini et al. (2007), are displayed also. Our calculations show that the observed line intensities can be reproduced when only of the order of 1% of the elemental silicon is initially in the grain mantles, as SiO. Core erosion alone is sufficient only at the higher shock speed, 50 km s^{-1}; Fig. 2 confirms the efficacy of mantle sputtering at lower speeds.
- Figure 3 presents the integrated intensities of other rotational transitions, relative to the (5–4) line; observational data relating to L1157 B1 are shown also. At the lower shock speed, only the SiO sputtered from the mantles contributes significantly to the line emission. Furthermore, as the SiO is released into regions of high temperature, the emission in the high rotational transitions becomes stronger as the amount of SiO in the mantles increases. At the lower shock speed, 5% seems adequate to fit the relative line intensities; but this model predicts a value of the (5–4) line intensity which is 3–10 times higher than observed in L1448–L1157 (cf. Fig. 2). A low effective surface filling factor of 0.3–0.1 would then be required to reconcile this model with the observations, and this is incompatible with the typical sizes of the SiO knots observed by Nisini et al. (2007), which are comparable with the thickness of the SiO emitting layer in the model. On the other hand, at the higher speed, models with less than 1% of silicon in the mantles fit satisfactorily both the relative and the absolute line intensities.

The motivation for considering SiO being present in grain mantles was its possible consequences for the widths of the emission lines. Figure 4 displays the line profiles obtained when 5% of elemental silicon is initially in the mantles. As SiO is now present in the gas phase over the full width of the shock wave, the lines are much broader than predicted when assuming that Si is released by erosion of the grain cores only; cf. G08, Fig. 8. However, the computed profiles vary considerably from line to line, whereas they are observed to be similar (see, for example, Fig. 9 of Nisini et al. 2007). Furthermore, as noted by Nisini et al. (2007), the line profiles in L1157 B1, considered

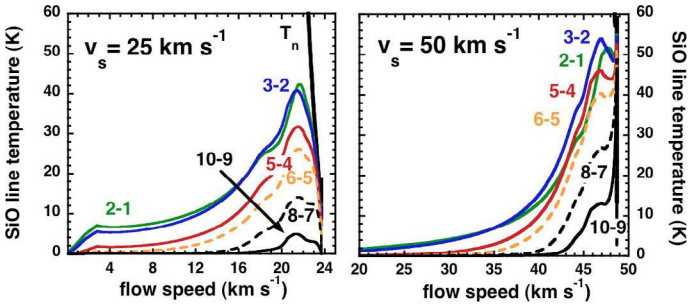

Fig. 4. Profiles of the SiO rotational transitions (2–1), (3–2), (5–4), (6–5), (8–7), and (10–9) computed in stationary C-type shock waves, for $n_H = 10^4$ cm^{-3}, $b = 1$, $v_s = 25$ km s^{-1} (*left panel*) and 50 km s^{-1} (*right panel*). 5% of the elemental silicon is assumed to be initially in the grain mantles, in the form of SiO. The flow speed is in the reference frame of the preshock gas. T_n is the temperature of the neutral fluid.

below, are reversed relative to those in the outflow L1448: in the former object, the maximum SiO line intensities occur close to the LSR velocity, with weaker emission from the higher velocity (more blue-shifted) gas. If the shock in L1157 B1 is moving towards the observer, the profiles plotted in Fig. 4 would correspond to maximum intensities at high blue shifts, as in L1448 but not as in L1157 B1. A possible explanation is that the SiO emission in L1157 B1 arises in a reverse shock. We shall return to the issue of line profiles in Sect. 3.3 below.

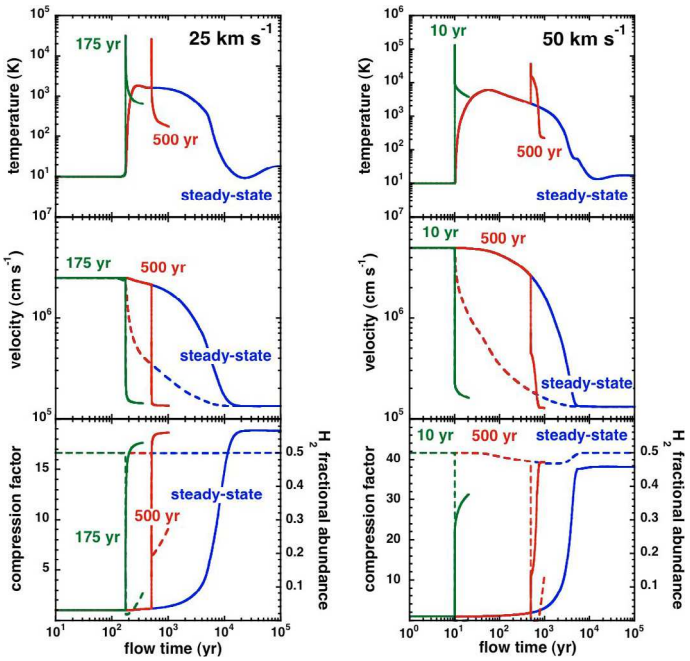

Fig. 5. Profiles of the CJ-type shocks specified in Sect. 3.1. The corresponding steady-state C-type shock models are shown also. *Left-hand panels*: $v_s = 25$ km s^{-1}; *right-hand panels*: $v_s = 50$ km s^{-1}. In *the middle panels*, the full curves correspond to the neutrals and the broken curves to the ions. In *the bottom panels*, the full curves correspond to the compression factor, and the broken curves to the fractional abundance of H_2.

3. Non-stationary shock waves

In the case of the SiO emission, stationary C-type shock waves have been shown to be able to account for the observed rotational line intensities (G08). However, the dynamical age of the blue lobe of the L1157 outflow, inferred from observations (see Gueth et al. 1998), is 2000–3000 yr, which is less than the time (of the order of 10^4 yr) required for a typical C-type shock wave to attain a steady state. Furthermore, previous studies (see, for example, Flower et al. 2003; Giannini et al. 2004, 2006) have demonstrated the necessity of considering non-stationary shock waves in order to account successfully for both the pure rotational and the rovibrational emission of molecular hydrogen observed in molecular outflows. The difficulty which has to be faced is that a single C-type shock fails to reproduce simultaneously the column densities of both the high (v, j) levels of H_2 and the column densities of the low ($v = 0$, j) levels. Accordingly, we proceed to consider non-stationary shock waves, which have developed a magnetic precursor but which retain a J-type discontinuity; see Chièze et al. (1998), Lesaffre et al. (2004b). We simulate such shock waves by introducing a discontinuity into the flow (by switching on artificial viscosity terms; see Flower & Pineau des Forêts 1999) at a given value of the fluid flow time, which becomes a parameter of the model. In practice, we introduce the discontinuity at one half of the flow time of the *charged* fluid (cf. Lesaffre et al. 2004b) to the point at which the flow is terminated; see Appendix C. We refer to such models as "CJ-type", as they possess both C- and J-type characteristics.

3.1. Molecular hydrogen cooling

By way of illustration, we consider the following models:

– $n_H = 10^4$ cm^{-3}, $b = 1$, $v_s = 25$ km s^{-1}; ages of 175 and 500 yr (and the limit of steady-state);

– $n_H = 10^4$ cm^{-3}, $b = 1$, $v_s = 50$ km s^{-1}; ages of 10 and 500 yr (and the limit of steady-state).

As the fractional abundance of SiO remains low, it plays only a minor role in the cooling of the medium. It follows that the choice of the initial repartition of silicon has negligible influence on the temperature profiles and on the fractional abundances of species other than those containing silicon. Accordingly, we assume initially that there is no elemental silicon in the grain mantles, i.e. that the silicon is in the form of silicates in the grain cores.

In Fig. 5, the neutral temperature profile, fluid velocities (charged and neutral), the compression factor, and the fractional abundance of molecular hydrogen are plotted against the flow time of the charged fluid, $t_i = \int (1/v_i) dz$, for the models specified above. It may be seen that the lower age, of 175 yr or 10 yr, respectively, is insufficient for a significant magnetic precursor to develop at the corresponding shock speed. In all cases, the initial rise in temperature is followed by radiative cooling and compression of the gas as it evolves towards its final state. The younger the shock, the higher is the compression factor and hence the initial, adiabatic increase in temperature at the J-discontinuity. Thus, even at 25 km s^{-1}, the CJ-type shock wave is sufficiently energetic to dissociate partially the ambient molecular hydrogen. At the higher shock speed, a much larger fraction of the H_2 is dissociated. The cooling of the gas occurs mainly through rovibrational transitions of H_2 and, in the region where the fractional abundance of molecular hydrogen is low, through fine-structure transitions of atomic oxygen. The compression of the gas and its falling temperature are accompanied by partial re-formation of H_2, on the grains. In the steady-state C-type shock models, H_2 remains the principal coolant throughout the shock wave, as the maximum temperature which is attained is not high enough

to give rise to significant dissociation. The flow time required for full compression of the gas to be attained is approximately 5×10^3 yr when $v_s = 50$ km s^{-1} and 10^4 yr when $v_s = 25$ km s^{-1}, as may be seen in the bottom panels of Fig. 5.

3.2. H_2 excitation diagrams

In molecular shock waves, H_2 is not only the major coolant but also comprises most of the mass and helps to define the chemical state of the gas. For these reasons, our numerical simulations include a detailed treatment of the physics of H_2, whose level populations are computed in parallel with the dynamical and chemical equations which determine the evolution of the shock wave: see Le Bourlot et al. (2002). At each point of the shocked region, the population densities of the rovibrational levels of molecular hydrogen are calculated. The corresponding column densities are determined by numerical quadrature.

Our analysis of the H_2 line emission from shocks makes use of excitation diagrams, which are plots of $\ln(N_{vj}/g_j)$ against E_{vj}/k_B, where N_{vj} (cm^{-2}) is the column density of the rovibrational level (v, J), E_{vj}/k_B is its excitation temperature and $g_j = (2j + 1)(2I + 1)$ its statistical weight. The nuclear spin quantum number is $I = 1$ for ortho-H_2 and $I = 0$ for para-H_2. If the gas is thermalized at a single temperature, all the points in the diagram lie on a straight line. In practice, thermalization is rarely realized, and the line is curved; then, the local values of the gradient of the curve provide an indication of the kinetic temperatures in the corresponding emitting regions. Our calculations incorporated all significant collisional and radiative transitions between rovibrational levels up to an excitation energy of almost 40 000 K. In partially dissociated gas, rovibrational excitation of H_2 can be dominated by collisions with H. For this process, we use the rate coefficients computed recently by Wrathmall & Flower (2007).

The excitation diagrams for the models specified above are plotted in Fig. 6. The younger the shock, the higher is its maximum temperature (and the smaller is its width). It follows that levels of high excitation energy tend to be more populated, relative to low levels, in younger shock waves. It is clear that the comparison of observed and calculated excitation diagrams has the potential for evolutionary age discrimination.

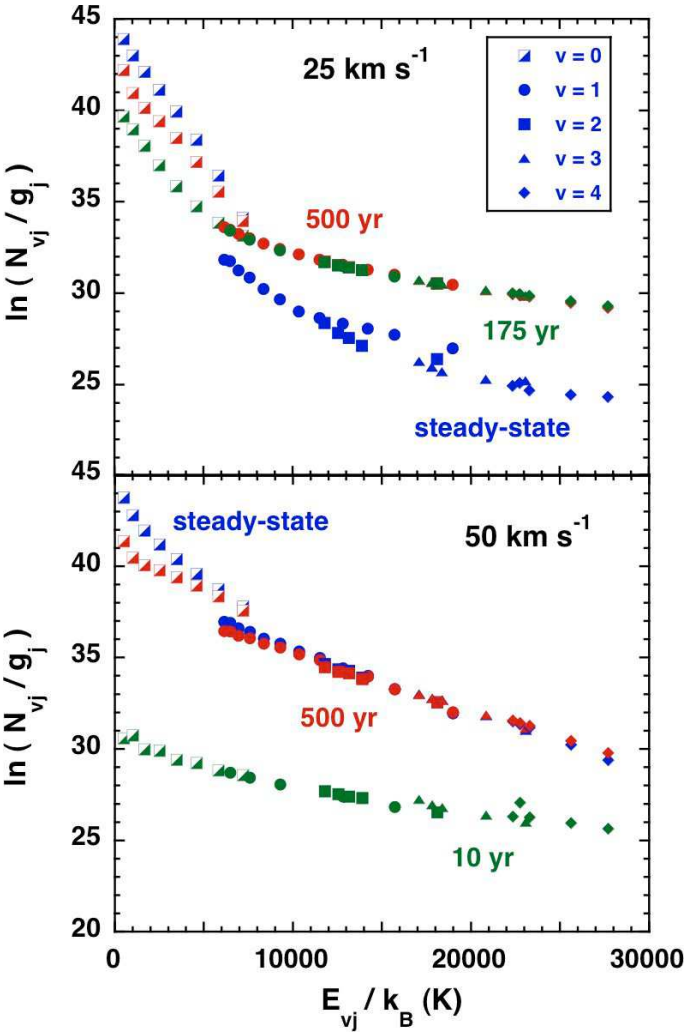

Fig. 6. Synthetic H_2 excitation diagrams for the CJ-type shocks specified in Sect. 3.1.

3.3. SiO emission

Our aim is to find a model that accounts for the observational data pertaining to both SiO and H_2, on the assumption that their emission is generated by the same non-stationary shock wave(s). The predictions of the SiO line intensities are not affected by our choice of shock termination point, which is taken to be twice the flow time at the J-discontinuity. The highly compressed gas behind the J-discontinuity does not contribute significantly to the line intensities.

We discuss first the emission from SiO which occurs following the erosion of Si from the grain cores, and then the corresponding results obtained on assuming that a small percentage of the silicon is initially in the form of SiO in the grain mantles.

3.3.1. SiO absent from the grain mantles

The erosion of Si from the grain cores occurs in the magnetic precursor of the CJ-type shock, where there is a non-zero drift velocity between charged and neutral species. We have noted already in Sect. 2 that core erosion is significant only in the case of the high-velocity shock, $v_s = 50$ km s^{-1}, and so this is the model which we consider. In order to enhance the extent of the region in which the flow velocities of the charged and the neutral fluids are decoupled, we consider evolved shock waves, with ages ≥500 yr. We recall that the pre-shock parameters are $n_H = 10^4$ cm^{-3} and $b = 1$.

Figure 7 illustrates the production of SiO in CJ-type shock waves with ages of 500, 1800 and 3800 yr; the corresponding stationary shock is shown also. There is a chemical delay to the formation of SiO, following the release of Si into the gas phase, due to the time required for oxidation to take place; this delay is significant in the case of non-stationary models, as it is comparable with the evolutionary ages being considered, i.e. of the order of 10^3 yr. Consequently, the maximum fractional abundance of SiO tends to increase with the shock age. In the CJ-type models, the flow speed becomes almost constant behind the J-discontinuity; this has consequences for the predicted SiO emission, as will be seen below.

Figure 8 shows the contributions to the intensities of three lines of SiO, (2–1), (5–4), and (10–9), as functions of the flow time of the charged fluid, for the CJ-type model specified above. In the magnetic precursor, Si is eroded from the grain cores and then oxidized to SiO in the gas phase, resulting in rotational line emission whose intensity increases through the shock wave. The emission saturates behind the discontinuity, owing to the low

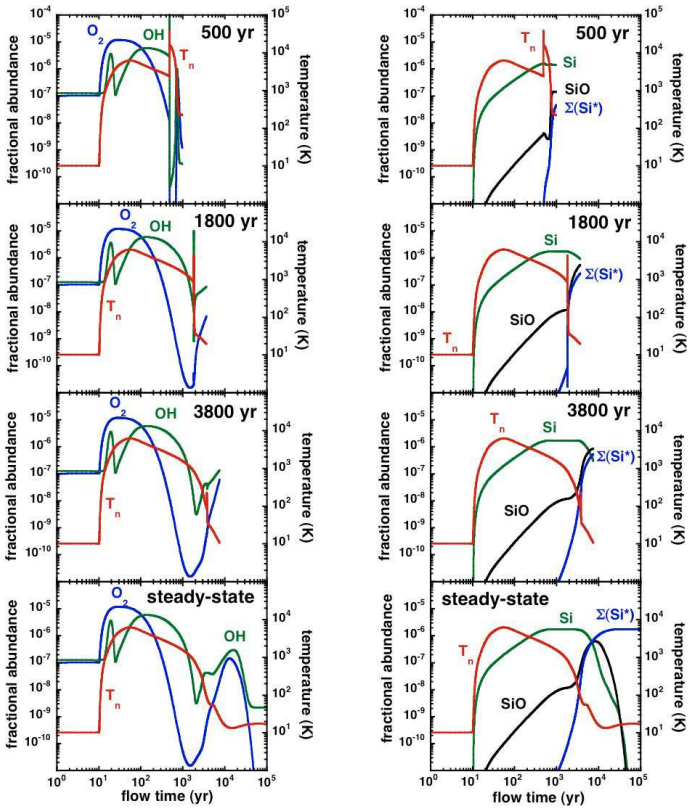

Fig. 7. The temperature of the neutral fluid, T_n, and the fractional abundances of OH and O_2 (*left-hand panels*) and of Si, SiO, and silicon in the grain mantles, Σ Si* (right–hand panels), as functions of the flow time of the charged fluid, for the CJ-type shock model in which $n_H = 10^4$ cm^{-3}, $b = 1$, and $v_s = 50$ km s^{-1}. The shock age increases *from top to bottom*: 500, 1800, 3800 yr, and steady-state. In these calculations, there is no SiO in the grain mantles, and the gas-phase silicon is produced solely by erosion of the silicate grain cores.

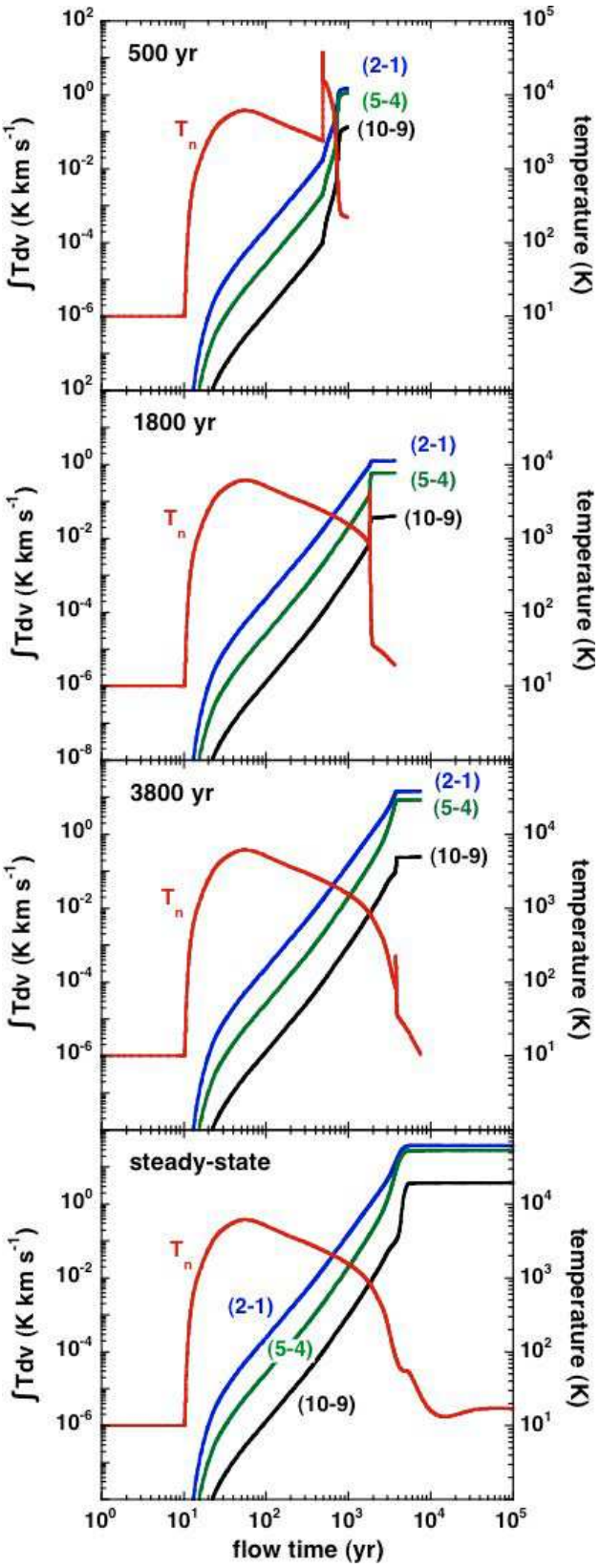

Fig. 8. The integrated intensities, $\int T\mathrm{d}v$, of the SiO (2–1), (5–4) and (10–9) rotational transitions, as functions of the flow time of the charged fluid, for the CJ-type shock model in which $n_H = 10^4$ cm^{-3}, $b = 1$, and $v_s = 50$ km s^{-1}. The shock age increases *from top to bottom*: 500, 1800, 3800 yr, and steady-state. The temperature of the neutral fluid, T_n, is plotted also. In these calculations, there is no SiO in the grain mantles, and the gas-phase silicon is produced solely by erosion of the silicate grain cores.

fluid velocity gradient. In the CJ-type models (top three panels of Fig. 8), the populations of excited rotational levels, and the intensity of, in particular, the (10–9) line, are given a boost whose significance increases with the temperature jump at the J-discontinuity, i.e. towards lower evolutionary ages; this explains the variations of the relative line intensities with the shock age, seen in Fig. 9. The younger the CJ-type shock, the larger is the temperature jump and the stronger are the lines from high rotational levels, relative to low levels.

In the case of the stationary (C-type) shock model, emission arises over almost the full width of the shock wave, including the SiO fractional abundance peak; this explains why all the lines have higher final integrated intensities. In addition, as the $j = 10$ level lies only 115 K above the ground state, it can be excited right through to the point where the fluid velocity reaches its (constant) post-shock value and the compression is highest, which accounts for the high relative integrated intensity of the (10–9) transition in the stationary shock model. On the other hand, at an age of 3800 yr, the J-discontinuity gives rise to a temperature blip which is followed by rapid cooling (see Fig. 8) to temperatures such that the highly rotationally excited levels, such as $j = 10$, become energetically inaccessible; this accounts for the deviation of the relative line intensities from the steady-state values, seen in Fig. 9.

Figure 9 shows that either a stationary C-type shock or young CJ-type shocks provide the best fits to the observations of L1157 B1. However, the lower panel of Fig. 10 shows that the

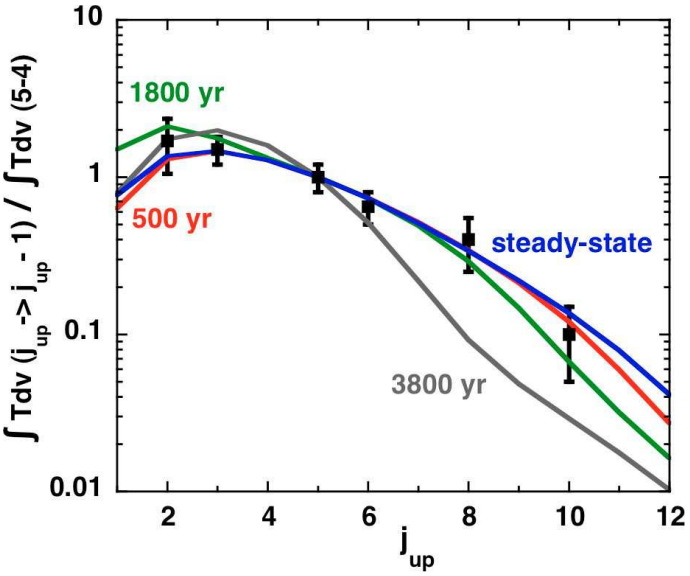

Fig. 9. Integrated SiO line intensities, relative to the (5–4) transition, for the CJ-type shock model in which $n_H = 10^4$ cm^{-3}, $b = 1$, and $v_s = 50$ km s^{-1}. The shock ages are 500, 1800, 3800 yr, and the corresponding steady-state results are plotted also. In these calculations, there is no SiO in the grain mantles, and the gas-phase silicon is produced solely by erosion of the silicate grain cores. The observed points, with error bars, relate to L1157 B1.

absolute SiO(5–4) line intensity is substantially underestimated by the young CJ-type shock models, if it is assumed that there is no SiO in the grain mantles and the gas-phase silicon is produced exclusively by erosion of the silicate grain cores. In this case, only the stationary shock model is a good candidate to fit the SiO observations.

3.3.2. SiO present in the grain mantles

We turn now to non-stationary shock models in which SiO is supposed to be present in the grain mantles; the fraction of the elemental silicon which is initially in the mantles is varied from 0% to 10%[2]. As in Sect. 2, we consider the following model parameters: $n_H = 10^4$ cm^{-3}, $b = 1$, $v_s = 25$ and 50 km s^{-1}.

First, we compare the computed values of the integrated SiO(5–4) line intensity with those observed in L1157 and L1448; see Fig. 10. As expected, the line emission increases with the amount of SiO in the grains mantles. We see also that the line intensity tends to increase with the evolutionary age of the shock, owing to the greater velocity extent of the emitting region. Exceptions to this general trend are young, high-velocity CJ-type shocks (cf. lower panel of Fig. 10), for which the temperature rise at the J-discontinuity is sufficient to cause partial dissociation of molecular hydrogen. Consequent to the reduction in the efficiency of H_2 cooling, the width of the cooling zone, behind the discontinuity, is greater and the SiO line intensity is enhanced.

Figure 10 shows that agreement can be found between the observed and calculated (5–4) line intensity for almost every

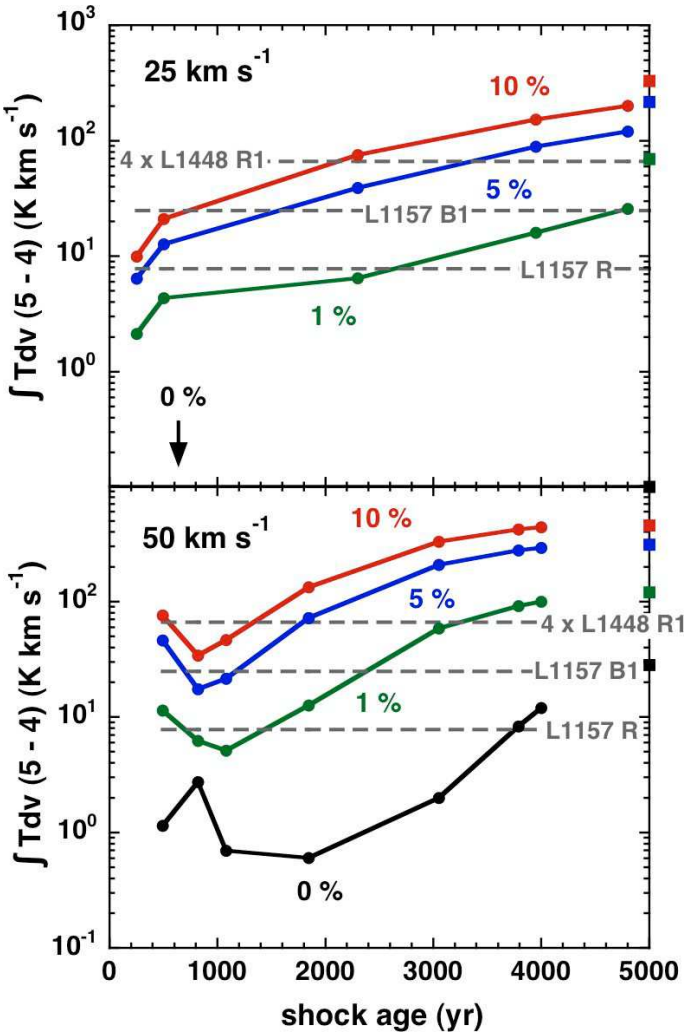

Fig. 10. The integrated intensity of the SiO(5–4) line, $\int T\mathrm{d}v(5{-}4)$, as a function of the age of the shock wave and the percentage of silicon initially in the form of SiO in the grain mantles; $n_H = 10^4$ cm^{-3}, $b = 1$, $v_s = 25$ km s^{-1} (*upper panel*) and 50 km s^{-1} (*lower panel*). The points corresponding to the limit of steady-state are plotted on the right-hand y-axis. The SiO(5–4) intensities observed in L1157 and L1448 are indicated by the horizontal lines.

model in which there is some SiO in the grain mantles. With a view to finding a means of discriminating between the models, we plot, in Fig. 11, the integrated SiO line intensities, relative to the (5–4) transition. In the calculations shown in this figure, it was assumed that 5% of the elemental silicon was initially in the form of SiO in the grain mantles.

At the lower shock speed, the populations of the high rotational levels are greater when the shock is young, owing to the larger jump in temperature at the J-discontinuity. The oldest shock (4000 yr) remains far from the steady-state limit. On the other hand, at the higher shock speed, the 3800 years-old CJ-type shock has almost attained steady state. The cooling efficiency behind the J-discontinuity in the youngest shock (with an age of 500 yr) is reduced by the partial dissociation of molecular hydrogen. Reasonable agreement with the observations is found for evolutionary ages of the order of a thousand years.

Owing to the presence of the embedded J-discontinuity, the profiles of the SiO lines predicted by CJ-type models are compressed in velocity space, as compared with the steady-state C-type models discussed in Sect. 2. The younger the shock wave,

[2] The possibility that solid SiO at the higher concentrations might be detectable in the infrared needs careful evaluation. The fundamental transition should fall around 8 μm, in a region of the infrared which is congested, owing to emission from ices and silicates. The first harmonic at 4 μm would probably also be difficult to detect (Dartois, personal communication).

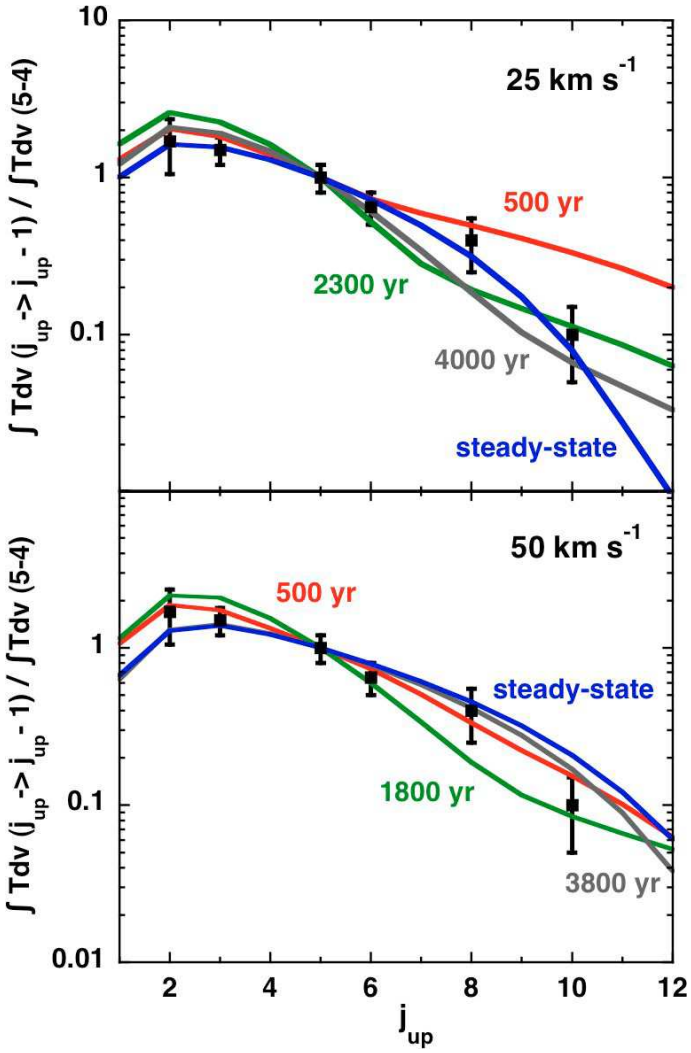

Fig. 11. Integrated SiO line intensities, relative to the (5–4) transition, for the CJ-type shock models in which $n_H = 10^4$ cm^{-3}, $b = 1$, and $v_s = 25$ km s^{-1} (*upper panel*) and $v_s = 50$ km s^{-1} (*lower panel*). The evolutionary ages of the shocks are indicated, and the corresponding steady-state results are plotted also. In these calculations, 5% of the elemental silicon is assumed to be initially in the grain mantles, in the form of SiO. The observed points, with error bars, relate to L1157 B1. The highest rotational level for which observations are available, $j_{up} = 10$, lies 115 K above the ground state.

the greater is the fraction of the emission that is contributed by the gas immediately behind the discontinuity. As the flow velocity of this gas becomes approximately constant, the lines become narrower than in the steady-state limit. The predicted widths decrease to the assumed turbulent width, which is smaller than the observed widths of 5–20 km s^{-1}, in 3″–10″ beams. In this respect, the CJ-type models face a problem which is analogous to that encountered by G08, and for which, in Sect. 5, we advance the same tentative explanation.

In the following Section, we consider the observations of L1157 B1 in more detail, considering both the H_2 and SiO emission lines.

4. A test case: L1157 B1

Observations of pure rotational lines of SiO (up to the (10–9) transition) in the L1157 outflow have been reported recently by Nisini et al. (2007). Caratti o Garatti et al. (2006) compiled observations of a large number of rovibrational lines of H_2, whereas Cabrit et al. (1999) observed pure rotational lines of molecular hydrogen, using ISO; see Appendix A. L1157 is a Class 0 object, at a distance of approximately 440 pc. The jet is highly collimated and inclined relative to the line of sight. L1157 is an example of a "chemically active outflow" (see Bachiller et al. 2001) and is an appropriate object with which to compare our simulations of H_2 and SiO emission from shock waves.

Nisini et al. (2007) studied the excitation of SiO in various knots of the blue and red lobes of L1157, whereas Caratti o Garatti et al. (2006) concentrated on the H_2 rovibrational lines in its blue lobe. Therefore, we focus our analysis on the B1 region; this refers to the SiO observations and corresponds approximately to the A1 and A2 regions observed in molecular hydrogen.

In order to compare with the observations of H_2 and SiO, a grid of models was computed, with the following ranges of parameters:

- shock speeds $10 \leq v_s \leq 45$ km s^{-1};
- preshock densities $10^4 \leq n_H \leq 10^6$ cm^{-3};
- preshock transverse magnetic field strengths determined by $0.1 \leq b \leq 2.0$.

In addition, we varied both the evolutionary age of the (CJ-type) shocks and the fraction of silicon that was initially in the grain mantles, as SiO.

Although the parameter space was not covered uniformly, i.e. not all possible combinations of the parameters above were used, the grid of C- and J-type models that was generated was sufficient to make meaningful comparisons with the observations. The grid will be made accessible from http://massey.dur.ac.uk/drf/outflows/

4.1. H_2 emission lines

We present in Fig. 12 the excitation diagram which derives from the H_2 rovibrational line intensities listed in Caratti o Garatti et al. (2006) and the pure rotational line intensities observed by Cabrit et al. (1999). When correcting the data for reddening, we adopted a visual extinction $A_V = 2$, which is an upper limit from Caratti o Garatti et al. (2006), and the interstellar extinction law of Rieke & Lebofsky (1985). Results are plotted for two single-pixel ("pix1" and "pix2") ISO measurements of the pure rotational line intensities (see Appendix A), and for the two regions, A1 and A2, observed in the near-infrared rovibrational lines. We note that the effects of the reddening correction on the observational points plotted in this diagram are minor.

Rotational and rovibrational temperatures, deduced from the excitation diagrams for each set of data, are compiled in Table 1. The excitation temperatures deduced for pix1 and pix2, and for A1 and A2, are similar. Furthermore, the reddening correction has only minor significance. Unsurprisingly, the rovibrational transitions trace hotter gas than the pure rotational transitions; cf. Le Bourlot et al. (2002), Giannini et al. (2006). There is no persuasive evidence for non-thermal values of the ortho:para H_2 ratio from the observational points in the excitation diagram. In the models, an initial (statistical) value of 3:1 was assumed, and the computed value of the ortho:para ratio remained unchanged (to better than 10%) through the shock wave. The timescale for thermalization under the conditions of the cold, preshock gas (via proton exchange reactions with H^+ or H_3^+) approaches 10^6 yr, which is much larger than the dynamical age

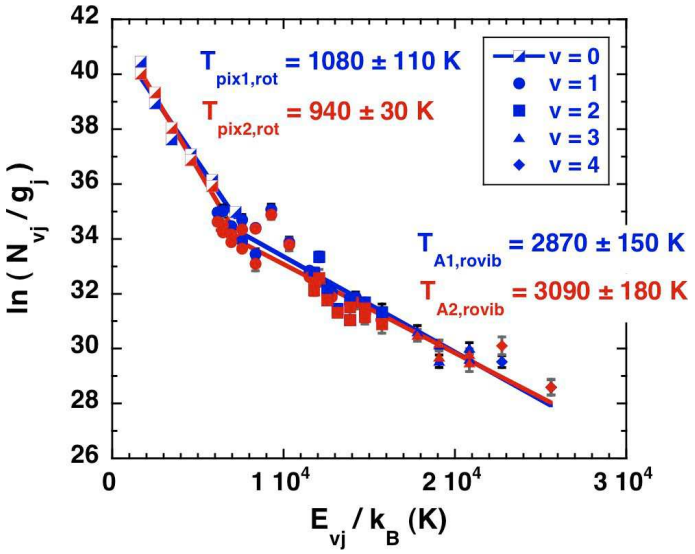

Fig. 12. Composite H_2 excitation diagrams, corrected for reddening with $A_V = 2$; see text, Sect. 4.1. The excitation temperatures deduced from each set of observations are indicated.

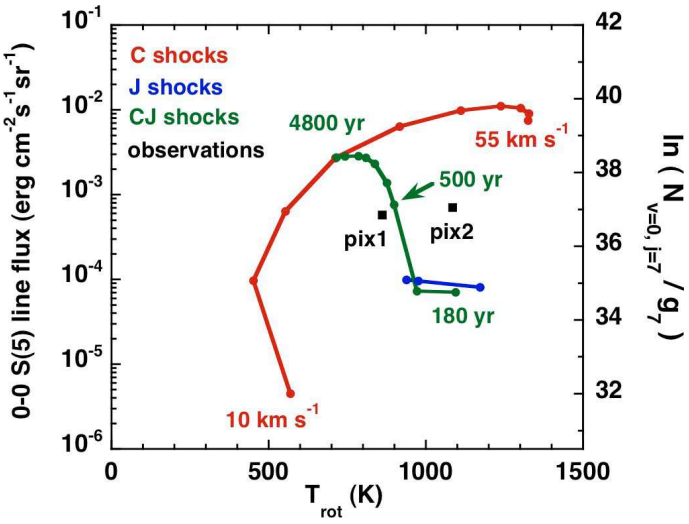

Fig. 13. The observed and calculated values of the H_2 0–0 S(5) emission line flux, plotted as functions of the mean excitation temperature of the rotational lines within the $v = 0$ vibrational ground state. The corresponding values of the column density per magnetic sub-level are given on the right–hand axis for the ($v = 0$, $j = 7$) emitting level, whose degeneracy is $g_7 = 45$. Results are given for L1157 B1, as observed by ISO (two separate pixels, pix1 and pix2) and for a series of models of (stationary) C-type ($b = 1$) shock waves (red curve) for ranges of the shock speed, v_s, in steps of 5 km s^{-1} between the limiting values indicated. Also shown are the results for an evolutionary sequence of non-stationary CJ-type ($b = 1$) models (green curve), for $v_s = 25$ km s^{-1}, and for J-type ($b = 0.1$) models (blue curve) with $v_s = 20$, 25 and 30 km s^{-1}. In all cases, the pre-shock density is $n_H = 10^4$ cm^{-3}.

Table 1. Excitation temperatures inferred from observations of H_2 rotational (pix1 and pix2) and rovibrational (A1 and A2) transitions in L1157.

T_{exc}(K)	Without reddening	With reddening
pix1	1090 ± 110	1080 ± 110
pix2	860 ± 50	940 ± 30
A1	2740 ± 130	2870 ± 150
A2	2940 ± 170	3090 ± 180

of L1157 B1. Thermalization in the hot gas of the shock wave occurs more rapidly, via hydrogen atom exchange reactions: see Wilgenbus et al. (2000).

We have already noted in Sect. 3 that previous studies (see, for example, Flower et al. 2003; Giannini et al. 2004, 2006) have suggested that only CJ-type shock waves can account for the molecular hydrogen emission observed in molecular outflows. Our preliminary investigations of L1157 B1 confirmed this conclusion: stationary C-type shocks cannot reproduce the observed H_2 excitation diagram. Accordingly, we concentrate on CJ-type models, for which the parameters to be varied include n_H, v_s, b, and the age of the shock wave. It follows that a procedure which restricts the range of the search of the parameter space is desirable, even essential.

Figures 6 and 12 show that most of the column density of H_2 is contributed by the rotational levels of the vibrational ground state. Consequently, the first restriction is to models that can reproduce the observed rotational excitation temperature (cf. Table 1), to within a reasonable tolerance. Adopting even a wide tolerance of 400 K restricts the parameter ranges to the following:

- $n_H = 10^4$ cm^{-3}, $15 \leq v_s \leq 35$ km s^{-1}, and $0.45 \leq b \leq 2.00$;
- $n_H = 10^5$ cm^{-3}, $10 \leq v_s \leq 20$ km s^{-1}, and $0.30 \leq b \leq 2.00$.

With $n_H = 10^6$ cm^{-3}, only models with evolutionary ages less than a few hundred years are able to fit the observed rotational temperature. We excluded such models on the grounds that the dynamical age deduced empirically is in the range 2000–3000 yr Gueth et al. (1998). The magnetic field parameter, b, is poorly constrained by the rotational line observations. A lower limit to the magnetic field strength is imposed by the requirement that the ion magnetosonic speed should exceed the shock speed, a necessary condition for a magnetic precursor to develop; see Flower & Pineau des Forêts (2003), Le Bourlot et al. (2002), Guillet et al. (2007).

In order to constrain the evolutionary age of the shock wave, we are guided by the rotational line spectrum, and initially by the 0–0 S(5) transition. In Fig. 13 is plotted the flux in this rotational line against the mean rotational excitation temperature in the vibrational ground state, $v = 0$. We show results for series of C- and J-type models, for the parameters specified and ranges of the shock speed, v_s, and of CJ-type models with $v_s = 25$ km s^{-1} and varying ages. The fluxes observed in L1157 B1 (pix1 and pix2) are shown also. The evolution of J-type models into C-type, through CJ-type of increasing ages, is well represented in this figure. It is clear that only CJ-type models provide a fit to the observations, a result which is consistent with earlier studies of ouflows, cited above, and which will receive further confirmation below. The steady-state C-type models consistently overestimate the intensity of the 0–0 S(5) transition, whatever value of b is adopted. Whilst the discrepancy might be resolved by assuming a small filling factor, this assumption would result in the intensities of lines from vibrational levels $v > 0$ being underestimated. When optimizing the values of the CJ-type model parameters, we shall make use of the entire H_2 excitation diagram, incorporating the emission observed from vibrationally excited levels.

We compute a small grid of CJ-type (non-stationary) shock models around our initial estimation of the shock age. The range

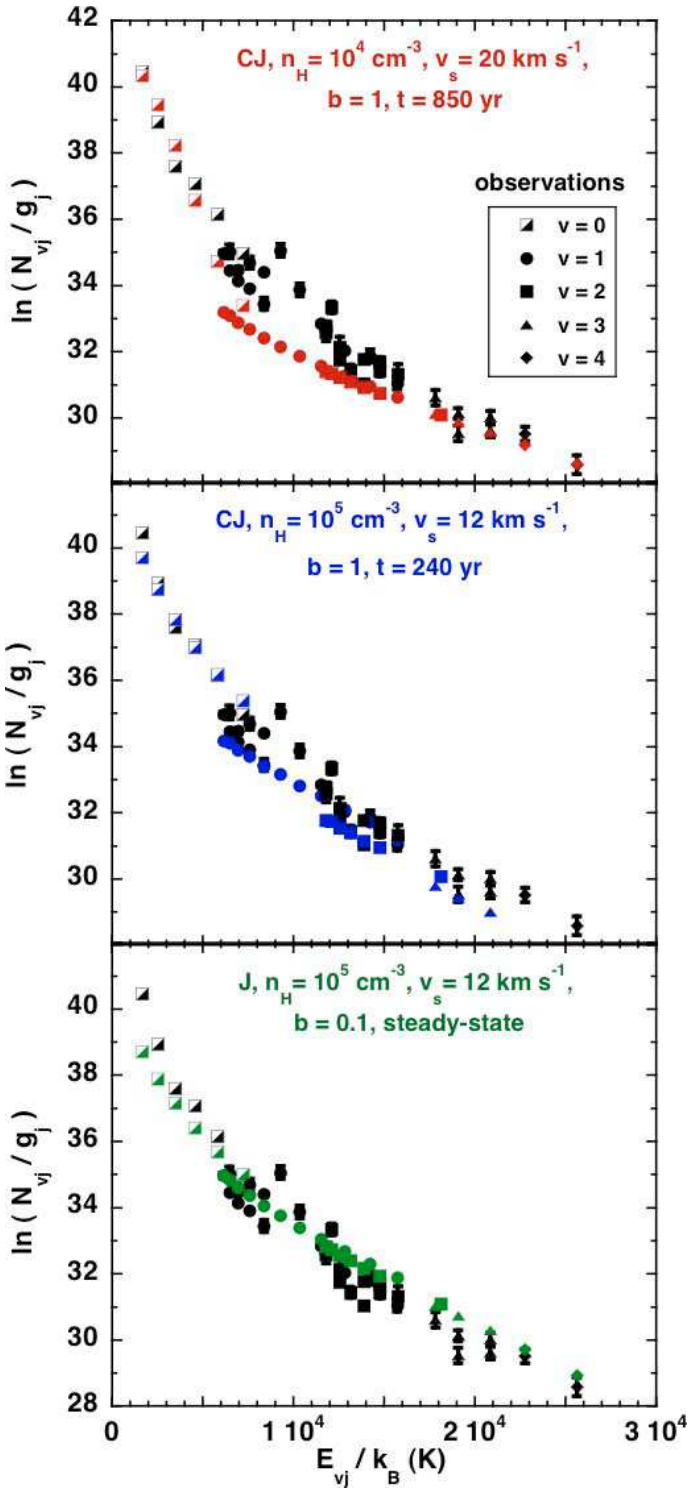

Fig. 14. Three models of the H_2 excitation diagram of L1157 B1: CJ-type $n_H = 10^4$ cm^{-3}, $v_s = 20$ km s^{-1}, $b = 1$, age 850 yr (*top panel*); CJ-type $n_H = 10^5$ cm^{-3}, $v_s = 12$ km s^{-1}, $b = 1$, age 240 yr (*middle panel*); J-type $n_H = 10^5$ cm^{-3}, $v_s = 12$ km s^{-1}, $b = 0.1$ (*bottom panel*). The observations are from Caratti o Garatti et al. (2006) and Cabrit et al. (1999); see also Appendix A.

of ages is sufficient to ensure that we do not exclude models which might yield acceptable excitation diagrams.

CJ-type shocks with a pre-shock density $n_H = 10^4$ cm^{-3}, shock velocities $v_s = 20$, 22, and 25 km s^{-1}, and $n_H = 10^5$ cm^{-3}, $v_s = 12$ and 15 km s^{-1} were found to give reasonable fits to the H_2 observations. In Fig. 14, we compare the H_2 excitation diagram derived from the observations of L1157 B1 with the predictions of two CJ-type models with pre-shock densities $n_H = 10^4$ and 10^5 cm^{-3}. We show also the results from the best-fitting J-type shock model. None of the models provides a completely satisfactory fit to the observations. As the shock evolves towards stationary C-type, i.e. as its age increases, the intensities of the rovibrational transitions decrease, relative to the pure rotational transitions within the vibrational ground state, $v = 0$. Thus, the J-type shock underestimates substantially the column densities of the $v = 0$ rotational levels. As these levels contribute most of the H_2 column density, we eliminate the J-type model from further consideration. On the other hand, the CJ-type shocks tend to underestimate the column densities of some of the vibrationally excited rotational levels. We defer further discussion of these remaining discrepancies until comparisons with the observations of the rotational transitions of SiO have been made.

4.2. SiO emission lines

After an initial selection of model parameters, based on H_2 observations, we proceed to comparisons with the observed SiO rotational line intensities. There is now an additional parameter, namely, the fraction of silicon present as SiO in the grain mantles.

As in Sect. 3.3, we consider first the integrated intensity of the SiO(5–4) line. It is clear that, for the low shock speeds which were derived from the analysis of the H_2 rovibrational spectrum, some silicon must be present in the grain mantles: grain-core erosion alone would not give rise to a sufficient amount of gas-phase SiO to account for the observations of its rotational lines. We assume that either 1% or 10% of the silicon is SiO in the mantles.

In Fig. 15 is plotted the SiO(5–4) integrated line intensity against the magnetic field parameter, b, for CJ-type shocks with a pre-shock density $n_H = 10^4$ cm^{-3}, shock velocities $v_s = 20$, 22, and 25 km s^{-1} (in the upper panel), and $n_H = 10^5$ cm^{-3}, $v_s = 12$ and 15 km s^{-1} (in the lower panel). We recall that these models were found to give acceptable fits to the H_2 observations. We note that the evolutionary age was varied simultaneously with b, in order to optimize the fits to the observed H_2 excitation diagram, giving rise to the variations which are seen in the (5–4) line intensity. This variation is particularly striking in the results for a pre-shock density of 10^5 cm^{-3} and shock velocity of 12 km s^{-1}: the model for which $b = 0.45$ (age 75 yr) incorporates a significant magnetic precursor, whereas, when $b = 0.6$ (age 75 yr), the precursor is negligible. In the latter case, there is much less sputtering of SiO from the grain mantles, and the SiO emission is correspondingly weaker. The results in Fig. 15 may be seen to support the higher percentage (10%) of silicon being present in the mantles.

Finally, we compare the integrated line intensities, relative to the (5–4) transition, with the observations. This comparison eliminates the models with $n_H = 10^5$ cm^{-3}, which are found to overestimate the intensities of the lines from high rotational levels. On the other hand, as may be seen from Fig. 16, a range of combinations of b and the shock age remains compatible with the relative line intensities for $n_H = 10^4$ cm^{-3} and the optimal shock speed of $v_s = 20$ km s^{-1}. The only observational point that is not well fitted by the models (the (10–9) transition) could be more closely approached by reducing the amount of SiO assumed to be initially in the mantles. The evolutionary ages of the models in Fig. 16 lie in the range 500–2000 yr, as compared with the dynamical age estimate of 2000–3000 yr, derived empirically

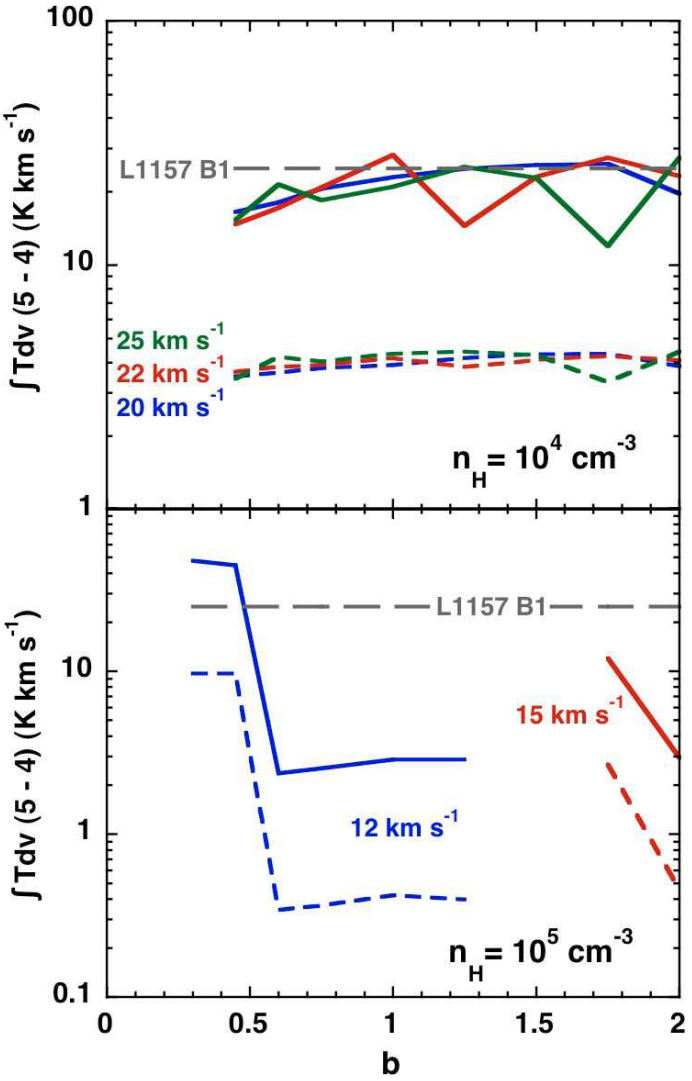

Fig. 15. The integrated intensity of the SiO(5–4) line, $\int T\mathrm{d}v(5-4)$, against the magnetic field parameter, b, for CJ-type shocks of various ages in which the pre-shock density $n_{\rm H} = 10^4$ cm^{-3}, the shock velocity $v_{\rm s}$ = 20, 22, and 25 km s^{-1} (*upper panel*), and $n_{\rm H} = 10^5$ cm^{-3}, $v_{\rm s}$ = 12 and 15 km s^{-1} (*lower panel*). Results were obtained assuming either 10% (full curves) or 1% (broken curves) of the silicon is initially SiO in the grain mantles.

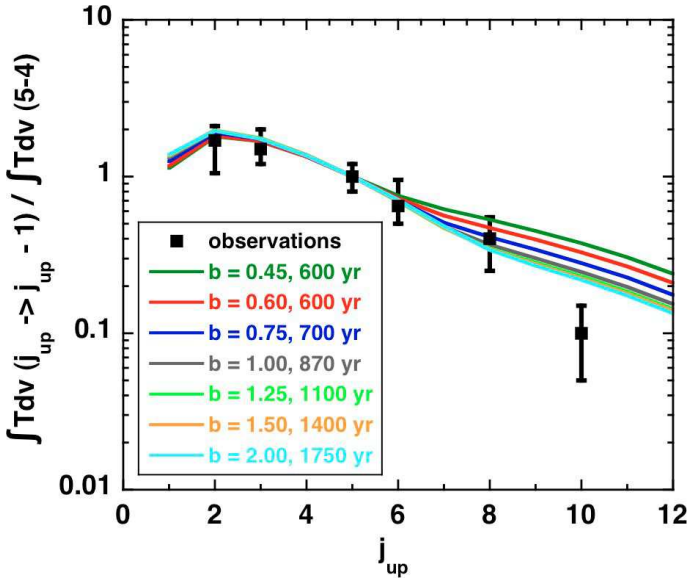

Fig. 16. The best-fitting models of the H_2 and SiO observations of L1157 B1: CJ-type shocks for which $n_{\rm H} = 10^4$ cm^{-3} and $v_{\rm s}$ = 20 km s^{-1}; the magnetic field parameter, b and the evolutionary age are varied simultaneously. 10% of the silicon is initially SiO in the grain mantles.

(Gueth et al. 1998). The models which fit the observations of H_2 and SiO have been found to be compatible with the integrated intensities of rotational lines of CO: see Appendix B.

5. Concluding remarks

We have extended a previous study (G08) of the emission of SiO from shock waves in molecular outflows by considering the possibility that a small percentage of the silicon is present, as SiO, in the grain mantles, rather than exclusively as silicates in the grain cores. The lower binding energy of the mantle material ensures that the constituents are rapidly sputtered by the light but abundant neutral species, H_2, He and H, which impact the grains (most of which are negatively charged, and hence flow with the charged fluid) at the ion-neutral drift speed. The sputtering process ensures that SiO emission occurs over the full width of the magnetic precursor and hence over a wide range of flow speeds. This situation contrasts with that studied by G08, in which Si was sputtered from the grain cores by the impact of heavy but scarce neutral species, such as CO, and subsequently oxidized to SiO in the gas phase. As a consequence, the SiO rotational line profiles predicted by steady-state C-type shock waves (see Fig. 4, above) are much broader than in our previous study (G08, Fig. 8) and, in this respect, in much better agreement with the observed line profiles. However, the computed profiles vary significantly with the emitting rotational level, $j_{\rm up}$, whereas the observed profiles are seen to be similar from line to line (see Fig. 9 of Nisini et al. 2007).

Additional constraints on the nature of the shock waves are provided by observations of molecular hydrogen. Previous comparisons with observed H_2 excitation diagrams for Cepheus A West, Orion OMC-1, and various Herbig-Haro objects have suggested that non-stationary (CJ-type) shock waves are required to reproduce simultaneously the column densities of the ground and the excited vibrational levels of H_2. This conclusion is confirmed by the present study. Furthermore, the derived evolutionary ages of the order of a thousand years are consistent with the empirically-derived dynamical age of L1157, the object that we have studied in most detail. We derive a pre-shock gas density $n_{\rm H} = 10^4$ cm^{-3} and a shock speed $v_{\rm s}$ = 20 km s^{-1}; approximately 10% of the elemental silicon is initially in the form of SiO in the grain mantles. The initial (transverse) magnetic field strength is not well constrained by the observations but is broadly compatible with the values derived by Crutcher (1999) from Zeeman measurements. The predictions of this model are found to be consistent also with the rotational line emission of CO (Appendix B). We consider that the level of agreement between the model predictions and the observations of H_2, SiO and CO is encouraging, though certainly not perfect. The optimal model (pre-shock density $n_{\rm H} = 10^4$ cm^{-3} and shock speed $v_{\rm s}$ = 20 km s^{-1}) tends to underestimate the column densities of the $v = 1$ and $v = 2$ vibrationally excited levels of H_2 and overestimate the emission from the $j = 10$ rotational level of SiO.

It would be naive to believe that a single plane-parallel shock wave could be completely successful in accounting for the emission from what is undoubtedly a complex flow. In order to explain the fact that the calculated SiO line widths were an order

of magnitude smaller than observed, G08 proposed that the observed lines are attributable to several shocks within the telescope beam, which appear spread out in radial velocity, owing to a range of inclination angles or propagation speeds (in the reference frame of the observer). In the case of CJ-type models, the discrepancy between the calculated and observed line widths is at least as great as in G08; but as the dimension of the emitting region is also reduced by the presence of the *J*-discontinuity, we may invoke the same explanation in this case, namely that there are several shocks within the telescope beam.

Acknowledgements. This study is based in part on observations with ISO, an ESA project with instruments funded by ESA Member States (especially the PI countries: France, Germany, the Netherlands and the United Kingdom) with the participation of ISAS and NASA. Antoine Gusdorf and the University of Durham acknowledge the support of the European Commission under the Marie Curie Research Training Network "The Molecular Universe" MRTN-CT-2004-512302. We thank Brunella Nisini for helpful correspondence relating to the SiO observations of Nisini et al. (2007), Emmanuel Dartois for discussions of the possibility of detecting SiO in grain mantles, and Malcolm Walmsley for his comments on the manuscript.

References

Bachiller, R., & Pérez Gutiérez, M. 1997, ApJ, 487, L93
Bachiller, R., Pérez Gutiérez, M., Kumar, M. S. N., & Tafalla, M. 2001, A&A, 372, 899
Balakrishnan, N., Yan, M., & Dalgarno, A. 2002, ApJ, 568, 443
Cabrit, S., Bontemps, S., Lagage, P. O., et al. 1999, in the Universe as seen by ISO, ed P. Cox, & M. F. Kessler, 449
Caratti o Garatti, A., Giannini, T., Nisini, B., & Lorenzetti, D. 2006, A&A, 449, 1077
Cecchi-Pestellini, C., Bodo, E., Balakrishnan, N., & Dalgarno, A. 2002, ApJ, 571, 1015
Chièze, J.-P., Pineau des Forêts, G., & Flower, D. R. 1998, MNRAS, 295, 672
Crutcher, R. M. 1999, ApJ, 520, 706
Davis, C. J., & Eisloeffel, J. 1995, A&A, 300, 851
Dayou, F., & Balança, C. 2006, A&A, 459, 297
Flower, D. R. 2001, J. Phys. B, 34, 2731
Flower, D. R., & Pineau des Forêts, G. 1999, MNRAS, 308, 271
Flower, D. R., & Pineau des Forêts, G. 2003, MNRAS, 343, 390
Flower, D. R., Le Bourlot, J., Pineau des Forêts, G., & Cabrit, S. 2003, MNRAS, 341, 70
Giannini, T., Nisini, B., & Lorenzetti, D. 2001, ApJ, 555, 40
Giannini, T., McCoey, C., Caratti o Garatti, A., et al. 2004, A&A, 419, 999
Giannini, T., McCoey, C., Nisini, B., et al. 2006, A&A, 459, 821
Guillet, V., Pineau des Forêts, G., & Jones, A. 2007, A&A, 476, 263
Gueth, F., Guilloteau, S., & Bachiller, R. 1998, A&A, 333, 287
Gusdorf, A., Cabrit, S., Flower, D. R., & Pineau des Forêts, G. 2008, A&A, 482, 809
Larsson, B., Liseau, R., Pagani, L., et al. 2007, A&A, 466, 999
Le Bourlot, J., Pineau des Forêts, G., Flower, D. R., & Cabrit, S. 2002, MNRAS, 332, 985
Lesaffre, P., Chièze, J.-P., Cabrit, S., & Pineau des Forêts, G. 2004a, A&A, 427, 147
Lesaffre, P., Chièze, J.-P., Cabrit, S., & Pineau des Forêts, G. 2004b, A&A, 427, 157
Nisini, B., Codella, C., Giannini, T., et al. 2007, A&A, 462, 163
Pagani, L., Olofsson, A. O. H., Bergman, P., et al. 2003, A&A, 402, L77
Rieke, G. H., & Lebofsky, M. J. 1985, ApJ, 288, 618
Schilke, P., Pineau des Forêts, G., Walmsley, C. M., & Martín-Pintado, J. 2001, A&A, 372, 291
Tafalla, M., & Bachiller, R. 1995, ApJ, 443, L37
Van der Tak, F. F. S., Black, J. H., Schöier, F. L., Jansen, D. J., & van Dishoeck, E. F. 2007, A&A, 468, 627
Walmsley, C. M., Pineau des Forêts, G., & Flower, D. R. 1999, A&A, 342, 542
Wilgenbus, D., Cabrit, S., Pineau des Forêts, G., & Flower, D. R., 2000, A&A, 356, 1010
Wrathmall, S. A., & Flower, D. R., 2007, J. Phys. B, 40, 3221
Zhang, Q., Ho, P. T. P., Wright, M. C. H., & Wilner, D. J. 1995, ApJ, 451, L71
Zhang, Q., Ho, P. T. P., & Wright, M. C. H. 2000, AJ, 119, 1345

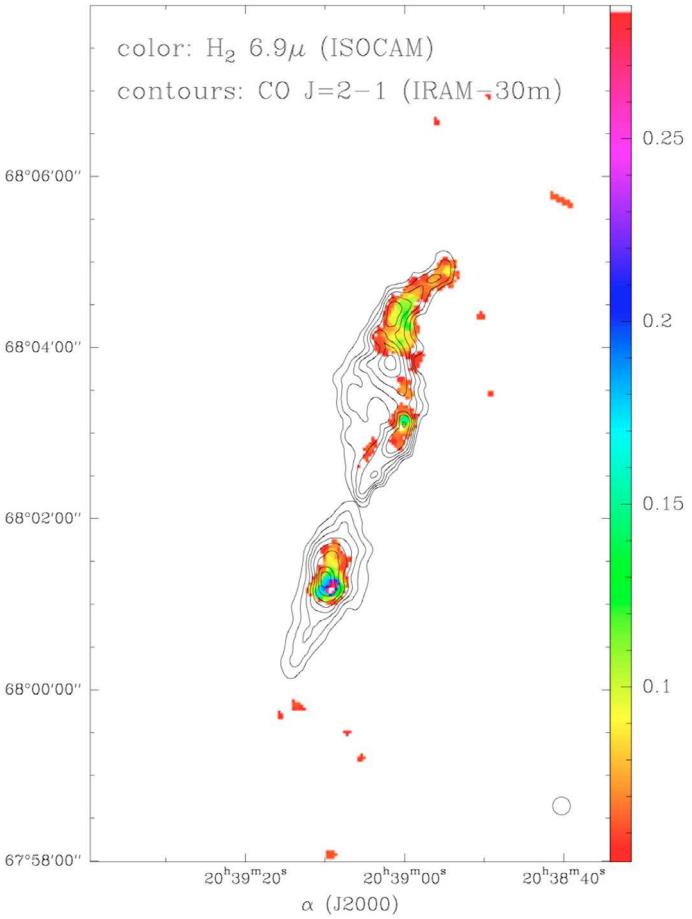

Fig. A.1. A map of the L1157 outflow (Cabrit et al. 1999) obtained with ISOCAM in a narrow filter ($R \approx 40$), centered on the 0–0 S(5) line at 6.9 μm, and superposed on the CO map of Bachiller & Pérez-Guttiérez (1997).

Appendix A: H_2 rotational lines observed with ISO

In order to illustrate the morphology of the H_2 emission, we show, in Fig. A.1, the map of the L1157 outflow obtained by Cabrit et al. (1999) with ISOCAM in a narrow filter ($R \approx 40$) centered on the 0–0 S(5) line at 6.9 μm, superposed on the CO map of Bachiller & Pérez-Guttiérez (1997). A curving chain of knots is seen along the outflow axis, coinciding with previously known shocked regions, traced by interferometric mapping in SiO (Gueth et al. 1998; Zhang et al. 1995, 2000) and NH_3 (Tafalla & Bachiller 1995), and in 2.12 μm H_2 rovibrational emission (Davis & Eisloeffel 1995). As may be seen in Fig. A.2, there is good spatial correspondence between the H_2 $v = 0$–0 lines and the SiO and rovibrational H_2 towards the southern blue lobe. The peak of H_2 $v = 0$–0 coincides with the brightest regions in SiO and 2.12 μm H_2. A second SiO knot at the tip of the southern lobe appears only in the longer wavelength LW3 filter that covers the 0–0 S(1) and 0–0 S(2) lines, indicating a lower degree of excitation.

Individual line fluxes of the 0–0 S(2) to 0–0 S(7) lines towards the peak were extracted from a full ISOCAM/CVF scan of this region obtained with 6″ per pixel resolution. By comparing the fluxes in the broad and the narrow filters, we established that there was negligible continuum contamination. The data were analyzed using "CIA", a joint development by the ESA Astrophysics Division and the ISOCAM Consortium led by the ISOCAM PI, C. Cesarsky, Direction des Sciences de la Matière, C.E.A., France. The most important sources of uncertainty are, in decreasing order, transient effect corrections, flat-field errors, and photometric conversion factors, giving a total uncertainty of ±20–30%. The observed fluxes after transient correction are listed in Table A.1.

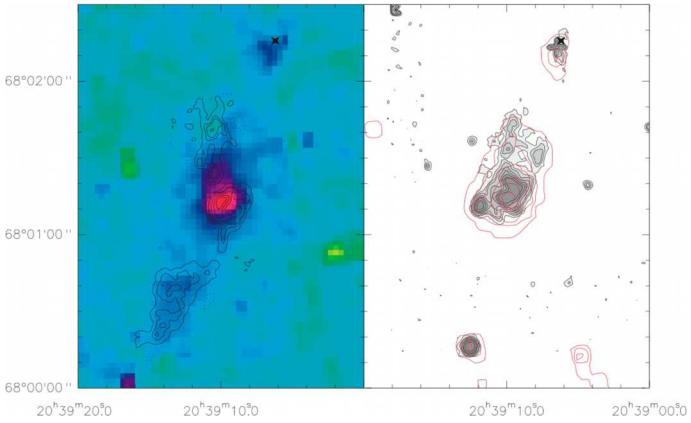

Fig. A.2. *Left panel*: the LW3 ISOCAM image of the southern blue lobe of L1157 superposed on the SiO (2–1) contours of Gueth et al. (1998). *Right panel*: the LW2 ISOCAM image of the southern blue lobe of L1157 superposed on the contours of the H_2 2.12 μm (plus continuum) emission from Davis & Eisloeffel (1995).

Table A.1. Values of $\ln(N_{up}/g_{up})$, derived from ISOCAM observations of H_2 rotational lines in L1157 (uncorrected for reddening), for the two brightest pixels of the knot B1 and also for a 3 × 3 pixel area which comprises the two peaks. The pixel size is 6″, which corresponds to 2600 AU at the distance of L1157.

Transition	E_{up} (K)	pix1	pix2	3 × 3
0–0 S(2)	1681.68	40.33	40.79	40.18
0–0 S(3)	2503.87	38.80	39.20	38.64
0–0 S(4)	3474.43	37.55	37.98	37.14
0–0 S(5)	4586.38	37.05	36.85	36.46
0–0 S(6)	5829.76	35.92	35.70	34.54
0–0 S(7)	7197.00	34.95	34.07	33.69

Appendix B: CO integrated line intensities

The treatment of the radiative transfer of the rotational lines of CO was completely analogous to that of SiO. In particular, the expression for the escape probability and the numerical implementation were identical; for more complete information, see G08, Appendix A. The Einstein A-values and the rotational constant for the ground vibrational state of $^{12}C^{16}O$ (B_0 = 57635.96828 MHz, corresponding to hB_0/k_B = 2.766 K) were taken from the NIST database (`http://www.nist.gov/data/`).

In the case of CO, rate coefficients for collisional excitation by H_2, He and H are available. We used the following sets of collisional data:

- collisions with H from Balakrishnan et al. (2002) for the 8 lowest rotational levels of CO and $5 \leq T \leq 100$ K, and also for the 17 lowest levels and $100 \leq T \leq 300$ K;
- collisions with He from Cecchi-Pestellini et al. (2002) for the 15 lowest rotational levels of CO and $5 \leq T \leq 500$ K;
- collisions with ortho-H_2 and para-H_2 from Flower (2001): the 20 lowest levels of CO for collisions with ortho-H_2, and the 29 lowest levels of CO for collisions with para-H_2; $5 \leq T \leq 400$.

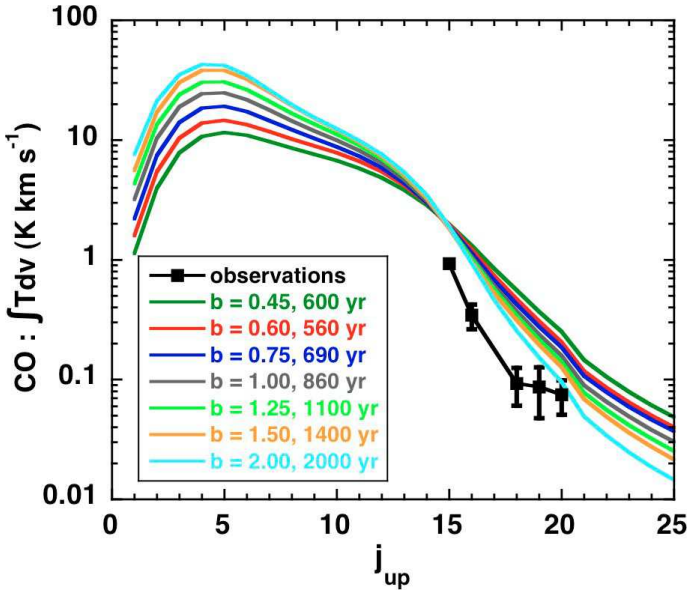

Fig. B.1. The integrated intensities of the CO rotational lines, $\int T\mathrm{d}v$, for CJ-type shocks for which $n_\mathrm{H} = 10^4$ cm^{-3} and $v_\mathrm{s} = 20$ km s^{-1}; the magnetic field parameter, b and the evolutionary age are varied simultaneously.

At temperatures higher than the specified upper limits, we assumed the rate coefficients to be constant.

Our code was tested against the online version of RADEX (http://www.sron.rug.nl/vdtak/radex/radex.php), which is appropriate to a turbulent homogeneous sphere (Van der Tak et al. 2007), adopting their expression for the escape probability and assuming that H_2 is the only collision partner; discrepancies never exceeded a few percent. As anticipated, the initial distribution of elemental oxygen (see Sect. 1 and G08) and of elemental silicon (see above) had no influence on the CO emission from the shock wave.

As in the case of SiO, we computed the CO integrated line intensities for all models which simulated the H_2 emission satisfactorily. Models for which $n_\mathrm{H} = 10^5$ cm^{-3} generated too much emission from the high rotational levels, relative to the low levels. CJ-type shock models with a preshock density $n_\mathrm{H} = 10^4$ cm^{-3} provided better fits to the observations. Figure B.1 shows a comparison between observed and calculated (absolute) integrated line intensities; the observations were compiled by Giannini et al. (2001). The model for which results are displayed is the same as in Fig. 16 and corresponds to $n_\mathrm{H} = 10^4$ cm^{-3} and $v_\mathrm{s} = 20$ km s^{-1}; there are various combinations of the magnetic field strength parameter, b, and the shock age. The shape of the theoretical curves in this Fig. B.1 is in good agreement with that observed, although there remains a discrepancy in the absolute values which may indicate an overestimation of the beam filling factor, for which we adopted a value of 1/16, corresponding to a beam diameter of 80″ and a source diameter of 20″. Figure B.1 suggests that the rotational transitions which were observed by ISO are not ideal discriminants of the models.

Appendix C: The age of a CJ-type shock wave

In the CJ-type models considered above, the termination point of the flow was determined such that the (ion) flow time in the C part of the shock wave, i.e. up to the J-discontinuity, and the flow time behind the discontinuity were equal. In so far as the models are perceived as a set of quasi-time-dependent simulations of the flow, the termination point should correspond to the location of the "piston" which drives the shock wave.

Let u_p be the speed of the piston (which is also the speed of the gas at the surface of the piston) and u_0 be the speed of the gas immediately upstream of the discontinuity, with these speeds being expressed in the shock frame. If ρ_p and ρ_0 are the corresponding mass densities, then

$$\rho_\mathrm{p} u_\mathrm{p} = \rho_0 u_0$$

from the equation of continuity. Hence

$$u_\mathrm{p} = \rho_0 u_0 / \rho_\mathrm{p}.$$

The discontinuity advances at u_0 relative to the gas immediately in front of it, and the velocity of the piston, relative to this same gas, is $(u_0 - u_\mathrm{p})$. Thus, the speed of the discontinuity minus the speed of the piston is u_p. In other words, the discontinuity moves away from the piston at speed u_p. As the discontinuity coincides with the surface of the piston at time $t = 0$, the age of the shock wave is

$$t_\mathrm{s} = \int_0^p [(\rho_\mathrm{p}/\rho_0)/u_0]\mathrm{d}z = [(\rho_\mathrm{p}/\rho_0)/u_0]\Delta z$$

where z is the position coordinate and Δz is the current distance between the discontinuity and the piston; t_s is the time required for the discontinuity to move to its current position from its initial position, at the surface of the piston.

Using t_s as defined above to define the shock age has the advantage of removing the ambiguity of the two flow times (ion and neutral): behind the discontinuity, $u_\mathrm{i} = u_\mathrm{n}$. Because the flow speed rapidly attains its postshock value ($=u_\mathrm{p}$) behind the discontinuity, the flow time behind the discontinuity is approximately equal to t_s. In the time t_s required for the discontinuity to separate from the piston and reach its current position, a magnetic precursor develops simultaneously upstream of the discontinuity.

Note, however, that the expression above for t_s does not give the shock age exactly, as it assumes that the speed of the discontinuity relative to the piston, u_p, remains constant, whereas Fig. 3d of Lesaffre et al. (2004a) shows that u_p decreases steadily as cooling sets in and the size of the velocity jump at the discontinuity decreases, following the growth of the precursor. A more accurate estimate of the age, under the (generally valid) condition that the width of the region downstream of the J-discontinuity is much smaller than the width of the C part of the shock wave, upstream of the discontinuity (i.e. the "magnetic precursor"), is the time of flow of the charged fluid through the precursor (Lessaffre et al. 2004b, Eq. (60)). It is this determination of the shock age that has been adopted in the present paper.

Mon. Not. R. Astron. Soc. **000**, 1–?? (2008) Printed 22 December 2008 (MN LATEX style file v2.2)

Emission and cooling by CO in interstellar shock waves

D. R. Flower[1⋆], A. Gusdorf[1,2]
[1]*Physics Department, The University, Durham DH1 3LE, UK*
[2]*Institut d'Astrophysique Spatiale (IAS), Bâtiment 121, F-91405 Orsay, France*

Accepted 2008 December 15. Received 2008 December 14; in original form 2008 October 11

ABSTRACT

We have calculated emission by CO molecules from interstellar shock waves. Two approximations have been used to determine the population densities, n_J, of the rotational levels, J: steady state ($\partial/\partial t \equiv 0$) and statistical equilibrium ($\mathrm{d}/\mathrm{d}t \equiv 0$). An LVG approximation to the line transfer problem was adopted in both cases. We find that there can be substantial differences between the values of the integrated rotational line intensities calculated in steady state and in the limit of statistical equilibrium. On the other hand, although CO can be the dominant coolant towards the rear of the cooling flow which follows the dynamical heating of the gas, the rate of cooling computed assuming statistical equilibrium is likely to be reasonably accurate, given that the limit of statistical equilibrium is approached in this region.

Key words:

1 INTRODUCTION

Carbon monoxide is one of the most widely observed and important molecules in the interstellar medium. After H_2, it is the most abundant molecular species [$n(\mathrm{CO})/n(\mathrm{H_2}) \approx 10^{-4}$], containing much of the elemental carbon. Because it is heavier than H_2, CO has a smaller rotational constant [$B(\mathrm{CO}) = 1.92$ cm^{-1}, $B(\mathrm{H_2}) = 59.3$ cm^{-1}], and its lowest rotational transitions are readily observed from the ground at mm wavelengths. Higher rotational transitions, at shorter wavelengths, have been observed with the ISO satellite (Giannini et al. 2001). Being an 'almost homonuclear' molecule, CO has only a weak dipole moment (0.11 debye), and the radiative lifetime of its first rotationally excited level, $J = 1$, for example, is very large (1.4×10^7 s $= 0.44$ yr). The small dipole moment inhibits the development of large optical depths in the rotational transitions, $J{+}1 \rightarrow J$. However, owing to the large fractional abundance of CO, transitions between the lowest rotational levels, at least, become optically thick under the conditions in the interstellar medium. It follows that any modelling of the emission of CO, and the associated cooling, needs to incorporate a treatment of radiative line transfer.

In shock waves, the flow velocity of the gas changes more or less abruptly, depending on the physical conditions in the medium into which the shock propagates and its speed. Under these circumstances, it would be expected that the 'large velocity gradient' (LVG) approximation to radiative line transfer would be valid. This method was applied to the study of the cooling of warm molecular gas – such as is generated by the passage of a shock wave – by Neufeld & Kaufman (1993). A more recent implementation of the LVG model of line transfer is the RADEX code of van der Tak et al. (2007).

The determination of the line optical depths requires the knowledge of the population densities of the energy levels; but the populations depend, in turn, on the line optical depths, as re-absorption of a line photon results in population transfer. Whilst the LVG approximation reduces the line transfer problem to being local – the large velocity gradient implies that the line photons are absorbed 'on the spot' – it does not remove the mutual inter–dependence of the level populations and the line optical depths. In most implementations of the LVG approach, the level populations are assumed to be in statistical equilibrium, and they are determined self–consistently with the line optical depths by means of iterative, algebraic methods. However, in dynamically active regions, where large velocity gradients occur, other physical parameters, such as the density and the kinetic temperature, may also vary rapidly. Under these conditions, the assumption of statistical equilibrium when determining the level populations needs careful validation.

In the present paper, we evaluate the emission and cooling by the CO molecule in interstellar shock waves, propagating in molecular gas. We compare results obtained using a conventional LVG code (Gusdorf et al. 2008a, hereafter G08a) with the predictions of a dynamical determination of the CO level populations and line intensities. Specifically, we integrate the equations for the population densities in parallel with the equations describing the evolution of the phys-

⋆ E-mail: david.flower@durham.ac.uk

ical and chemical variables. This implementation not only eliminates the assumption of statistical equilibrium but obviates the need to solve iteratively for the level populations and the line optical depths. We find significant differences between predictions based on the conventional LVG method and the dynamical approach, as will be seen below.

In Section 2, we formulate our approach. Section 3 contains the numerical applications and comparisons, and, in Section 4, we make our concluding remarks.

2 FORMULATION

The equations describing the temporal evolution of the level populations may be written as

$$\frac{\mathrm{d}n_J}{\mathrm{d}t} = \sum_{J'} n_{J'} R(J' \rightarrow J) - n_J \sum_{J'} R(J \rightarrow J') \tag{1}$$

where n_J is the population density (cm^{-3}) of rotational level J and $R(J' \rightarrow J)$, $R(J \rightarrow J')$ are the total rates (s^{-1}) of population transfer from and to other rotational levels, J'. Transfer of population is induced by collisional and radiative processes. The principal collision partners are ortho– and para–H_2, H, and He, of which H_2 and H are dominant under the conditions of the models considered below. Radiative excitation and de-excitation occur through absorption and emission of photons at the frequencies of the rotational lines. The photon field is generated by collisional excitation of the molecule, followed by radiative decay, and there is a 'background' field, which, in practice, is taken to be the cosmic black–body radiation at temperature $T_{\mathrm{bb}} = 2.73$ K. When the assumption of statistical equilibrium is made, the lhs of Equ. (1) is set equal to zero, leaving a set of homogeneous, first–order algebraic equations for the level population densities, which are complemented by the closure relation

$$n(\mathrm{M}) = \sum_J n_J, \tag{2}$$

which states that the number density of molecular species M is the sum of the population densities of its rotational levels.

The equation of radiative transfer of the line photons takes the form

$$\frac{\mathrm{d}I_\nu}{\mathrm{d}\tau_\nu} = -I_\nu + S_\nu \tag{3}$$

where I_ν is the local radiation intensity at frequency ν, τ_ν is the optical depth at this frequency, and S_ν is the source function. We consider one–dimensional models, and τ_ν is the optical depth in this dimension, z, taken to be the direction of propagation of the shock wave. The expression for the source function is

$$S_\nu = \frac{2h\nu^3}{c^2} \frac{1}{\frac{n_J/g_J}{n_{J'}/g_{J'}} - 1} \tag{4}$$

where h is Planck's constant and c is the velocity of light; $g_J = 2J + 1$ and $g_{J'} = 2J' + 1$ are the degeneracies of the rotational levels J, J'. As we consider only dipole transitions, the upper level $J' = J + 1$. The dependence of the source function on the level population densities is explicit in Equ. (4). If the large–velocity–gradient assumption is made, the transfer equation (3) may be integrated to yield

$$I_{\nu_0} = S_{\nu_0}(1 - \mathrm{e}^{-\tau_{\nu_0}}) + B_{\nu_0}(T_{\mathrm{bb}})\mathrm{e}^{-\tau_{\nu_0}} \tag{5}$$

where ν_0 is the frequency at the line centre and B_ν is the Planck (black–body) function. The probability of escape of a photon, of frequency ν_0, from the region in which it is produced is

$$\beta = \frac{1 - \mathrm{e}^{-\tau_{\nu_0}}}{\tau_{\nu_0}}, \tag{6}$$

although other forms have been suggested in the literature. In particular, Neufeld & Kaufman (1993) proposed

$$\beta = \frac{1}{1 + 3\tau_{\nu_0}} \tag{7}$$

as being more appropriate in the case of a plane–parallel model. We shall compare below results obtained using both expressions for the escape probability, (6) and (7), **when calculating the level population densities. However, when evaluating the line temperatures, we used Equ. (6), which is appropriate to isotropic emission, because the line of sight will not be along the direction of propagation of the shock wave, in general.**

An approximation which is superior to the assumption of statistical equilibrium ($\mathrm{d}/\mathrm{d}t \equiv 0$) when solving Equ. (1) is that of steady state ($\partial/\partial t \equiv 0$). Then, $\mathrm{d}/\mathrm{d}t = v\mathrm{d}/\mathrm{d}z$, where v is the fluid flow velocity in the z-direction, and Equ. (1) takes the form of an ordinary, first–order differential equation, in which there appear, on the rhs, the dependent variables: dynamical, chemical, and the rotational level populations themselves. Such differential equations may be integrated in parallel by means of the method for solving 'stiff' ordinary differential equations developed originally by Gear (1971) and subsequently by A. C. Hindmarsh and his colleagues. The most recent implementation of this method is DVODE (http://www.llnl.gov/CASC/odepack/). By means of this technique, the level populations can be determined simultaneously with the physical and chemical variables, and iterative methods become redundant. The closure relation (2) was incorporated explicitly into the solutions, thereby ensuring conservation of the total CO population density. We note that Neufeld & Kaufman (1993) also integrated Equ. (1) by means of the Gear (1971) method; but they used this technique to determine the level populations at large times, when statistical equilibrium is attained, and not to determine the evolution of the level populations in parallel with the other dependent variables of the model, as is done here.

As is shown in Appendix A of G08a, the intensity of radiation at frequency ν in a given rotational line, observed using the background subtraction technique, is

$$I_{\mathrm{obs}}(\nu) = [B_\nu(T_{\mathrm{ex}}) - B_\nu(T_{\mathrm{bb}})]\left(1 - \mathrm{e}^{-\tau_\nu}\right) \tag{8}$$

where T_{ex} is the excitation temperature. The line radiation temperature is defined as

$$T_{\mathrm{R}} \equiv \frac{I_{\mathrm{obs}}c^2}{2k_{\mathrm{B}}\nu^2} \tag{9}$$

in which k_{B} is the Boltzmann constant, and the integrated line temperature (in K km s^{-1}) is obtained by integrating T_{R} with respect to the flow speed of the neutral fluid, $v(z)$.

As shown by Elitzur & Watson (1978), when statistical equilibrium applies, the population densities of successive rotational levels J and $J+1$ are related by

$$\frac{n_{J+1}}{n_J} = \frac{C_{J,J+1}}{C_{J+1,J} + A_{J+1,J}}$$

for an optically thin transition $J+1 \rightarrow J$. In this equation, $A_{J+1,J}$ is the spontaneous radiative transition probability and the collisional rates are connected through the detailed balance relation,

$$(2J+1)C_{J,J+1} = (2J+3)C_{J+1,J}\exp[-(E_{J+1}-E_J)/k_{\rm B}T],$$

where E denotes the energy of the level and T is the kinetic temperature. For electric dipole transitions, $A_{J+1,J} \propto (E_{J+1}-E_J)^3$ and $E_{J+1}-E_J \approx 2B(J+1)$, where B is the rotational constant. The rate of collisional de-excitation, $C_{J+1,J}$, is approximately independent of J.

3 RESULTS AND DISCUSSION

The validity of the assumption of statistical equilibrium is usually assessed by comparing the timescale for population transfer by collisions with a dynamical timescale, determined by the conditions of the flow. In the case of a shock wave, the latter may be taken to be the flow time of the neutral fluid through the relevant part of the shock wave. For the former timescale, one might take $[n({\rm H_2})q(J+1 \rightarrow J)]^{-1}$, where $q(J+1 \rightarrow J)$ is the rate coefficient for transfer of population between adjacent rotational levels through collisions with hydrogen molcules; $q(J+1 \rightarrow J) \approx 10^{-10}$ cm^3 s^{-1} is a representative numerical value, at kinetic temperatures of a few hundred kelvin, believed to be appropriate to many interstellar shock waves. Taking $n({\rm H_2}) = 10^4$ cm^{-3} for the density of the molecular gas yields a timescale for population transfer of 10^6 s $= 0.03$ yr. Given that this value is smaller, or much smaller, than typical flow times, it is tempting to conclude that the assumption of statistical equilibrium is valid. However, as we shall show, this conclusion is not necessarily correct.

In the cold, preshock gas, CO is found predominantly in its lowest rotational states. As the kinetic temperature increases, due to heating by the shock wave, more highly excited rotational states become populated through inelastic collisions, principally with H_2 and H. This process involves climbing the ladder of rotational energy levels, mainly in single-level steps ($J \rightarrow J+1$). Thus, to populate level $J+10$ from level J requires ten successive steps, enhancing the corresponding timescale by an order of magnitude, to 0.3 yr; but there is an additional effect acting which increases substantially the timescale for population transfer up the rotational ladder. By level $J=3$, the probability of spontaneous radiative decay, $A(3 \rightarrow 2) = 2.5 \times 10^{-6}$ s^{-1}, already exceeds the probability of collisional transfer upwards, to $J=4$, for the conditions adopted above. The A–values continue to increase with J and approach 10^{-3} for $J=20$. It follows that less than 1% of the population transferred by collisions from $J=17$ to $J=18$, for example, is available for subsequent transfer to $J=19$. We conclude that the timescale for population transfer to such highly excited rotational levels is typically of the order of 100 yr, which is comparable with the dynamical timescale, as will be seen below. **If the collisional rate coefficients are (artificially) enhanced by a factor of 100, the delay in populating the excited states, following the temperature rise, practically disappears, as we have verified numerically.**

We shall compare first the numerical results obtained for representative C-type ('continuous') and J-type ('jump') shock models, and then for a CJ-type model, which incorporates both a J-discontinuity and a magnetic precursor.

3.1 C-type shocks

We consider a C-type shock wave of speed $v_{\rm s} = 30$ km s^{-1}, propagating into gas of density $n_{\rm H} \equiv n({\rm H}) + 2n({\rm H_2}) = 10^5$ cm^{-3}; the initial value of the transverse magnetic field strength is $B = 200$ μG. These parameters are representative of shocks in molecular outflows. In Fig. 1 are plotted the fractional population densities, $n_J/n({\rm CO})$, of a sample of the rotational levels of CO, $J = 0$, 6, 12, 16. In the upper panel of Fig. 1 are the statistical equilibrium values, in the lower panel are the steady state solutions.

Figure 1 demonstrates that the approximation of statistical equilibrium leads to the population densities of the highly excited rotational levels, such as $J=12$ and $J=16$, being overestimated immediately beyond the region in which the initial rise in the temperature of the neutral fluid takes place. In effect, there is a delay in populating such excited states, in response to the rise in temperature, compared with the predictions of statistical equilibrium. Following the discussion above, and allowing for the higher preshock density $[n({\rm H_2}) = 10^5$ cm$^{-3}]$ of the model illustrated in Fig. 1, we expect the timescale for populating the high rotational levels, following the temperature rise, to be of the order of 10 yr, whereas the temperature increases in a flow time of approximately 1 yr. Subsequently, as the temperature begins to fall and the gas to be compressed (thereby reducing the timescale for collisional population transfer), the solutions in the two cases become indistinguishable, as may be seen in Fig. 1.

We mentioned in the Introduction that one of the motivations for studying the emission by CO is its potential significance as a coolant; this is especially true in shock waves, owing partly to the collisional dissociation of molecular hydrogen in the hot gas, but mainly to the large rotational constant of H_2, which causes the rates of collisional excitation of its rotational levels to decrease rapidly at temperatures below about 500 K.

In Fig. 2, we show the rates of cooling per unit volume by CO, as predicted by the statistical equilibrium and the steady state approximations, and by H_2. **The cooling rate was evaluated as the rate of removal of kinetic energy from the gas, the difference of collisional excitation (kinetic energy loss) and de-excitation (kinetic energy gain) processes:**

$$\sum_J (n_J C_{J,J+1} - n_{J+1}C_{J+1,J})(E_{J+1}-E_J).$$

We emphasize that, as above, the results refer to the *same* shock model, and, in particular, the differences in the CO cooling rate have not been fed back into the calculation of

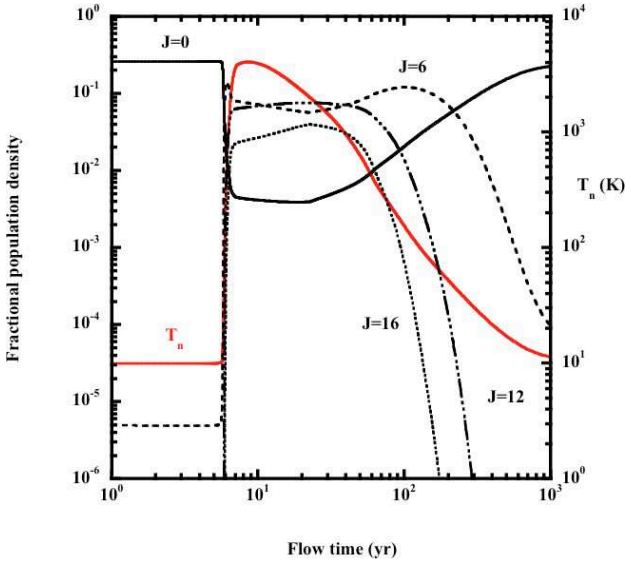

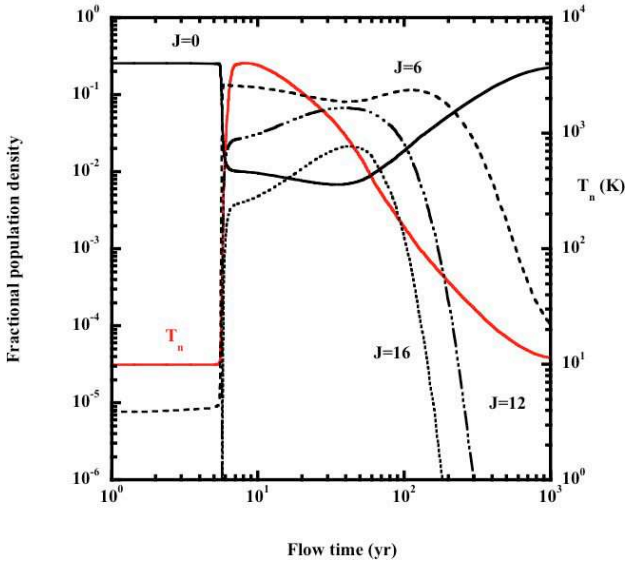

Figure 1. The fractional population densities, $n_J/n(\mathrm{CO})$, of the rotational levels $J = 0$, 6, 12, 16 of CO, as functions of the flow time of the neutral fluid through a C-type shock wave; see Section 3.1. In the upper panel are plotted the statistical equilibrium values, in the lower panel are the steady state solutions. The temperature of the neutral fluid, T_n, is shown also.

the thermal profile, which remains identical in the two cases. As might have been anticipated from the comparison of the level populations, the statistical equilibrium solution overestimates, by approximately an order of magnitude, the rate of CO cooling in the region immediately beyond the temperature rise. The two calculations of the rate of cooling by CO become identical subsequently, as the gas cools and is compressed. Cooling by H_2 dominates initially but then falls below that of CO as the temperature decreases. However, by

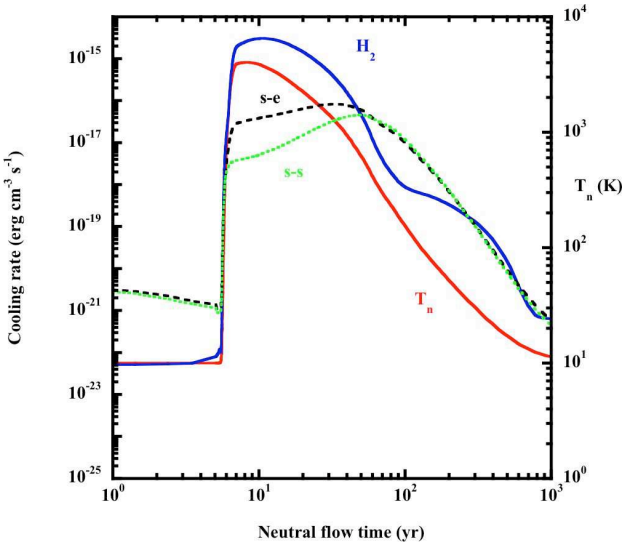

Figure 2. The rates of cooling per unit volume by CO, as predicted by the statistical equilibrium (s–e) and the steady state (s–s) approximations, and by H_2, for the same shock model as in Fig. 1: $v_\mathrm{s} = 30$ km s^{-1}, $n_\mathrm{H} = 10^5$ cm^{-3}, $B = 200$ μG. The temperature of the neutral fluid, T_n, is shown also.

the time that the CO cooling comes to exceed that by H_2, the two calculations of the CO cooling rate have converged.

3.2 J-type shocks

It might be anticipated that the significance of the delay in transferring population up the CO rotational ladder would be greater behind the 'discontinuity' in J-type shock waves, at which the temperature rise is much more rapid than in C-type shock waves. Accordingly, we compared the fractional populations of the CO rotational levels, in statistical equilibrium and steady state, for a J-type (single–fluid) model in which $v_\mathrm{s} = 25$ km s^{-1}, $n_\mathrm{H} = 10^4$ cm^{-3}, and $B = 10$ μG. Our expectation is seen to be justified only partially by the numerical results in Fig. 3. The time delay between the statistical equilibrium and steady state solutions is of the order of one year, which is less than the estimate of 10^2 yr made above, for the preshock density $n_\mathrm{H} = 10^4$ cm^{-3} of this model. A combination of factors results in the reduced delay time: the compression of the gas (by a factor of 4) at the J-'discontinuity', which continues into the cooling flow; the high kinetic temperature behind the 'discontinuity', which enhances the collisional excitation rates; and the dissociation of H_2 to H, which leads to a higher perturber density ($n(\mathrm{H}) = n_\mathrm{H}$ in atomic gas, whereas $n(\mathrm{H_2}) = n_\mathrm{H}/2$ in molecular gas. Furthermore, the rate coefficients for rotationally inelastic collisions of CO with H are larger than for collisions with H_2 by a factor of typically 3–4).

Once again, however, the effects on the thermal balance of the medium are mitigated by the high postshock temperature, which enhances the rate of cooling by molecular hydrogen. Although H_2 is collisionally dissociated in the hot gas behind the 'discontinuity', CO is dissociated chemically in this region, owing to the reaction H(CO, OH)C, which is rapid at high temperatures; see Fig. 4. Consequently, cooling by H_2 dominates.

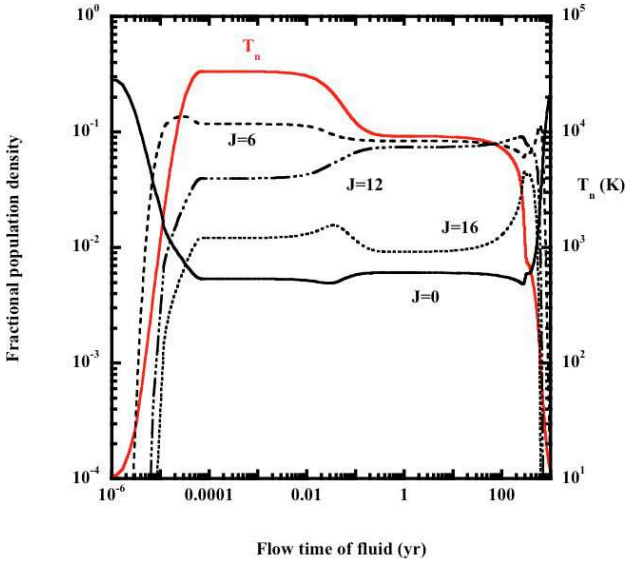

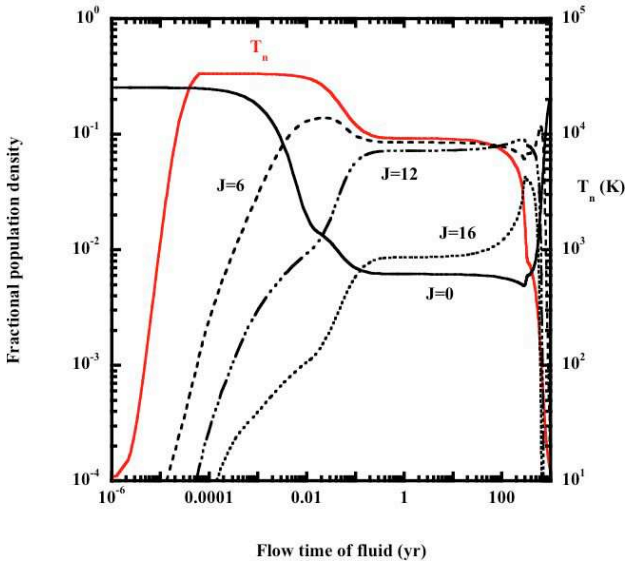

Figure 3. The fractional population densities, $n_J/n(\mathrm{CO})$, of the rotational levels $J = 0$, 6, 12, 16 of CO, as functions of the flow time of the neutral fluid through a J-type shock wave; see Section 3.2. In the upper panel are plotted the statistical equilibrium values, in the lower panel are the steady state solutions. The temperature of the fluid is plotted also. Results are shown for $v_\mathrm{s} = 25$ km s^{-1}, $n_\mathrm{H} = 10^4$ cm^{-3}, and $B = 10$ μG; see text, Section 3.2.

It should be noted that, in the models of J-type shock waves, the J-'discontinuity' is smoothed numerically, by introducing an artificial viscosity; see Flower et al. (2003).

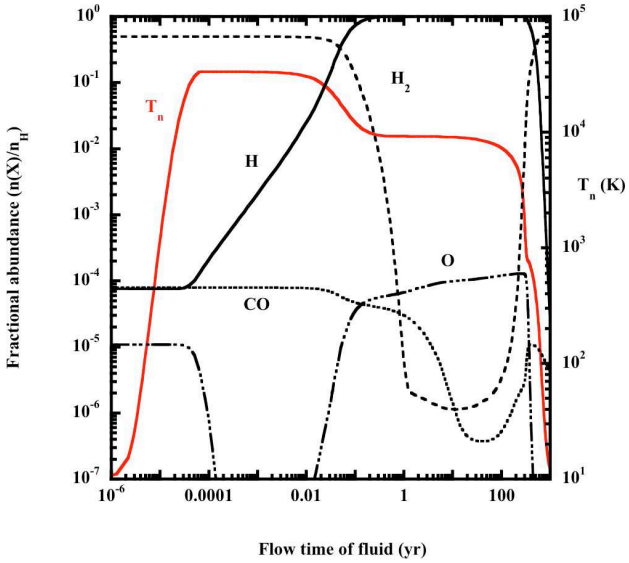

Figure 4. Illustrating the collisional dissociation of H_2 and the chemical dissociation of CO, in the reaction H(CO, OH)C, which is followed by H(OH, H_2)O; both these reactions are rapid in the hot gas, where the hydrogen is in mainly atomic form. The J-'discontinuity' is smoothed numerically by means of an artificial viscosity; see text, Section 3.2. Results are shown for $v_\mathrm{s} = 25$ km s^{-1}, $n_\mathrm{H} = 10^4$ cm^{-3}, and $B = 10$ μG.

3.3 CJ-type shocks

In a recent study (Gusdorf et al. 2008b, hereafter G08b), we modelled the emission of H_2, SiO, and CO from shocks in molecular outflows, particularly L1157 B1. We confirmed a result of earlier work, which showed that, in order to fit the observations of the rotational and rovibrational lines of H_2, CJ-type models, which comprise a magnetic precursor and a J-discontinuity, are necessary. The discontinuity is introduced at a specified value of the flow time of the charged fluid, identified with the evolutionary age of the shock wave (see G08b Appendix C).

In Fig. 5, we compare the integrated CO line temperatures (K km s^{-1}) predicted by the two approximations to the CO level populations, statistical equilibrium and steady state. The upper panel of Fig. 5 contains the results of the two models which define the envelope of the results plotted in Fig.B.1 of G08b: a shock speed $v_\mathrm{s} = 20$ km s^{-1}, preshock density $n_\mathrm{H} = 10^4$ cm^{-3}, and the preshock magnetic field strengths, B, and shock ages, t_s, specified in the Figure. The ISO oservations of the blue lobe of L1157 (Giannini et al. 2001) are plotted also. The lower panel of Fig. 5 contains the corresponding steady state results.

Figure 5 shows that, whilst the variation of the line intensities with the emitting rotational level, as predicted by the two approximations, is broadly similar, the differences between them are nonetheless significant. In the limit of statistical equilibrium, both models yield line intensities which exceed those observed for $15 \leqslant J \leqslant 20$, whereas the steady state results pass through or fall somewhat below the observed points. G08b commented that these high-J observations provide inadequate discrimination between the models. Unfortunately, combining high-J (satellite) and low-J (ground based) observations of L1157 (Giannini et

al. 2001, Hirano & Taniguchi 2001) involves using measurements made with different instruments and beam sizes and is consequently a non-trivial task.

We mentioned in Section 2 that different expressions have been suggested for the line escape probability. In Fig. 6 are compared the results obtained for the specified CJ-type model, using either Equ. (6), or Equ. (7) of Neufeld & Kaufman (1993), for the escape probability. We see that the form adopted for the escape probability has negligible consequences for the line intensities: the populations of the lower rotational levels are thermalized by collisions, whereas transitions from higher levels are optically thin.

4 CONCLUDING REMARKS

We have investigated the implications for interstellar shock waves of the finite time which is required to populate by collisions the excited rotational states of the CO molecule. We find that there is a significant delay in populating the highly excited states in both J-type and C-type shock waves. In CJ-type shock waves, which are believed to be relevant to the emission from dynamically young flows, such as L1157, allowance for the finite flow speed has consequences for the predicted values of the integrated rotational line intensities over the entire range of quantum number ($0 \leqslant J \leqslant 20$) that we considered.

Carbon monoxide was selected for study because of its importance as a coolant of molecular gas. In practice, our calculations suggest that departures from statistical equilibrium have limited consequences for the rate of cooling of the medium. Although CO can become the principal coolant in shock waves, as the kinetic temperature falls, following the initial dynamical heating, the CO cooling rate has become, by this point in the flow, almost the same in steady state as in the limit of statistical equilibrium.

The results presented here for CO beg the question of the importance of departures from statistical equilibrium in the case of SiO, studied by G08a,b, and so we have performed separate calculations to investigate the significance of these effects in the context of SiO emission. Owing to the lower elemental abundance of silicon, relative to carbon, SiO is not a significant coolant of the medium. The dipole moment of SiO in its ground vibrational state (3.1 debye) is much larger than that of CO, and the radiative transition probabilities of the corresponding transitions, $J + 1 \rightarrow J$, in SiO are approximately 40 times larger than in CO. As a consequence of the larger radiative transition probabilities, the timescale for climbing the rotational ladder of SiO is larger than for CO; the optical depths in the lines of SiO tend to be larger also. G08a,b considered rotational transitions in SiO up to $11 \rightarrow 10$, as observed by Nisini et al. (2007). Owing to the larger reduced mass of SiO, the level $J = 11$ lies only 138 K above the $J = 0$ ground state, as compared with 365 K in CO. Thus, the emission from SiO tends to arise from the compressed and relatively cold gas, towards the rear of the cooling flow of the shock wave. **This tendency is reinforced by the chemical delay associated with the formation of SiO in the gas phase, if it forms by oxidation of Si that is released by the sputtering of silicate grains (cf. Gusdorf et al. 2008a).** As a consequence, departures from statistical equilibrium prove to be less important for the emission of SiO than CO. On the other hand, the integrated intensities of the rotational transitions of SiO are more sensitive to the form adopted for the escape probability [Equ. (6) or Equ. (7)].

ACKNOWLEDGMENTS

Antoine Gusdorf and the University of Durham acknowledge the support of the European Commission under the Marie Curie Research Training Network "The Molecular Universe" MRTN-CT-2004-512302. **We thank the referee for some perceptive comments.**

REFERENCES

Elitzur M, Watson W. D. 1978, A&A, 70, 443
Flower D. R., Le Bourlot J., Pineau des Forêts G., Cabrit S. 2003, MNRAS, 341, 70
Gear C. W., 1971, Numerical Initial Value Problems in Ordinary Differential Equations, Prentice-Hall (Englewood Cliffs, NJ)
Giannini T., Nisini B., Lorenzetti D. 2001, ApJ, 555, 40
Gusdorf A., Cabrit S., Flower D. R., Pineau des Forêts G. 2008a, A&A, 482, 809
Gusdorf A., Pineau des Forêts G., Cabrit S., Flower D. R. 2008b, A&A, in press
Hirano N., Taniguchi Y. 2001, ApJ, 550, L219
Neufeld D. A., Kaufman M. J. 1993, ApJ, 418, 263
Nisini B., Codella C., Giannini T., Santiago Garcia J., Richer J. S., Bachiller R., Tafalla M. 2007, A&A, 462, 163
Van der Tak, F. F. S., Black, J. H., Schöier, F. L., Jansen, D. J., van Dishoeck, E. F. 2007, A&A. 468, 627

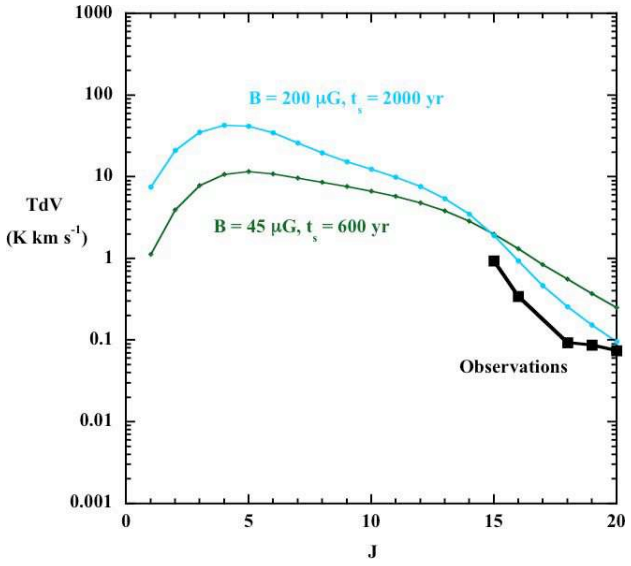

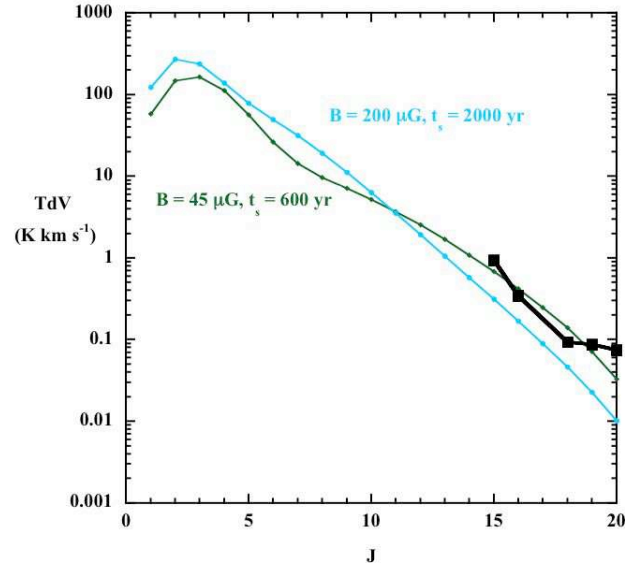

Figure 5. The integrated line CO rotational intensities, $T\mathrm{d}V$ (K km s^{-1}), predicted in the statistical equilibrium (upper panel) and steady state (lower panel) approximations. Results are shown for two models: $v_\mathrm{S} = 20$ km s^{-1}, $n_\mathrm{H} = 10^4$ cm^{-3}, $B = 200$ μG and $t_\mathrm{S} = 2000$ yr (full blue circles), $B = 45$ μG and $t_\mathrm{S} = 600$ yr (full green lozenges); see text, Section 3.3. The observations of L1157 B1 compiled by Giannini et al. (2001) are plotted in both panels as full black squares.

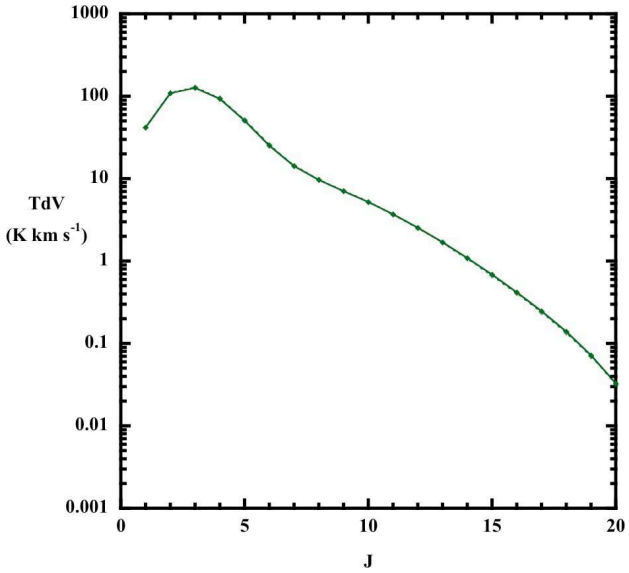

Figure 6. A comparison of the integrated line CO rotational intensities, $T\mathrm{d}V$ (K km s^{-1}), predicted in steady state, using different expressions for the escape probability: Equ. (6) (broken curve); Equ. (7) of Neufeld & Kaufman (1993) (full curve); the two curves appear superposed. Results are shown for the CJ-type model in which $v_\mathrm{S} = 20$ km s^{-1}, $n_\mathrm{H} = 10^4$ cm^{-3}, $B = 45$ μG and $t_\mathrm{S} = 600$ yr; see text, Section 3.3.

Mon. Not. R. Astron. Soc. **382,** 133–138 (2007) doi:10.1111/j.1365-2966.2007.12420.x

The excitation of molecular hydrogen by atomic hydrogen in astrophysical media

S. A. Wrathmall,★ A. Gusdorf and D. R. Flower
Department of Physics, The University of Durham, Durham DH1 3LE

Accepted 2007 August 27. Received 2007 August 3; in original form 2007 July 17

ABSTRACT

We report calculations of rate coefficients for the rovibrational excitation of H_2 and HD by H. The calculations relate explicitly to non-reactive scattering, excluding the proton-exchange channels. For vibrationally inelastic transitions, the new rate coefficients at $T \approx 1000$ K are larger than the results of earlier calculations in which the vibrational motion was treated approximately, by means of a simple harmonic oscillator model. As a result, much better agreement is obtained with the empirical estimates by Allers et al. of the rate coefficients for vibrational relaxation of the levels $(v, j) = (1, 3)$ and $(2, 3)$ of H_2. However, the effects of the new data on the results of illustrative astrophysical models – of a C-type shock wave and of the gravitational collapse of a condensation of the primordial gas – are less pronounced than the changes to the rate coefficients for vibrationally inelastic transitions might suggest; we explain why this is the case.

Key words: molecular data – shock waves – ISM: molecules – cosmology: miscellaneous

1 INTRODUCTION

As a consequence of its high elemental abundance, hydrogen is usually the most abundant molecular species and can be also the most abundant atomic species in interstellar clouds. In some regions, atomic and molecular hydrogen have comparable number densities; examples are shock-heated gas and photon-dominated regions (PDRs). In such structures, the kinetic temperature is enhanced relative to the ambient gas, and collisions with H contribute significantly to the rotational excitation of H_2 and may dominate its rovibrational excitation. In the primordial gas, subsequent to the recombination of H^+ with electrons at a redshift $z \approx 1000$, the most abundant species was H, followed by He; but there were trace amounts (fractional abundance $\approx 10^{-6}$) of H_2 (Stancil, Lepp & Dalgarno 1998). Although its fractional abundance was low, molecular hydrogen and its singly deuterated form, HD, were the only species which could contribute significantly to the cooling of the gas during the early stages of gravitational collapse of inhomogeneities in the medium.

H–H_2 and H–HD are ostensibly the simplest atom–molecule systems, involving only three singly charged nuclei and three electrons. Accordingly, it might be anticipated that the cross-sections for rotational and rovibrational excitation of H_2 and HD by H would be well established. However, this is not the case: the H–H_2 interaction comprises a very shallow Van der Waals potential well (≈20 K), where the atom–molecule interaction is only weakly anisotropic. Because the region of the Van der Waals minimum is crucial in calculations of rotational excitation cross-sections at low collision energies, such calculations impose stringent requirements on the accuracy to which the absolute H–H_2 interaction energy must be calculated. Furthermore, as the collision energy increases, approaching values comparable to the barrier to proton exchange (≈5000 K), reactive scattering can occur. At such energies, the H–H_2 interaction gives rise to strong collisional coupling between the vibrational manifolds of the molecule. As a consequence, (i) the rovibrational cross-sections converge only slowly with the size of the set of rovibrational states and (ii) more than usual care must be taken with the representation of the rovibrational wavefunctions of the molecule.

In spite of the difficulties outlined above, the H–H_2 system offers a perhaps unique opportunity to perform essentially exact calculations of rovibrational cross-sections. Owing to its low mass, and hence large rotational constant, there are 'only' 318 bound rovibrational levels, with the largest value of the rotational quantum number being $j = 29$. Consequently, quantum mechanical calculations using the exact coupled-channels method, with a complete or near-complete basis of bound rovibrational states, might be envisaged.

In an earlier paper (Wrathmall & Flower 2007), we presented and discussed the results of our calculations of cross-sections for the rovibrational excitation of H_2 by H. In this work, we extend the calculations to the H–HD system. Unlike H_2, HD has a small but finite permanent dipole moment. It follows that radiative transitions which change the rotational quantum number, j, by $\Delta j = 1$ are permitted in HD, whereas the (electric quadrupole) selection rule in H_2 is $\Delta j = 2$. Similarly, in collisions with H, transitions of HD involving odd values of Δj can occur, even in the case of non-reactive scattering, when there is no exchange of protons. On the other hand, during non-reactive scattering of H on H_2, only those transitions with even values of Δj are permitted, thus preserving ortho-H_2 (j odd) and para-H_2 (j even) as distinct species.

★E-mail: s.a.wrathmall@durham.ac.uk

We will discuss the differences between the results of the present calculations of the rate coefficients for rovibrational excitation of H_2 and HD by H and those published previously, which made use of an earlier H–H_2 interaction potential and a simple harmonic oscillator (SHO) approximation to the vibrational motion. We illustrate the effects of the new rate coefficients on astrophysical models. Specifically, we consider a C-type shock wave and the gravitational collapse of an inhomogeneity in the primordial gas.

2 CALCULATIONS OF CROSS-SECTIONS AND RATE COEFFICIENTS

Our approach to solving the problem of H–H_2 scattering was described in a previous paper (Wrathmall & Flower 2007). In essence, we adopted a fully quantum mechanical approach, without further approximation to the scattering equations. Furthermore, the rovibrational wavefunctions of the isolated H_2 molecule were computed exactly. The accuracy of the cross-sections is then limited by (i) that of the H–H_2 interaction potential and (ii) the completeness of the set of rovibrational states representing the H_2 molecule. As regards the potential, we used the most recent determination (Mielke, Garrett & Peterson 2002), which should also be the most reliable, according to the precision quoted for the calculations. The H_2 rovibrational basis set has been extended to comprise the energetically lowest 54 levels of ortho- and para-H_2, that is, 108 of the total of 318 bound levels; to our knowledge, this is the largest calculation of its kind to date for the H–H_2 system. In the case of HD, we included the lowest 120 of the total of 399 bound rovibrational levels.

Using the above basis sets and the same ab initio interaction potential, we generated the cross-sections on a grid of barycentric collision energies extending to 60 000 K. The expansion of the interaction potential in terms of the inter- and the intra-molecular coordinates differs between H_2 and HD because of the shift of the centre of mass of HD from the mid-point of the internuclear axis. In order to obtain rate coefficients as functions of the kinetic temperature, T, of the gas, one has to integrate over a Maxwellian velocity distribution. Care must be taken to ensure that the grid of collision energies is adapted to the opening of new thresholds: the cross-sections vary relatively rapidly with energy as threshold is approached, and so the cross-sections must be calculated for collision energies which are sufficiently close to threshold to define this increase satisfactorily. The rate coefficients were computed numerically, on a grid of temperatures extending to 6000 K. We interpolated between the grid points by means of cubic splines in order to be able to use a simple quadrature method, in practice, the trapezoidal rule. For the purposes of subsequent applications, described in Section 4, the rate coefficients have been fitted to the following function of temperature, T:

$$q(T) = a + \frac{b}{t} + \frac{c}{t^2},$$

where $t = 10^{-3}T + \delta$, and $\delta = 1.0$ ensures that the rate coefficients remain well behaved at low T. The results of these fits are available from http://ccp7.dur.ac.uk/pubs.html.

3 RESULTS

3.1 H–H_2

In the previous section, we referred to the difficulties involved in computing the H–H_2 interaction to an accuracy which is sufficient for the calculation of rotational excitation cross-sections at low collision energies. The interaction potential that we have employed (Mielke et al. 2002) yields lower values of these cross-sections, as threshold is approached, than the earlier potential of Boothroyd et al. (1996). On the other hand, the use of exact vibrational wavefunctions, in this work, gives rise to a more rapid increase from threshold of cross-sections for rovibrationally inelastic scattering than when SHO functions are adopted. For a more complete discussion of the determination of the cross-sections for H–H_2 scattering, the reader is referred to paper of Wrathmall & Flower (2007). We summarize below the analogous results for H–HD collisions.

3.2 H–HD

The electrostatic interaction between H and HD is identical to that between H and H_2, but the centre of mass of HD is displaced from the mid-point of its internuclear axis. As the (Jacobi) coordinates of the incoming atom are expressed relative to the centre of mass of the molecule, the corresponding interaction potential contains terms which give rise to inelastic scattering in which the rotational quantum number, j, of the HD molecule changes by both even and odd integers, Δj. For example, transitions with $\Delta j = 1$, forbidden in non-reactive H–H_2 scattering, are allowed in collisions of H with HD.

In Fig. 1, we compare the results of calculations of the pure rotational (de-excitation) cross-sections from $(v, j) = (0, 1)$ and $(0, 2)$ to the $(0, 0)$ ground state of HD. The calculations were performed using the most recent H–H_2 potential (Mielke et al. 2002) and either a SHO approximation to the vibrational wavefunctions or their 'exact' numerical representations. Comparing with the corresponding results for the $(0, 2) \rightarrow (0, 0)$ transition in H_2, we find a broadly similar trend, with the SHO model giving rise to a higher maximum cross-section and tending to the 'exact' cross-section at high collision energies, E. The H–HD cross-section is smaller at $E =$ 60 000 K than is the case for H–H_2; this difference relates to the presence of additional terms, of odd parity, in the H–HD interaction potential, which 'dilute' the even parity terms, responsible for transitions with Δj even. The rate of increase from threshold of the cross-sections plotted in Fig. 1 may be seen to be similar in the two models (SHO and 'exact'), whereas the SHO model gives rise to a slower increase in the case of H–H_2 scattering. We believe that this difference is attributable to the larger reduced mass of HD; this results in smaller separations of the rotational energy levels, which are consequently lower in the molecular potential well, where the harmonic approximation is more valid.

In Fig. 2 are compared exact and SHO results for vibrationally inelastic transitions out of $v = 1$. The $(1, 2) \rightarrow (0, 0)$ cross-section exhibits trends similar to those observed for H–H_2 scattering, with the 'exact' cross-section being much larger than is predicted by the SHO model, near threshold; this cross-section is smaller in absolute magnitude than the cross-section for the corresponding transition in H_2, and is also smaller than the $(1, 1) \rightarrow (0, 0)$ cross-section in HD, as may be seen from Fig. 2. Once again, these differences are related to the presence of odd parity terms in the H–HD interaction potential.

3.3 Comparison with previous results for vibrational relaxation of H_2

Allers et al. (2005, table 6) listed determinations of the rate coefficients for vibrational relaxation of the level $(v, j) = (1, 3)$ of H_2 to all lower rotational levels of the $v = 0$ manifold, and similarly for

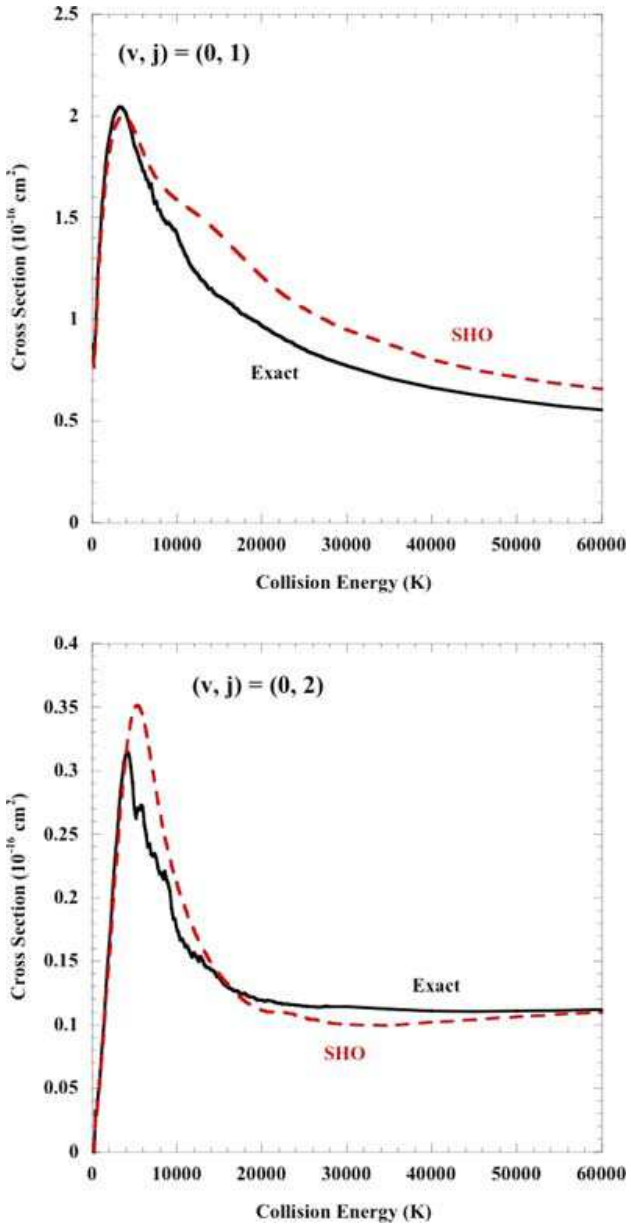

Figure 1. A comparison of cross-sections for de-excitation of the indicated level (v, j) to the $v = 0, j = 0$ ground state of HD in collisions with H; E is the barycentric collision energy, expressed in kelvin through division by Boltzmann's constant.

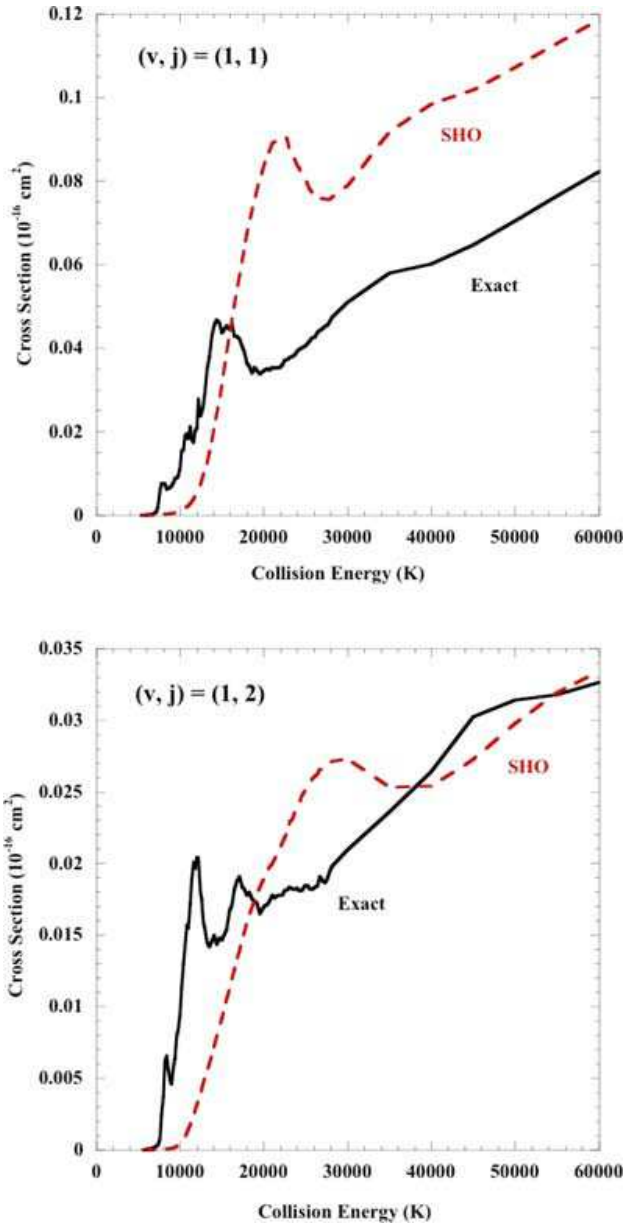

Figure 2. A comparison of cross-sections for de-excitation of the indicated level (v, j) to the $v = 0, j = 0$ ground state of HD in collisions with H; E is the barycentric collision energy, expressed in kelvin through division by Boltzmann's constant.

$(v, j) = (2, 3)$ to $v = 0$ and $v = 1$, at $T = 1000$ K, along with their own estimates, based on the observations of the Orion bar PDR; their tabulated values are reproduced in Table 1, where the results of this work have been incorporated. To our rate coefficients for non-reactive scattering, computed explicitly, we have added estimates of the contributions of the reactive scattering channels, using the prescription of Le Bourlot, Pineau des Forêts & Flower (1999). For $(v, j) = (1, 3)$, the estimated reactive scattering contribution is 54 per cent of the total, and for $(v, j) = (2, 3)$, the contribution of reactive scattering is 57 per cent. Flower & Roueff (1998) have observed that the quasi-classical trajectory calculations of Garcia & Laganà (1986) and Mandy & Martin (1993) show that the reactive and the non-reactive contributions to the rate coefficient for vibrational relaxation $v = 1 \rightarrow v = 0$ at $T = 300$ K of H_2 by H are related by $q_r \approx 2q_{nr}$. This relationship, which probably relates to the larger number of final rotational states accessible in reactive scattering, where j may change by both even and odd integers, is consistent with the present estimate of the contribution of the reactive scattering channels to the total rate coefficient for vibrational relaxation of H_2. None the less, the contribution of the reactive scattering channels remains a significant source of uncertainty, which can be removed only by quantum mechanical calculations which allow for proton exchange.

In the case of HD, the contribution of reactive scattering may be expected to be smaller, by a factor of 2, as only one proton is available for exchange. We have not applied any correction for

Table 1. Values of the total rate coefficients for vibrational relaxation of the specified upper rovibrational level, (v, j), of H_2, in units of $cm^3\,s^{-1}$. The numerical values were evaluated for $T = 1000$ K by summing the rate coefficients from the initial level, (v, j), to all lower levels with $v' < v$. Numbers in parentheses are powers of 10.

	$(v, j) = (1, 3)$	$(v, j) = (2, 3)$
Sternberg & Dalgarno (1989)	5.5 (−10)	7.5 (−10)
Mandy & Martin (1993)	6.3 (−12)	3.6 (−11)
Le Bourlot et al. (1999)	6.3 (−13)	9.2 (−13)
Allers et al. (2005)	5.4 (−11)	7.9 (−11)
This work (see Section 3.3)	1.5 (−11)	1.4 (−10)

reactive scattering of H on HD. Cooling by HD is significant in the context of the second application considered below (in Section 4.2), where pure rotational excitation within the $v = 0$ vibrational state, at temperatures $T \lesssim 1000$ K, is dominant. In this case, the contribution of exchange scattering may be expected to be small.

We note the wide range of the various determinations, reported in Table 1, owing to differences in the calculations of the H–H_2 interaction potential, representations of the vibrational eigenfunctions and treatments of the collision problem. We note also that the results of the present, ab initio study are in remarkably good agreement with the empirical estimates of Allers et al. The discrepancies with the earlier study of Le Bourlot et al. are attributable essentially to the improved representation of the vibrational eigenfunctions in this work, rather than changes in the H–H_2 interaction potential, for which we have adopted the results of the calculations of Mielke et al. (2002), whereas Le Bourlot et al. (1999) used the potential calculated by Boothroyd et al. (1996). We believe that the long-standing uncertainties in the rate coefficients for rovibrational excitation of H_2 (and HD) by H have finally been put to rest. Allers et al. (2005) are to be congratulated on their empirical determinations, particularly as the derivation of atomic and molecular data from astronomical observations is a procedure fraught with dangers for the unwary.

4 ILLUSTRATIVE APPLICATIONS

Although the changes (between the present and the previous results of Le Bourlot et al. 1999) in the values of individual rate coefficients at a given temperature are substantial, it does not follow automatically that the consequences for astrophysical models will be as significant. Even when the dominant excitation mechanism is collisions with H atoms, the populations of the rovibrational levels of H_2 depend on the relative importance of radiative (electric quadrupole) and collisional de-excitation. If the density is sufficiently high, collisional de-excitation dominates and the relative level populations tend to a Boltzmann distribution. The values of the collisional rate coefficients are then irrelevant, except in so far as they determine the 'critical density', at which the Boltzmann distribution begins to be approached. At densities much less than the critical density, collisional excitation is followed by radiative decay, and so the collisional excitation rates determine the emission line intensities. However, the spontaneous transition probabilities of H_2 are small, because electric dipole transitions are not allowed. Consequently, the critical density tends to be low, and regimes of even lower density may have only limited significance, in the context of the model.

With the above considerations in mind, we present some illustrative calculations, comparing models in which the current and the former H–H_2 rate coefficients have been employed.

4.1 C-type shock waves in molecular clouds

The rate coefficients for the rovibrational excitation of H_2 by H may be expected to play a significant role in C-type shock waves, propagating in molecular gas. Shock wave heating leads to partial dissociation of H_2, enriching the gas in atomic H. Rotational and particularly rovibrational excitation of H_2 takes place, under conditions in which the excited vibrational levels are depopulated principally by spontaneous radiative decay to lower vibrational levels, rather than collisionally. Under these circumstances, the relative populations of the vibrational manifolds do not approach a Boltzmann distribution.

In Fig. 3, we plot the 'excitation diagram' of H_2 for a C-type shock model with the following parameters: shock speed $v_s = 30\,km\,s^{-1}$, pre-shock gas density $n_H = 10^4\,cm^{-3}$ and pre-shock magnetic field strength, transverse to the direction of the (one-dimensional) flow, $B = 100\,\mu G$. The initial chemical composition of the gas was calculated assuming that a steady state prevailed.

If the populations of the rovibrational levels conformed to a Boltzmann distribution at a given kinetic temperature, T, the data points in Fig. 3 would fall on a single straight line, whose gradient is proportional to T^{-1}; in practice, this is not the case. However, within each vibrational manifold, the rotational levels fall approximately on straight lines corresponding to temperatures which tend to increase with the vibrational quantum number, v. Differences are apparent, for $v > 0$, between the results obtained using the present H–H_2 rate coefficients and those of Le Bourlot et al. (1999).

The results plotted in Fig. 3 are readily understandable in the light of the previous discussion. For the populations of the levels of the $v = 0$ manifold, only the vibrationally elastic (and rotationally inelastic) rate coefficients are important, for which the 'old' and the 'new' values do not differ substantially at the temperatures relevant to the formation of the corresponding emission lines. On the other hand, for vibrationally excited levels, the new rate coefficients yield larger populations and column densities. None the less, the

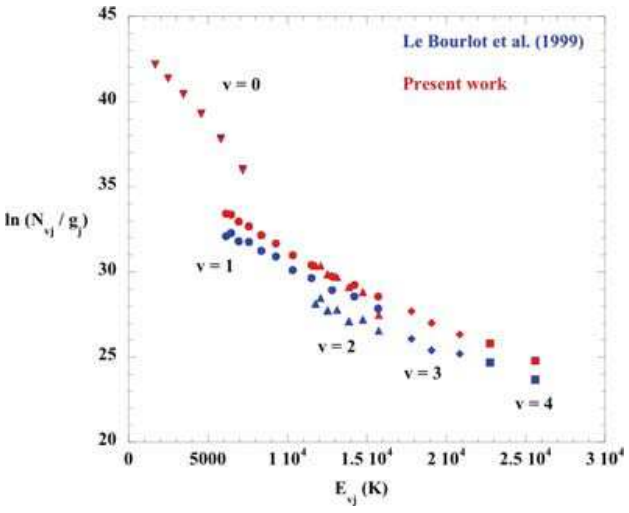

Figure 3. The excitation diagram computed for a C-type shock model (see the text Section 4.1), using the H–H_2 rate coefficients of Le Bourlot et al. (1999) (in blue) and the present values (in red). Results are plotted for rotational levels in vibrational manifolds $0 \leqslant v \leqslant 4$. For $v = 0$, the blue and the red symbols overlap.

changes are not as large as might have been anticipated from a glance at Table 1. The gas which is heated in the shock wave undergoes compression also, leading to an approximate thermalization of the populations of the rotational levels within a given vibrational manifold. Furthermore, to the larger rates of rovibrational excitation corresponds a higher rate of cooling by H_2. Because H_2 is a major coolant, the kinetic temperature falls, thereby reducing (exponentially) the rates of rovibrational excitation. In other words, there is a feedback loop which maintains the rate of cooling by H_2 at an approximately constant value.

4.2 Gravitational collapse of an inhomogeneity in the primordial gas

It is believed that the initial gravitational collapse of inhomogeneities in the primordial gas was made possible through radiative cooling by the trace amounts of molecular hydrogen which were produced in the post-recombination era (Palla, Salpeter & Stahler 1983). The cooling by HD can be comparable to that by H_2, owing to: (i) chemical fractionation, which enhances the deuterium content of molecular hydrogen; (ii) the lower rotational constant of HD, which makes its rotational levels more energetically accessible and (iii) the fact that HD has a permanent electric dipole moment, and hence transitions between adjacent rotational states can occur.

We have run a model of gravitational collapse of a spherical condensation of the primordial gas, starting from the conditions of the primordial gas at a redshift $z \approx 40$ and attaining $z \approx 10$ asymptotically. A comparison of the thermal profiles obtained with the present and the previous values of the rate coefficients for the excitation of H_2 (Le Bourlot et al. 1999) and HD (Flower et al. 2000) by H is shown in Fig. 4, through to a density $n_{\rm H} \equiv n({\rm H}) + 2n({\rm H_2}) + n({\rm HD}) + n({\rm H^+}) = 10^{12}\,{\rm cm^{-3}}$.

In the initial phase of the collapse, the kinetic temperature, T, increases adiabatically: the density is so low that the rate of cooling by H_2 and HD is negligible. Approaching $n_{\rm H} = 10\,{\rm cm^{-3}}$, collisional cooling assumes significance, and its rate increases quadratically with the density, $n_{\rm H}$. As a consequence, T decreases, reaching a minimum for $n_{\rm H} \approx 10^4\,{\rm cm^{-3}}$. The increases in the rate coefficients for rovibrationally inelastic scattering of H on both H_2 and HD (see Section 3) lead to lower temperatures; but the progressive thermalization of first the rotational levels and then, at higher densities, the vibrational levels (cf. Flower & Harris 2007) mitigates the effects on T. Furthermore, as the temperature does not exceed $T \approx 1000$ K over the range of density in Fig. 4, the contribution of cooling due to vibrationally inelastic scattering is limited, as the $v = 1$ vibrational threshold is approximately 6000 K.

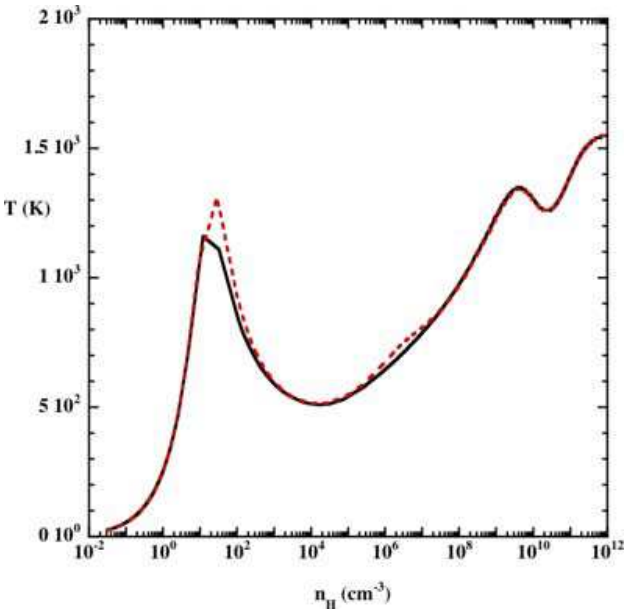

Figure 4. The temperature profile of a gravitationally collapsing spherical condensation of the primordial gas. The full curve was calculated with the present H–H_2 and H–HD rate coefficients, the broken curve using the earlier data of Le Bourlot et al. (1999) and Flower et al. (2000).

5 CONCLUDING REMARKS

We have reported the results of calculations of rate coefficients for the rovibrational excitation of H_2 by H, during non-reactive scattering. We have discussed also the cross-sections and rate coefficients for rovibrationally inelastic collisions of H and HD, obtained with the same ab initio interaction potential. The new rate coefficients were incorporated into illustrative astrophysical models – of a C-type shock wave propagating in an interstellar molecular cloud and of the gravitational collapse of a condensation of the primordial gas. Our conclusions may be summarized as follows.

(i) The cross-sections for rovibrational excitation of H_2 and HD are much larger, near threshold, when the numerically exact vibrational wavefunctions are employed, as in this work, compared with earlier studies, based on the SHO approximation to the wavefunctions. As a result, the rate coefficients for vibrational relaxation of the levels $(v, j) = (1, 3)$ and $(2, 3)$ are in much better agreement with estimates by Allers et al. (2005), based on the observations of the Orion bar PDR.

(ii) There are significant consequences for the H_2 excitation diagram predicted by an illustrative C-type shock model of speed $v_{\rm s} = 30\,{\rm km\,s^{-1}}$, propagating into molecular gas of density $n_{\rm H} = 10^4\,{\rm cm^{-3}}$; the new rate coefficients give rise to larger values of the column densities of the vibrationally excited levels. However, the increases in the column densities are much smaller than might be anticipated on the basis of a comparison of the 'new' and the 'old' rate coefficients, owing to the existence of a feedback loop, which maintains an approximately constant rate of cooling by H_2.

(iii) In the model of the gravitational collapse of a condensation of the primordial gas, there is little modification of the thermal profile when the new rate coefficents are introduced. In this case, pure rotational excitation within the vibrational ground state, $v = 0$, is more important to the thermal balance than vibrational excitation, and the changes in the rate coefficients for pure rotational excitation are less pronounced. Furthermore, the populations of rotational levels within a given vibrational manifold thermalize at lower gas densities, $n_{\rm H}$, than do the relative populations of levels belonging to different vibrational states.

ACKNOWLEDGMENTS

SAW was supported by a studentship from the Particle Physics and Astronomy Research Council, and AG by the Marie-Curie Research Training Network 'The Molecular Universe'. SAW would like to thank Jacques Le Bourlot for his assistance with fitting the rate coefficients.

REFERENCES

Allers K. N., Jaffe D. T., Lacy J. H., Draine B. T., Richter M. J., 2005, ApJ, 630, 368
Boothroyd A. I., Keogh W. K., Martin P. G., Peterson M. R., 1996, J. Chem. Phys., 104, 7139
Flower D. R., Harris G. J., 2007, MNRAS, 377, 705
Flower D. R., Roueff E., 1998, J. Phys. B, 31, L955
Flower D. R., Le Bourlot J., Pineau des Forêts, G., Roueff E., 2000, MNRAS, 314, 753
Garcia E., Laganà A., 1986, Chem. Phys. Lett., 123, 365
Le Bourlot J., Pineau des Forêts G., Flower D. R., 1999, MNRAS, 305, 802
Mandy M. E., Martin P. G., 1993, ApJS, 86, 199
Mielke S. L., Garrett B. C., Peterson K. A., 2002, J. Chem. Phys., 116, 4142
Palla F., Salpeter E. E., Stahler S. W., 1983, ApJ, 271, 632
Stancil P. C., Lepp S., Dalgarno A., 1998, ApJ, 509, 1
Sternberg A., Dalgarno A., 1989, ApJ, 338, 197
Wrathmall S. A., Flower D. R., 2007, J. Phys. B., 40, 3221

This paper has been typeset from a TEX/LATEX file prepared by the author.

A&A 468, L29–L32 (2007)
DOI: 10.1051/0004-6361:20077387

Astronomy & Astrophysics
Special feature

Extended baselines for the IRAM Plateau de Bure interferometer: First results

Letter to the Editor

PdBI sub-arcsecond study of the SiO microjet in HH212

Origin and collimation of class 0 jets

S. Cabrit[1], C. Codella[2], F. Gueth[3], B. Nisini[4], A. Gusdorf[5], C. Dougados[6], and F. Bacciotti[7]

[1] LERMA, UMR 8112 du CNRS, Observatoire de Paris, 61 Av. de l'Observatoire, 75014 Paris, France
e-mail: sylvie.cabrit@obspm.fr
[2] INAF, Istituto di Radioastronomia, Sezione di Firenze, Largo E. Fermi 5, 50125 Firenze, Italy
[3] IRAM, 300 rue de la Piscine, 38406 Grenoble Cedex, France
[4] INAF-Osservatorio Astrofisico di Roma, via di Frascati 33, 00040 Monte Catone, Italy
[5] Physics Department, The University, Durham DH1 3LE, UK
[6] Laboratoire d'Astrophysique de l'Observatoire de Grenoble, BP 53, 38041 Grenoble Cedex, France
[7] INAF-Osservatorio Astrofisico di Arcetri, Largo E. Fermi 5, 50125 Firenze, Italy

Received 1 March 2007 / Accepted 3 April 2007

ABSTRACT

Context. The bipolar HH 212 outflow has been mapped in SiO using the extended configuration of the Plateau de Bure Interferometer (PdBI), revealing a highly collimated SiO jet closely associated with the H_2 jet component.
Aims. We study at unprecedented resolution (0.″34 across the jet axis) the properties of the innermost SiO "microjet" within 1000 AU of this young Class 0 source, to compare it with atomic microjets from more evolved sources and to constrain its origin.
Methods. The SiO channel maps are used to investigate the microjet collimation and velocity structure. A large velocity gradient analysis is applied to SiO (2−1), (5−4) and (8−7) data from the PdBI and the Submillimeter Array to constrain the SiO opacity and abundance.
Results. The HH212 Class 0 microjet shows striking similarities in collimation and energetic budget with atomic microjets from T Tauri sources. Furthermore, the SiO lines appear optically thick, unlike what is generally assumed. We infer $T_k \simeq 50-500$ K and an SiO/H_2 abundance $\geq 4\times10^{-8}-6\times10^{-5}$ for $n(H_2) = 10^7-10^5$ cm^{-3}, i.e. 0.05−90% of the elemental silicon.
Conclusions. This similar jet width, regardless of the presence of a dense envelope, definitely rules out jet collimation by external pressure, and favors a common MHD self-collimation (and possibly acceleration) process at all stages of star formation. We propose that the more abundant SiO in Class 0 jets could mainly result from rapid (≤25 yrs) molecular synthesis at high jet densities.

Key words. stars: formation – radio lines: ISM – ISM: jets and outflows – ISM: molecules – ISM: individual objects: HH212

1. Introduction

Millimeter interferometric studies of the L1448 and HH211 Class 0 sources have identified high-velocity SiO jet-like emission possibly related to the primary protostellar wind (Guilloteau et al. 1992; Chandler & Richer 2001; Hirano et al. 2006; Palau et al. 2006; Gueth et al. 2007). A similar SiO jet has recently been discovered by Codella et al. (2007, hereafter Paper I) in the HH212 H_2 outflow in Orion ($d \simeq 450$ pc) using the new extended configuration of the PdBI. This study revealed highly collimated SiO emission with a close spatial and kinematic correspondence to near-IR H_2 knots, indicating that both are tracing the same molecular jet component. In addition, an inner pair of SiO knots with no near-IR H_2 counterparts was identified at ±1.″5 of the central source, with a radial velocity range pointing to a high degree of collimation. Continuum data at 1mm further reveal a compact, optically thick source probably tracing a disk of diameter ≤ 120 AU. Similar conclusions were reached by Lee et al. (2007) in a lower resolution, multi-species study with the Submillimeter Array (SMA).

In this second paper, we further exploit the unprecedented resolution of 0.″34 *HPBW* across the jet axis provided by the extended configuration of the PdBI to carry out the first comparison of the properties of the Class 0 SiO "microjet" in HH212 with atomic microjets from Class I/II sources observed on similar scales. We identify several similarities suggesting that the same collimation (and possibly acceleration) mechanism is at work in Class 0 jets as in later stages. We also demonstrate that SiO is optically thick and close to LTE in the inner knots (as is not generally assumed) and discuss possible origins for the abundant SiO in Class 0 jets, compared to their more evolved counterparts.

2. Jet collimation and velocity structure

2.1. Present SiO observations

Figure 1 presents PdBI SiO 5–4 maps from Paper I of the inner jet knots, separated into three velocity intervals. The SiO microjet is *extremely narrow*, with a typical transverse *FWHM* ≃ 0.″4 at all velocities, i.e. an intrinsic width of 0.″2 = 90 AU after correction for the PdBI *HPBW* of 0.″34 in the same direction[1].

[1] A slightly larger width of 0.″35 was quoted in Paper I, where cleaning had not been optimized for the innermost jet regions.

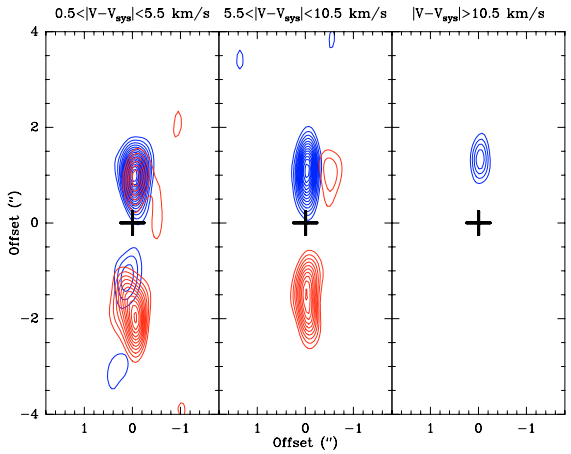

Fig. 1. SiO (5–4) emission maps of the HH212 microjet in 3 different velocity ranges. Blue and red contours refer to blueshifted and redshifted gas, respectively. A cross marks the position of the continuum source from Paper I: $\alpha(2000) = 05^h43^m51\overset{s}{.}41$, $\delta(2000) = -01°02'53\overset{''}{.}160$. Contour spacing is 50 mJy/beam km s^{-1} with the first contour at 100 mJy/beam km s^{-1}.

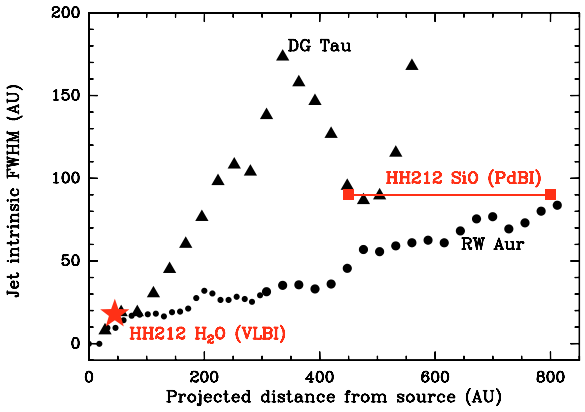

Fig. 2. HH212 intrinsic jet width compared to the range spanned by atomic microjets from Class II sources, corrected for the instrumental PSF (small dots: Woitas et al. 2002; large dots and triangles: Dougados et al. 2000); Our SiO PdBI measurements are shown as filled squares; the H_2O maser width from Claussen et al. (1998) as a filled star.

Figure 1 also shows that, in both lobes, the region of blue/red overlap is not coincident with the region of highest radial velocities, but is slightly *trailing behind it* by about 0.″4. The lack of blue/red contamination towards the fastest gas requires that its motions are highly forward-directed with a semi-opening angle ≤4° (see Paper I). The blue/red overlap at low velocities ≃3−4 km s^{-1} traces less collimated, slower material in the wake of the fastest gas.

2.2. Comparison with jets from more evolved sources

The width of atomic jets from T Tauri Class II sources spans a relatively broad range, depending on the brightness of bow-shock wings driven by internal working surfaces. In Fig. 2, the intrinsic *FWHM* of the HH212 SiO microjet is compared to the broadest (DG Tau) and narrowest (RW Aur) atomic microjets from Class II sources studied so far using ground-based adaptive optics or HST (Dougados et al. 2000; Woitas et al. 2002). We find that the HH212 SiO microjet falls exactly in the same range as Class II jets on scales 500−1000 AU. Similar results are found for the SiO jet from the HH211 Class 0 source (width of 95−125 AU at distances of 300−600 AU; Gueth et al. 2007).

Also indicated in Fig. 2 is the width of the HH212 jet at 50 AU from the source, ≃40 mas = 18 AU, as inferred from the bow shape of H_2O maser spots within 100 mas (Claussen et al. 1998). Again it is undistinguishable from that of atomic microjets at the same distance. We thus find no evidence of a higher jet collimation in Class 0 sources compared to the T Tauri stage where only a thin disk is present, although the dense infalling envelopes characterizing the Class 0 stage would be capable of strongly reconfining a radially expanding wind (Delamarter et al. 2000). This definitely rules out collimation by external pressure gradients and requires that jets from young stellar objects are self-collimated by internal magnetic stresses. The jet MHD collimation process appears to be the same at all phases, with all fast material confined within a beam diameter of about 15−20 AU over a distance ≃50 AU.

We further note that the HH212 Class 0 microjet follows interesting scalings compared with Class II microjets concerning its energetics and kinematics. (i) The mass ejection to accretion rate in HH212 estimated by Lee et al. (2007) from CO emission farther out along the jet is 15% (scaling with V_{jet}/100 km s^{-1}). This is similar to the ratio of 10% found for spatially resolved Class II jets (e.g. Woitas et al. 2002). (ii) The HH212 knot speed of 100−150 km s^{-1} is typically half that in T Tauri jets (e.g. Dougados et al. 2000), for a four times lower stellar mass of 0.15 $M_\odot$ (Lee et al. 2006). Hence the jet speed appears reduced in the same proportion as the escape speed from the central object. Such scalings would be consistent with the jet acceleration mechanism and launching zone also possibly being the same at all phases. However, similar data in a larger sample of Class 0 jets would be needed to confirm this conjecture.

3. SiO abundance in the HH 212 microjet

3.1. SiO line ratios and brightness temperatures

In order to constrain the physical conditions associated with the SiO emission in the inner jet, we compared the $J = 2-1$ and 5−4 line intensities from Paper I. For proper comparison, the SiO(5−4) map, originally obtained with a 0.″78×0.″34 resolution, was reconstructed at the lower resolution of the SiO(2−1) map (1.″89 × 0.″94). Figure 3 plots on a main beam ("MB") scale the reconstructed 5−4 line profiles at the peaks of the inner SiO knots, and the ratio $T_{MB}(5-4)/T_{MB}(2-1)$ as a function of velocity (bottom panels). It can be seen that the ratio is ≃0.75−1.1 across the blue knot profile, and ≃0.5−0.85 across the red knot profile. Relative calibration uncertainties between the 2−1 and 5−4 lines are estimated to be ≃20%. We similarly evaluate the SiO (8−7) to (5−4) intensity ratio by degrading our PdBI map to the 0.″96 × 0.″69 SMA beam of Lee et al. (2007). The resulting (5−4) spectra towards the inner SiO knots are also plotted in Fig. 3. Comparison with Fig. 10 of Lee et al. (2007) yields an (8−7)/(5−4) ratio in the range 0.7−1 at all velocities. The relative calibration uncertainty could reach 30%.

A third constraint is provided by the peak main beam temperatures $T_{MB}(5-4) \simeq 25$ K in both knots in our original PdBI beam (top curve in Fig. 3). As the jet is broadened by a factor ≃2 by beam convolution across the jet (cf. Sect. 2), the intrinsic line temperature $T_R(5-4)$ is at least $25 \times 2 = 50$ K. Including beam dilution along the jet axis with 0.″78 *HPBW*, the intrinsic line brightness could reach 200 K if the knot is roughly circular.

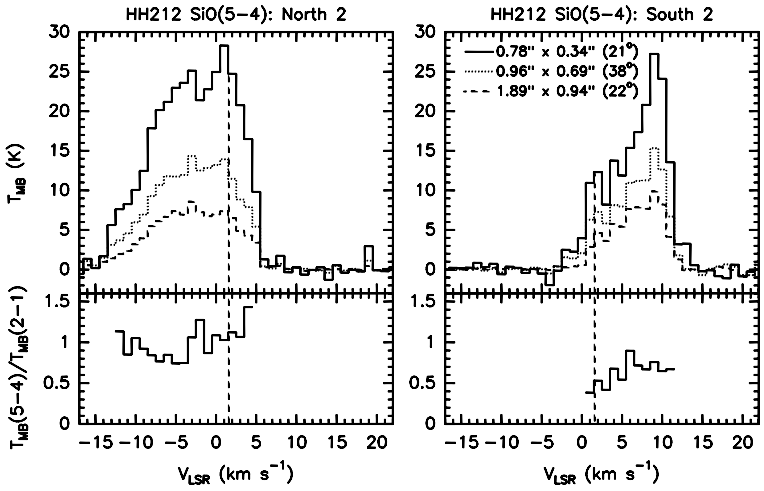

Fig. 3. *Top panels*: line profiles in SiO J = 5−4 towards the inner SiO knots at various resolutions: the original PdBI beam (solid histogram), the SMA J = 8−7 beam (dotted histogram), and the PdBI SiO J = 2−1 beam (dashed histogram). Beam PAs are listed between parentheses. Note the dramatic decrease in brightness temperature with increasing beam dilution. The vertical dashed line marks the ambient LSR velocity (+1.6 km s^{-1}; Wiseman et al. 2001). Bottom panels: Line temperature ratio $T_{\rm MB}(5{-}4)/T_{\rm MB}(2{-}1)$ at the resolution of the PdBI SiO J = 2−1 map, as a function of velocity.

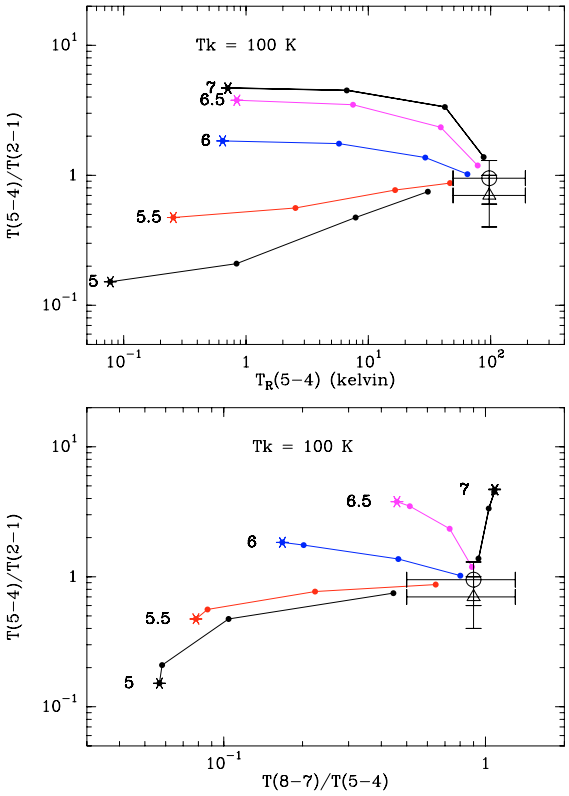

Fig. 4. *Top*: SiO line temperature ratio $T(5{-}4)/T(2{-}1)$ versus intrinsic line temperature $T_{\rm R}(5{-}4)$ for LVG slab models at $T_{\rm k}$ = 100 K. Each curve corresponds to the labelled $\log(n(\mathrm{H_2}))$, with dots marking values of $N_{\rm SiO}/\Delta V$ increasing (*left to right*) from 10^{12} to 10^{15} cm^{-2} (km s^{-1})$^{-1}$ by factors of 10. Symbols with error bars illustrate the range in line ratio in the inner SiO knots of HH212 (including calibration uncertainties) and the range in $T_{\rm R}(5{-}4)$ after correction for beam dilution. *Bottom*: same as above for the $T(5{-}4)/T(2{-}1)$ ratio versus $T(8{-}7)/T(5{-}4)$.

3.2. LVG modelling: evidence for optically thick SiO

The line ratios and (5−4) intrinsic brightness are compared with the result of a large velocity gradient (LVG) code, which considers the first 20 levels of SiO and the rate coefficients for collisions with H_2 reported by Turner et al. (1992) up to $T_{\rm k}$ = 300 K. We explored H_2 densities from 10^5 to 10^7 cm^{-3} (see Sect. 3.3) and an LVG optical depth parameter $n(\mathrm{SiO})/(\mathrm{d}V/\mathrm{d}z) = N_{\rm SiO}/\Delta V$ ranging from 10^{12} to 10^{17} cm^{-2} (km s^{-1})$^{-1}$, i.e. from the fully optically thin to optically thick regime. Our typical model results are illustrated graphically for $T_{\rm k}$ = 100 K in Fig. 4, and compared with observed values in HH212.

We find that the usual approach of assuming optically thin emission to derive $n(\mathrm{H_2})$ and $T_{\rm k}$ from line ratios (e.g. Gibb et al. 2004; Nisini et al. 2007) would give inaccurate results in our case: As shown in Fig. 4 (bottom panel), no optically thin model (starred symbols in the curves) can *simultaneously* reproduce the observed values of both SiO(8−7)/(5−4) and SiO(5−4)/(2−1). Values ≃ 1 for both ratios are only achieved when approaching the optically thick LTE regime ($T_{\rm R} \simeq T_{\rm k}$), which is the point of convergence of all density curves at sufficiently high opacity. We infer that $N_{\rm SiO}/\Delta V$ must be greater than $\simeq 10^{15}$ cm^{-2} (km s^{-1})$^{-1}$, while $n(\mathrm{H_2})$ is not well-constrained. The high (5−4) intrinsic brightness of 50 K−200 K also independently argues for a large optical depth parameter (Fig. 4, top). It also indicates that $T_{\rm k}$ lies in the range 50−500 K, or else the predicted $T_{\rm R}(5{-}4)$ close to LTE would be too low/high.

We note that substantial SiO optical depth could be rather common in the innermost part of Class 0 jets, if they are as narrow as in HH212. In the L1448 jet, for example, a column density $\sim 10^{14}$ cm^{-2} has been derived from single-dish measurements of the 5−4 transition assuming a jet width of 2″ (Nisini et al. 2007). A narrower width of ∼0.2″ would result in a column density higher by an order of magnitude, implying, as in HH212, a line optical depth larger than unity. Hence the low $T_{\rm MB}(5{-}4) \simeq$ 0.1−1 K in single-dish observations could result mainly from severe beam dilution of the SiO emission, as argued previously by Gibb et al. (2004) and illustrated in Fig. 3. The SiO abundances would then be substantially larger than previously reported.

3.3. SiO abundance and H_2 density

Noting that $N_{\rm SiO}/\Delta V = n(\mathrm{SiO})/(\mathrm{d}V/\mathrm{d}z)$, the SiO abundance with respect to H_2 may be written:

$$X(\mathrm{SiO}) \;=\; 4\times10^{-7}\left(\frac{N_{\rm SiO}/\Delta V}{10^{15}\ \mathrm{cm^{-2}\,km^{-1}\,s}}\right)\left(\frac{10^6}{n(\mathrm{H_2})}\right) \times\left(\frac{\mathrm{d}V/\mathrm{d}z}{4\times10^{-11}\ \mathrm{s^{-1}}}\right). \quad (1)$$

The adopted line-of-sight velocity gradient $\mathrm{d}V/\mathrm{d}z$ is typical of cooled regions with $T_{\rm k} \le 100$ K at the rear of planar C-shocks and is probably a lower limit. A steeper gradient $\mathrm{d}V/\mathrm{d}z$ is given by the ratio of the FWZI of the SiO line profile (≃10 km s^{-1}) to the knot width (0.″2 = 100 AU), which would increase X(SiO) by a factor 16 from the above formula.

The main uncertainty in X(SiO) stems from the unknown H_2 density in the SiO knots. A reasonable range may be inferred from the presence of shock-excited H_2O masers at 0.1″ from the source. Magnetic field strengths and line ratios in H_2O masers around YSOs typically require preshock H nuclei densities $n_H \simeq 10^7$–10^8 cm^{-3}(Kaufman & Neufeld 1996). Assuming that density roughly drops with distance as $1/r^2$ (cf. the DG Tau jet; Lavalley-Fouquet et al. 2000), one infers a preshock density $\simeq 10^5$–10^6 cm^{-3} at the SiO knots. Shock compression could increase these values by a about an order or magnitude (e.g. Kaufman & Neufeld 1996), so that the density is in the range $\simeq 10^5$–10^7 cm^{-3}. The resulting *minimum* SiO abundance for optically thick emission is $X(\mathrm{SiO}) \geq (4 \times 10^{-8}$–$4 \times 10^{-6}) \times$ (1–16), with the higher value corresponding to the lower density, and the additional factor 1–16 arising from the uncertainty in velocity gradient. Assuming a solar abundance of $(\mathrm{Si/H})_\odot \simeq 3.5 \times 10^{-5}$ (Grevesse & Sauval 1998), between 0.05% and 90% of the elemental silicon is in the form of SiO.

3.4. Origin of the SiO component

Our PdBI observations of the HH212 microjet set stronger constraints than previously on the origin of the SiO in protostellar outflows, because of the shorter timescales involved and the unusually high collimation and SiO column densities indicated by our data.

Given the proper motions of 60–150 km s^{-1} for H_2O masers and H_2 knots (Claussen et al. 1998; McCaughrean et al. 2002), the dynamical time of inner SiO peaks at 500 AU is only 25 yr. SiO should thus be incorporated very rapidly in the flow. The formation of SiO in outflows is usually attributed to sputtering of Si atoms from charged grains in a magnetized C-shock with ion-neutral drift speeds $\geq$25 km s^{-1} (Schilke et al. 1997). Updated C-shock models with improved sputtering yields, SiO formation rates, and molecular cooling (Gusdorf et al., in preparation) show that the required conditions for optically thick emission are reached for shock speeds 35–45 km s^{-1} and preshock densities of 10^5–10^6 cm^{-3} but only at the rear of the shock where velocity gradients are small, i.e. after 400–150 yrs. As this exceeds the knot dynamical time, non-steady truncated C-shocks need to be considered to model SiO-emitting shocks on such small scales.

Another long-standing issue is whether SiO molecules originate from shocked ambient material or trace the primary jet itself. The SiO microjet diameter of 100 AU is comparable to the centrifugal disk diameter of 120 AU indicated by our 1mm continuum size (Paper I) and by envelope kinematics (Lee et al. 2006). Hence we would expect little infalling molecular material left on-axis to refill the jet path between successive ejection episodes, unless this material is very warm. This would appear to favor an origin of the SiO in the jet itself. The option is appealing, as the higher densities of Class 0 jets, and the accompanying low temperature and ionization, are indeed conducive to molecular formation. In an early study of chemistry in protostellar winds, Glassgold et al. (1991) found that Si atoms are quickly converted into SiO at high mass-loss rates $\dot{M}_{\rm jet} > 10^{-6} M_\odot$ yr^{-1}. For a dust-free wind, the predicted SiO abundances are $\simeq$50–100% of the total elemental silicon. However, the recent finding of a substantial depletion of Fe and Ca at the base of several Class I jets (Podio et al. 2006) indicates that jets are not dust-free and that grains are only partly eroded along the flow. In the HH34 jet, 13% of Fe has been returned to the gas at distances $\geq$1500 AU. The same process at work in Class 0 jets would release Si atoms in a sufficient amount to produce optically thick SiO emission if $\dot{M}_{\rm jet} \geq 10^{-6}\ M_\odot$ yr^{-1}. In the inner SiO knots of HH212, this mass-flux is achieved for $n(\mathrm{H_2}) \geq 10^6$ cm^{-3} (with $V_{\rm jet} = 100$ km s^{-1} and a jet radius of 50 AU), thus only 0.5%–9% of Si would be needed, if all is converted into SiO (see Eq. (1)).

4. Conclusions

Our finding that jet collimation in the HH212 Class 0 source is similar to that in T Tauri stars favors a collimation mechanism independent of the presence of a dense envelope, i.e. most probably internal MHD stresses. The ejection/accretion ratio and the jet speed/escape speed ratio also appear to be similar to those in Class II, possibly suggesting the same acceleration mechanism as well. The main difference between Class 0 jets and their more evolved analogs would then be their differing chemical composition, with abundant molecules at the Class 0 stage, a mixed atomic-molecular composition at the Class I stage (Davis et al. 2001, 2003), and a purely atomic flow at the Class II stage.

We also find that SiO is optically thick, so that its abundance is larger than previously estimated. The extremely narrow width of the SiO jet revealed by PdBI further argues that this species is not formed in swept-up material, but more likely within the jet itself. We thus propose that the higher SiO content of Class 0 jets could mainly reflect an increase in jet density (hence, a higher efficiency of molecular formation), linked to the increased mass-accretion rate at earlier stages.

Acknowledgements. We are grateful to R. Cesaroni, J. Ferreira, and an anonymous referee for helpful comments. This work is supported in part by the European Community's Marie Curie Research Training Network JETSET under contract MRTN-CT-2004-005592. It benefited from research funding by the European Community's sixth Framework Programme under RadioNet R113CT 2003 5058187. A. Gusdorf acknowledges support through the European Community's Human Potential Programme under contract MRTN-CT-2004-512302, Molecular Universe.

References

Chandler, C. J., & Richer, J. S. 2001, ApJ, 555, 139
Claussen, M. J., Marvel, K. B., Wootten, A., & Wilking, B. A. 1998, ApJ, 507, L79
Codella, C., Cabrit, S., Gueth, F., et al. 2007, A&A, 462, L53 (Paper I)
Davis, C. J., Ray, T. P., Desroches, L., & Aspin, C. 2001, MNRAS, 326, 524
Davis, C. J., Whelan, E., Ray, T. P., & Chrysostomou, A. 2003, A&A, 397, 693
Dougados, C., Cabrit, S., Lavalley-Fouquet, C., & Ménard, F. 2000, A&A, 357, L61
Delamarter, Frank, & Hartmann 2000, ApJ, 530, 923
Gibb, A. G., Richer, J. S., Chandler, C. J., & Davis, C. J. 2004, ApJ, 603, 198
Glassgold, A. E., Mamon, G. A., & Huggins, P. J. 1991, ApJ, 373, 254
Grevesse, N., & Sauval, A. J. 1998, Space Sci. Rev., 85, 161
Gueth, F., et al. 2007, in preparation
Guilloteau, S., Bachiller, R., Fuente, A., & Lucas, R. 1992, A&A, 265, L49
Hirano, N., Liu, S.-Y., Shang, H., et al. 2006, ApJ, 636, L141
Kaufman, M. J., & Neufeld, D. A. 1996, ApJ, 456, 250
Lavalley-Fouquet, C., Cabrit, S., & Dougados, C. 2000, A&A, 356, L41
Lee, C.-F., Ho, P. T. P., Beuther, H., et al. 2006, ApJ, 639, 292
Lee, C.-F., Ho, P. T. P., Beuther, H., et al. 2007, ApJ, in press
McCaughrean, M., Zinnecker, H., Andersen, M., Meeus, G., & Lodieu, N. 2002, Msngr, 109, 28
Nisini, B., Codella, C., Giannini, T., et al. 2007, A&A, 462, 163
Palau, A., Ho, P. T. P., Zhang, Q., Estalella, R., et al. 2006, ApJ, 636, L137
Podio, L., Bacciotti, F., Nisini, B., et al. 2006, A&A, 456, 189
Schilke, P., Walmsley, C. M., Pineau des Forêts, G., & Flower, D. R. 1997, A&A, 321, 293
Turner, B. E., Chan, K. W., Green, S., & Lubowich, D. A. 1992, ApJ, 399, 114
Woitas, J., Ray, T. P., Bacciotti, F., Davis, C. J., & Eislöffel, J. 2002, ApJ, 580, 336
Wiseman, J., Wootten, A., Zinnecker, H., & McCaughrean, M. 2001, ApJ, 550, L87

Bibliographie

M. A. Albrecht. Approximated collisional rates for CS-H2 (J = 0). *A&A*, 127 :409–+, Nov. 1983.

P. Andre. The Initial Conditions for Protostellar Collapse : observational constraints. In *Formation stellaire et physique des etoiles jeunes*, Ecole d'Aussois, 2000.

P. Andre. The Evolution of Flows and Protostars. In B. Reipurth and C. Bertout, editors, *Herbig-Haro Flows and the Birth of Stars*, volume 182 of *IAU Symposium*, pages 483–494, 1997.

P. Andre, J. Martin-Pintado, D. Despois, and T. Montmerle. Discovery of a remarkable bipolar flow and exciting source in the Rho Ophiuchi cloud core. *A&A*, 236 :180–192, Sept. 1990a.

P. Andre, T. Montmerle, E. D. Feigelson, and H. Steppe. Cold dust around young stellar objects in the Rho Ophiuchi cloud core. *A&A*, 240 :321–330, Dec. 1990b.

P. Andre, D. Ward-Thompson, and M. Barsony. Submillimeter continuum observations of Rho Ophiuchi A - The candidate protostar VLA 1623 and prestellar clumps. *ApJ*, 406 :122–141, Mar. 1993. doi : 10.1086/172425.

P. Andre, D. Ward-Thompson, and M. Barsony. From Prestellar Cores to Protostars : the Initial Conditions of Star Formation. *Protostars and Planets IV*, pages 59–+, May 2000.

P. André, F. Motte, and A. Belloche. The Youngest Accreting Protostars : Implications for Collapse Models. In T. Montmerle and P. André, editors, *From Darkness to Light : Origin and Evolution of Young Stellar Clusters*, volume 243 of *Astronomical Society of the Pacific Conference Series*, pages 209–+, 2001.

P. André, S. Basu, and S.-i. Inutsuka. The Formation and Evolution of Prestellar Cores. *ArXiv e-prints*, Jan. 2008.

G. Anglada. Radio Jets in Young Stellar Objects. In A. R. Taylor and J. M. Paredes, editors, *Radio Emission from the Stars and the Sun*, volume 93 of *Astronomical Society of the Pacific Conference Series*, pages 3–7, 1996.

H. G. Arce and A. A. Goodman. The Episodic, Precessing Giant Molecular Outflow from IRAS 04239+2436 (HH 300). *ApJ*, 554 :132–151, June 2001. doi : 10.1086/321334.

H. G. Arce and A. A. Goodman. The Great PV Cephei Outflow : A Case Study in Outflow-Cloud Interaction. *ApJ*, 575 : 911–927, Aug. 2002a. doi : 10.1086/341427.

H. G. Arce and A. A. Goodman. Bow Shocks, Wiggling Jets, and Wide-Angle Winds : A High-Resolution Study of the Entrainment Mechanism of the PV Cephei Molecular (CO) Outflow. *ApJ*, 575 :928–949, Aug. 2002b. doi : 10.1086/341426.

H. G. Arce and A. I. Sargent. Outflow-Infall Interactions in Early Star Formation and Their Impact on the Mass-assembling Process in L1228. *ApJ*, 612 :342–356, Sept. 2004. doi : 10.1086/422552.

H. G. Arce, D. Shepherd, F. Gueth, C.-F. Lee, R. Bachiller, A. Rosen, and H. Beuther. Molecular Outflows in Low- and High-Mass Star-forming Regions. In B. Reipurth, D. Jewitt, and K. Keil, editors, *Protostars and Planets V*, pages 245–260, 2007.

H. G. Arce, J. Santiago-García, J. K. Jørgensen, M. Tafalla, and R. Bachiller. Complex Molecules in the L1157 Molecular Outflow. *ApJ*, 681 :L21–L24, July 2008. doi : 10.1086/590110.

F. Bacciotti, R. Mundt, T. P. Ray, J. Eislöffel, J. Solf, and M. Camezind. Hubble Space Telescope STIS Spectroscopy of the Optical Outflow from DG Tauri : Structure and Kinematics on Subarcsecond Scales. *ApJ*, 537 :L49–L52, July 2000. doi : 10.1086/312745.

R. Bachiller and M. Perez Gutierrez. Shock Chemistry in the Young Bipolar Outflow L1157. *ApJ*, 487 :L93+, Sept. 1997. doi : 10.1086/310877.

R. Bachiller and M. Tafalla. Bipolar Molecular Outflows. In C. J. Lada and N. D. Kylafis, editors, *NATO ASIC Proc. 540 : The Origin of Stars and Planetary Systems*, pages 227–+, 1999.

R. Bachiller, J. Martin-Pintado, and A. Fuente. High-velocity SiO emission in the L 1448 outflow - Evidence for dense shocked gas in the molecular bullets. *A&A*, 243 :L21–L24, Mar. 1991.

R. Bachiller, J. Martin-Pintado, and A. Fuente. High-Velocity Hot Ammonia in Bipolar Outflows. *ApJ*, 417 :L45+, Nov. 1993. doi : 10.1086/187090.

R. Bachiller, M. Pérez Gutiérrez, M. S. N. Kumar, and M. Tafalla. Chemically active outflow L 1157. *A&A*, 372 :899–912, June 2001. doi : 10.1051/0004-6361 :20010519.

N. Balakrishnan, M. Yan, and A. Dalgarno. Quantum-Mechanical Study of Rotational and Vibrational Transitions in CO Induced by H Atoms. *ApJ*, 568 :443–447, Mar. 2002. doi : 10.1086/321434.

J. Ballesteros-Paredes, E. Vázquez-Semadeni, and J. Kim. Star Formation Efficiency in Driven, Supercritical, Turbulent Clouds. In *Protostars and Planets V*, pages 8630–+, 2005.

J. Bally and B. Reipurth. Irradiated Herbig-Haro Jets in the Orion Nebula and near NGC 1333. *ApJ*, 546 :299–323, Jan. 2001. doi : 10.1086/318258.

J. Bally, D. Devine, and V. Alten. A Parsec-Scale Herbig-Haro Jet in Barnard 5. *ApJ*, 473 :921–+, Dec. 1996. doi : 10.1086/178203.

J. Bally, C. R. O'Dell, and M. J. McCaughrean. Disks, Microjets, Windblown Bubbles, and Outflows in the Orion Nebula. *AJ*, 119 :2919–2959, June 2000. doi : 10.1086/301385.

J. Bally, E. Feigelson, and B. Reipurth. X-Rays from the Vicinity of the Protostar L1551 IRS 5 : Reflection or Fast Shocks ? *ApJ*, 584 :843–852, Feb. 2003. doi : 10.1086/345850.

D. S. Balsara, R. M. Crutcher, and A. Pouquet. Turbulent Flows within Self-gravitating Magnetized Molecular Clouds. *ApJ*, 557 :451–463, Aug. 2001. doi : 10.1086/323679.

J. F. Barral and J. Canto. A Stellar Wind Model for Bipolar Nebulae. *Revista Mexicana de Astronomia y Astrofisica*, 5 : 101–+, June 1981.

S. Basu and T. C. Mouschovias. Magnetic braking, ambipolar diffusion, and the formation of cloud cores and protostars. 1 : Axisymmetric solutions. *ApJ*, 432 :720–741, Sept. 1994. doi : 10.1086/174611.

M. R. Bate. Collapse of a Molecular Cloud Core to Stellar Densities : The First Three-dimensional Calculations. *ApJ*, 508 : L95–L98, Nov. 1998. doi : 10.1086/311719.

R. Beck. Galactic and Extragalactic Magnetic Fields. *Space Science Reviews*, 99 :243–260, Oct. 2001.

M. T. Beltrán, F. Gueth, S. Guilloteau, and A. Dutrey. L1157 : Interaction of the molecular outflow with the Class 0 environment. *A&A*, 416 :631–640, Mar. 2004. doi : 10.1051/0004-6361 :20034123.

M. Benedettini, T. Giannini, B. Nisini, E. Tommasi, D. Lorenzetti, A. M. Di Giorgio, P. Saraceno, H. A. Smith, and G. J. White. The ISO spectroscopic view of the HH 24-26 region. *A&A*, 359 :148–158, July 2000.

M. Benedettini, S. Viti, C. Codella, R. Bachiller, F. Gueth, M. T. Beltrán, A. Dutrey, and S. Guilloteau. The clumpy structure of the chemically active L1157 outflow. *MNRAS*, 381 :1127–1136, Nov. 2007. doi : 10.1111/j.1365-2966.2007.12300.x.

P. J. Benson and P. C. Myers. A survey for dense cores in dark clouds. *ApJS*, 71 :89–108, Sept. 1989. doi : 10.1086/191365.

H. Beuther and D. Shepherd. Precursors of UCHII Regions and the Evolution of Massive Outflows. In M. S. N. Kumar, M. Tafalla, and P. Caselli, editors, *Cores to Clusters : Star Formation with Next Generation Telescopes*, pages 105–119, Nov. 2005.

H. Beuther, P. Schilke, and F. Gueth. Massive Molecular Outflows at High Spatial Resolution. *ApJ*, 608 :330–340, June 2004. doi : 10.1086/386543.

J. H. Bieging, M. Cohen, and P. R. Schwartz. VLA observations of T Tauri stars. II - A luminosity-limited survey of Taurus-Auriga. *ApJ*, 282 :699–708, July 1984. doi : 10.1086/162251.

J. H. Black and E. F. van Dishoeck. Fluorescent excitation of interstellar H2. *ApJ*, 322 :412–449, Nov. 1987. doi : 10.1086/165740.

L. Blitz. Giant molecular clouds. In E. H. Levy and J. I. Lunine, editors, *Protostars and Planets III*, pages 125–161, 1993.

L. Blitz and F. H. Shu. The origin and lifetime of giant molecular cloud complexes. *ApJ*, 238 :148–157, May 1980. doi : 10.1086/157968.

S. Bonazzola, J. Heyvaerts, E. Falgarone, M. Perault, and J. L. Puget. Jeans collapse in a turbulent medium. *A&A*, 172 : 293–298, Jan. 1987.

I. A. Bonnell, M. R. Bate, C. J. Clarke, and J. E. Pringle. Accretion and the stellar mass spectrum in small clusters. *MNRAS*, 285 :201–208, Feb. 1997.

W. B. Bonnor. Boyle's Law and gravitational instability. *MNRAS*, 116 :351–+, 1956.

S. Bontemps, P. Andre, S. Terebey, and S. Cabrit. Evolution of outflow activity around low-mass embedded young stellar objects. *A&A*, 311 :858–872, July 1996.

A. Boothroyd, W. Keogh, P. Martin, and M. Peterson. A Refined H_3 Potential Energy Surface. *Journal of Chemical Physics*, 104 :7139–7152, 1996.

A. P. Boss. Collapse and fragmentation of molecular cloud cores. 2 : Collapse induced by stellar shock waves. *ApJ*, 439 : 224–236, Jan. 1995. doi : 10.1086/175166.

T. L. Bourke, P. C. Myers, G. Robinson, and A. R. Hyland. New OH Zeeman Measurements of Magnetic Field Strengths in Molecular Clouds. *ApJ*, 554 :916–932, June 2001. doi : 10.1086/321405.

J. V. Buckle and G. A. Fuller. Sulphur-bearing species as chemical clocks for low mass protostars ? *A&A*, 399 :567–581, Feb. 2003. doi : 10.1051/0004-6361 :20021816.

S. Cabrit. Constraints on Accretion-ejection Structures in Young Stars. In *Formation stellaire et physique des etoiles jeunes*, Ecole d'Aussois, 2000.

S. Cabrit. Jets from Young Stars : The Need for MHD Collimation and Acceleration Processes. In J. Ferreira, C. Dougados, and E. Whelan, editors, *Lecture Notes in Physics, Berlin Springer Verlag*, volume 723 of *Lecture Notes in Physics, Berlin Springer Verlag*, pages 21–+, 2007.

S. Cabrit and C. Bertout. CO line formation in bipolar flows. II - Decelerated outflow case and summary of results. *ApJ*, 348 :530–541, Jan. 1990. doi : 10.1086/168261.

S. Cabrit, A. Raga, and F. Gueth. Models of Bipolar Molecular Outflows. In B. Reipurth and C. Bertout, editors, *Herbig-Haro Flows and the Birth of Stars*, volume 182 of *IAU Symposium*, pages 163–180, 1997.

S. Cabrit, S. Bontemps, P. O. Lagage, M. Sauvage, F. Boulanger, P. Andr'e, L. Nordh, G. Olofsson, C. J. Cesarsky, O. de Boula, F. Sibille, and R. Siebenmorgen. ISOCAM mapping and spectro-imaging of bipolar outflows. In P. Cox and M. Kessler, editors, *The Universe as Seen by ISO*, volume 427 of *ESA Special Publication*, pages 449–+, Mar. 1999.

N. Calvet, L. Hartmann, and S. E. Strom. Evolution of Disk Accretion. *Protostars and Planets IV*, pages 377–+, May 2000.

J. Canto and A. C. Raga. Mixing layers in stellar outflows. *ApJ*, 372 :646–658, May 1991. doi : 10.1086/170007.

J. Cantó, A. C. Raga, and A. Riera. A Model for the Cross Section of a Turbulent, Radiative Jet or Wake. *Revista Mexicana de Astronomia y Astrofisica*, 39 :207–212, 2003.

A. Caratti o Garatti, T. Giannini, B. Nisini, and D. Lorenzetti. H_2 active jets in the near IR as a probe of protostellar evolution. *A&A*, 449 :1077–1088, Apr. 2006. doi : 10.1051/0004-6361 :20054313.

P. Caselli, T. W. Hartquist, and O. Havnes. Grain-grain collisions and sputtering in oblique C-type shocks. *A&A*, 322 : 296–301, June 1997.

C. Ceccarelli, M. R. Haas, D. J. Hollenbach, and A. L. Rudolph. O I 63 Micron-determined Mass-Loss Rates in Young Stellar Objects. *ApJ*, 476 :771–+, Feb. 1997. doi : 10.1086/303643.

C. Cecchi-Pestellini, E. Bodo, N. Balakrishnan, and A. Dalgarno. Rotational and Vibrational Excitation of CO Molecules by Collisions with ^{4}He Atoms. *ApJ*, 571 :1015–1020, June 2002. doi : 10.1086/340020.

J. Cernicharo. *The Physics of Star Formation and Early Stellar Evolution.* Kluwer academic publishing, 2001.

R. Cesaroni. Outflow, Infall, and Rotation in High-Mass Star Forming Regions. *Ap&SS*, 295 :5–17, Jan. 2005. doi : 10.1007/s10509-005-3651-8.

D. Cesarsky, P. Cox, G. Pineau des Forêts, E. F. van Dishoeck, F. Boulanger, and C. M. Wright. ISOCAM spectro-imaging of the H_2 rotational lines hfill in the supernova remnant IC 443. *A&A*, 348 :945–949, Aug. 1999.

C. J. Chandler and J. S. Richer. Subarcsecond Imaging of SiO in the HH 211 Protostellar Jet. *ApJ*, 555 :139–145, July 2001. doi : 10.1086/321463.

S. Chandrasekhar and E. Fermi. Magnetic Fields in Spiral Arms. *ApJ*, 118 :113–+, July 1953. doi : 10.1086/145731.

S. B. Charnley. Sulfuretted Molecules in Hot Cores. *ApJ*, 481 :396–+, May 1997. doi : 10.1086/304011.

H. Chen, P. C. Myers, E. F. Ladd, and D. O. S. Wood. Bolometric temperature and young stars in the Taurus and Ophiuchus complexes. *ApJ*, 445 :377–392, May 1995. doi : 10.1086/175703.

L. M. Chernin. Water masers in the L1448C outflow. *ApJ*, 440 :L97–L99, Feb. 1995. doi : 10.1086/187770.

L. M. Chernin and C. R. Masson. A nearly unipolar CO outflow from the HH 46 - 47 system. *ApJ*, 382 :L93–L96, Dec. 1991. doi : 10.1086/186220.

L. M. Chernin and C. R. Masson. Momentum Distribution in Molecular Outflows. *ApJ*, 455 :182–+, Dec. 1995. doi : 10.1086/176566.

J. P. Chieze. The fragmentation of molecular clouds. I - The mass-radius-velocity dispersion relations. *A&A*, 171 :225–232, Jan. 1987.

J.-P. Chieze, G. Pineau des Forets, and D. R. Flower. Temporal evolution of MHD shocks in the interstellar medium. *MNRAS*, 295 :672–+, Apr. 1998. doi : 10.1046/j.1365-8711.1998.01391.x.

M. J. Claussen, K. B. Marvel, A. Wootten, and B. A. Wilking. Distribution and Motion of the Water Masers near IRAS 05413-0104. *ApJ*, 507 :L79–L82, Nov. 1998. doi : 10.1086/311669.

C. Codella, R. Bachiller, and B. Reipurth. Low and high velocity SiO emission around young stellar objects. *A&A*, 343 : 585–598, Mar. 1999.

C. Combet, T. Lery, and G. C. Murphy. Transit Flow Models for Low- and High-Mass Protostars. *ApJ*, 637 :798–810, Feb. 2006. doi : 10.1086/498612.

R. M. Crutcher. Magnetic Fields in Molecular Clouds : Observations Confront Theory. *ApJ*, 520 :706–713, Aug. 1999. doi : 10.1086/307483.

K. M. Cudworth and G. Herbig. Two large-proper-motion Herbig-Haro objects. *AJ*, 84 :548–551, Apr. 1979. doi : 10.1086/112447.

A. Cunningham, A. Frank, and L. Hartmann. Wide-Angle Wind-driven Bipolar Outflows : High-Resolution Models with Application to Source I of the Becklin-Neugebauer/Kleinmann-Low OMC-I Region. *ApJ*, 631 :1010–1021, Oct. 2005. doi : 10.1086/432658.

S. Curiel, L. F. Rodriguez, J. M. Moran, and J. Canto. The triple radio continuum source in Serpens - The birth of a Herbig-Haro system ? *ApJ*, 415 :191–203, Sept. 1993. doi : 10.1086/173155.

S. Curiel, J. M. Torrelles, L. F. Rodríguez, J. F. Gómez, and G. Anglada. A Study of the Kinematics and Temperature of the High-Density Molecular Gas Surrounding L1448C. *ApJ*, 527 :310–320, Dec. 1999. doi : 10.1086/308049.

G. Danby, D. Flower, E. Kochansky, K. L., and V. P. Rotational Excitation of ortho-NH_3 by para-H_2. *Journal of Physics B : Atomic, Molecular and Optical Physics*, 19 :2891–2906, 1986.

E. Dartois, A. Dutrey, and S. Guilloteau. Structure of the DM Tau Outer Disk : Probing the vertical kinetic temperature gradient. *A&A*, 399 :773–787, Feb. 2003. doi : 10.1051/0004-6361 :20021638.

R. D. Davies and W. L. H. Shuter. An experiment to measure the magnetic field of the Galaxy, III. *MNRAS*, 126 :369–+, 1963.

C. J. Davis and J. Eisloeffel. Near-infrared imaging in H_2 of molecular (CO) outflows from young stars. *A&A*, 300 :851–+, Aug. 1995.

C. J. Davis, R. Mundt, J. Eislöffel, and T. P. Ray. Shocks in the L 1551-IRS 5 outflow optical and near-infrared imaging. *Ap&SS*, 233 :51–54, Nov. 1995. doi : 10.1007/BF00627330.

F. Dayou and C. Balança. Rotational excitation of SiO by collisions with helium. *A&A*, 459 :297–305, Nov. 2006. doi : 10.1051/0004-6361 :20065718.

E. M. de Gouveia Dal Pino. Three-dimensional Simulations of Jet/Cloud Interactions : Structure and Kinematics of the Deflected Jets. *ApJ*, 526 :862–873, Dec. 1999. doi : 10.1086/308037.

T. de Jong, A. Dalgarno, and S.-I. Chu. Carbon monoxide in collapsing interstellar clouds. *ApJ*, 199 :69–78, July 1975. doi : 10.1086/153665.

W. M. Decampli. T Tauri winds. *ApJ*, 244 :124–146, Feb. 1981. doi : 10.1086/158691.

G. Delamarter, A. Frank, and L. Hartmann. Interaction of Infall and Winds in Young Stellar Objects. *ApJ*, 530 :923–938, Feb. 2000. doi : 10.1086/308389.

A. DePristo, S. Augustin, R. Ramaswamy, and R. H. Quantum Number and Energy Scaling for Nonreactive Collisions. *Journal of Chemical Physics*, 71 :850–855, 1979.

D. F. Dickinson. Detection of Silicon Monoxide at 87 GHz. *ApJ*, 175 :L43+, July 1972. doi : 10.1086/180981.

C. Dougados, S. Cabrit, C. Lavalley, and F. Ménard. T Tauri stars microjets resolved by adaptive optics. *A&A*, 357 : L61–L64, May 2000.

T. P. Downes and S. Cabrit. The mass-velocity and intensity-velocity relations in jet-driven molecular outflows. *A&A*, 403 : 135–140, May 2003. doi : 10.1051/0004-6361 :20030363.

T. P. Downes and T. P. Ray. On the transfer of momentum from stellar jets to molecular outflows. *A&A*, 345 :977–985, May 1999.

B. T. Draine. Interstellar shock waves with magnetic precursors. *ApJ*, 241 :1021–1038, Nov. 1980. doi : 10.1086/158416.

B. T. Draine, W. G. Roberge, and A. Dalgarno. Magnetohydrodynamic shock waves in molecular clouds. *ApJ*, 264 :485–507, Jan. 1983. doi : 10.1086/160617.

M.-L. Dubernet and A. Grosjean. Collisional excitation rates of H_2O with H_2 . I. Pure rotational excitation rates with para-H_2 at very low temperature. *A&A*, 390 :793–800, Aug. 2002. doi : 10.1051/0004-6361 :20020800.

C. P. Dullemond, D. Hollenbach, I. Kamp, and P. D'Alessio. Models of the Structure and Evolution of Protoplanetary Disks. In B. Reipurth, D. Jewitt, and K. Keil, editors, *Protostars and Planets V*, pages 555–572, 2007.

A. K. Dupree, N. S. Brickhouse, G. H. Smith, and J. Strader. A Hot Wind from the Classical T Tauri Stars : TW Hydrae and T Tauri. *ApJ*, 625 :L131–L134, June 2005. doi : 10.1086/431323.

A. Dutrey, S. Guilloteau, and R. Bachiller. Successive SiO shocks along the L1448 jet axis. *A&A*, 325 :758–768, Sept. 1997.

J. E. Dyson. The interpretation of flows in molecular clouds. *Ap&SS*, 106 :181–197, Nov. 1984. doi : 10.1007/BF00653925.

R. Ebert. Zur Instabilität kugelsymmetrischer Gasverteilungen. Mit 2 Textabbildungen. *Zeitschrift fur Astrophysik*, 42 : 263–+, 1957.

J. Eisloffel, M. D. Smith, C. J. Davis, and T. P. Ray. Molecular Hydrogen in the Outflow From CEP E. *AJ*, 112 :2086–+, Nov. 1996. doi : 10.1086/118165.

J. Eisloffel, R. Mundt, T. P. Ray, and L. F. Rodriguez. Collimation and Propagation of Stellar Jets. *Protostars and Planets IV*, pages 815–+, May 2000.

M. Elitzur and A. Asensio Ramos. A new exact method for line radiative transfer. *MNRAS*, 365 :779–791, Jan. 2006. doi : 10.1111/j.1365-2966.2005.09770.x.

A. Faure, N. Crimier, C. Ceccarelli, P. Valiron, L. Wiesenfeld, and M. L. Dubernet. Quasi-classical rate coefficient calculations for the rotational (de)excitation of H{2}O by H{2}. *A&A*, 472 :1029–1035, Sept. 2007. doi : 10.1051/0004-6361 :20077678.

C. Fendt and M. Čemeljić. Formation of protostellar jets - effects of magnetic diffusion. *A&A*, 395 :1045–1060, Dec. 2002. doi : 10.1051/0004-6361 :20021442.

J. Ferreira, G. Pelletier, and S. Appl. Reconnection X-winds : spin-down of low-mass protostars. *MNRAS*, 312 :387–397, Feb. 2000. doi : 10.1046/j.1365-8711.2000.03215.x.

J. D. Fiege and R. N. Henriksen. A global model of protostellar bipolar outflow - I. *MNRAS*, 281 :1038–1054, Aug. 1996a.

J. D. Fiege and R. N. Henriksen. A global model of protostellar bipolar outflow - II. *MNRAS*, 281 :1055–1072, Aug. 1996b.

D. Field, P. W. May, G. Pineau des Forets, and D. R. Flower. Sputtering of the refractory cores of interstellar grains. *MNRAS*, 285 :839–846, Mar. 1997.

D. R. Flower. The rotational excitation of CO by H_2. *Atomic and Molecular, Optical Physics*, 34 :2731–2738, 2001.

D. R. Flower. Atomic and molecular physics of interstellar heating and cooling. In D. J. Hollenbach and H. A. Thronson, Jr., editors, *Interstellar Processes*, volume 134 of *Astrophysics and Space Science Library*, pages 745–761, 1987.

D. R. Flower. Rotational excitation of HCO^+ by H_2. *MNRAS*, 305 :651–653, May 1999. doi : 10.1046/j.1365-8711.1999.02451.x.

D. R. Flower and A. Gusdorf. Emission and cooling by CO in interstellar shock waves, submitted. *MNRAS*, 2008.

D. R. Flower and G. Pineau des Forêts. The influence of grains on the propagation and structure of C-type shock waves in interstellar molecular clouds. *MNRAS*, 343 :390–400, Aug. 2003. doi : 10.1046/j.1365-8711.2003.06716.x.

D. R. Flower and G. Pineau-Des-Forets. Multicomponent Reacting Magnetohydrodynamics Flows - a Reply. *MNRAS*, 220 : 149–+, May 1986.

D. R. Flower and G. Pineau des Forets. Grain / Mantle Erosion in Magnetohydrodynamic Shocks. *MNRAS*, 268 :724–+, June 1994.

D. R. Flower and G. Pineau des Forets. Non-thermal sputtering of interstellar grains in magnetohydrodynamic shocks. *MNRAS*, 275 :1049–1056, Aug. 1995.

D. R. Flower and G. Pineau des Forêts. H_2 emission from shocks in molecular outflows : the significance of departures from a stationary state. *MNRAS*, 308 :271–280, Sept. 1999. doi : 10.1046/j.1365-8711.1999.02729.x.

D. R. Flower, G. Pineau des Forets, and T. W. Hartquist. Theoretical studies of interstellar molecular shocks. I - General formulation and effects of the ion-molecule chemistry. *MNRAS*, 216 :775–794, Oct. 1985.

D. R. Flower, G. Pineau-Des-Forets, and T. W. Hartquist. Theoretical studies of interstellar molecular shocks. II - Molecular hydrogen cooling and rotational level populations. *MNRAS*, 218 :729–741, Feb. 1986.

D. R. Flower, G. Pineau des Forets, D. Field, and P. W. May. The structure of MHD shocks in molecular outflows : grain sputtering and SiO formation. *MNRAS*, 280 :447–457, May 1996.

D. R. Flower, J. Le Bourlot, G. Pineau des Forêts, and S. Cabrit. The contributions of J-type shocks to the H_2 emission from molecular outflow sources. *MNRAS*, 341 :70–80, May 2003. doi : 10.1046/j.1365-8711.2003.06463.x.

J. Franklin, R. L. Snell, M. J. Kaufman, G. J. Melnick, D. A. Neufeld, D. J. Hollenbach, and E. A. Bergin. SWAS Observations of Water in Molecular Outflows. *ApJ*, 674 :1015–1031, Feb. 2008. doi : 10.1086/524924.

D. Froebrich, M. D. Smith, K.-W. Hodapp, and J. Eislöffel. Far-infrared photometry of deeply embedded outflow sources. *MNRAS*, 346 :163–176, Nov. 2003. doi : 10.1046/j.1365-2966.2003.07072.x.

A. Fuente, J. Martın-Pintado, R. Bachiller, A. Rodrıguez-Franco, and F. Palla. The history of mass dispersal around Herbig Ae/Be stars. *A&A*, 387 :977–992, June 2002. doi : 10.1051/0004-6361 :20020470.

R. S. Furuya, Y. Kitamura, M. Saito, R. Kawabe, and H. A. Wootten. VLA Observations of H_2O Masers in the Class 0 Protostar S106 FIR : Evidence for a 10 AU Scale Accelerating Jetlike Flow. *ApJ*, 525 :821–831, Nov. 1999. doi : 10.1086/307913.

R. S. Furuya, Y. Kitamura, H. A. Wootten, M. J. Claussen, and R. Kawabe. Water Maser Survey toward Low-Mass Young Stellar Objects in the Northern Sky : Observational Constraints on Maser Excitation Conditions. *ApJ*, 559 :L143–L147, Oct. 2001. doi : 10.1086/324012.

D. Galli and F. H. Shu. Collapse of Magnetized Molecular Cloud Cores. I. Semianalytical Solution. *ApJ*, 417 :220–+, Nov. 1993a. doi : 10.1086/173305.

D. Galli and F. H. Shu. Collapse of Magnetized Molecular Cloud Cores. II. Numerical Results. *ApJ*, 417 :243–+, Nov. 1993b. doi : 10.1086/173306.

G. Garay, D. Mardones, and L. F. Rodríguez. Silicon Monoxide and Methanol Emission from the NGC 2071 Molecular Outflow. *ApJ*, 545 :861–873, Dec. 2000. doi : 10.1086/317853.

R. P. Garden, M. Hayashi, T. Hasegawa, I. Gatley, and N. Kaifu. A spectroscopic study of the DR 21 outflow source. III - The CO line emission. *ApJ*, 374 :540–554, June 1991. doi : 10.1086/170143.

T. A. Gardiner, A. Frank, and L. Hartmann. Stellar Outflows Driven by Magnetized Wide-Angle Winds. *ApJ*, 582 :269–276, Jan. 2003. doi : 10.1086/344609.

T. Giannini, B. Nisini, and D. Lorenzetti. Far-Infrared Investigation of Class 0 Sources : Line Cooling. *ApJ*, 555 :40–57, July 2001. doi : 10.1086/321451.

T. Giannini, C. McCoey, A. Caratti o Garatti, B. Nisini, D. Lorenzetti, and D. R. Flower. On the excitation of the infrared knots along protostellar jets. *A&A*, 419 :999–1014, June 2004. doi : 10.1051/0004-6361 :20040087.

T. Giannini, C. McCoey, B. Nisini, S. Cabrit, A. Caratti o Garatti, L. Calzoletti, and D. R. Flower. Molecular line emission in HH54 : a coherent view from near to far infrared. *A&A*, 459 :821–835, Dec. 2006. doi : 10.1051/0004-6361 :20065127.

C. Giovanardi, S. Lizano, A. Natta, N. J. Evans, II, and C. Heiles. Neutral winds from protostars. *ApJ*, 397 :214–224, Sept. 1992. doi : 10.1086/171780.

J. M. Girart, S. Viti, R. Estalella, and D. A. Williams. The molecular condensations ahead of Herbig-Haro objects. III. Radiative and dynamical perturbations of the HH 2 condensation. *A&A*, 439 :601–612, Aug. 2005. doi : 10.1051/0004-6361 :20041720.

R. Goldflam, S. Green, and K. D.J. Infinite order sudden approximation for rotational energy transfer in gaseous mixtures. *The Journal of Chemical Physics*, 67 :4149–4161, 1977.

P. Goldreich and J. Kwan. Molecular Clouds. *ApJ*, 189 :441–454, May 1974. doi : 10.1086/152821.

M. M. Graff. Fast neutral reactions in cold interstellar clouds. *ApJ*, 339 :239–243, Apr. 1989. doi : 10.1086/167291.

J. S. Greaves, M. Ohishi, and L.-A. Nyman. The abundance of SiO in 'spiral arm' clouds. *A&A*, 307 :898–902, Mar. 1996.

R. Gredel. Quantitative optical and near-infrared spectroscopy of H2 towards HH91A. *A&A*, 474 :941–950, Nov. 2007. doi : 10.1051/0004-6361 :20078260.

S. Green. Collisional excitation of interstellar sulfur monoxide. *ApJ*, 434 :188–191, Oct. 1994. doi : 10.1086/174715.

S. Green and P. Thaddeus. Rotational Excitation of HCN by Collisions. *ApJ*, 191 :653–658, Aug. 1974. doi : 10.1086/153006.

S. Green, S. Maluendes, and A. D. McLean. Improved collisional excitation rates for interstellar water. *ApJS*, 85 :181–185, Mar. 1993. doi : 10.1086/191760.

T. P. Greene, B. A. Wilking, P. Andre, E. T. Young, and C. J. Lada. Further mid-infrared study of the rho Ophiuchi cloud young stellar population : Luminosities and masses of pre-main-sequence stars. *ApJ*, 434 :614–626, Oct. 1994. doi : 10.1086/174763.

A. Grosjean, M.-L. Dubernet, and C. Ceccarelli. Collisional excitation rates of H_2O with H_2. II. Rotational excitation with ortho-H_2 at very low temperature and application to cold molecular clouds. *A&A*, 408 :1197–1203, Sept. 2003. doi : 10.1051/0004-6361 :20030969.

C. Gry, F. Boulanger, E. Falgarone, G. Pineau des Forets, and J. Lequeux. High velocity gas and dust evolution in Chamaeleon clouds. *A&A*, 331 :1070–1077, Mar. 1998.

F. Gueth and S. Guilloteau. The jet-driven molecular outflow of HH 211. *A&A*, 343 :571–584, Mar. 1999.

F. Gueth, S. Guilloteau, and R. Bachiller. SiO shocks in the L1157 molecular outflow. *A&A*, 333 :287–297, May 1998.

F. Gueth, P. Schilke, and M. J. McCaughrean. An interferometric study of the HH 288 molecular outflow. *A&A*, 375 : 1018–1031, Sept. 2001. doi : 10.1051/0004-6361 :20010896.

V. Guillet. *Evolution des Poussieres dans les Chocs.* PhD thesis, Universite Paris XI-Orsay, 2008.

V. Guillet, G. Pineau Des Forêts, and A. P. Jones. Shocks in dense clouds. I. Dust dynamics. *A&A*, 476 :263–277, Dec. 2007. doi : 10.1051/0004-6361 :20078094.

S. Guilloteau, R. Bachiller, A. Fuente, and R. Lucas. First observations of young bipolar outflows with the IRAM interferometer - 2 arcsec resolution SiO images of the molecular jet in L 1448. *A&A*, 265 :L49–L52, Nov. 1992.

E. Gullbring, L. Hartmann, C. Briceno, and N. Calvet. Disk Accretion Rates for T Tauri Stars. *ApJ*, 492 :323–+, Jan. 1998. doi : 10.1086/305032.

A. Gusdorf, S. Cabrit, D. R. Flower, and G. Pineau Des Forêts. SiO line emission from C-type shock waves : interstellar jets and outflows. *A&A*, 482 :809–829, May 2008a. doi : 10.1051/0004-6361 :20078900.

A. Gusdorf, G. Pineau Des Forêts, S. Cabrit, and D. R. Flower. SiO line emission from interstellar jets and outflows : silicon-containing mantles and non-stationary shock waves. *A&A*, 490 :695–706, Nov. 2008b. doi : 10.1051/0004-6361 :200810443.

G. Haro. Herbig's Nebulous Objects Near NGC 1999. *ApJ*, 115 :572–+, May 1952. doi : 10.1086/145576.

P. Hartigan, J. A. Morse, and J. Raymond. Mass-loss rates, ionization fractions, shock velocities, and magnetic fields of stellar jets. *ApJ*, 436 :125–143, Nov. 1994. doi : 10.1086/174887.

P. Hartigan, S. Edwards, and L. Ghandour. Disk Accretion and Mass Loss from Young Stars. *ApJ*, 452 :736–+, Oct. 1995. doi : 10.1086/176344.

P. Hartigan, J. Bally, B. Reipurth, and J. A. Morse. Shock Structures and Momentum Transfer in Herbig-Haro Jets. *Protostars and Planets IV*, pages 841–+, May 2000.

P. Hartigan, S. Edwards, and R. Pierson. Going Slitless : Images of Forbidden-Line Emission Regions of Classical T Tauri Stars Observed with the Hubble Space Telescope. *ApJ*, 609 :261–276, July 2004. doi : 10.1086/386317.

L. Hartmann. On Age Spreads in Star-forming Regions. *AJ*, 121 :1030–1039, Feb. 2001. doi : 10.1086/318770.

L. Hartmann, N. Calvet, and A. Boss. Sheet Models of Protostellar Collapse. *ApJ*, 464 :387–+, June 1996. doi : 10.1086/177330.

F. Heitsch, M.-M. Mac Low, and R. S. Klessen. Gravitational Collapse in Turbulent Molecular Clouds. II. Magnetohydrodynamical Turbulence. *ApJ*, 547 :280–291, Jan. 2001a. doi : 10.1086/318335.

F. Heitsch, E. G. Zweibel, M.-M. Mac Low, P. Li, and M. L. Norman. Magnetic Field Diagnostics Based on Far-Infrared Polarimetry : Tests Using Numerical Simulations. *ApJ*, 561 :800–814, Nov. 2001b. doi : 10.1086/323489.

P. Hennebelle and M. Pérault. Dynamical condensation in a magnetized and thermally bistable flow. Application to interstellar cirrus. *A&A*, 359 :1124–1138, July 2000.

R. N. Henriksen, I. F. Mirabel, and V. S. Ptuskin. Bipolar radio sources in star-forming regions ? *A&A*, 248 :221–226, Aug. 1991.

G. H. Herbig. The Spectra of Two Nebulous Objects Near NGC 1999. *ApJ*, 113 :697–699, May 1951. doi : 10.1086/145440.

E. Herbst, T. J. Millar, S. Wlodek, and D. K. Bohme. The chemistry of silicon in dense interstellar clouds. *A&A*, 222 : 205–210, Sept. 1989.

G. A. Hirth, R. Mundt, and J. Solf. Spatial and kinematic properties of the forbidden emission line region of T Tauri stars. *A&AS*, 126 :437–469, Dec. 1997. doi : 10.1051/aas :1997275.

D. G. Hummer and G. B. Rybicki. A unified treatment of escape probabilities in static and moving media. I - Plane geometry. *ApJ*, 254 :767–779, Mar. 1982. doi : 10.1086/159788.

I. Jiménez-Serra, J. Martín-Pintado, A. Rodríguez-Franco, and N. Marcelino. Tracing the Shock Precursors in the L1448-mm/IRS 3 Outflows. *ApJ*, 603 :L49–L52, Mar. 2004. doi : 10.1086/382784.

I. Jiménez-Serra, J. Martín-Pintado, A. Rodríguez-Franco, and S. Martín. Grain Evolution across the Shocks in the L1448-mm Outflow. *ApJ*, 627 :L121–L124, July 2005. doi : 10.1086/432467.

C. E. Jones, S. Basu, and J. Dubinski. Intrinsic Shapes of Molecular Cloud Cores. *ApJ*, 551 :387–393, Apr. 2001. doi : 10.1086/320093.

P. Kendall and P. C. *Magnetohydrodynamics with Hydrodynamics, vol I.* Pergamon Press, The MacMillan Company, 1964.

S. J. Kenyon and L. Hartmann. Pre-Main-Sequence Evolution in the Taurus-Auriga Molecular Cloud. *ApJS*, 101 :117–+, Nov. 1995. doi : 10.1086/192235.

W.-T. Kim and E. C. Ostriker. Amplification, Saturation, and Q Thresholds for Runaway : Growth of Self-Gravitating Structures in Models of Magnetized Galactic Gas Disks. *ApJ*, 559 :70–95, Sept. 2001. doi : 10.1086/322330.

L. B. G. Knee and G. Sandell. The molecular outflows in NGC 1333. *A&A*, 361 :671–684, Sept. 2000.

A. Kolmogorov. The Local Structure of Turbulence in Incompressible Viscous Fluid for Very Large Reynolds' Numbers. *Akademiia Nauk SSSR Doklady*, 30 :301–305, 1941.

A. Konigl. On the nature of bipolar sources in dense molecular clouds. *ApJ*, 261 :115–134, Oct. 1982. doi : 10.1086/160324.

A. Konigl and R. E. Pudritz. Disk Winds and the Accretion-Outflow Connection. *Protostars and Planets IV*, pages 759–+, May 2000.

L. E. Kristensen, T. L. Ravkilde, G. Pineau Des Forêts, S. Cabrit, D. Field, M. Gustafsson, S. Diana, and J.-L. Lemaire. Observational 2D model of H_2 emission from a bow shock in the Orion Molecular Cloud. *A&A*, 477 :203–211, Jan. 2008. doi : 10.1051/0004-6361 :20078100.

R. Kulsrud and W. P. Pearce. The Effect of Wave-Particle Interactions on the Propagation of Cosmic Rays. *ApJ*, 156 : 445–+, May 1969. doi : 10.1086/149981.

J. Kwan and E. Tademaru. Disk Winds from T Tauri Stars. *ApJ*, 454 :382–+, Nov. 1995. doi : 10.1086/176489.

C. J. Lada and M. Fich. The Structure and Energetics of a Highly Collimated Bipolar Outflow : NGC 2264G. *ApJ*, 459 : 638–+, Mar. 1996. doi : 10.1086/176929.

W. D. Langer and A. E. Glassgold. Silicon chemistry in interstellar clouds. *ApJ*, 352 :123–131, Mar. 1990. doi : 10.1086/168519.

W. D. Langer, E. F. van Dishoeck, E. A. Bergin, G. A. Blake, A. G. G. M. Tielens, T. Velusamy, and D. C. B. Whittet. Chemical Evolution of Protostellar Matter. *Protostars and Planets IV*, pages 29–+, May 2000.

R. B. Larson. Numerical calculations of the dynamics of collapsing proto-star. *MNRAS*, 145 :271–+, 1969.

B. Larsson, R. Liseau, and A. B. Men'shchikov. The ISO-LWS map of the Serpens cloud core. II. The line spectra. *A&A*, 386 :1055–1073, May 2002. doi : 10.1051/0004-6361 :20020168.

B. Larsson, R. Liseau, L. Pagani, P. Bergman, P. Bernath, N. Biver, J. H. Black, R. S. Booth, V. Buat, J. Crovisier, C. L. Curry, M. Dahlgren, P. J. Encrenaz, E. Falgarone, P. A. Feldman, M. Fich, H. G. Florén, M. Fredrixon, U. Frisk, G. F. Gahm, M. Gerin, M. Hagström, J. Harju, T. Hasegawa, Å. Hjalmarson, L. E. B. Johansson, K. Justtanont, A. Klotz, E. Kyrölä, S. Kwok, A. Lecacheux, T. Liljeström, E. J. Llewellyn, S. Lundin, G. Mégie, G. F. Mitchell, D. Murtagh, L. H. Nordh, L.-Å. Nyman, M. Olberg, A. O. H. Olofsson, G. Olofsson, H. Olofsson, G. Persson, R. Plume, H. Rickman, I. Ristorcelli, G. Rydbeck, A. A. Sandqvist, F. V. Schéele, G. Serra, S. Torchinsky, N. F. Tothill, K. Volk, T. Wiklind, C. D. Wilson, A. Winnberg, and G. Witt. Molecular oxygen in the ρ Ophiuchi cloud. *A&A*, 466 :999–1003, May 2007. doi : 10.1051/0004-6361 :20065500.

C. Lavalley, S. Cabrit, C. Dougados, P. Ferruit, and R. Bacon. Sub-arcsecond morphology and kinematics of the DG Tauri jet in the [O I]λ6300 line. *A&A*, 327 :671–680, Nov. 1997.

J. Le Bourlot, G. Pineau des Forêts, and D. R. Flower. The cooling of astrophysical media by H_2. *MNRAS*, 305 :802–810, May 1999. doi : 10.1046/j.1365-8711.1999.02497.x.

J. Le Bourlot, G. Pineau des Forêts, D. R. Flower, and S. Cabrit. New determinations of the critical velocities of C-type shock waves in dense molecular clouds : application to the outflow source in Orion. *MNRAS*, 332 :985–993, June 2002. doi : 10.1046/j.1365-8711.2002.05373.x.

S. D. Le Picard, A. Canosa, G. Pineau des Forêts, C. Rebrion-Rowe, and B. R. Rowe. The $Si(^3_J P)$ + O_2 reaction : A fast source of SiO at very low temperature ; CRESU measurements and interstellar consequences. *A&A*, 372 :1064–1070, June 2001. doi : 10.1051/0004-6361 :20010542.

Y. H. Le Teuff, T. J. Millar, and A. J. Markwick. The UMIST database for astrochemistry 1999. *A&AS*, 146 :157–168, Oct. 2000. doi : 10.1051/aas :2000265.

C.-F. Lee and P. T. P. Ho. Outflow Interaction in the Late Stages of Star Formation. *ApJ*, 624 :841–852, May 2005. doi : 10.1086/429535.

C.-F. Lee, L. G. Mundy, B. Reipurth, E. C. Ostriker, and J. M. Stone. CO Outflows from Young Stars : Confronting the Jet and Wind Models. *ApJ*, 542 :925–945, Oct. 2000. doi : 10.1086/317056.

C.-F. Lee, J. M. Stone, E. C. Ostriker, and L. G. Mundy. Hydrodynamic Simulations of Jet- and Wind-driven Protostellar Outflows. *ApJ*, 557 :429–442, Aug. 2001a. doi : 10.1086/321648.

C. W. Lee, P. C. Myers, and M. Tafalla. A Survey for Infall Motions toward Starless Cores. II. CS (2-1) and N_2H^+ (1-0) Mapping Observations. *ApJS*, 136 :703–734, Oct. 2001b. doi : 10.1086/322534.

B. Lefloch, A. Castets, J. Cernicharo, and L. Loinard. Widespread SiO Emission in NGC 1333. *ApJ*, 504 :L109+, Sept. 1998. doi : 10.1086/311581.

J. Lequeux, F. E., and R. C. *Le milieu interstellaire*. EDP Sciences, CNRS Editions, 2002.

T. Lery. New ideas on jets and outflows interactions. *Ap&SS*, 287 :35–38, 2003. doi : 10.1023/B :ASTR.0000006197.57413.bc.

T. Lery, R. N. Henriksen, and J. D. Fiege. Magnetised protostellar bipolar outflows. I. Self-similar model with Poynting flux. *A&A*, 350 :254–274, Oct. 1999.

T. Lery, R. N. Henriksen, J. D. Fiege, T. P. Ray, A. Frank, and F. Bacciotti. A global jet/circulation model for young stars. *A&A*, 387 :187–200, May 2002. doi : 10.1051/0004-6361 :20020369.

P. Lesaffre, J.-P. Chièze, S. Cabrit, and G. Pineau des Forêts. Temporal evolution of magnetic molecular shocks. I. Moving grid simulations. *A&A*, 427 :147–155, Nov. 2004a. doi : 10.1051/0004-6361 :20035867.

P. Lesaffre, J.-P. Chièze, S. Cabrit, and G. Pineau des Forêts. Temporal evolution of magnetic molecular shocks. II. Analytics of the steady state and semi-analytical construction of intermediate ages. *A&A*, 427 :157–167, Nov. 2004b. doi : 10.1051/0004-6361 :20035873.

M. Lesieur. *Turbulence in Fluids*. Kluwer Publishing, 1997.

A. Li and B. T. Draine. Infrared Emission from Interstellar Dust. II. The Diffuse Interstellar Medium. *ApJ*, 554 :778–802, June 2001. doi : 10.1086/323147.

Z.-Y. Li and F. H. Shu. Magnetized Singular Isothermal Toroids. *ApJ*, 472 :211–+, Nov. 1996. doi : 10.1086/178056.

S. Lizano and F. H. Shu. Molecular cloud cores and bimodal star formation. *ApJ*, 342 :834–854, July 1989. doi : 10.1086/167640.

S. Lizano, C. Heiles, L. F. Rodriguez, B.-C. Koo, F. H. Shu, T. Hasegawa, S. Hayashi, and I. F. Mirabel. Neutral stellar winds that drive bipolar outflows in low-mass protostars. *ApJ*, 328 :763–776, May 1988. doi : 10.1086/166335.

M. Lombardi and G. Bertin. Boyle's law and gravitational instability. *A&A*, 375 :1091–1099, Sept. 2001. doi : 10.1051/0004-6361 :20010857.

L. W. Looney, J. J. Tobin, and W. Kwon. A Flattened Protostellar Envelope in Absorption around L1157. *ApJ*, 670 : L131–L134, Dec. 2007. doi : 10.1086/524361.

M.-M. Mac Low. The Energy Dissipation Rate of Supersonic, Magnetohydrodynamic Turbulence in Molecular Clouds. *ApJ*, 524 :169–178, Oct. 1999. doi : 10.1086/307784.

M.-M. Mac Low and R. S. Klessen. Control of star formation by supersonic turbulence. *Reviews of Modern Physics*, 76 : 125–194, Jan. 2004. doi : 10.1103/RevModPhys.76.125.

M.-M. Mac Low, R. S. Klessen, A. Burkert, and M. D. Smith. Kinetic Energy Decay Rates of Supersonic and Super-Alfvénic Turbulence in Star-Forming Clouds. *Physical Review Letters*, 80 :2754–2757, Mar. 1998. doi : 10.1103/PhysRevLett.80.2754.

M. N. Machida, S.-i. Inutsuka, and T. Matsumoto. Magnetic Fields and Rotations of Protostars. *ApJ*, 670 :1198–1213, Dec. 2007a. doi : 10.1086/521779.

M. N. Machida, S.-i. Inutsuka, and T. Matsumoto. Driving Mechanism of Jets and Outflows in Star Formation Process. *ArXiv e-prints*, May 2007b.

L. Machin and E. Roueff. Rotational Excitation and De-excitation of Interstellar Ammonia in Collisions with Helium. *Journal of Physics B : Atomic, Molecular and Optical Physics*, 38 :1519–1534, 2005.

M.-M. MacLow. *Turbulence and Magnetic Fields in Astrophysics*. Springer, Heidelberg, 2002.

S. Maret, C. Ceccarelli, A. G. G. M. Tielens, E. Caux, B. Lefloch, A. Faure, A. Castets, and D. R. Flower. CH3OH abundance in low mass protostars. *A&A*, 442 :527–538, Nov. 2005. doi : 10.1051/0004-6361 :20052899.

J. Martin-Pintado, R. Bachiller, and A. Fuente. SIO Emission as a Tracer of Shocked Gas in Molecular Outflows. *A&A*, 254 :315–+, Feb. 1992.

H. Masunaga, S. M. Miyama, and S.-I. Inutsuka. A Radiation Hydrodynamic Model for Protostellar Collapse. I. The First Collapse. *ApJ*, 495 :346–+, Mar. 1998. doi : 10.1086/305281.

R. D. Mathieu, A. M. Ghez, E. L. N. Jensen, and M. Simon. Young Binary Stars and Associated Disks. *Protostars and Planets IV*, pages 703–+, May 2000.

J. S. Mathis, W. Rumpl, and K. H. Nordsieck. The size distribution of interstellar grains. *ApJ*, 217 :425–433, Oct. 1977. doi : 10.1086/155591.

S. Matt, A. P. Goodson, R. M. Winglee, and K.-H. Böhm. Simulation-based Investigation of a Model for the Interaction between Stellar Magnetospheres and Circumstellar Accretion Disks. *ApJ*, 574 :232–245, July 2002. doi : 10.1086/340896.

C. D. Matzner and C. F. McKee. Efficiencies of Low-Mass Star and Star Cluster Formation. *ApJ*, 545 :364–378, Dec. 2000. doi : 10.1086/317785.

C. D. Matzner and C. F. McKee. Bipolar Molecular Outflows Driven by Hydromagnetic Protostellar Winds. *ApJ*, 526 : L109–L112, Dec. 1999. doi : 10.1086/312376.

P. W. May, G. Pineau des Forêts, D. R. Flower, D. Field, N. L. Allan, and J. A. Purton. Sputtering of grains in C-type shocks. *MNRAS*, 318 :809–816, Nov. 2000. doi : 10.1046/j.1365-8711.2000.03796.x.

M. J. McCaughrean, J. T. Rayner, and H. Zinnecker. Discovery of a molecular hydrogen jet near IC 348. *ApJ*, 436 : L189–L192, Dec. 1994. doi : 10.1086/187664.

C. F. McKee, E. G. Zweibel, A. A. Goodman, and C. Heiles. Magnetic Fields in Star-Forming Regions - Theory. In E. H. Levy and J. I. Lunine, editors, *Protostars and Planets III*, pages 327–+, 1993.

F. Ménard and G. Duchêne. On the alignment of Classical T Tauri stars with the magnetic field in the Taurus-Auriga molecular cloud. *A&A*, 425 :973–980, Oct. 2004. doi : 10.1051/0004-6361 :20041338.

M. Micono, S. Massaglia, G. Bodo, P. Rossi, and A. Ferrari. Kelvin-Helmholtz instabilities in stellar jets. IV. On the origin of the emission knots. *A&A*, 333 :1001–1006, May 1998.

M. Micono, G. Bodo, S. Massaglia, P. Rossi, and A. Ferrari. On the matter entrainment by stellar jets and the acceleration of molecular outflows. *A&A*, 364 :318–326, Dec. 2000.

S. Mielke, B. Garrett, and K. Peterson. A Hierarchical Family of Global Analytic Born-Oppenheimer Potential Energy Surfaces for the H + H_2 Reaction Ranging in Quality from Double-Zeta to the Complete Basis Set Limit. *Journal of Chemical Physics*, 116 :4142–4161, 2002.

M.-A. Miville-Deschenes, G. Joncas, and D. Durand. The H II Region Sharpless 170 : a Multiscale Analysis of the H alpha Velocity Field. *ApJ*, 454 :316–326, 1995.

K. Motoyama and T. Yoshida. High accretion rate during class 0 phase due to external trigger. *MNRAS*, 344 :461–467, Sept. 2003. doi : 10.1046/j.1365-8711.2003.06833.x.

T. C. Mouschovias. Magnetic braking, ambipolar diffusion, cloud cores, and star formation - Natural length scales and protostellar masses. *ApJ*, 373 :169–186, May 1991. doi : 10.1086/170035.

T. C. Mouschovias and S. A. Morton. Ambipolar diffusion, cloud cores, and star formation : Two-dimensional, cylindrically symmetric contraction. I - The issues, formulation of the problem, and method of solution. *ApJ*, 371 :296–316, Apr. 1991. doi : 10.1086/169893.

T. C. Mouschovias and E. V. Paleologou. Magnetic braking of an aligned rotator during star formation - an exact, time-dependent solution. *ApJ*, 237 :877–899, May 1980. doi : 10.1086/157936.

R. Mundt and J. W. Fried. Jets from young stars. *ApJ*, 274 :L83–L86, Nov. 1983. doi : 10.1086/184155.

L. G. Mundy, L. W. Looney, and W. J. Welch. The Structure and Evolution of Envelopes and Disks in Young Stellar Systems. *Protostars and Planets IV*, pages 355–+, May 2000.

P. C. Myers and P. J. Benson. Dense Cores in Dark Clouds - Part Two - NH3 Observations and Star Formation. *Revista Mexicana de Astronomia y Astrofisica, vol. 7*, 7 :238–+, Aug. 1983.

P. C. Myers and E. F. Ladd. Bolometric temperatures of young stellar objects. *ApJ*, 413 :L47–L50, Aug. 1993. doi : 10.1086/186956.

T. Nakano. Star Formation in Magnetic Clouds. *ApJ*, 494 :587–+, Feb. 1998. doi : 10.1086/305230.

A. Natta, C. Giovanardi, F. Palla, and N. J. Evans, II. Neutral winds from cool young stars - A solution to the line deficit problem. *ApJ*, 327 :817–821, Apr. 1988. doi : 10.1086/166239.

D. A. Neufeld and M. J. Kaufman. Radiative Cooling of Warm Molecular Gas. *ApJ*, 418 :263–+, Nov. 1993. doi : 10.1086/173388.

B. Nisini, M. Benedettini, T. Giannini, C. Codella, D. Lorenzetti, A. M. di Giorgio, and J. S. Richer. Far infrared mapping of the gas cooling along the L1448 outflow. *A&A*, 360 :297–310, Aug. 2000.

B. Nisini, C. Codella, T. Giannini, R. Bachiller, J. Santiago Garcia, and J. S. Richer. Physical conditions of molecular bullets along protostellar outflows probed through high-J SiO emission. In A. Wilson, editor, *ESA Special Publication*, volume 577 of *ESA Special Publication*, pages 397–398, Jan. 2005.

B. Nisini, C. Codella, T. Giannini, J. Santiago Garcia, J. S. Richer, R. Bachiller, and M. Tafalla. Warm SiO gas in molecular bullets associated with protostellar outflows. *A&A*, 462 :163–172, Jan. 2007. doi : 10.1051/0004-6361 :20065621.

A. R. Offer and E. F. van Dishoeck. Rotational excitation of interstellar OH by para- and ortho-H2. *MNRAS*, 257 :377–390, Aug. 1992.

S. Ogino, K. Tomisaka, and F. Nakamura. Gravitational Collapse of Spherical Interstellar Clouds. *PASJ*, 51 :637–+, Oct. 1999.

D. E. Osterbrock. Two Dense Nebulae. *PASP*, 70 :399–+, Aug. 1958. doi : 10.1086/127245.

D. E. Osterbrock. *Astrophysics of gaseous nebulae and active galactic nuclei.* Research supported by the University of California, John Simon Guggenheim Memorial Foundation, University of Minnesota, et al. Mill Valley, CA, University Science Books, 1989, 422 p., 1989.

L. Pagani, A. O. H. Olofsson, P. Bergman, P. Bernath, J. H. Black, R. S. Booth, V. Buat, J. Crovisier, C. L. Curry, P. J. Encrenaz, E. Falgarone, P. A. Feldman, M. Fich, H. G. Floren, U. Frisk, M. Gerin, E. M. Gregersen, J. Harju, T. Hasegawa, Å. Hjalmarson, L. E. B. Johansson, S. Kwok, B. Larsson, A. Lecacheux, T. Liljeström, M. Lindqvist, R. Liseau, K. Mattila, G. F. Mitchell, L. H. Nordh, M. Olberg, G. Olofsson, I. Ristorcelli, A. Sandqvist, F. von Scheele, G. Serra, N. F. Tothill, K. Volk, T. Wiklind, and C. D. Wilson. Low upper limits on the O_2 abundance from the Odin satellite. *A&A*, 402 :L77–L81, May 2003. doi : 10.1051/0004-6361 :20030344.

F. Palla and S. W. Stahler. Star Formation in Space and Time : Taurus-Auriga. *ApJ*, 581 :1194–1203, Dec. 2002. doi : 10.1086/344293.

N. Panagia. Ionized Winds From Young Stellar Objects. In C. J. Lada and N. D. Kylafis, editors, *NATO ASIC Proc. 342 : The Physics of Star Formation and Early Stellar Evolution*, pages 565–+, 1991.

T. R. Phillips, S. Maluendes, and S. Green. Collisional Excitation of H 2O by H 2 Molecules. *ApJS*, 107 :467–+, Nov. 1996. doi : 10.1086/192372.

G. Pineau des Forets, E. Roueff, P. Schilke, and D. R. Flower. Sulphur-bearing molecules as tracers of shocks in interstellar clouds. *MNRAS*, 262 :915–928, June 1993.

G. Pineau des Forets, D. R. Flower, and J.-P. Chieze. The physical and chemical effects of C-shocks in molecular outflows. In B. Reipurth and C. Bertout, editors, *Herbig-Haro Flows and the Birth of Stars*, volume 182 of *IAU Symposium*, pages 199–212, 1997.

R. E. Pudritz and R. Banerjee. The disc-jet connection. In R. Cesaroni, M. Felli, E. Churchwell, and M. Walmsley, editors, *Massive Star Birth : A Crossroads of Astrophysics*, volume 227 of *IAU Symposium*, pages 163–173, 2005. doi : 10.1017/S1743921305004497.

A. Raga and S. Cabrit. Molecular outflows entrained by jet bowshocks. *A&A*, 278 :267–278, Oct. 1993.

A. Raga, S. Cabrit, C. Dougados, and C. Lavalley. A precessing, variable velocity jet model for DG Tauri. *A&A*, 367 : 959–966, Mar. 2001. doi : 10.1051/0004-6361 :20000415.

A. C. Raga and J. Canto. The steady structure of a jet/cloud interaction - II. The case of a spherically symmetric stratification. *MNRAS*, 280 :567–571, May 1996.

A. C. Raga and L. Kofman. Knots in stellar jets from time-dependent sources. *ApJ*, 386 :222–228, Feb. 1992. doi : 10.1086/171008.

A. C. Raga, S. Cabrit, and J. Canto. Mixing layers in stellar outflows-II. Interfaces between two moving fluids. *MNRAS*, 273 :422–430, Mar. 1995.

R. J. Rand and S. R. Kulkarni. The local Galactic magnetic field. *ApJ*, 343 :760–772, Aug. 1989. doi : 10.1086/167747.

R. J. Rand and A. G. Lyne. New Rotation Measures of Distant Pulsars in the Inner Galaxy and Magnetic Field Reversals. *MNRAS*, 268 :497–+, May 1994.

J. M. C. Rawlings, M. P. Redman, E. Keto, and D. A. Williams. HCO^+ emission excess in bipolar outflows. *MNRAS*, 351 : 1054–1062, July 2004. doi : 10.1111/j.1365-2966.2004.07855.x.

T. Ray, C. Dougados, F. Bacciotti, J. Eislöffel, and A. Chrysostomou. Toward Resolving the Outflow Engine : An Observational Perspective. In B. Reipurth, D. Jewitt, and K. Keil, editors, *Protostars and Planets V*, pages 231–244, 2007.

B. Reipurth and J. Bally. Herbig-Haro Flows : Probes of Early Stellar Evolution. *ARA&A*, 39 :403–455, 2001. doi : 10.1146/annurev.astro.39.1.403.

B. Reipurth and C. Bertout, editors. *Herbig-Haro Flows and the Birth of Stars ; IAU Symposium No. 182*, volume 182 of *IAU Symposium*, 1997.

B. Reipurth, J. Bally, and D. Devine. Giant Herbig-Haro Flows. *AJ*, 114 :2708–+, Dec. 1997. doi : 10.1086/118681.

S. P. Reynolds. Continuum spectra of collimated, ionized stellar winds. *ApJ*, 304 :713–720, May 1986. doi : 10.1086/164209.

J. S. Richer, R. E. Hills, and R. Padman. A fast CO jet in Orion B. *MNRAS*, 254 :525–538, Feb. 1992.

J. S. Richer, D. S. Shepherd, S. Cabrit, R. Bachiller, and E. Churchwell. Molecular Outflows from Young Stellar Objects. *Protostars and Planets IV*, pages 867–+, May 2000.

G. H. Rieke and M. J. Lebofsky. The interstellar extinction law from 1 to 13 microns. *ApJ*, 288 :618–621, Jan. 1985. doi : 10.1086/162827.

L. F. Rodriguez. Subarcsecond Observations of Radio Continuum from Jets and Disks. In S. Lizano and J. M. Torrelles, editors, *Revista Mexicana de Astronomia y Astrofisica Conference Series*, volume 1 of *Revista Mexicana de Astronomia y Astrofisica Conference Series*, pages 1–+, Apr. 1995.

L. F. Rodriguez, G. Anglada, and A. Raga. Radio Continuum Detection of the Exciting Sources of the DG Tauri B and L1551NE Outflows. *ApJ*, 454 :L149+, Dec. 1995. doi : 10.1086/309797.

L. F. Rodríguez, B. Reipurth, A. C. Raga, and J. Cantó. VLA Detection of the Exciting Source of the "Deflected" HH 270/110 System. *Revista Mexicana de Astronomia y Astrofisica*, 34 :69–72, Oct. 1998.

A. Rosen and M. D. Smith. Numerical simulations of highly collimated protostellar outflows. The effects of relative density. *A&A*, 413 :593–607, Jan. 2004. doi : 10.1051/0004-6361 :20031566.

A. Rudolph and W. J. Welch. Evidence for a wind-swept cavity in HH 34 ? *ApJ*, 395 :488–493, Aug. 1992. doi : 10.1086/171669.

A. P. G. Russell, J. Bally, R. Padman, and R. E. Hills. Atomic and molecular outflow in DR 21. *ApJ*, 387 :219–228, Mar. 1992. doi : 10.1086/171073.

G. B. Rybicki and D. G. Hummer. An accelerated lambda iteration method for multilevel radiative transfer. I - Non-overlapping lines with background continuum. *A&A*, 245 :171–181, May 1991.

B. S. Ryden. The Shapes of Dense Cores and BOK Globules. *ApJ*, 471 :822–+, Nov. 1996. doi : 10.1086/178010.

P. Schilke, C. M. Walmsley, G. Pineau des Forets, and D. R. Flower. SiO production in interstellar shocks. *A&A*, 321 : 293–304, May 1997.

P. Schilke, G. Pineau des Forêts, C. M. Walmsley, and J. Martín-Pintado. Observations of SiO towards photon dominated regions. *A&A*, 372 :291–301, June 2001. doi : 10.1051/0004-6361 :20010470.

F. Schmitz. The effect of a poloidal magnetic field on the stability of a rotating self-gravitating disc. *A&A*, 179 :167–170, June 1987.

F. Schmitz. Equilibrium structures of differentially rotating self-gravitating gases. *A&A*, 200 :127–134, July 1988.

F. L. Schöier, F. F. S. van der Tak, E. F. van Dishoeck, and J. H. Black. An atomic and molecular database for analysis of submillimetre line observations. *A&A*, 432 :369–379, Mar. 2005. doi : 10.1051/0004-6361 :20041729.

R. D. Schwartz. T Tauri Nebulae and Herbig-Haro Nebulae - Evidence for excitation by a strong stellar wind. *ApJ*, 195 : 631–642, Feb. 1975. doi : 10.1086/153364.

D. Shepherd. The Energetics of Outflow and Infall from Low to High Mass YSOs (Invited Review). In J. M. De Buizer and N. S. van der Bliek, editors, *Galactic Star Formation Across the Stellar Mass Spectrum*, volume 287 of *Astronomical Society of the Pacific Conference Series*, pages 333–344, 2003.

D. Shepherd. Massive star outflows. In R. Cesaroni, M. Felli, E. Churchwell, and M. Walmsley, editors, *Massive Star Birth : A Crossroads of Astrophysics*, volume 227 of *IAU Symposium*, pages 237–246, 2005. doi : 10.1017/S174392130500459X.

D. S. Shepherd, K. C. Yu, J. Bally, and L. Testi. The Molecular Outflow and Possible Precessing Jet from the Massive Young Stellar Object IRAS 20126+4104. *ApJ*, 535 :833–846, June 2000. doi : 10.1086/308873.

F. H. Shu. Self-similar collapse of isothermal spheres and star formation. *ApJ*, 214 :488–497, June 1977. doi : 10.1086/155274.

F. H. Shu, F. C. Adams, and S. Lizano. Star formation in molecular clouds - Observation and theory. *ARA&A*, 25 :23–81, 1987. doi : 10.1146/annurev.aa.25.090187.000323.

F. H. Shu, S. P. Ruden, C. J. Lada, and S. Lizano. Star formation and the nature of bipolar outflows. *ApJ*, 370 :L31–L34, Mar. 1991. doi : 10.1086/185970.

F. H. Shu, A. Allen, H. Shang, E. C. Ostriker, and Z.-Y. Li. Low-Mass Star Formation : Theory. In C. J. Lada and N. D. Kylafis, editors, *NATO ASIC Proc. 540 : The Origin of Stars and Planetary Systems*, pages 193–+, 1999.

M. D. Smith and A. Rosen. The instability of fast shocks in molecular clouds. *MNRAS*, 339 :133–147, Feb. 2003. doi : 10.1046/j.1365-8711.2003.06155.x.

R. L. Snell, R. B. Loren, and R. L. Plambeck. Observations of CO in L1551 - Evidence for stellar wind driven shocks. *ApJ*, 239 :L17–L22, July 1980. doi : 10.1086/183283.

R. L. Snell, D. Hollenbach, J. E. Howe, D. A. Neufeld, M. J. Kaufman, G. J. Melnick, E. A. Bergin, and Z. Wang. Detection of Water in the Shocked Gas Associated with IC 443 : Constraints on Shock Models. *ApJ*, 620 :758–773, Feb. 2005. doi : 10.1086/427231.

U. J. Sofia, B. D. Savage, and J. A. Cardelli. High-resolution ultra-violet observations of the interstellar diffuse clouds toward MU Columbae. *ApJ*, 413 :251–267, Aug. 1993. doi : 10.1086/172993.

J. Solf. Spectroscopic Signatures of Microjets. In B. Reipurth and C. Bertout, editors, *Herbig-Haro Flows and the Birth of Stars*, volume 182 of *IAU Symposium*, pages 63–72, 1997.

P. K. Sollins, T. R. Hunter, J. Battat, H. Beuther, P. T. P. Ho, J. Lim, S. Y. Liu, N. Ohashi, T. K. Sridharan, Y. N. Su, J.-H. Zhao, and Q. Zhang. Mapping the Outflow from G5.89-0.39 in SiO J = 5 - 4. *ApJ*, 616 :L35–L38, Nov. 2004. doi : 10.1086/421294.

P. M. Solomon, A. R. Rivolo, J. Barrett, and A. Yahil. Mass, luminosity, and line width relations of Galactic molecular clouds. *ApJ*, 319 :730–741, Aug. 1987. doi : 10.1086/165493.

S. W. Stahler. Deuterium and the stellar birthline. *ApJ*, 332 :804–825, Sept. 1988. doi : 10.1086/166694.

S. W. Stahler, D. G. Korycansky, M. J. Brothers, and J. Touma. The early evolution of protostellar disks. *ApJ*, 431 : 341–358, Aug. 1994. doi : 10.1086/174489.

T. Stanke, M. J. McCaughrean, and H. Zinnecker. Giant protostellar outflows revealed by infrared imaging. *A&A*, 355 : 639–650, Mar. 2000.

J. M. Stone, E. C. Ostriker, and C. F. Gammie. Dissipation in Compressible Magnetohydrodynamic Turbulence. *ApJ*, 508 : L99–L102, Nov. 1998. doi : 10.1086/311718.

J. Surdej. Contribution to spectral line formation in moving stellar envelopes - Radiation field and statistical equilibrium equations. *A&A*, 60 :303–311, Sept. 1977.

M. Tafalla and P. C. Myers. Velocity Shifts in L1228 : The Disruption of a Core by an Outflow. *ApJ*, 491 :653–+, Dec. 1997. doi : 10.1086/304968.

S. Terebey, F. H. Shu, and P. Cassen. The collapse of the cores of slowly rotating isothermal clouds. *ApJ*, 286 :529–551, Nov. 1984. doi : 10.1086/162628.

T. H. Troland and C. Heiles. Interstellar magnetic field strengths and gas densities Observational and theoretical perspectives. *ApJ*, 301 :339–345, Feb. 1986. doi : 10.1086/163904.

B. E. Turner. The Physics and Chemistry of Small Translucent Molecular Clouds. X. SiO. *ApJ*, 495 :804–+, Mar. 1998. doi : 10.1086/305319.

B. E. Turner, K.-W. Chan, S. Green, and D. A. Lubowich. Tests of shock chemistry in IC 443G. *ApJ*, 399 :114–133, Nov. 1992. doi : 10.1086/171908.

F. F. S. van der Tak, A. M. S. Boonman, R. Braakman, and E. F. van Dishoeck. Sulphur chemistry in the envelopes of massive young stars. *A&A*, 412 :133–145, Dec. 2003. doi : 10.1051/0004-6361 :20031409.

E. F. van Dishoeck and G. A. Blake. Chemical Evolution of Star-Forming Regions. *ARA&A*, 36 :317–368, 1998. doi : 10.1146/annurev.astro.36.1.317.

E. F. van Dishoeck, D. J. Jansen, and T. G. Phillips. Submillimeter observations of the shocked molecular gas associated with the supernova remnant IC 443. *A&A*, 279 :541–566, Nov. 1993.

E. F. van Dishoek, G. A. Blake, B. T. Draine, and J. I. Lunine. The chemical evolution of protostellar and protoplanetary matter. In E. H. Levy and J. I. Lunine, editors, *Protostars and Planets III*, pages 163–241, 1993.

E. Vázquez-Semadeni, A. Gazol, and J. Scalo. Is Thermal Instability Significant in Turbulent Galactic Gas ? *ApJ*, 540 : 271–285, Sept. 2000. doi : 10.1086/309318.

T. Velusamy and W. D. Langer. Outflow-infall interactions as a mechanism for terminating accretion in protostars. *Nature*, 392 :685–687, Apr. 1998. doi : 10.1038/33624.

S. Viti and D. A. Williams. Chemical evolution ahead of Herbig-Haro objects. *MNRAS*, 310 :517–526, Dec. 1999. doi : 10.1046/j.1365-8711.1999.02962.x.

S. Viti, C. Codella, M. Benedettini, and R. Bachiller. The origin and structure of clumps along molecular outflows : the test case of CB3. *MNRAS*, 350 :1029–1037, May 2004. doi : 10.1111/j.1365-2966.2004.07722.x.

V. Wakelam, P. Caselli, C. Ceccarelli, E. Herbst, and A. Castets. Resetting chemical clocks of hot cores based on S-bearing molecules. *A&A*, 422 :159–169, July 2004. doi : 10.1051/0004-6361 :20047186.

V. Wakelam, C. Ceccarelli, A. Castets, B. Lefloch, L. Loinard, A. Faure, N. Schneider, and J.-J. Benayoun. Sulphur chemistry and molecular shocks : The case of NGC 1333-IRAS 2. *A&A*, 437 :149–158, July 2005. doi : 10.1051/0004-6361 :20042566.

C. M. Walmsley, G. Pineau des Forêts, and D. R. Flower. Silicon chemistry in PDRs. *A&A*, 342 :542–550, Feb. 1999.

D. Ward-Thompson, P. F. Scott, R. E. Hills, and P. Andre. A Submillimetre Continuum Survey of Pre Protostellar Cores. *MNRAS*, 268 :276–+, May 1994.

D. Ward-Thompson, F. Motte, and P. Andre. The initial conditions of isolated star formation - III. Millimetre continuum mapping of pre-stellar cores. *MNRAS*, 305 :143–150, May 1999. doi : 10.1046/j.1365-8711.1999.02412.x.

D. Ward-Thompson, P. André, and J. M. Kirk. The initial conditions of isolated star formation - V. ISOPHOT imaging and the temperature and energy balance of pre-stellar cores. *MNRAS*, 329 :257–276, Jan. 2002. doi : 10.1046/j.1365-8711.2002.04969.x.

J. C. Weingartner and B. T. Draine. Photoelectric Emission from Interstellar Dust : Grain Charging and Gas Heating. *ApJS*, 134 :263–281, June 2001. doi : 10.1086/320852.

A. P. Whitworth, A. S. Bhattal, N. Francis, and S. J. Watkins. Star formation and the singular isothermal sphere. *MNRAS*, 283 :1061–1070, Dec. 1996.

D. Wilgenbus, S. Cabrit, G. Pineau des Forêts, and D. R. Flower. The ortho :para-H_2 ratio in C- and J-type shocks. *A&A*, 356 :1010–1022, Apr. 2000.

J. P. Williams, L. Blitz, and C. F. McKee. The Structure and Evolution of Molecular Clouds : from Clumps to Cores to the IMF. *Protostars and Planets IV*, pages 97–+, May 2000.

R. W. Wilson, A. A. Penzias, K. B. Jefferts, M. Kutner, and P. Thaddeus. Discovery of Interstellar Silicon Monoxide. *ApJ*, 167 :L97+, Aug. 1971. doi : 10.1086/180769.

J. Woitas, T. P. Ray, F. Bacciotti, C. J. Davis, and J. Eislöffel. Hubble Space Telescope Space Telescope Imaging Spectrograph Observations of the Bipolar Jet from RW Aurigae : Tracing Outflow Asymmetries Close to the Source. *ApJ*, 580 : 336–342, Nov. 2002. doi : 10.1086/343124.

M. G. Wolfire, D. Hollenbach, C. F. McKee, A. G. G. M. Tielens, and E. L. O. Bakes. The neutral atomic phases of the interstellar medium. *ApJ*, 443 :152–168, Apr. 1995. doi : 10.1086/175510.

S. A. Wrathmall, A. Gusdorf, and D. R. Flower. The excitation of molecular hydrogen by atomic hydrogen in astrophysical media. *MNRAS*, 382 :133–138, Nov. 2007. doi : 10.1111/j.1365-2966.2007.12420.x.

T. Xie, M. Allen, and W. D. Langer. Turbulent Diffusion and Its Effects on the Chemistry of Molecular Clouds. *ApJ*, 440 : 674–+, Feb. 1995. doi : 10.1086/175305.

H. W. Yorke and C. Sonnhalter. On the Formation of Massive Stars. *ApJ*, 569 :846–862, Apr. 2002. doi : 10.1086/339264.

K. C. Yu, Y. Billawala, and J. Bally. Parsec-Scale CO Outflow and H_2 Jets in Barnard 5. *AJ*, 118 :2940–2961, Dec. 1999. doi : 10.1086/301123.

M. R. Zachariah and W. Tsang. Theoretical Calculation of Thermochemistry, Energetics, and Kinetics of High-Temperature $Si_xH_yO_z$ Reactions. *Journal of Physical Chemistry*, 99 :5308–5318, 1995.

Q. Zhang, P. T. P. Ho, M. C. H. Wright, and D. J. Wilner. Emission in a Jetlike Molecular Outflow toward L1157. *ApJ*, 451 :L71+, Oct. 1995. doi : 10.1086/309690.

Q. Zhang, T. R. Hunter, J. Brand, T. K. Sridharan, R. Cesaroni, S. Molinari, J. Wang, and M. Kramer. Search for CO Outflows toward a Sample of 69 High-Mass Protostellar Candidates. II. Outflow Properties. *ApJ*, 625 :864–882, June 2005. doi : 10.1086/429660.

L. M. Ziurys, P. Friberg, and W. M. Irvine. Interstellar SiO as a tracer of high-temperature chemistry. *ApJ*, 343 :201–207, Aug. 1989. doi : 10.1086/167696.